PMM/A-227

COMISION NACIONAL DE ENERGIA ATOMICA
DEPENDIENTE DE LA PRESIDENCIA DE LA NACION

PROGRAMA MULTINACIONAL DE METALURGIA
(Programa Regional de Desarrollo Científico y Tecnológico-OEA)

GENERAL THEORY OF PASSIVITY

Dr. Norio Sato

Tercer Seminario Latinoamericano en el Nivel de Postdoctorado

Tema: CORROSION

Buenos Aires - Argentina
1977

PMM/A-227

COMISION NACIONAL DE ENERGIA ATOMICA
DEPENDIENTE DE LA PRESIDENCIA DE LA NACION

PROGRAMA MULTINACIONAL DE METALURGIA
(Programa Regional de Desarrollo Científico y Tecnológico-OEA)

GENERAL THEORY OF PASSIVITY

Dr. Norio Sato

Tercer Seminario Latinoamericano en el Nivel de Postdoctorado

Tema: CORROSION

Buenos Aires - Argentina
1977

C O N T E N T S

FIGURES

1. INTRODUCTION TO METAL PASSIVITY

1.1. Iron Passivation in Nitric Acid

Iron corrodes vigorously in dilute nitric acid, but its corrosion virtually stops in concentrated nitric acid (Fig. 1-1). It was as early as 1790 that iron was found to become chemically inert or passive when immersed in concentrated nitric acid.

Faraday noted in 1836 "the surface is oxidized to form a superficial film of oxide so thin as not to be sensible but enough to prevent corrosion of iron". An alternative explanation was that the iron is transformed into an inert allotropic modification when it becomes passive and hence behaves as a noble metal.

(1) The oxide film theory

(2) The allotropy theory

Other metals also passivate in nitric acid of 90 wt% HNO_3 for Fe below 75°C, Co below 10°C, Ni below 30°C, Cu below 30°C. Zn and Hg were not rendered passive at -11°C.

1.2. Anodic Passivation of Iron

When iron is made an anode in H_2SO_4 by using an electrolytic cell with a counter electrode (Fig. 1-2), iron becomes passive at anodic bias voltages larger than a critical voltage (Fig. 1-3).

The device that applies an anodic bias voltage to an iron electrode with respect to a standard reference electrode is an electrochemical polarization cell in which a

bias voltage controlling unit is included. Commercial devices called the potentiostat are available which will hold a test electrode at any prechosen potential. The potentiostat circuitry consists of a low voltage d.c. source and extremely low impedance circuit, while the galvanostat circuitry contains a high voltage d.c. source and high impedance circuit.

1.3. Electrochemical Reaction on Metal Electrodes

When a metal is immersed in an electrolyte solution, there are two directions in which an electro-chemical reaction can proceed on the metal surface.

a) Anodic, electron-donating reaction, involving loss of electrons, which is chemical oxidation by definition.

$$A \rightarrow A^{m+} + me \quad ; \text{ ionization of A atom} \qquad (1.1)$$

$$B^{n-} \rightarrow B + ne \quad ; \text{ discharge of } B^{n-} \text{ ion} \qquad (1.2)$$

b) Cathodic, electron-accepting reaction, involving gain of electrons, which is chemical reduction by definition.

$$X^{p+} + pe \rightarrow X \quad ; \text{ discharge of } X^{p+} \text{ ion} \qquad (1.3)$$

$$Y + qe \rightarrow Y^{q-} \quad ; \text{ ionization of Y atom} \qquad (1.4)$$

The rate of anodic and cathodic reactions is a function

of electrode potential of the metal (bias voltage with respect to a reference electrode). The anodic reaction rate increases with increasing potential and conversely the cathodic reaction rate increases with decreasing potential. Both rates are non-ohmic and hence the potential-reaction rate relationship is not linear (Fig. 1-4).

1.4. Oxidation-Reduction Balance on a Corroding Metal

When a metal is corroding spontaneously in acid solution, anodic oxidation and cathodic reduction take place simultaneously;

Anodic oxidation

$$Fe \rightarrow Fe^{2+} + 2e \qquad (1.5)$$

Cathodic reduction

$$2H^{+} + 2e \rightarrow H_2 \qquad (1.6)$$

The electron donation rate in the oxidation must be exactly equal to the rate of electron acceptance in the reduction under steady state conditions. On a plott of E - j curves for both anodic oxidation and cathodic reduction, this oxidation-reduction balance occurs at a particular potential, which is often denoted by E_{corr}. This is the rest potential, corrosion potential, or spontaneous potential of a corroding metal. It is this potential that we measure with a spontaneously corroding metal by use of a reference electrode and high impedance voltometer (Fig. 1-5).

1.5. Corrosion-Balancing Reactions

The hydrogen evolution reaction which balances the

anodic metal dissolution reaction tends to be dominant in acidic solution because of the high level of availability of hydrogen ions, but it becomes more difficult as the hydrogen ion concentration decreases.

$$2H^+ + 2e \rightarrow H_2 \qquad (1.7)$$

The most important alternative reaction of accepting and consuming electrons produced by metal dissolution is the oxygen reaction (Fig. 1-5).

$$\frac{1}{2}O_2 + H_2O + 2e \rightarrow 2OH^- \qquad (1.8)$$

or

$$\frac{1}{2}O_2 + 2H^+ + 2e \rightarrow 2H_2O \qquad (1.9)$$

There are many other more or less complicated reduction reactions capable of sustaining a corrosion reaction. One of them is the reduction of nitric acid HNO_3 to nitrous acid HNO_2 ; (Fig. 1-5).

$$NO_3^- + 3H^+ + 2e \rightarrow HNO_2 + H_2O \qquad (1.10)$$

$$E^o = + 0.935V$$

$$NO_3^- + H_2O + 2e \rightarrow NO_2^- + 2OH^- \qquad (1.11)$$

$$E^o = + 0.01V$$

The reaction mechanism in acid solution is

$$H^+ + HNO_2 \rightarrow H_2O + NO^+ \qquad \text{slow} \qquad (1.12)$$

$$NO^+ + NO_3^- \rightleftharpoons N_2O_4 \qquad \text{fast} \qquad (1.13)$$

$$N_2O_4 \rightleftharpoons 2NO_2 \qquad \text{fast} \qquad (1.14)$$

$$2(H^+ + NO_2 + e \rightarrow HNO_2) \qquad \text{slow} \qquad (1.15)$$

The reaction rate is catalysed by HNO_2 and hence increases with increasing concentration of HNO_2.

1.6. Anodic Passivation and Spontaneous Passivation

Suppose that a passivable metal is studied in three different aqueous solutions in which the rate of corrosion-balancing reactions is characterised by cathodic reduction curve 1, 2, or 3 (Fig. 1-6), then the balancing condition of anodic and cathodic reactions appears in different states. The solution 1 allows a balance only at $E_{corr,1}$ and will always produce passivity under steady state conditions. The solution 3 also allows a single balance point at $E_{corr.3}$ in the active potential region. The "in between" solution 2 allows two possible balance potentials $E_{corr.2}$ and $E'_{corr.2}$. Then if the metal is already passive when immersed in solution 2, the corrosion-balancing reduction reaction will be capable of maintaining passivity by balancing the comparatively slow dissolution of the passive metal at $E_{corr.2}$. But if the metal is not initially passive and enters the solution in the active state it will corrode at $E_{corr.2}$.

It is noted that concentrated HNO_3 readily passivates iron, that dilute HNO_3 causes fairly rapid corrosion of iron, and that moderately concentrated HNO_3 is capable of maintaining passivity but not capable of producing passivity of iron (Fig. 1-7).

Spontaneous passivation of nickel in aerated sulphate solutions is illustrated to occur in neutral and alkaline pH ranges (Fig. 1-8). In this system the anodic metal dissolution $Ni \rightarrow Ni^{2+} + 2e$ balances the cathodic oxygen reduction $1/2\ O_2 + 2H^+ + 2e \rightarrow H_2O$ or $1/2\ O_2 + H_2O + 2e \rightarrow 2OH^-$.

1.7. Thermodynamic Stability of H_2O, H^+ and O_2 in Aqueous Solution

In aqueous solutions water is stable in the potential range between the hydrogen electrode potential $E^o(H)$ and the oxygen electrode potential $E^o(O)$

$$2H^+ + 2e \rightleftharpoons H_2 \qquad (1.16)$$

$$E^o(H) = 0 - 0.059\ pH \quad Volt$$

$$\frac{1}{2}O_2 + 2H^+ + 2e \rightleftharpoons 2H_2O \qquad (1.17)$$

$$E^o(O) = + 1.18 - 0.059\ pH \quad Volt$$

Above $E^o(O)$ water is oxidized to oxygen gas and below $E^o(H)$ water is reduced to hydrogen gas (Fig. 1-9).

In the potential-pH diagram there are the hydrogen ion reduction region (I), the oxygen gas reduction region (I)-(II), and the region (III) where water is oxidized to oxygen.

1.8. Thermodynamic Stability of Metals in Aqueous Solutions

The metallic state of the majority of structural metals under atmospheric conditions and in a number of aqueous media is thermodynamically unstable. The tendency of metals to pass from the metallic state into a more stable state is quit different for different metals and is characterized by the reduction of free energy corresponding to the corrosion reaction taking place under specific conditions. An approximate evaluation of the degree of thermodynamic instability for various metals in aqueous solutions can be made from the standard electrode potential of the metal (Table 1-1).

For those metals whose standard potential is in the region where hydrogen ions are reduced (region I), the anodic metal dissolution can be coupled with the hydrogen ion reduction; Li, Mg, Al, Ti, Zr, Zn, Cr, Fe. For other metals whose potential is in the region where water is stable (region II), the anodic metal dissolution can not be coupled with hydrogen ion reduction but can be coupled with oxygen reduction reaction if oxygen is present in the solution; Bi, Sb, As, Cu, Ag. For a few metals whose potential is in the region where water is oxidized to oxygen (region III), the anodic metal dissolution can not be coupled with both hydrogen ion reduction and oxygen reduction and hence no corrosion occurs; Au.

The anodic reactions that occur on metal can be

classified as follows;

1) Anodic Metal Oxidation

a) Metal dissolution

$M \rightarrow M^{2+} + 2e$, acid (1.18)

$M + OH^- \rightarrow MOH^+ + 2e$, neutral (1.19)

$M + 2OH^- \rightarrow MO^- + H_2O + 2e$, alkaline (1.20)

$M + A^- \rightarrow MA^+ + 2e$, anion-complex (1.21)

b) Metal oxide formation

$M + 2H_2O \rightarrow M(OH)_2 + 2H^+ + 2e$ (1.22)

$M + H_2O \rightarrow MO + 2H^+ + 2e$ (1.23)

2) Oxide Precipitation

$M^{2+} + 2OH^- \rightarrow M(OH)_2$ (1.24)

$M^{2+} + OH^- \rightarrow MO + H^+$ (1.25)

3) Anodic Deposition of Oxides

$2M^{2+} + 3H_2O \rightarrow M_2O_3 + 6H^+ + 2e$ (1.26)

$M^{2+} + 3H_2O \rightarrow M(OH)_3 + 3H^+ + e$ (1.27)

1.9. Potential-pH Diagram for Iron

The thermodynamic stability and instability of a metal in aqueous solutions can be illustrated in a potential-pH diagram, for the metal corrosion is determined by the potential and the hydrogen ion concentration. This is an electrochemical potential diagram and may also be named a corrosion diagram.

The full potential-pH diagram for iron is quite complex

because of many reaction equilibria involved. A useful simplified diagram is illustrated (Fig. 1-10). In the diagram there are the immunity region where iron is thermodynamically stable, the corrosion region where iron dissolves as soluble iron ions, and the passivity region where a solid oxide film prevents the dissolution of iron.

There appear two passivity regions in the diagram:

1) Thermodynamic passivity region, where the surface oxide film is thermodynamically stable.

2) Kinetic passivity region, where the surface oxide film is thermodynamically unstable but its dissolution rate is very small.

2. ANODIC POLARIZATION CURVES OF METALS

2.1. The Potential Difference Across The Metal/Solution Interface

When a metal of electronic conductor is immersed in an electrolyte solution of ionic conductor, an electrified interface is formed (Fig. 2-1, 2-2, and 2-3) and a potential difference developes across the interface (Fig. 2-4 and 2-5).

The absolute value of this potential difference can not be measured but the relative value can be measured by using an etra electrode called the reference electrode. The two electrode system consisting of the test electrode and the reference electrode is in fact a potential-difference measuring cell for the test electrode/solution interface. A potentiometer in the outercircuit of the cell measures the potential difference between the two electrode without producing appreciable flow of electric current in the cell circuit (Fig. 2-6, 2-7, 2-8, and 29).

The reference electrodes commonly used are the hydrogen electrode ($2H^+ + 2e \rightleftharpoons H_2$), the calomel electrode ($Hg_2Cl_2 + 2e \rightleftharpoons 2Hg + 2Cl^-$), and the silver chloride electrode ($AgCl_2 + e \rightleftharpoons AgCl + Cl^-$).

$$E_{NHE} = E_{SCE} - 0.242\ V = E_{NSCE} - 0.222\ V \qquad (2.1)$$

The electrode potential measured by a potential measuring cell is the sum of potential differences across interfaces present in the cell circuit;

$$E = \Delta\Phi + \Delta\Phi_{contact} + \Delta\Phi_{ref} \qquad (2.2)$$

where E is the electrode potential, $\Delta\Phi$ is the pd across the test metal/solution interface, $\Delta\Phi_{ref}$ is the pd across the reference electrode/solution interface, and $\Delta\Phi_{contact}$ is the pd across other interfaces in the circuit.

The electrode potential at which the metal/solution interface is not electrified and hence no excess or deficient charge exist on both sides of the interface is called the potential of zero charge. There is, to first approximation, no potential difference across the interface at pzc.

2.2. Electrode Polarization Changing The Potential Difference Across The Metal/Solution Interface

The electrochemical polarization of a metal means changing the metal potential and hence changing the potential difference across the metal/solution interface. To change the metal potential, we need an additional electrode as a counter electrode to apply a bias voltage to the test electorde (Fig. 2-10 and 2-11), which constitutes a polarization circuit or cell beside the potential measuring cell.

An electronic device called the potentiostat is usually used for controlling the test electrode potential (Figure 2-12). At constant potential, an electronic current flows in the polarization cell, which is equivalent to the rate of an electrochemical reaction occurring at the test electrode/solution interface.

2.3. Charge Transfer Across The Metal/Solution Interface

The transfer of electronic or ionic charge across the metal electrode/solution interface is in fact the occurrence of electrochemical reactions. A metal may dissolve into a solution producing hydrated metal ions and leaving electrons in the metal phase;

$$M(\text{metal}) \rightarrow M^{2+}(\text{solution}) + 2e(\text{metal}) \qquad (2.3)$$

This is the anodic metal dissolution and is classified electrochemically in the oxidation, electron-donating reaction or de-electronation (Fig. 2-13).

When hydrogen ions are discharged on a metal electrode to produce hydrogen gas molecules, there occurs an exchange of electrons between the metal and the hydrogen ions,

$$2H^{+}(\text{solution}) + 2e(\text{metal}) \rightarrow H_2(\text{gas}) \qquad (2.4)$$

This is the cathodic hydrogen evolution reaction and is classified into the reduction, electron-acception reaction or electronation (Fig. 2-13).

The electrons consumed or produced by an electrochemical reaction of a metal electrode flow in the outer circuit of the polarization cell and its current can be measured, which in fact is equivalent to the rate of the electrochemical reaction at the metal/solution interface.

The interphase regions constitute the essential parts of an electrochemical system. The basic law of charge-transfer reaction across the interface has been expressed through

the Butler-Volmer equation of electrode kinetics.

For an anodic reaction it is

$$j = j_a^o \exp(\alpha F \Delta\Phi/RT) \tag{2.5}$$

where $\Delta\Phi$ is the pd across the metal/solution interface and α is a kinetic constant (Fig. 2-14).

Actually, the anodic metal dissolution rate is a function of the metal electrode potential, and the relationship measured between the potential and the reaction current is called the current-potentail or the polarization curve.

If the above Butler-Volmer equation is applicable, there would be a linear relationship between log j and E;

$$E = a + b \log j, \tag{2.6}$$

which is called the Tafel relation. This equation is usually valid only in a narrow potential region. Extending the potential range for anodic polarization often gives rise to a complicated E - j curve particularly for passivable metals.

2.4. The Form of Anodic Polarization Curves of Passivable Metals

The anodic current-potential curve is characteristic for passivation of metals showing a steep decrease in the anodic current above a critical potential called the passivation potential.

A typical anodic polarization curve of passivable metals comprises (I) the active metal dissolution region, (II) the transition region from the active to the passive

states, (III) the passive region, (IV) the transpassive region, and (V) the oxygen evolution region (Fig. 2-15).

The curve however varies with different metals and environmental solutions. Generally, there are three types of the curve for the active and active-passive transition regions (Fig. 2-16a). The curve showing a single current peak is of the most simple form. The second form is characterized by a limiting current, and the third form posses more than one current peak.

In the passive region, for most of metals, the anodic current under steady state conditions is independent of potential. Some metals however exhibit different degrees of passivity with the anodic potential-independent current which differs in different potential regions. Furthermore, there are a few metals such as nickel in which the passive dissolution current increases with potential (Fig. 2-16b).

Transpassivity is characterized by a sudden increase of the anodic dissolution current with rise of the potential of passivated metals. Chromium is typical for the transpassivation which occurs above a critical potential. The critical transpassivation potential is either less noble or more noble than the oxygen evolution potential (Fig. 2-16c). As the potential is raised further, the transpassive dissolution current approaches a limiting value and frequently leads to the brightening or polishing of the metal surface.

For some metals such as iron, nickel, and cobalt, the

anodic oxygen evolution takes place at noble potentials no matter whether the transpassivation might occur. For those metals on which an insulating oxide film is formed, such as Al and Ta, the anodic oxygen evolution reaction does not proceed.

In the presence of passivity-breaking anions, the pitting type of anodic dissolution is observed above a critical potential called the pitting potential (Fig. 2-16d). Occasionally, hysteresis appears in the polarization curve around the pitting potential, depending on the pit geometry and hydrodynamic conditions of the solution.

The measured polarization curves are illustrated (Fig. 2-17 and 2-18).

The anodic polarization curve in the passive region is somewhat deformed when dissolved metal ions are being oxidized to a higher oxidation state. For instance, iron in the active state dissolves to form Fe(II) ions, which are then anodically oxidized to form a deposit film of iron(III) oxyhydroxide on the passive iron electrode (Fig. 2-19).

$$Fe^{2+} + 2H_2O \rightarrow FeOOH + 3H^+ + e \qquad (2.7)$$

Similarly, titanium in sulphuric acid produces a deposit oxide film in the passive potential region (Fig. 2-10).

$$Ti^{3+} + 2H_2O \rightarrow TiO_2 + 3H^+ + e \qquad (2.8)$$

2.5. Surface Morphology of Anodically Polarized Metals

The etch figure of anodically polarized metal surface varies with different potentials. In the active state the anodic dissolution leaves a characteristic etch pattern dependent on the crystallographic orientation of the surface, i.e. a crystallographic orientation-dependent etch pattern (Fig. 2-21).

The transpassive dissolution, on the other hand, produces a relatively uniform etch pattern independent of the crystallographic orientation of the crystal grain, indicating that the dissolution takes place through a surface film slightly influenced by the crystallographic orientation of the substrate metal (Fig. 2-21).

2.6. Anodic Polarization Curve Depending on The Electrolyte Concentration

The anodic polarization curve of passible metals is affected by the electrolyte concentration and the effect is particularly noticable in concentrated solutions. The joint influence of the anodic potential and the electrolyte concentration on the occurrence of active, passive, transpassive, or brightening metal is illustrated (Fig. 2-22 and 2-23).

For iron in phosphoric acid solutions, the active dissolution current decreases with increasing concentration of phosphoric acid, and eventually it concides with the passive dissolution current at a critical concentration, above which the brightening dissolution will take place (Fig. 2-24).

In concentrated solutions of passivity-breaking anions such as chloride, two apparently different modes of general dissolution occur corresponding to the active and the brightening states, between which an intermediate mode of pitting dissolution appears (Fig. 2-25 and 2-26).
The active dissolution is directly followed by the brightening dissolution if the chloride concentration suffices for the full depassivation of the metal.

2.7. Non-Aqueous Media

Those metals which are passivable in aqueous solutions do not necessarily passivate in nonaqueous media. No passivation is observed with chromium in acidic methanol, iron in acidic dimethylformamid (Fig. 2-27), iron in nonaqueous acetic acid (Fig. 2-28), and tungsten in LiCl methanol solution (Fig. 2-29). It is noted that a small quantity of water contribute to the passivation of metals even in non-aqueous media.

Molybdenum shows no active dissolution in aqueous solutions because of its spontaneous passivation due to the oxidation by hydrogen ions, but it exhibits an active-passive transition in 0.25 M KOH ethanol solution (Fig. 2-30).

The active-passive transition of silicon in gaseous oxygen-helium mixtures has been found; at low oxygen pressures the rate of attack of silicon due to the formation of volatile silicon mono-oxide increases with increasing oxygen pressure until a critical oxygen pressure is reached above

which a solid silica film forms to decrease the rate of attack by several orders of magnitude (Fig. 2-31).

Anodic passivation of metals is also observed in molten salts (Fig. 2-32).

2.8. Effect of Metallurgical Factors on the Active-Passive Transition Polarization Curve

The metallurgical factors such as crystal orientation, grain size, and plastic deformation possibly affect the passivation behaviour of metals. The effects, however, may differ depending on the metal and environment. Examples of the effect on the passivation of nickel of the grain size and strain are illustrated together with the passivation of amorphous and crystalline alloys of the same composition (Fig. 2-33 and 2-34).

3. ANODIC ACTIVE DISSOLUTION OF METALS

3.1. Anodic Metal Dissolution in the Active State

In the active state the anodic metal dissolution is an electrochemical transfer of metal atoms from the surface lattice sites to the hydrated metal ions in solution. This transfer occurs across the electrified double layer (Helmholtz layer) established between the metal surface and the closest plane of approach of hydrated ions to the metal. The rate of anodic metal dissolution is therefore dependent on the potential difference across the Helmholtz layer and hence on the electrode potential of the metal. Furthermore, the metal dissolution rate is often influenced by the concentration of anions in the solution (Fig. 3-1, 3-2, 3-3 and 3-4).

Experimental and theoretical investigations on the kinetics of anodic active metal dissolution have suggested the following reaction mechanisms; Non-ligand mechanism, hydroxo-ligand mechanism, and anionic ligand mechanism.

3.2. The Non-Ligand Mechanism

This mechanism is apparently the simplest mechanism and involves no association of metal ions with specific ligands in solution during the metal dissolution. The reaction pathway is either a single step of ionizing metal atom transfer or multiple steps with partially ionizing metal atoms.

For divalent metal ion dissolution, the mechanism

may be written as follows,

$$a)\quad M \rightarrow M^{2+}_{aq} + 2e \qquad (3.1)$$

or

$$a')\quad M \rightarrow M^{+}_{ad} + e \qquad (3.2)$$

$$b')\quad M^{+}_{ad} \rightarrow M^{2+}_{aq} + e \qquad (3.3)$$

where M^{+}_{ad} is an intermediate monovalent metal ion adsorbed on the metal surface and M^{2+}_{aq} is aquo-metal ion which is hydrated by coordination to water molecules.

3.3. The Hydroxo-Ligand Mechanism

This mechanism considers metal dissolution to take place producing hydroxo-metal ions, which may or may not be dissociated finally into hydroxide ions and quo-metal ions in solution depending on their thermodynamic stability. The reaction pathway for divalent metals may be represented by;

$$a)\quad M + H_2O \rightarrow M{\cdot}OH_{ad} + H^{+}_{aq} + e \qquad (3.4)$$

$$b)\quad M{\cdot}OH_{ad} \rightarrow MOH^{+}_{aq} + e \qquad (3.5)$$

$$c)\quad MOH^{+}_{aq} \rightarrow M^{2+}_{aq} + OH^{-}_{aq} \qquad (3.6)$$

where MOH^{+}_{aq} is a hydroxo-metal ion and $M{\cdot}OH_{ad}$ is an adsorbed hydroxide radical -OH or partially ionized hydroxo-metal intermediate on the surface. The rate of metal dissolution

in this mechanism is expected to increase with increasing concentration of hydroxide ions in the solution.

The anodic active dissolution of iron in acid solution obeys this mechanism (Fig. 3-5). In this case, the mechanism is written as

$$Fe + (OH^-)_{ads} \underset{k_1'}{\overset{k_1}{\rightleftharpoons}} (FeOH)_{ad} + e \qquad (3.7)$$

$$(FeOH)_{ads} \overset{k_2}{\rightarrow} FeOH^+ + e \qquad (3.8)$$

$$FeOH^+ + H^+ \rightleftharpoons Fe^{2+} + H_2O \qquad (3.9)$$

The reaction rate is pH-dependent as long as the surface coverage of $FeOH_{ad}$ is sufficiently small but it becomes pH-independent as $\theta_{FeOH_{ad}}$ reaches its maximum superficial density.

3.4. The Anionic Ligand Mechanism

This mechanism is essentially the same as and in general sense includes the hydroxo-ligand mechanism, but the reaction involves association of metal ions with anionic ligands other than hydroxide ions.

$$a)\quad M + A^-_{aq} \rightarrow M{\cdot}A_{ad} + e \qquad (3.10)$$

$$b)\quad M{\cdot}A_{ad} \rightarrow MA^+_{aq} + e \qquad (3.11)$$

$$c)\quad MA^+_{aq} \rightarrow M^{2+}_{aq} + A^-_{aq} \qquad (3.12)$$

The reaction rate then depends on the concentration of ligand-forming anions in the solution as long as $\theta_{MA_{ad}}$ is sufficiently small (Fig. 3-1, 3-2, 3-3, and 3-4).

3.5. Effectiveness of The Ligand Mechanisms

The effectiveness of the ligand mechanisms is based on the adsorbability of hydroxide and other ligand-forming anions on the metal surface. If hydroxide ions or hydroxide radicals are more readily adsorbed than other anions in the competition for surface sites, the hydroxo-ligand mechanism will be predominating, whereas anions adsorbed more stably than hydroxide ions make the hydroxo-ligand mechanism less effective.

In the range of adsorption where both ligand-forming anions and hydroxide ions are simultaneously adsorbed on the metal surface, the two mechanism will operate in proportions of their degree of adsorption

$$\text{a)}\quad M + xH_2O + (1-x)A^-_{aq} \rightarrow \begin{bmatrix} xMOH_{ad} \\ (1-x)\ MA_{ad} \end{bmatrix} + xH^+ + e \qquad (3.13)$$

$$\text{b)}\quad \begin{bmatrix} xMOH_{ad} \\ (1-x)MA_{ad} \end{bmatrix} \rightarrow xMOH^+_{aq} + (1-x)\ MA^+_{aq} + e \qquad (3.14)$$

where x is the proportion of OH_{ad}, and $0 < x < 1$.
What ratio these mechanisms bare in the rate of metal dissolution is of course dependent on their kinetic parameters

as well as adsorption proportions.

Generally, adsorbed ions either accelerate (Fig. 3-3) or inhibit (Fig. 3-6) the metal dissolution. The effect of anions on the metal dissolution rate may be explained by the relative energy level of the adsorbed intermediate to the energy level of the hydrated metal ions at the outer Helmholtz plane in solution (Fig. 3-7).

It is to be noted that those anions which are more readily adsorbable on the metal surface than hydroxide ions are not necessarily more stable ligands to metal ions in solution than hydroxide ions. If the anion in the solution forming no anionic ligand to metal ions is strongly adsorbed, the following mechanism would be conceivable;

$$\text{a)}\quad M + xH_2O + (1-x)A^-_{aq} \rightarrow \left[M(OH)_x A_{(1-x)}\right]_{ad} + xH^+ + e \qquad (3.15)$$

$$\text{b)}\quad \left[M(OH)_x A_{(1-x)}\right]_{ad} \rightarrow MOH^+_{aq} + {}^{\cdot}A^-_{(1-x)\ ad} + x\,e \qquad (3.16)$$

where the adsorbed intermediate is a complex species.

It is evident that the adsorbed species on surface sites together with the ligand-forming anions in solution play a decisive role in the kinetics of anodic metal dissolution.

4. ACTIVE-PASSIVE TRANSITION AND PASSIVATION PROCESSES

4.1. Possible Reactions

There are three alternative processes which possibly lead to the formation of passive films on metals: 1) the direct film formation, 2) the dissolution-precipitation, and 3) the anodic deposition.

The first process is the direction reaction of metal with solution to form an oxygen adsorption film, a compact oxide film, or a protecting solid salt film on the metal surface:

$$M + H_2O \rightarrow M{\cdot}O_{ad} + 2H^+_{aq} + 2e \qquad (4.1)$$

$$M + H_2O \rightarrow MO_{oxide} + 2H^+_{aq} + 2e \qquad (4.2)$$

$$M + A^{2-}_{aq} \rightarrow MA_{salt} + 2e \qquad (4.3)$$

where $M{\cdot}O_{ad}$ represents an oxygen adsorption film, MO_{oxide} a passive oxide film, and MA_{salt} a passivating insoluble salt film.

The second process consists of the anodic metal dissolution followed by a precipitation of dissolved metal ions to form a passivating oxide or insoluble salt film:

$$M \rightarrow M^{2+}_{aq} + 2e \qquad (4.4)$$

$$M^{2+}_{aq} + H_2O \rightarrow MO_{oxide} + 2H^+ \qquad (4.5)$$

$$M^{2+}_{aq} + A^{2-}_{aq} \rightarrow MA_{salt} \qquad (4.6)$$

The third process is a consecutive reaction of anodic dissolution followed by an electrochemical oxidation of dissolved metal ions to form an anodic deposit oxide or salt film:

$$M \rightarrow M^{2+}_{aq} + 2e \qquad (4.7)$$

$$2M^{2+}_{aq} + 3H_2O \rightarrow M_2O_3 \text{ oxide} + 6H^+ + 6e \qquad (4.8)$$

$$2M^{2+}_{aq} + 3A^{2-}_{aq} \rightarrow M_2A_3 \text{ salt} + 2e \qquad (4.9)$$

It is noted that the passivating film is not in the fully dehydrated state but is more or less hydrated particularly in the outermost part of the film in contact with the solution. The nature of the film will be discussed later.

4.2. Electrode Impedance in The Active-Passive Transition

The electrode impedance measured by using alternative current or voltage at various frequencies provides information about the structure and property of the electrified double layer at the metal/solution interface. For instance, the impedance spectrum of a rotating iron disc electrode in the active dissolution region in sulphuric acid solution changes with potential (Fig. 4-1). The impedance spectrum can be illustrated in the complex impedance plane with the real part of resistance R and the imaginary part of $jG = (\frac{1}{\omega C})$.

$$Z = R - j\ (\frac{1}{\omega C}) \qquad (4.10)$$

where ω is the frequency and C is the capacitance.

There are two semicircles in the impedance diagram for an actively dissolving iron disc electrode. Semicircule 1 at high frequency represents the relaxation of the electric double layer. Semicircle 2 is related to the relaxation of adsorbed species on the surface, which appears as a psudo-self inductance at low current density (a) and as a faradic psudo-capacitance at high current density (b).

In the potential region where a rotating iron disc is in midway between the active and the passive states (c and d), the impedance falls in a high frequency semicircle 1 of the electric double layer and in a low frequency semicircle 2 which represents the relaxation of a passivating species on the surface and moreover in a very low frequency semi-circle 3 which arises from a convective diffusion near the surface at high current density (Fig. 4-2).

Based on the impedance measurements, Epelboin and his coworker (1975) suggested the following mechanism for iron passivation in acid solution:

$$FeOH^{+}_{aq} \rightleftharpoons Fe^{2+}_{aq} + OH^{-}_{aq} \qquad (4.11)$$

$$Fe \rightarrow (FeOH)_{ad} \rightleftharpoons [Fe(OH)_2]_{ad} \rightarrow [Fe(OH)_3]_{ad} \qquad (4.12)$$

where $[Fe(OH)_2]_{ad}$ and $[Fe(OH)_3]_{ad}$ are passivating species

and $(FeOH)_{ad}$ is an adsorbed reaction intermediate for both active dissolution and passivation.

Although uncertainities are always involved in analyzing the impedance spectrum because of unavoidable assumptions, distinction may be made at least qualitatively between the intermediate adsorption of active dissolution and the adsorption that leads to passivation (Fig. 4-3).

At infinite or very high frequencies the electrode impedance gives the electric double layer capacity at frozen coverages of adsorbed species (Fig. 4-4). There is a discontinuity in the capacity-potential curves somewhere between the active and the passive states, indicating that the occurrence of metal passivation is associated with a radical change of the electrical double layer at the metal/solution interface.

4.3. The Flade Potential

It was noted as early as 1911 by Flade that upon interruption of the anodic current, the potential of a passivated metal decreases to an arrest potential before decaying rapidly to the active state (Fig. 4-5). This arrest potential is later called the Flade potential. For those metals which exhibit different degree of passivity, there are more than one Flade potential (Fig. 4-5).

Bonhoeffer (1953) suggested that the Flade potential was equal to the passivation potential observed in the potentiostatic anodic polarization curve. Although agreement

between the two potentials is not always satisfactory in that the potential arrest often occurs in a range of potential instead of appearing at a constant potential, the Flade potential has been considered to represent a characteristic potential for passivation.

The Flade potential and its pH dependence are characteristics of the passive film on metals (Fig. 4-6). It is a linear function of pH and in most cases is given by:

$$E_F = E_F^o - 0.059\ pH. \tag{4.13}$$

It has been considered that the Flade potential is the potential of an oxide-covered metal electrode. The overall reactions which may determine the potential of this type of electrode are,

$$M + nH_2O \rightleftharpoons MO_n + 2\,n\,H^+ + 2\,n\,e \tag{4.14}$$

and

$$MO_n + mH_2O \rightleftharpoons MO_{n+m} + 2\,m\,H^+ + 2\,m\,e. \tag{4.15}$$

Göhr and Lange (1957) explained the Flade potential of iron as the equilibrium potential of the following reaction,

$$2Fe_3O_4 + H_2O \rightleftharpoons 3\gamma \cdot Fe_2O_3 + 2H^+_{aq} + 2\,e. \tag{4.16}$$

Along the same line, Pryor (1959) assumed the Flade potential to be determined by the reaction between excess oxygen in the

passive film and hydrogen ions and electrons. Wagners (1973) also described the Flade potential of iron as the potential of an iron-deficient magnetite in which excess oxygen reacts with hydrogen ions and electrons: The thermodynamic calculation shows that the iron deficit Δ in $Fe_{3-\Delta}O_4$ changes from $\Delta = 0$ for Fe_3O_4 to $\Delta = 1/3$ for $Fe_2O_3 = Fe_{2.67}O_4$ in a relatively narrow potential range from +0.5 V to +0.7 V, which is agreeable to the Flade potential of iron $E_F = -0.58$ V at pH = 0. The potential determining reaction in this case may be written as,

$$(3-\Delta-x)\ Fe_{3-\Delta}O_4 + 4xH_2O \rightleftharpoons (3-\Delta)\ Fe_{3-\Delta-x}O_4 + 8xH^+ + 8xe \qquad (4.17)$$

where Δ changes from $\Delta = 0$ to $\Delta = 1/3$ and $x \rightarrow 0$. The Flade potential may correspond to $\Delta = 1/6$, half-way between the two limiting compositions.

$$2FeOH^+_{aq} + H_2O \rightleftharpoons \gamma \cdot Fe_2O_3 + 4H^+_{aq} + 2\,e \qquad (4.18)$$

Nagayama and Cohen (1963) found later that in a limited range of neutral pH, the rest potential of passive iron was a function of iron(II) ion concentration as well as pH.

Another approach was made by Uhlig (1958, 1967) who suggested a passivating layer of chemisorbed atomic and molecular oxygen on the surface and described the Flade potential as determined by the following reactions,

$$Fe(surface) + 3H_2O \rightleftharpoons O{\cdot}O_2(ads\ on\ Fe) + 6H^+_{aq} + 6\,e \qquad (4.19)$$

or

$$Fe + O{\cdot}O_2(ads\ on\ Fe) + 6H^+_{aq} + 3\,e \rightleftharpoons Fe^{3+}_{aq} + 3H_2O \qquad (4.20)$$

Possibly, there are a number of electrochemical reactions which may determine the electrode potential of a passivated metal. It should however be noted that, when more than one reaction is expected to occur, the prevailing reaction in determining the potential is of the largest exchange current density. The potential-determining reaction can therefore be altered depending on the solution composition and the property of the passive film.

Divergent views still exists as to whether the rest potential is determined by the bulk of the passive film itself or by the outermost, adsorption-like layer of the film adjacent to the solution.

4.4. Galvanostatic Passivation

When an anodic current greater than the minimum passivation current j_m is applied to a metal electrode in solution, it takes an induction time τ_p before the metal goes from the active to the passive state (Fig. 4-7). This induction time τ_p, often called the passivation time, depends on the current density applied and obeys the following equation,

$$\tau_p = k\ (j - j_m)^n \qquad (4.21)$$

where constant n has been found to be -1 for iron and -2 for nickel. The fact that n = -1 indicates that a constant anodic charge is required for passivation in addition to a minimum charge which inevitably goes into the anodic metal dissolution. This amount of charge was measured to be 1700 - 1800 m coulomb cm^{-2} for iron in acid and 2.3 m coulomb cm^{-2} for chromium in acid, suggesting that a thick hydrated salt layer is deposited prior to the formation of passive film on iron, while the direct formation of passive film is likely to occur in the case of chromium.

It is also suggested from n = -2 that the passivation of nickel requires some diffusing species, probably hydrogen ions, to be depleted in solution adjacent to the metal surface.

During galvanostatic passivation, the potential is arrested for a short time at a certain potential that seems to separate the active state from the passive state. This anodic arrest potential (anodic Flade potential) corresponds with the cathodic arrest potential (cathodic Flade potential) which appears during galvanostatic activation of passivated iron. These two Flade potentials as well as the open circuit Flade potential are again indicative of a critical potential for passivation.

4.5. Potentiostatic Passivation

When a metal having no surface film is anodically polarized at a constant potential in the passive state, the

anodic current decreases with time forming a passive film on the metal (Fig. 4-8 and 4-9).

For iron in neutral solution, a large anodic current flows in an early stage, which seems to carries mainly the actively dissolving iron ions before the passive film starts to form; experimentally, the initial current somehow depends on the impedance of cell circuit, but it does not rule out the distinct difference in time variation of anodic current between the initial stage and the later stage (Fig. 4-8).

For nickel in neutral solution, the passive film formation appears to occur first and then the anodic nickel dissolution proceeds through the passive film formed (Fig. 4-9). It is anticipated that the sequence of reactions that occur during passivation is determined by the kinetic properties of the film formation and dissolution reactions and hence varies with different metals and solutions.

4.6. Passivation Kinetics

(I) Competitive Model

The simplest model for passivation kinetics is that the active metal dissolution competes with the passive film formation. The typical kinetic equation for this model was derived by Schwabe et al. (1967). Simultaneous occurrence of anodic metal dissolution and film formation on the film-free portion of the surface,

$$M + 2H_2O \rightarrow MOH^+_{aq} + H^+_{aq} + 2e \qquad (4.22)$$

$$M + H_2O \rightarrow MO + 2H^+_{aq} + 2e\,, \qquad (4.23)$$

leads to the total anodic current j

$$j = (j_d + j_f)(1 - \theta) \tag{4.24}$$

where j_d is the current density of the active dissolution, j_f the c_d of the film formation, and θ the fraction of passivated portion of the surface. In the first approximation, the change of θ with time at constant potential may be expressed,

$$\left[\frac{\partial \theta}{\partial t}\right]_E = C\, j_f\, (1 - \theta) - B\theta \tag{4.25}$$

where C is the covered area per unit anodic change of the film formation and B is the rate of dissolution or degradation of the film. The total anodic current j then becomes

$$j = (j_d + j_f)\left[1 - \frac{C\, j_f}{C\, j_f + B}\{1 - \exp[-(C\, j_f + B)t]\}\right] \tag{4.26}$$

with

$$j_d = j_d^o \exp\left[\frac{\alpha z}{RT}(E - E_d^o)\right] \tag{4.27}$$

$$j_f = j_f^o \exp\left[\frac{\alpha' z}{RT}(E - E_f^o)\right] \tag{4.28}$$

where j^o denotes the exchange cd, E^o is the equilibrium potential. By use of reasonable values for the kinetic parameters, the anodic current-potential curve can be calculated and compared with experiments (Fig. 4-10).

The above equation for j always gives a current peak in the active-passive transition if the following conditions are satisfied: a) j_d^o and j_f^o are of similar order of magnitude, b) E_d^o and not too far apart, and c) B is not too great. If $j_d^o \gg j_f^o$ and $E_d^o \gg E_f^o$, the metal dissolution predominates and the passivation that can be expected to occur under such conditions is only the salt layer passivation resulting from the super-saturation of metal ions.

(II) Two Adsorbed Species Model

Gelain, Cassuto and LeGoff (1971) described the kinetic conditions that determine the occurrence of passivity in the presence of two adsorbed species on the metal surface. They dealt with the passivation of silicon in low pressure oxygen gas, but we shall deal the passivation of a metal in aqueous solution in analogy with their treatment.

Suppose the following reactions are taking place on the metal surface.

$$(1)\quad M + H_2O \rightarrow MOH_{ad} + H^+ + e \qquad (4.29)$$

$$(2)\quad MOH_{ad} \rightarrow MOH^+_{aq} + e \qquad (4.30)$$

$$(3)\quad MOH_{ad} \rightarrow MO_{ad} + H^+ + e \qquad (4.31)$$

$$(4)\quad M + MO_{ad} + H_2O \rightarrow 2MOH_{ad} \qquad (4.32)$$

$$(5)\quad MO_{ad} + H^+ \rightarrow MOH^+_{aq} \qquad (4.33)$$

where MOH_{ad} and MO_{ad} are two adsorbed species (Fig. 4-11).

Under steady state conditions the surface coverage do not change with time,

$$\frac{d\,\theta_{OH}}{dt} = k_1\theta_M - (k_2 + k_3)(1 - \theta_M - \theta_o) + 2\,k_4\theta_M\theta_o = 0 \qquad (4.34)$$

$$\frac{d\,\theta_o}{dt} = k_3\,\theta_{OH} - k_4\,\theta_M\theta_o - k_5\,\theta_o \qquad (4.35)$$

$$\theta_M + \theta_{OH} + \theta_o = 1 \qquad (4.36)$$

where k represents the rate constant of the reactions given above. From the above three equations we obtain

$$\theta_M = \frac{(k_2 + k_3)\ (1 - \theta_o)}{k_1 + k_2 + k_3 + 2k_4\,\theta_o} \qquad (4.37)$$

$$\theta_M = \frac{k_3 - (k_3 + k_5)\theta_o}{k_3 + k_4\,\theta_o} \qquad (4.38)$$

These equations can be solved graphically (to obtain) two hyperbolic curves for the relationship between θ_M and θ_o (Fig. 4-11). If $k_5 \gg k_3$ and hence if the rate of passive film formation is much greater than the rate of passive film dissolution, the two hyperbolic curves intersect each other at only one point somewhere apart from $\theta_o = 1$, leading no complete coverage of the passive film. If $k_3 \gg k_4$, however, the two parabolic curves always intersect at two points, one apart

from $\theta_o = 1$ and the other being characterised by $\theta_o = 1$ and $\theta_M = 0$. The former is the active state with a fraction of the passivating adsorption and the latter is the passive state. The existence of two steady states represented by two intersecting points is the necessary condition for the transition from the active to the passive states.

(III) Three Adsorbed Species Model

Among many other theoretical models not much different from each other, the kinetic treatment made recently by Lorenz et al. (1975) for iron in weak acid solution may be instructive. They assumed three different species to be adsorbed on the surface (Fig. 4-12).

$$Fe + H_2O \rightleftharpoons (FeOH)_{ad} + H^+ + e \qquad (4.39)$$

$$(FeOH)_{ad} \rightleftharpoons (FeO)_{ad} + H^+ + e \qquad (4.40)$$

$$(FeO)_{ad} + H_2O \rightleftharpoons (FeOOH) + H^+ + e \qquad (4.41)$$

Furthermore the metal dissolution was assumed to take place by the following three different reactions,

$$(FeOH)_{ad} \rightarrow FeOH^+_{aq} + e \qquad [I] \quad (4.42)$$

$$(FeO)_{ad} + H^+ \rightarrow FeOH^+_{aq} \qquad [II] \quad (4.43)$$

$$Fe + (FeO)_{ad} + H_2O \rightarrow (FeOH)_{ad} + FeOH^+_{aq} + e \qquad [III] \quad (4.44)$$

The kinetic equation derived from this model gives a computer-simulated anodic polarization curve and adsorption isotherm, which can be compared with experiments (Fig. 4-13).

4.7. Effects of Anions

Anions in solution affect the active-passive transition of metals. For instance, addition of phosphate ions in borate solutions causes the active-passive transition to proceed in two stage instead of one (Fig. 4-14). The primary stage probably corresponds to the formation of an involuble iron phosphate or basic phosphate layer and the secondary stage to the formation of an oxide film. The primary salt layer passivation is facilitated by increasing the phosphate ion concentration, but it breaks down in the presence of sulphate ions.

Nickel in sulphate solution adsorbs sulphate ions to cause a primary passivation (Fig. 4-15). Sulphate ions however were desorbed above a certain potential which is less noble than the Flade potential. There are therefore two current peaks in the active-passive transition polarization curve of nickel in sulphuric acid solution (Fig. 4-15). When nickel is pre-immersed in sulphuric acid for an extended time (70 hours), the first current peak tends to disappear owing to the complete coverage of adsorbed sulphate ions and only the second current peak remains increasing with pre-immersion time.

Generally, anions in solution either facilitate or retard the passivation of metals through their adsorption

or salt layer formation on the metal surface.

a) Adsorption accelerating or retarding passivation;

$$M + x\,H_2O + (1-x)\,A^-_{aq} \rightarrow \begin{bmatrix} xMOH_{ad} \\ (1-x)MA_{ad} \end{bmatrix} + 2\,xH^+ + x\,e \quad \ldots (4.45)$$

$$\begin{bmatrix} x\,MOH_{ad} \\ (1-x)MA_{ad} \end{bmatrix} \rightarrow x\,MOH^+_{aq} + (1-x)MA^+_{aq} + e \quad (4.46)$$

b) Salt or basic salt layer formation

$$MA^+_{aq} + A^-_{aq} \rightarrow MA_2 \quad (4.47)$$

$$[MA^+_{aq}] + H_2O \rightarrow MAOH + H^+_{aq} \quad (4.48)$$

$$[MA_{ad}] + A^-_{aq} \rightarrow MA_2 \quad (4.49)$$

5. PASSIVE FILMS ON METALS

5.1. Morophology and Thickness

The passive films on metals may be classified into five types (Fig. 5-1).

Type 1: the adsorption film consisting of a monoatomic or multimolecular layer of oxygen or other species. The effectiveness of an adsorbed film in causing passivity of an iron-chromium alloy in acid solution was recently examined by Frankenthal ; an adsorbed 0.36 mC/cm^2 film of oxygen or oxyhydroxo-chromium monolayer was found to sustain a potential difference of 0.1 ∿ 0.2V (10^6∿ 10^7V/cm) without appreciable increase in anodic current of the order of 10 $\mu A/cm^2$ at potentials slightly more positive than the passivation potential.

Type 2: the barrier film of a three-dimentional oxide polymer layer sustaining the potential of 10^6 ∿ 10^7V/cm. It it probably difficult to draw a dividing line between a multimolecular adsorption film and a thin three-dimensional barrier film, for an oxygen adsorption layer often grows to an oxide barrier film. On chromium, for instance, the film thickness of about 1.2 nm/V increasing from the order of monoatomic layer in acid and neutral solutions (Fig. 5-2). The most typical is the passive barrier film on iron in acid solution, which possesses the thickness of 1.6 nm/V consisting of an inner Fe_3O_4 and an outer γ-Fe_2O_3 barrier layers (Fig. 5-3). Generally, the barrier film thickness

at steady state is a linear function of potential if the passivity-maintaining current is independent of potential, but this is no longer the case when the passive dissolution current is potential-dependent, as in the case of nickel (Fig. 5-4).

Type 3: the barrier film formed on a less protecting layer. This type of passive film is exemplified by cobalt in which three degrees of passivity occur in neutral solution (Fig. 5-5). The primary passivity is due to a single CoO layer, and the secondary passivity is due to a Co_3O_4 film formed on a less protecting CoO layer. The barrier Co_3O_4 film grows nearly linearly with potential, whereas the inner CoO layer thickness appears not to be a simple function of potential but rather determined by the history of its formation. Thermodynamically, a constant potential drop is expected to occur in the inner CoO layer whatever its thickness, and if this potential drop controls ionic current, the CoO layer thickness would eventually became constant irrespective of the electrode potential. The quasi-passive film on copper in neutral solution is also of this type consisting of Cu_2O and CuO (Fig. 5-6). It is anticipated that the existence of a non- or less protective layer between the metal and the passivating layer makes the passivity unstable in acid solution.

Type 4: the barrier film covered with a hydrated deposit layer. Iron in neutral solution forms this type of

passive films (Fig. 5-7). The barrier oxide layer thickness is a linear function of potential with the slope of about 1.7 nm/V, while the outer deposit layer thickness is nearly independent of potential except for potentials close to the passivation potential. Cobalt in alkaline solution forms a precipitate layer of $Co(OH)_2$ on the passivating barrier film (Fig. 5-8), and titanium in acid solution has non-protective crystalline TiO_2(rutile) deposits on the passive barrier film of TiO_2(anatase) (Fig. 5-9).

Type 5: the barrier film covered with a porous layer of the same composition. In anodic oxidation of aluminum, pores are formed on the barrier oxide film in acid solution and the outer porous layer thickens continuously (Fig. 5-10). By contrast, no pore formation occurs in neutral solutions and the barrier film grows to a limiting thickness. It seems likely that the pore formation on barrier oxide films is determined by the mechanical property of the films as well as the kinetics of film growth and dissolution.

5.2. Composition, Nonstoichiometry And Semiconductor Properties

The composition of the passivating film on a metal is a function of potential and environmental solution if the rate of film dissolution and reformation is large enough for establishing the steady state. Otherwise, the film initially formed remains to exist or at least excerts influence to the film composition.

A variety of chemical, optical, electrochemical and

electro-optical techniques have been applied to measure the composition of passivating films on metals. Among them, a photoelectric polarization method developed by Oshe and Rosenfeld (1970) deserves attention (Fig. 5-11).

The photoelectric polarization measures a generation of hole-electron pairs caused by the illumination of short time light pulses in a semiconductor surface film on metals. The oxide films on metals show n-type conductivity when metal ions are in excess, whereas they show p-type conductivity when oxygen ions are in excess. According to the thoery of of photo-electric polarization (Oshe and Rosenfeld, 1969), the semiconducting character and the degree of deviation from the oxide stoichiometry are connected with the sign and amplitude of the photoresponse potential by the equation,

$$V_{pep} = \frac{kT}{2e} \quad n \frac{[V_c^{m+}]}{[V_A^{n-}]} - C \qquad (5.1)$$

where $[V_c^{m+}]$ and $[V_A^{n-}]$ are the concentrations of cationic and anionic vacancies in the oxide film, and C is a constant. The sign of the photopotential indicates which of the two over-stoichiometric components, metal or oxygen, privails. The amplitude of the photopotential, measured in volts, allows determination of the excess of one of the overstoichiometric components.

The passivating film on iron in acid solutions, where the

film dissolution and reformation rate is relatively large, consists of only the barrier layer of oxide, which is bi-layered with probably an inner Fe_3O_4 layer and an outer γ-Fe_2O_3 layer (Fig. 5-3). Its nonstoichiometry and semiconductor properties have been measured by photoelectric potential measurements to be of n-type semiconducting oxides with overstoichiometric excess iron ions (Fig. 5-12). In neutral solution where a deposit-covered barrier film is formed on iron, electrolyte anions affect the composition of the barrier layer; it is an iron(III) oxide in borate solution and an iron(II)-(III) mixed oxide in phosphate solution (Fig. 5-13). The anion effect arises from two reasons; one is the initially formed, primary passive film which differs in different anion solutions, and the other is the ion-selectivity of the deposit layer which is anion-selective in a borate-containing deposit layer but is cation-selective in a phosphate-containing deposit layer.

The composition of passivating barrier films often changes with potential; for example, the barrier film on cobalt changes from Co_3O_4 to Co_2O_3 (Fig. 5-14), and the film on copper changes from p-type CuO to n-type CuO in neutral solution (Fig. 5-15). Changes in the film composition necessarily induce changes in the electronic band structure of the film, which can be measured by modulated reflectance spectra, as described later.

The passivating film on nickel is a p-type semiconductor of probably NiO_{1+x} whose composition seems to change over a

wide range of potential (Fig. 5-16). The secondary passivation is due likely to the formation of a NiOOH layer by anodic deposition from dissolved nickel(II) ions (Sato, 1971). In the potential range where the passive dissolution current increases with potential in acid solution, the electronic band gap of the film changes continuously with potential (Paatsch et al. 1971 , Heusler et al. 1973).

The passivating film on chromium is likely to be a CrOOH layer. This film and the film on nickel as well are so thin that unambiguous assignment to an absorbed film or to a barrier oxide film may hardly be made from the present stage of analysis.

For alloy, enrichment of some of alloying elements in the passivating film was noted, for instance, for iron-chromium alloys (Asami et al. 1976) and for stainless steel (Sugimoto et al. 1974, Okamoto et al. 1974). It was also noted that there was enrichment or depletion of alloying elements in a substrate metal layer 1~5 nm thick (Seo and Sato, 1977). Newly developed surface analysis techniques such as XPS, AES, SIMS, ISS, and APS will provide in near future much deeper insight into the compositional profile of the passivating film on alloys. Up to now, however, there has been no systematic study of the effect of alloying composition on the nature of passive films.

Evidence was given for the presence of water in the passive film on iron and stainless steel. It is highly

probable that all the passivating films formed in aqueous solution contain a quantity of water. Since the water excerts various influences on the physical and chemical properties of the film, its role on the passivity should not be ignored; it affects for instance the ionic conductivity, electronic configuration, band structure, dielectric property, and mechanical property, all of which more or less contribute to the passivability and the stability of passivating films.

There is no general agreement as to whether the passivating film is crystalline or amorphous. Electron diffraction measurements gave crystalline or diffused crystalline films of Fe_3O_4, FeOOH and γ-Fe_2O_3 for iron at room temperature in aqueous solutions (Kruger et al. 1967), and an anatase TiO_2 with rutile TiO_2 deposits for titanium at 100°C in acid (Koizumi, 1968), while an amorphous film was suggested for stainless steel (Rodin, 1956). It is also anticipated and asserted that the amorphous film is more protective than the ctystalline film of the same thickness probably because of it uniformity and deformability.

5.3. Electronic Property

The electronic property, particularly electronic conductivity, has been one of the points of dispute for the passed years. At the present state of knowledge, it is highly probable that in most of passivable metals the passivating film is a poor electronic conductor ranging from semiconductor to insulator. Redox reactions, however, are allowed to occur by

the electronic tunnelling if the passivating film is sufficiently thin.

Evidence was given for the electronic tunnelling which controlled the oxygen evolution reaction on passivated zirconium (Fig. 5-10). In the potentiodynamic polarization curve and the passive film thickness of zirconium in ammonium borate solution, the oxygen current j_{O_2} occurs only in the first potential sweep where the passive film is growing in very small thickness, and suddenly decreases when the film thickness exceeds a critical value. Once a thick film has been formed, the oxygen current no longer occurs in the succeeding potential sweeps. Comparison between the observed oxygen current and the tunnel current calculated after Hartman (1964) shows a good agreement at high overpotentials where the electronic conduction is the rate-determining step; at low overpotentials the electrochemical reaction at the film/solution interface is determining the rate so that the observed current is smaller than the calculated one (Fig. 5-18).

Hartman's equation for the electronic tunnel conduction is,

$$je = \frac{4\Pi m^* e}{h^3 C^2}\left\{\frac{\Pi C kT}{\sin [\Pi C kT]}\right\} \exp[-B]\{1-\exp[C\cdot e\eta]\} \qquad (5.2)$$

with B and C for low bias voltage ($e\eta < \Phi_1$)

$$B(\eta) = 2\alpha L[(\Phi_1 - \eta)^{3/2} - \Phi_2^{3/2}] / 3(\Phi_1 - \Phi_2), \qquad (5.3)$$

$$C(\eta) = \alpha L [(\Phi_1 - e\eta)^{1/2} - \Phi_2^{1/2}] (\Phi_1 - \Phi_2 - e\eta) \qquad (5.4)$$

and for high bias voltage ($e\eta > \Phi_1$),

$$B(\eta) = - 2\alpha L \Phi_2^{3/2}/3(\Phi_1 - \Phi_2 - e\eta) \qquad (5.5)$$

$$C(\eta) = - \alpha L \Phi_2^{1/2}/(\Phi_1 - \Phi_2 - e\eta), \qquad (5.6)$$

where $\alpha = 4 (2m^*)^{1/2}/hL$, L is the film thickness, m^* the electron effective mass, η the overpotential (bias voltage), and h the Phanck constant. Φ_1 and Φ_2 are the energy barrier hights at the metal/film interface and at the film/solution interface, respectively.

Redox reactions other than oxygen electrode reaction may also take place on passive metal surface covered with a thin passive film through electron tunnelling; For instance, Ce^{2+}/Ce^{4+} reaction (Franck et al. 1952), Fe^{2+}/Fe^{3+} reaction (Makrides, 1964), and $[Fe(CN)_6]^{4-}/[Fe(CN)_6]^{3-}$ reaction (Moshtev, 1972; Schultze et al. 1976). Generally, the redox reaction current density tends to decrease with increasing thickness of the passive film, although depending on the overpotential (Fig. 5-19). The redox reaction current density appears also to depend on the semi-conductor property of the passive film. The anodic and cathodic polarization curve for iron(II) - (III) cyanide redox reactions with the current

density normalized for unit concentration of on various passive metal electrodes (Fig. 5-20). Obviously, the exchange current density is the largest on Pt.

If the passive film is a semiconductor, both semiconduction and tunnel mechanisms are operative, the former depending on the concentration of electron or hole in the film and the latter depending on the film thickness. When the passive film is not sufficiently thin for electron tunnelling, the semiconduction mechanism is privailing and the passive electrode behaves as a semiconductor electrode rather than a metal electrode. In such a case, the redox reaction occur with electrons or holes in the film:

$$\text{Red} \rightleftharpoons \text{Ox} + e \quad \text{(the electron transfer)} \qquad (5.7)$$

$$\text{Red} + p \rightleftharpoons \text{Ox} \quad \text{(the hole transfer)} \qquad (5.8)$$

The electron transfer between the conduction band of semiconductor and the redox system in solution is likely to occur with redox reactions whose equilibrium potential is low or not noble, while the hole transfer is likely to occur with redox reaction whose euqilibrium potential is high or noble. Furthermore, the semiconductor electrode kinetics predicts that the electron transfer reaction proceeds much more rapidly in cathodic direction than in anodic direction, and that the reverse is the case of hole transfer reaction (Fig. 5-21).

The passive films on titanium, iron, and niobium are of

n-type semiconductor. For a redox reaction of iron(II)-(III) cyanides on these passive films, the cathodic current flows more easily than the anodic current which appears to level off with increasing potential (Fig. 5-20).

The semiconducting property for the passive film on iron in neutral solution has recently been studied by capacitance measurements to demonstrate an electronic band model for the film (Fig. 5-22). Also instructive is a p-type/intrinsic semiconductor/n-type junction model suggested for the anodic oxide film on tantalum.

5.4. Ionic Conduction

The ionic current in the passivating film follows either the field-assisted ion conduction in which the activation energy is a function of the electric field in the film (Weil, 1955, Moshtev 1967) or the place exchange mechanism in which the activation energy is a function of the film thickness as well as the electric field (Sato and Cohen, 1963), probably depending on the film thickness. Experimentally, these two mechanisms are hardly differentiated unless the range of film thickness is extended.

The rate equation for the field-assisted conduction (Cabrera and Mott, 1949) is,

$$j = j_o \exp\left(\frac{\alpha azF}{RT}\frac{\Delta\Phi}{L}\right) = j_o \exp\left(B\,\Phi\Delta/L\right) \qquad (5.9)$$

where αaz is the activation dipole and $\Delta\Phi/L$ is the field in

the film. For the place exchange mechanism (Sato et al. 1963), it is

$$j = j_o' \exp(-L/B_1) \exp(B_2 E), \qquad (5.10)$$

where E is the electrode potential and B_1 and B_2 are the kinetic parameters.

The ionic current in the passivating film plotted according to the field-assisted conduction mechanism as a function of the electronic field $\Delta\Phi/L$ (= E) for the barrier layer on iron at pH 1 ∿ 6, on nickel at pH 8.42, on cobalt at pH 8.42, and on zirconium in 0.1 M Na_2CO_3; all show nearly the same field-dependence except for nickel (Fig. 5-23). The extremely small field-dependence of the ionic current for nickel can hardly be explained by a simple, field-assisted ion conduction mechanism. Sato (1976) suggested that the space charge created in an oxide film having no intrinsic vacant ion sites such as NiO and CoO suppresses the formation of cationic vacancies in the outermost layer of the film and thus decreases the field-dependence of ion migration current.

5.5. Mechanical Property

The mechanical properties of the passivating film are little understood. They seem almost hopelessly difficult to be revealed if the film thickness is of the order of 1 nm thickness. The interfacial and hence environmental effects on the mechanical properties increase as the film is thinner.

It was found that the solution pH affects the ultimate tensile strain of a barrier oxide film on an aluminum alloy; a peak of the strain is noted at the zero-point-of-charge pH (Fig. 5-24). From this result it is highly probable that adsorbed ions facilitate the mechanical breakdown of the passivating film.

Stresses in the passivating film can arise from various reasons; (a) interfacial tension, (b) electrostriction pressure normal to the film surface, (c) lateral stress due to epitaxial lattice misfit called the Pilling-Bedworth ratio (d) normal stress due to electrochemical potential gradient responsible for mass transport through the film, (e) stress due to partial hydration or dehydration, and (f) local stress due to impurities.

The electrostriction pressure modified by the surface tension (a + b) is given by,

$$p = \frac{\epsilon(\epsilon - 1) E^2}{8 \Pi} - \frac{\gamma}{L} \qquad (5.11)$$

where E is the electric field in the film, ϵ the dielectric constant, L the film thickness, and γ the surface tension of the film. This electrostriction pressure may exceed the ultimate compressive stress of oxides to cause the mechanical breakdown of the passive films (Fig. 5-25, 5-26, and 5-27).

Furthermore, the mass transport (d) produces the resultant

force acting on each volume element,

$$F = -E\, C_s(x)\, d\,\tilde{\mu}_s(x)/dx, \qquad (5.12)$$

where $C_s(x)$ is the concentration of diffusing species s at position x and $\tilde{\mu}_s(x)$ is the electrochemical potential of s (Fromhold, 1970). It is compressive if anions are more mobile than cations. Namely, the oxide film grown by anion (oxygen) migration induces a compress stress in it, while the cation migration produces tensile stress or no stress.

The stress in anodic 40~300 nm oxide films formed on tantalum, niobium, aluminum, zirconium, and tungusten was measured and found to be tensile except for zirconium (Vermilyea, 1963). The stress in the film on zirconium is compressive in borate solution but turns to be tensile in the presence of fluoride ions (Fig. 5-28). After the film breakdown due to fluoride ions, however, the stress turns again to be compressive. This peculiar phenomenon was suggested to be due to a shift in the ionic transport numbers due to the presence of the fluoride ions (Fig. 5-29). Whatever the mechanism, it is evident that the fluoride ions played a decisive role in the mechanical deformation of the film.

5.6. Modulation Electroreflectance Spectroscopy of Passive Films

The reflectivity of the surface of metal electrode is

usually a function of electrode potential, and will provide information about the optical property of the metal surface or the surface oxide film on metals. Experimentally, however, it is difficult to measure the absolute value of the reflectivity of the metal surface. To overcome such difficulties, a variety of modulation techniques have been applied to the reflectivity measurements.

The modulation electroreflectance technique measures the electroreflectance signal that responds to an ac modulation of the electrode potential at constant bias voltage of electrode potential (Fig. 5-30). The derivative of the reflectance obtained in this way yields very sharp spectra and as a result more precise information about the electronic optical properties of the surface film than that obtained by conventional reflectivity measurements (Fig. 5-31).

The modulated electroreflectance spectra of passive nickel a sulphuric acid solution (Fig. 5-32) show a negative spectrum peak at 4 eV photon energy for the passive film formed in the passive potential region where the passive current is almost potential-independent. This photon energy 4 eV is equal to the band gap in NiO and thus the film may be identified with NiO. For the film formed in the potential region where the passive current increases with potential, the negative spectrum peak shifts to higher photon energy values than 4 eV as the potential becomes noble. The band gas estimated from the spectrum peak changes from

a steady value of 4 eV (NiO) to another steady value of 4.2eV (NiO_{1+x}) with increasing potential (Fig. 5-33).

Modulation electroreflectance measurements have also been made for iron in alkaline solution (Fig. 5-34), and for titanium in acid solution (Fig. 5-35 and 5.36). For titanium the critical wave length where the modulated electroreflectance $\Delta R/R = 0$, increases with potential exhibiting three straight lines corresponding probably $TiO_{1\sim2}$, TiO_2, and Ti_3O_5. At the same time, the potopolairzation potential measured indicates the passive film to be an electronic semiconductor of n-type with the band gap changing from 3.75 eV of TiO_2 to 3.64 eV of Ti_3O_5 with increasing potential (Fig. 5-36). This increase in the band gap may be attributed to the formation of oxygen vacancies in the film.

With a passive chromium in sodium sulphate solution at pH 2.0, the modulation electroreflectance spectra show a peak at 5 eV corresponding probably Cr_2O_3 at lower potentials and two peaks at 5 eV and 3.1 eV at higher potentials where the transpassivation occurs (Fig. 5-37).

5.7. Ellipsometry of Passive Films

Ellipsometry is in the broadest sense the method of measuring and analyzing elliptical polarization of light. It provides a very sensitive optical technique for measuring the thickness of thin surface films on metals without disturbing their nature by the use of polarized light which

reflects from the surface in question. Upon reflection from a metal surface the polarized light changes in the state of polarization depending on the optical property of the surface. Since the change in polarization of light is a function of the optical property of the surface, we can measure the property of the surface and any films overlaying it by monitoring the change in the state of polarization of light upon reflection.

The state of polarized light is usually expressed by the complex amplitude attenuation between the electric vectors, E_p and E_s, vibrating parallel (p) and perpendicular (s) to the plane of incidence:

$$\rho' = \frac{E_p}{E_s} = \tan \Psi' \exp (i\Delta') \qquad (5.13)$$

where $\tan \Psi'$ is the amplitude attenuation, Δ' is the phase difference, and i is the imaginary unit $\sqrt{-1}$. After reflection the state of polarization changes to

$$\rho'' = \frac{E_p}{E_s} = \tan \Psi'' \exp (i\Delta'') \qquad (5.14)$$

The change in the state of polarization caused by reflection is given by the complex relative amplitude attenuation – the complex relative reflection coefficient –,

$$\rho = \frac{\tan \Psi'}{\tan \Psi''} \exp i(\Delta' - \Delta'') \qquad (5.16)$$

$$\rho = \tan \Psi \exp (i\Delta) \qquad (5.17)$$

Here $\tan \Psi$ represents the relative amplitude attenuation and Δ is the relative phase change upon reflection.

Δ and Ψ are the two reflection parameters and can be measured experimentally by ellipsometry. On the other hand, accoring to Drude (1889 - 91), the theory of metal optics gives ρ for a metal surface in contact with a transparent aqueous solution as a function of the refractive index of the solution n_s, the complex refractive index of the metal N_m, the angle of incident, ψ_o, and the wave length of light, λ:

$$\rho = \tan \Psi \exp (i\Delta) = f(n_s, N_m, \psi_o, \lambda) \qquad (5.18)$$

If the metal surface is covered with a film, ρ is then given as

$$\rho = \tan \Psi \exp (i\Delta) = f(n_s, N_f, N_m, d, \psi_o, \lambda) \qquad (5.19)$$

where N_f is the complex refractive index of the film and d is the film thickness. At constant ψ_o and λ, therefore, becomes a function of the optical property (N_f and d) of the film, provided that n_s and N_m are known.

The complex refractive index may be formulated for the metal

$$N_m = n_m - ik_m \tag{5.20}$$

and for the film

$$N_f = n_f - ik_f \ , \tag{5.21}$$

where n_m and n_f are the refractive indexes, and k_m and k_f are the extinction indexes. If the film is optically transparent, k_f vanishes and the index is then given by n_f which is a real number.

In the case of absence of any surface films, it is evident from the above equation that the refractive index n_m and the extinction index k_m of the metal can be estimated from the two reflection parameters Δ and Ψ , provided that the angle of incidence ψ_o, the wave length λ , and the refractive index n_s of the solution are known. In the case of presence of a surface film, however, the two parameters Δ and Ψ are not sufficient to determine straightforward the three unknowns, the complex refractive index of the film $n_f = n_f - ik_f$ and the film thickness d, even if n_s, N_s, N_m, ψ_o and λ are known. In the latter case, therefore, the trial-and-error method has to be employed and therefore large amounts of computation is usually required to estimate n_f, k_f and d. For this computation a Fortran computer program (1971) has been developed in our laboratory, which makes it possible to calculate not only the theoretical reflection parameters

(Δ and Ψ) as a function of the optical constants of the metal substrate and the surface film, the film thickness, and the angle of incidence, but also the optical constant and thickness of the surface film within a specified experimental error by comparing the calculated reflection parameter with the ellipsometrically measured reflection parameters.

The ellipsometer we used (Fig. 5-38) is one of the standard type with a polarizer and a compensator (quarter-wave-quartz plate) placed on the side of incident beam and an analyzer on the side of reflected beam. The polarizer and analyzer are Glam-Thompson prisms mounted in divided circles by which rotations can be measured within the accuracy of 20' (1/180 deg) in angle.

The light source consists of a mercury arc lamp, a pin-hole collimator, an interference filter, and two lenses. It emits a collimated, monochromatic beam of light, $3 \sim 5$ mm in diameter and 5461 Å in wavelength, which is one of the prominent lines of the Hg-discharge spectrum. The light beam goes through the polarizer which makes the light plane-polarized and the compensator which changes the polarization to elliptical before incidence on the surface to be examined. Upon reflection, the light turns again into plane-polarized, provided that azimuthal setting of the polarizer is properly made so as to meet the optical requirements that depends on the optical property of the surface being examined. The analyzer can now measure the azimuth of plane-polarization

of the reflected light with the aid of a photomultiplier in the last unit of ellipsometer.

Thus, measurements in ellipsometry are made of the azimuths of the polarizer and analyzer at which extinction of the reflected light after passing through the analyzer is observed: These measured azimulths of the polarizer and analyzer will be denoted herein by P and A.

From the measured values of P and A it is straightforward to calculate a pair of reflection parameters, Δ and tan Ψ, with the aid of the following equations derived theoretically:

$$\cot(\pi - \Delta) = \tan 2P / \sin \delta_k \tag{5.22}$$

$$\tan \Psi = \tan \ell \tan A \tag{5.23}$$

$$\cos 2\ell = \cos 2P \cos \delta \tag{5.24}$$

where δ_k is the phase shift given by the compensator. If the compensator gives the phase difference exactly equal to a quarter wave, i.e. $\delta_k = \pi/2$, then we obtain

$$\Delta = 2P + 90^{\circ} \tag{5.25}$$

$$\Psi = A \tag{5.26}$$

In this simplest case, therefore, the azimuths of the polarizer and analyzer correspond to the relative phase change Δ and the relative amplitude attenuation tan Ψ, respectively.

Since P and A are directly related with Δ and Ψ in the above equation, we can make a computor program for ellipsometry in terms of P and A instead of using Δ and Ψ. It is such a computor program that we have developed and used for various ellipsometric calculations in our laboratory.

One of the cells we have used for simultaneous measurements of ellipsometry and electrochemical polarization (Fig. 5-39) is a glass vessel of 100 ml capacity connected to a 2000-ml solution reservoir, and consisted of a gas bubbler, a platinum counter-electrode 5 cm^2 in area, a Luggin capillary leading to a saturated calomel electrode, a specimen holder adjustable in position through a spherical joint, and a rubber tube on top of the cell, and two optical plate-glass windows 1.5 mm thick and 20 mm in diameter fixed at an angle of $118^{\circ}50'$.

Ellipsometry has been applied by Sato and his coworkers (1971-74) to the measurement of the passive film formed on iron in neutral solution. In borate buffer solution at pH 8.42 the passive dissolution current of iron is virtually zero (Fig. 5-40), and a film-free surface is obtained by cathodic reduction of passive iron. Ellipsometric measurements of the iron surface during a cycle of anodic one-hour oxidation of iron at a passivity potential followed by cathodic galvanostatic reduction of the anodically oxidized iron reveals the formation and reduction of a passive oxide film (Fig. 5-41). At the end of the oxidation-reduction cycle both P and A return to their original value corresponding

to the oxide-free surface of iron.

In this solution at pH 8.42 the cathodic reduction gives an oxide-free surface but the current efficiency for the cathodic reduction is not 100% but about 80%. From further experiments we have found that the passive oxide films can be dissolved by galvanostatic reduction in a de-aerated borate buffer solution at pH 6.35. During the cathodic reduction at pH 6.35 the reaction

$$Fe_2O_3 + 6H^+ + 2e \rightarrow 2Fe^{2+} + 3H_2O \qquad (5.27)$$

proceeds at 100% current efficiency and hence no other reactions occur that might cause the film composition to change (Fig. 5-42). This means that the passive films is dissolved layer by layer without producing any change in ints composition during the reduction, if we use the borate solution of pH 6.35 and the cd of about 5 μ A/cm^2. It is also found from the slope of $W_{Fe} - Q_c$ curve (the amount of iron dissolved from the film versus the amount of cathodic charge passed) that the valency of iron ions in the film iS Fe(III), i.e. ferric oxide or hydroxide.

The change in ellipsometric parameters P and A during the cathodic reduction of the film in this solution is plotted to illustrate a P - A curve which consists of two straight lines (Fig. 5-43), indicating that the film is bilayered. Computer calculation gives the best fit between

the measured P - A curve and a theoretical curve for the removal of 30 Å of an outer layer with the refractive index

$$II^{N}_{f} = (1.8 \pm 0.1) - (0.1 \pm 0.05)i \qquad (5.28)$$

followed by the removal of 23.5 Å of an inner layer with the refractive index

$$I^{N}_{f} = (3.0 \pm 0.1) - (0.5 \pm 0.1)i. \qquad (5.29)$$

In this iterative calculation the range of refractive index for the film has been limited in $n = 1.5 \sim 3.5$ and $k = 0.0 \sim 1.0$, within which all the refractive indices of iron oxides in the literature are found.

By using the above refractive indices the film thickness can be estimated as a function of cathodic charge passed during the cathodic reduction at pH 6.35 of the passive film formed on iron in a borate solution of pH 8.42 (Fig. 5-44). From the W_{Fe} versus Q_c and L versus Q_c curves, the relation between the film thickness L and the amount of iron in the film $W^{T}_{Fe} - W_{Fe}$ is obtained, giving the iron density 32.9 ng/Å cm^2 to the inner layer and 14.6 ng/Åcm^2 to the outer layer (Fig. 5-45). In terms of the iron density in the layer, the inner layer is close to γ-Fe_2O_3, which may contain water to the limit $Fe_2O_3 \cdot 0.2\,H_2O$, and the outer layer appears to be a hydrous iron(III) oxide containing water more than $Fe_2O_3 \cdot 1.8\,H_2O$.

The inner layer thickness increases nearly linearly with potential, while the outer layer is almost constant except for the film formed at potentials less noble than the Flade potential (Fig. 5-46). The intercept of the inner layer thickness versus potential curve at zero film thickness comes close to the equilibrium potential of the following reaction,

$$2Fe + 6H_2O \rightleftharpoons \gamma\text{-}Fe_2O_3 + 6e \qquad (5.30)$$

$$E_o = -0.015 - 0.059\ pH \quad V\ nhe$$

$$= -0.505 \quad V\ nhe \quad at\ pH\ 8.42. \qquad (5.31)$$

Since the outer layer thickness is nearly independent of potential and since the inner layer thickness is a linear function of potential, it is likely that most of the over-voltage occurs in the inner layer. The average field strength in the inner layer is

$$(\Delta E/\Delta L) = (5.60 \pm 0.45) \times 10^6\ V/cm. \qquad (5.32)$$

It should be noted that the film composition described in this section is that of the passive film formed on iron in neutral borate solutions. It has later been found that the film composition and layer structure are dependent on the environmental solution, particularly anions in the solution, in which the film has been formed.

6. DISSOLUTION OF PASSIVE FILMS

6.1. Dissolution in Steady States

The dissolution of passivated metals proceeds through the passivating film;

$$M(\text{metal}) \rightarrow M^{2+}(\text{in the film}) + 2e, \qquad (6.1)$$

$$M^{2+}(\text{in the film}) \rightarrow M^{2+}(\text{aqueous solution}). \qquad ...(6.2)$$

In the steady state the ionic current through the film is equal to the film dissolution current across the electrified double layer (simply the Helmholtz layer) at the film/solution interface (Fig. 6-1). The rate of film dissolution is controlled by the Helmholtz layer potential difference Φ_H;

$$j_d = j_d^o \exp\left(\frac{\alpha z F \Phi_H}{RT}\right) \qquad (6.3)$$

where α is the ionic transfer coefficient.

Φ_H can be related to the electric field $E_F (= \Delta\Phi/L)$ in the film if no electronic surface states exist on the interface. From the equation of electrostatic inductions $E_F \epsilon_F = E_H \epsilon_H$, one obtains

$$\Phi_H = E_H \delta = E_F \delta \ (\epsilon_F/\epsilon_H) \qquad (6.4)$$

where E_H is the electric field in the Helmholtz layer of thickness δ, and ϵ_F and ϵ_H are the dielectric constants.

In what follows, we simply assume $\delta \approx 0.5$ nm and $\epsilon_F/\epsilon_H \approx 1$ to estimate Φ_H from the existing data of E_F, and illustrate the dissolution current j_d found in the literatures for iron and nickel as a function of Φ_H.

The log j_d - Φ_H curves thus estimated from experiments for iron in acid solutions (Sato, 1976) and nickel in a neutral solution (Sato, 1976), fit well in the rate equation derived above, indicating that the film dissolution is an electrochemical reaction occurring at the film/solution interface (Fig. 6-2). Assuming $\alpha \approx 0.5$, we estimate the transferring ionic charge $z \approx 3$ for iron and suggest the following mechanism,

$$Fe^{3+}(\text{oxide}) \rightarrow Fe^{3+}(\text{solution}). \qquad (6.5)$$

For nickel the estimated z is much less than 1 so that at simple mechanism similar to iron may not be valid, presumably because of the influence of potential and space charge on the dissolution site density and/or because of the electronic surface states at the film/solution interface affecting the distribution of potential.

An alternative approach has been made by Vetter (1955) who assumed the Helmholtz layer potential difference Φ_H to be determined by the oxygen reaction in equilibrium at the film/solution interface in the steady state,

$$H_2O_{aq} = O^{2-}(\text{oxide}) + 2H^+_{aq}, \qquad (6.6)$$

and obtained the rate equation,

$$\log j_d = - \alpha z \text{ pH} + \text{constant}, \qquad (6.7)$$

which agreed with the experiments for iron in acid solution (Fig. 6-1). Similarly, Vetter (1963) also explained the potential-dependent dissolution current of passive nickel by assuming a non-stoichiometric oxide film with the rate equation being

$$\log j_d = K \log a_o(\text{ox}) - \alpha z \text{ pH} + \text{constant}, \qquad (6.8)$$

where $a_o(\text{ox})$ is the activity of oxygen ion in the outermost layer of the film. If a_o increases with potential, then j_d also increase with potential. Essentially, no difference exists between Vetter's approach and ours, both emphasizing the role of Φ_H on the film dissolution.

6.2. Dissolution in Non-Steady State

It was recently noted that the dissolution rate of the passive film on iron in non-steady states was not equal to the potential-independent, steady state dissolution rate (Fig. 6-3). This is the fact which rules out the conventional interpretation of passive metal dissolution based on the

simple chemical dissolution of metal oxide. The non-steady state dissolution rate of passive iron is not constant but increases with increasing anodic current applied.

Under non-steady state conditions, two different electrochemical reactions occur at the film/solution interface; one is the iron ion transfer into the solution, Fe^{3+}(oxide → Fe^{3+}_{aq}, and the other is the oxygen ion incorporation into the film, $H_2O_{aq} \rightarrow O^{2-}$(oxide) + $2H^+_{aq}$. The electrochemical kinetics gives the rate equation $j_d = j_d^o \exp(3\alpha F\Phi_H/RT)$ for the former, and $j_\ell = j_\ell^o \exp(2\alpha' F\Phi_H/RT)$ for the latter. Accordingly, we obtain after Vetter (1973),

$$2\alpha' \log j_d = 3\alpha \log j_\ell + \text{constant}, \qquad (6.9)$$

The experimental results by Heusler (1968) and by Vetter and Gorn (1973) appear to fit in the above equation (Fig. 6-4 and 6-5).

It is also possible to derive from the previously given equations a linear relationship between the logarithm of ionic current j through the film and the logarithm of dissolution current j_d,

$$\frac{\epsilon_H B}{\epsilon_F \delta} \log j_d = \left(\frac{\alpha zF}{RT}\right) \log j + \text{const.} \qquad (6.10)$$

This equation also appears to fit in the experimental results for iron (Fig. 6-6). The dissolution current of passive

aluminum in acid and neutral sulphate solutions also shows a linear curve in log j_d - log j plot and, alternatively, in log j_d - log j plot.

The above two equations appear to fit equally in the experimental results (Fig. 6-7).

It is fairly certain from the above that, whatever the detailed mechanism, the dissolution rate of the passivating barrier layer on metal under steady and non-steady conditions is a function of the Helmholtz layer potential difference at the film/solution interface. This conclusion is of importance in understanding the passivity and also in developing the general theory to be described later.

7. THEORY OF PASSIVITY

7.1. General Theory

Many passivity theories have so far been presented in the literatures all of which fall into the categories of adsorption theory and polyatomic three-dimensional oxide theory. The divergence in existing theories has recently been made consistent into a general theory offered by Sato (1976). In the following we discuss his theoretical approach to the general passivity behaviour of metals.

As has been described, the potential difference between the metal and the solution plays a decisive role on the anodic metal dissolution. If no film exists on the surface, the potential difference is located across the electrified double layer (simply the Helmholtz layer) separating the metal phase by about 0.5 nm from the closest plane of approach of hydrated ions (the outer Helmholtz plane). The formation of a thin film of monoatomic or polyatomic oxide on the surface exerts great effects on the electrified double layer structure changing an initial single Helmholtz layer to at least a bilayered structure consisting of a thin film formed and an Helmholtz layer which is now located at the film/solution interface. Consequently, the metal ion to dissolve must move through the bilayered electric double layer *via* at least three consecutive reactions comprizing the metal ion transfer from the metal phase into the surface film, the ionic diffusion in the film, and the metal ion

transfer and hydration across the Helmholtz layer at the film/solution interface. This last reaction is in fact the dissolution of the film, and it is this last reaction that determines the rate of the overall reactions of metal dissolution in the steady state.

The potential difference Φ_H across the Helmholtz layer at the film/solution interface is in general a complicated function of the overall potential difference Φ_M between the metal and the solution. In the simple case of a thin intrinsic semiconductor film, having no electronic surface state, Φ_H may be related to Φ_M as follows (Kuznetsov, 1964);

$$\Phi_H = \Phi_M \left(1 + \frac{L}{\delta} \frac{\epsilon_H}{\epsilon_F}\right)^{-1} \qquad (7.1)$$

where L is the film thickness, δ the Helmholtz layer thickness, and ϵ_F and ϵ_H are respectively the dielectric constants of the film and the Helmholtz layer. If no surface film exists, $\Phi_H = \Phi_M$.

From the above equation, it is obvious that Φ_H/Φ_M decreases with increasing thickness of the passive film (Fig. 7-1). We assume $\delta \approx 0.5$ nm and $\epsilon_H \approx \epsilon_F$, then the potential difference Φ_H can be calculated as a function of Φ_M (Fig. 7-2). Several possible $\Phi_H - \Phi_M$ curves are also shown for the metal surfaces having no film, a monatomic oxygen film, and an oxide film growing as a function of Φ_M at different growth rates. It appears that the adsorption of monoatomic oxygen

layer does decrease the potential difference Φ_H and hence does decrease the anodic dissolution rate, which in some cases may lead to passivation. The dissolution rate, however, will increase with increasing the metal potential Φ_M unless the adsorbed layer grows to a polyatomic thickness. In comfirming with this conclusion, the sulphide monolayer passivation of mercury in sulphide ion solutions gives rise to a potential-dependent dissolution current (Fig. 7-3).

The general theory also predicts that even if a passivating film exists the passive dissolution current will increase, remain constant, or decrease depending on the relationship between the film thickness and the potential Φ_M; the potential-independent dissolution current may result from a linear relation between L and Φ_M. The $\Phi_H - \Phi_M$ curve calculated from experimental results for iron in the passive state gives a constant Φ_H independent of Φ_M in agreement with the potential-independent dissolution current (Fig. 7-4), while that of nickel shows an increasing Φ_H with increasing Φ_M in agreement with the potential-dependent passive dissolution current (Fig. 7-5).

Beside the general theory which is rather phenomenological, there are three molecular mechanisms that cause passivation; electron-configuration-induced adsorption passivity, ionic space-charge-induced passivity, and ionselective fixed charge-induced passivity.

7.2. Electron-Configuration-Induced Adsorption Passivity

Uhlig (1958) stated the important role played by chemisorption of oxygen in the occurrence of passivity of metals and alloys. The passivefilm, when consisting of chemisorbed oxygen, is favored by those transition metals with uncoupled d electrons with which adsorbed oxygen can interact. The assumed number of uncoupled electrons per atom of transition metal at any given atom percent in alloys was approximated by,

$$v_g - (v_g - v_m) \frac{at.\%}{100} \qquad (7.2)$$

where v_g are vacancies per atom in the gas, and v_m are vacancies in the solid. The donor electrons from monotransition metal like alloyed Cu, Al, and Zn in the Cu-Ni series were found empirically to equal 0.8 per s electron (Uhlig, 1971). In other words, 80% of an s electron from a donor component was found to be coupled with electrons from alloyed Ni. For transition metals, the donor electrons and d electrons that are coupled with neighboring atoms of the solid. The number of donor d electrons per atom is given by,

$$(v_g - e_p - v_m) \frac{at.\%}{100} \qquad (7.3)$$

where e_p is the number of electrons per atom coupled with adsorbed oxygen of the passive film.

In iron-chromium alloys, the more passive component of chromium is the electron acceptor and iron is the donor. From the electron configuration of Cr($3d^5$ 4s), $v_g = 5$, and $v_m = 0.4$. Then the uncoupled electrons per Cr atom equal 5 - (5 - 0.4) at.% Cr/100 = 5 - 0.046 at.% Cr. For iron Fe($3d^6 4s^2$), $v_g = 4$, $v_m = 2.2$, and e_p is arbitraily assumed equal to 1. The donor electrons per Fe atom then equal (4 - 1 - 2.2) at.% Fe/100 = 0.008 at.% Fe.

To obtain the critical percentage of Cr in the binary alloy, the number of available uncoupled electrons in Cr is set equal to the number of available electrons from Fe or

$$(5 - 0.046 \text{ at.\% Cr}) \text{ at.\% Cr} = 0.008(\text{at.\% Fe})^2$$
$$= 0.008(100 - \text{at.\% Cr})^2 \quad (7.4)$$

or at.% = 13.6. This value is comparable with the observed 12.7 at,% Cr (12 wt.%), which is well known value for corrosion resistance minimum.

For Cu-Ni alloys, the critical composition reparating a filled d band from an unfild band comes at about 4% Ni, which is the composition range separating alloys showing a passive current from those that do not (Fig. 7-6).

This model is concerned only with the oxygen adsorption on metals and refers nothing of the kinetic stability of the passive films.

7.3. Ionic Space-Charge-Induced Passivity

Fromhold and Kruger (1973) and Fromhold (1976) proposed

the space-charge induced passivity model that the ionic current in the barrier layer can be reduced by orders of magnitude by the ionic space charge within the layer, as compared with the corresponding rate expected in the absence of appreciable space charge. Their approach is based on the field-assisted ion conduction current and the ionic space charge is taken into account using Poisson's equation. The numerical evaluation based on a computer-controlled iterative techniques was carried out to reveal the effects of the space charge on the ionic current for the passive film on iron. The computed ionic current in the presence and absence of the ionic space charge as a function of the film thickness at constant potential reveals the space charge effect, which can be noted to be an order of magnitude at a thickness of 3 nm ($\approx$10 monolayers) and increases with increasing thickness of the film, reaching a value of two orders of magnitude or so at 10 nm (Fig. 7-7).

The space charge effects are of course dependent on the charged ionic defect concentration. In general they are important whenever the charged defect density exceeds 10^{18} defects/cm^3, while the homogeneous field limit is a good approximation whenever the charged defect density is lower than 10^{16} defects/cm^3.

This mechanism, dealing with only the ionic current in the film, is not directly concerned with the dissolution rate of the barrier film which eventually determines the

steady state dissolution rate of passive metals. The ionic space charge may affect to the dissolution reaction in two ways; one is the Helmholtz double layer potential difference Φ_H and the other is the dissolution site density. It is anticipated that if the ionic space charge density in an outermost layer of the film increases with the potential Φ_M, the passive dissolution current will increase with potential. This is considered to explain the potential-dependent passive dissolution current of nickel, as suggested elsewhere (Sato, 1976).

7.4. Bipolar Fixed Charge-Induced Passivity

Sakashita and Sato (1977) suggested recently that the ion-selectivity due to the fixed charge in hydrated oxide membranes on metals plays an important part in producing passivity, and proposed the bipolar fixed charge-induced passivity model that a bipolar film consisting of an anion-selective layer on the metal side and an cation-selective layer on the solution side, which is inherently capable of rectifying ionic migration, retards the ionic current in the anodic direction (Fig. 7-8). In fact the rectification of ionic current was found in a hydrous nickel(II) oxide membrane bipolarized with the positive fixed charge Ni^{2+} and the negative fixed charge WO_4^{2-} (Fig. 7-9). The anodic current is obviously reduced in the bipolarized membrane, as compared with the corresponding current in the absence of the bipolarity.

Hydrated metal oxide membranes are either anion-selective with the positive fixed charge or cation-selective with the negative fixed charge; Hydrous iron(II), nickel(II) and chromium(III) oxide membranes are highly anion-selective in mono-monovalent electrolyte solutions while they are rather cation-selective in the presence of some multivalent anions in the solution (Sakashita et al. 1976-7). It is therefore very likely that hydrous oxide deposits on the metal surface in the presence of multivalent anions is bipolarized with an intrinsic anion-selective inner layer on the metal side and a cation-selective outer layer in which multivalent anions incorporate. The anodic bias voltage imposed with then causes dehydration of the deposit layer with hydrogen ions moving in the cation-selective layer toward the solution and with metal ions whose movement is retarded in the anion-selective inner layer, and eventually a dehydrated protective oxide film is formed on the metal surface (Fig. 7-10).

If the bipolarity is reversed, the dehydration of hydrous oxide deposits does not occur and a less protective hydrous oxide film continues growing under anodic bias conditions without producing the passive and almost dehydrated oxide film (Fig. 7-10). This ionic selectivity effect is suggested to provide the explanation for the curious nature of the occurrence of passivation in various metals and environmental solutions.

8. BREAKDOWN OF PASSIVE FILMS

8.1. Passivity Breakdown due to Aggressive Anions

When the solution contains aggressive anions, the passive film often locally breaks down and the pitting type of localized metal dissolution is initiated at the surface sites of film breakdown. The anodic polarization curve of passive metals such as zirconium and stainless steel in halide-containing solutions shows a steep increase of anodic current in the otherwise passive potential region as a result of chemical breakdown of passive films due to halide ions (Fig. 8-1).

The critical potential for pit initiation is called the pitting potential. It is a function of the nature and concentration of aggressive and inhibitive anions. Generally, the pitting potential is more positive (noble), the smaller the aggressive anion concentration and the greater the inhibitive anion concentration. There is, therefore, a critical concentration of aggressive ions for a given concentration of inhibitive anions, below which no pitting occurs in the passive potential region.

Sulphate ions are inhibitive against chloride-pitting of stainless steel, and shift the pitting potential in the anodic direction. Nitrate ions are also inhibitive, and are able to completely inhibit chloride-pitting to recover the passivity of stainless steel at more anodic passivating potentials (Fig. 8-2).

There exists an induction period for pit initiation after introduction of chloride to prepassivated metals at constant potential anodic to the pitting potential. Examples are illustrated showing the change in anodic current with time after introduction of chloride for passive iron in sulphuric acid and for passive stainless steel in sulphate solution (Fig. 8-3). As a general tendency, the induction period is shorter, the greater the overpotential exceeding the pitting potential.

8.2. Film Breakdown

During the induction period for chloride pit initiation in passivated iron, the passive film dissolution rate ocillates irregularly around a mean value which increases with increasing chloride concentration (Fig. 8-4). The ocillation continues to occur even after appearance of the pits. Such effects of chloride on the film dissolution occurs no matter whether the potential is above or below the pitting potential. The passive film is always breaking down and reparing in greater or lesser degree depending on the nature and concentration of anions in the solution. If the repair rate is not sufficient to prevent propagation of pits, the anodic pitting takes place. The pit initiation is therefore a process in which two competitive reactions of film breakdown and repair are involved.

The observations by McBee and Kruger (1971) for iron and by Paatsch (1975) for nickel showed that the property

of the passive film as measured optically changes in the presence of chloride (Fig. 8-5). Although the changes are subtle and can not presently interpreted, it is evident that chlorides influence the passive film itself.

Okamoto et al. (1975) measured the noise in the passive current of stainless steels in sulphuric acid solutions in the presence or absence of chloride (Fig. 8-6). In the range of noise frequency from 4Hz to 40 Hz, the mean square of the noise current does not depend on whether chloride ions are present or absent, whereas in the frequency range lower than 4 Hz the passive current noise represented by the root mean square values of noise voltage increases with time during the induction period of chloride-pit initiation. This is indicative of the breaking down and repairing of the passive film.

8.3. Film Breakdown Models

According to Kruger (1975), theoretical models that have been proposed to describe the events leading to passive film breakdown are classified into three groups; adsorbed ion displacement models, ion migration or penetration models, and chemomechanical models.

The first groups of models consider that breakdown occurs when a more strongly adsorbing damaging anion displaces the oxygen forming the passive film or that a small number of aggressive anions jointly adsorb to form a high energy complex on the surface of the passive film. The film of oxygen

monolayer adsorption is thus locally removed at the site of anion adsorption, or the passive polyatomic phase oxide film is made thinner at the site where adsorbing damaging anion readily remove the cation from the passive film lattice. When other anions are present, they can compete with the damaging anion for sites and inhibit breakdown.

The second group models assume the migration or penetration of aggressive anions through the passive film. The processes which involve ion migration or penetration can occur in a variety of ways, such as the pore mechanism in which preexisting pores or defects provide the penetration path, and the anion or cation vacancy mechanism in which a path of high ionic conductivity is created.

The last group models involve chemically induced mechanical disruption of the passive film. Stress in the passive film can arise for several reasons such as interfacial tension, electrostriction pressure, volume ratio of oxide and metal, hydration or dehydration, and impurities. According to Sato (1971), the electrostriction pressure and interfacial tension generate the pressure acting normal to the passive film which could exceed fracture strengths of the film and lead to the mechanical rupture of passive films.

7.4. Pit Generation Kinetics

The generation of pits in passive metals is a random phenomenon discrete in time and location on the surface, and hence may be regarded as a stochastic process (Shibata and

Takeyama, 1976). According to Sato (1976), the time interval, Δ , for chloride-pits successively breaking out in rotating stainless steel electrode scatters in such a manner as to satisfy the Markov restriction that the probability $P(\Delta t)$ for a pit to break out in a time interval greater than Δt after the preceding pit has opened is given by,

$$dP(\Delta t)/P(\Delta t) = - \lambda \, dt, \qquad (8.1)$$

and hence by

$$d \log P(\Delta t)/dt = - \lambda /2.3026, \qquad (8.2)$$

where λ is the pit generation intensity and equivalent to the pit generation probability for unit time at any time Δt (the probability of a pit opening to occur in the range of time $\Delta t \sim \Delta t +$ unit time). λ may or may not depend on Δt; Strictly, it is a function of Δt, but in a simple case it is often independent of Δt.

The relative frequency of pit breakdown for a time interval between Δt and $\Delta t + \delta t$ may be written as $N_{\Delta t \sim \Delta t + \delta t}/N_T$, where N_T is the total number of pits that appear during measurements. This relative frequency of pit breakdown can be determined as a function of Δt to obtain a histogram. This relative frequency is related to the probability $P(\Delta t)$ as follows,

$$P(\Delta t) = \frac{\sum_{\delta t = 0}^{\infty} N_{\Delta t \sim \Delta t + \delta t}}{N_T} \qquad (8.3)$$

which may be called the cumulative relative frequency.

For potentiostatic generation of pits in a rotating 18 Cr-8Ni stainless steel, the probability $P(\Delta t)$ estimated from a relative frequency histogram (Fig. 8-7) gives a linear relation between $\log P(\Delta t)$ and Δt (Fig. 8-8). Thus, we obtain

$$2.3026 \log P(\Delta t) = -\lambda \Delta t \qquad (8.4)$$

and λ is independent of Δt.

Pit generation intensity, for unit area of the surface decreases with decreasing potential (Fig. 8-9). In view of stochastic process, the critical potential for pit generation may be defined as the least noble potential at which the pit generation intensity is practically recognizable. Notice that the pit generation intensity depends on the area of the metal surface.

8.5. Stability of Pitting

According to Franck (1960), the active and passive states can not stably coexist on the same surface (all-or-nothing law). In the presence of aggressive ions, however, the active surface in growing pits is stable with the passive surface surrounding the pits. Such coexistence of two different states, from the viewpoint of irreversible thermodynamics, is possible only when certain transport processes are taking place to stabilize a heterogeneous pattern created on the surface.

Hisamatusu (1975) has suggested that the mass transport between the pit inside and the bulk of solution determins the stability of a growing pit. The transport equation is given by;

$$\Delta \Sigma C = \frac{j_w \cdot \gamma}{n F D} \; [\text{mol/cm}^3] \qquad (8.5)$$

where $\Delta \Sigma C = C_{pit} - \Sigma C_{out}$ denotes the total concentration difference for all ionic species between the solution within the pit and the solution outside the pit, n the metal ion valency, D the diffusion coefficient of metal ions, I_w the anodic dissolution current density at pit wall, and γ the pit mouth radius. He found experimentally that, independent of the pit radius, a growing pit was stable unless the total concentration difference $\Delta \Sigma C$ decreased below a critical value, $(\Delta \Sigma C)^*$, which was 1.8 m/cm^3 for 18Cr - 8Ni stainless steel in sodium chloride solution.

Essentially the same transport equation was presented by Pickering and Frankenthal (1972) and was modified by Galvale (1976), who emphasized the local acidification due to metal ion hydrolysis within the pit rather than the local concentration of salts.

Eq.(43) may also be applied to describing the critical condition for pit initiation. Substituting a Tafel equation $j_w = j_w^o \exp(\beta E)$ in the above equation leads to the critical potential for pit initiation,

$$E^* = \frac{1}{\beta} \ln \frac{nFD\ (\Delta\Sigma C)^*}{r^*\ j_w^o} \qquad (8.6)$$

where r^* is the size of pit-embryo, which was estimated to be about 10 $\sim$ 20 μm for stainless steels.

9. PASSIVITY OF IRON

9.1. Iron in Neutral Solutions

a) Anodic polarization curves.

b) Anodic dissolution in the active state.

c) Metal dissolution and film formation at low potentials.

d) Transpassive dissolution.

e) Anodic charge for the passive film.

f) Film thickness depending on the speed of passivation.

g) A cathodic reduction technique to analyze the film.

h) Transpassive film thickness.

i) Measurement of water in the film.

9.2. Depth-Analysis of Passive Film in Neutral Solution

a) Cathodic reduction of the film.

b) Ellipsometry during cathodic reduction.

c) Depth-profile.

d) Film composition depending on the history of film formatic

e) Film composition changing with time.

f) Conclusions.

The galvanostatic cathodic reduction technique employing appropriate solution and current density provides a depth profiling analysis of the passive film on iron.

The potential region of iron passivity in borate solution at pH 8.42 may be divided by the Flade potential into two regions, I and II, with which the passive barrier layer changes in composition and refractive index.

In region I, the barrier layer was an iron(II-III) mixed

oxide and its thickness for unit voltage at steady state was 1.54 nm/V (6.5×10^6 V/cm). In region II, it was an iron(III) oxide (probably γ-iron(III) oxide) with thickness 1.75 nm/V (5.7×10^6 V/cm).

Transpassivation caused the barrier layer to cease growing with rise of potential and to reduce its oxidized stage to less than $z_{Fe} = +3$.

The deposit layer, which was always formed on the barrier layer, was a hydrated iron(III) oxide (probably γ-FeOOH) and exhibited no significant composition change with potential, except for an absorption of iron(II) ions in region I.

There was a peak or a decrease in iron ion concentration at the barrier/deposit boundary in the depth profile of the film. At relatively less noble potentials the boundary absorbed excess iron ions, which were gradually replaced by iron ion vacancies as the potential was more noble.

It is the barrier layer alone that increased in thickness during the growth of the passive film in the potential region II.

9.3 Dependence of pH on Passive Films on Iron

a) pH-dependence of anodic dissolution.

b) pH-dependence of film thickness-potential curves.

c) Barrier layer determined by potential.

d) Deposit layer depending on pH and anion.

9.4. Ion Migration in the Barrier Oxide Film

a) Field-assisted ion migration

$$j = j_o \exp\left(B \frac{\Delta E}{L}\right) \qquad (9.1)$$

b) Kinetic parameters B and j_o

$$B = Zae/kT = 3.25 \times 10^{6} cmV^{-1} \quad (9.2)$$

$$j_o = 2.0 \times 10^{-14} A\ cm^{-2} \quad (9.3)$$

c) Ionic conductivity κ

$$\kappa = \{ \partial j/\partial(\Delta E/L) \}_{(\Delta E/L) \to 0} = j_o B \quad (9.4)$$

d) Diffusion constant D

$$D = \kappa kT/Z^2e^2C = j_o BkT/Z^2e^2C \quad (9.5)$$

$$C = 3.7 \times 10^{22} \text{ ions } cm^{-3} \quad (9.6)$$

e) Activation energy A^*

$$D = D_o \exp (A^*/RT) \quad (9.7)$$

f) Conclusion

The ionic current in the anodic barrier oxide layer on iron at the steady state in acidic phosphate solutions is a high field ion conduction and the classical rate equation, $i_a = i_{ao} \exp (B\Delta E/L)$, is hold.

The diffusion coefficient and the activation energy for diffusion of migrating ions in the barrier oxide layer at 25^oC are estimated to be $D = 3 \sim 5 \times 10^{-26} cm^2/sec$ and $A^* = 10 \sim 15$ Kcal/mol, respectively.

By comparing these two diffusion parameters with those of high temperature diffusion in iron oxides, it is suggested that the ionic current is carried by oxygen ions rather than iron ions in the anodic barrier oxide layer.

10. PASSIVITY OF NICKEL

10.1. Nickel in Acid Solutions

10.2. Nickel in Neutral Solutions

11. PASSIVITY OF CHROMIUM

11.1. Chromium in Acid Solutions

11.2. Chromium in Neutral Solutions

12. PASSIVITY OF COBALT

12.1. Cobalt in Neutral Borate Solutions

12.2. Cobalt in Acid Solutions

12.3. Cobalt in Alkaline Solutions

12.4. pH-Dependence of Passive Films on Cobalt

13. PASSIVITY OF STAINLESS STEEL IN ACID SOLUTION

13.1. Anodic Polarization Curve

13.2. Effect of Heat Treatment of Stainless Steels on Anodic Dissolution

13.3. Cathodic Reduction of Various Oxidants on Stainless Steels

13.4. Corrosion of Stainless Steel in Aerated 5 % H_2SO_4 Solution

13.5. Anodic Passivation and Chemical Passivation

13.6. Strauss Test

13.7. Huey Test

14. PASSIVITY OF IRON-BASE ALLOYS

14.1. Fe - Ni Alloys

14.2. Fe - Cr Alloys

14.3. Stainless Steels

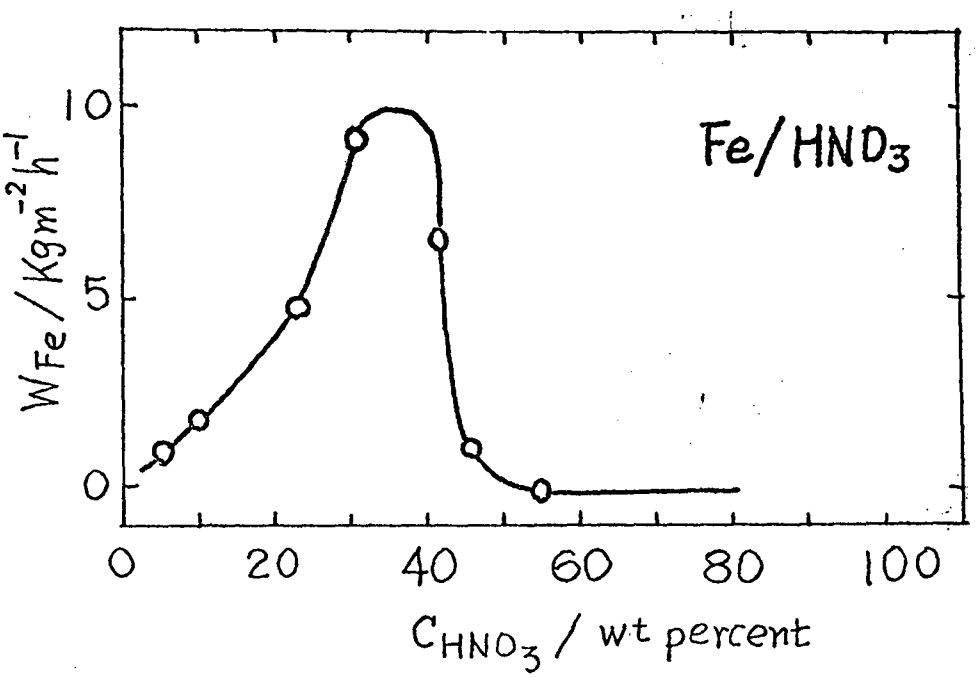

Fig. 1-1. Corrosion of iron in nitric acid solution as a function of HNO_3 concentration; passivation occurs above a critical concentration (Tomashov, 1966).

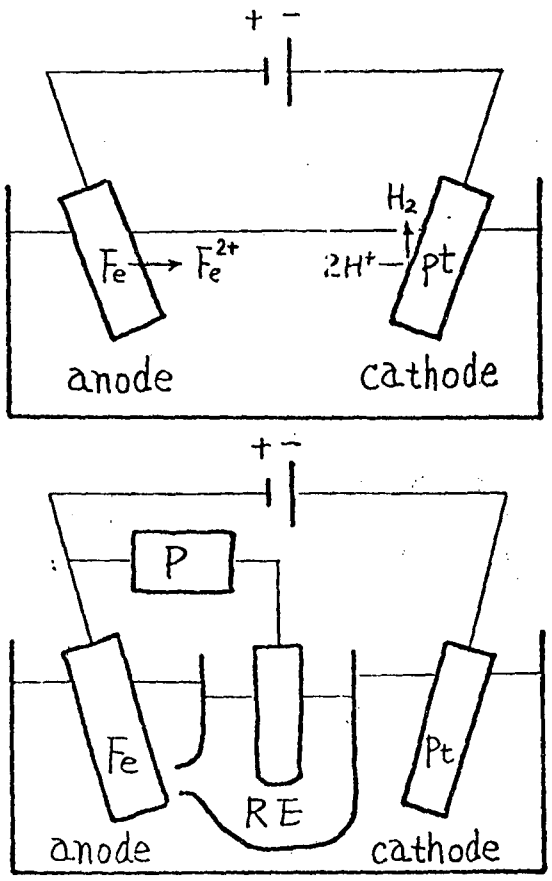

Fig. 1-2. Electrolytic cell to produce anodic passivity of iron and three electrode cell for measurement of anodic current-potential curve of iron.

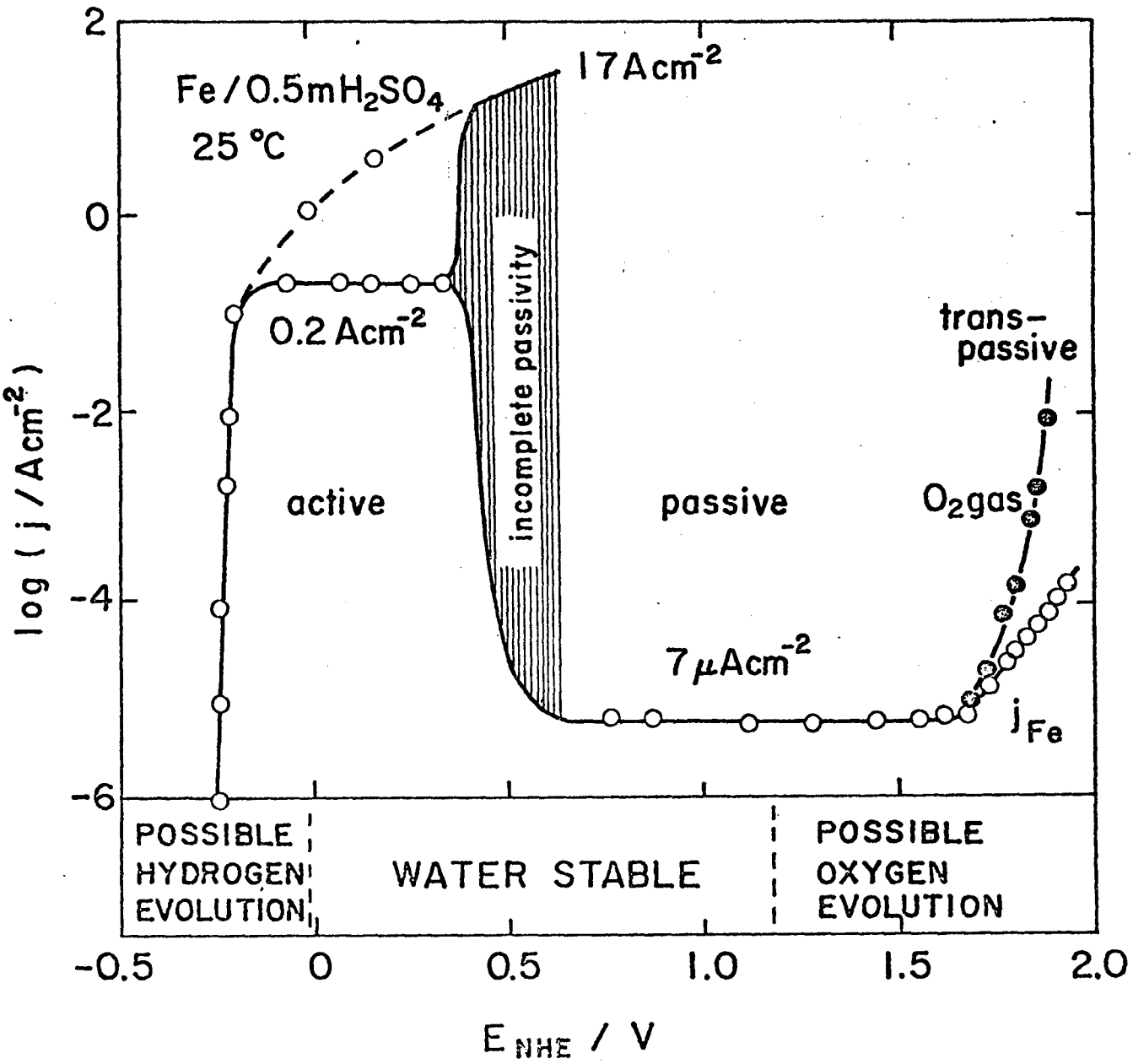

Fig. 1-3. Anodic current-potential curve of iron in 0.5 M H_2SO_4 solution (Franck and Weil, 1952 - 53).

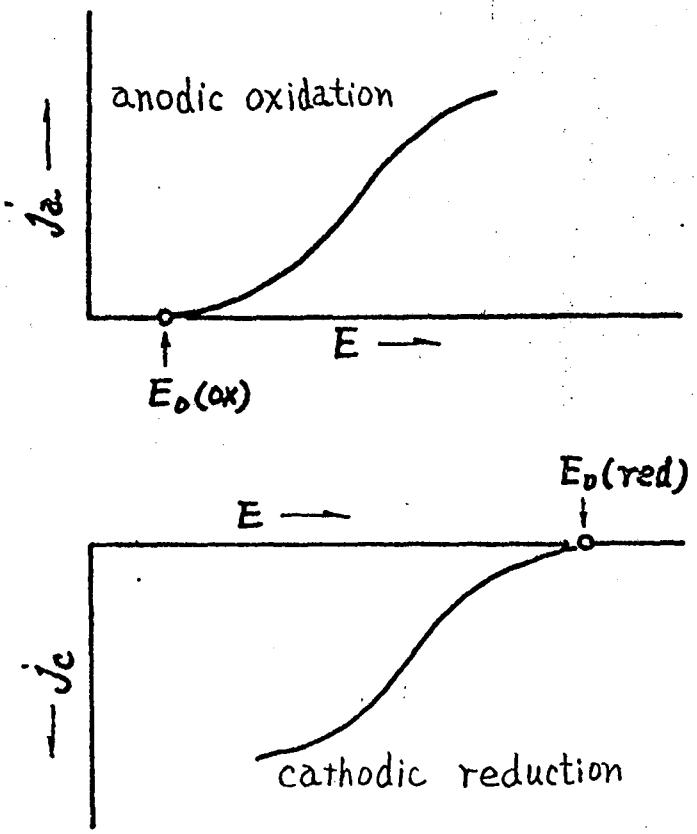

Fig. 1-4. Electrochemical reaction rates depending on the electrode potential; anodic oxidation rate j_a increasing with increasing potential and cathodic reduction rate j_c increasing with decreasing potential.

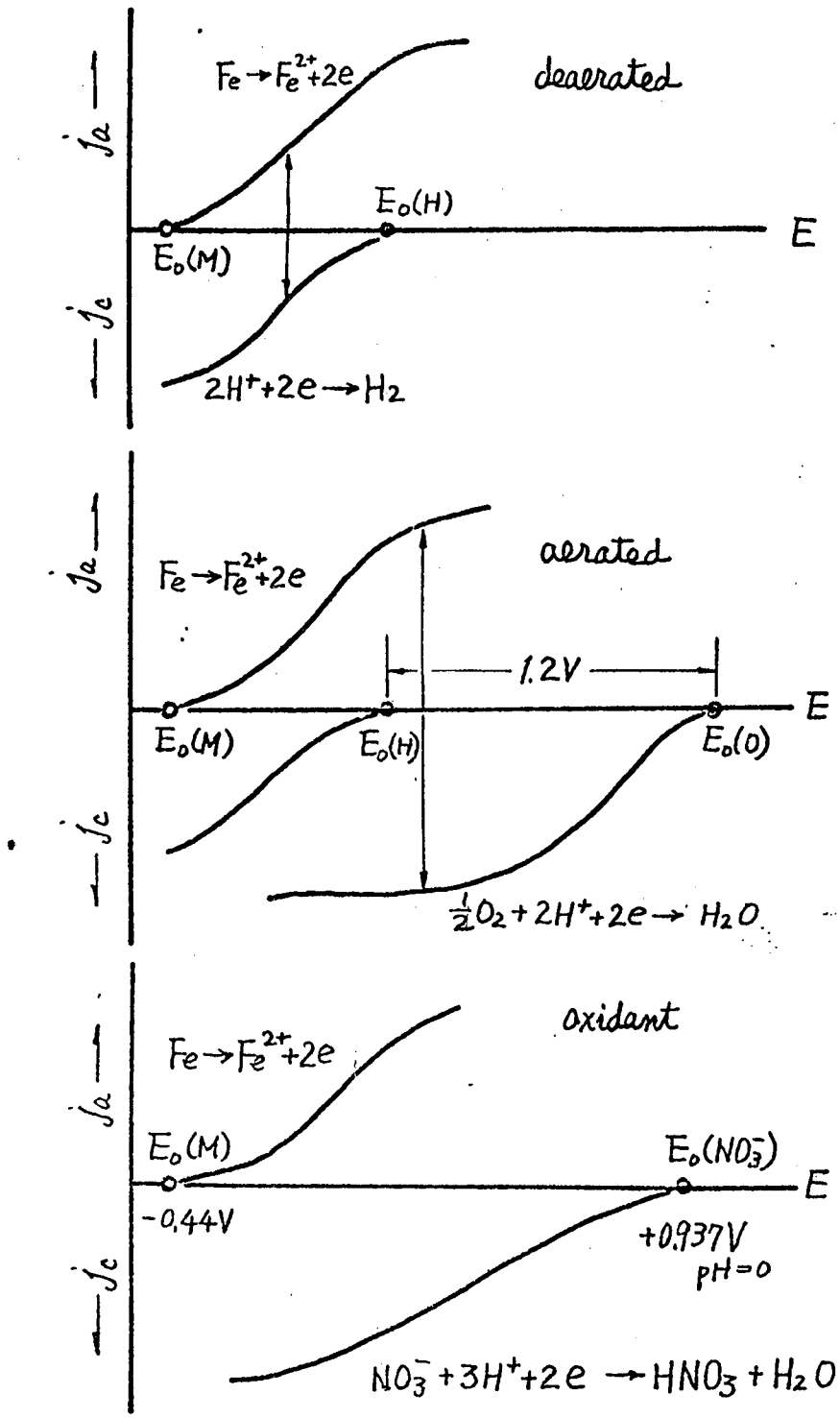

Fig. 1-5. Corrosion-balancing reactions and schematic anodic and cathodic reaction rate (current)-potential curves.

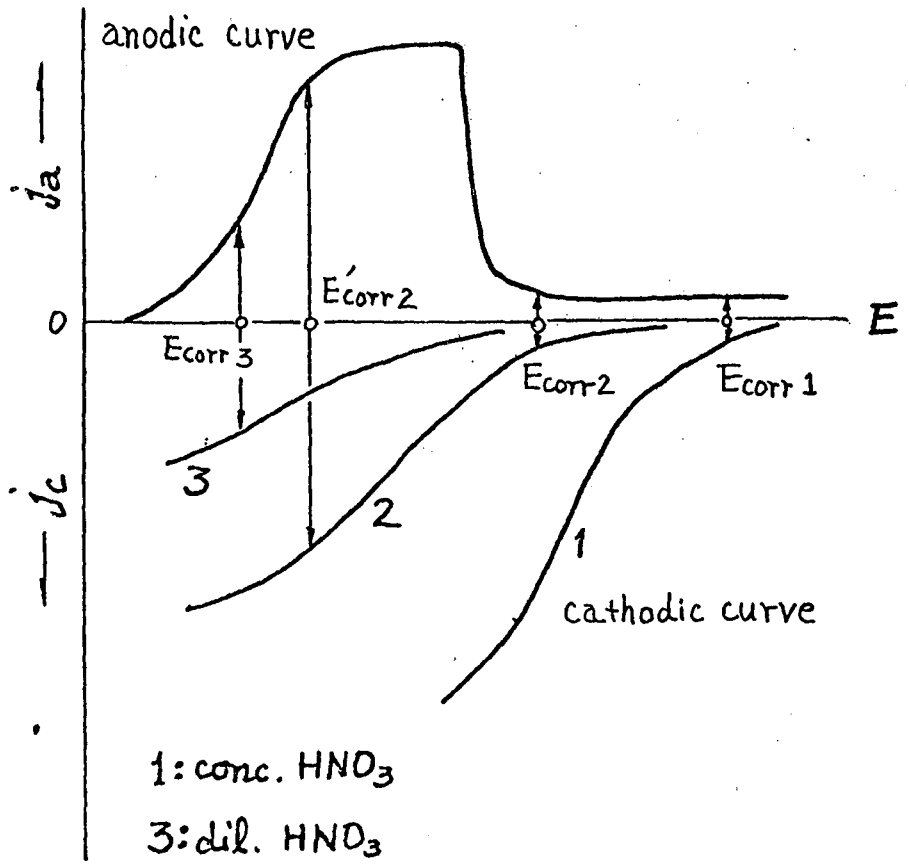

Fig. 1-6. Schematic anodic and cathodic polarization curves of iron in nitric acid of various concentrations; the balancing points represent the corrosion potential and current of iron.

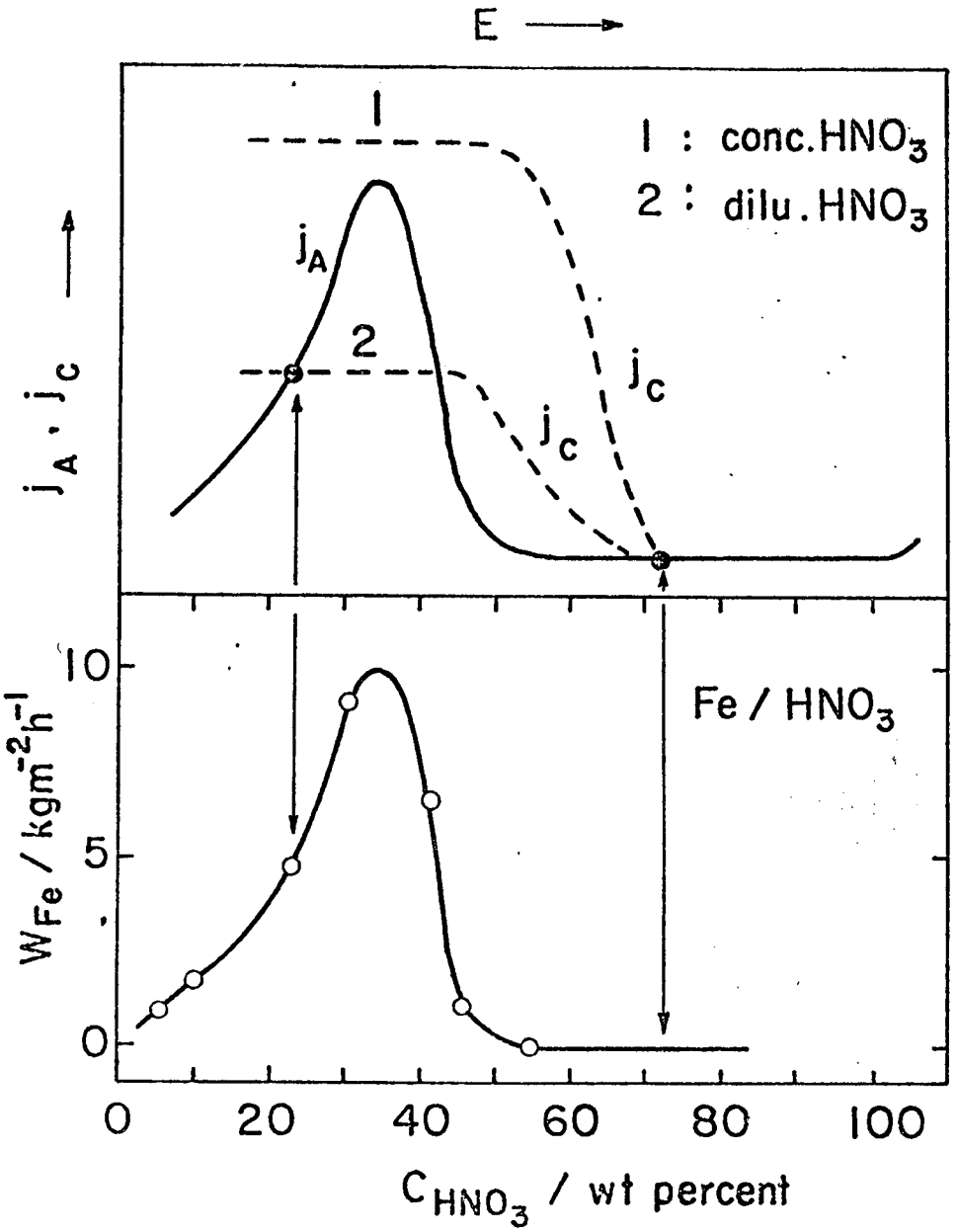

Fig. 1-7. Corrosion of iron in nitric acid determined by the electrochemical balancing of anodic polarization curve of metal dissolution and cathodic polarization curve of nitric acid reduction.

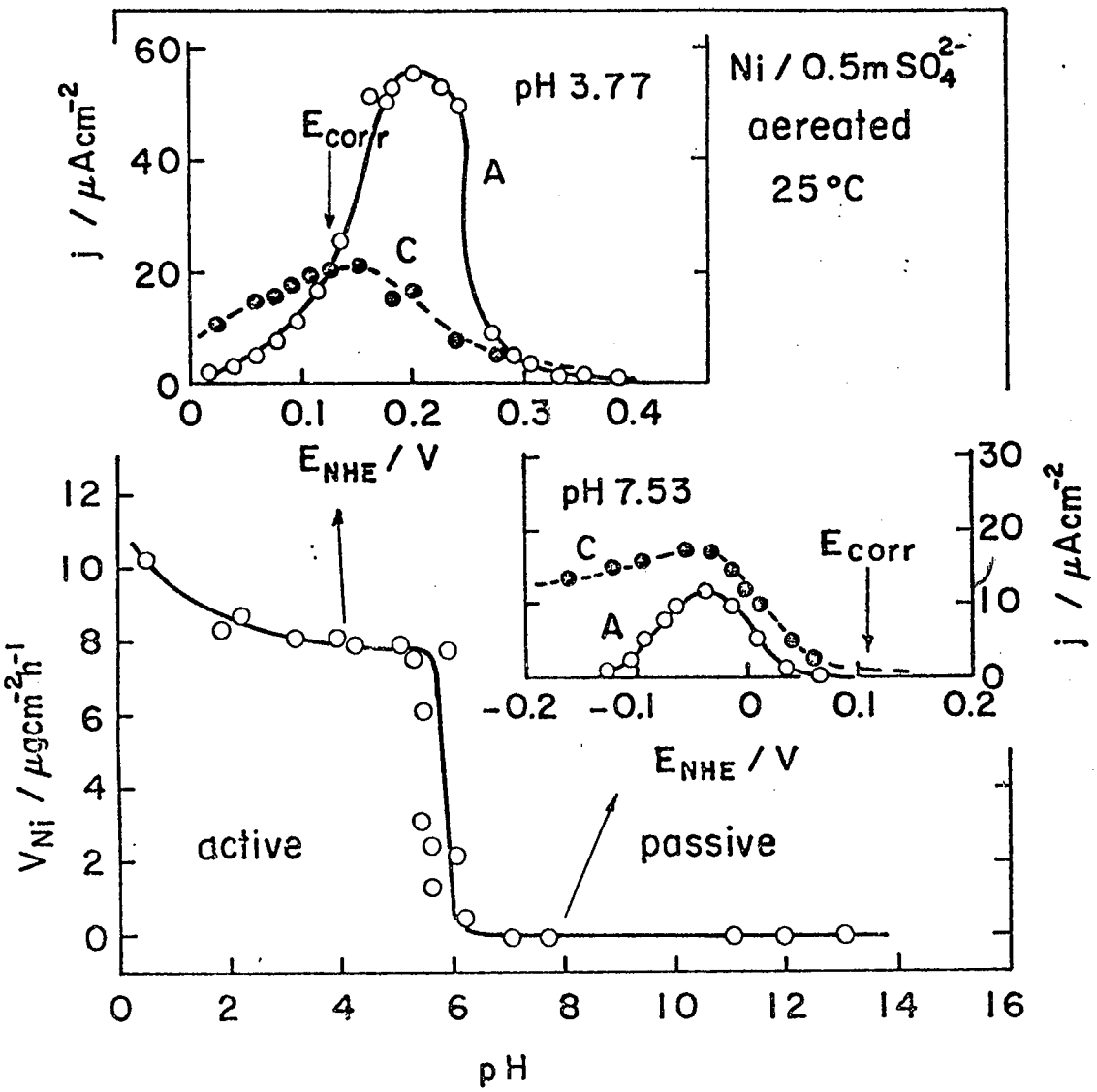

Fig. 1-8. Corrosion of nickel in aerated sulphate solutions determined by the electrochemical balancing of anodic polarization curve of nickel dissolution and cathodic polarization of oxygen reduction (Sato, 1959).

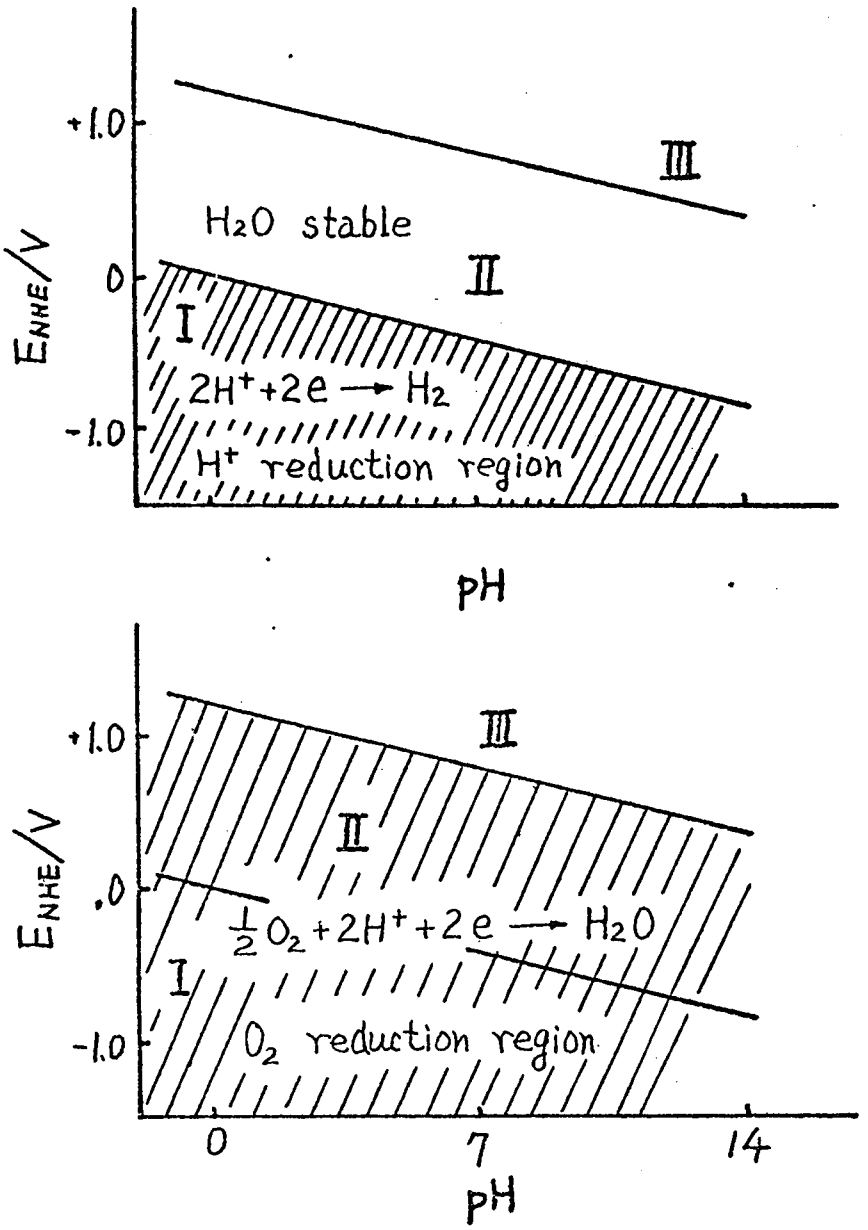

Fig. 1-9. Thermodynamic stability of H_2O, H^+ and O_2 in the potential-pH diagram.

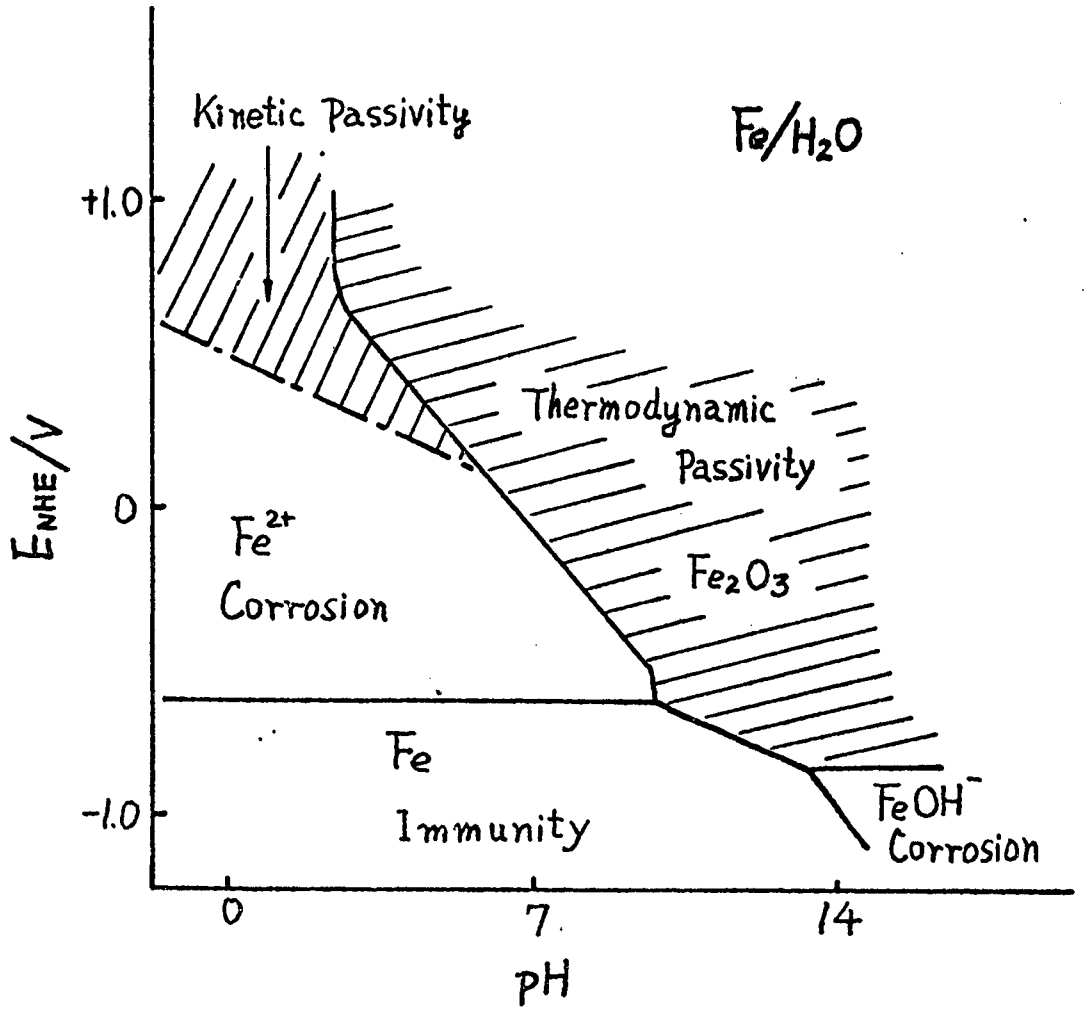

Fig. 1-10. Simplified potential-pH diagram for iron in aqueous solution.

Table 1. General Thermodynamic Stability of Metals and Their Standard Electrode Potentials

Group No.	General thermodynamic stability	Electrode reactions*	E^0, V
1	Metals of high thermodynamic instability (active). Can corrode even in neutral aqueous media which do not contain oxygen or oxidizers.	Li−e	−3.045
		Rb−e	−2.925
		K−e	−2.925
		Cs−e	−2.923
		Ra−e	−2.92
		Ba−e	−2.90
		Sr−e	−2.89
		Ca−2e	−2.87
		Na−e	−2.714
		La−3e	−2.52
		Mg−2e	−2.37
		Am−3e	−2.32
		Pu−3e	−2.07
		Th−4e	−1.90
		Np−3e	−1.86
		Be−2e	−1.85
		V−3e	−1.80
		Hf−4e	−1.70
		Al−3e	−1.66
		Ti−2e	−1.63
		Zr−4e	−1.53
		Ti−3e	−1.21
		V−2e	−1.18
		Mn−2e	−1.18
		Nb−3e	−1.1
		Ta−Ta_2O_5	−0.81
		Zn−2e	−0.762
		Cr−3e	−0.74
		Ga−3e	−0.53
		Fe−2e	−0.440
2	Metals thermodynamically unstable (active). Stable in neutral media in the absence of O_2; in acid media they can corrode in the absence of O_2.	Cd−2e	−0.402
		In−3e	−0.342
		Tl−3e	−0.336
		Mn−3e	−0.283
		Co−2e	−0.277
		Ni−2e	−0.250
		Mo−3e	−0.2
		Ge−4e	−0.15
		Sn−2e	−0.136
		Pb−2e	−0.126
		W−3e	−0.11
3	Metals of intermediate thermodynamic stability (semi-noble). Are stable in acid and neutral media in the absence of O_2 and oxidizers.	Bi−3e	+0.226
		Sb−3e	+0.24
		Re−3e	+0.30
		As−3e	+0.30
		Cu−2e	+0.337
		Hg−e	+0.789
		Ag−e	+0.799
		Rh−3e	+0.80
4	Metals of high stability (noble); do not corrode in neutral media in the presence of O_2. Can corrode in acid media in the presence of O_2 or oxidizers.	Pd−2e	+0.987
		Ir−3o	+1.000
		Pt−2e	+1.19
5	Metals of complete stability. Stable in acid media in the presence of O_2. Can dissolve in complex-forming solutions in the presence of oxidizers.	Au−3e	+1.50

*Electrode reactions $Me \rightleftarrows Me^{n+} + ne$ are abbreviated to Me − ne.

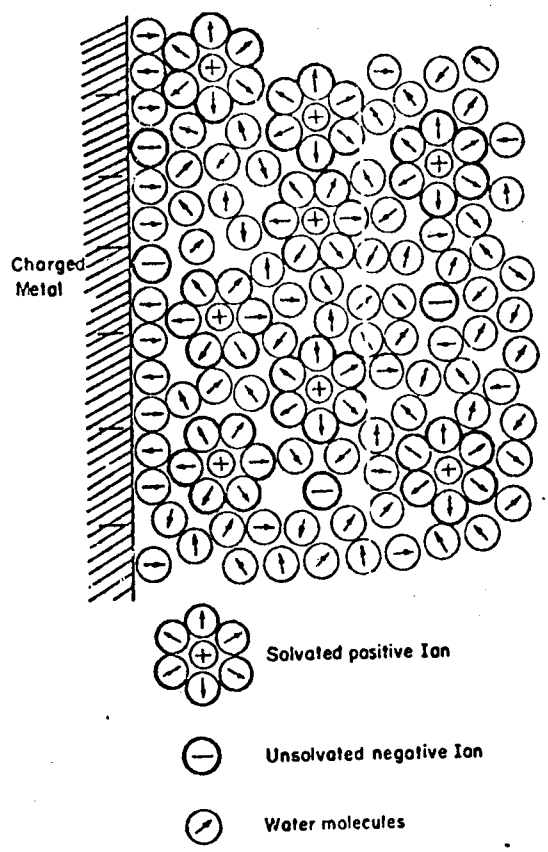

Fig. 2-1. Schematic representation of the structure of an electrified interface. The small, positive ions tends to be solvated, while the layer, negative ions are usually unsolvated.

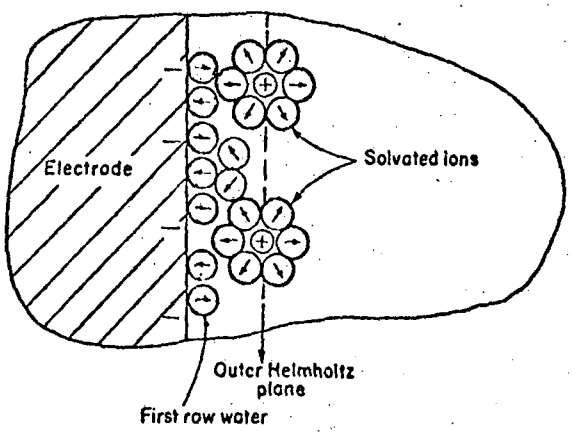

Fig. 2-2. An electrified layer of solvated ions on the layer of first-raw water.

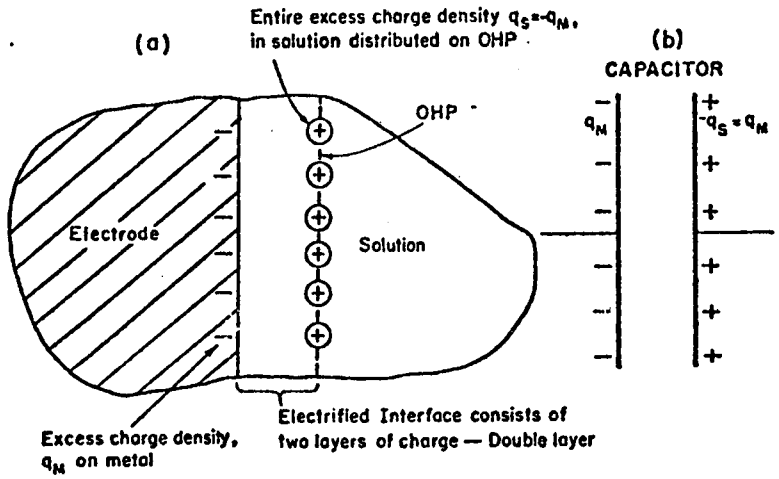

Fig. 2-3. An electrified double layer of a simple type in which a layer of the outer Helmholtz plane constitutes the entire excess charge q_S in the solution, and the electrical equivalent of such a double layer is a parallel condenser.

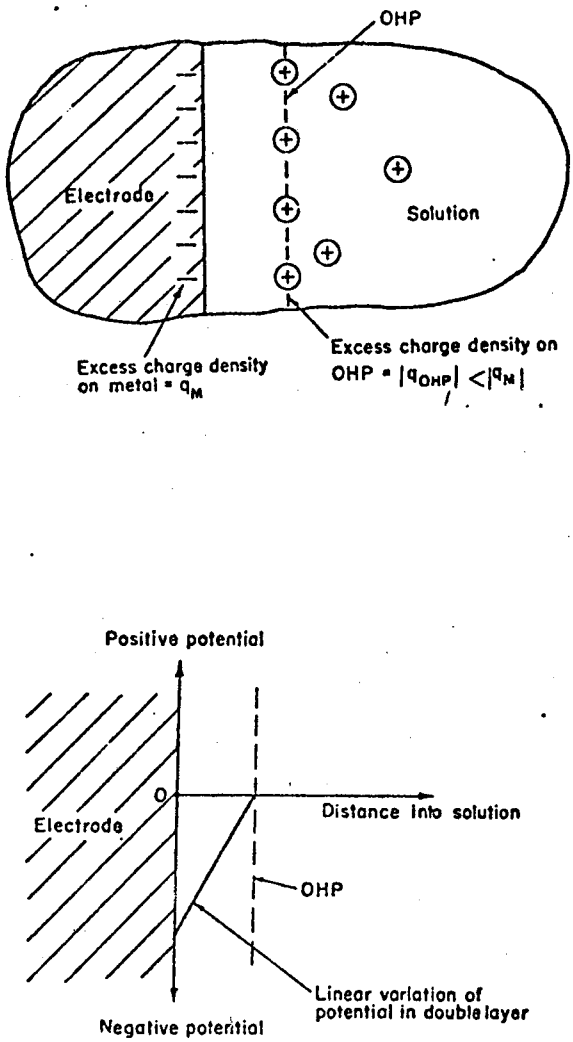

Fig. 2-4. The linear variation of potential corresponding to a simple double layer.

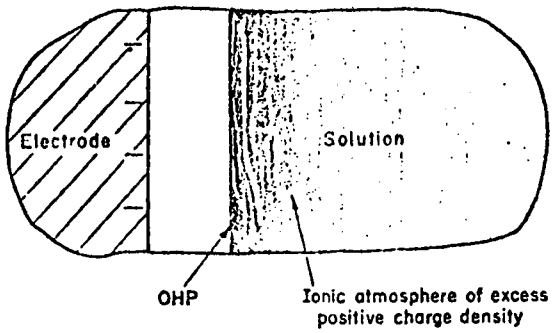

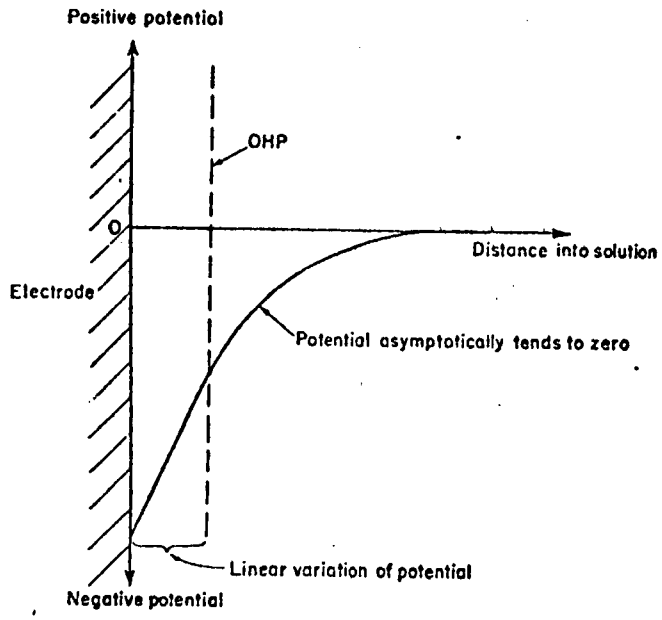

Fig. 2-5. The variation of potential corresponding to a double layer in which the excess charge diffuses from the OHP to the bulk solution.

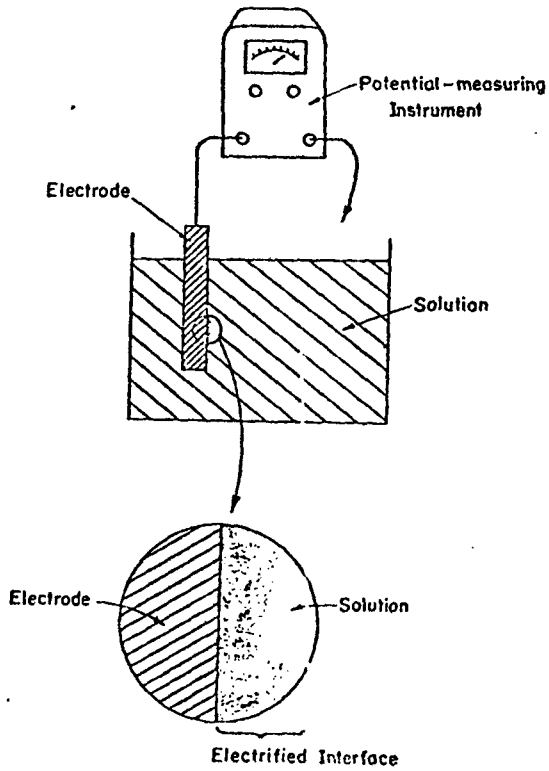

Fig. 2-6. To measure the potential difference across a metal/solution electrified interface, one terminal of the potentiometer is connected to the metal electrode. What is to be done with the second terminal?

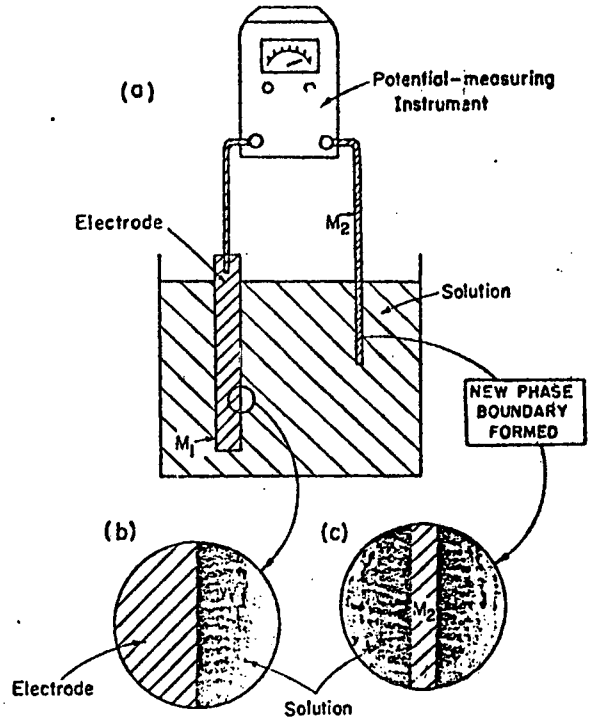

Fig. 2-7. If the second terminal M_2 of potentiometer is dipped into the solution, an extra M_2/solution interface is formed.

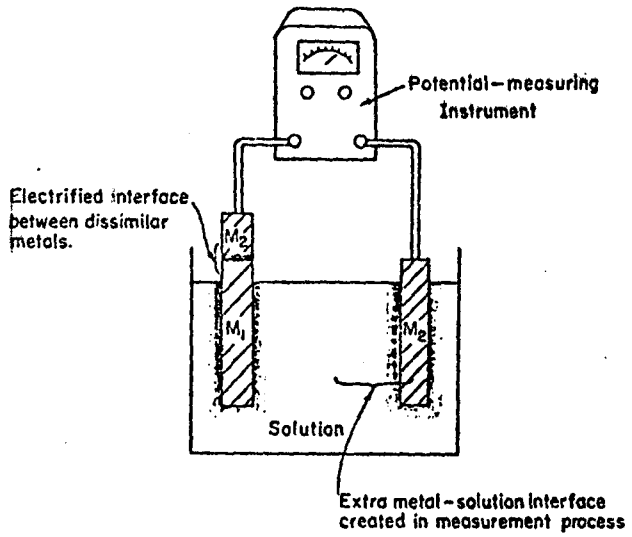

Fig. 2-8. If electrode M_1 and the connecting wire M_2 are dissimilar metals, a contact potential difference pd M_2/M_1 at the metal M_1/metal M_2 interface is generated in the measurement process in addition to the extra metal-solution potential difference pd M_2/sol.

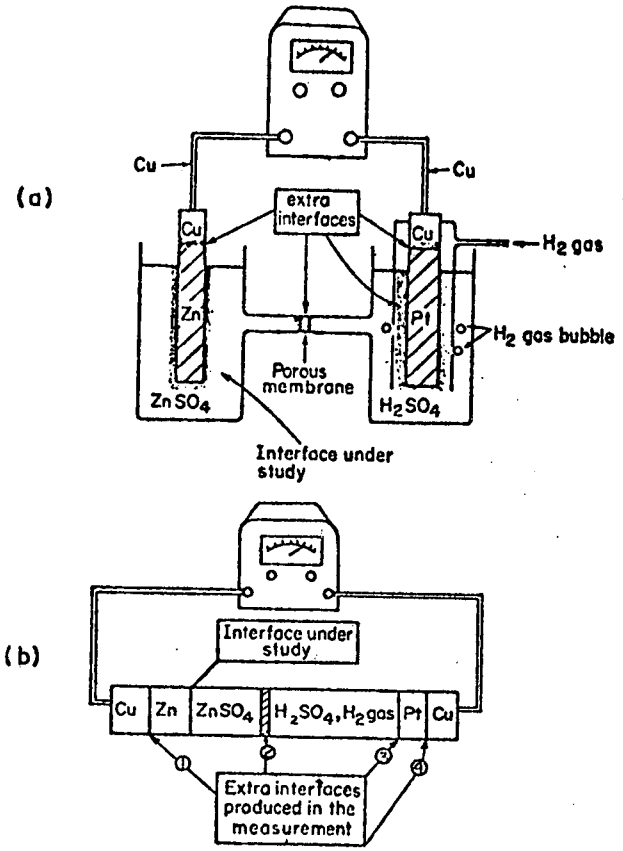

Fig. 2-9. A more complex cell in which two electrodes both differ in nature from the cupper connecting wires of the potentiometer.

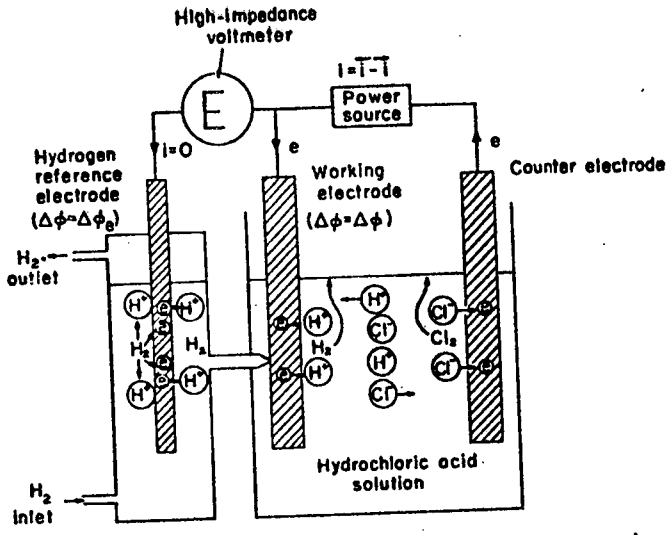

. The three-electrode system required to measure electrode overpotentials, i.e., $\Delta\phi - \Delta\phi_e$. The potential between the working electrode and the reference electrode when both $\Delta\phi$ and $\Delta\phi_e$ correspond to the same reaction is equal to the overpotential η. The tube joining reference electrode and working electrode is called a Luggin capillary. It helps diminish the inclusion of illicit *IR* drop in the measurement.

Fig. 2-10. The three electrode system required to measure electrode potentials. The tube joining reference electrode and working electrode is called a Luggin capillary, which helps diminish the inclusion of illicit IR drop in the measurements.

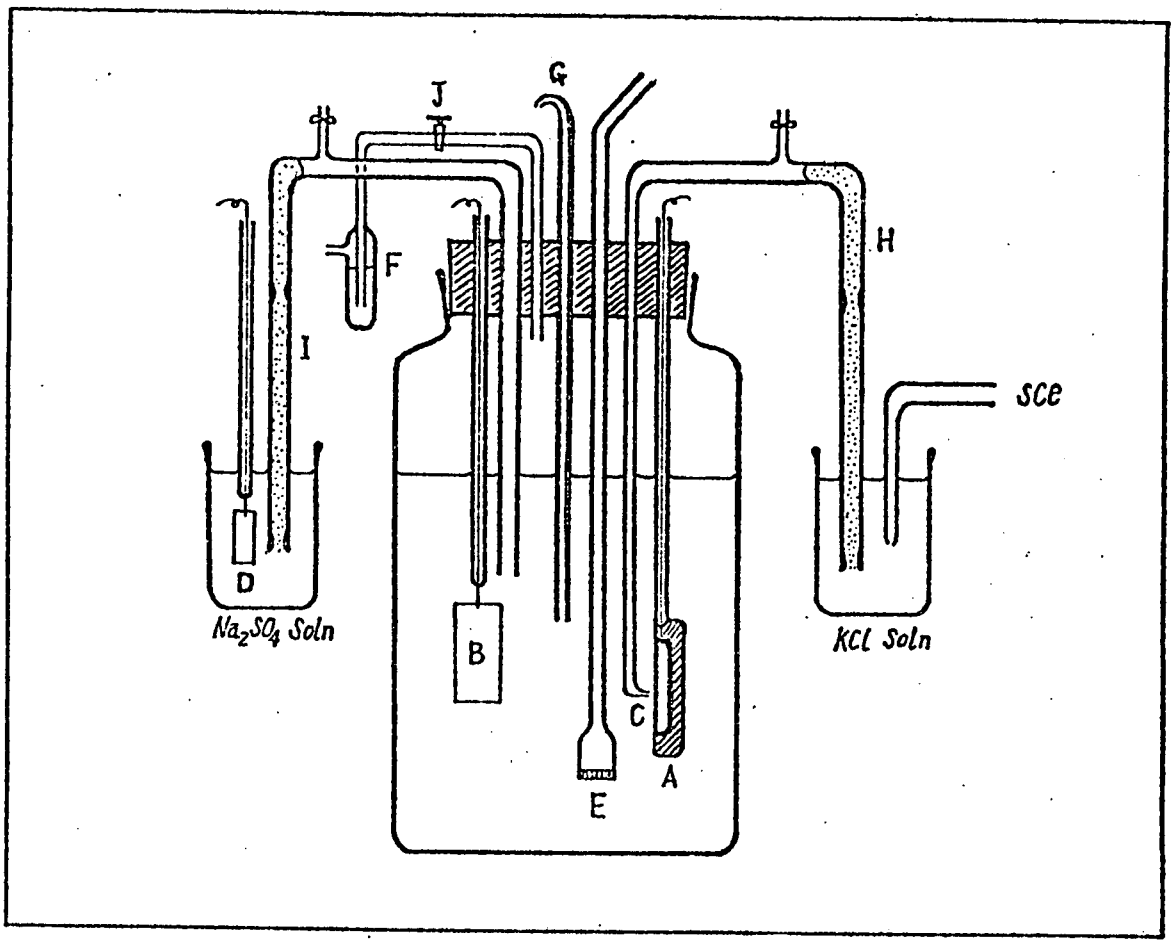

Fig. 2-11. A conventional electrolytic cell for metal polarization: A = test specimen, B = counter Pt electrode for polarization, C = Luggin capillary, D = auxiliary Pt electrode for pre-electrolysis, E = nitrogen gas inlet, F = water sealed gas outlet, G = capillary tube for sampling the solution, J = stop cock, H = agar saturated with KCl, and I = agar saturated with the salt of electrolyte.

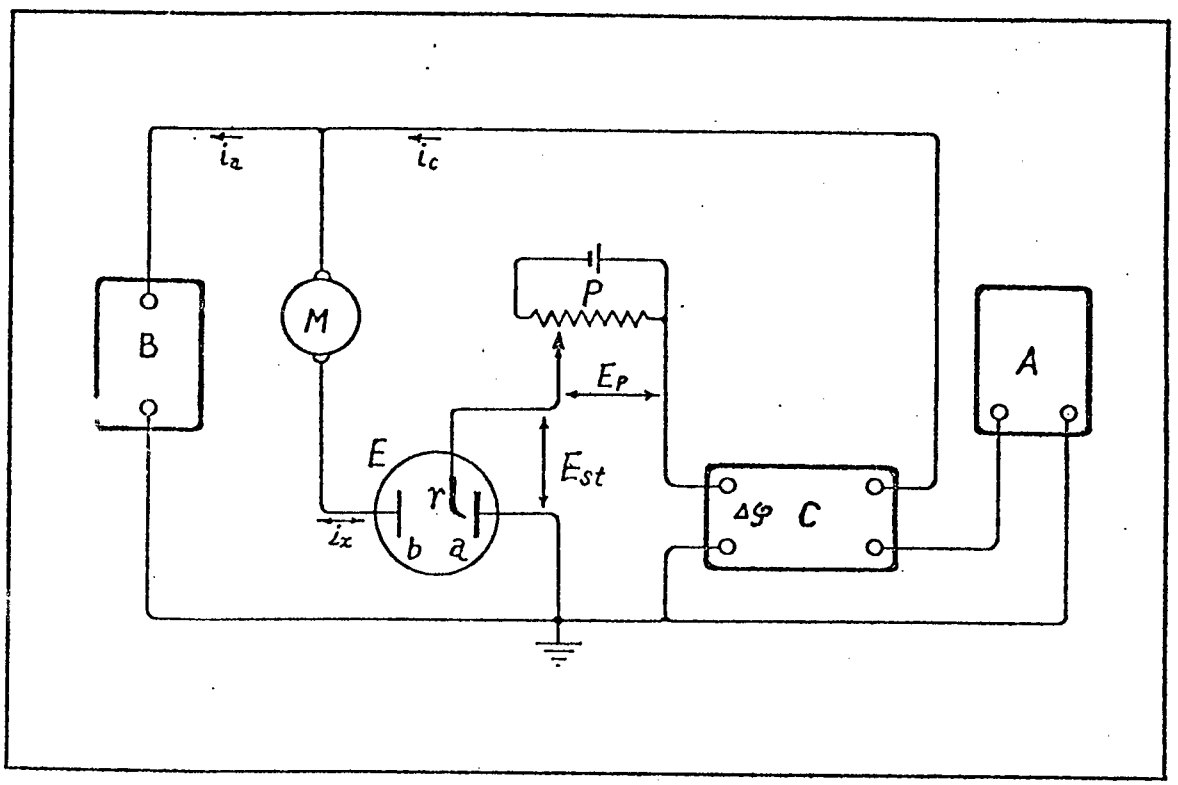

Fig. 2-12. Block diagram of an electronic potentiostat: E = electrolytic cell, a = test specimen, b = counter Pt electrode, r = reference electrode, P = potentiometer, C = electronic controller, A = dc source for cathodic direction, M= ampere meter, B = dc source for anodic direction.

(a) Anodic Reaction , Oxidation
Electron-Donating Reaction
De-Electronation

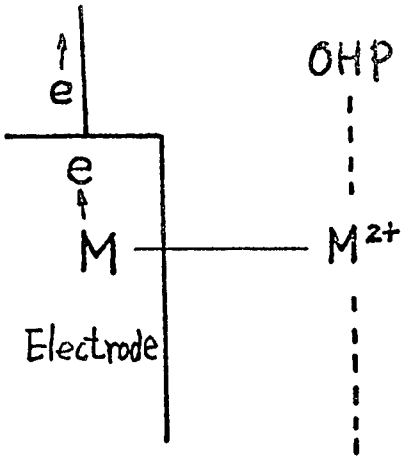

(b) Cathodic Reaction , Reduction
Electron-Accepting Reaction
Electronation

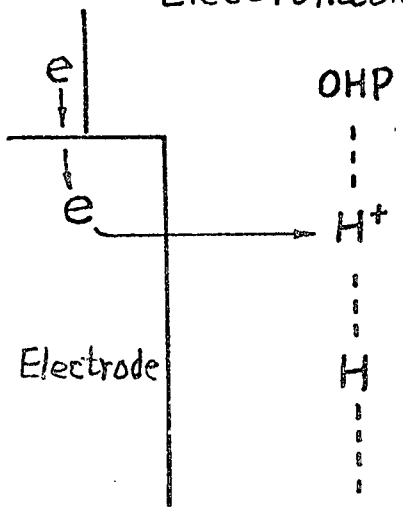

Fig. 2-13. Two kinds of electrochemical reactions to occur on metal electrodes.

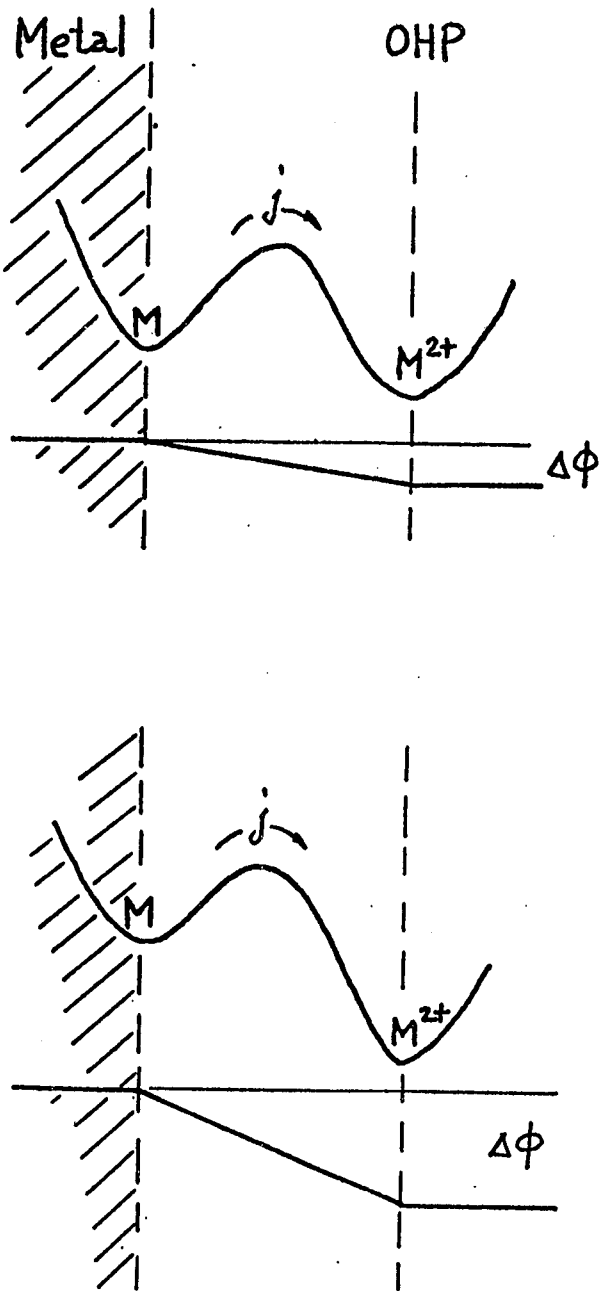

Fig. 2-14. Energy profile for transfer of a metal ion from the metal lattice to the OHP in solution.

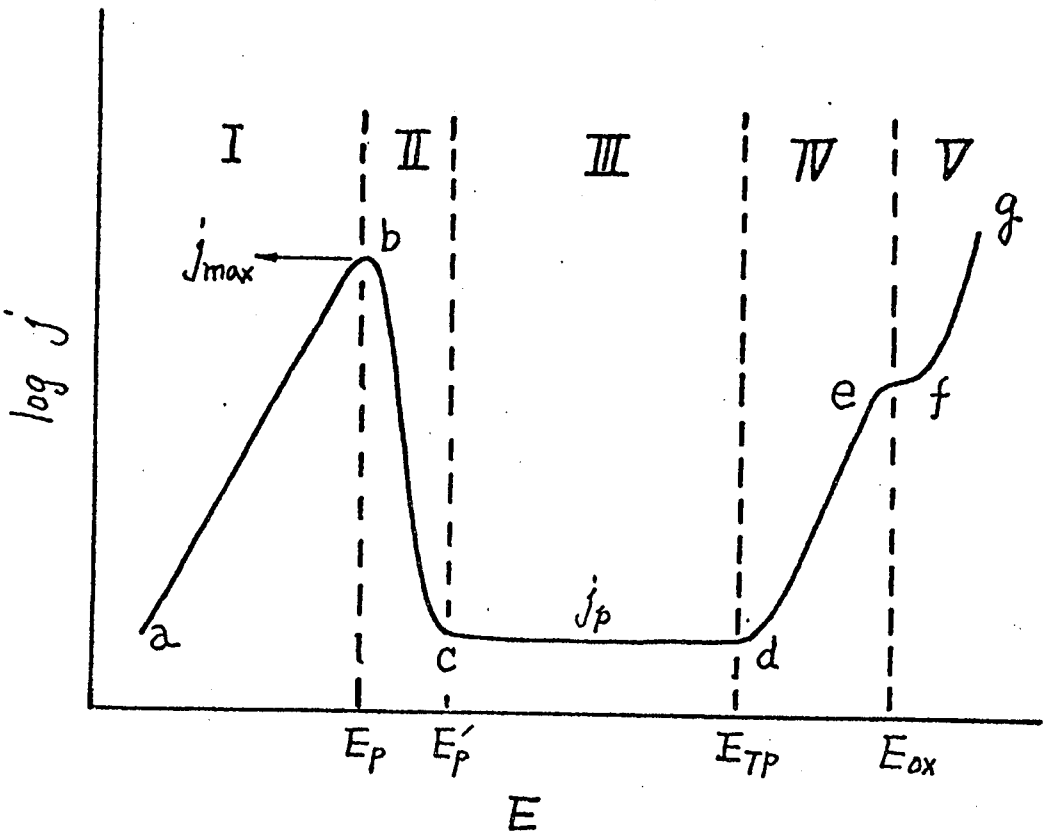

Fig. 2-15. Typical anodic polarization curve of passivable metals in aqueous solution.

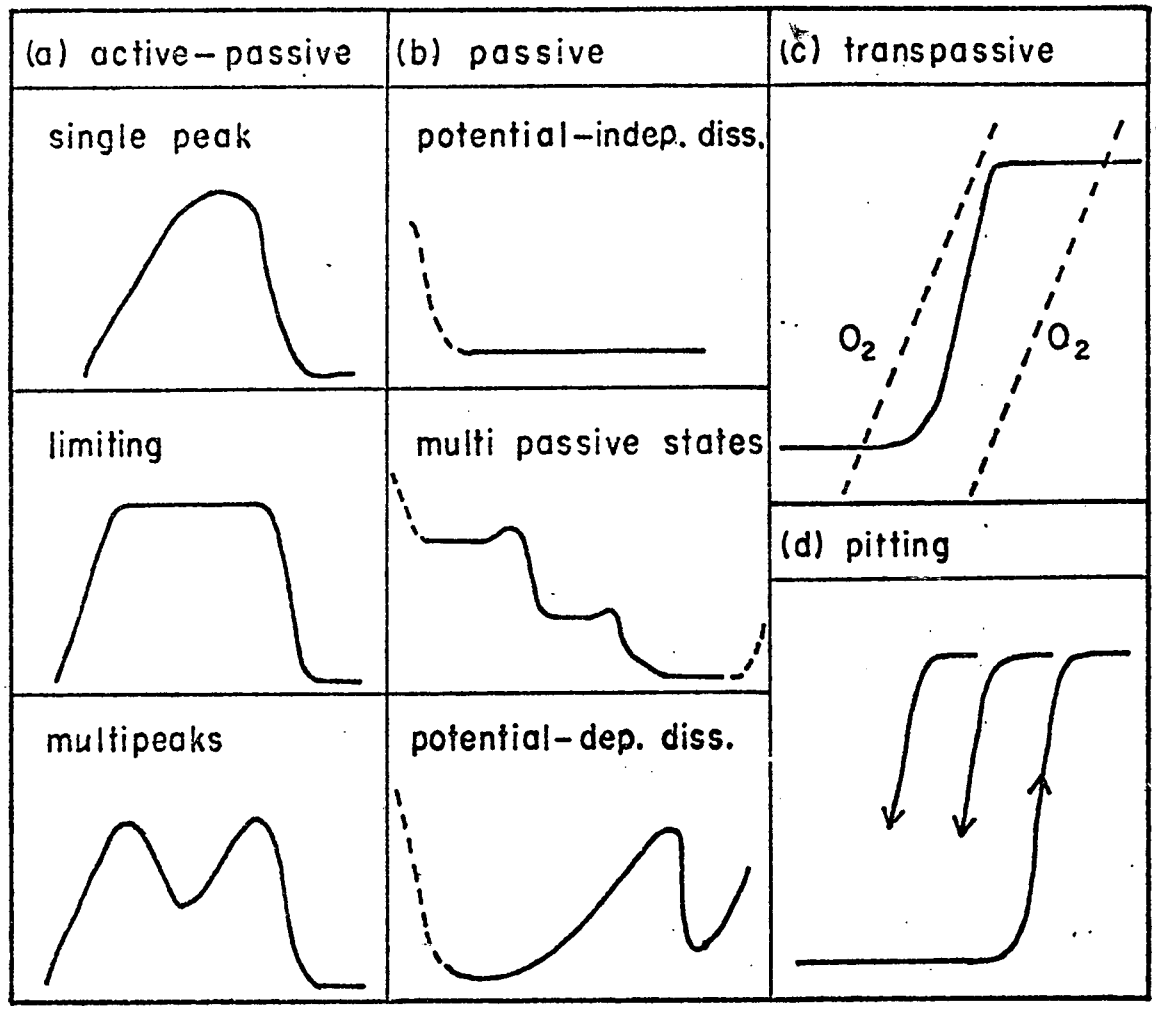

Fig. 2-16. Types of anodic polarization curves of metals in the active-passive transition, the passive state, and the transpassive state in aqueous solution.

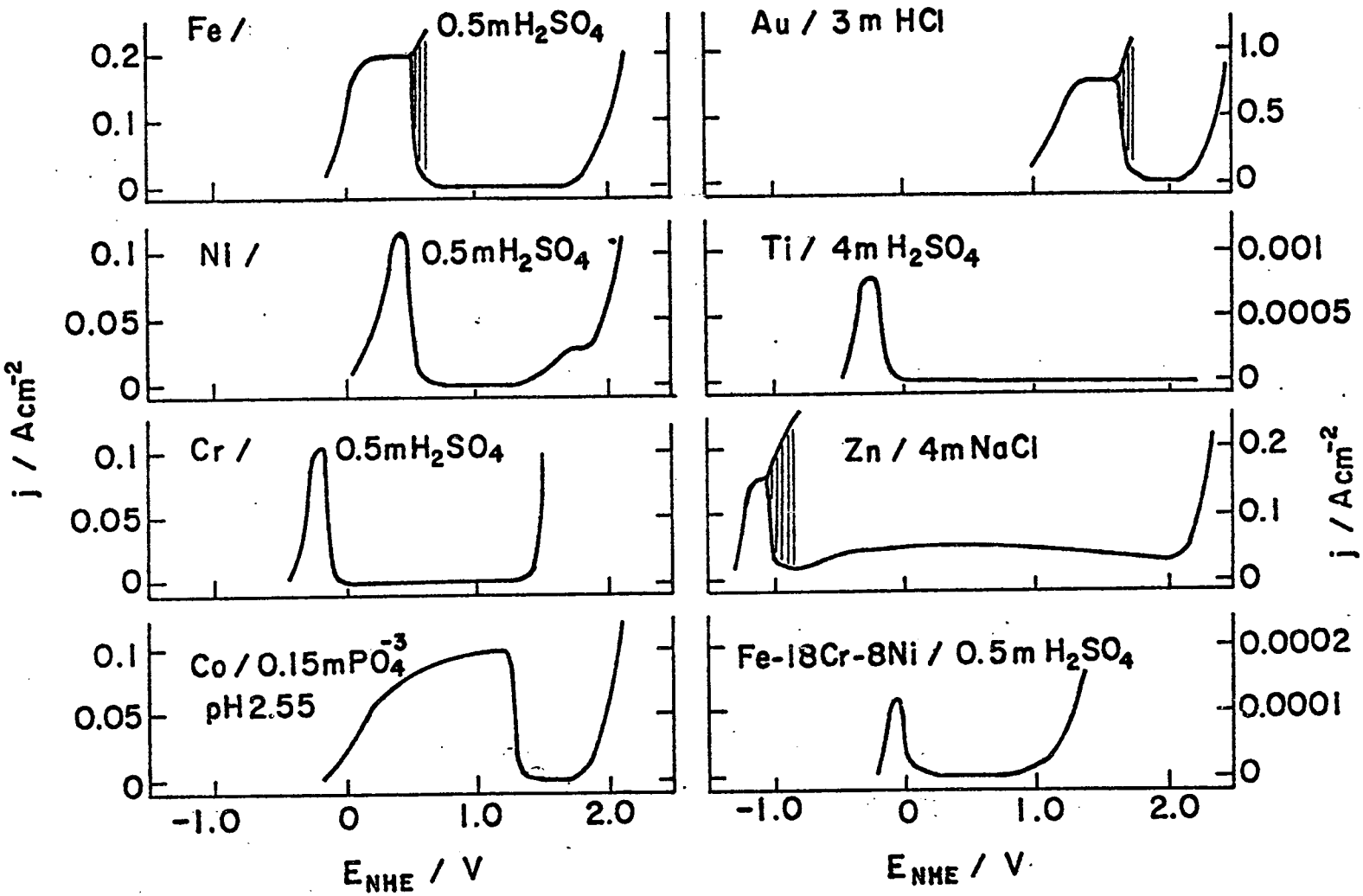

Fig. 2-17. Anodic polarization curves of various passivable metal in aqueous solutions.

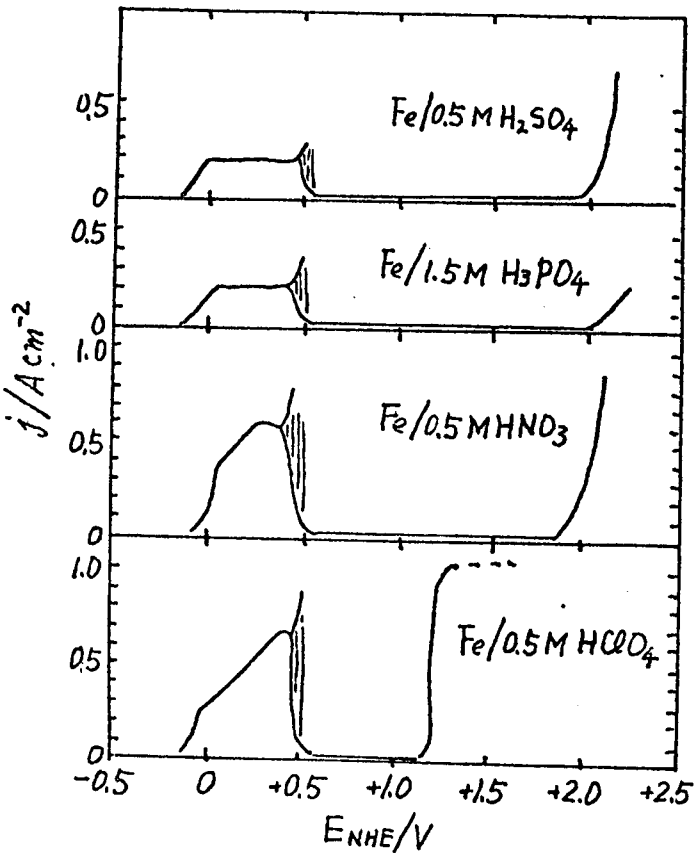

Fig. 2-18. Anodic polarization curves of iron in various acid solutions (Franck, 1958).

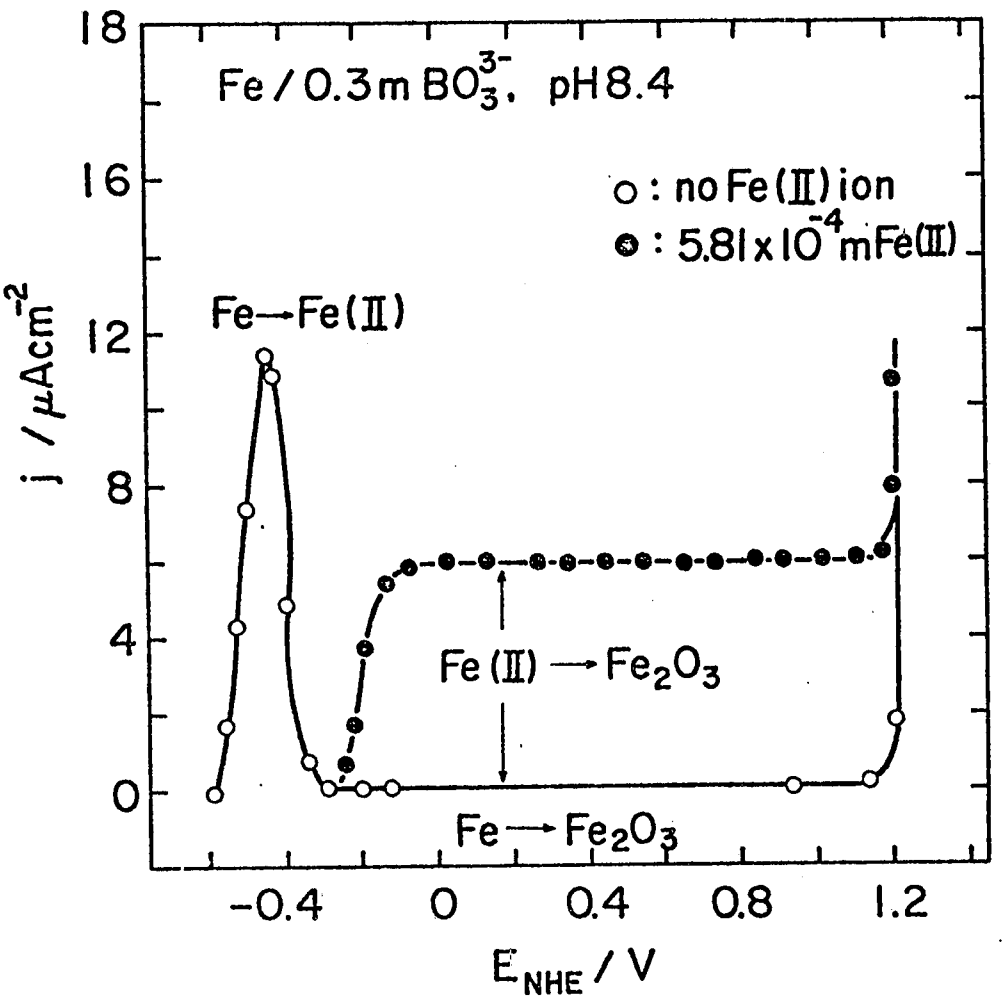

Fig. 2-19. Anodic polarization curves of iron in 0.3 M BO_3^{3-} buffer solutions at pH 8.4 containing no Fe(II) ion and a quantity of Fe(II) ion (Nagayama and Cohen, 1963).

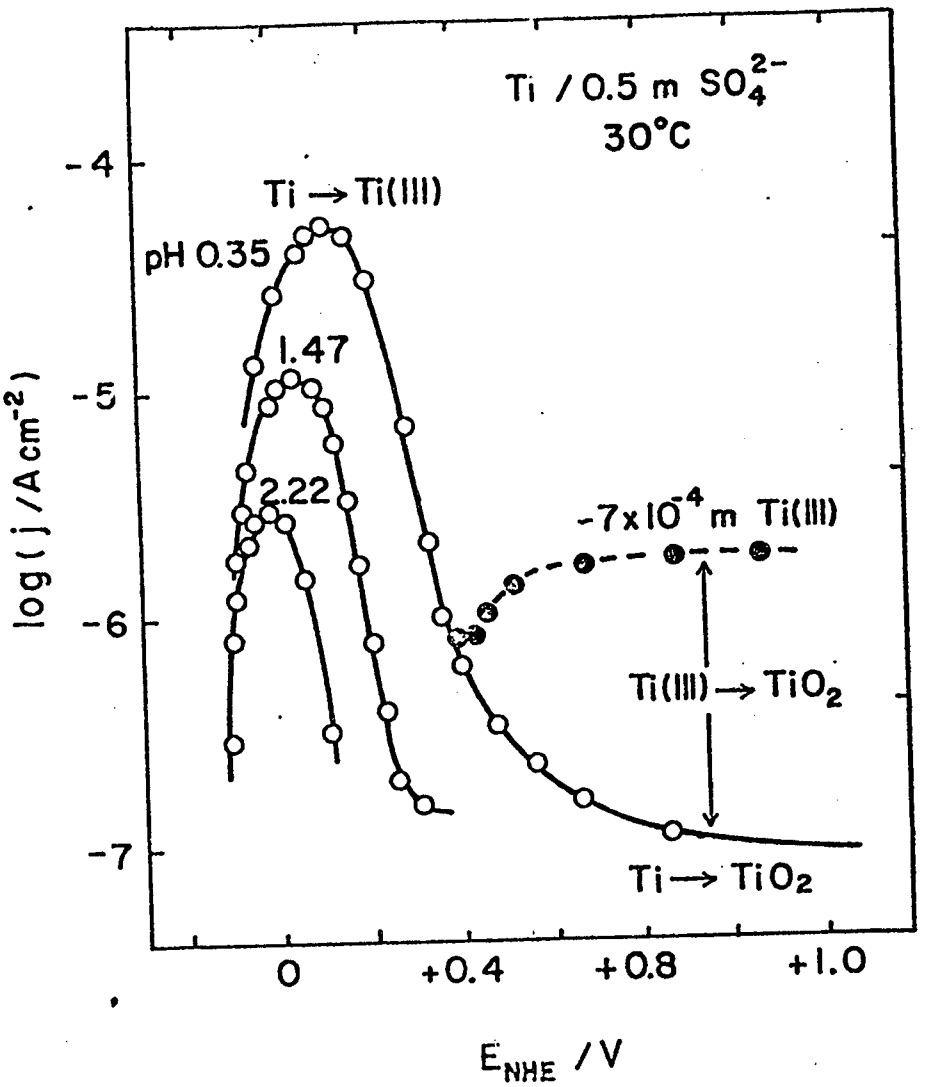

Fig. 2-20 Anodic polarization curve of titanium in sulphuric acid solutions containing no Ti(III) ion and a quantity of Ti(III) ion (Kelley, 1976).

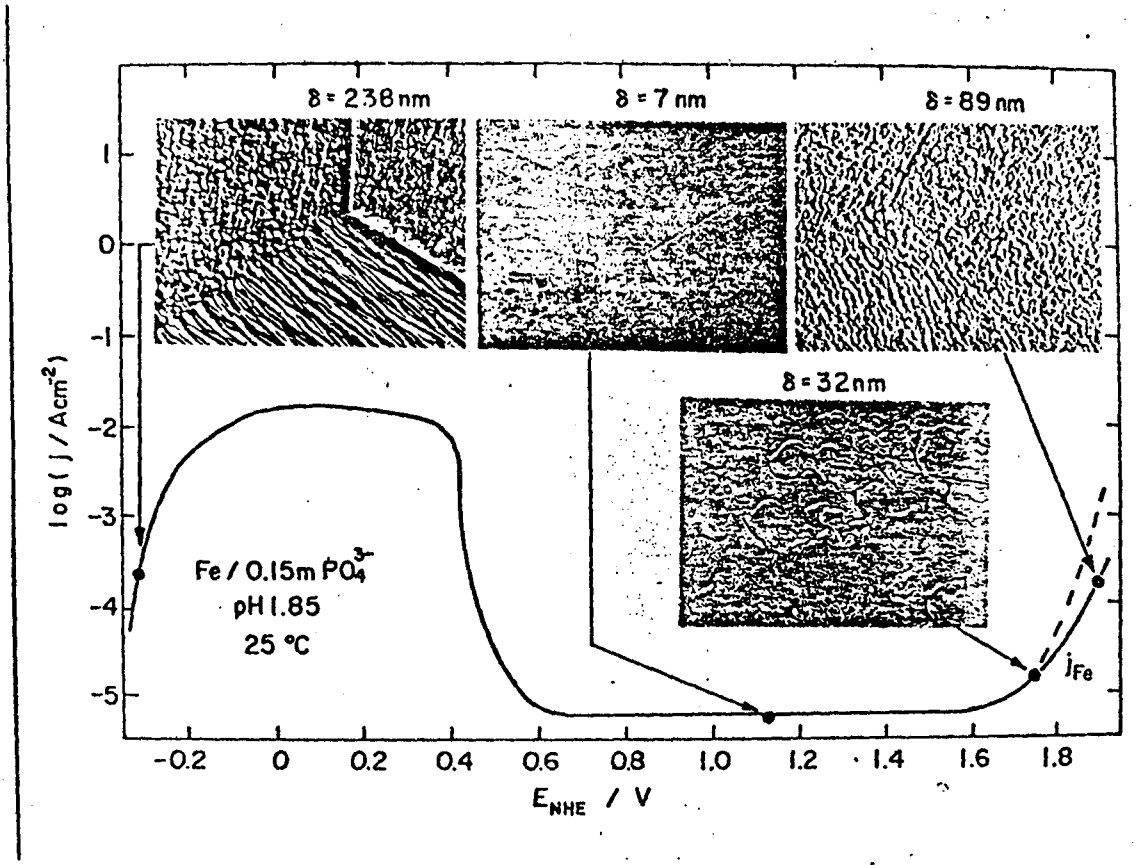

Fig. 2-21. Microscopic appearance of iron surfaces anodically polarized in the active, passive and transpassive states (Noda, 1973).
δ = the surface layer thickness removed during anodic polarization.

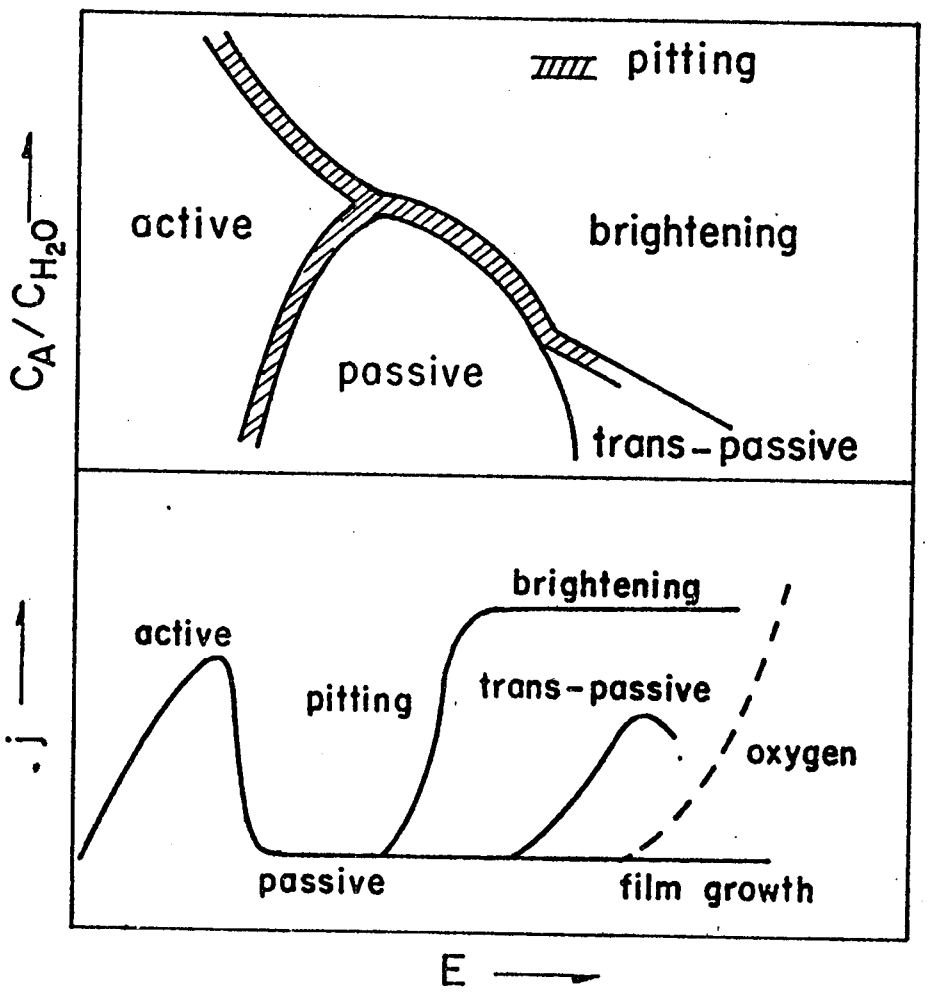

Fig. 2-22. Diagram showing metal anode behaviour at various potentials in solutions of various anion/water concentration ratio and several modes of anodic polarization curves at potentials more positive than the passive range (Hoar, 1967).

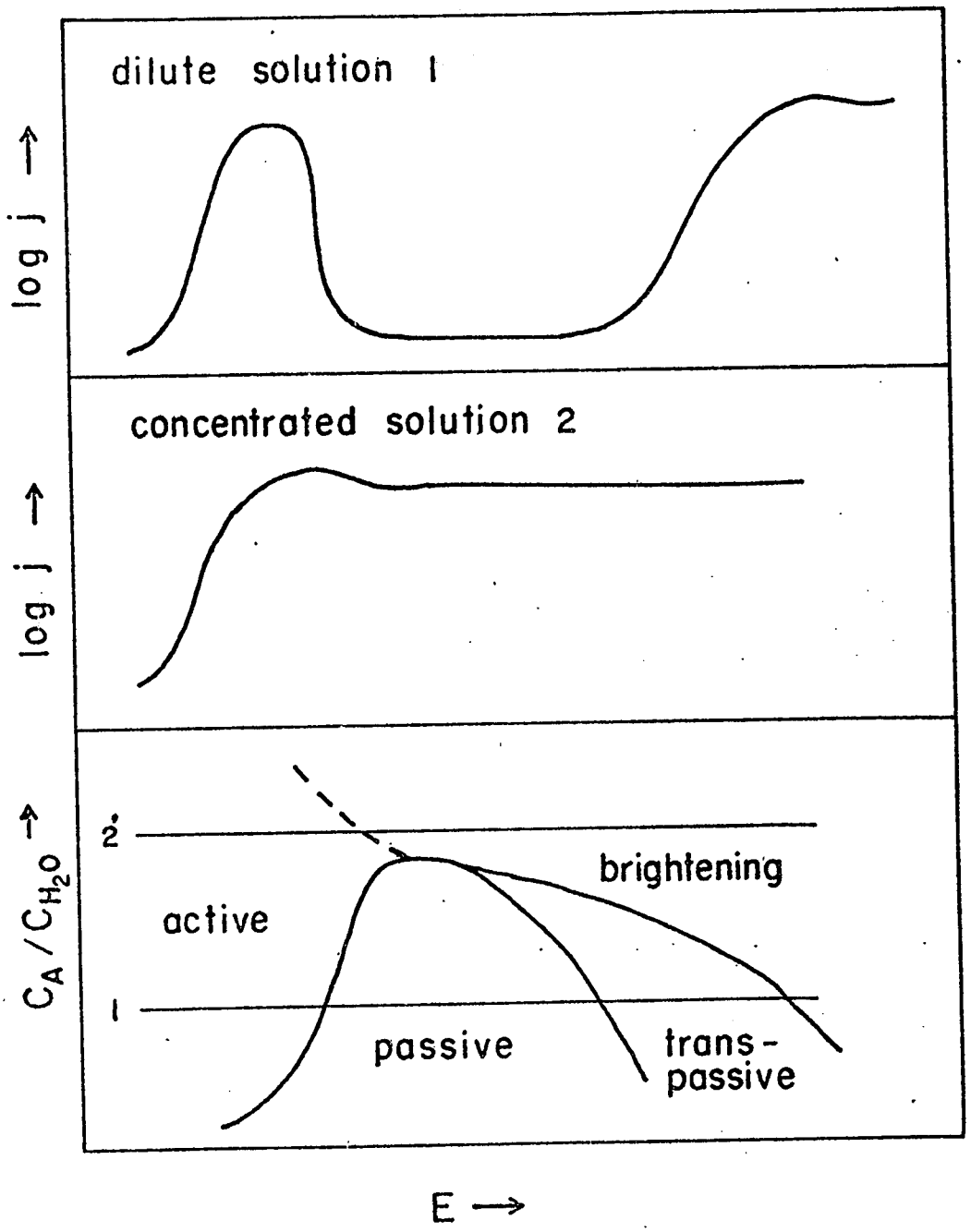

Fig. 2-23. Anodic polarization curves of metals in dilute and concentrated aqueous electrolyte solutions and electrolyte concentration versus potential diagram for anodic behavior of metals.

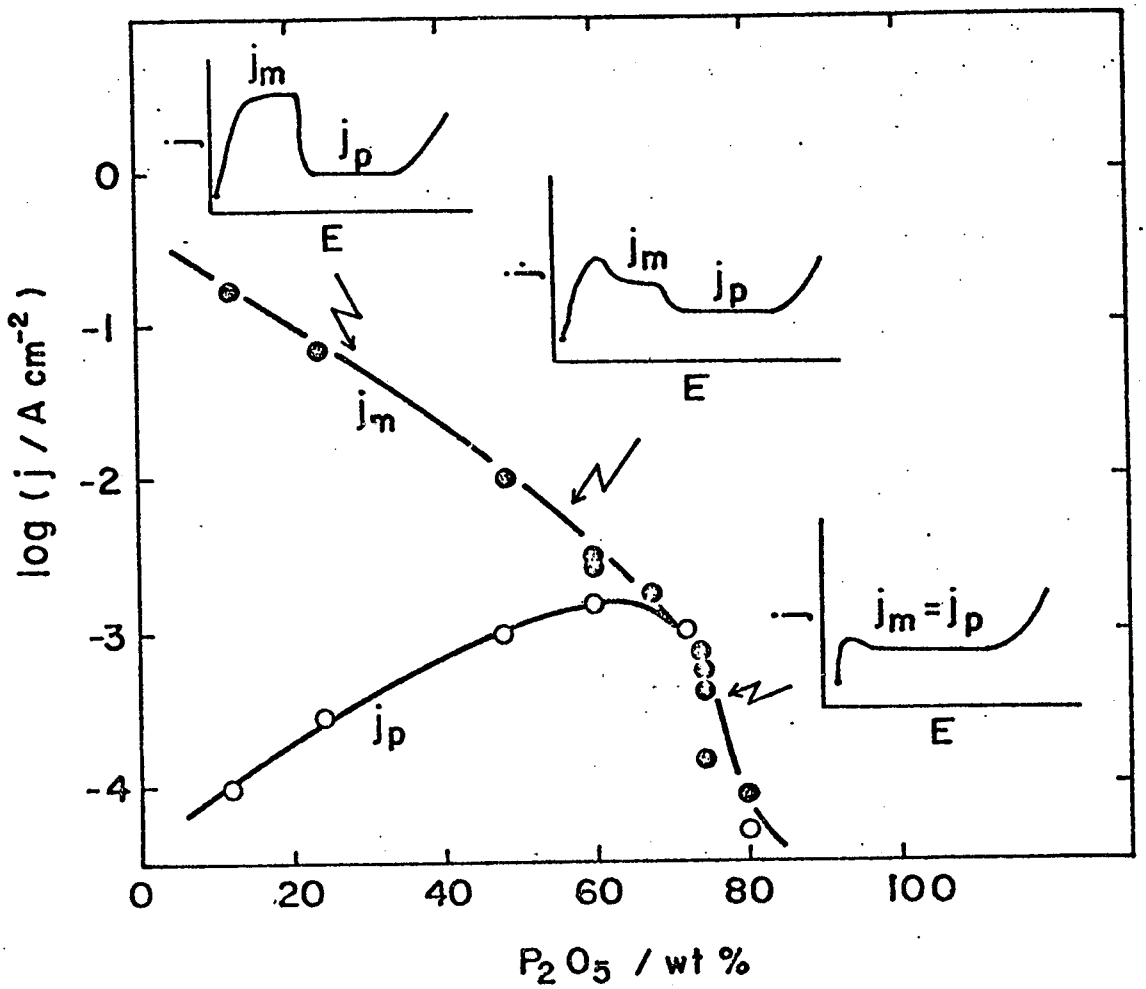

Fig. 2-24. Effect of P_2O_5 concentration on the anodic active dissolution peak current, on the passive dissolution current, and on the anodic polarization curve of iron in phosphoric acid solutions (Zucchi et al., 1971, Kanda et al., 1973).

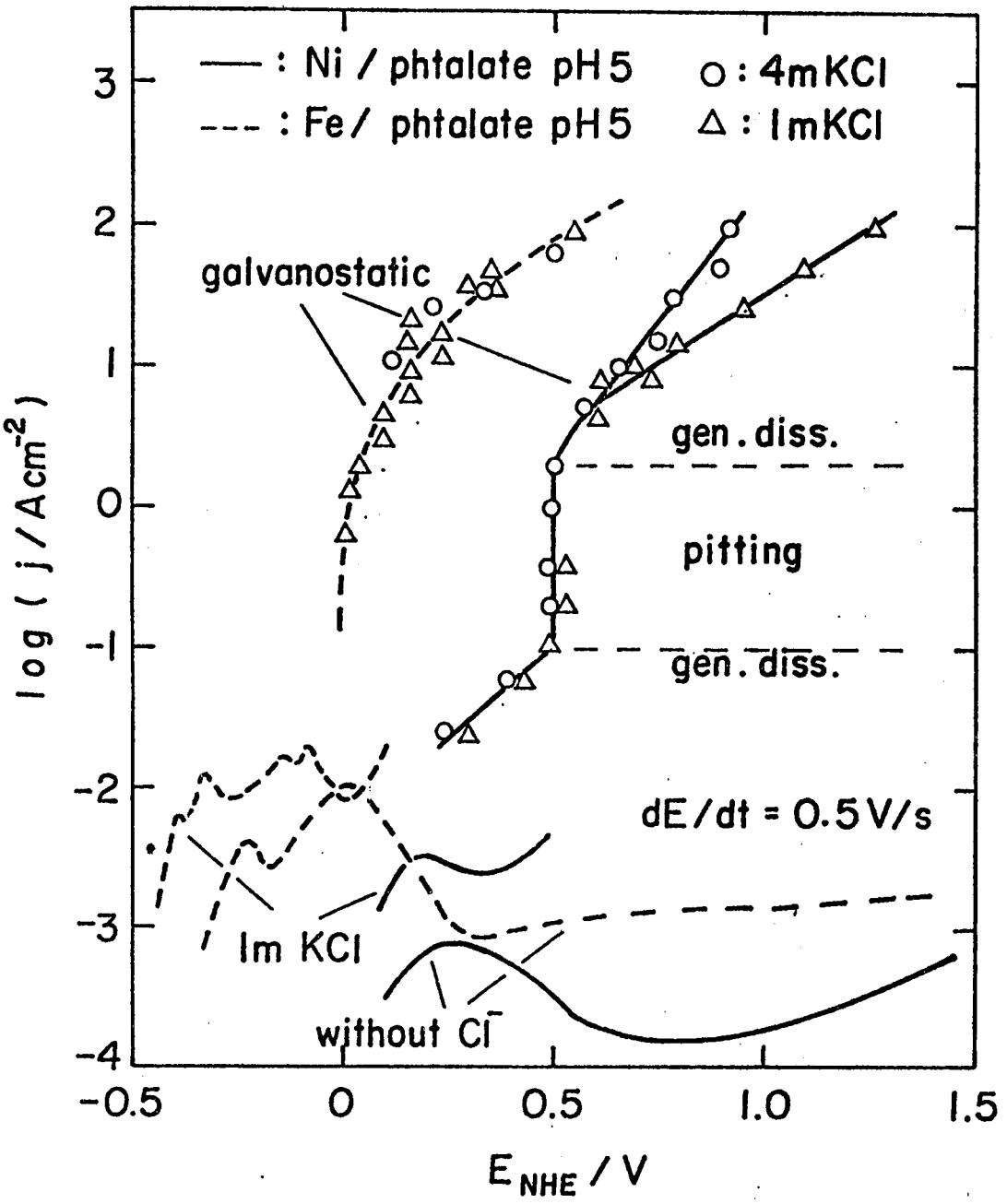

Fig. 2-25. Anodic polarization curves of iron and nickel in dilute 0.05 M H_3PO_4 solution and in concentrated 1 M and 4 M NaCl solutions (Strehblow et al., 1975).

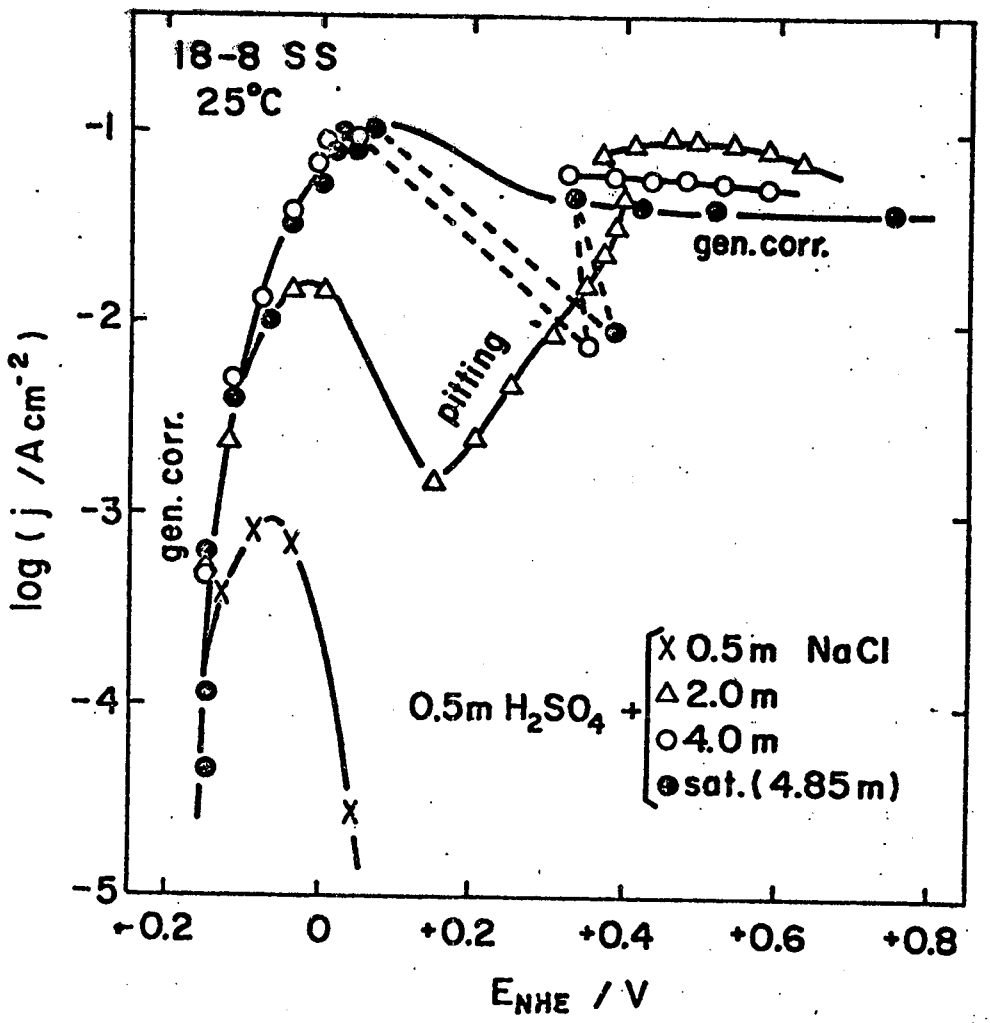

Fig. 2-26. Anodic polarization curves of an austenitic 18 Cr 8 Ni stainless steel in concentrated NaCl solutions containing 0.5 M H_2SO_4 (Hisamatsu et al., 1971).

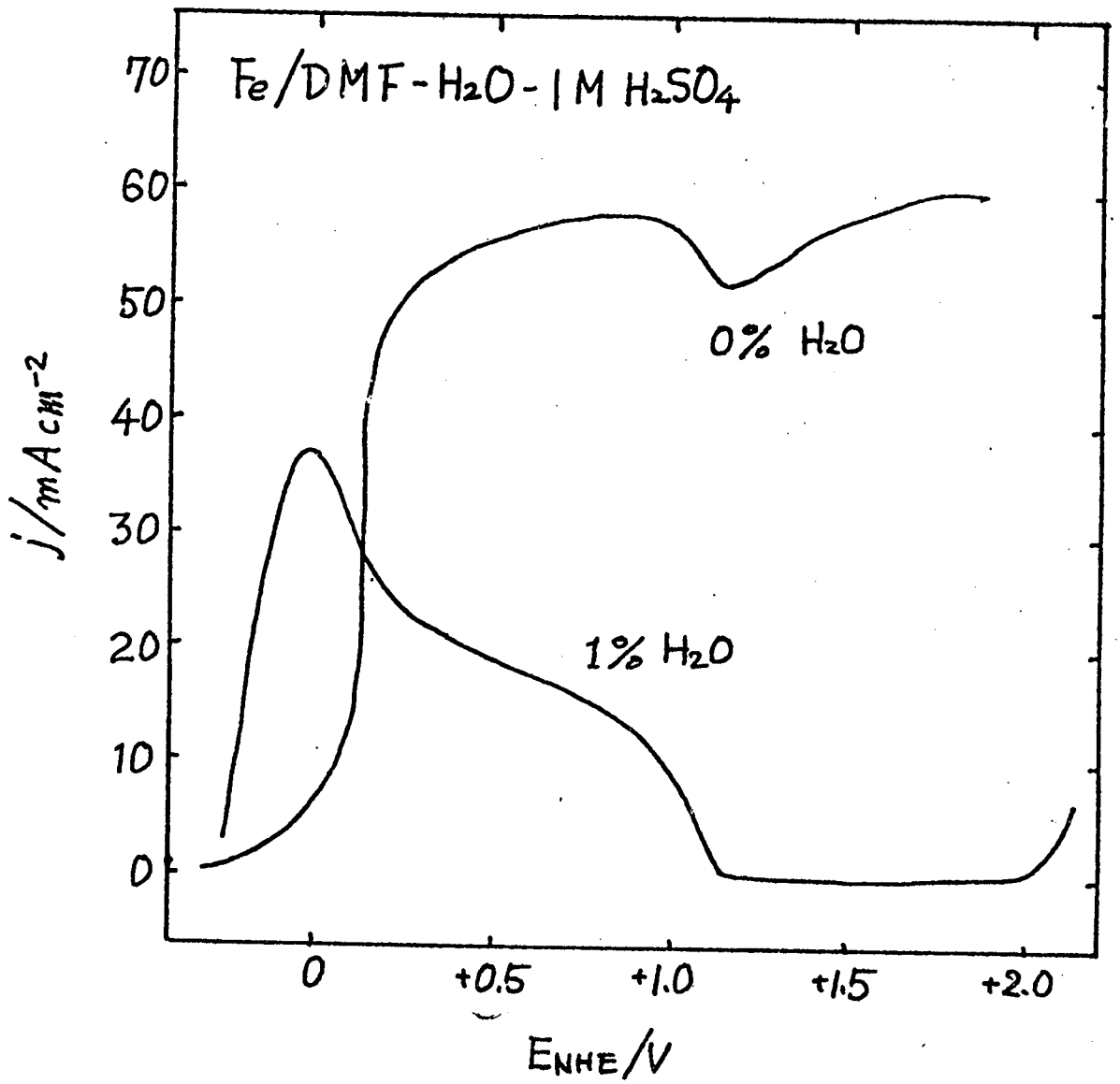

Fig. 2-27. Anodic polarization curve of iron in acid dimethylformamid solutions with and without water (Schwabe et al., 1976).

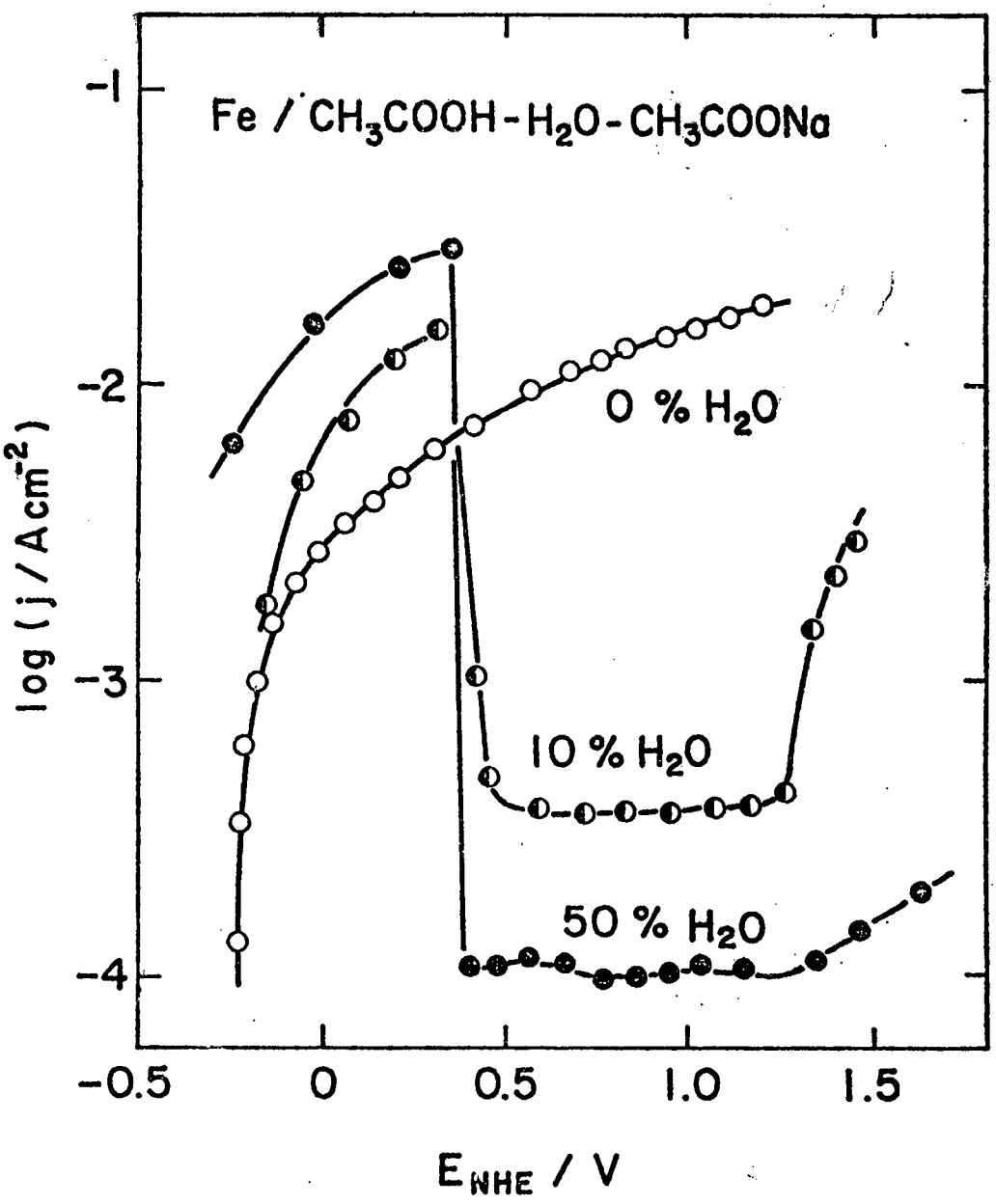

Fig. 2-28. Anodic polarization curve of iron in acetic acid-sodium acetate solutions with and without water (Kiss et al., 1971).

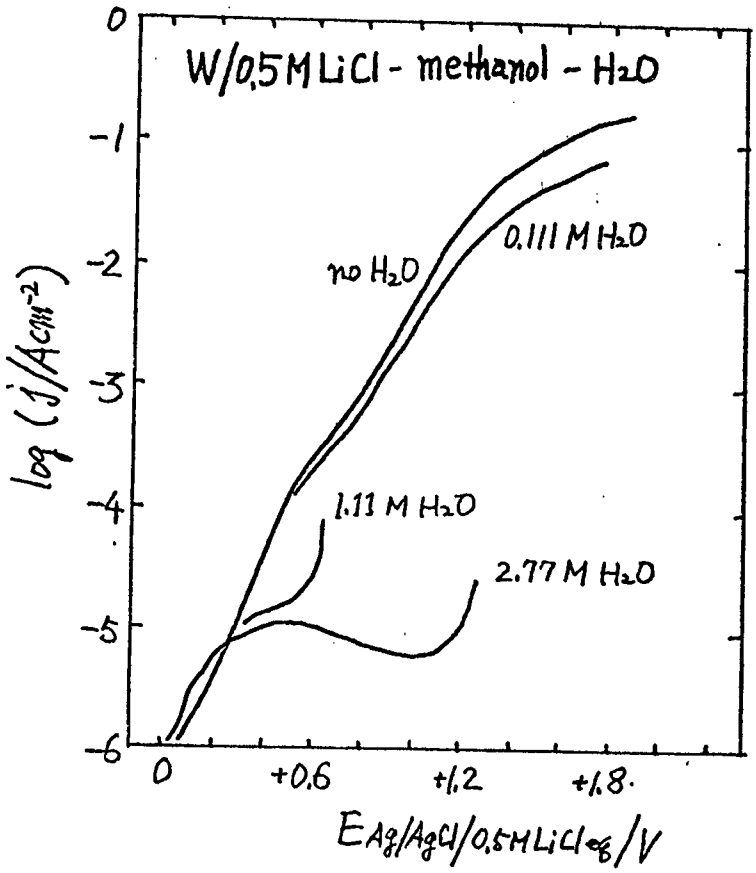

Fig. 2-29. Anodic polarization curves of tungusten in LiCl methanol solutions with and without water (Stolica, 1972).

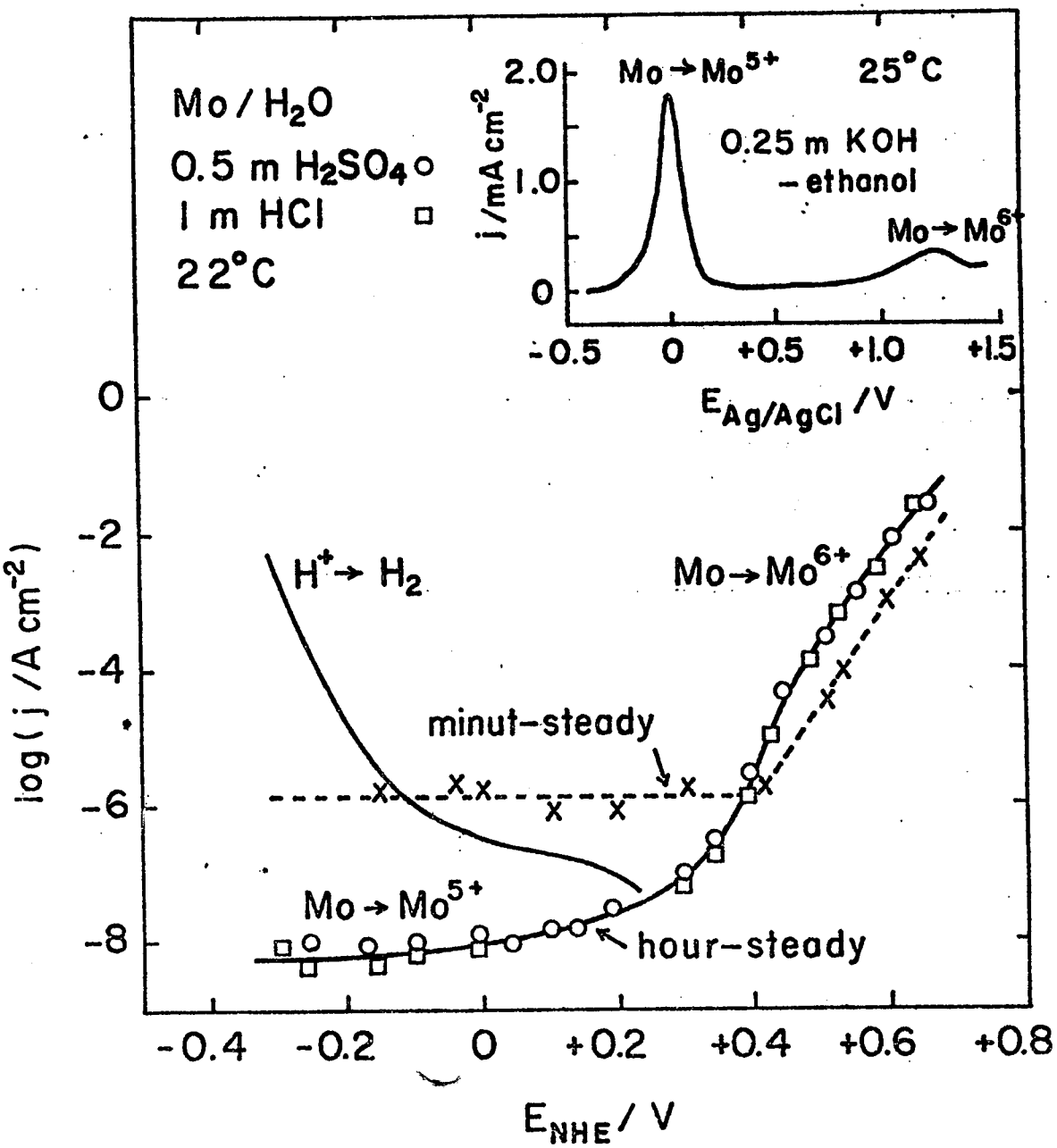

Fig. 2-30. Anodic dissolution current versus potential curve of molybdenum in 0.5 M H_2SO_4 and 1 M HCl solutions (Pozdeeza et al., 1966) and anodic polarization curve in 0.25 M KOH ethanol solution (Heumann et al., 1975).

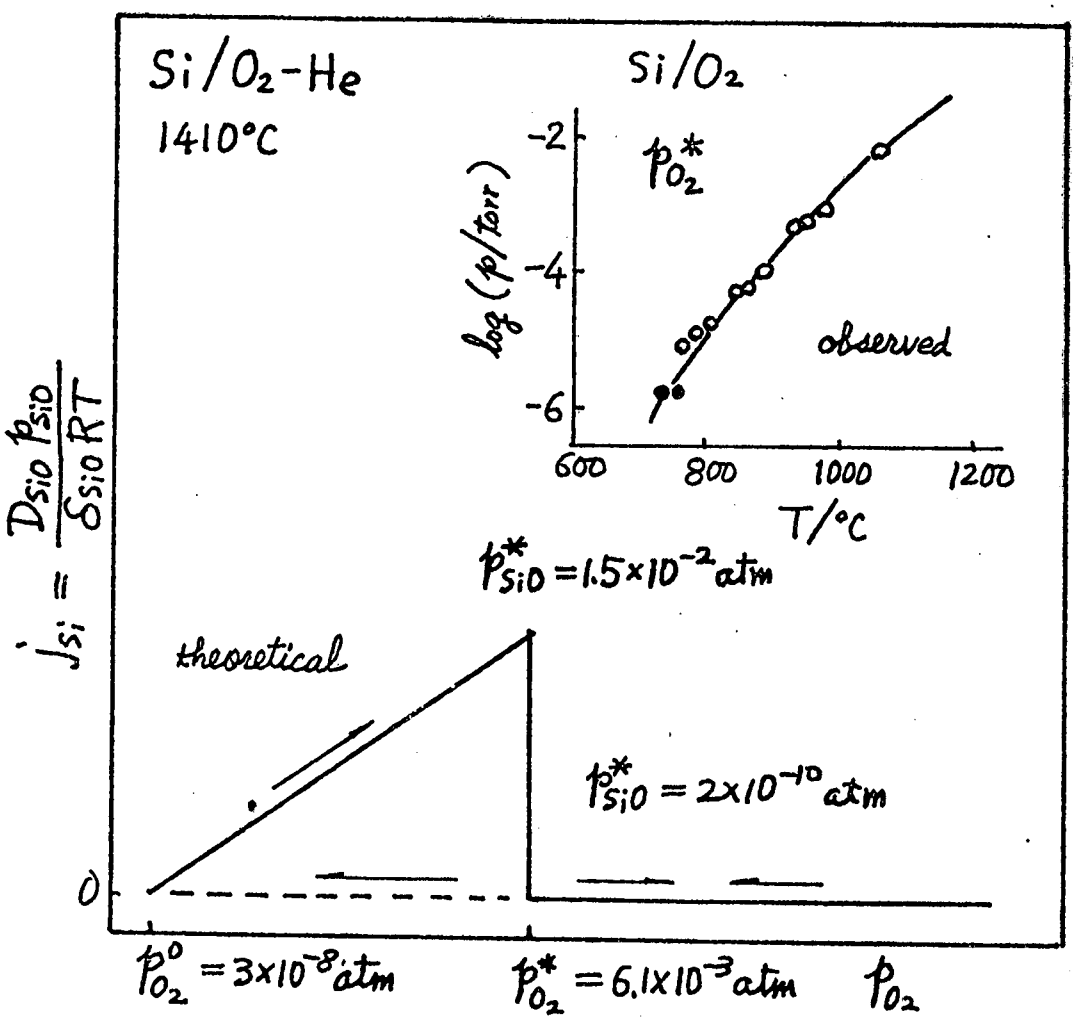

Fig. 2-31. Passivation of silicon in low pressure of oxygen gas at high temperatures (Wagner, 1958 and Galain et al., 1971).

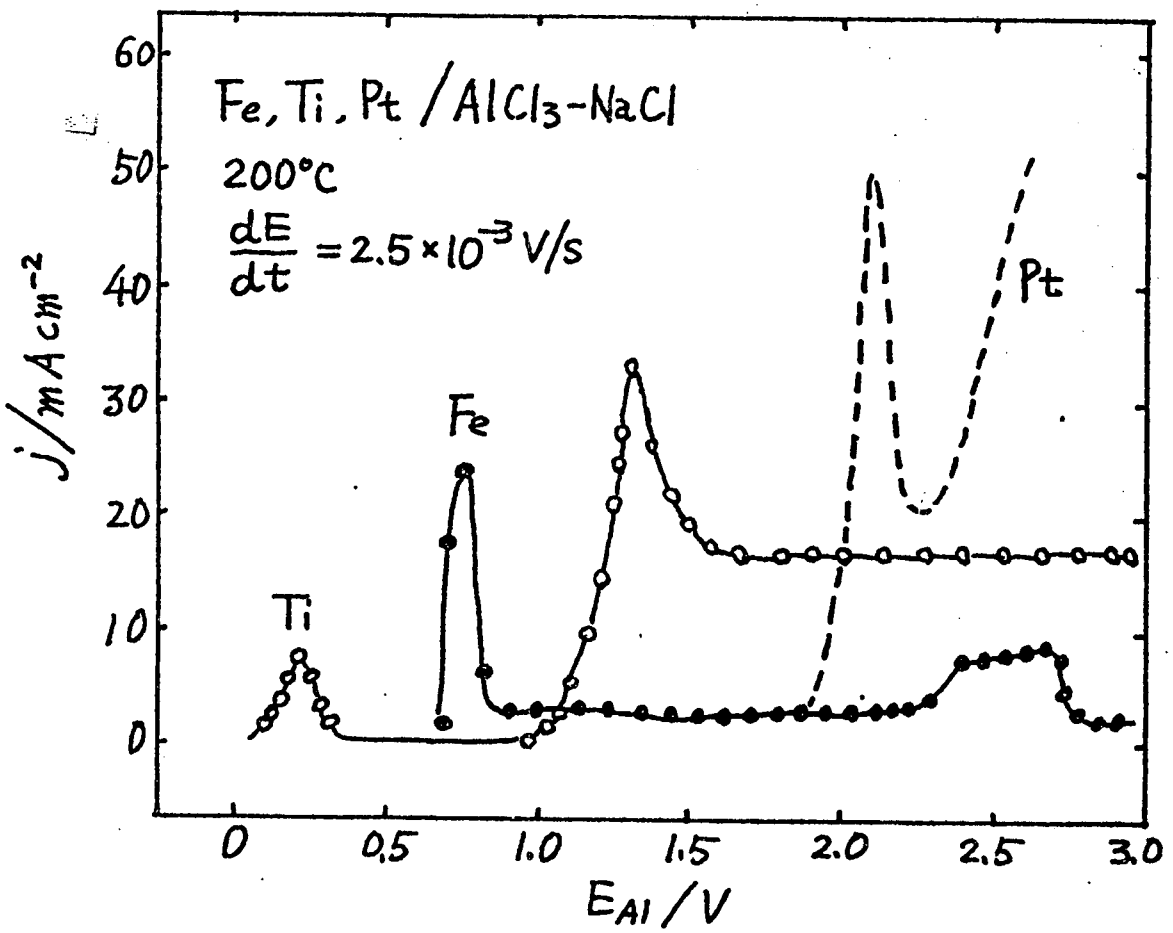

Fig. 2-32. Anodic polarization curves of Fe, T, and Pt in a melt of $AlCl_3$ - NaCl mixture at 200°C (Notoya et al., 1968).

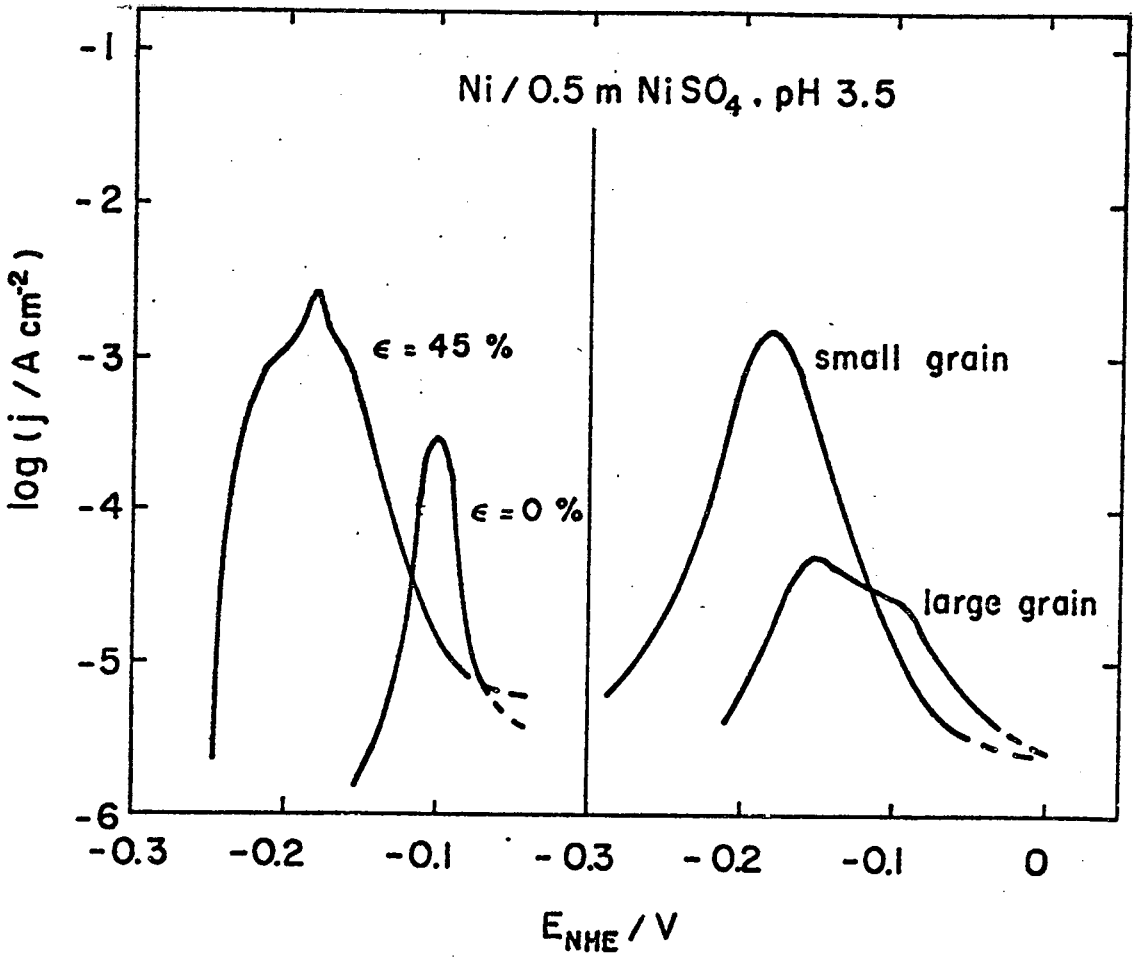

Fig. 2-33. Effects of mechanical strain and xrystal grain size on anodic polarization curve for passivation of nickel in 0.5 M $NiSO_4$ solution (Garz et al., 1971).

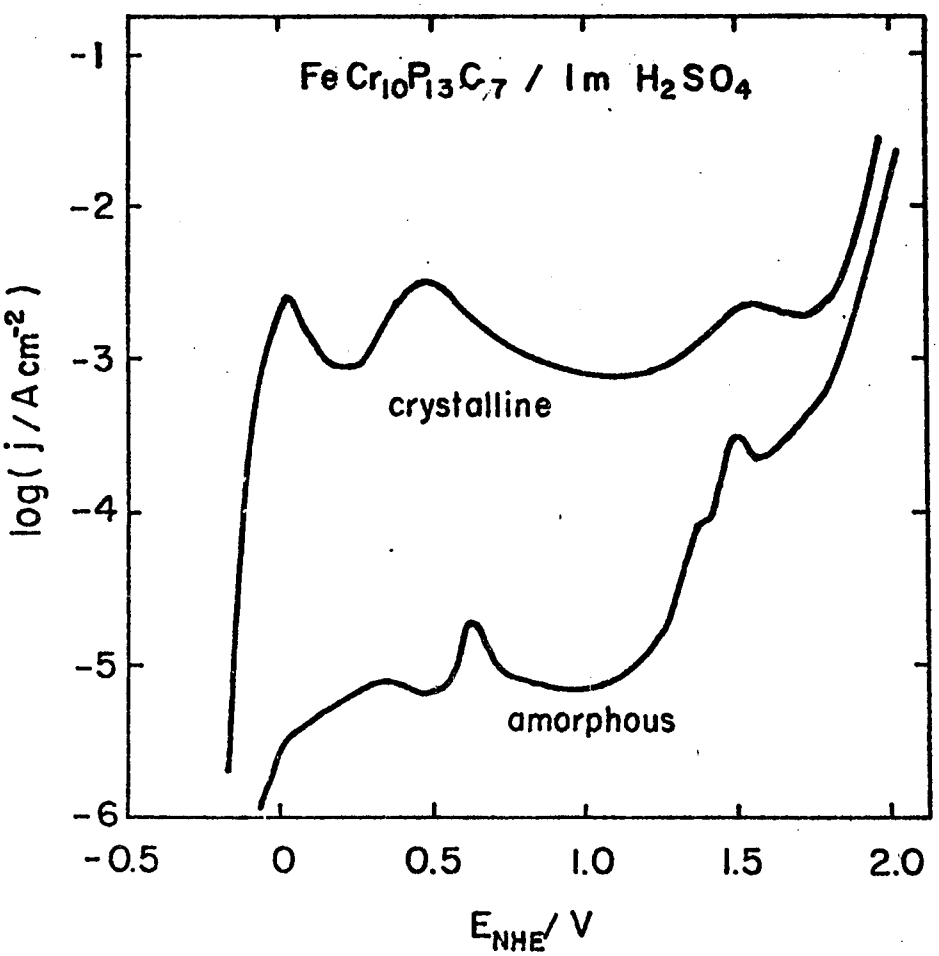

Fig. 2-34. Anodic polarization curves measured by a potential sweep method of an amorphous and crystalline Fe - Cr(10 at %) - P (13 at %) alloy (Hashimoto, 1976).

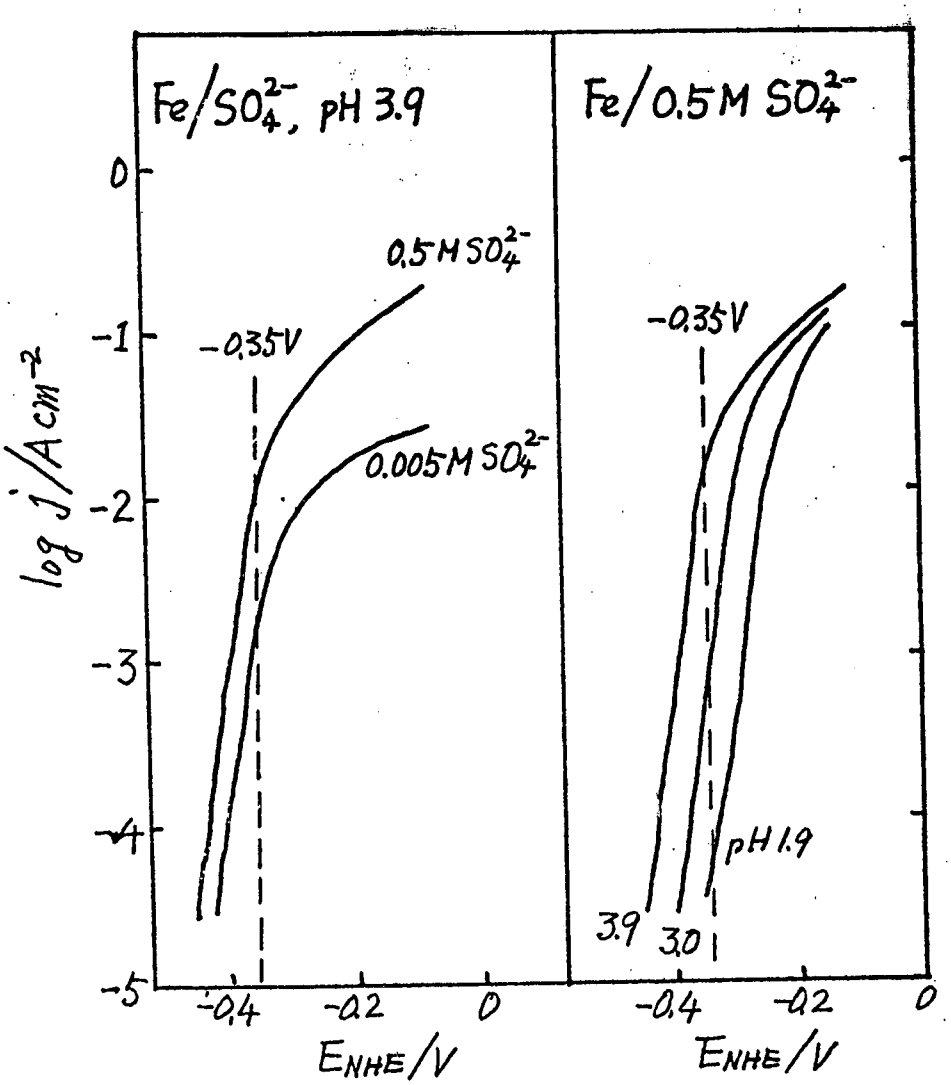

Fig. 3-1. Anodic polarization curves of iron dissolution in the active state in sulphate solutions of different sulphate concentrations and pH (Kolotyrkin dt al., 1967).

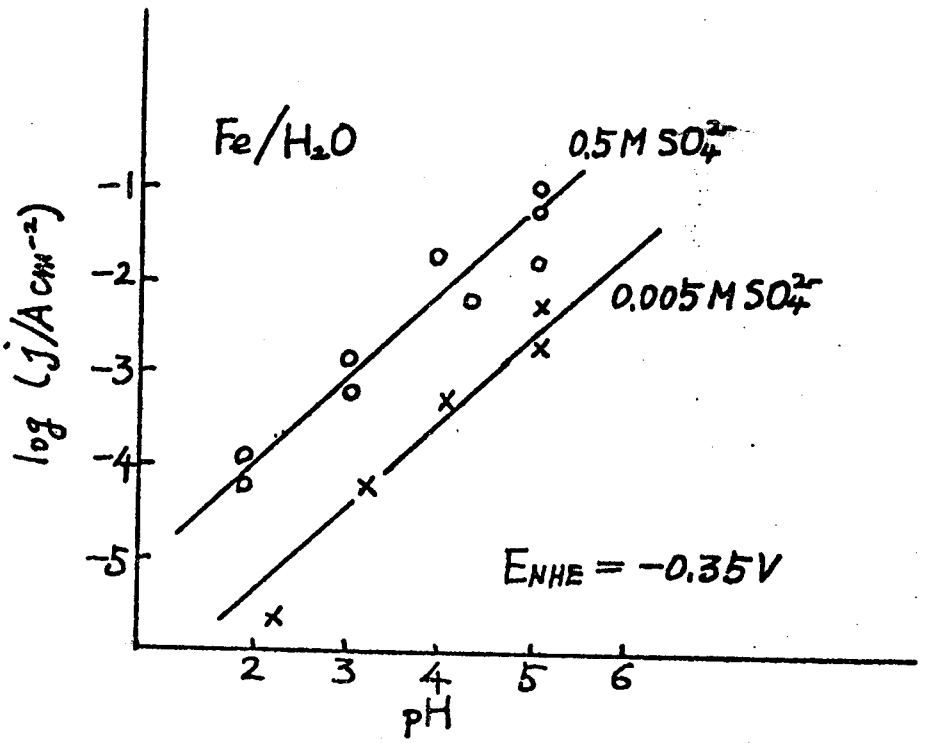

Fig. 3-2. Dependence of the anodic dissolution rate of iron at a constant potential -0.35 V(NHE) on pH in solution with constant sulphate concentration (Kolotyrkin et al., 1967).

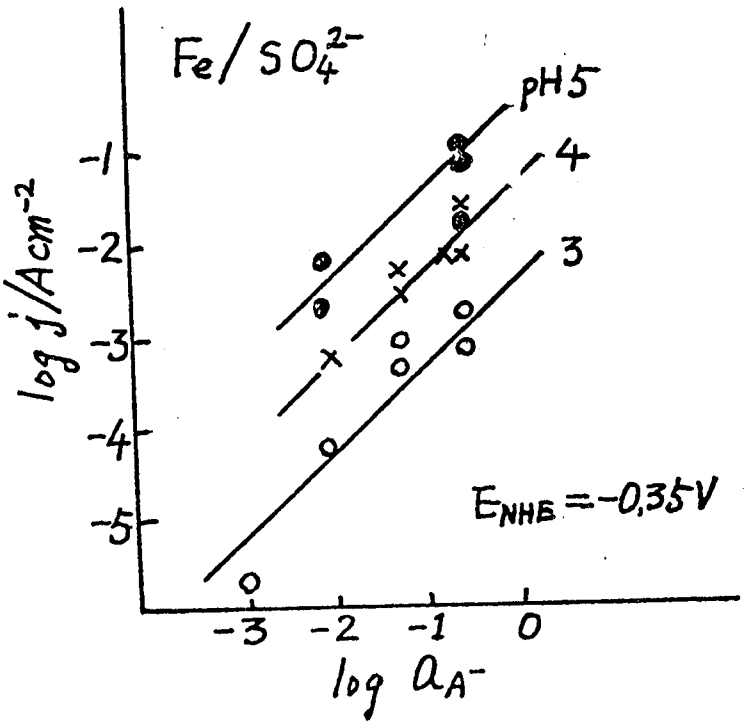

Fig. 3-3. Anodic dissolution rate at a constant potential -0.35 V(NHE) as a function of sulphate activity in solutions of different pH (Kolotyrkin et al., 1967).

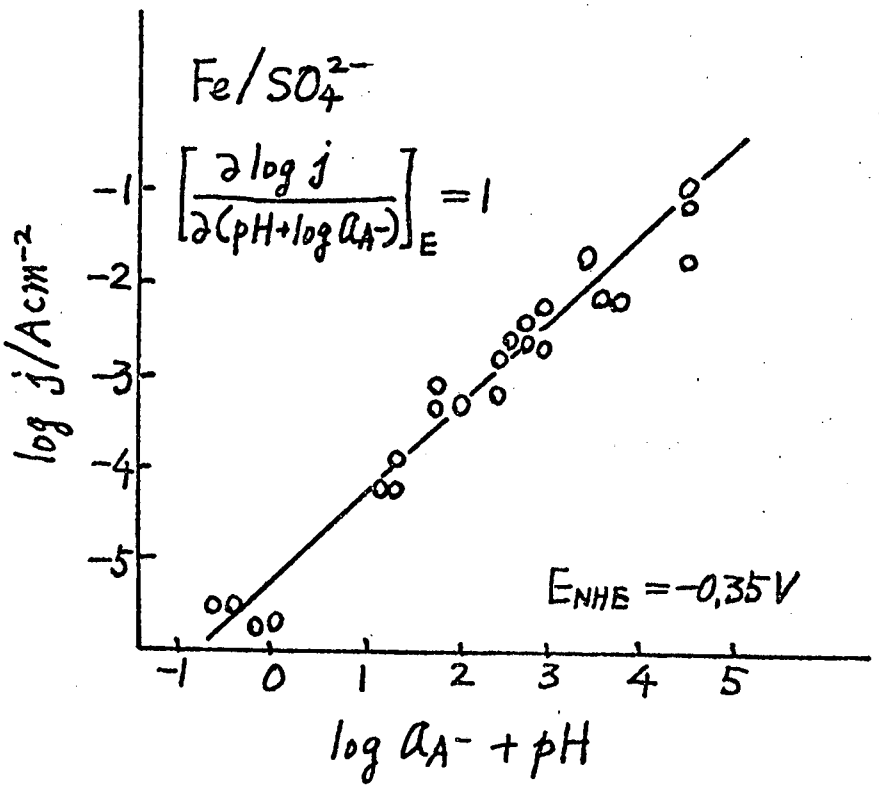

Fig. 3-4. Dependence of the rate of iron dissolution at a constant potential -0.35 V(NHE) on the value of log a_{A^-} + pH for sulphate solutions of different compositions (Kolotyrkin et al., 1967).

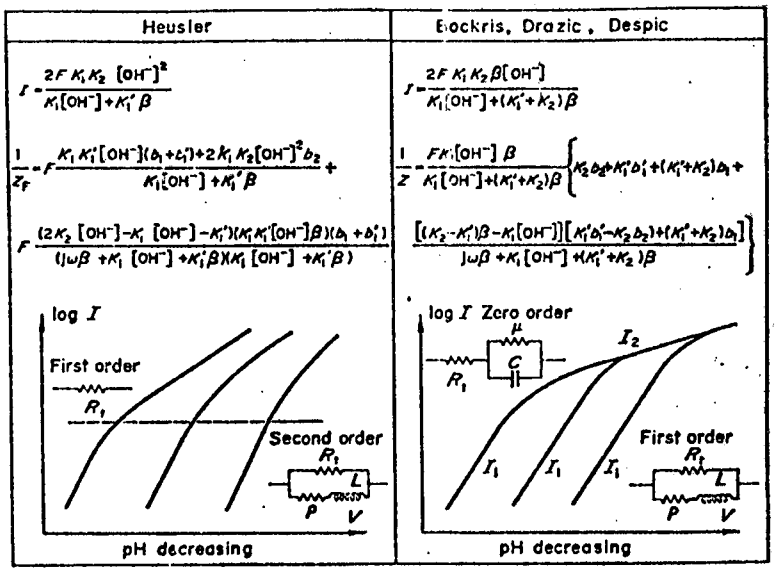

Theoretical behaviour established for mechanisms I and II using the method of Gerischer and Mehl. Expressions of steady-state anodic current I and faradaic impedance Z_F as function of electrochemical rate constants. Schematic I/V curves and equivalent circuit for Z_F at three different pH values.

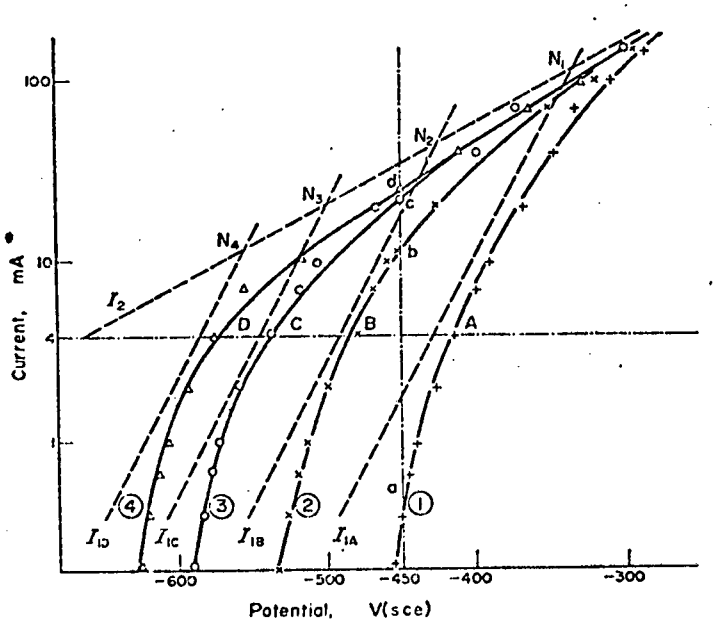

Steady-state current/potential curves for the anodic dissolution of a rotating disk of Johnson–Matthey iron 0·5 cm dia. 2000 rev/min; 25 ± 0·1°C.
1, 1 M H_2SO_4, pH 0·03; 2, 0·1 M H_2SO_4, 0·9 M Na_2SO_4, pH 1·61; 3, 0·01 M H_2SO_4, 0·99 M Na_2SO_4, pH 2·68; 4, 0·0012 M H_2SO_4, 1 M Na_2SO_4, pH 3·50.

Fig. 3-5. Steady-state current/potential curves for the anodic dissolution of a rotating disk of iron in 1 M H_2SO_4 at pH 0.03 (1), 0.1 M H_2SO_4 + 0.9 M Na_2SO_4 at pH 1.61 (2), 0.01 M H_2SO_4 + 0.99 Na_2SO_4 at pH 2.68 (3), and 0.0012 M H_2SO_4 + 1 M Na_2SO_4 at pH 3.50 (4). (Epelboin and Keddam, 1972).

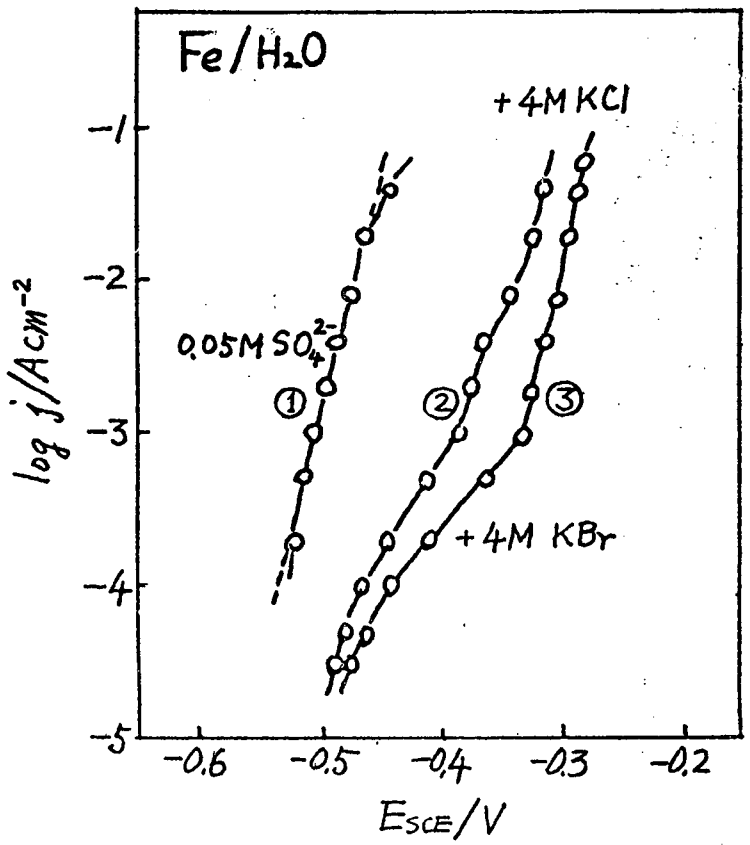

Fig. 3-6. Anodic polarization curves of iron dissolution in 0.05 M H_2SO_4 solutions with and without halide ions (Schwabe and Voigt, 1969).

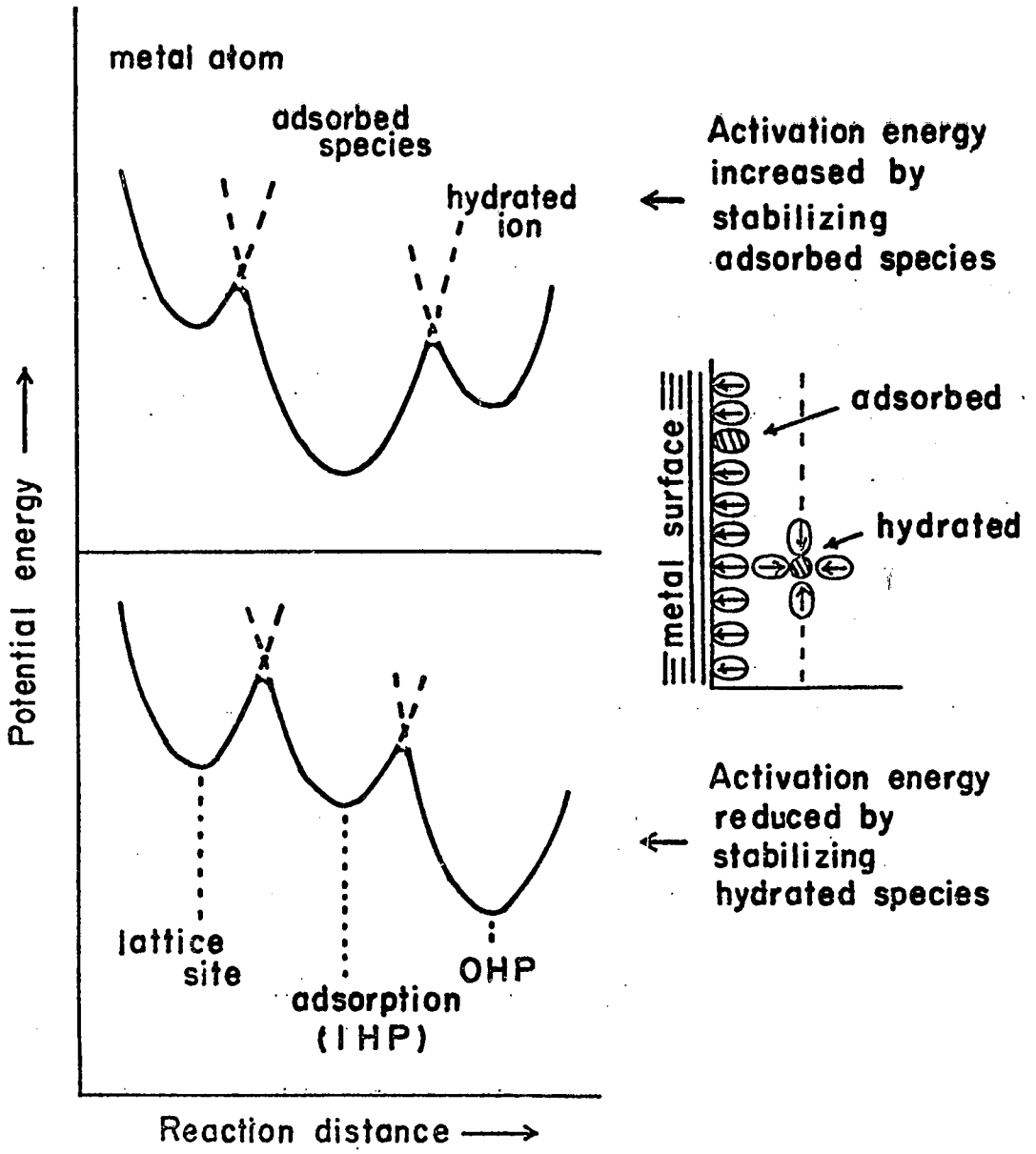

Fig. 3-7. Energy profile for metal atom at surface sites, adsorbed intermediate and hydrated metal ion at the OHP. The relative energy level of adsorbed intermediate and hydrated metal ion control the activation energy of anodic metal dissolution.

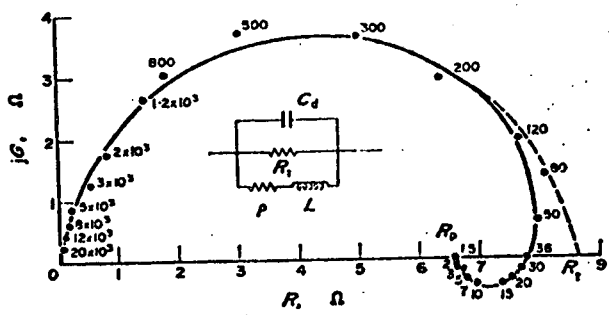

(a)

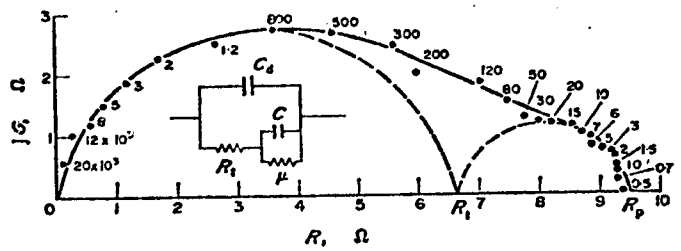

(b)

Fig. 4-1. Complex impedance diagrams R versus jG for a rotating iron electrode in the active dissolution regions in sulphuric acid solutions at lower dissolution current (a) and at higher dissolution current (b) (Epelboin et al., 1972).

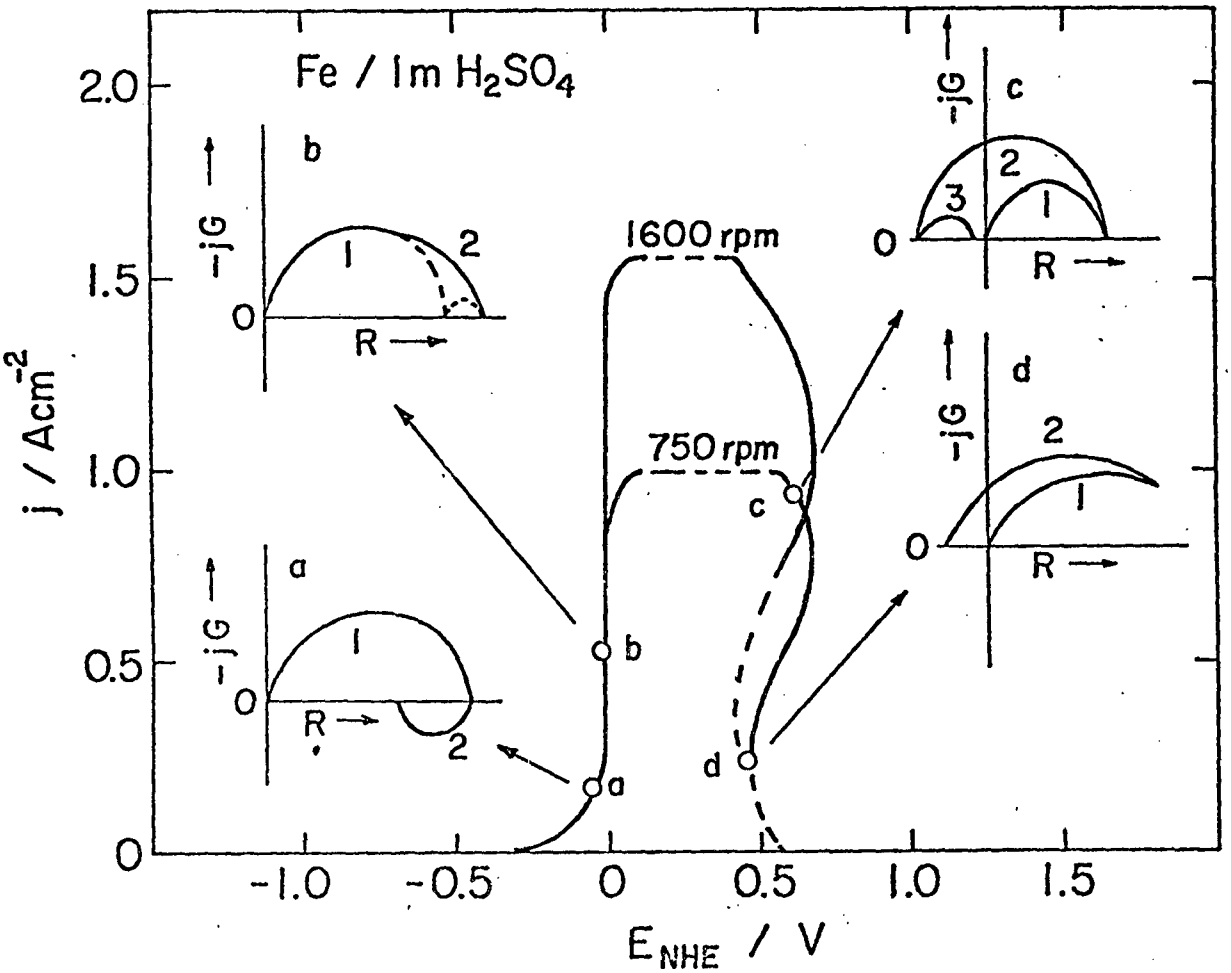

Fig. 4-2. Steady-state polarization curve of a rotating iron electrode at two different speeds in 1 M H_2SO_4 and schematic impedance spectra (R versus jG curves) at from different potentials, a) active dissolution at low current, b) active dissolution at high current, c) passivity at high current, and passivity at low current (Epelboin et al., 1975).

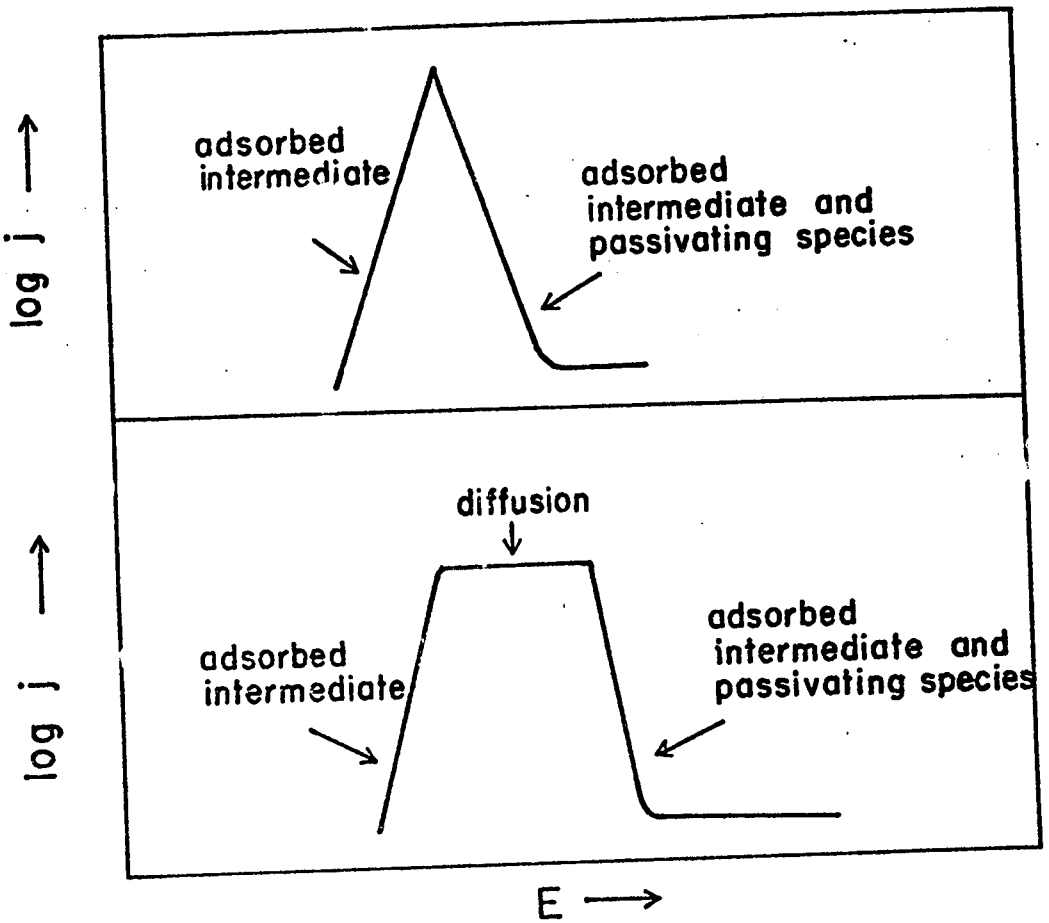

Fig. 4-3. Schematic anodic polarization curves and adsorption versus potential curves anticipated from impedance measurements.

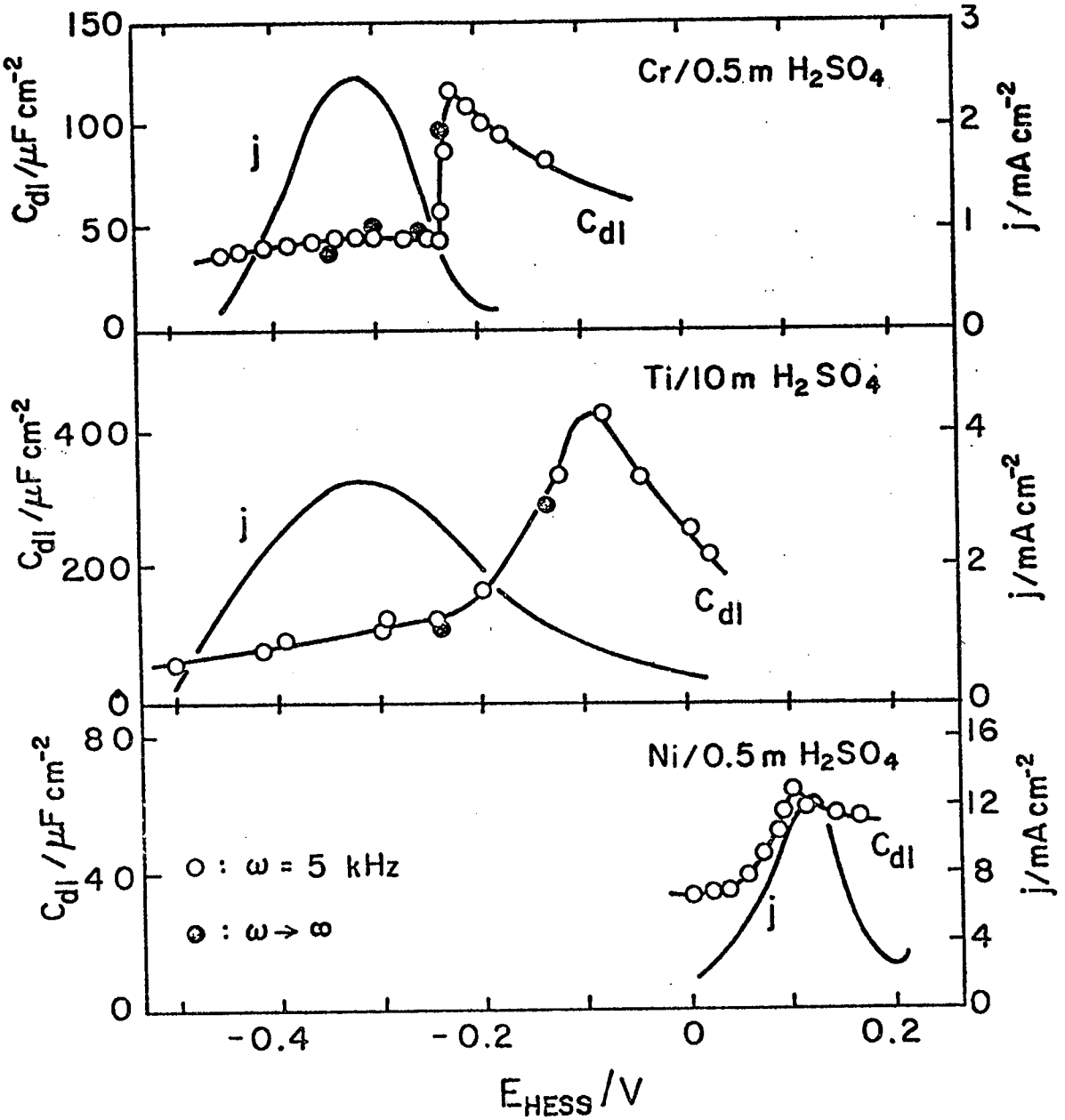

Fig. 4-4. Electrical double layer capacity and anodic current versus potential in the active-passive transition for chromium, titanium, and nickel in acid solutions (Armstrong et al., 1972).

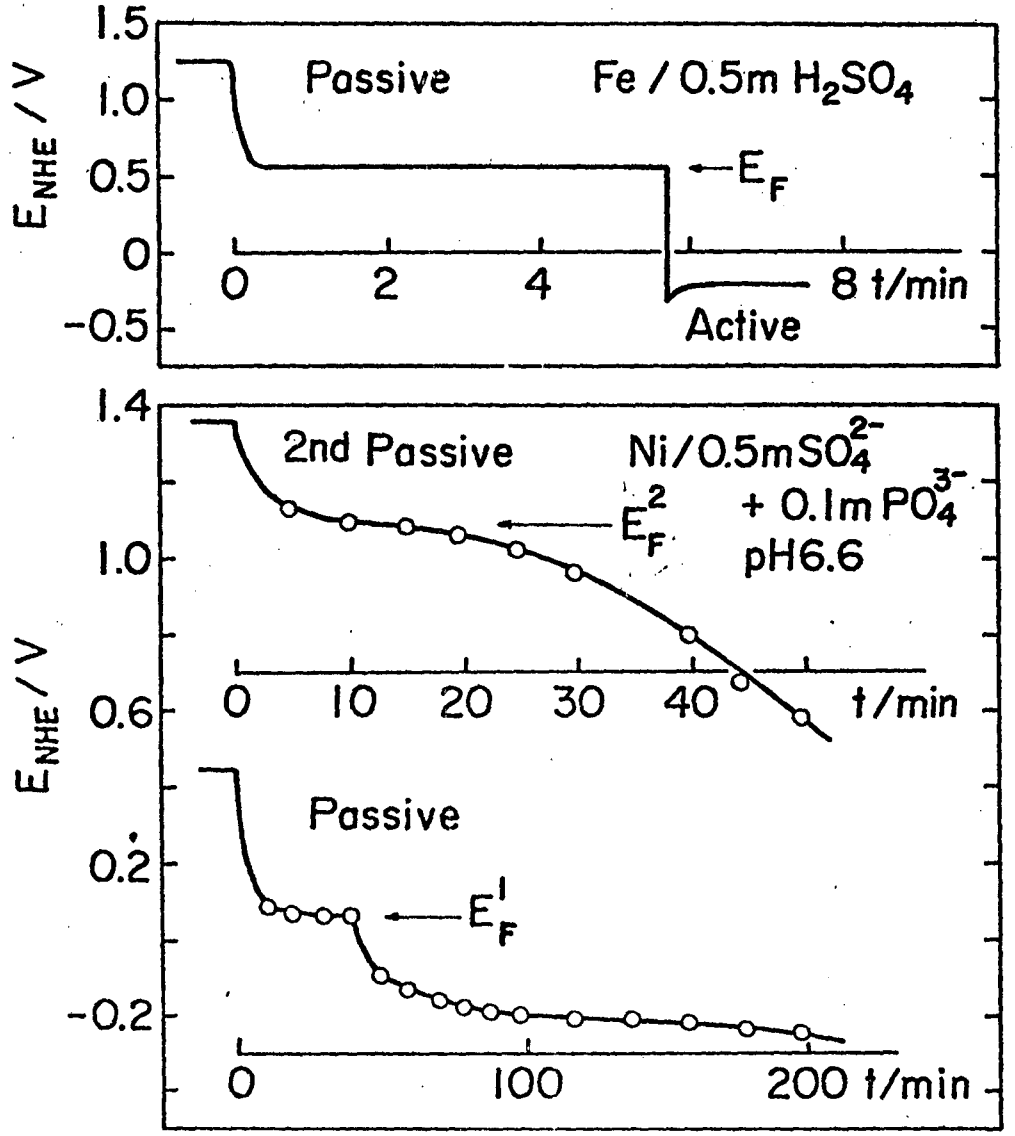

Fig. 4-5. Open-circuit decay of passivity as a function of time, showing the Flade potential of iron in 0.5 M H_2SO_4 (Franck et al., 1952) and Nickel in 0.5 M SO_4^{2-} solution at pH 6.6 (Okamoto and Sato, 1963).

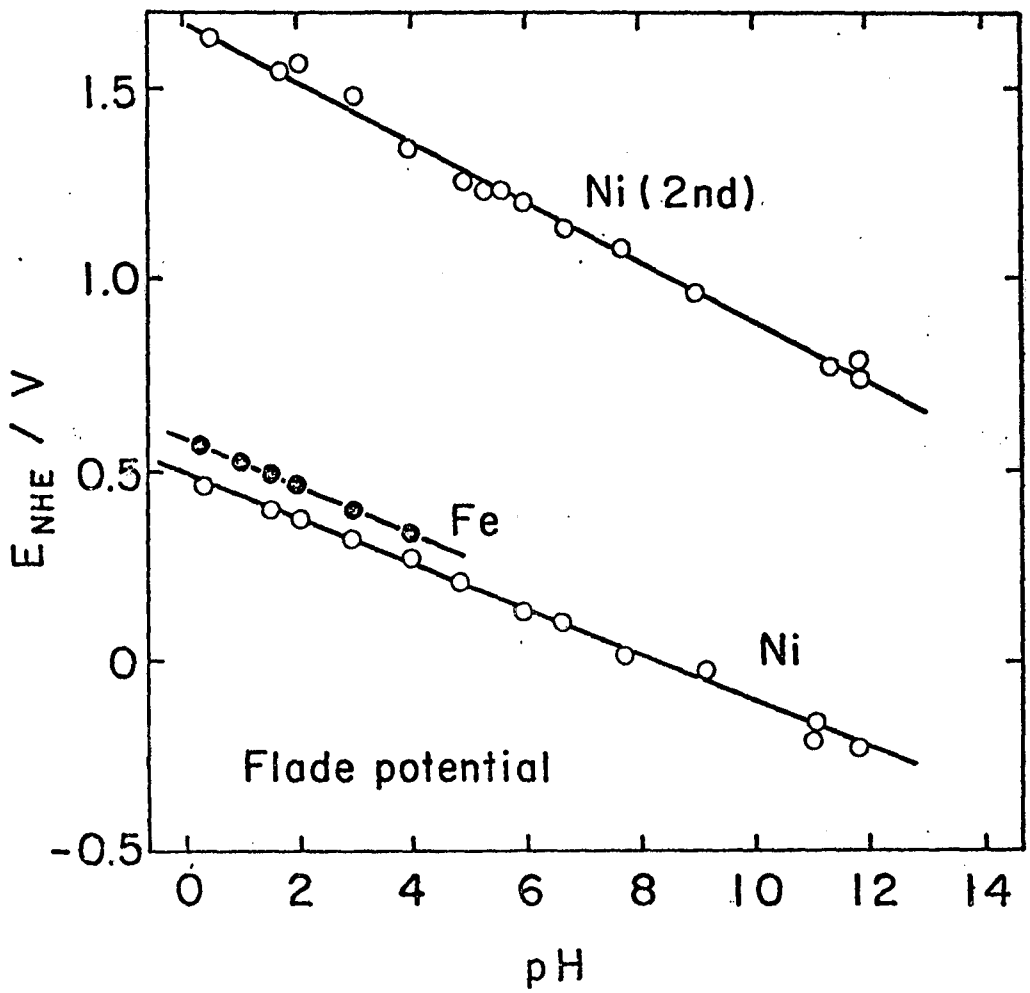

Fig. 4-6. pH-dependence of the Flade potential of iron (Franck, 1948) and nickel (Sato, 1963). E_F(iron) = +0.58 - 0.058 pH, E_F(nickel, primary) = + 0.48 - 0.058 pH, E_F(nickel, secondary) = + 1.60 - 0.095 pH.

Fig. 4-7. Potential versus time for galbanostatic passivation of iron in 0.5 M H_2SO_4 (Franck, 1947), nickel in 0.5 M Na_2SO_4 at pH 6.6 (Sato, 1963), and chromium in 0.1 M H_2SO_4 (Heumann, et al., 1958).

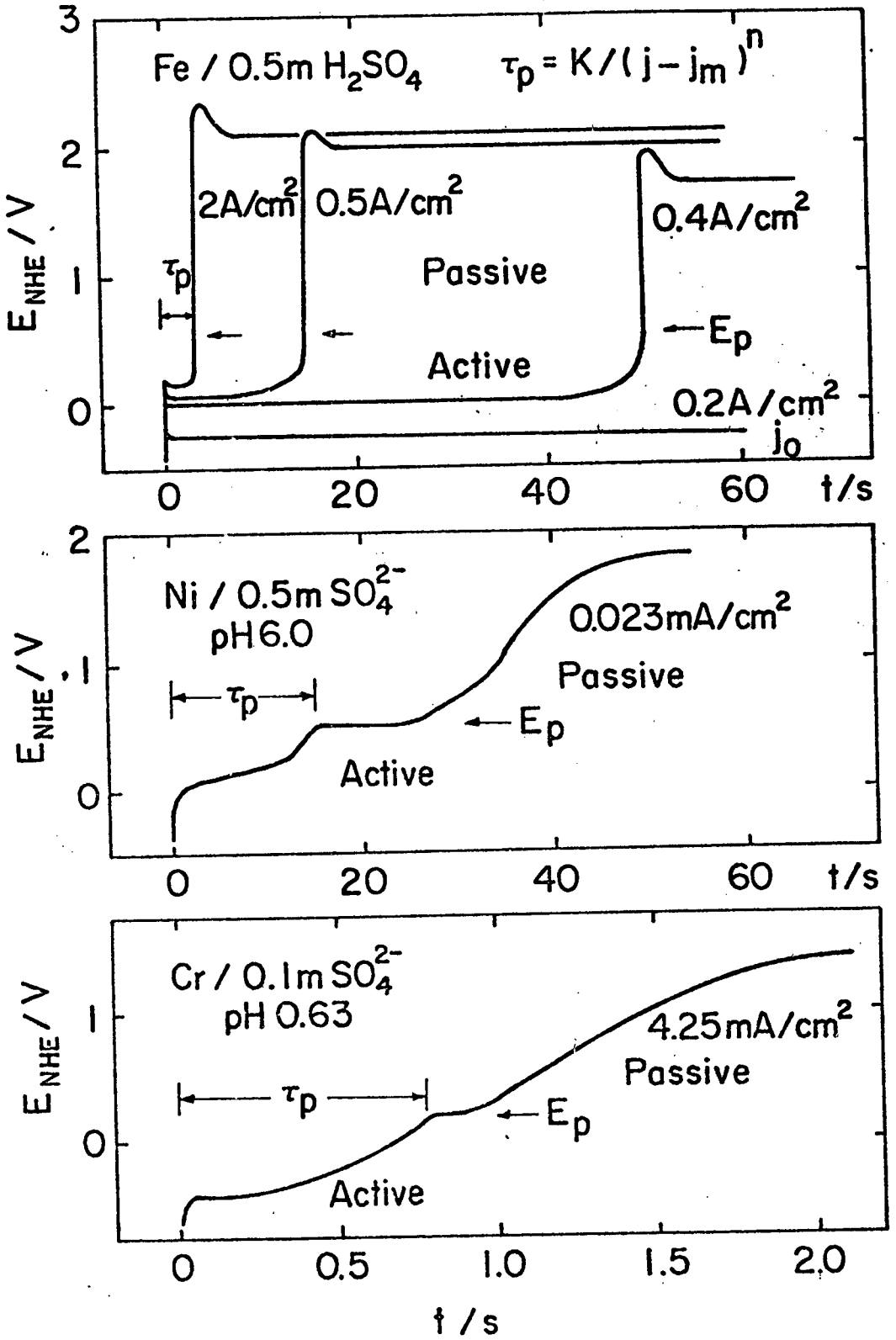

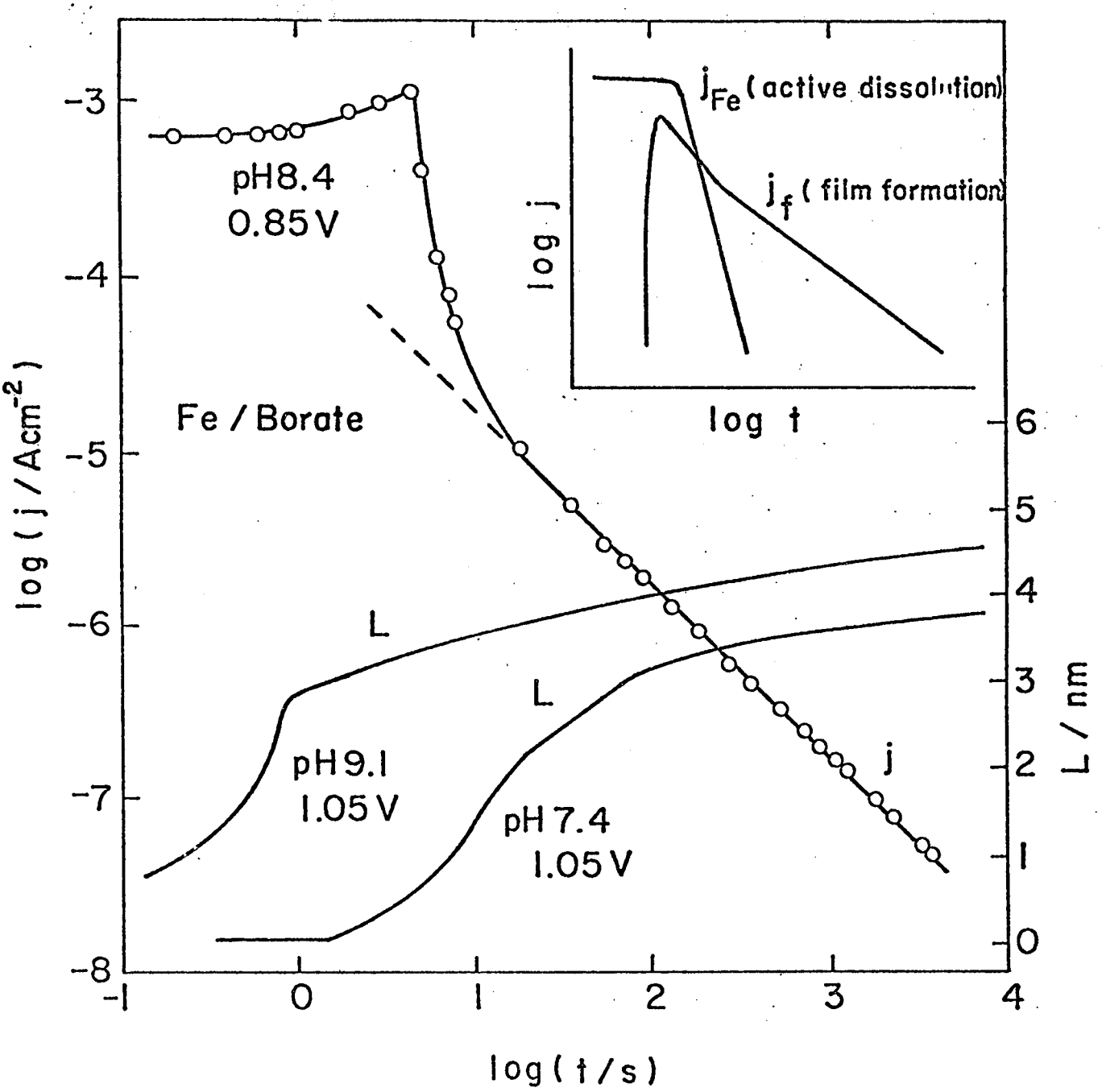

Fig. 4-8. Anodic current (Nagayama et al., 1962) and film thickness (Kruger et al., 1960) versus time during potentiostatic passivation of iron in borate buffer solutions, and schematic representation of active dissolution current j_{Fe} and film formation current j_f changing with time.

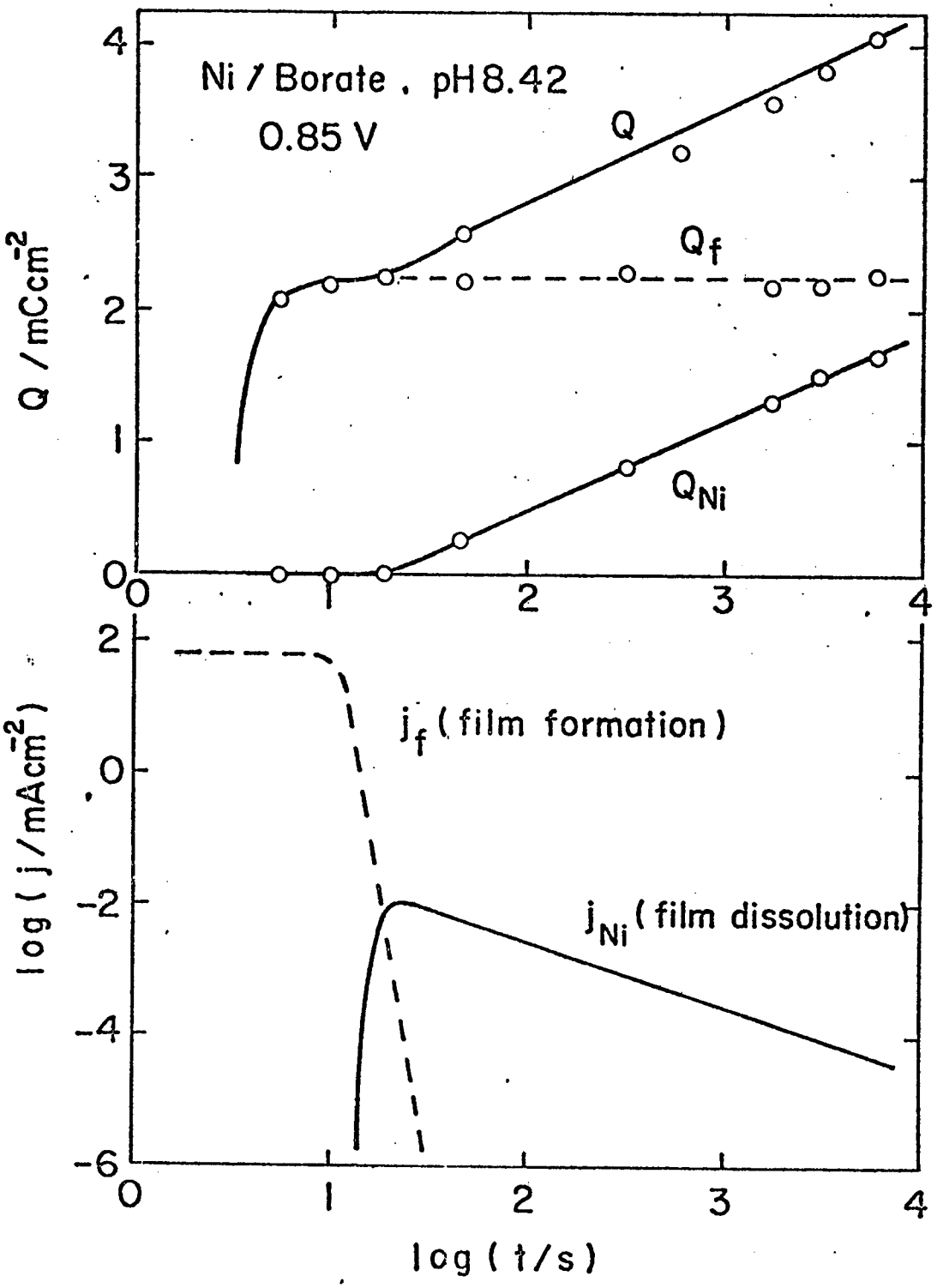

Fig. 4-9. Total anodic charge Q, dissolution charge Q_{Ni}, and film formation charge $Q_f = Q - Q_{Ni}$ versus time during potentiostatic passivation of nickel in a borate solution at pH 8.42, and expected time variation of dissolution current j_{Ni} and of film formation current j_f (Sato et al., 1971).

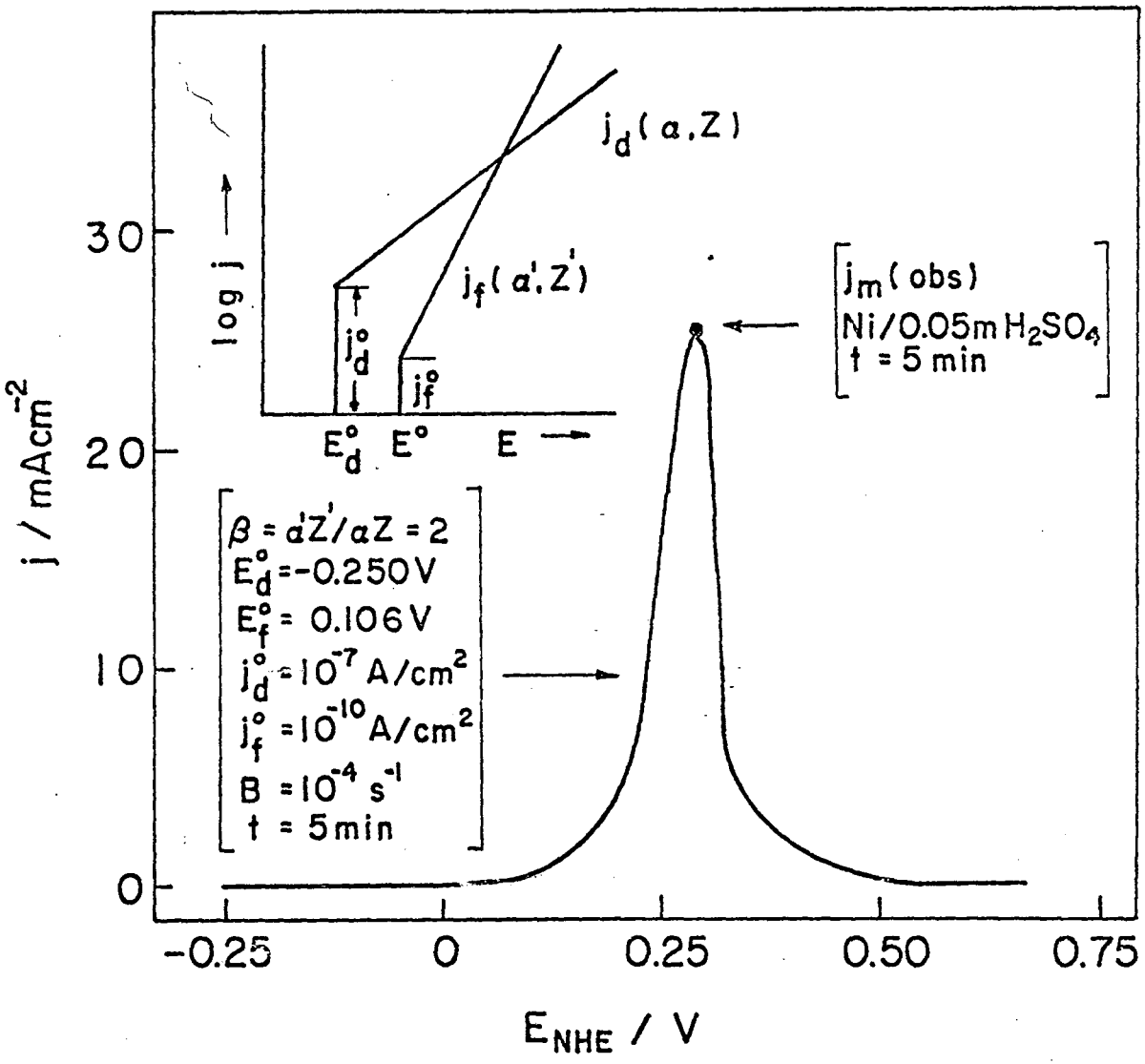

Fig. 4-10. Potentiostatic anodic polarization curve calculated from a simple competitive model for passivation using kinetic parameters typical for nickel, and experimentally estimated peak current in active dissolution of nickel in 0.05 M H_2SO_4 for passivation time t = 5 min (Ebersbach et al., 1967).

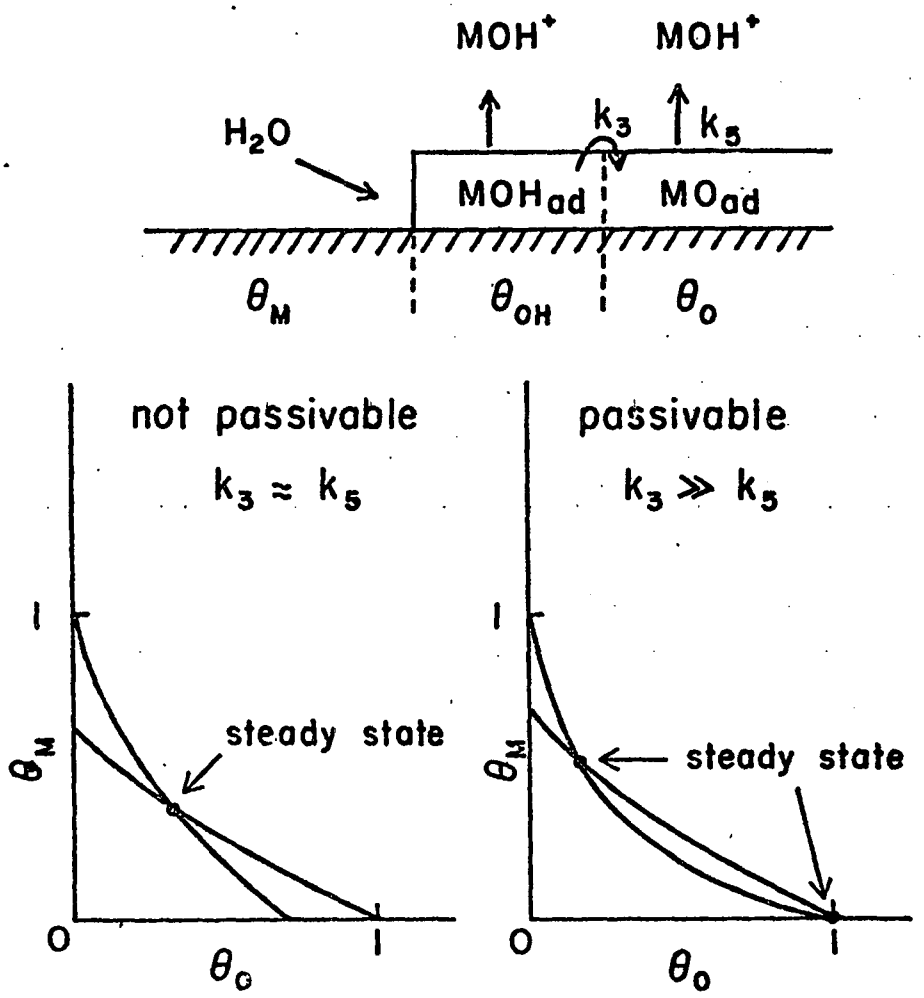

Fig. 4-11. Two adsorbed species whose kinetic properties determining the occurrence of passivation.

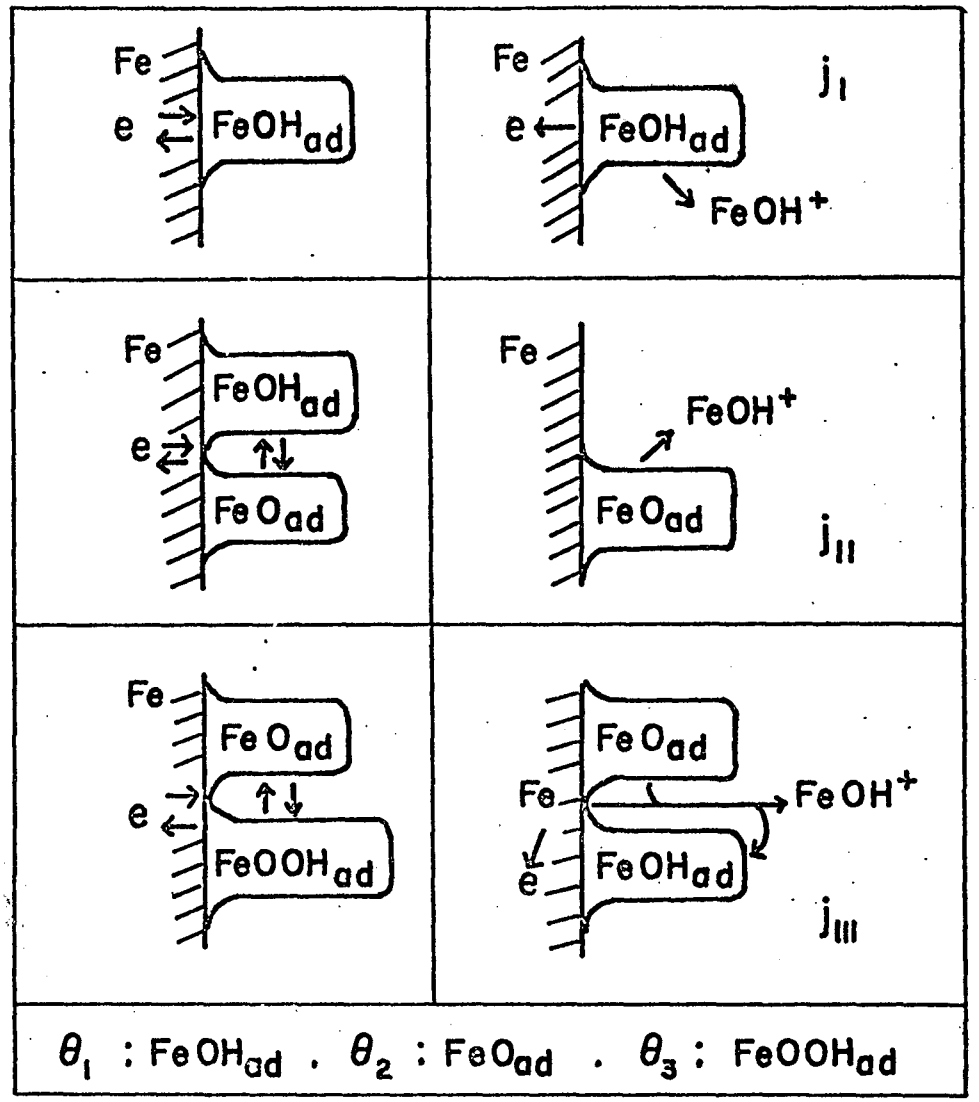

Fig. 4-12. Three adsorbed species contributing anodic dissolution and passivation.

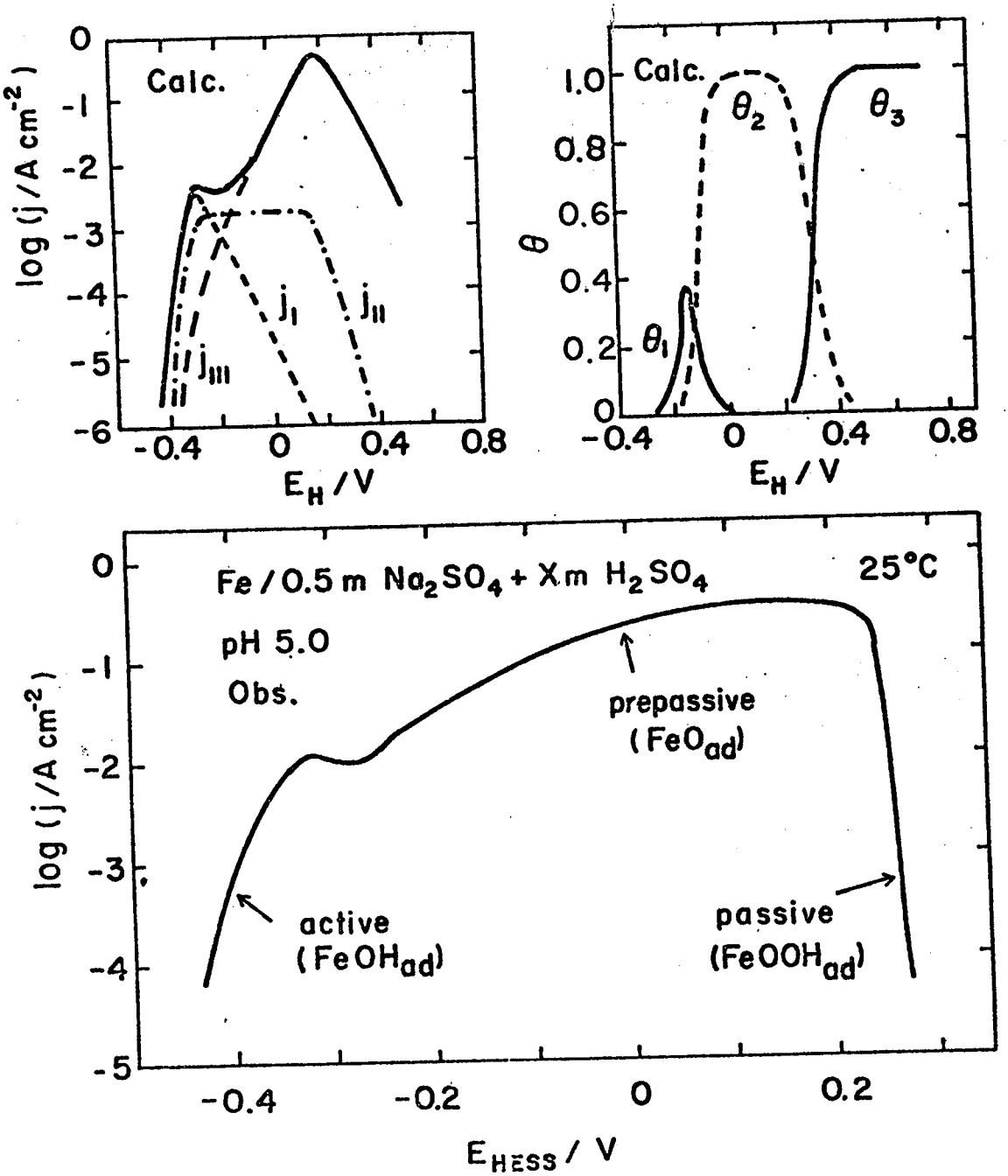

Fig. 4-13. Computor evaluation of anodic dissolution currents and adsorption coverages for three adsorbed species as a function of potential in comparison with observed current versus potential curve of iron in a neutral sulphate solution (Lorenz et al., 1967).

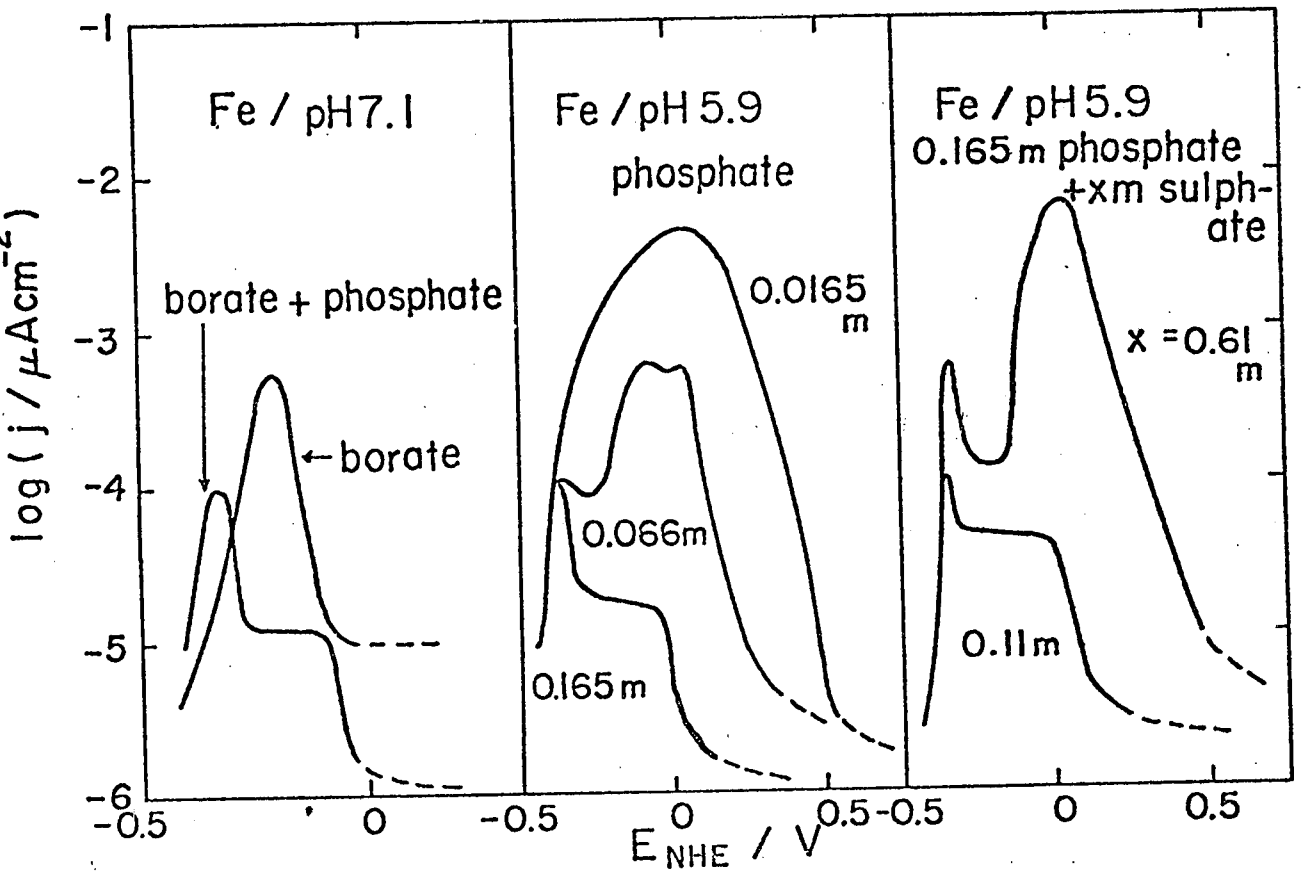

Fig. 4-14. Effects of anions on anodic polarization curve for active-passive transition of iron in neutral solutions (Kolotyrkin et al., 1969).

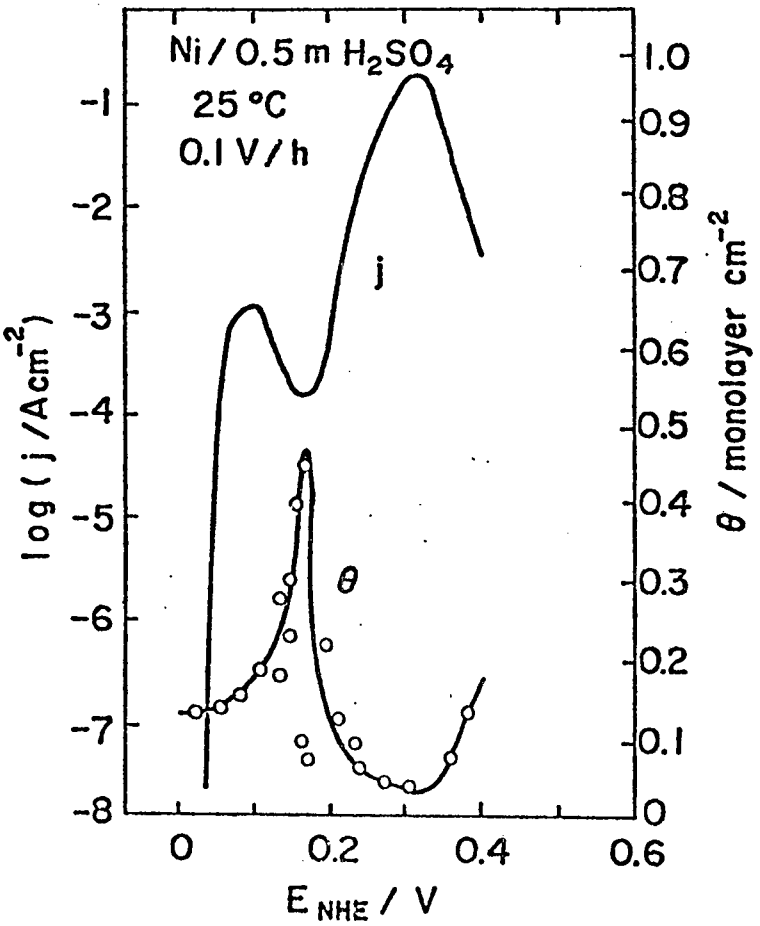

Fig. 4-15. Anodic potential-sweep polarization curve and adsorption coverage of sulphate ion as a function of potential for nickel pre-immersed for 18 hours in 0.5 M H_2SO_4 (Feller et al., 1972).

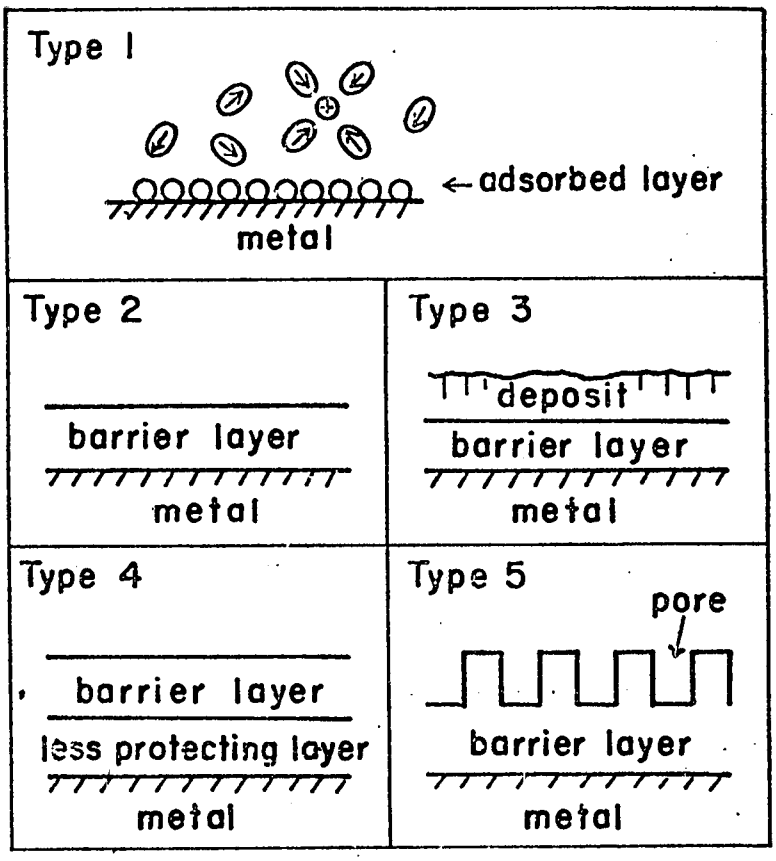

Fig. 5-1. Five types of passive films on metals (Sato, 1977).

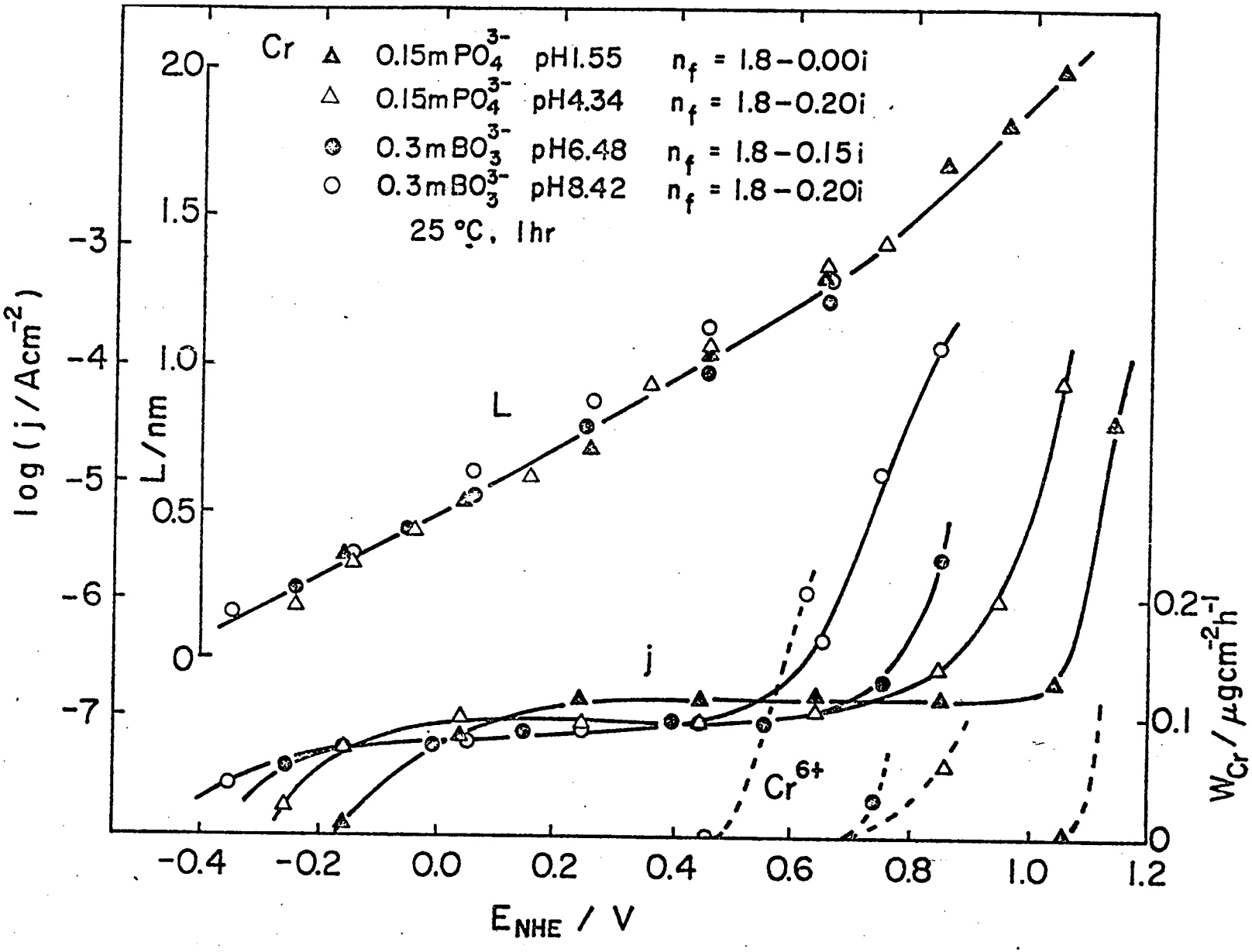

Fig. 5-2. Passive film thickness and anodic current versus potential for chromium in acid phosphate and neutral borate solutions (Saito and Sato, to be published).

L = thickness measured by ellipsometry, n_f = optical constant of the film.

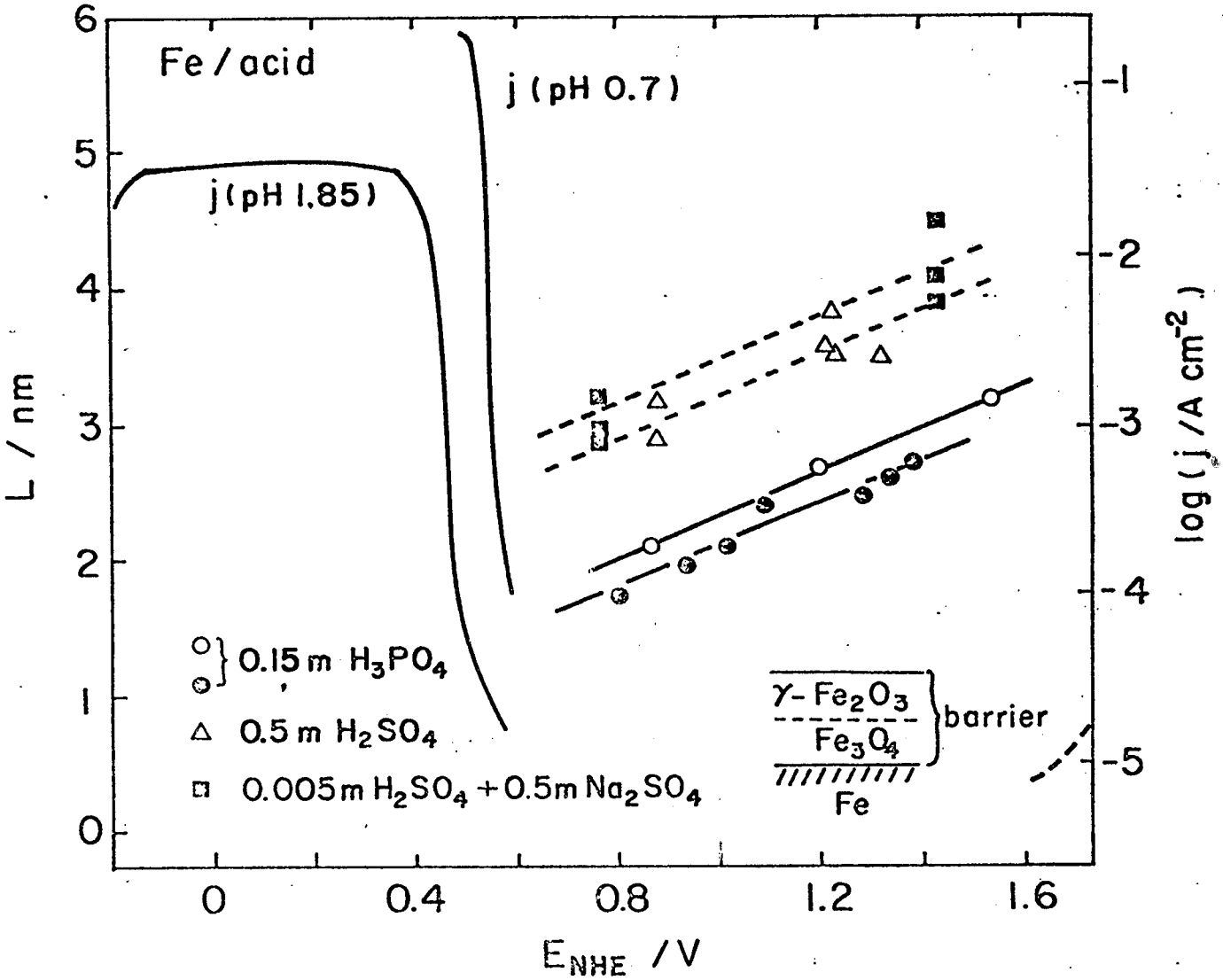

Fig. 5-3. Passive film thickness versus potential for iron in acid solutions. L= thickness measured by ellipsometry ○ ◉ : Sato et al. (1973-75), ■△ Vetter et al. (1973).

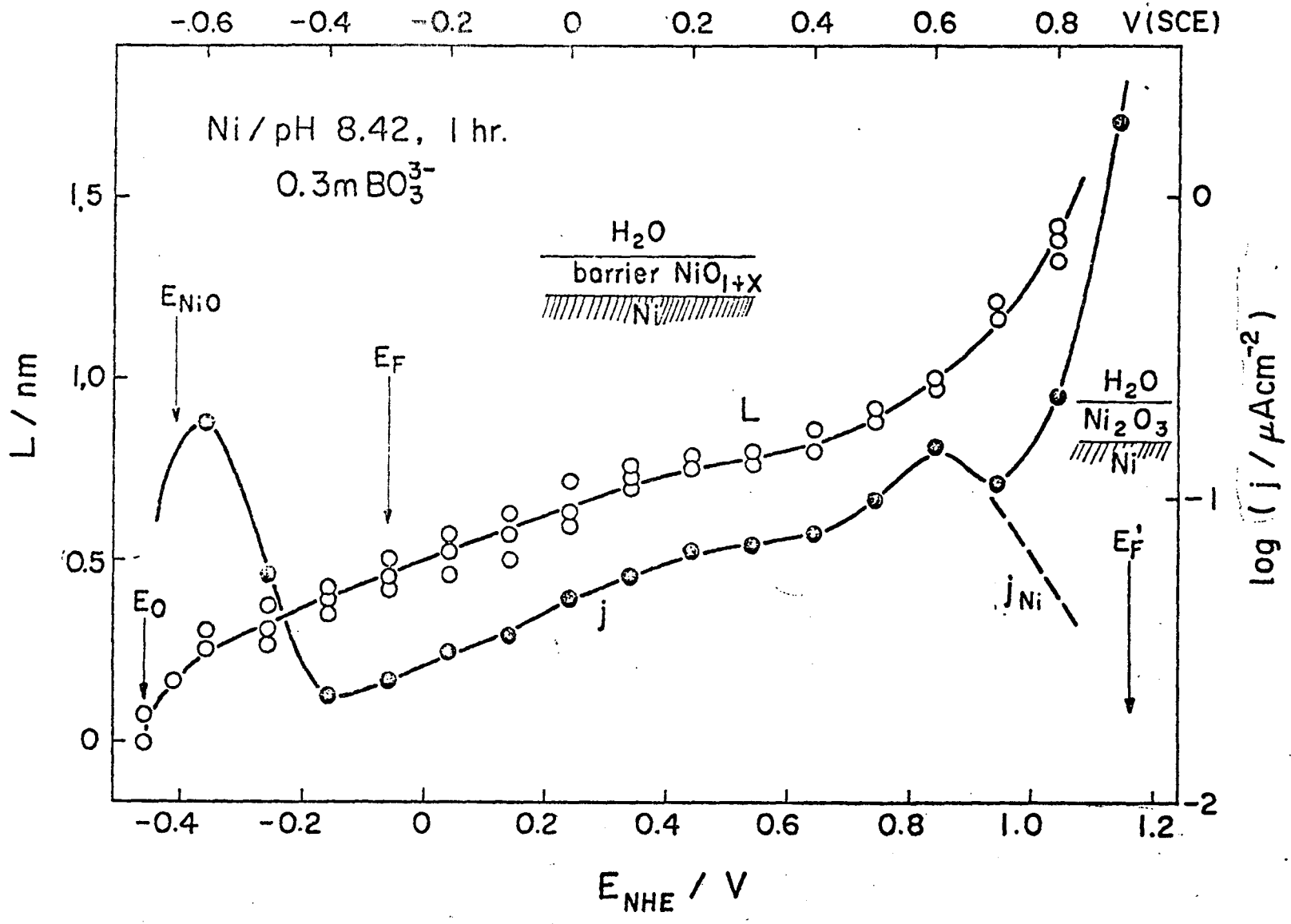

Fig. 5-4. Passive film thickness and anodic current versus potential for nickel in a borate solution (Sato et al. 1974). L = thickness measured by ellipsometry.

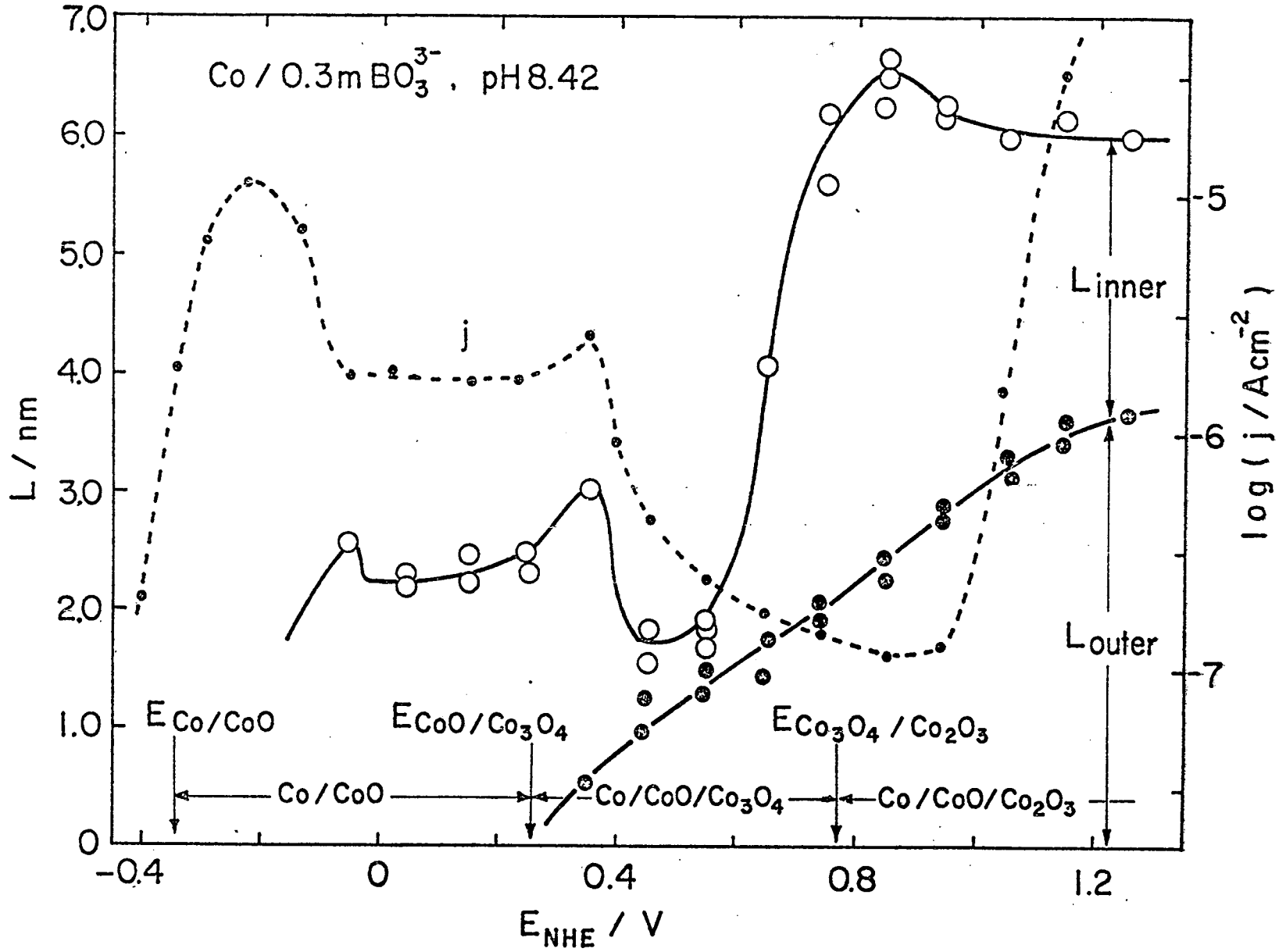

Fig. 5-5. Passive film thickness versus potential for cobalt in a borate solution (Ohtsuka et al., 1974). L = thickness measured by ellipsometry.

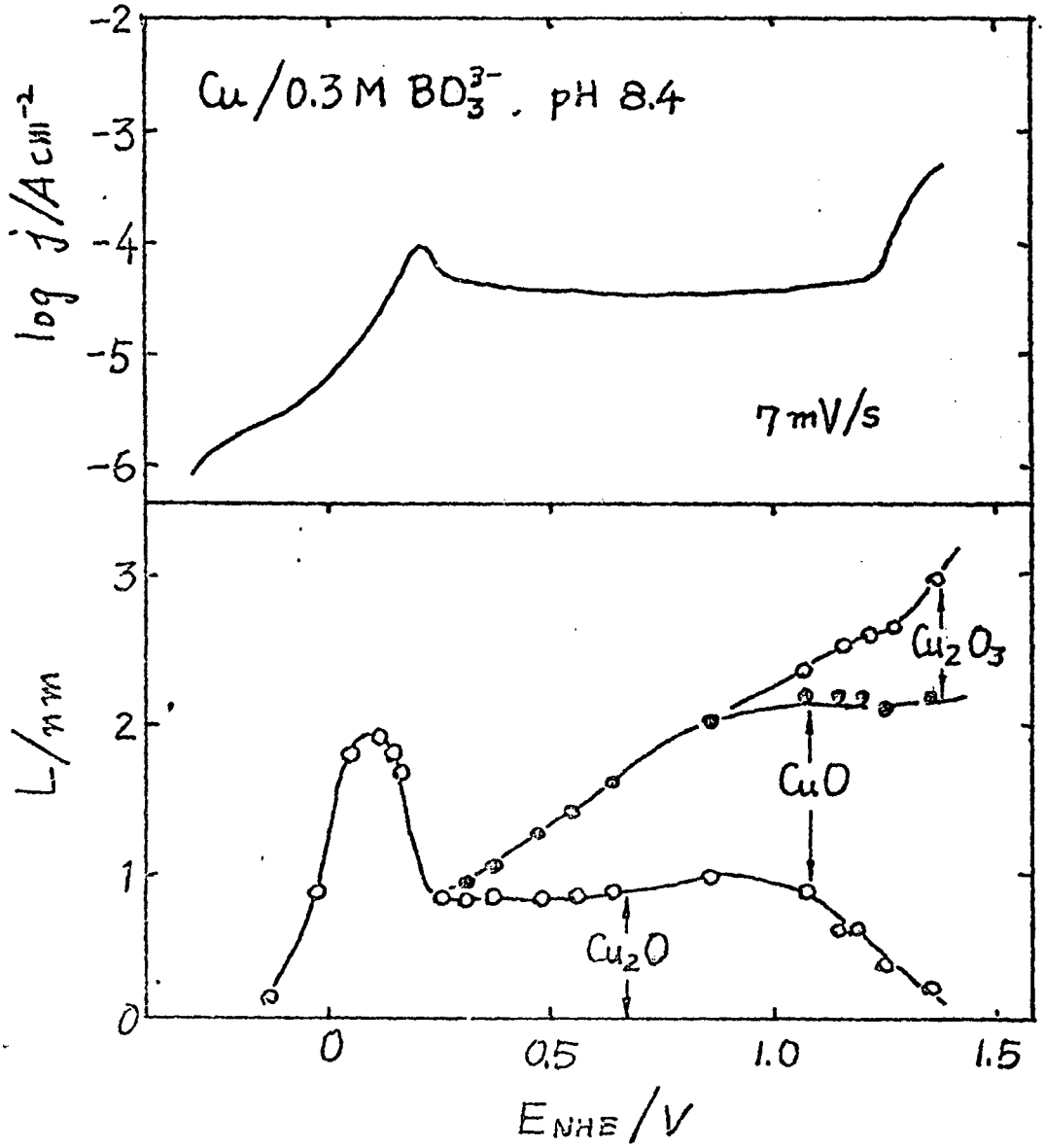

Fig. 5-6. Passive film thickness and anodic current versus potential for cupper in a borate solution (Haruyama et al., 1976). L = thickness measured by cathodic coulometry.

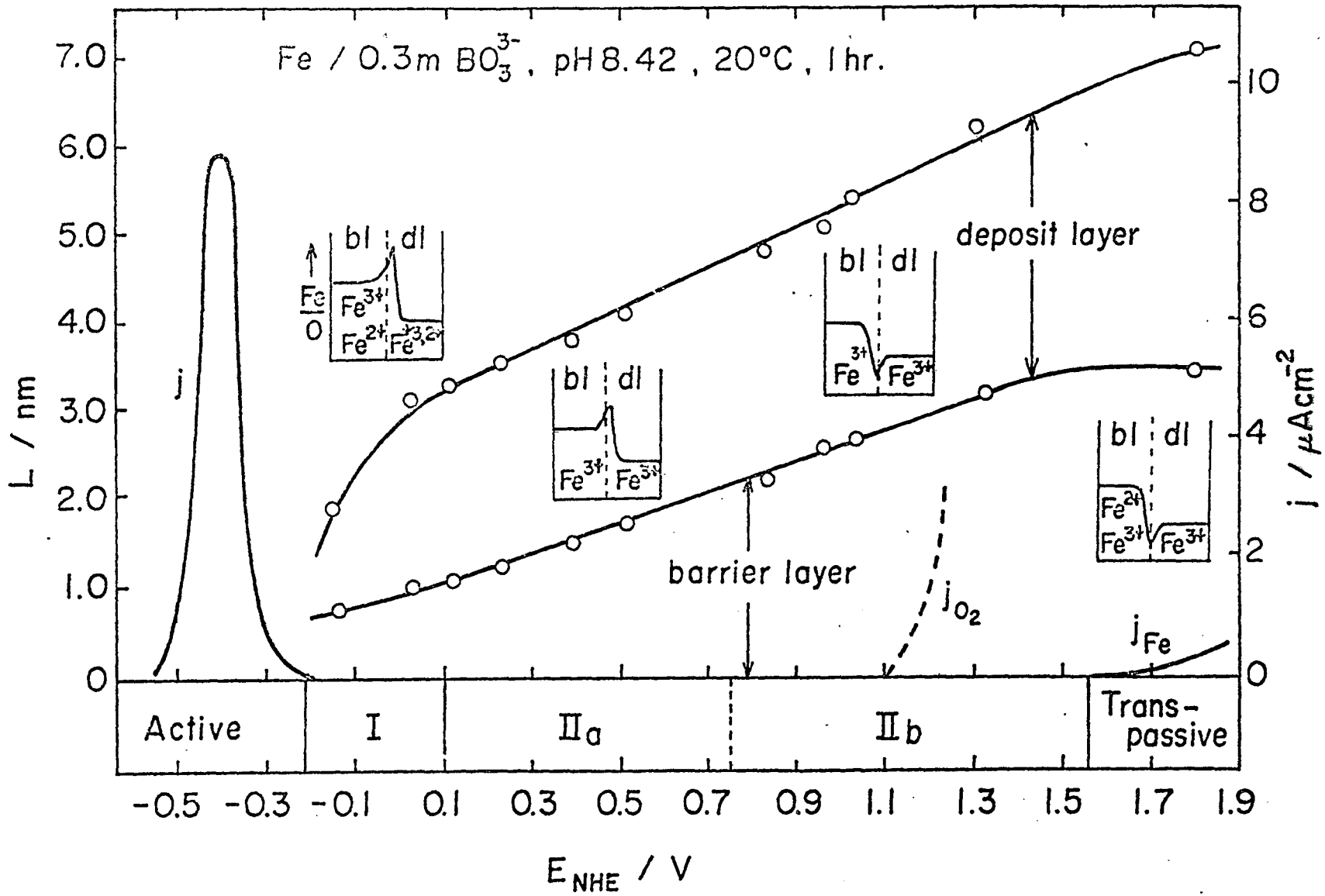

Fig. 5-7. Passive film thickness versus potential and schematic compositional in-depth profile for the passivating film of barrier and deposit layers on iron in a neutral solution (Sato et al., 1976). L = thickness measured by ellipsometry.

Fig. 5-8. Passive film thickness and anodic dissolution current versus solution pH for the passivating film formed for one hour on cobalt at a constant overpotential in phosphate and borate solutions (Ohtsuka et al., to be published).
L = thickness measured by ellipsometry.

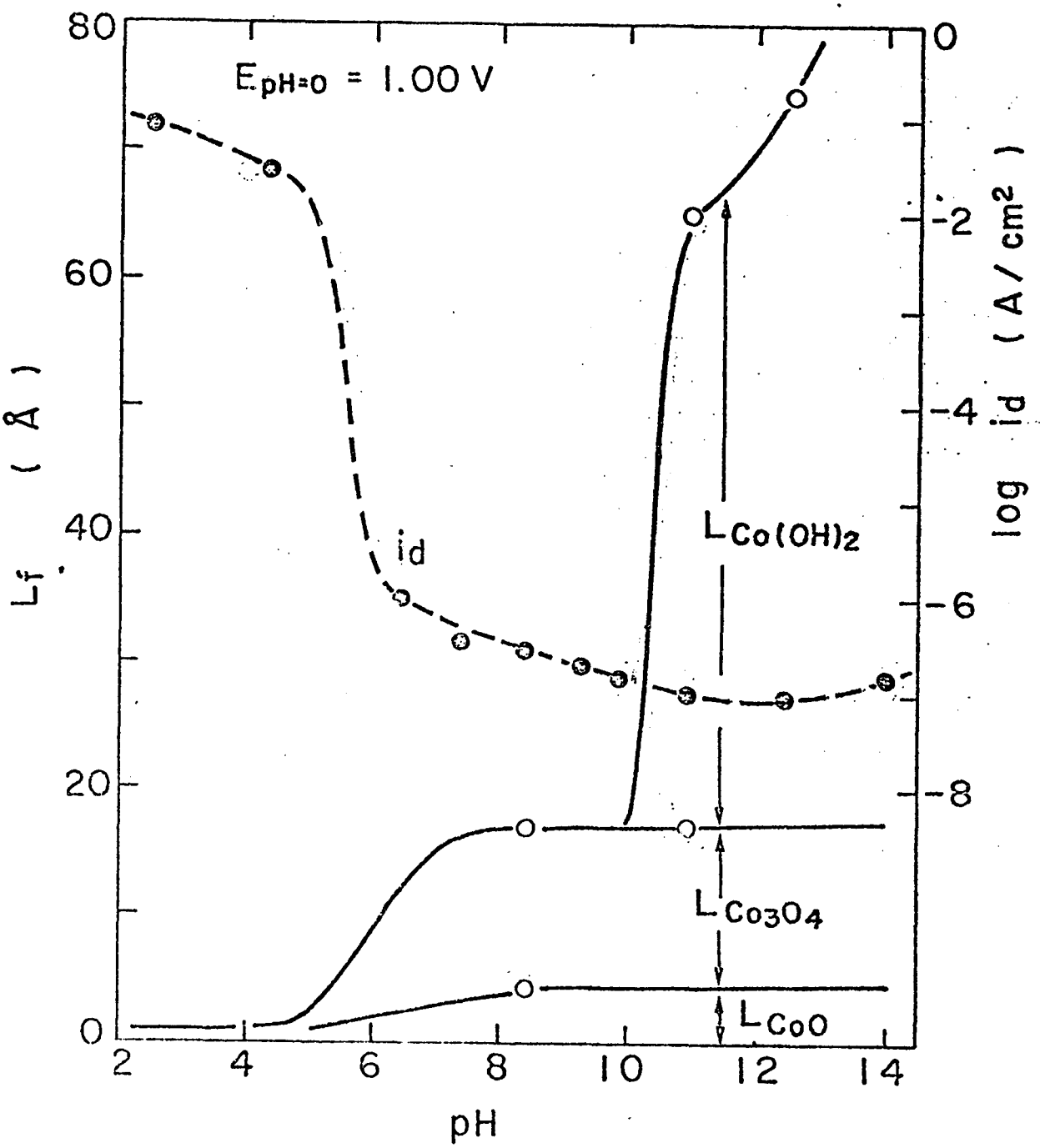

Film thickness and dissolution current of secondary passivity.

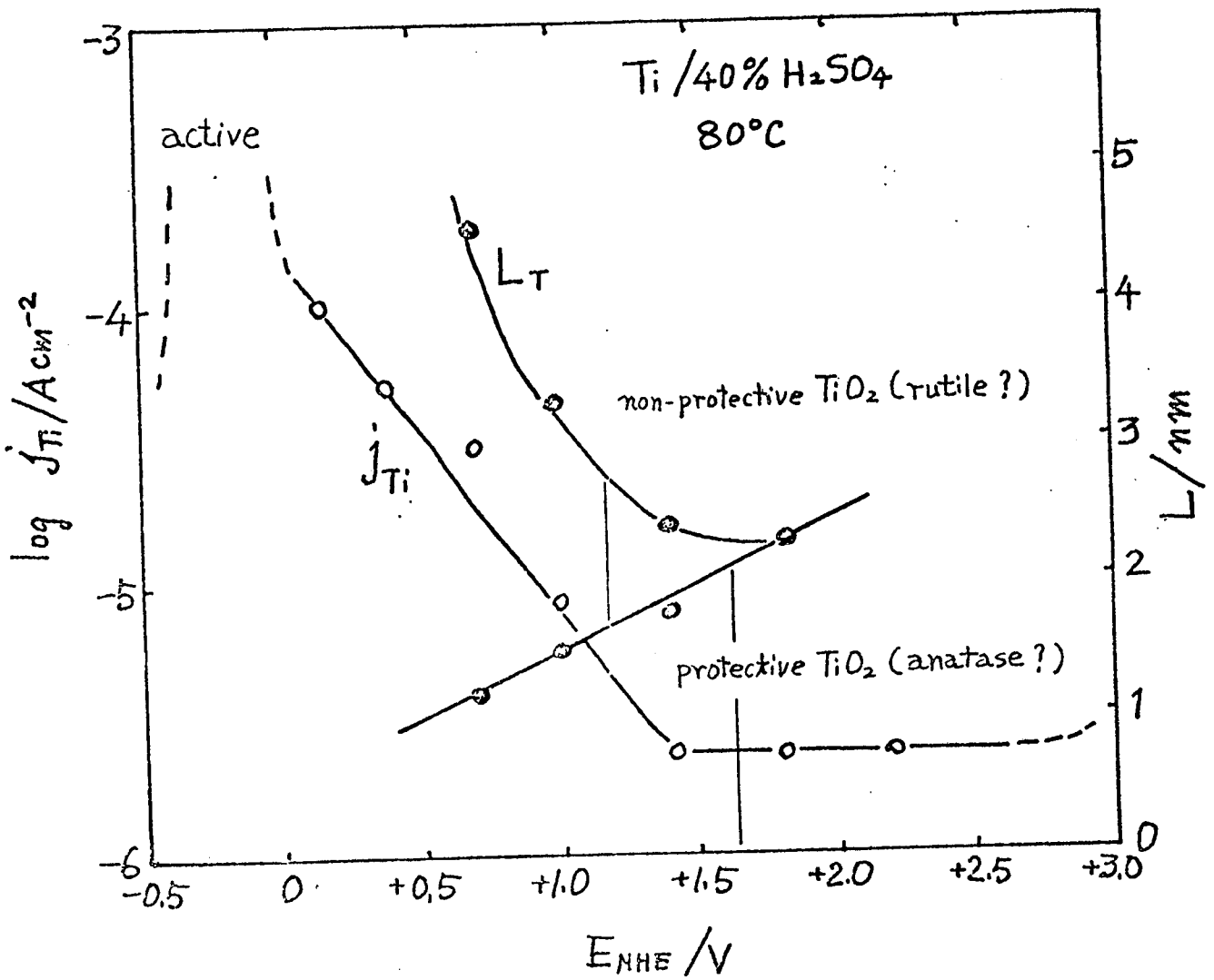

Fig. 5-9. Passive film thickness and anodic dissolution current versus potential for titanium in sulphuric acid solution (Tomashov et al., 1972). L = thickness measured by coulometry and gravimetry.

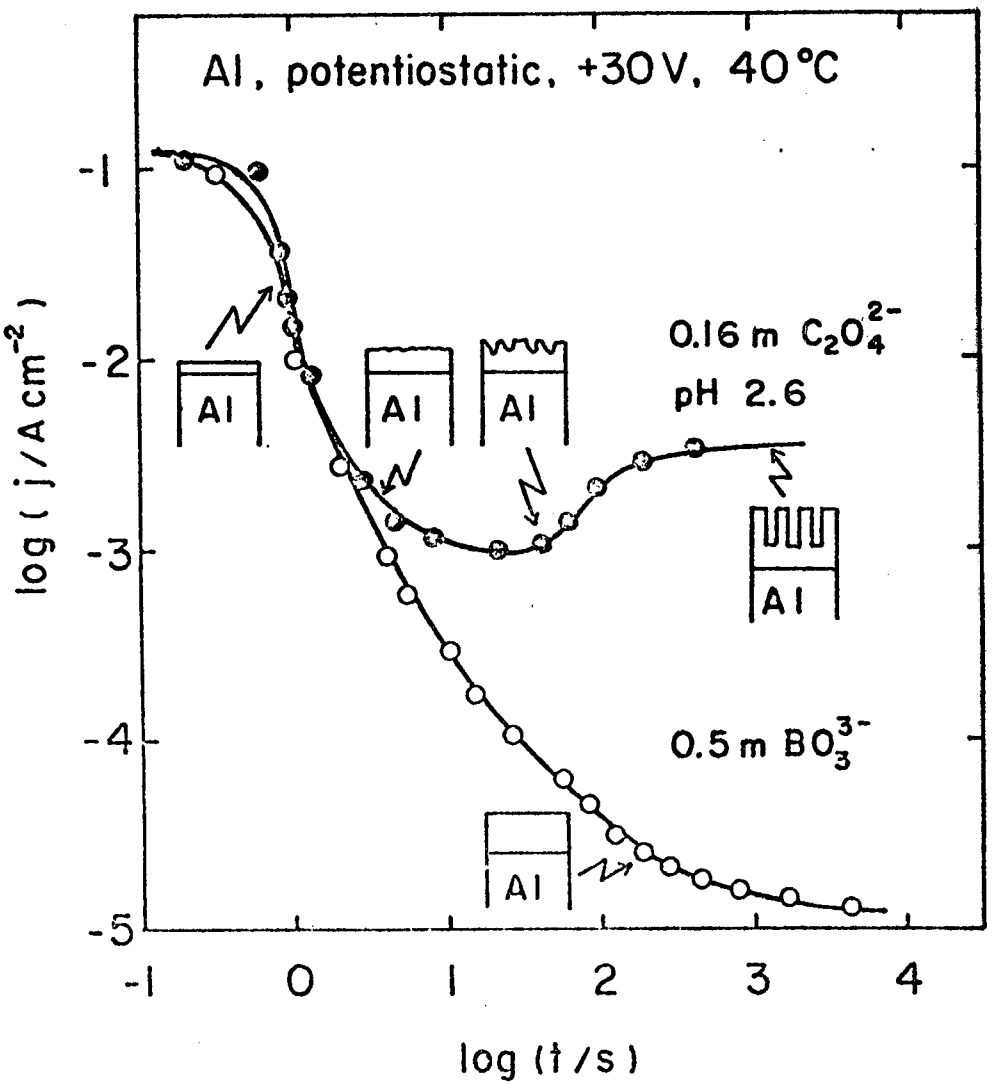

Fig. 5-10. Anodic current and morphology of anodic oxide films versus potentiostatic passivation time for aluminum in oxalic acid and neutral borate solutions (Nagayama et al., 1972).

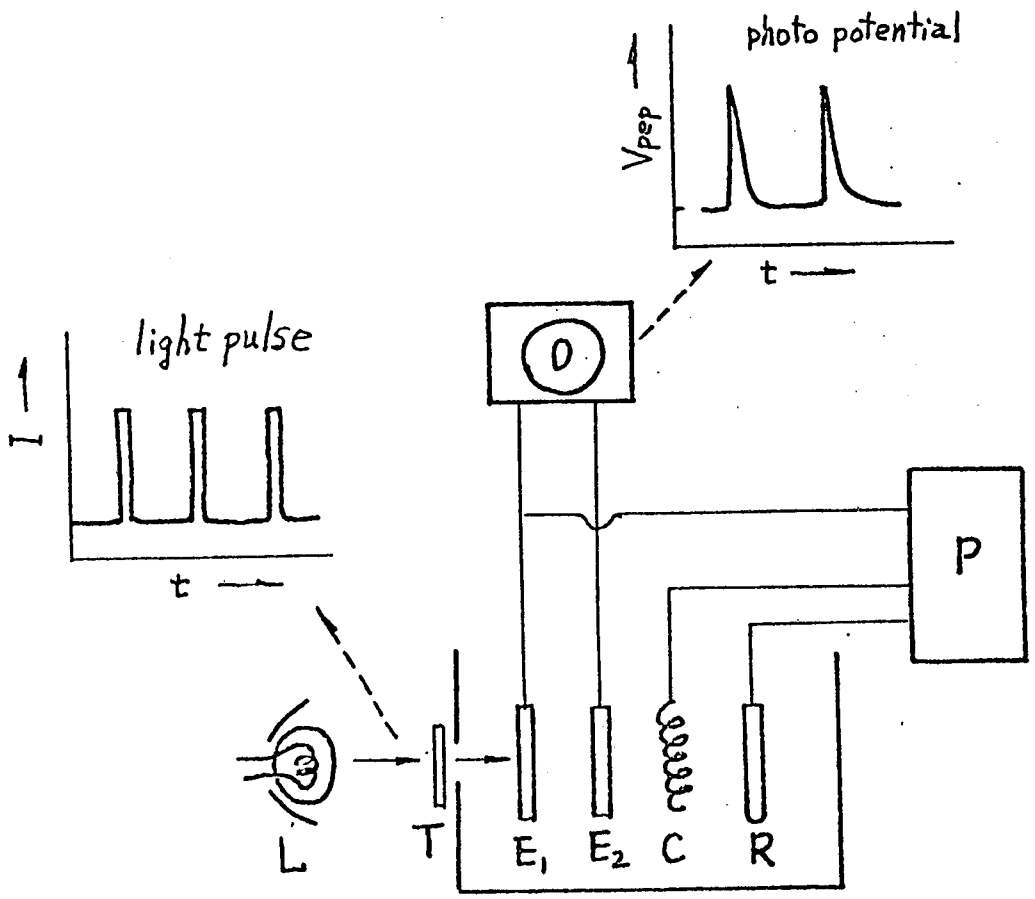

Fig. 5-11. Experimental apparatus for photoelectric polarization potential of metal electrodes. L = lamp, T = chopping photo-trigger, E_1 = test electrode E_2 = counter electrode for photopotential measurement, C = counter electrode for potentiostat, R = reference electrode, O= sinchronized oscilloscope.

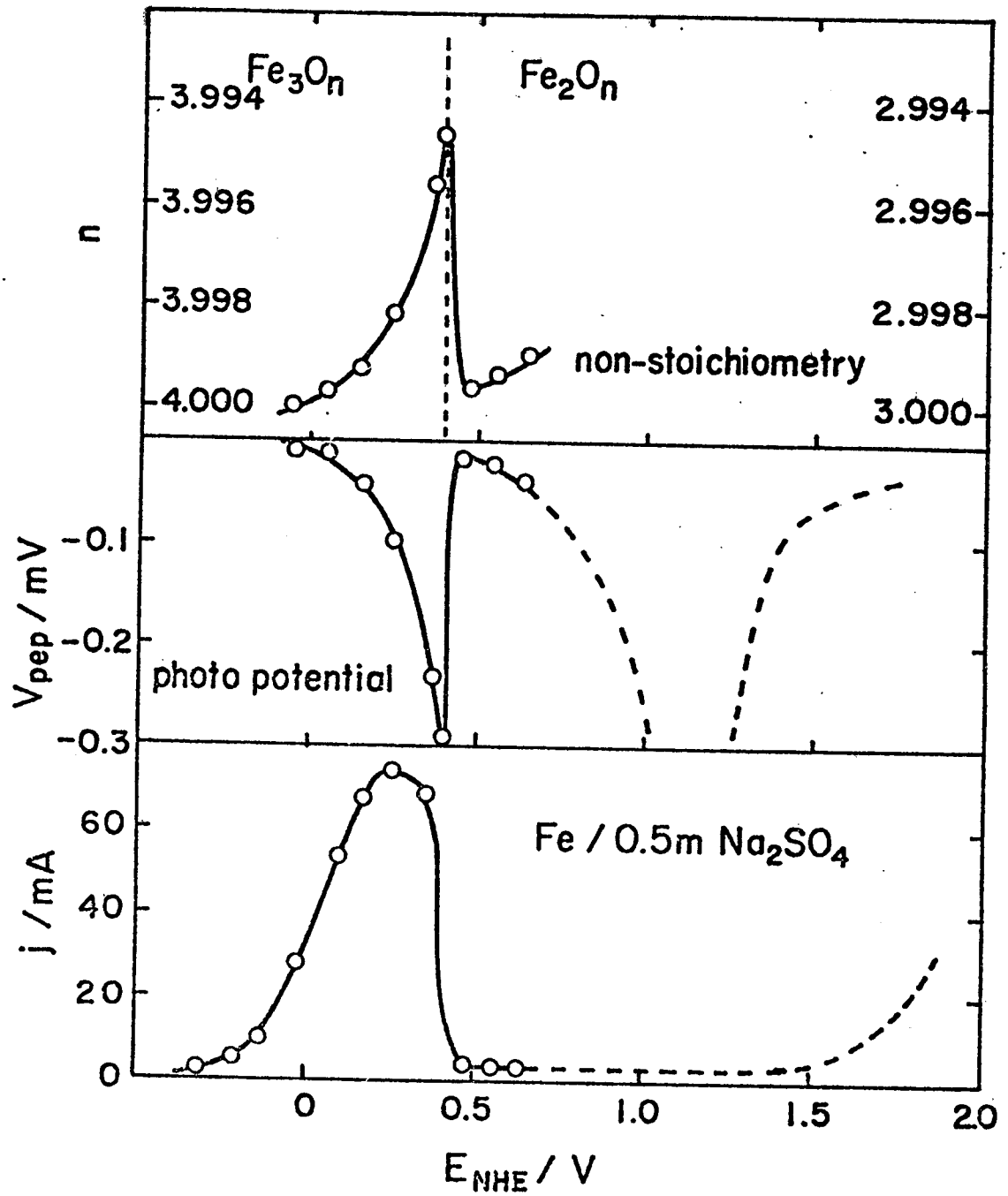

Fig. 5-12. Anodic current j, photoelectric polarization potential V_{pep}, and nonstoichiometry n for the passivating oxide film on iron in 0.5 M Na_2SO_4 solution as a function of potential (Oshe et al., 1970).

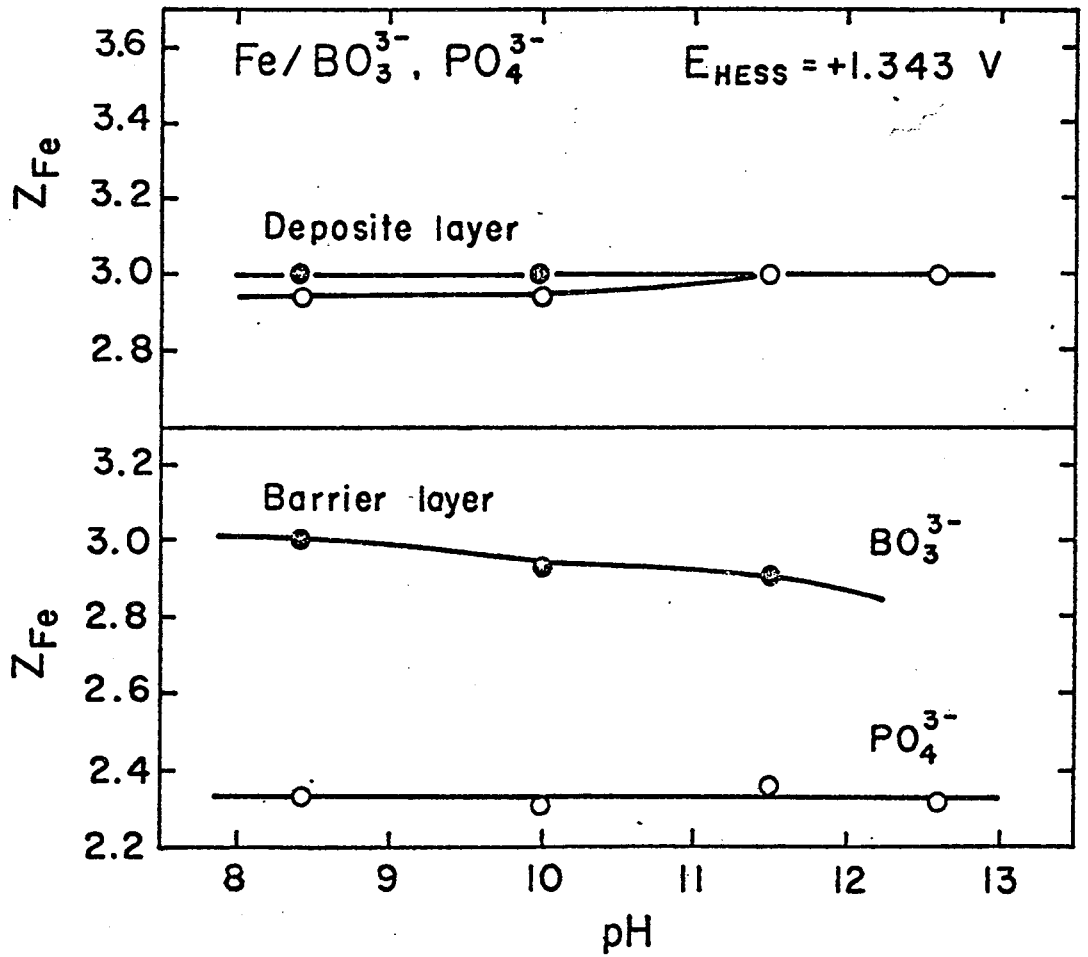

Fi g. 5-13. Valency of iron ions in the barrier and deposit layers of the passive film on iron in borate and phosphate solutions as a function of pH (Nishimura and Sato, to be published). The valency was estimated by coulometry and chemical analysis.

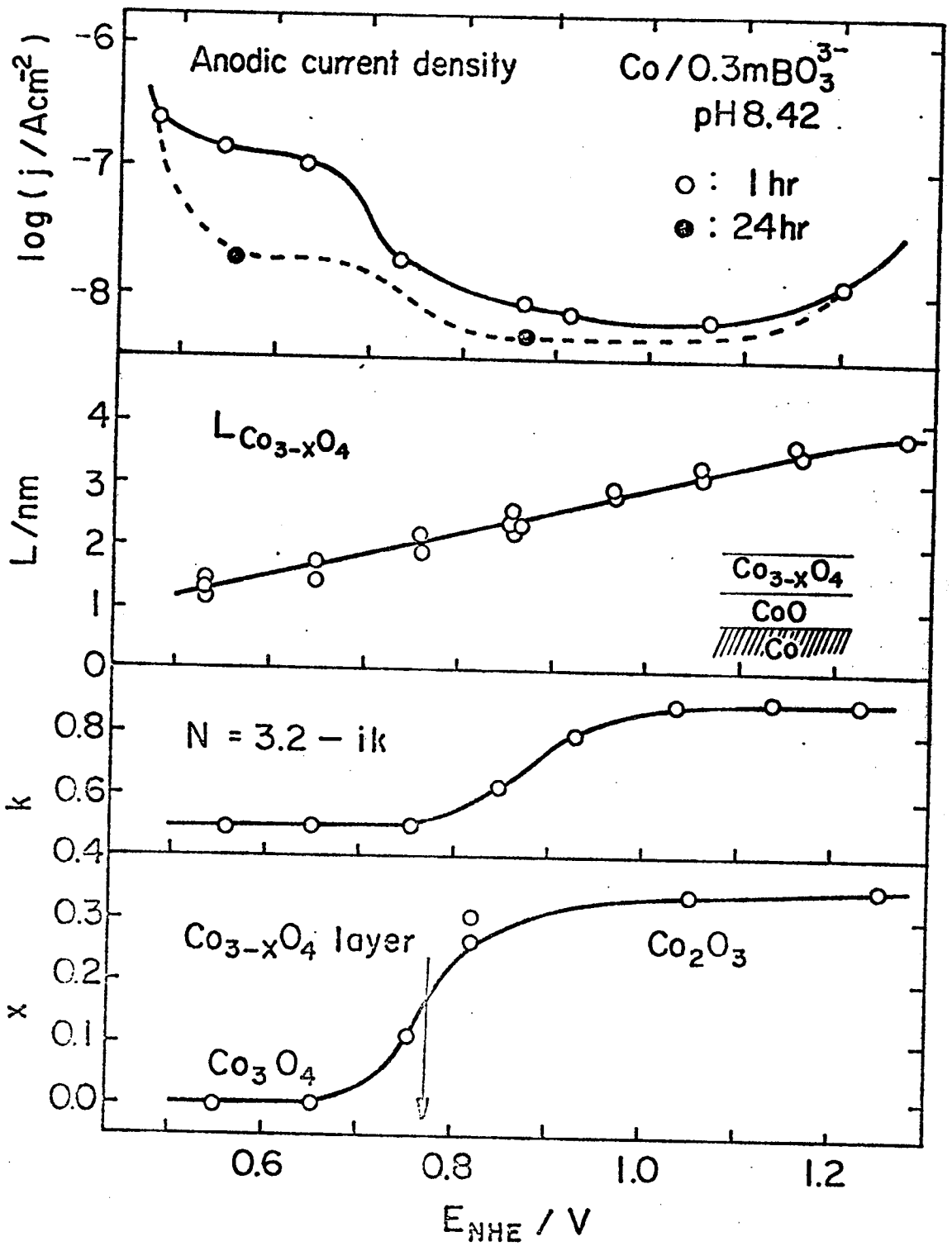

Fig. 5-14. Anodic current j, barrier layer thickness L, optical constant N, and nonstoichiometry x versus potential for the passive film on cobalt in borate solution (Ohtsuka et al., to be published).

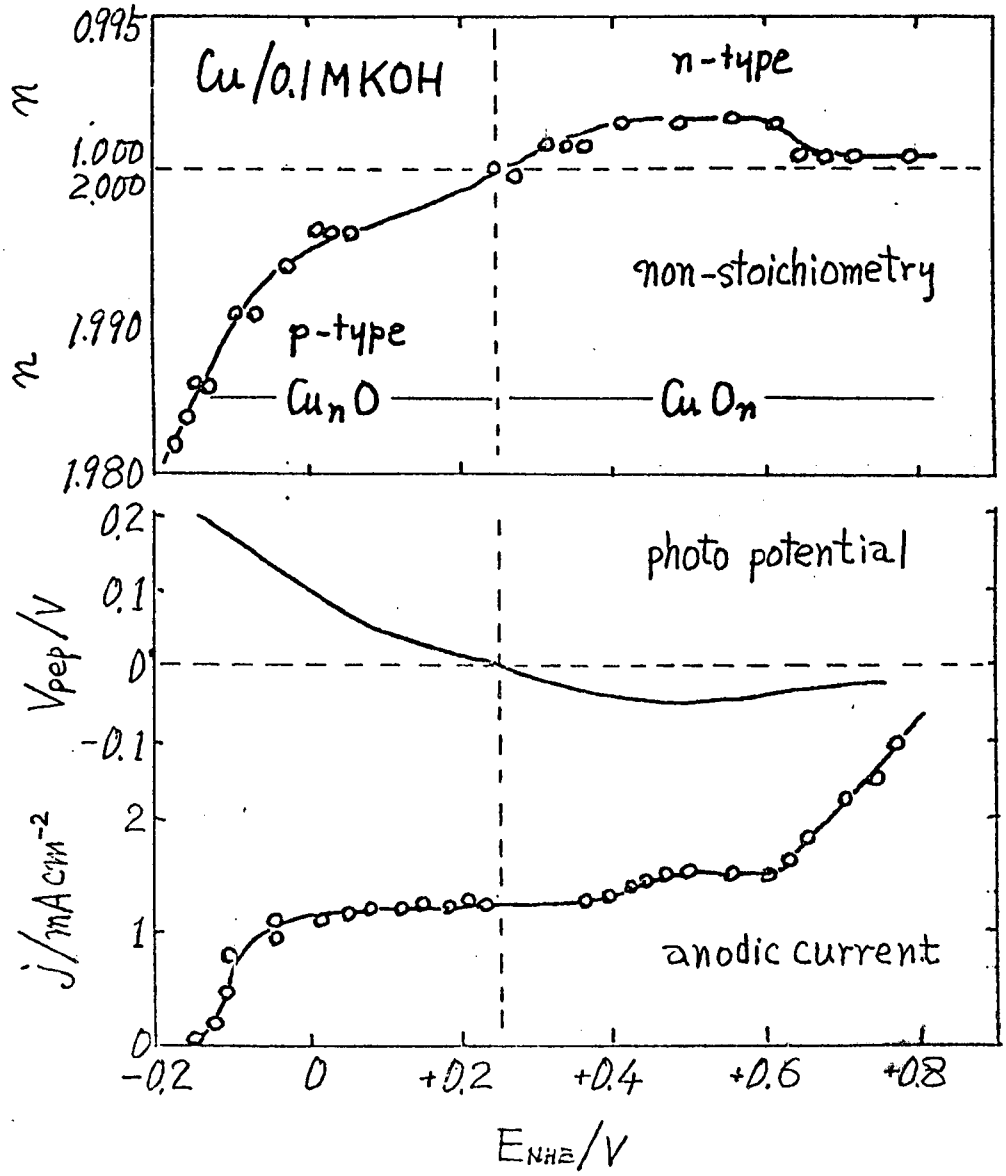

Fig. 5-15. Anodic current j, photoelectric polarization potential V_{pep}, and nonstoichiometry n versus potential the anodic oxide film on cupper in alkaline solution (Oshe et al., 1969).

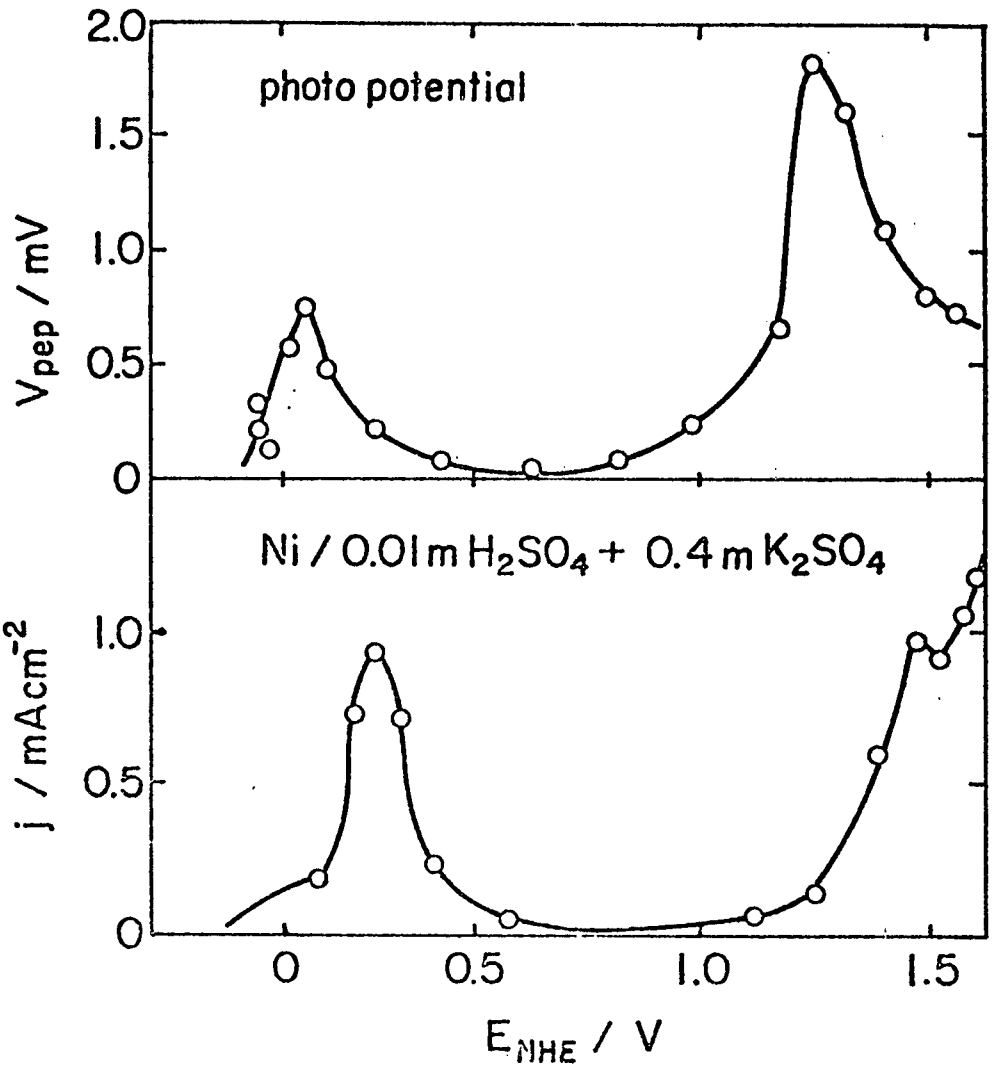

Fig. 5-16. Anodic current j and photoelectric polarization potential versus potential for nickel in acidic 0.5 M H_2SO_4 solution (Oshe et al., 1975).

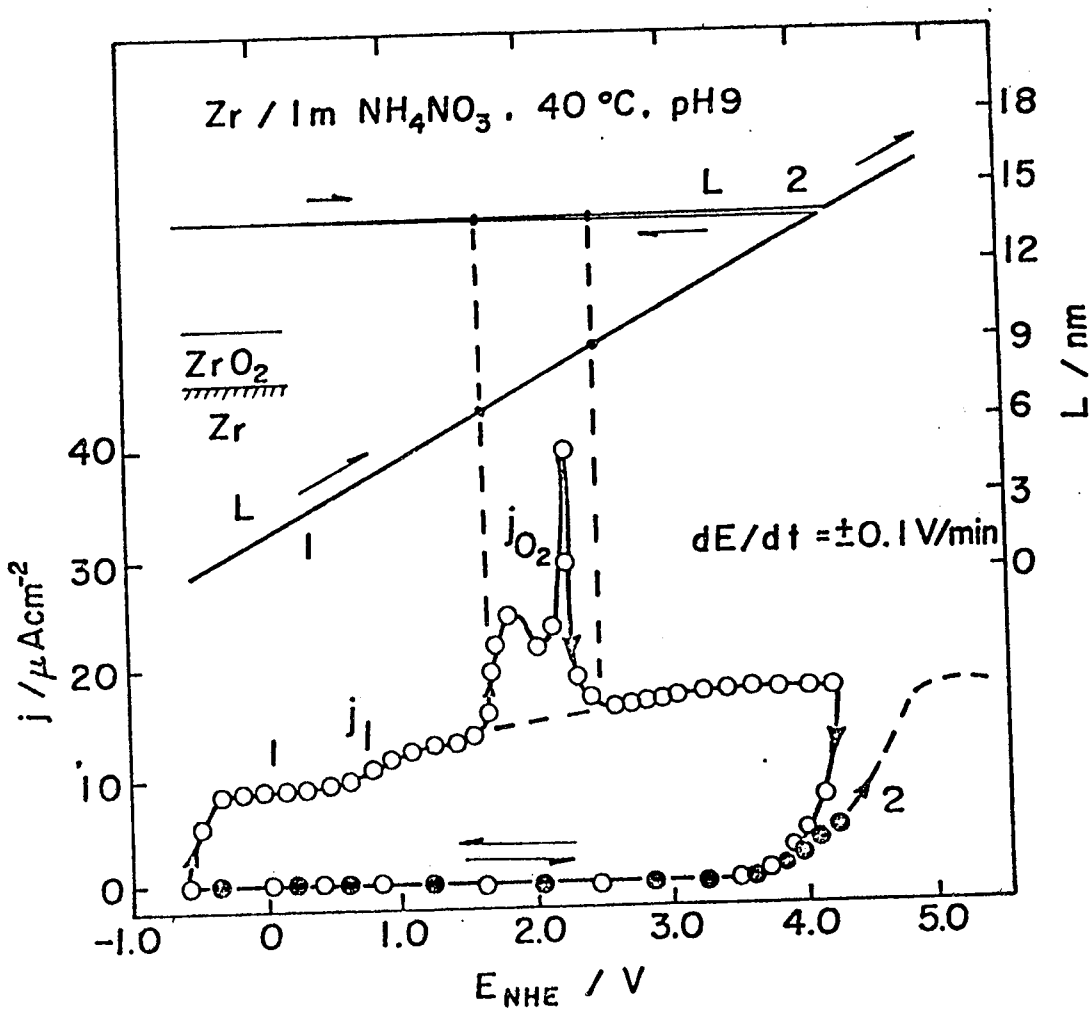

Fig. 5-17. Anodic current and film thickness versus potential of zirconium in an ammonium nitrate solution during anodic-and-cathodic potential sweep (Morozumi et al., 1975). j_{O_2} = oxygen current, j_ℓ = film formation current.

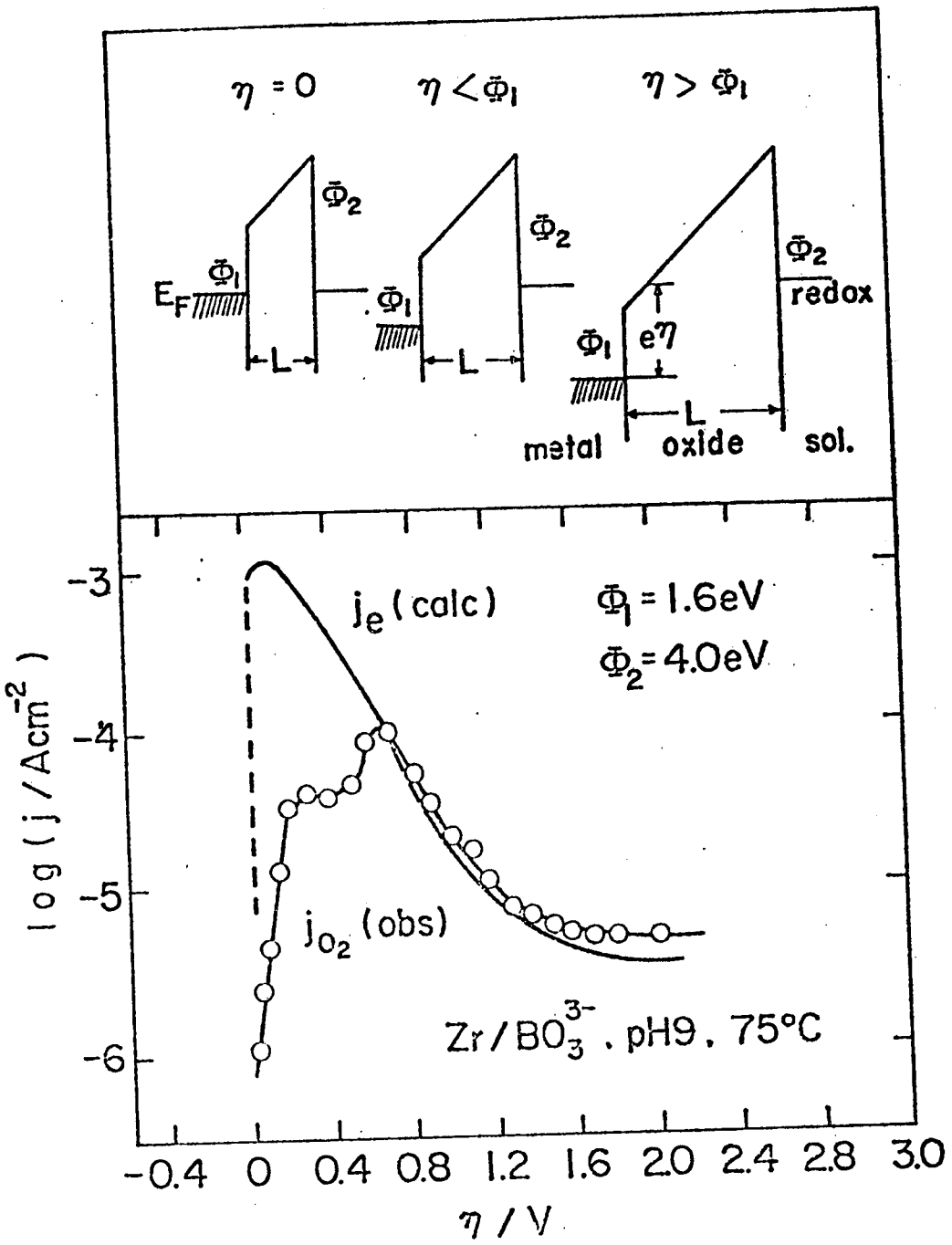

Fig. 5-18. Electron energy band model and comparison between calculated electron tunnel current j_e(calc.) and observed oxygen current j_{O_2}(obs.) for zirconium covered with a passive film growing with potential at weep rate dE/dt = 0.1 V/min. in saturated ammonium borate solution at 75°C (Morozumi et al., 1975).

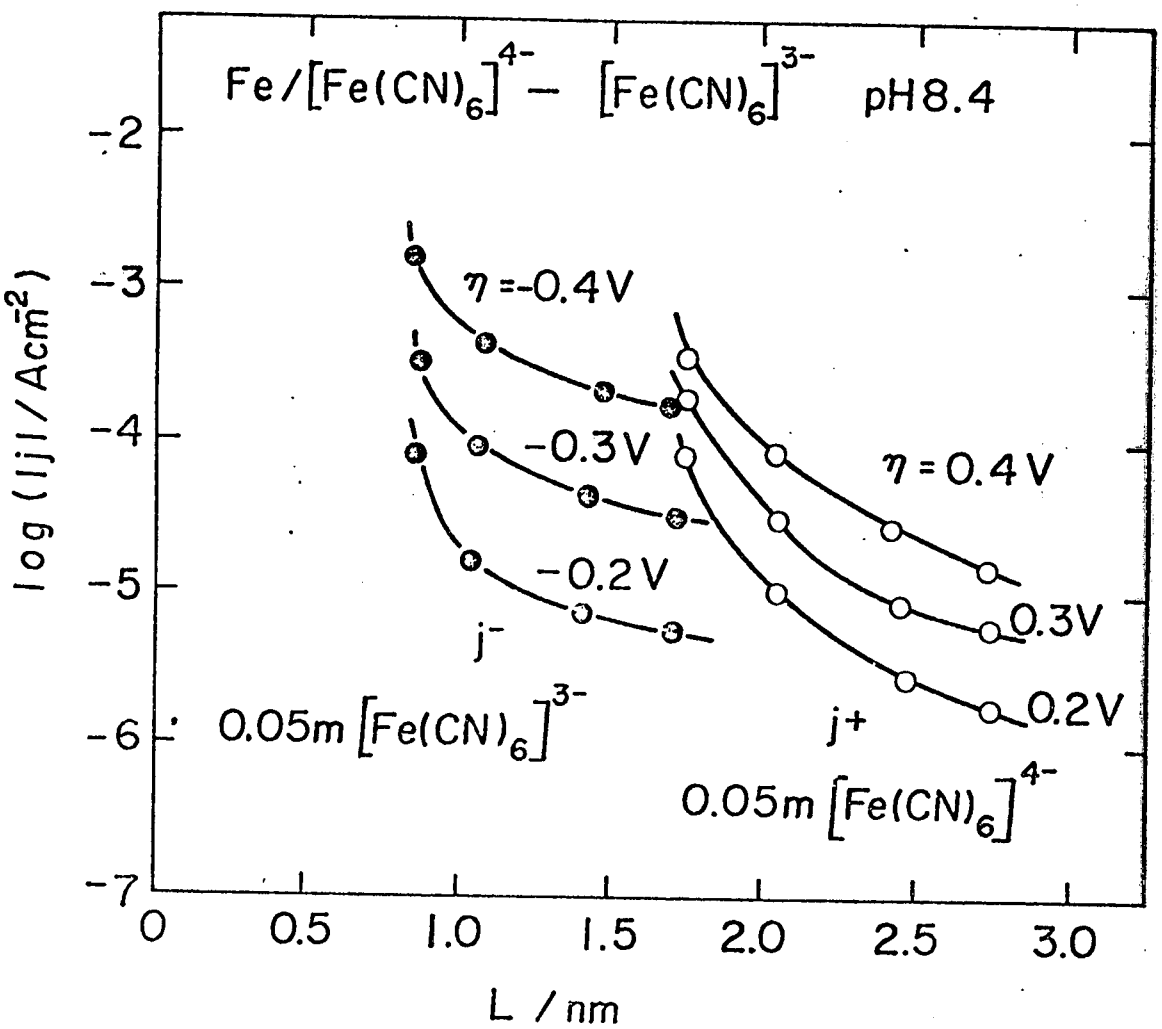

Fig. 5-19. Anodic and cathodic current of iron(II)-(III) cyanides redox reaction at different overpotentials on passive iron electrode as a function of the passive film thickness (Schultze et al., 1976).

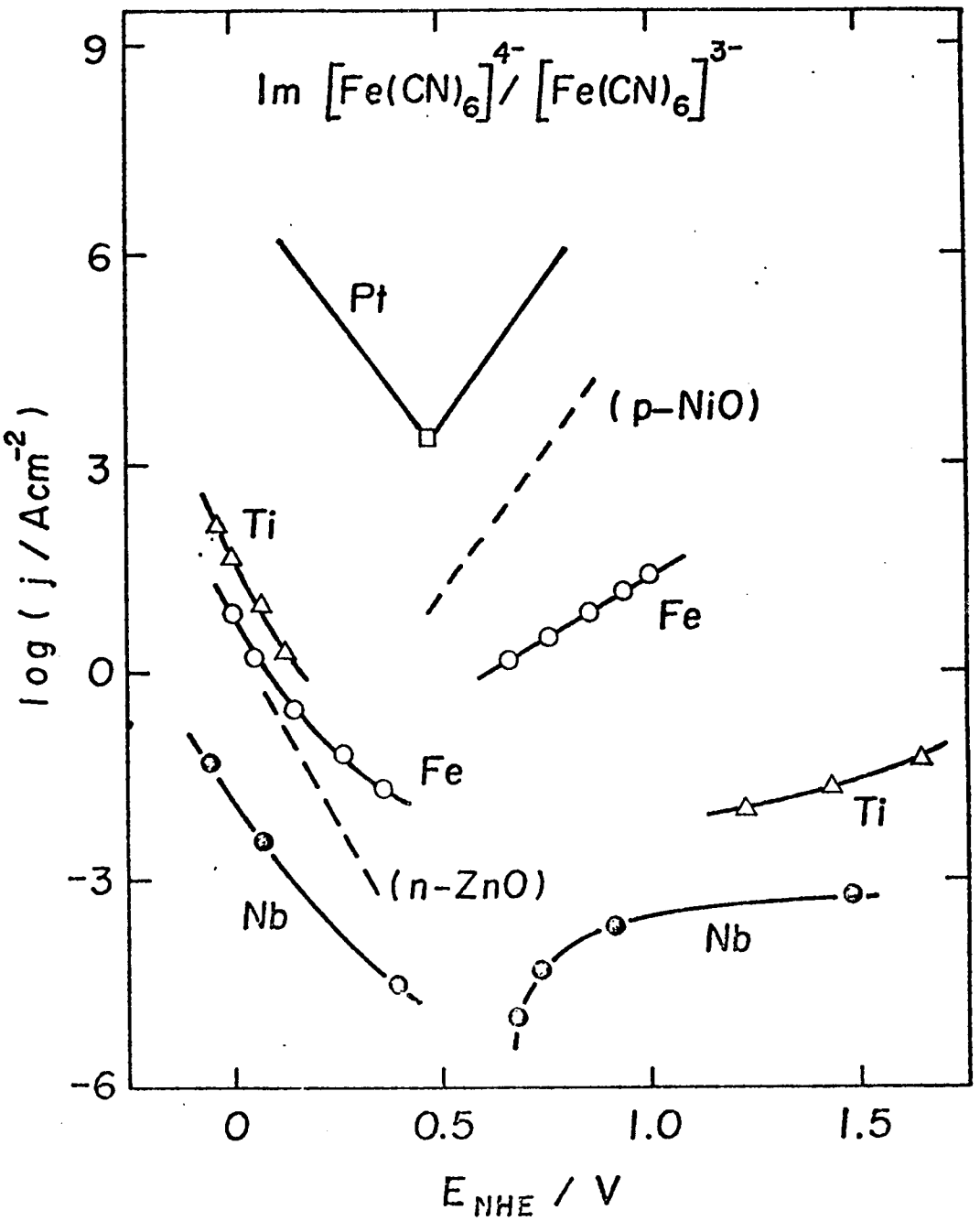

ig. 5-20. Anodic and cathodic polarization curve of iron(II)-(III) cyanides redox reaction on passive electrodes of Pt, Ti, Fe, Nb, p-type NiO, and n-type ZnO (Schultze et al., 1976). The cd is normalized for 1 M iron cyanide concentration. The passive film thickness is 5.0 nm for Ti/TiO_2, 1.7 nm for $Fe/\gamma\text{-}Fe_2O_3$, and 12 nm for Nb/Nb_2O_5.

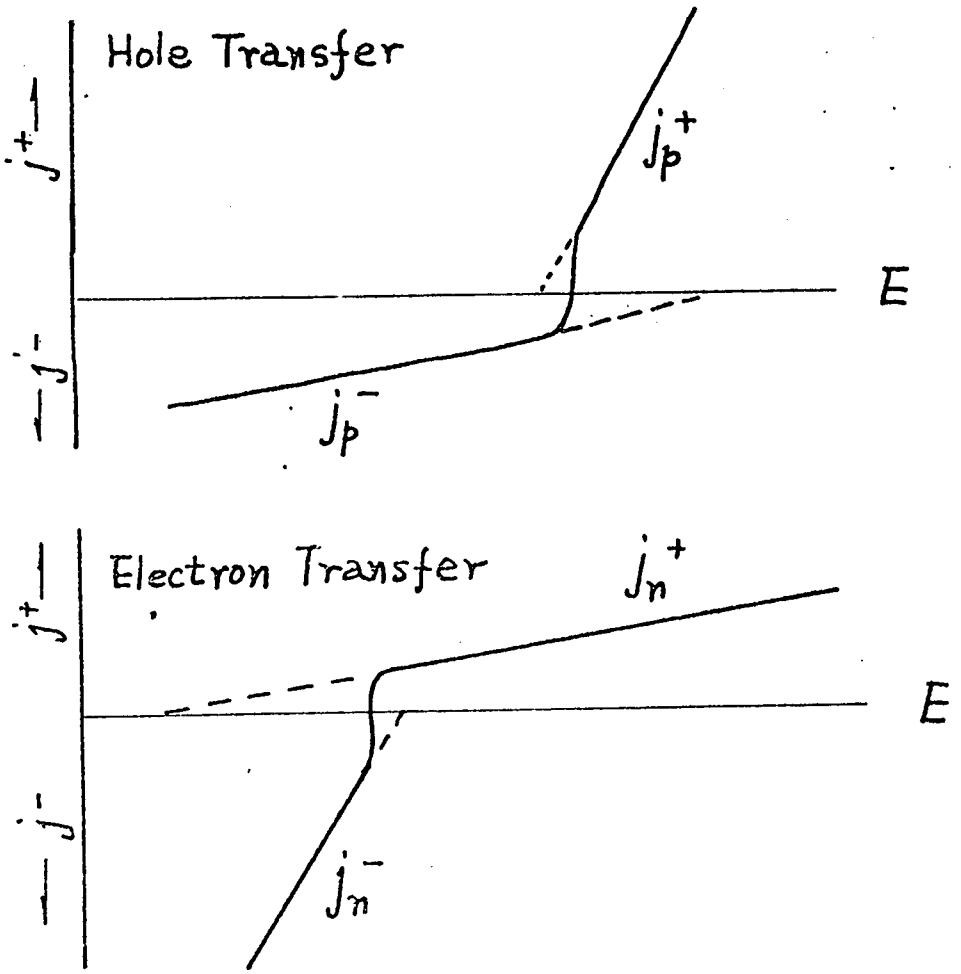

Fig. 5-21. General tendency of potential-dependence of hole and electron transfer redox reaction rates on semiconductor electrodes.

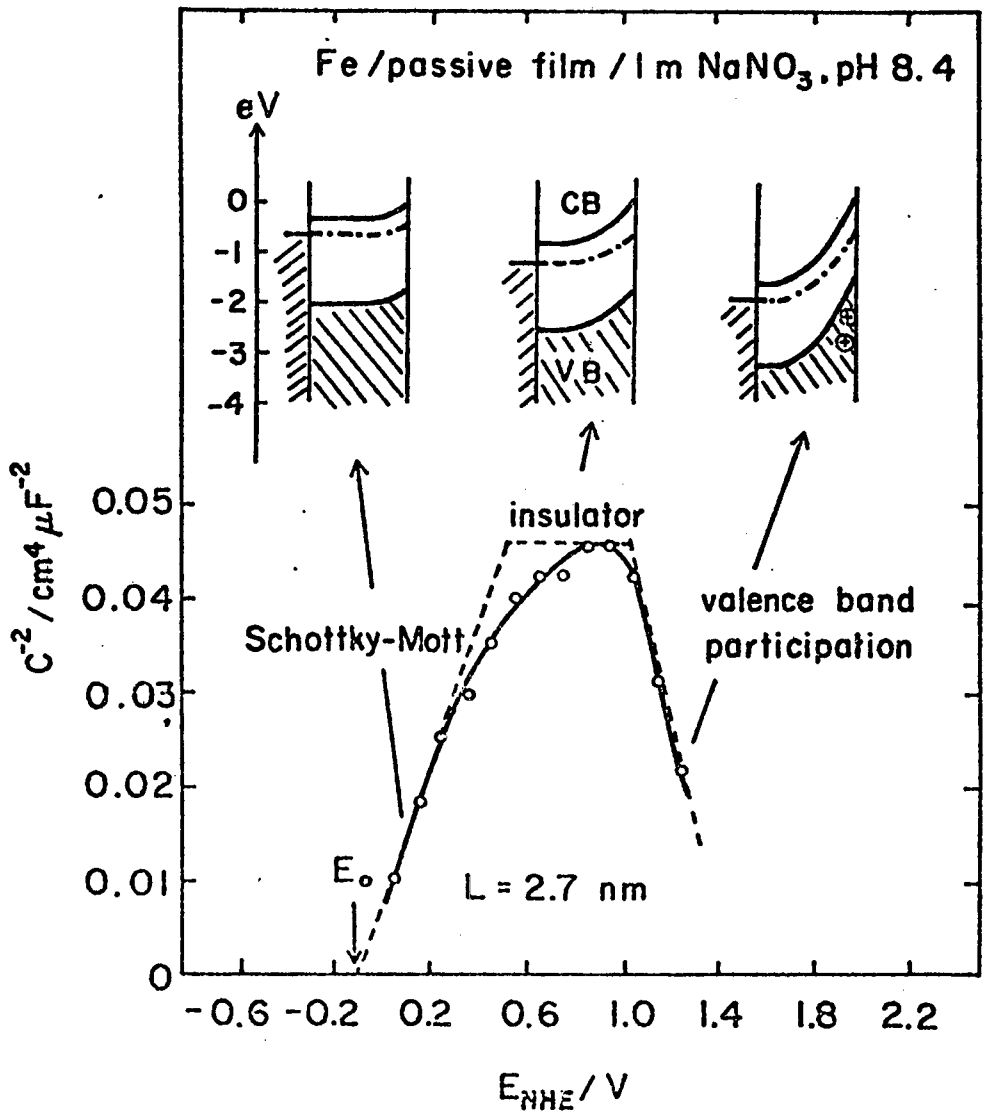

Fig. 5-22. Schottky-Mott plot of electrode capacitance and electron energy band model for the passive film 2.7 nm thick on iron in 1 M $NaNO_3$ solution at pH 8.4 (Schultze et al., 1977). The slope of the Schottky-Mott line gives the donor concentration $N = 1.5 \times 10^{20}/cm^3$, if assuming the dielectric constant $\epsilon = 12$. The donors are exhausted at high potentials. The flat band potential E_{FB} is obtained from E_o, which involves an additional potential drop in the Helmholtz layer.

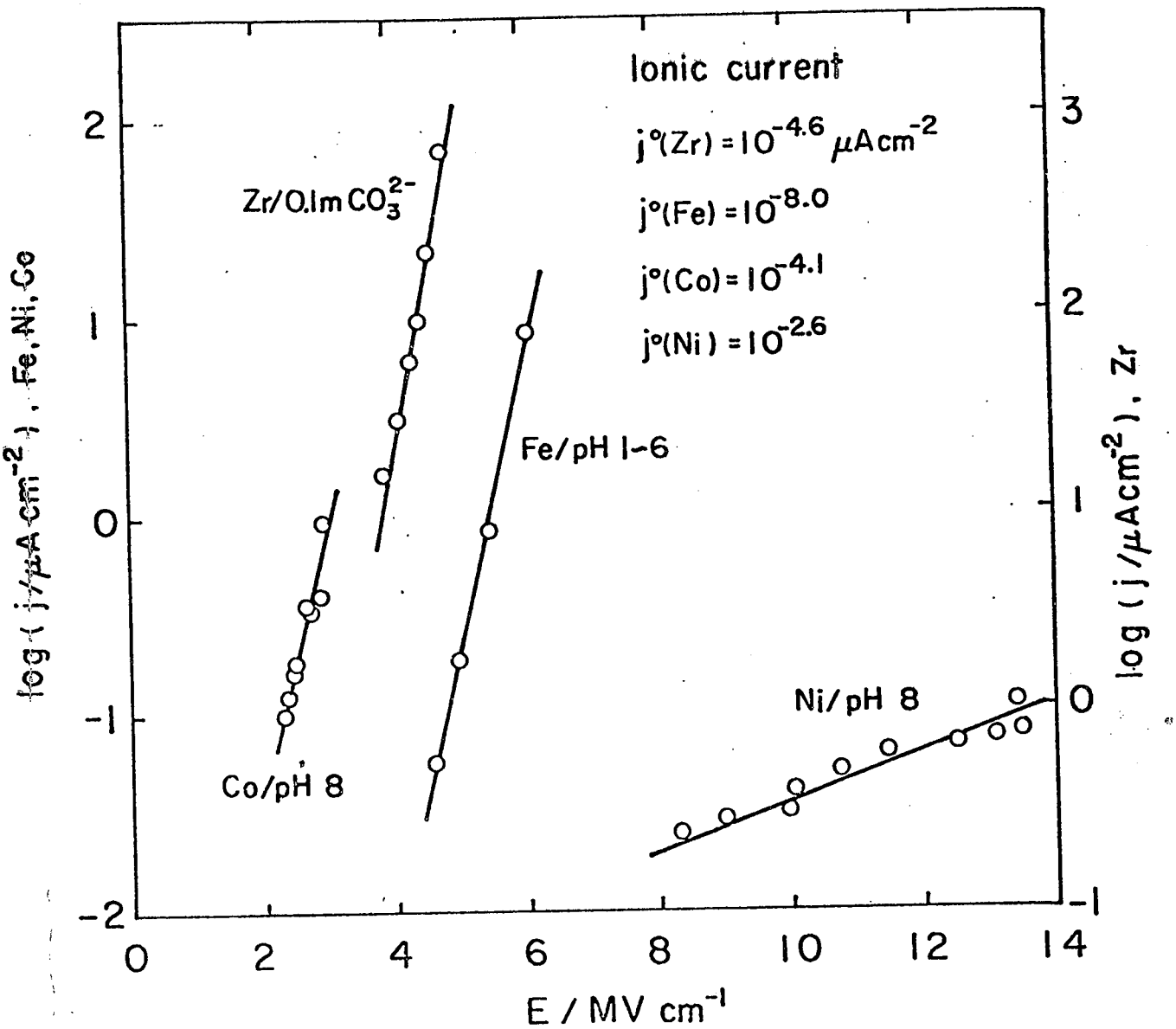

Fig. 5-23. Logarithm of ionic current versus electric field in the passive films on iron, nickel, cobalt and zirconium (Sato, 1977). $j = j_o \exp(BE)$.

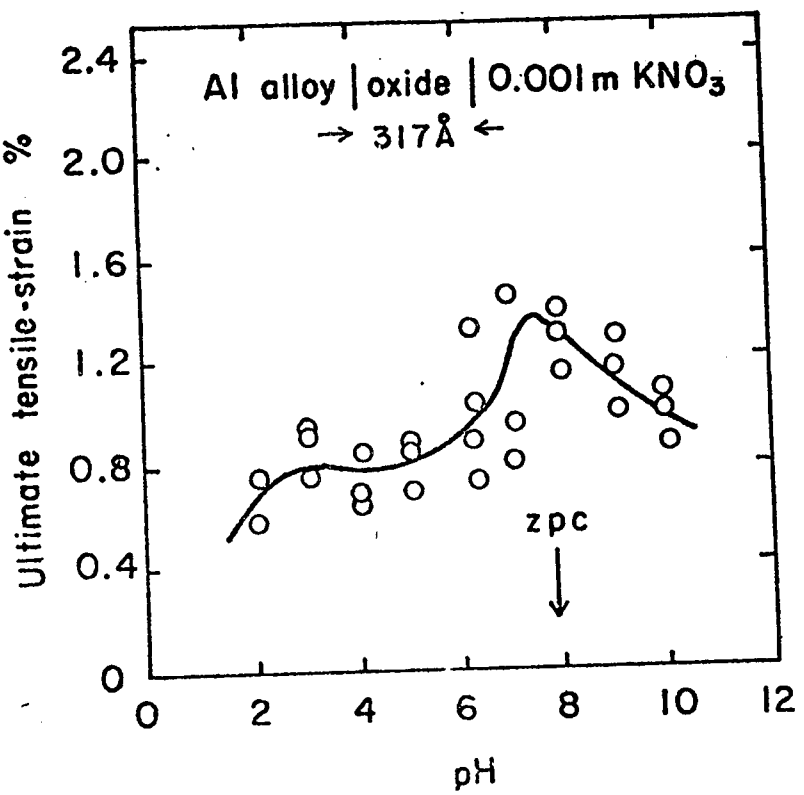

Fig. 5-24. Ultimate tensile strain of an anodic oxide film 31.7 nm thick on a Cu(4.4%) - Mg(1.6%) - Mn(0.6%) - Al alloy as a function of pH at which the film has been formed (Devereux et al., 1975).

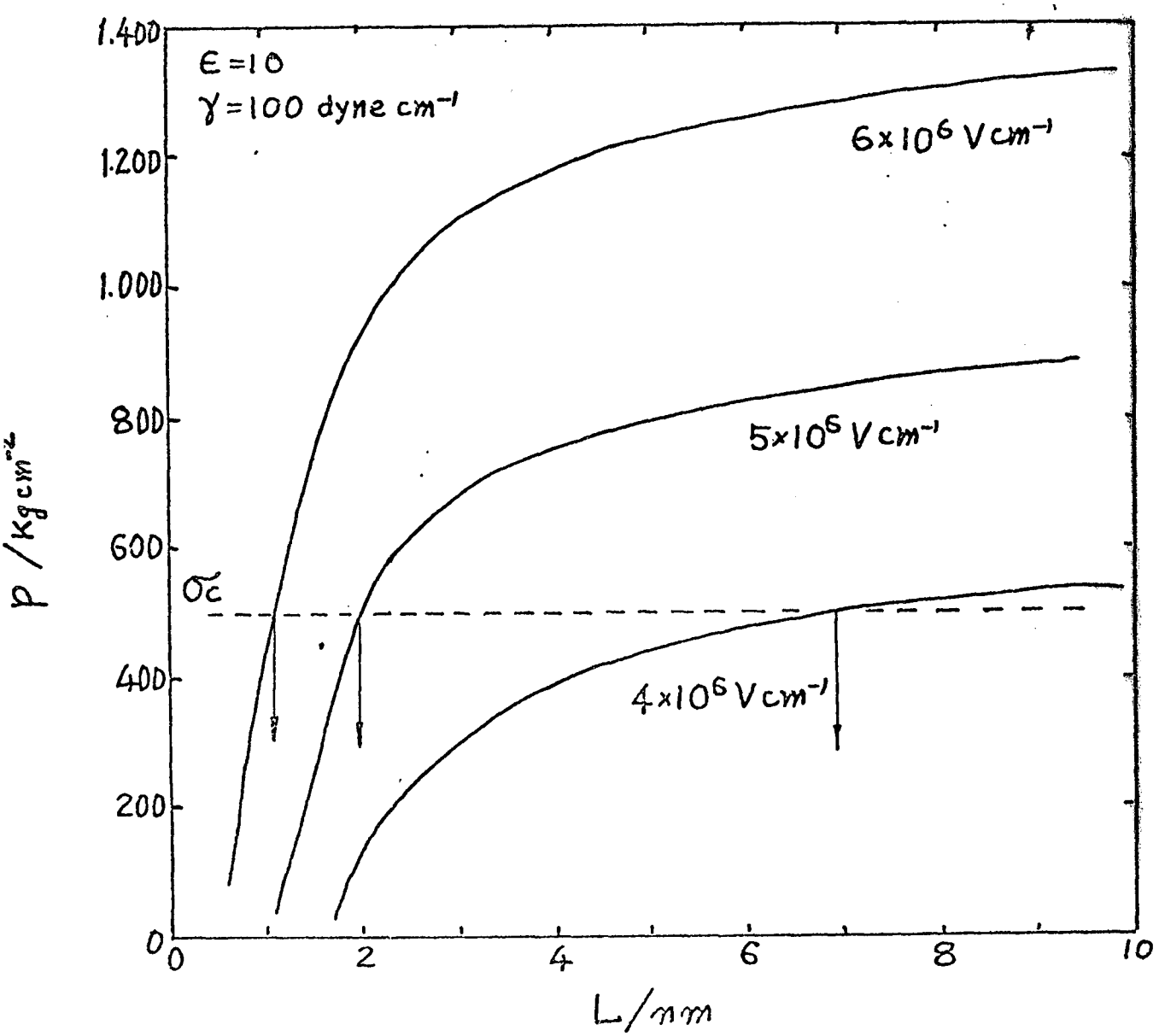

Fig. 5-25. Pressure normal to the film surface due to the electrostriction modified by surface tension as a function of film thickness calculated for a u surface film with the dielectric constant $\epsilon = 10$ surface tension $\gamma = 100$ and different electric field strength in the film $E = 4 \times 10^6$ and 6×10^6 V/cm (Sato, 1971).

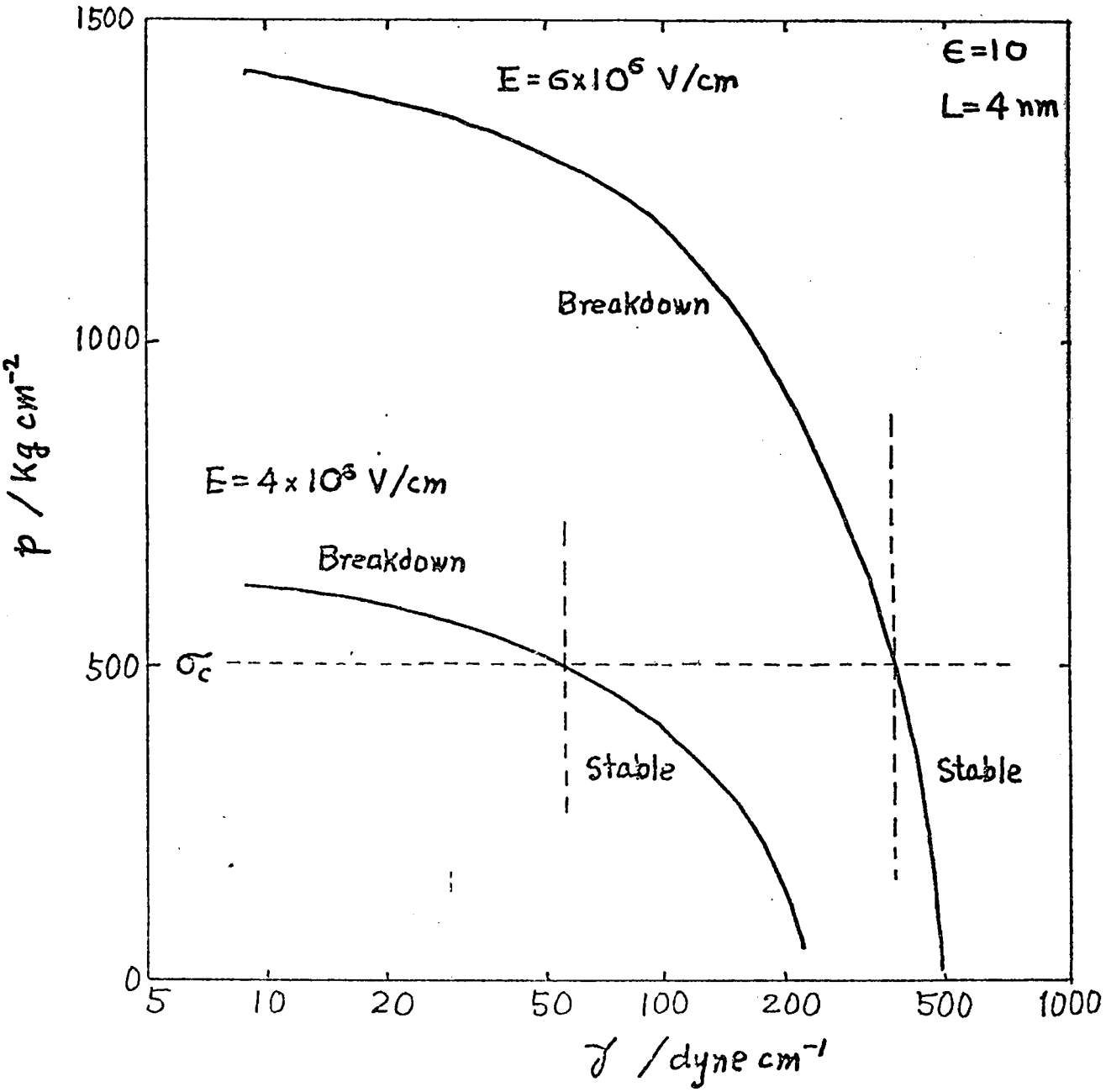

Fig. 5-26. Pressure normal to the film surface due to the electrostriction modified by surface tension calculated for a surface film with the dielectric constant ϵ = 10 and electric field strength E = 4 x 10^6 and 6 x 10^6 V/cm (Sato, 1971).

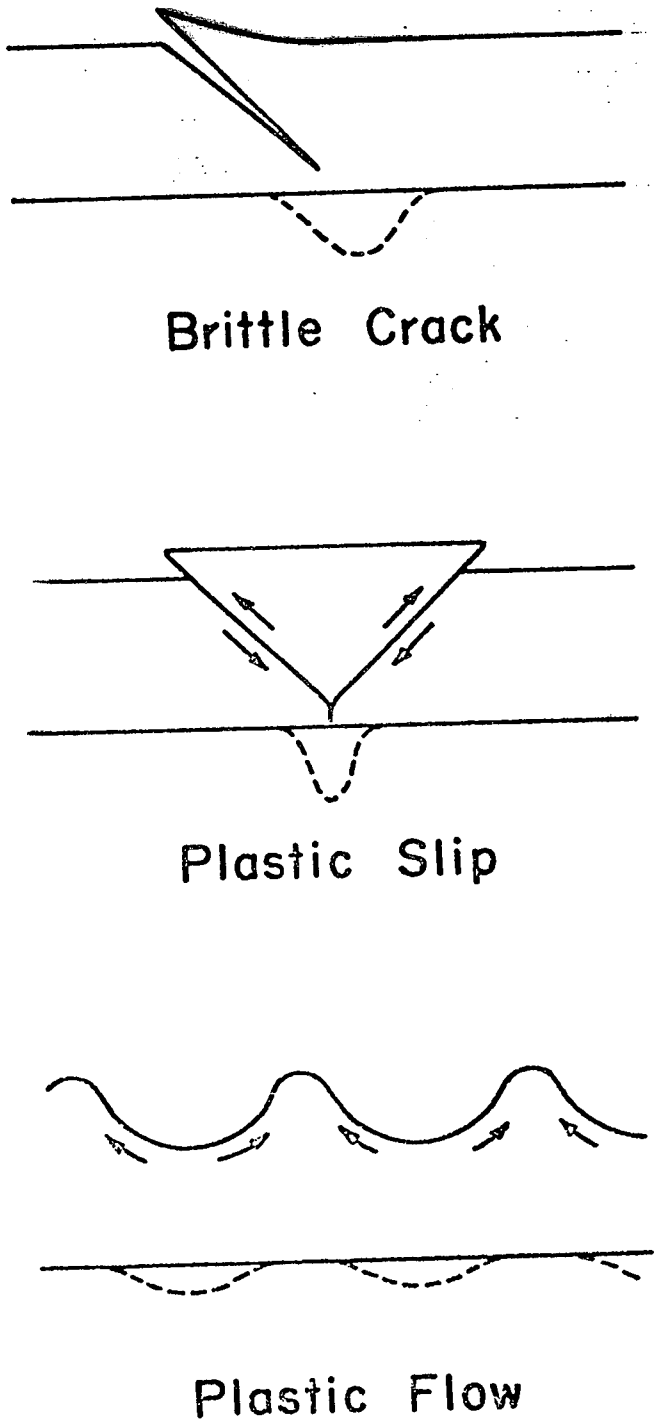

Fig. 5-27. Breakdown mode of passive films (Sato, 1971).

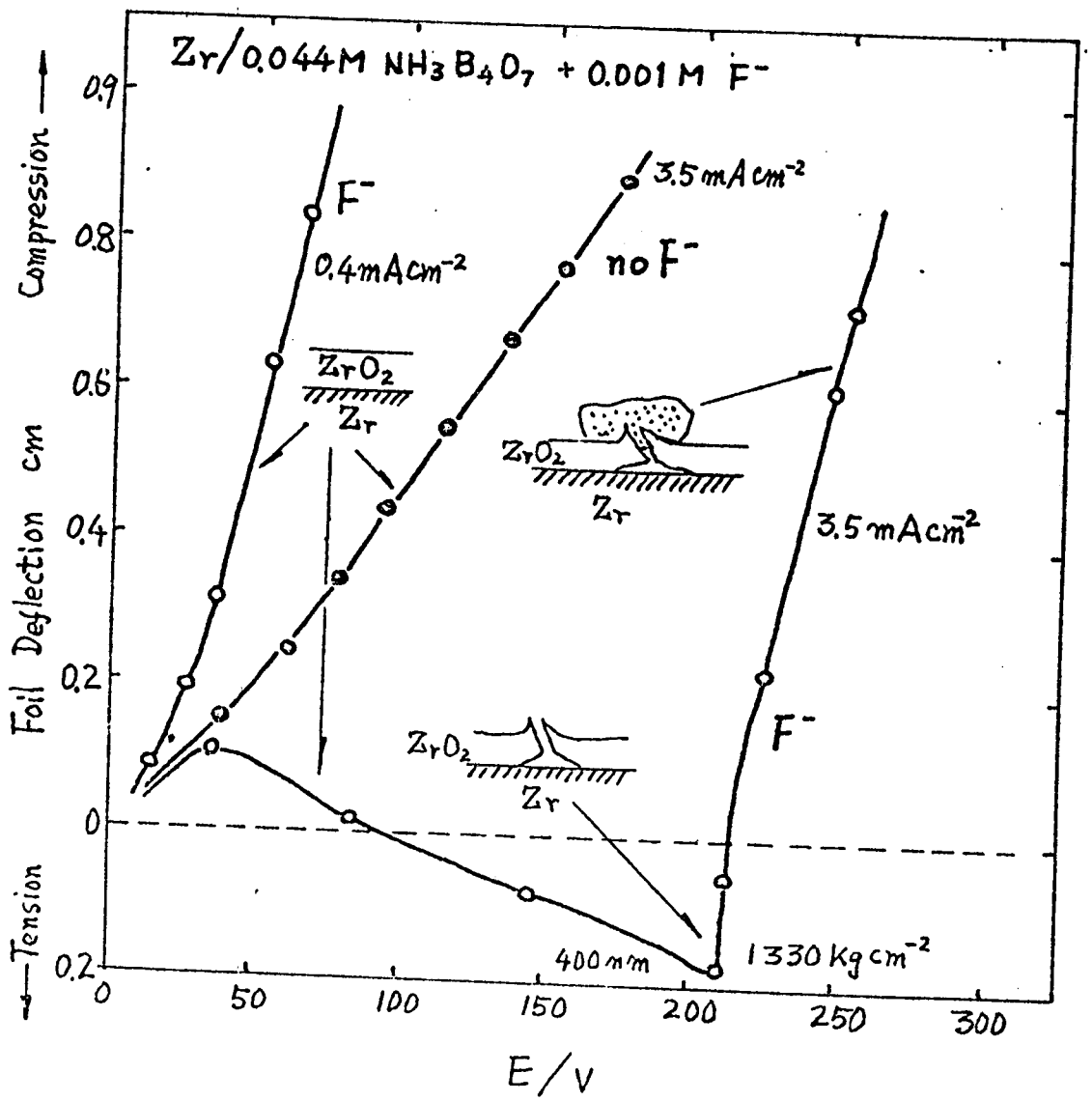

Fig. 5-28. Effect on foil deflection of adding F^- ions to the electrolyte 0.044 M $NH_3B_4O_7$ for zirconium anodized at constant current (Leach et al., 1977).

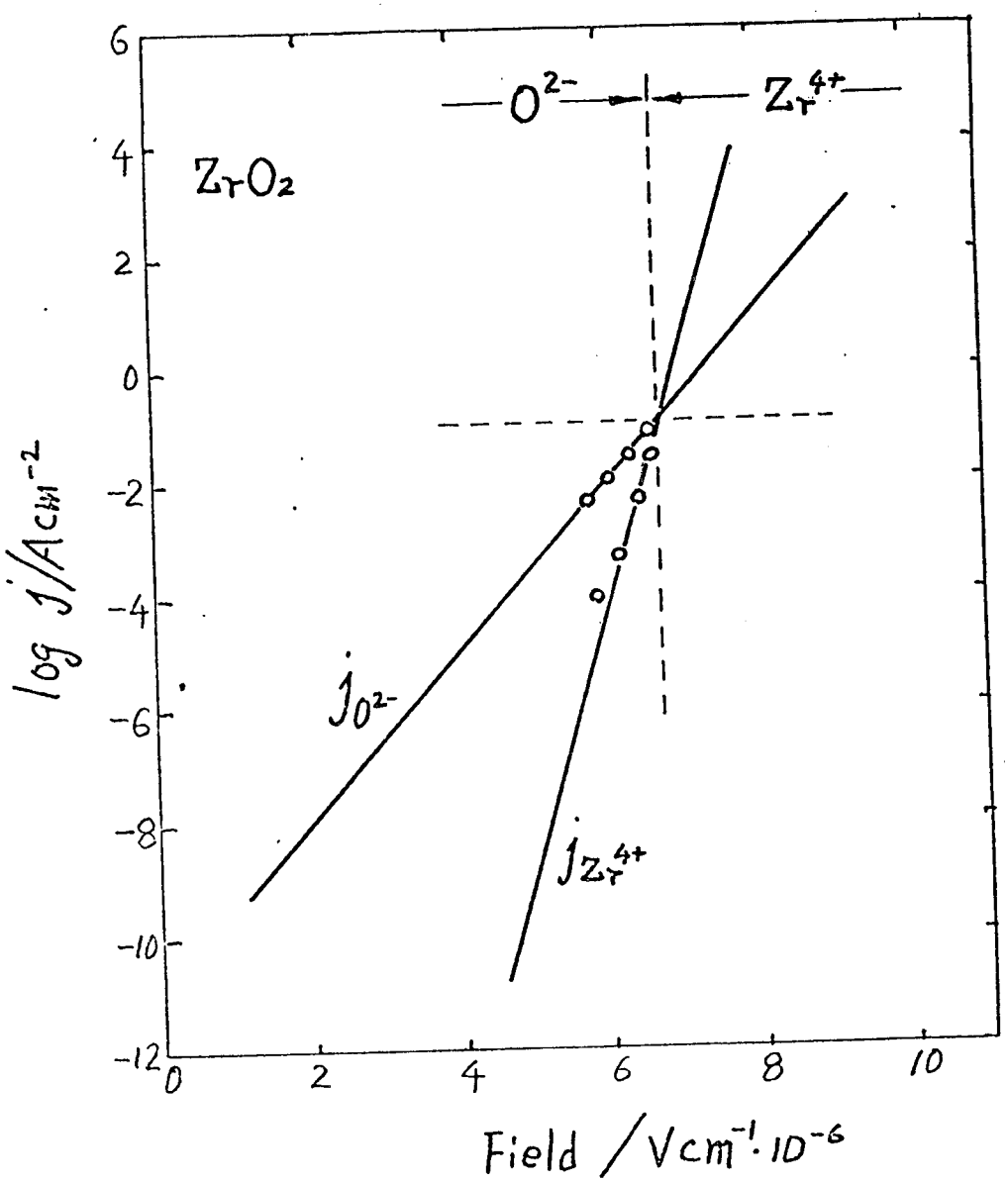

Fig. 5-29. Field-dependence of ionic diffusion current of zirconium ion and oxygen ion in an anodic oxide film of ZrO_2 (Leach et al., 1972). Metal ion and oxygen ion diffusion currents are estimated from the transport number of each ion.

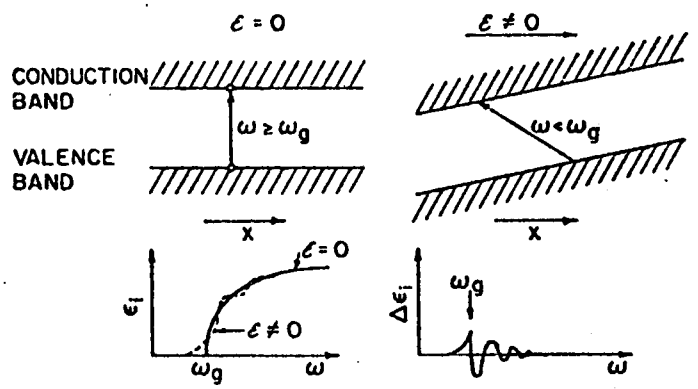

Effect of an electric field $\mathscr{E}$ on interband transitions near an M_0 energy gap. The upper drawings represent the "local" energy gap as a function of the space coordinate along $\mathscr{E}$.

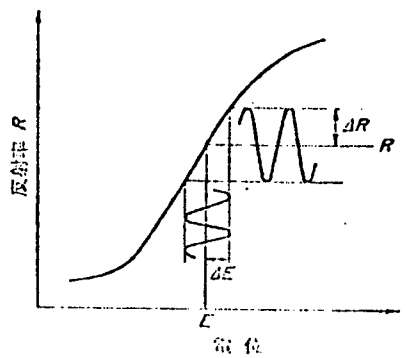

Fig. 5-30. Principle of modulation electroreflection measurement of metal electrode, and effect of an electric field on interband transitions near an energy gap.

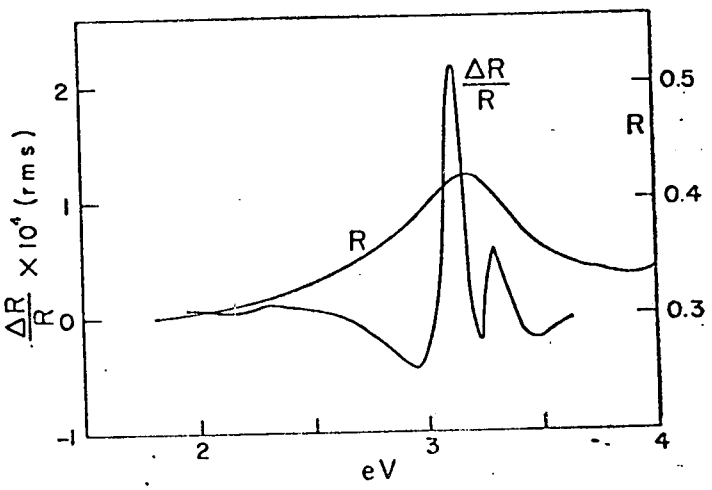

Fig. 5-31. Modulated electroreflectance ΔR/R and reflection R spectra of InP measured in electrolyte (Shaklee et al., 1965). The sign of ΔR/R is that which corresponds to a positive half-cycle applied to the sample.

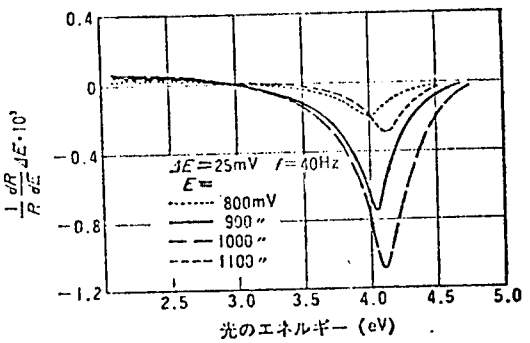

Fig. 5-32. Modulated electroreflectance spectra of nickel at 0.8, 0.9, 1.0 and 1.1 V in 0.05 M H_2SO_4 solution (Paatsch, 1971-73).

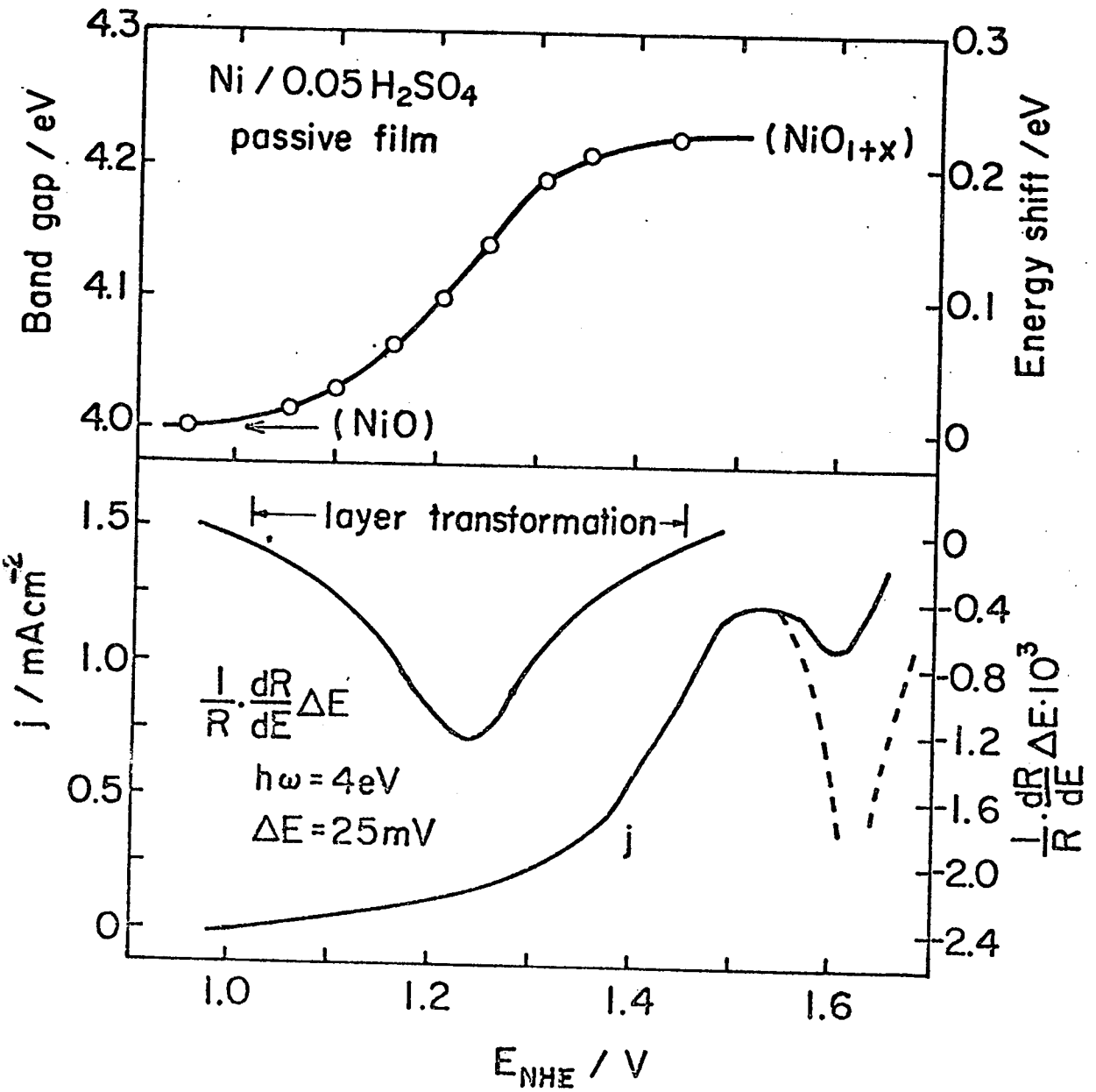

Fig. 5-33. Anodic current, modulated electroreflectance at photon energy 4 eV, and electron energy band gap estimated from electroreflectance spectra as a function of potential for the passive film on nickel in 0.05 M H_2SO_4 solution (Paatsch, 1971-73).

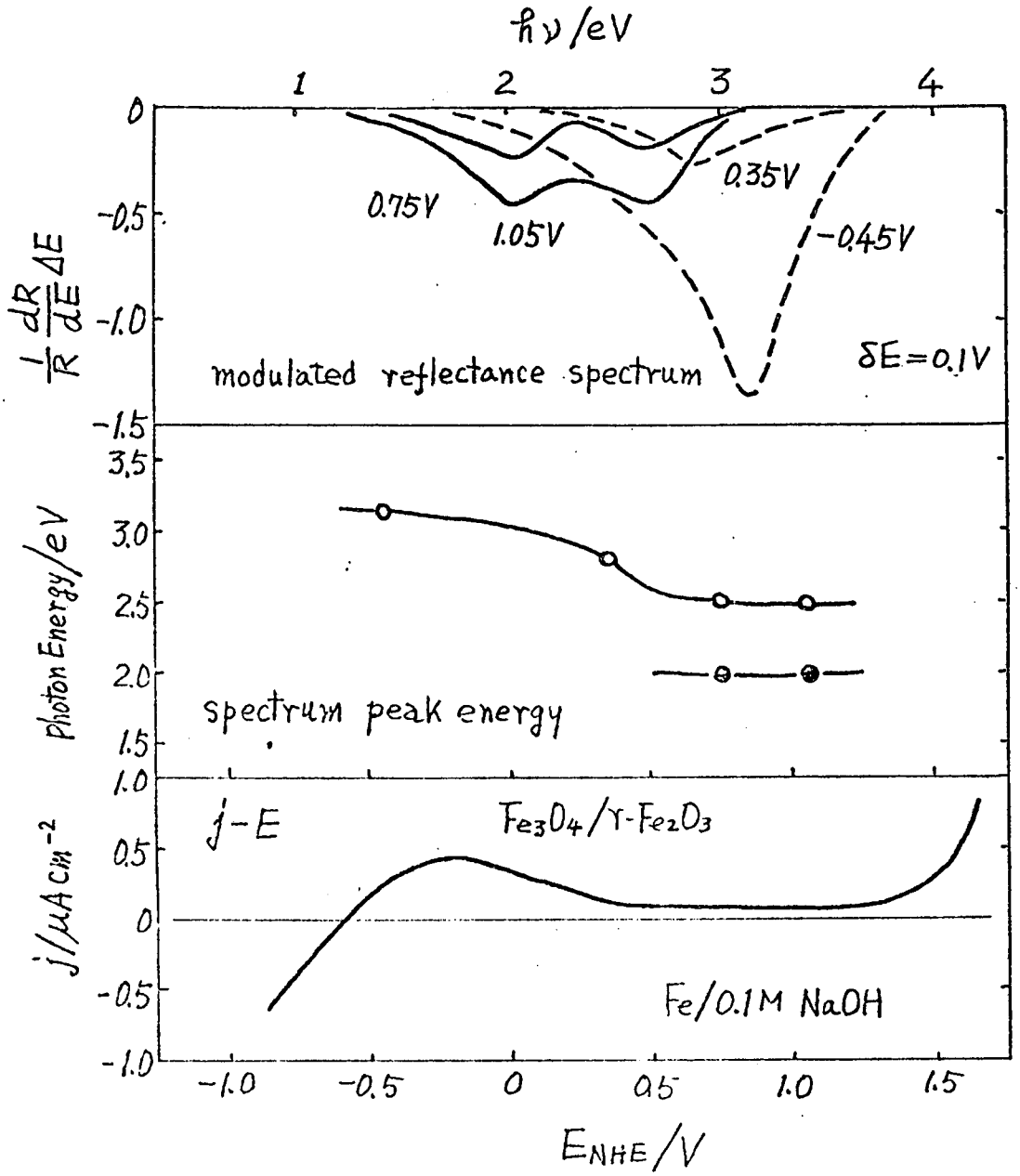

Fig. 5-34. Modulated electroreflectance spectra at different potentials, spectrum peak energy versus potential, and anodic current versus potential of iron in 0.1 M NaOH (Paatsch, 1973). ΔE = modulation voltage 0.1 V.

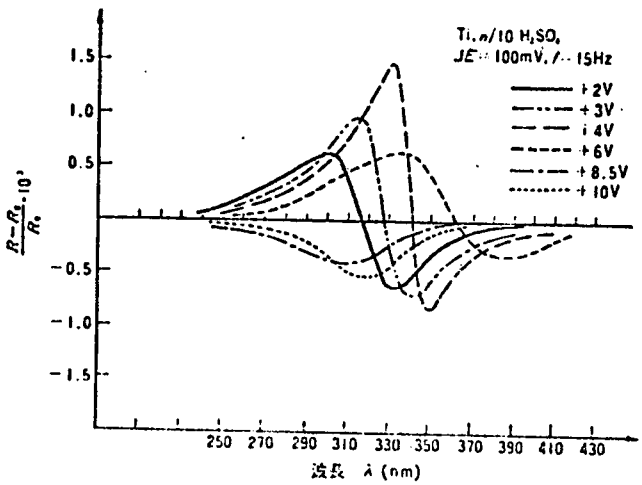

Fig. 5-35. Modulated electroreflectance spectra of titanium at six different potentials in 0.05 M H_2SO_4 (Paatsch, 1975).

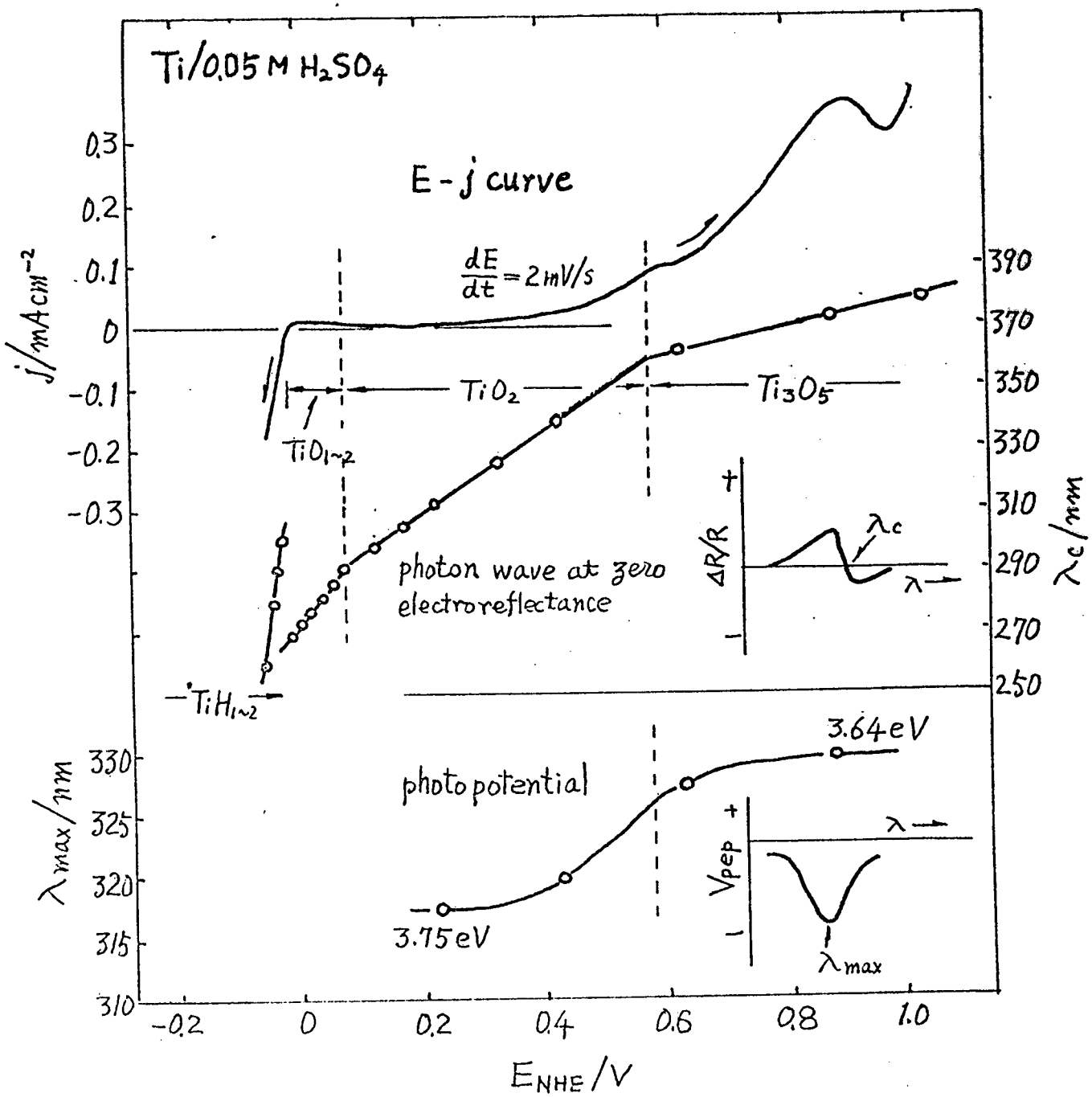

Fig. 5-36. Anodic current, critical photon wave length at zero electroreflectance, and critical pholon wave length at a spectrum peak of photoelectric polarization potential versus electrode potential of titanium in 0.05 M H_2SO_4 solution (Paatsch, 1975).

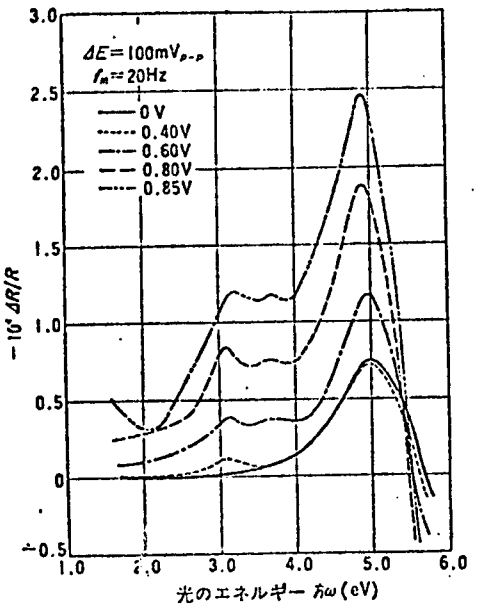

Fig. 5-37. Modulated electroreflectance of chromium at five different potential in 1 M Na_2SO_4 solution of pH 2 (Sugimoto et al., 1977).

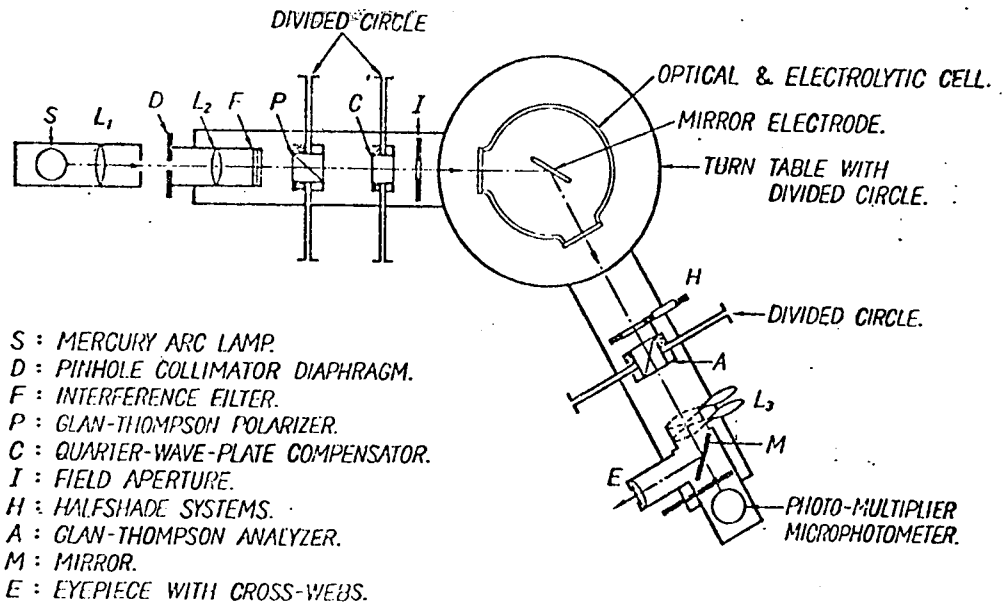

Fig. 5-38. Ellipsometer arrangement.

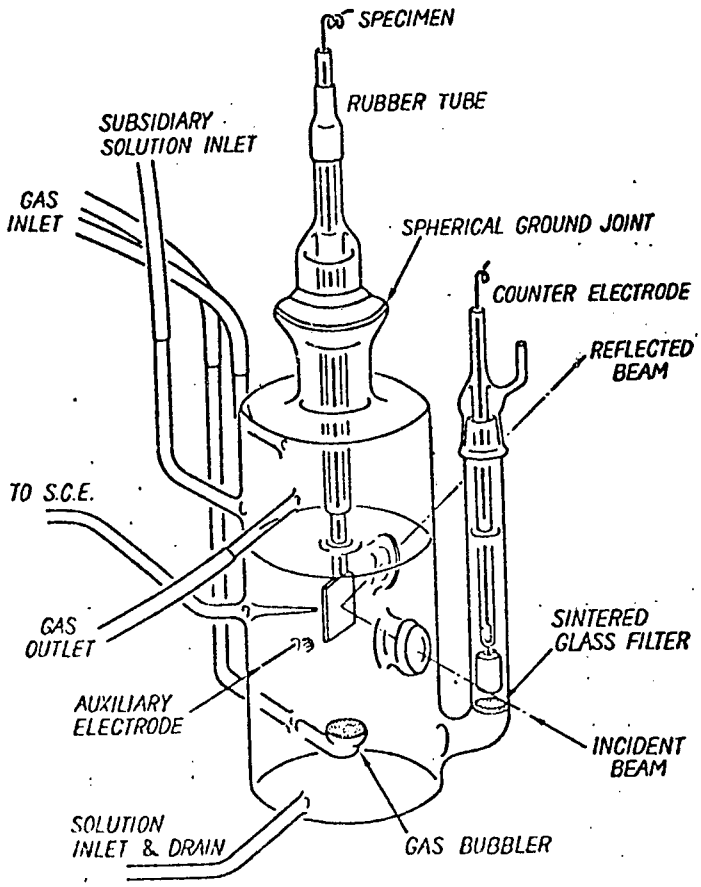

Fig. 5-39. An electrolytic cell for in-situ ellipsometry of the surface of electrodes.

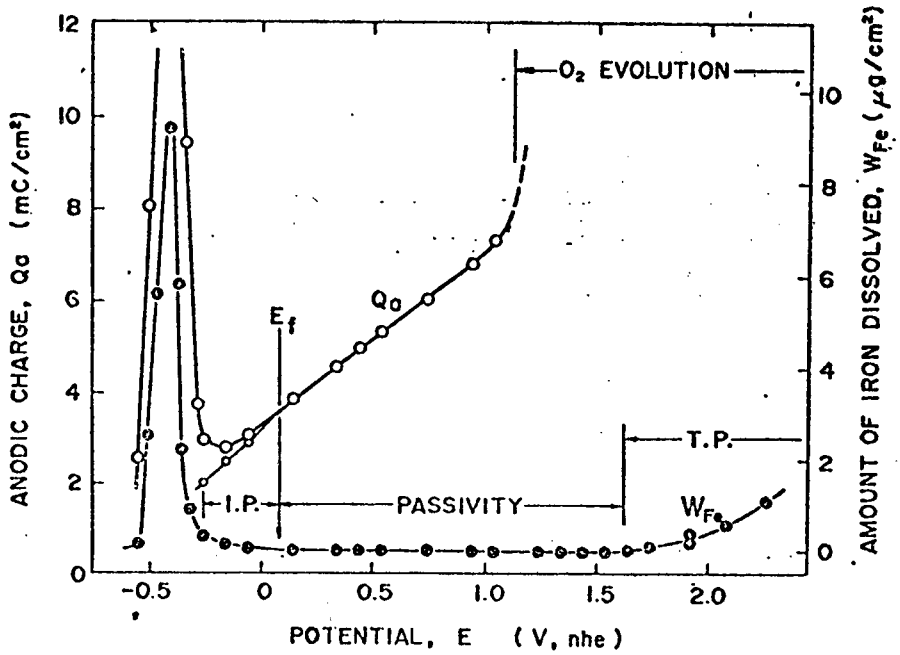

Fig. 5-40. Anodic charge Q_a and amount of iron dissolved during anodic-potentiostatic one-hour oxidation of iron in a deaerated borate solution at pH 8.4 as a function of potential (Sato et al., 1974).

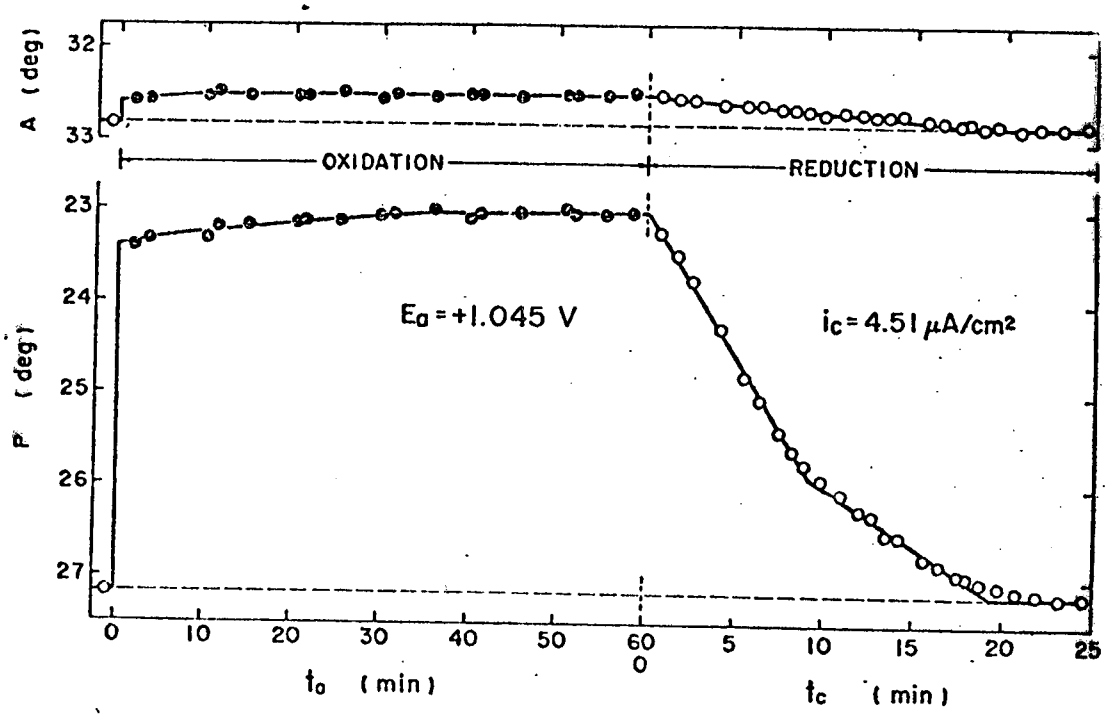

Fig. 5-41. Change in ellipsometric parameters P and A during one-hour potentiostatic oxidation followed by galvanostatic reduction of iron in a borate solution at pH 8.42 (Sato et al., 1971). Incident angle $\Phi = 59^{o}25'$

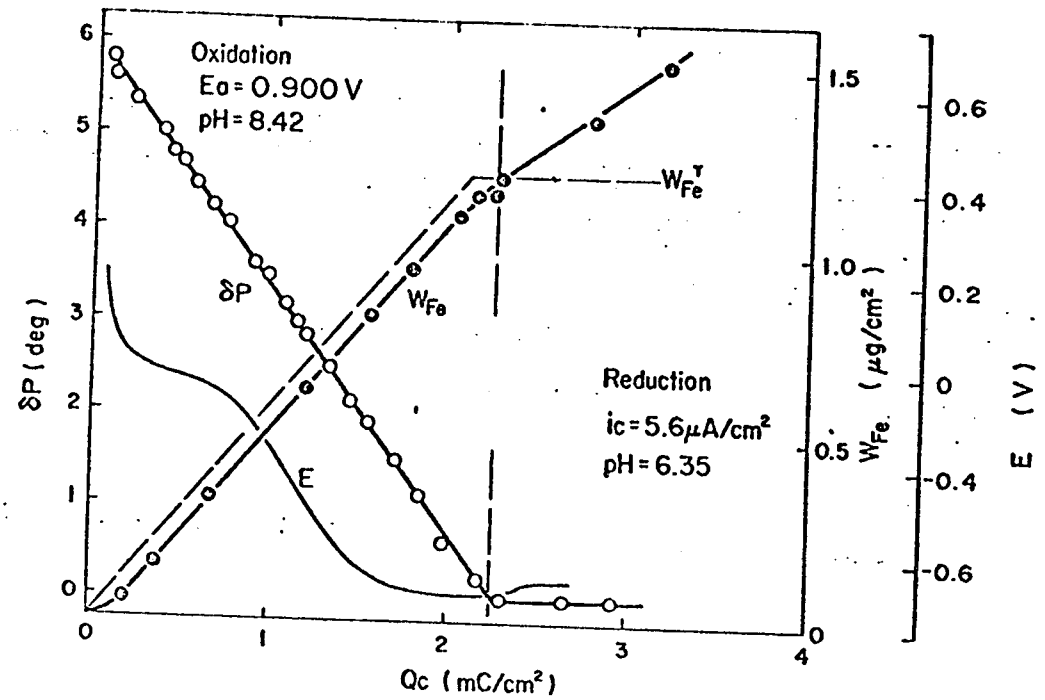

Fig. 5-42. Amount of iron cathodically dissolved from the passive film, potential, and ellipsometric parameter P and a function of cathodic charge passed during galvanostatic-cathodic reduction of a passive iron in a borate buffer solution at pH 6.35 (Sato, et al., 1973). Incident angle $\Phi = 73^{o}16'$. The film was formed at pH 8.42 and reduced at pH 6.35.

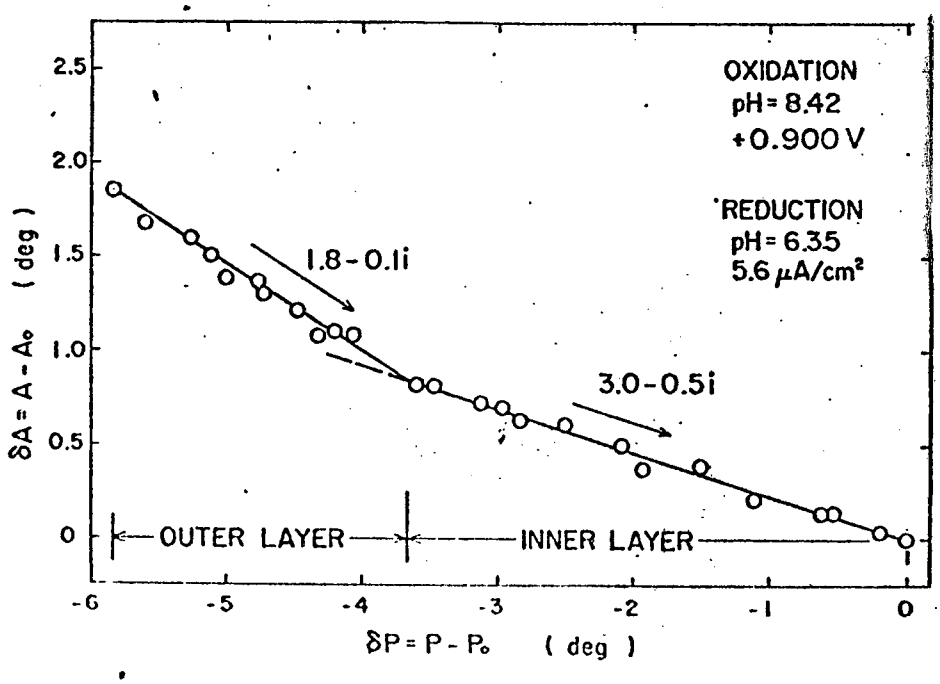

Fig. 5-43. Change in P and A during galvanostatic-cathodic reduction of the passive film on iron in a borate solution at pH 6.35 (Sato et al., 1973). $\Phi = 73^{\circ}16'$. The film was formed at pH 8.42 and reduced at pH 6.35.

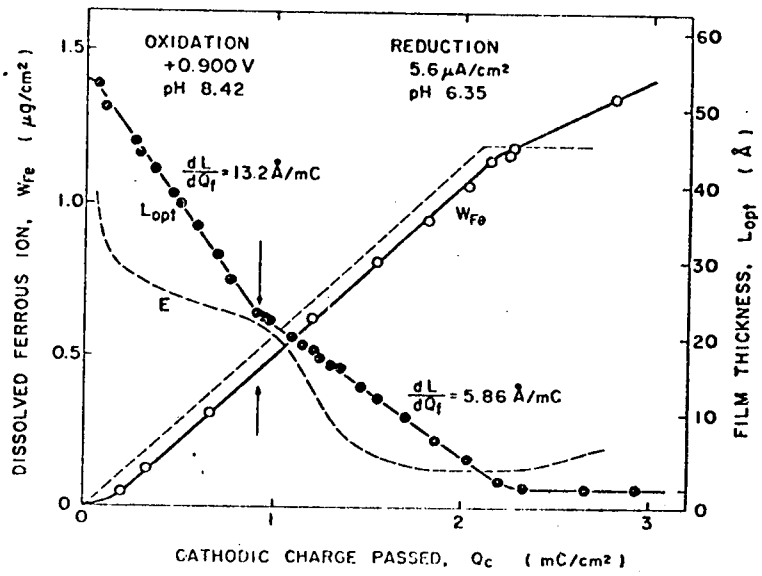

Fig. 5-44. Change in film thickness and amount of iron dissolved from the passive film on iron during galvanostatic-cathodic reduction in a borate solution at pH 6.35 (Sato et al., 1973).

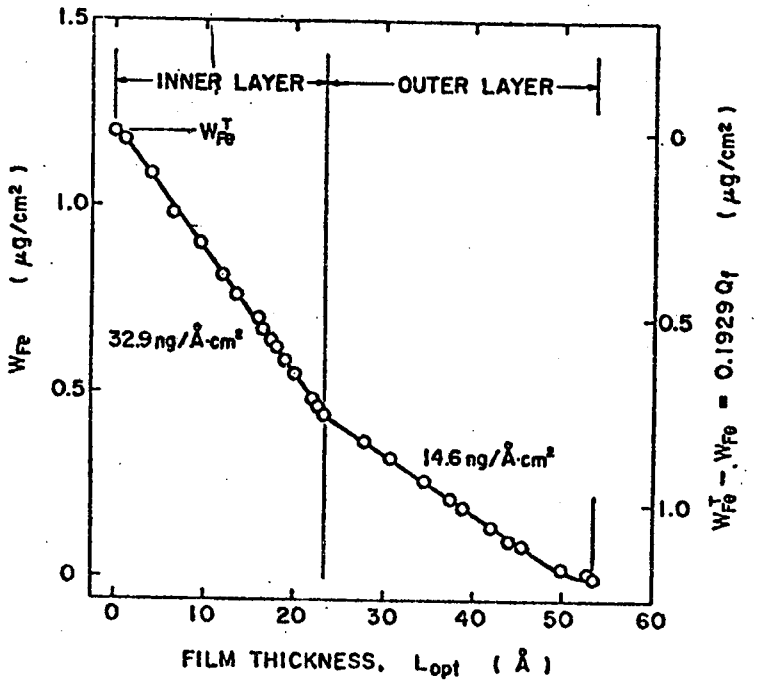

Fig. 5-45. Relation between thickness L and amount of iron in the passive film $W_{Fe}^T - W_{Fe}$ estimated during galvanostatic-cathodic reduction of a passive iron: Data are based on the result shown in Fig. 5-44 (Sato et al., 1973).

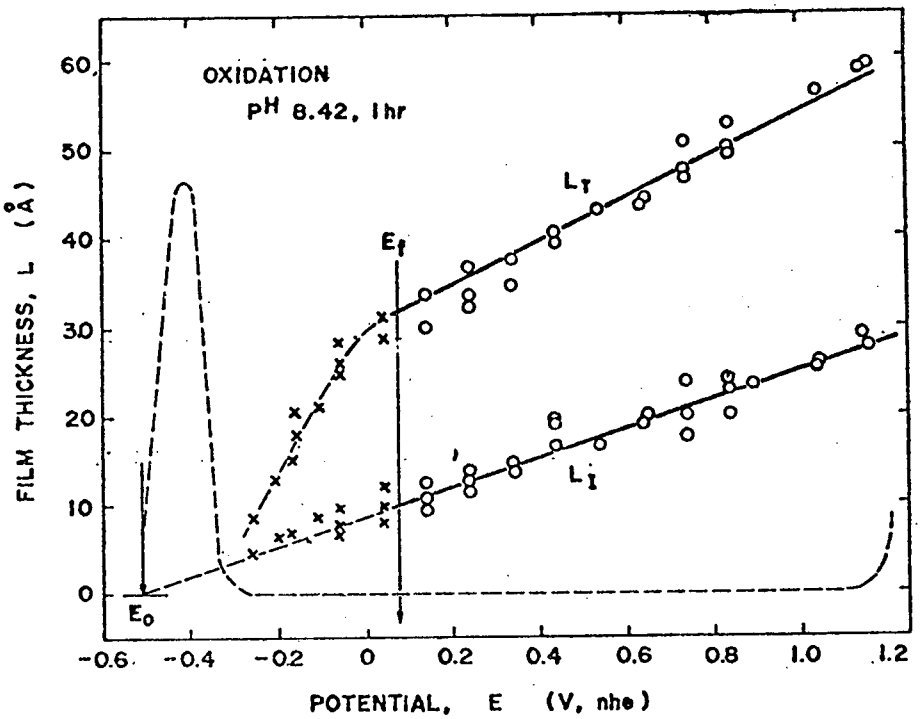

Fig. 5-46. Thickness of the inner layer (barrier layer) and the outer layer (deposit layer) of the passive film formed by potentiostatic one-hour oxidation in a borate solution at pH 8.42 as a function of potential (Sato et al.,1973).

Table 1. Optical constants of iron for wavelength 5461 Å.

2.29—3.29i*		Minor (1903)[14]
2.19—3.19i*		Bernoulli (1909)[15]
2.34—3.17i*		Tool (1910)[16]
2.7—2.7i		Leberknight & Lustman (1939)[17]
3.06—3.67i	$\Phi=60°$	Winterbottom (1950)[18]
2.75—3.65i	45°	Winterbottom (1955)[19]
2.98—3.99i	60°	Winterbottom (1955)[19]
2.78—3.87i	75°	Winterbottom (1955)[19]
3.23—3.84i	70°	Menzel & Gebhart (1962)[20]
3.35—3.84i†	66°	Yolken & Kruger (1965)[21]
3.50—3.66i†	60°	Ord & DeSmet (1966)[22]
3,18—3.85i†	59°25′	Kudo, Sato & Okamoto (1968)[10]
3.21—3.79i†		McBee & Kruger (1969)[23]
3.24—3.98i†	68°05′	Bockris, *et al.* (1971)[24]
3.52—3.54i†	73°16′	Sato & Noda (1972)[25]

* Interpolated, Φ=Angle of incidence.
† Electrochemically reduced surfaces in solution.

Table 3. Density, ρ, and iron ion density, W_{Fe}/L, calculated from the lattice constants of iron oxides and hydroxides.

Compound	Cell Constant (Å)	ρ (g/cm³)	W_{Fe}/L (ng/Å·cm²)
γ-Fe_2O_3	8.30[29] − 8.34		
$\square_8H_0Fe_{64}O_{96}$ [28]		4.91±0.4	34.3±2.3
$\square_8H_{12}Fe_{60}O_{96}$		4.71±0.4	32.3±2.0
α-Fe_2O_3		5.24[30]	37.1
Fe_3O_4	8.397[31]	5.20	37.6
γ-FeOOH	a= 3.06[32] b=12.4 c= 3.87	4.01	25.2
$Fe_2O_3\cdot1.8H_2O$	a= 5.08[33] b= 9.4	3.29	19.1
Inner layer*	Measured		32.9±0.8[25]
Outer layer*	Measured		14.6±1.2

* Thickness-charge ratio, L/Q, is 5.86±0.2 (Å·cm²/mC) for the inner layer and 13.2±1.2 (Å·cm²/mC) for the outer layer.

Table 2. Optical constants of iron oxides for wavelength 5461 Å.

Magnetite, cubic	
2.58—0.28i	Leberknight & Lustman (1939)[17]
2.5—0.3i	Winterbottom (1950)[18]
2.39—0.249i	Bockris, *et al.* (1971)[24]
Hematite rhombohedral	
3.20—0.97i*	Leberknight & Lustman (1939)[17]
3.46—1.07i	Winterbottom (1950)[18]
2.88—0.378i	Bockris, *et al.* (1971)[24]
Hydrated ferric oxide, amorphous	
2.5—0.0i	Winterbottom (1950)[18]
($2.0<n<2.5$, $k<0.1$)	
1.87	Kodama (1972)[26]
Anodic oxide film	
2.6—0.4i	Ord & DeSmet (1966)[22]
2.55—0.35i	Kudo, Sato & Okamoto (1968)[10]
2.48—0.273i	Goswami & Staehle (1971)[27]
(2.7±0.1)—(0.13±0.05)i	Bockris, *et al.* (1971)[24]
Inner layer of anodic oxide film	
(3.0±0.1)—(0.5±0.1)i	Sato & Noda (1972)[25]
Outer layer of anodic oxide film	
(1.8±0.1)—(0.1±0.05)i	Sato & Noda (1972)[25]

* Calculated.

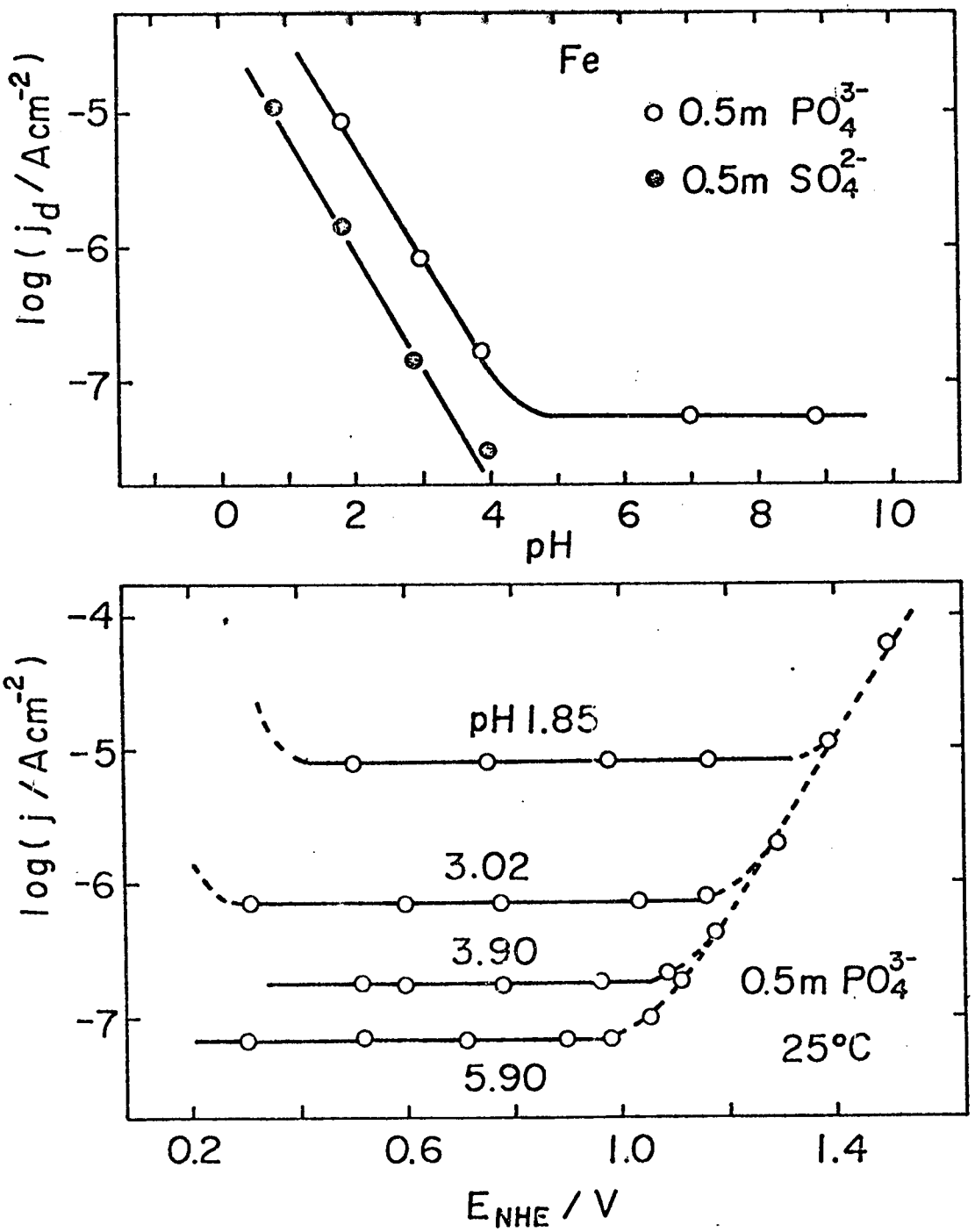

Fig. 6-1. Potential-independent dissolution current of passive iron under one-hour steady state condition in phosphate solutions (Sato et al., 1974) and in sulphate solutions (Vetter, 1955) as a function of pH.

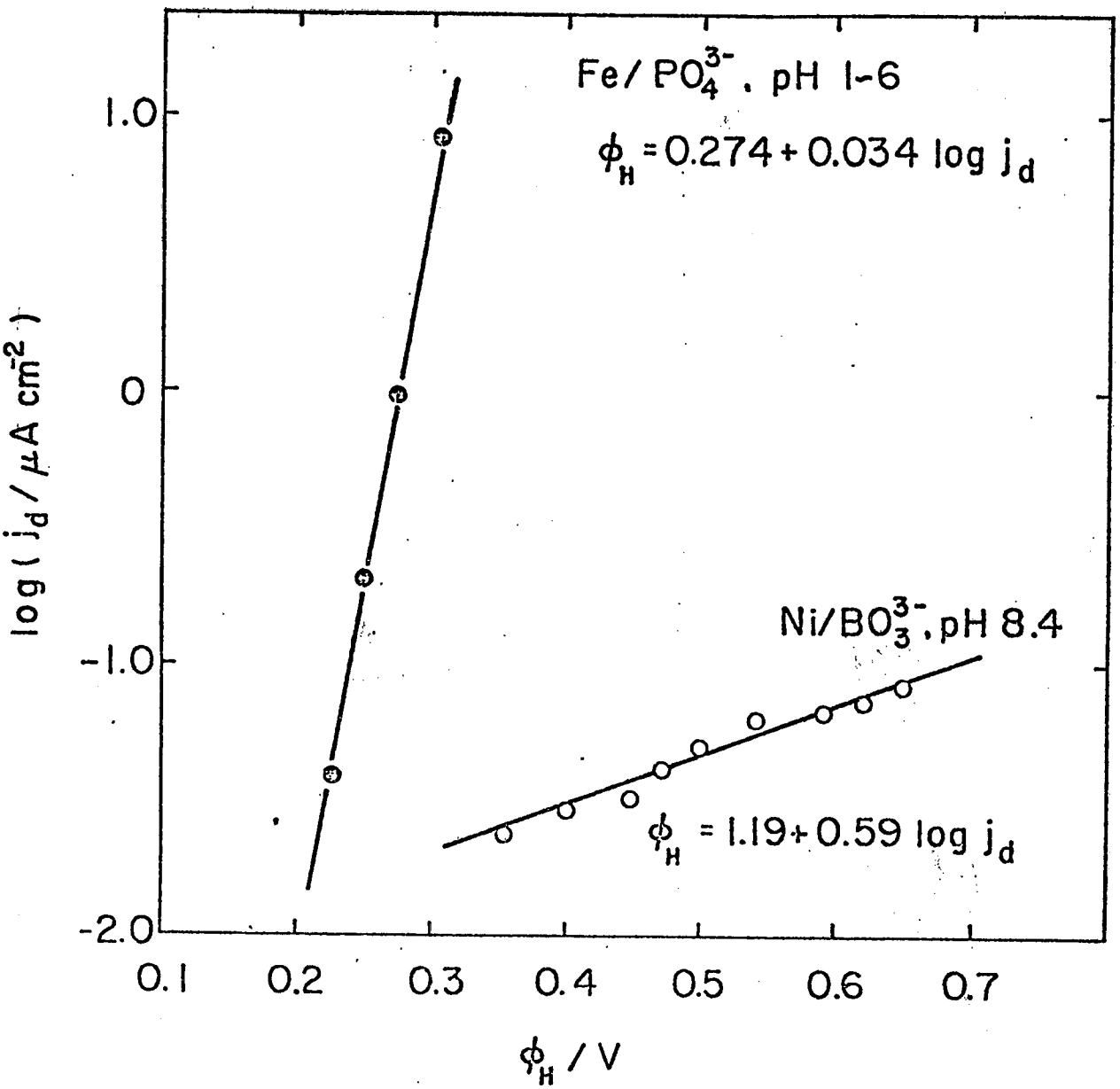

Fig. 6-2. Steady state dissolution current of the passive film versus potential difference across the Helmholtz layer at the film/solution interface for, iron and nickel (Sato, 1976). Φ_{II} was calculated from the mean electric field in the film.

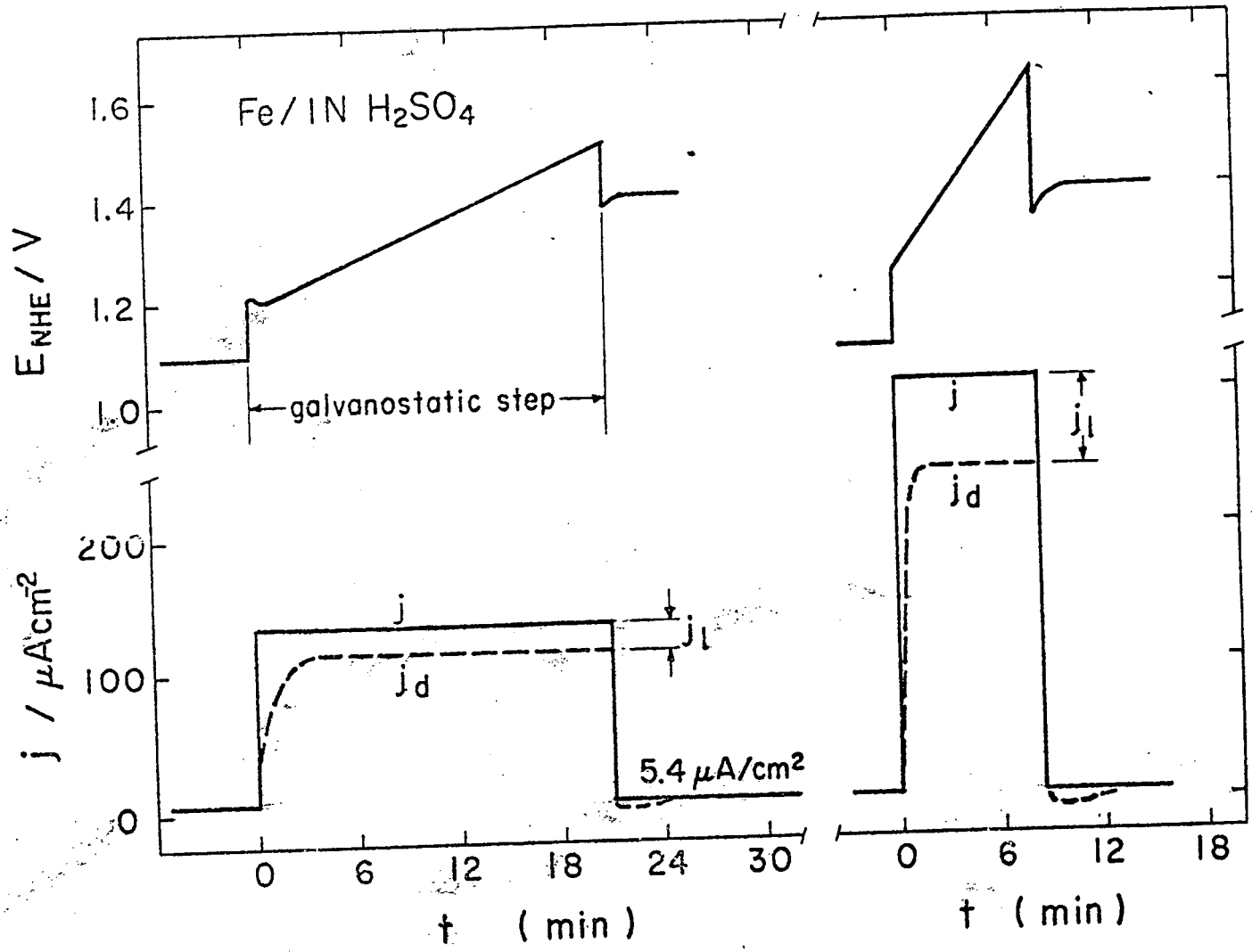

Fig. 6-3. Non-steady state dissolution current j_d, anodic current j, and potential of a passive iron as a function of time during galvanostatic step from a steady state in 0.5 M H_2SO_4 solution (Vetter et al., 1970). $j_\ell = j - j_d$ is the current for the rate of film growth.

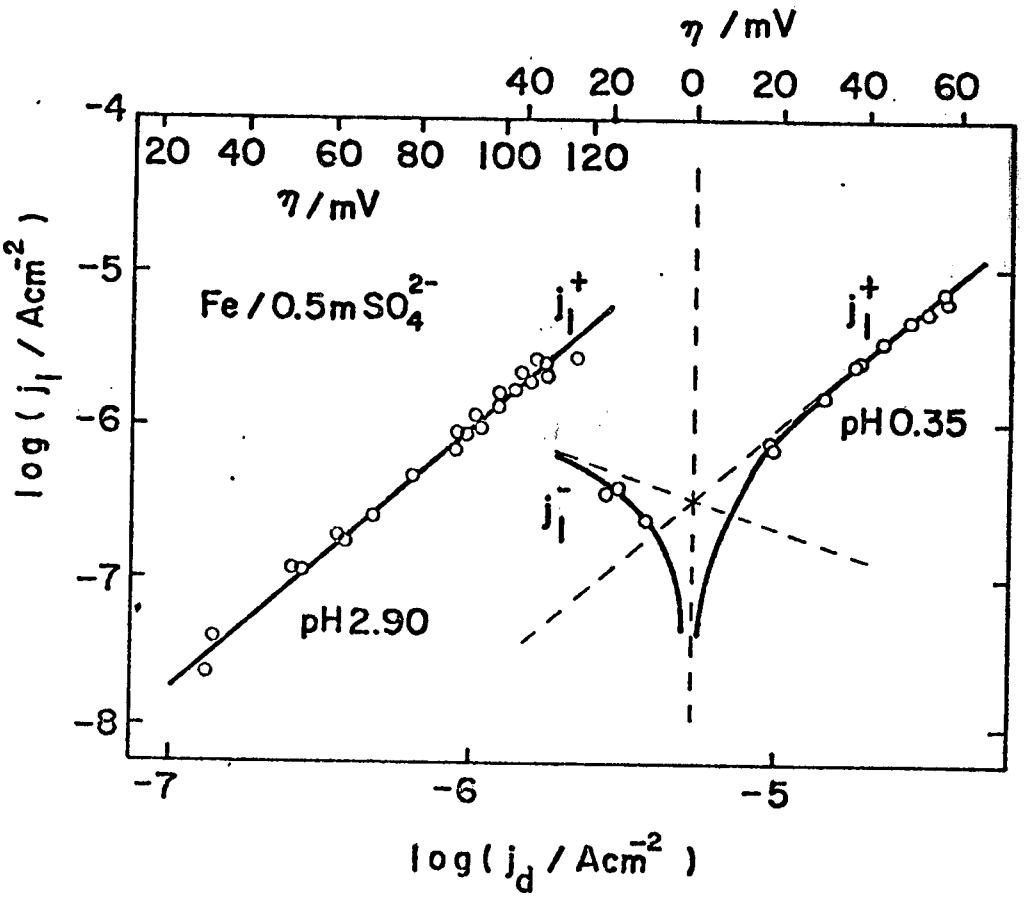

Fig. 6-4. Relation between film growth current j and film dissolution current j_d at the passive film/solution interface for passive iron under non-steady state conditions in 0.5 M sulphate solutions at pH 0.35 and 2.90 (Vetter et al., 1973). j_ℓ^+ = film growth current, j_ℓ^- = film removal current, and η = the overpotential at the film/solution interface.

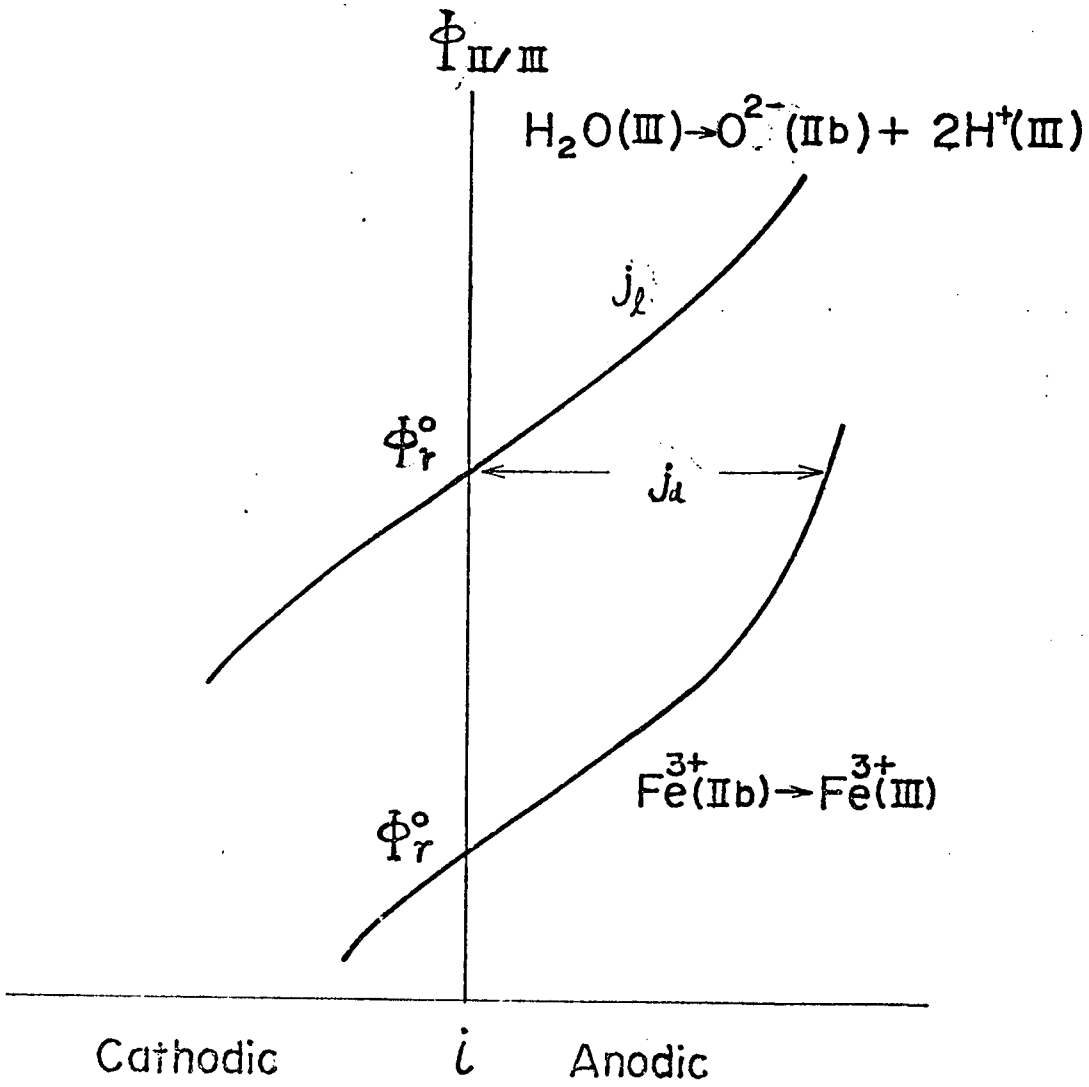

Fig. 6-5. Schematic polarization curve of passive film dissolution; The currents of iron ion transfer j_d and oxygen ion transfer j_ℓ versus the Helmholtz layer potential difference $\Phi_{II/III}$ at the passive film/solution interface.

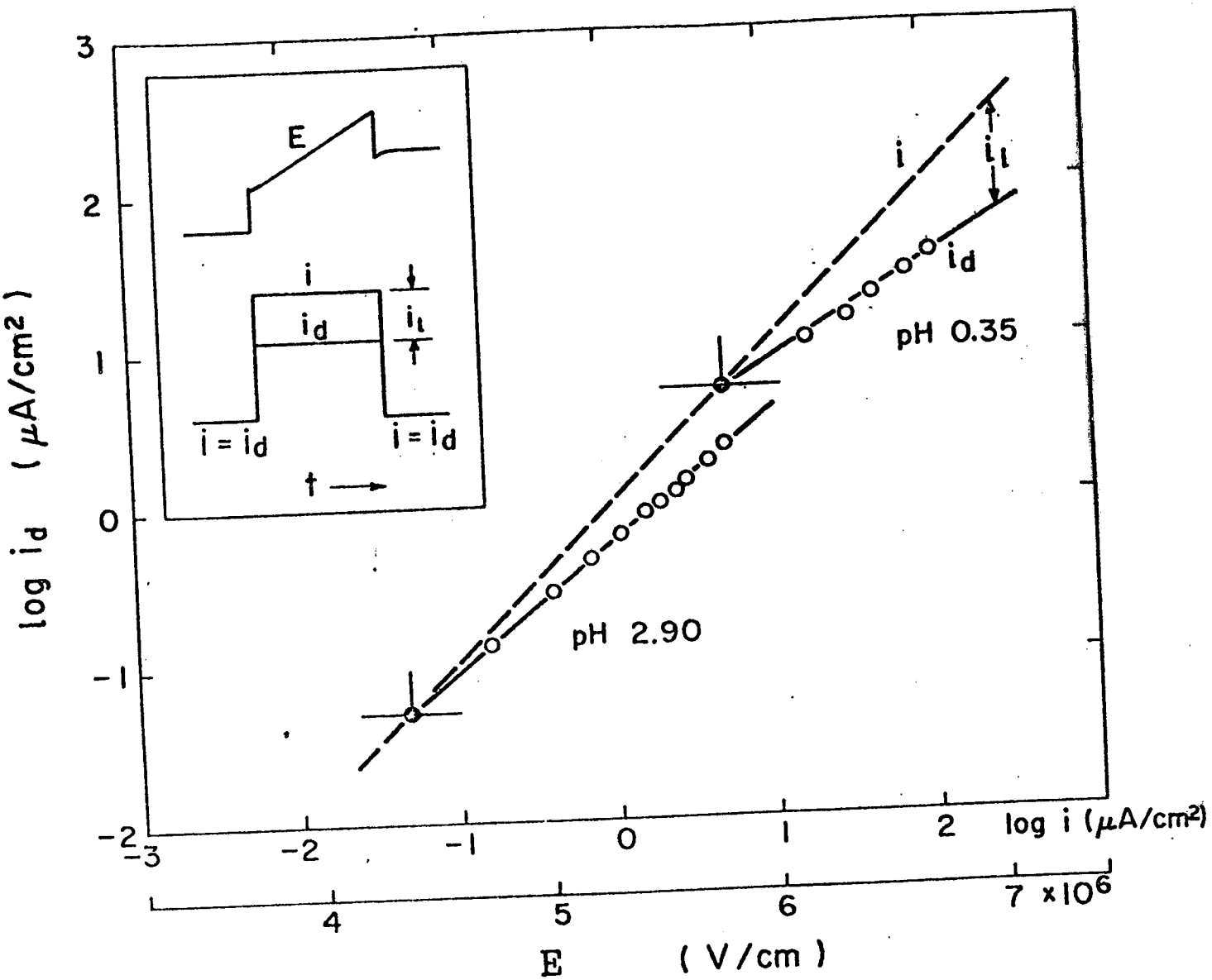

Fig. 6-6. Relation between the ionic current in the passive film j and the film dissolution current j_d for passive iron under non-steady state conditions in 0.5 M sulphate solutions at pH 0.35 and pH 2.90 (Sato, 1976). Data are based on the results shown in Fig. 6-4.

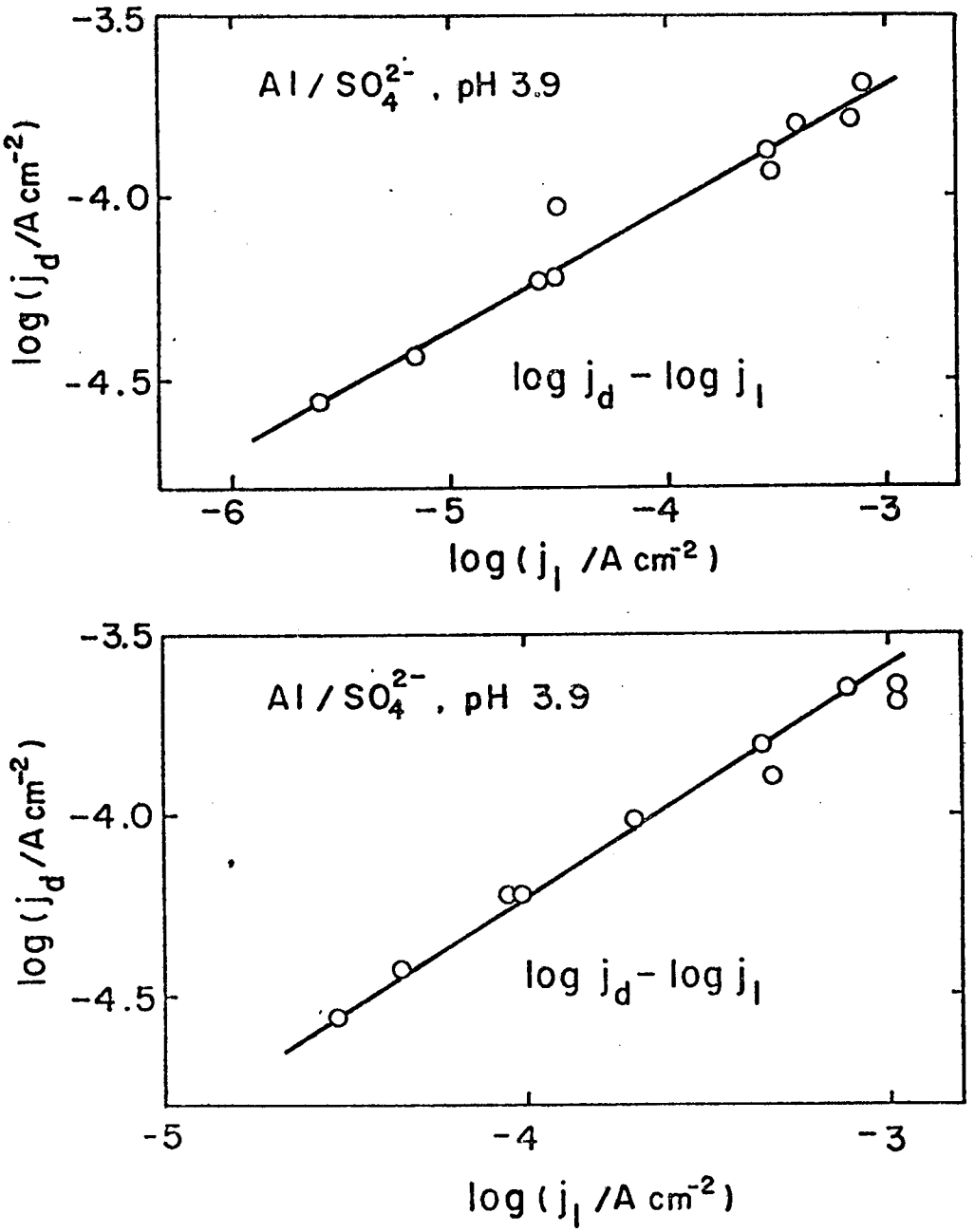

Fig. 6-7. Dissolution current j_d of an anodic oxide film on aluminum in 0.5 M Na_2SO_4 solution at pH 3.9 as functions of film formation current j_ℓ and total ionic current j in the film (Gorn, 1975).

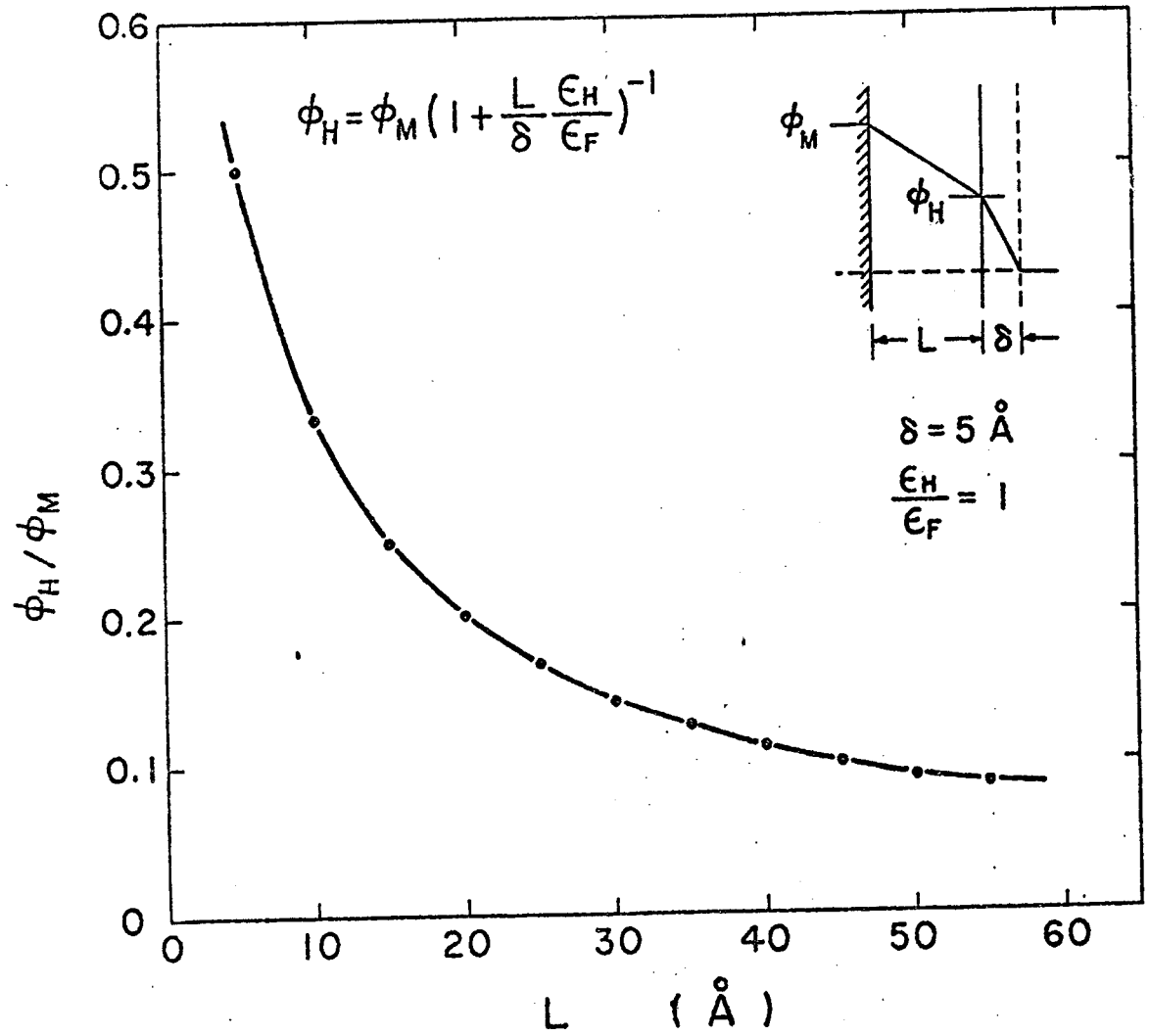

Fig. 7-1. Ratio of Helmholtz layer potential Φ_H to metal potential Φ_M as a function of thickness of a thin semiconductor film on metal electrodes (Sato, 1976).

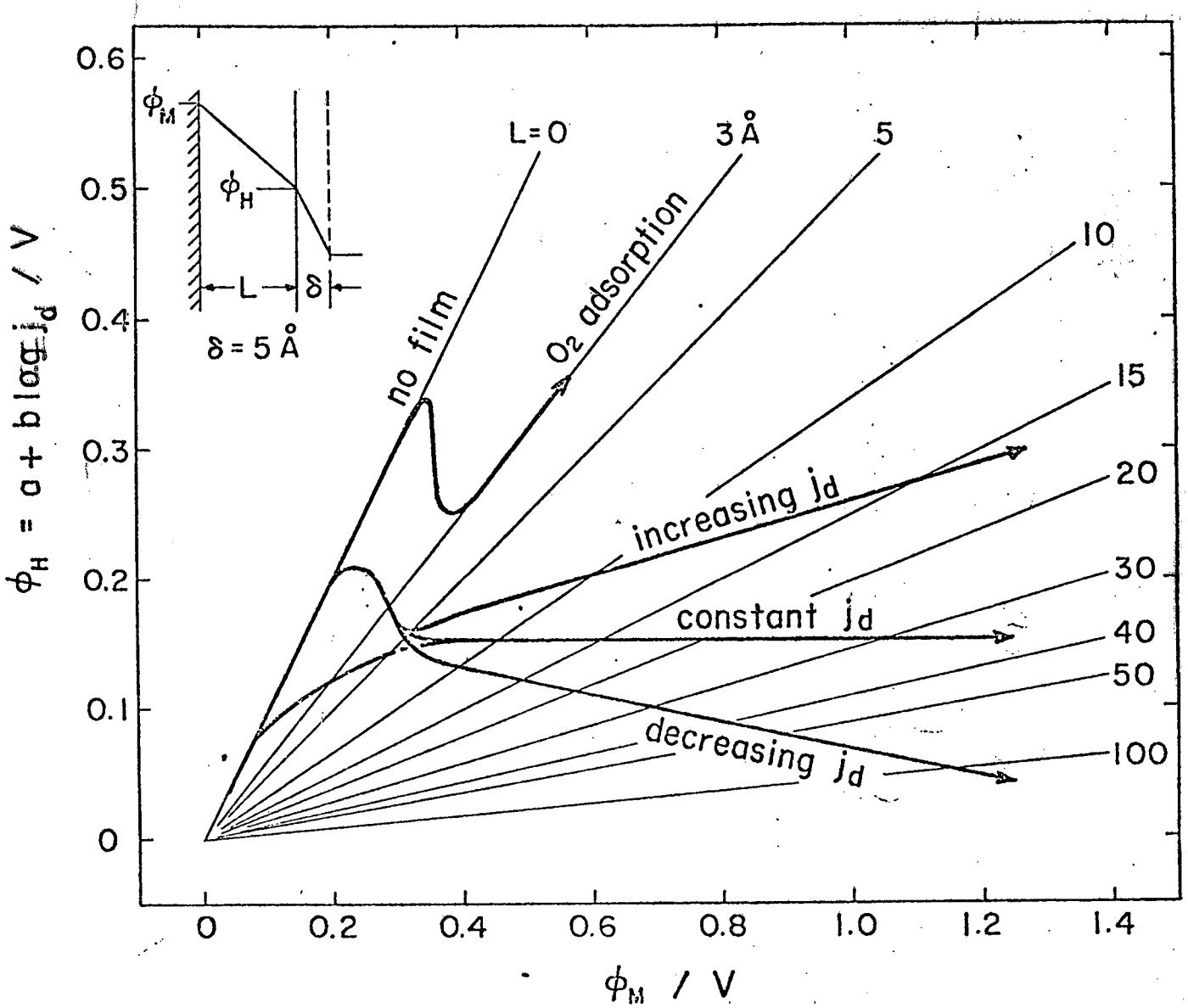

Fig. 7-2. Helmholtz layer potential Φ_H versus metal potential Φ_M for a metal electrode covered with a thin semiconductor film of various thickness from L = 0 to L = 100Å, and possible shapes of $\Phi_H - \Phi_M$ curve and hence log j - Φ_M curve for anodic metal dissolution and passivation (Sato, 1976).

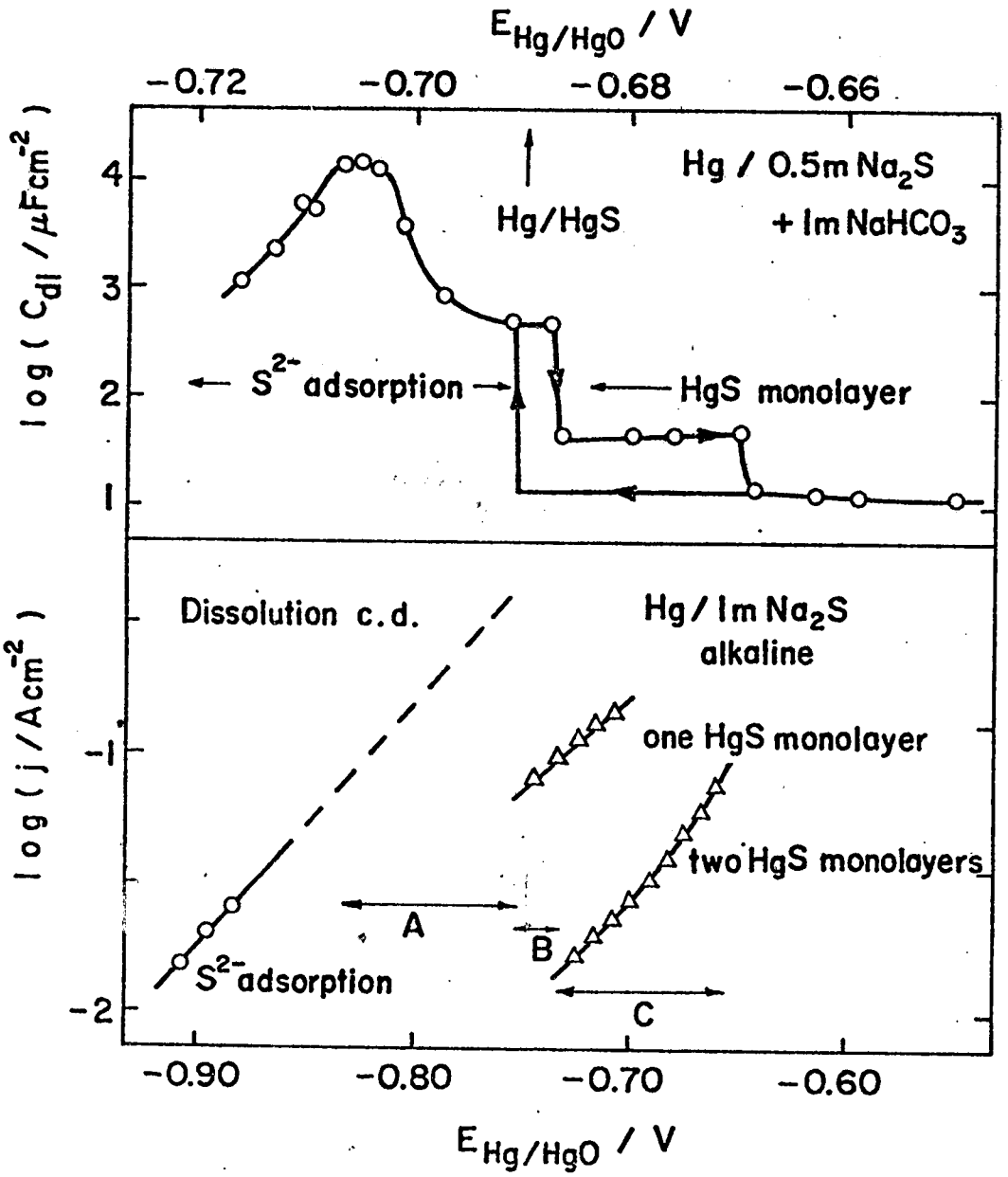

Fig. 7-3. Anodic dissolution current and electrode double layer capacity versus potential of mercury in sulphide ion solutions, indicating monolayer sulphide passivity (Armstrong et al., 1968). Strong S^{2-} ion adsorption occurs in potential range A, the first HgS monolayer in B, and the second monolayer in C.

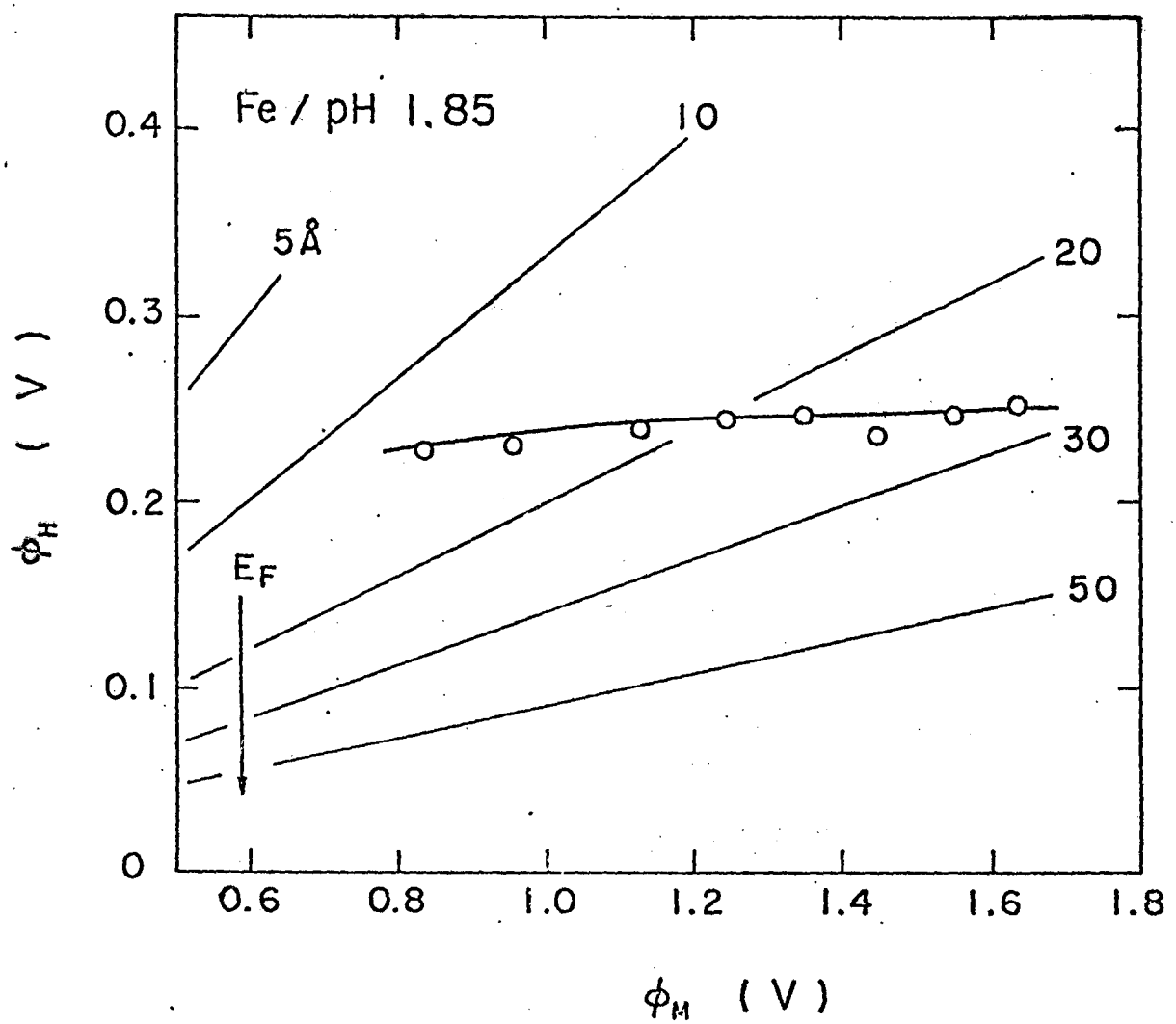

Fig. 7-4. Helmholtz layer potential Φ_M at the passive barrier film surface versus metal potential Φ_M for passive iron in phosphate solution at pH 1.85 (Sato, 1976). Φ_H is calculated from experimentally estimated thickness L of the passive film by using the equation

$$\Phi_H = \Phi_M / \left(1 + \frac{L}{\delta} \frac{\epsilon_H}{\epsilon_F} \right) \quad \text{with } \delta = 5\,\text{Å} \text{ and } \epsilon_H = \epsilon_F.$$

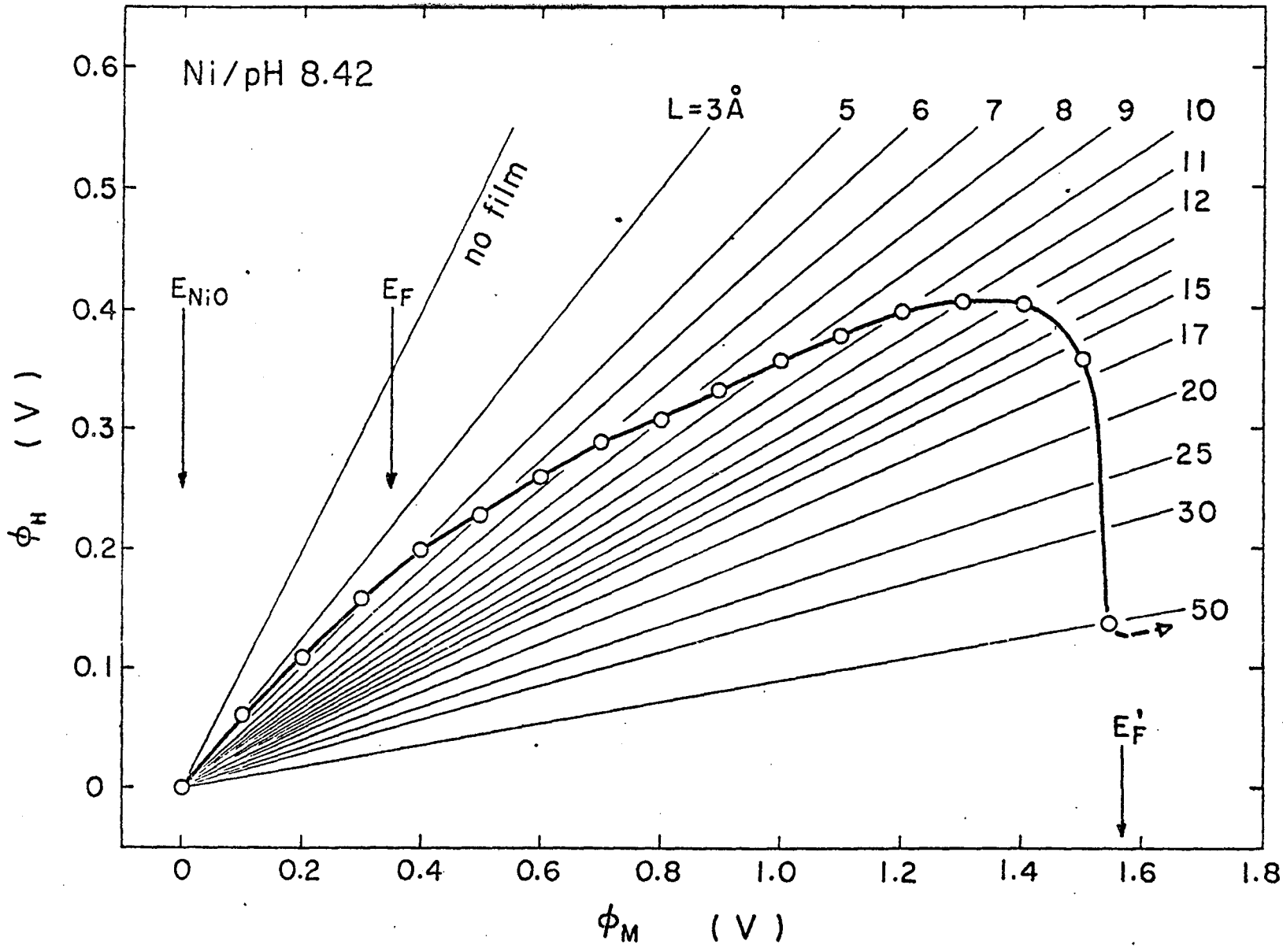

Fig. 7-5. Helmholtz layer potential Φ_M at the passive barrier film surface versus metal potential Φ_M for the passive film on nickel in steady state in borate solution at pH 8.42 (Sato, 1976).

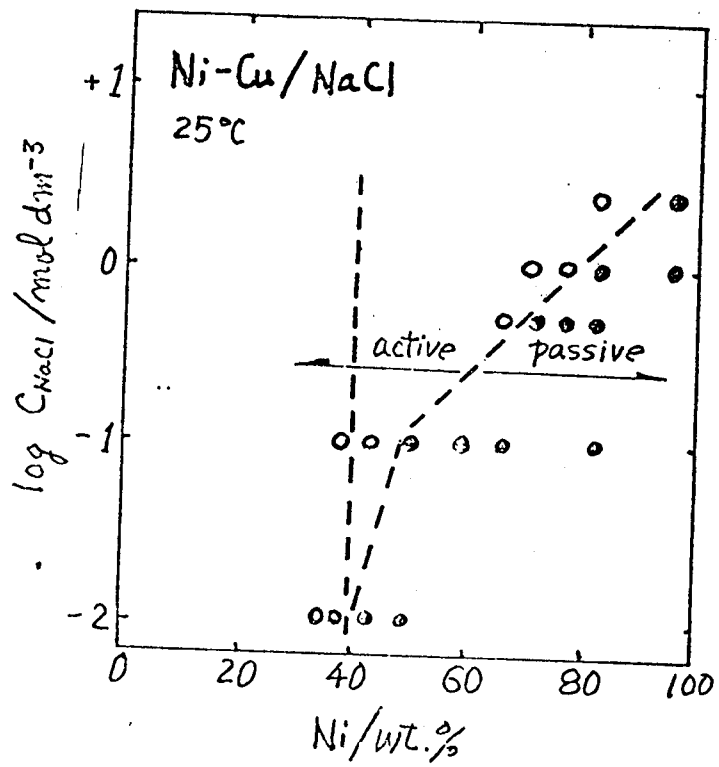

Fig. 7-6. Stability of active and passive states of nickel-cupper alloys in NaCl solutions, showing that all alloys lose passivity regardless of pH or presence of Cl^- below 40 % Ni, which is close to the critical composition established for anodic passivity in 0.5 M H_2SO_4 (Uhlig, 1975).

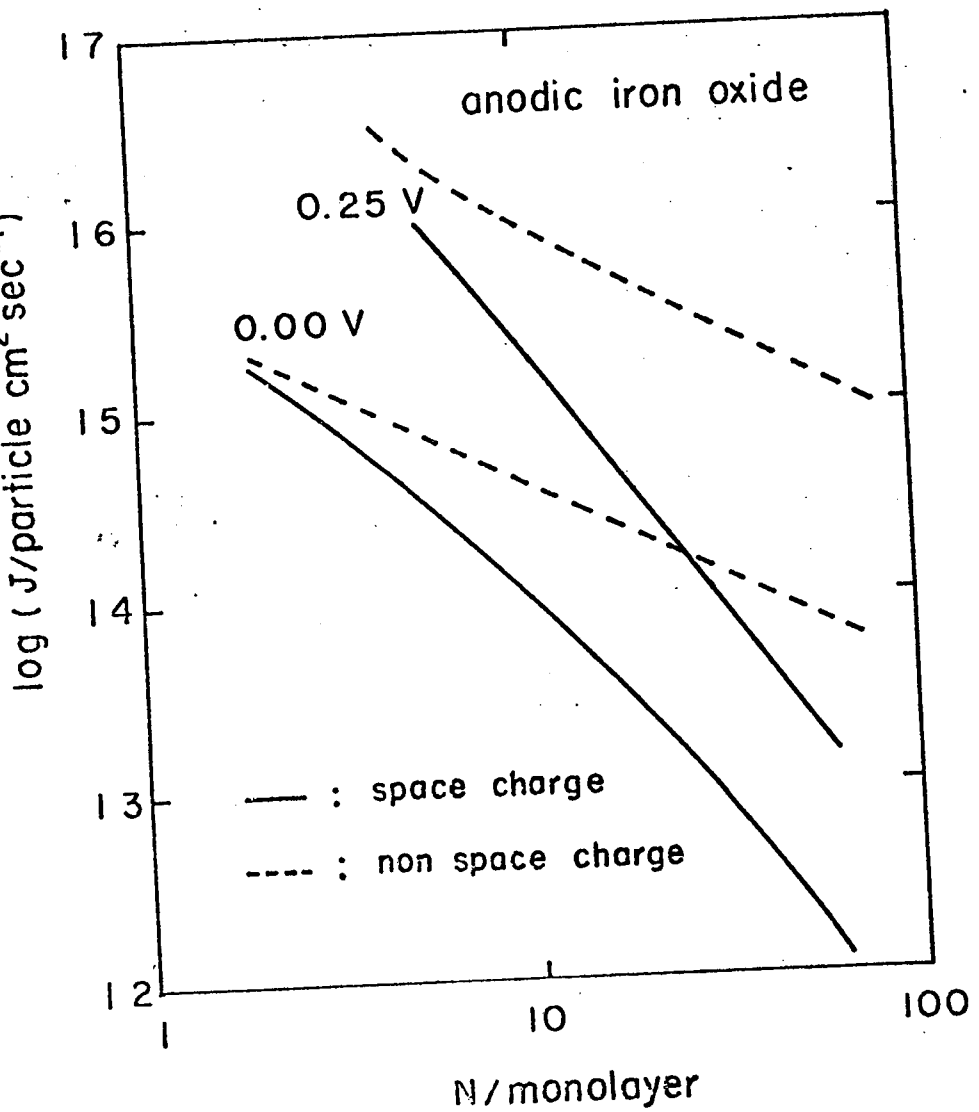

Fig. 7-7. Logarithm of ionic current versus logarithm of anodic oxide film thickness for film growth with and without space charge at constant potential difference across the film (Fromhold, 1976).

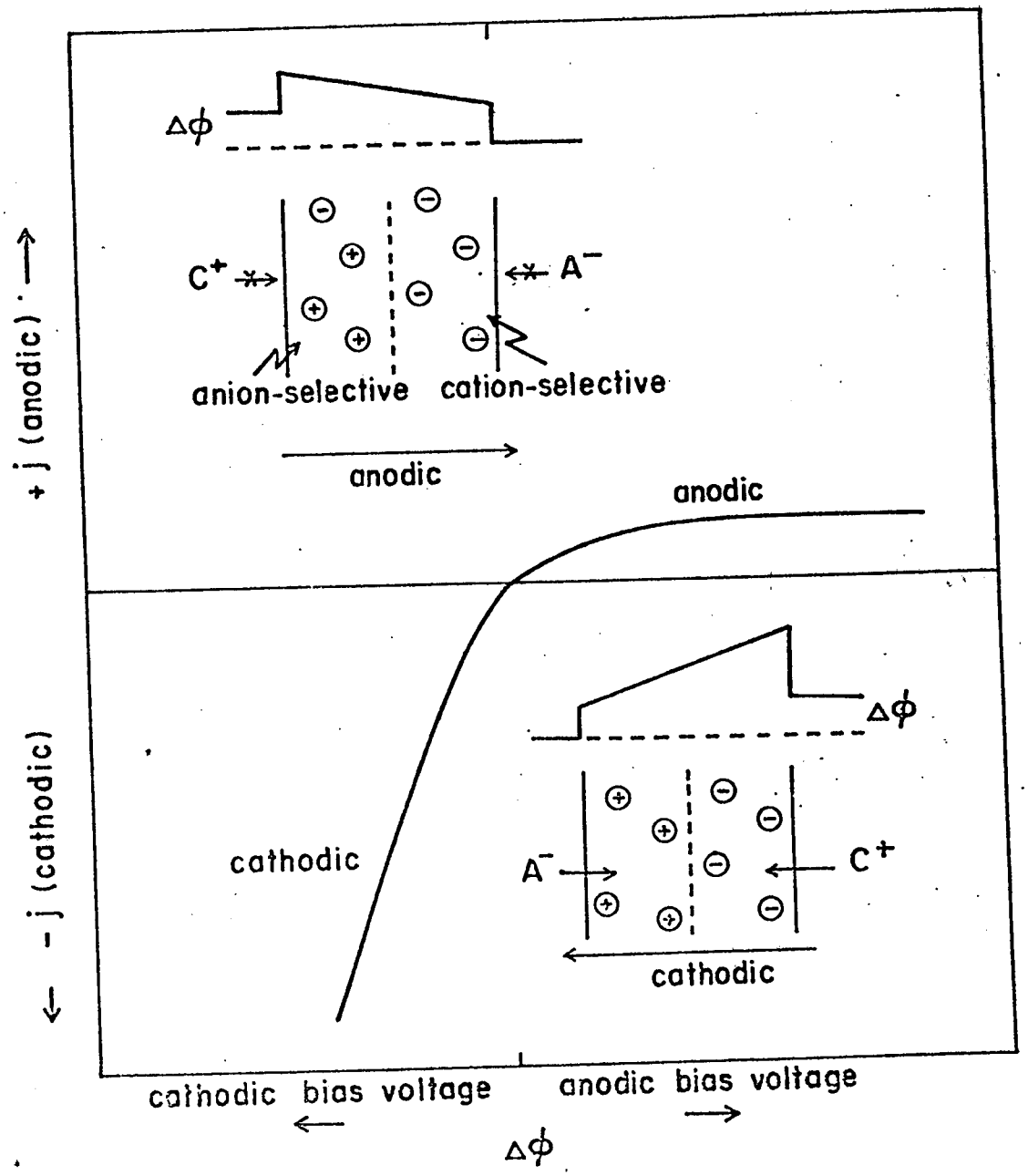

Fig. 7-8. Rectification of ionic current through bi-polar membrane with a positive fixed charge on the one side and a negative fixed charge on the other side (Sato, 1977).

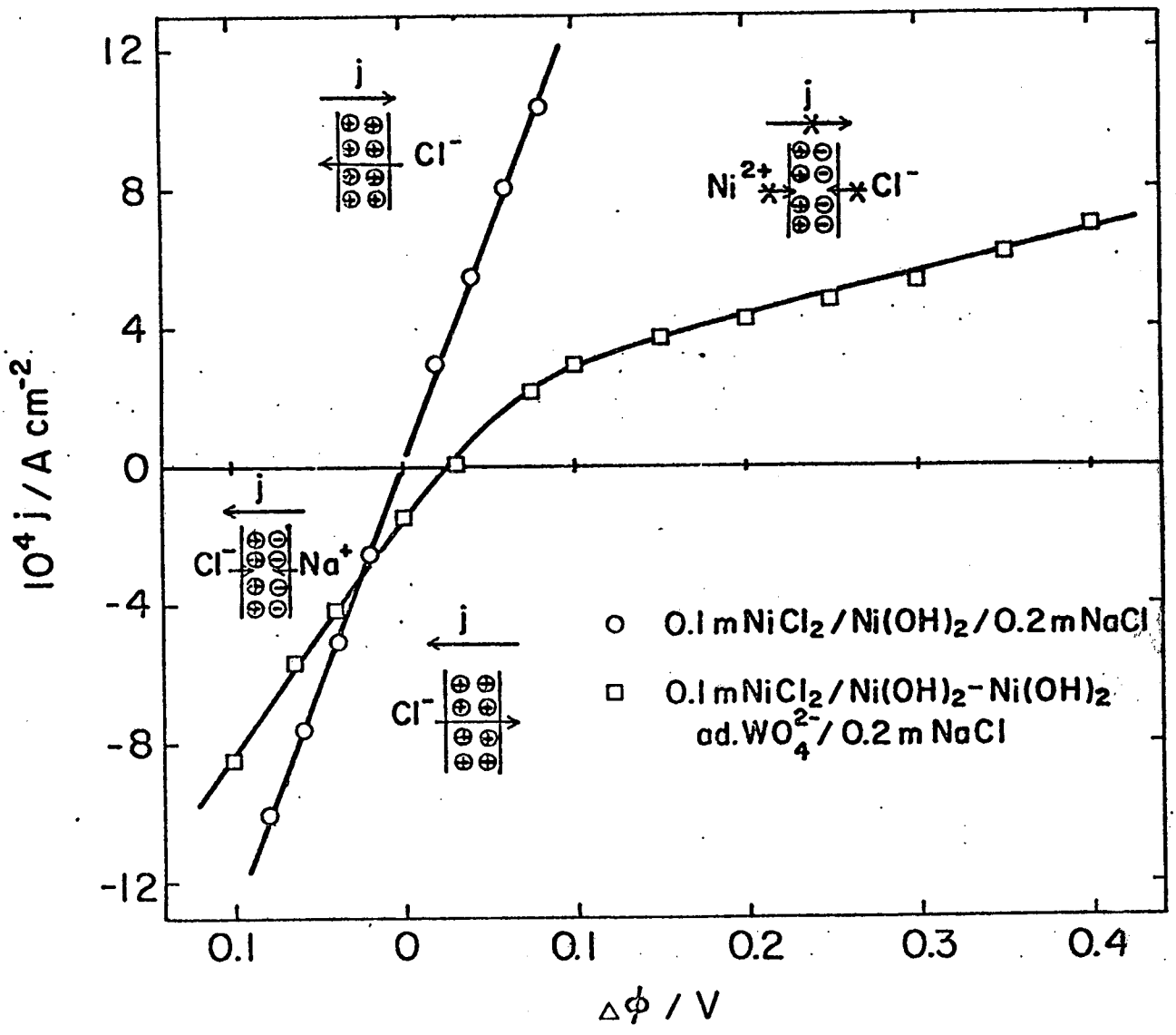

Fig. 7-9. Ionic current versus bias voltage for hydrous nickel(II) oxide membranes with intrinsic unipolar positive fixed charge Ni^{2+} and with bipolar fixed charge $Ni^{2+} - WO_4^{2-}$ separating 0.1 M $NiCl_2$ from 0.2 M NaCl solutions (Sakashita and Sato, to be published).

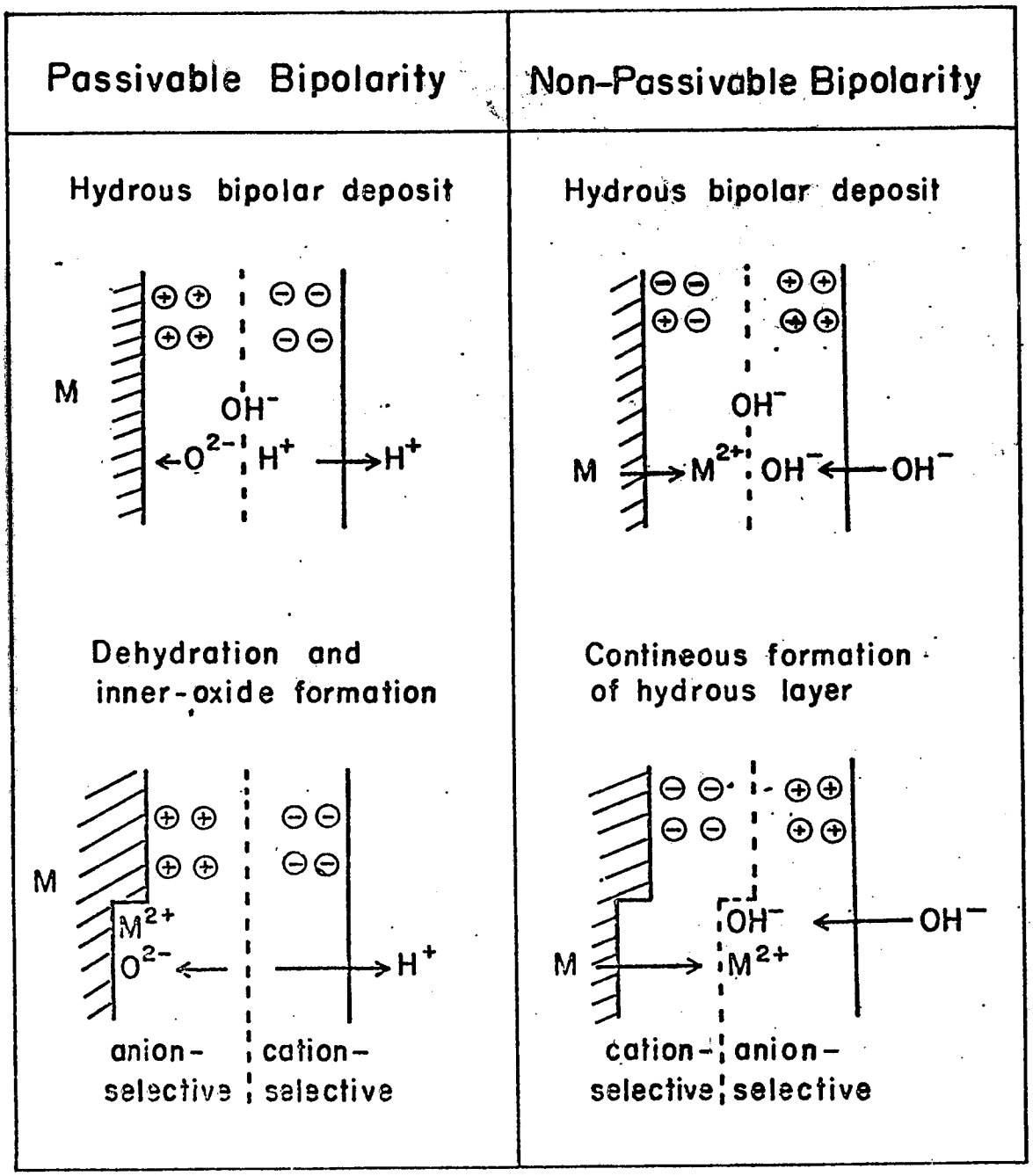

Fig. 7-10. Bipolar fixed charge in hydrous metal oxide films leading to the formation of protective metal oxide films and to the continuous growth of non-protective hydrous oxide films (Sato, 1977).

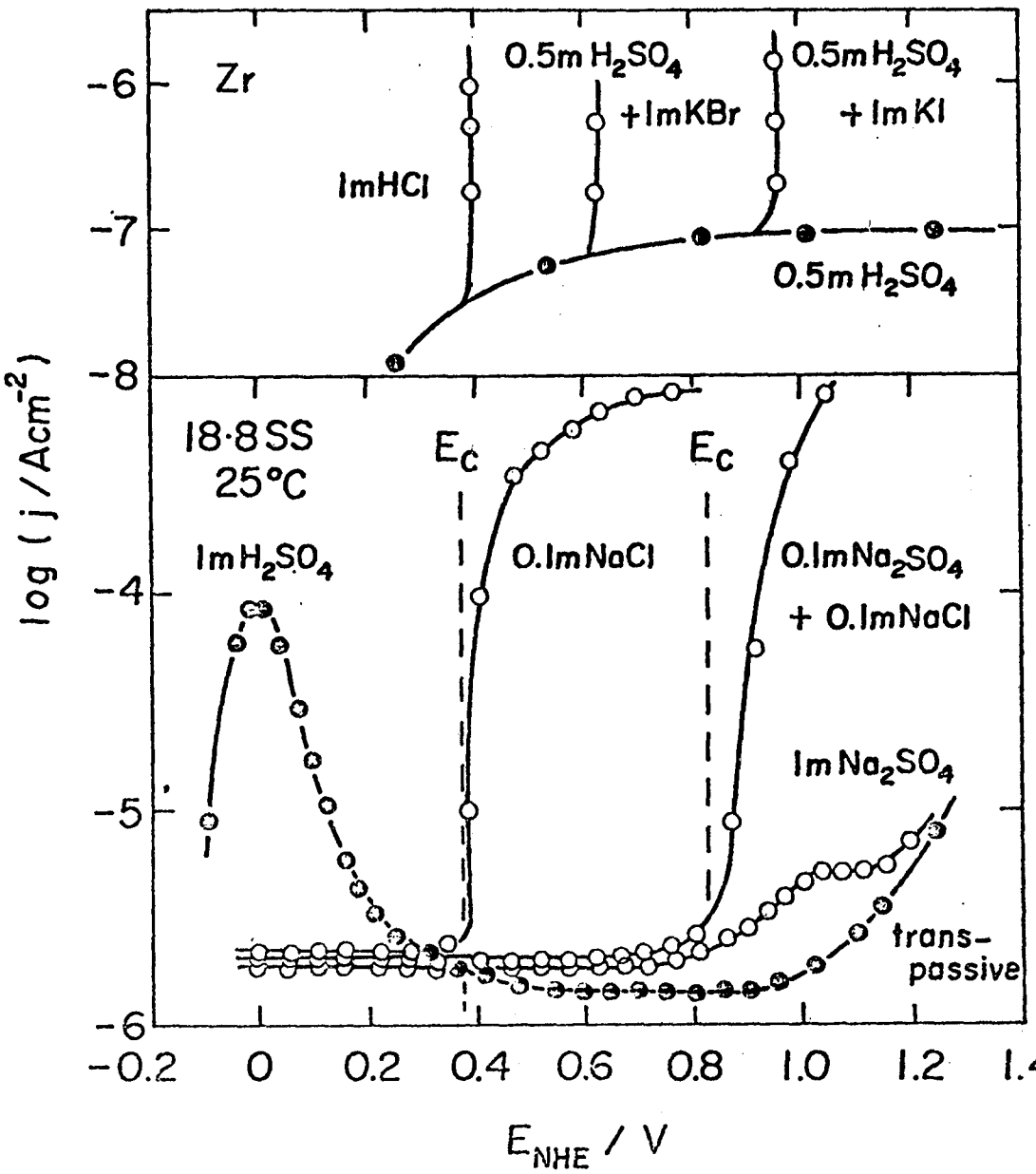

Fig. 8-1. Anodic polarization curves of austenitic 18 Cr - 8Ni stainless steel in solutions of H_2SO_4, NaCl, Na_2SO_4, and Na_2SO_4 containing Cl^- ions (Uhlig et al., 1966), and of zirconium in solutions of H_2SO_4, HCl, H_2SO_4 containing Br^- ions, and H_2SO_4 containing I^- ions (Kolotyrkin, 1961), showing the critical potential of pitting dissolution in presence of halide ions.

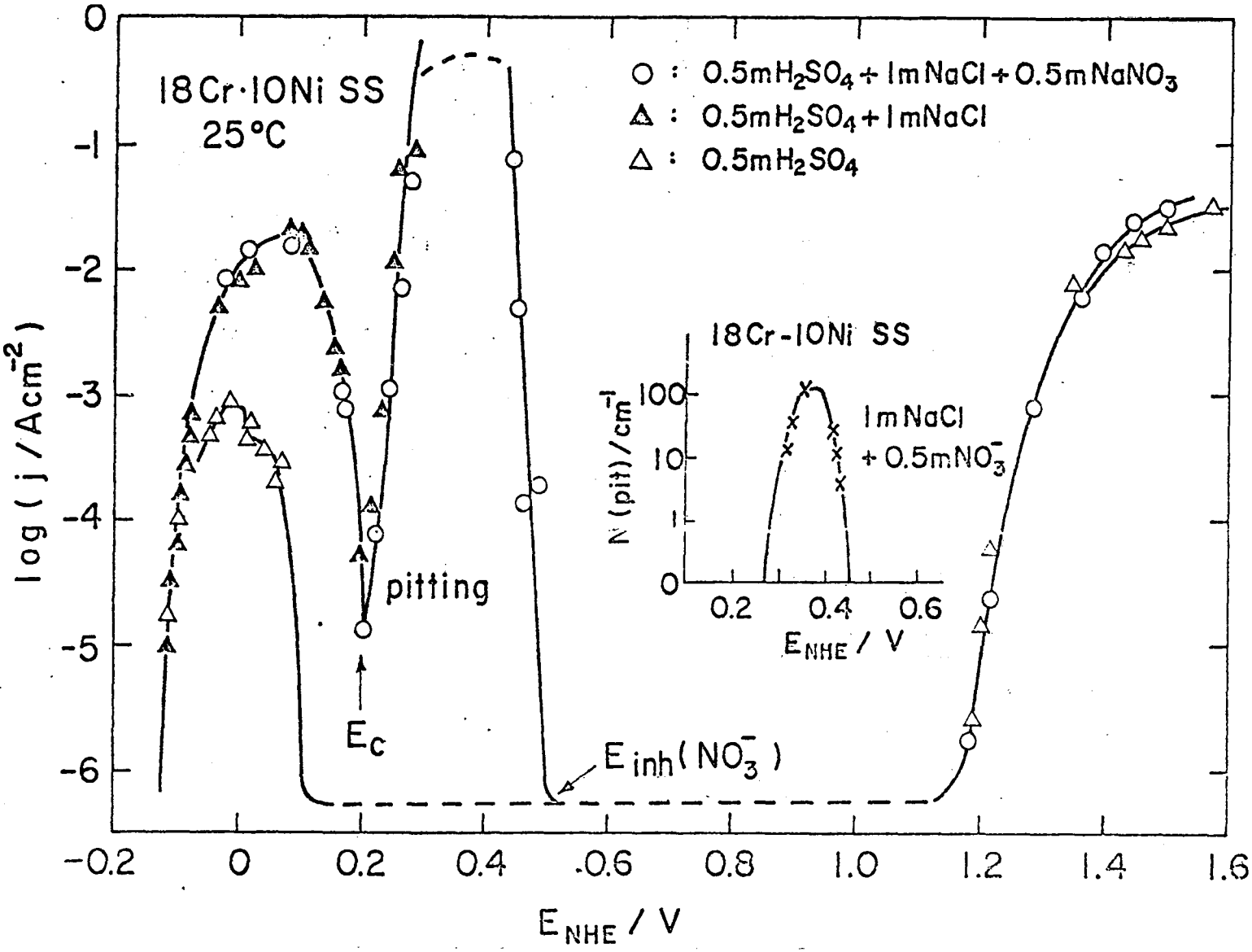

Fig. 8-2. Anodic polarization ourves of austenitic 18 Cr - 10 Ni stainless steel in H_2SO_4, H_2SO_4 + NaCl, and H_2SO_4 + NaCl + $NaNO_3$ (Schwenk, 1961 ∿ 64), and pit density versus potential curve of the steel potentiostated for 24 hours in HCl solution oontaining No_3^- ions (Herbsleb, 1965)

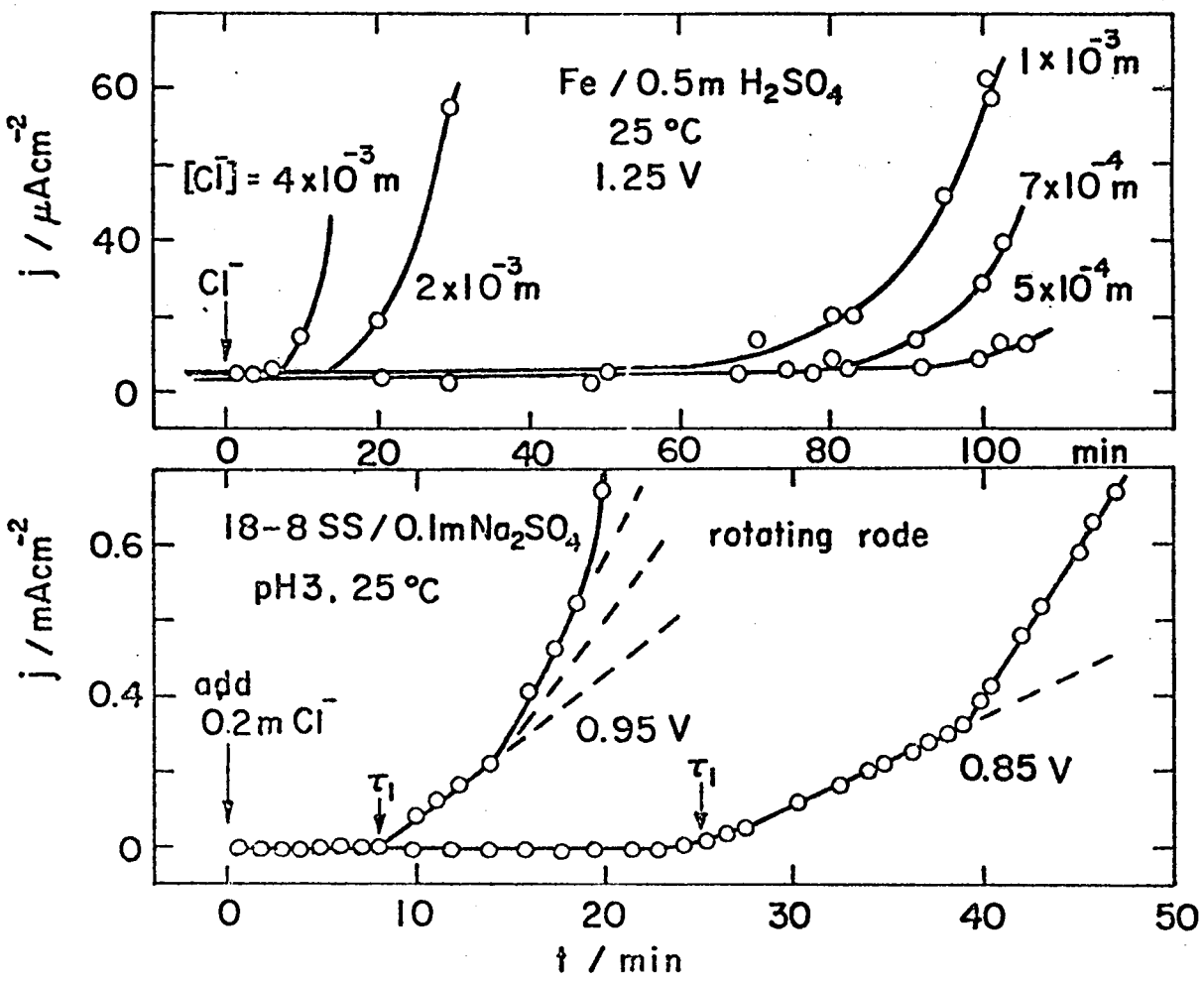

Fig. 8-3. Anodic current at constant potential as a function of time after addition of chloride ions for prepassivated iron in H_2SO_4 (Engell et al., 1959) and for prepassivated 18 Cr - 8 Ni stainless steel in Na_2SO_4 solution (Sato et al., 1974), showing the incubation time for initiation of pitting dissolution.

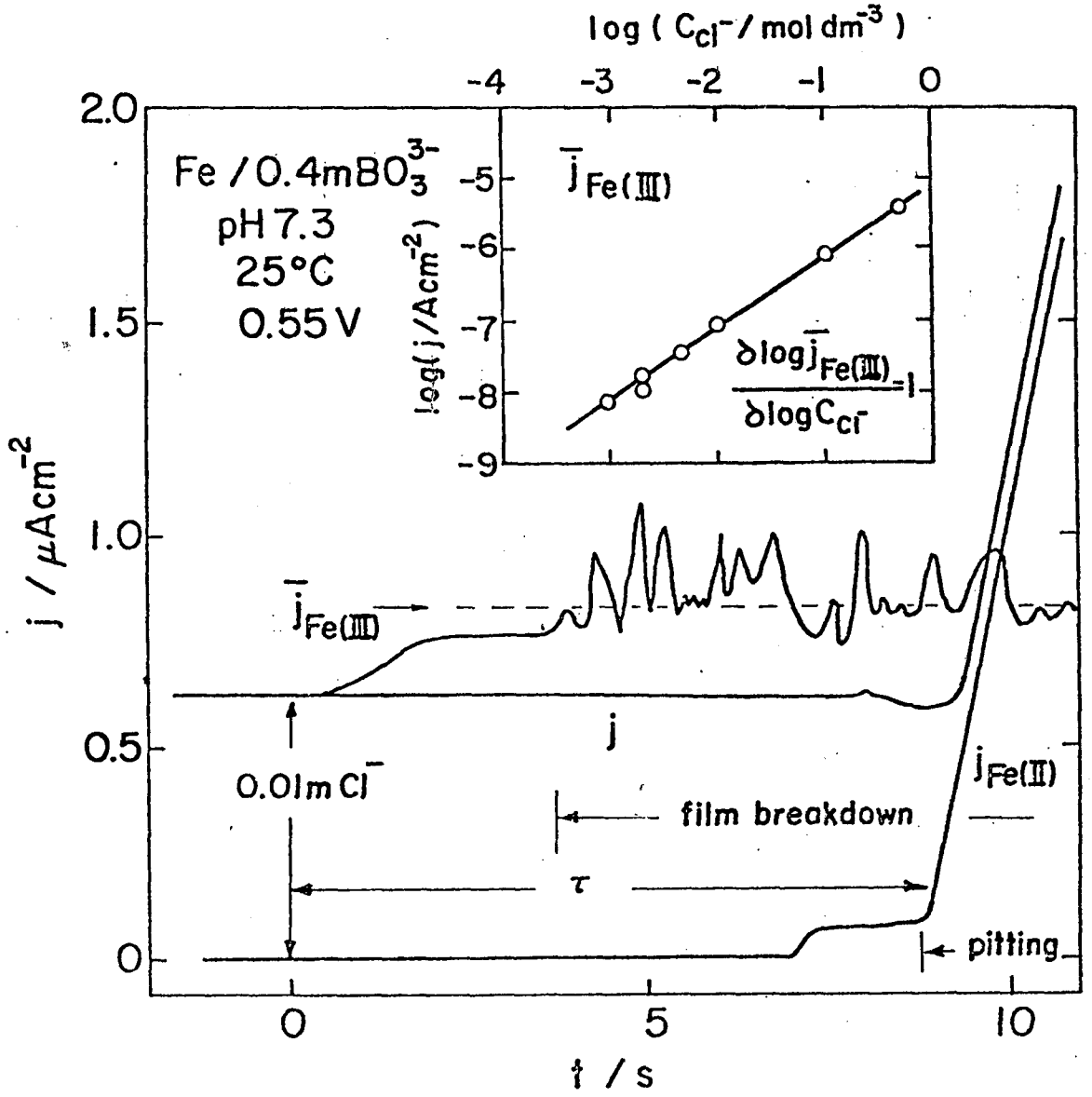

Fig. 8-4. Change in anodic current j, iron(III) ion dissolution current $j_{Fe(III)}$ (passive film dissolution current), and iron(II) ion dissolution current $j_{Fe(II)}$ (pitting dissolution current) of a passive iron in borate solution as a function of time after introduction of chloride ions (Heusler et al., 1976).

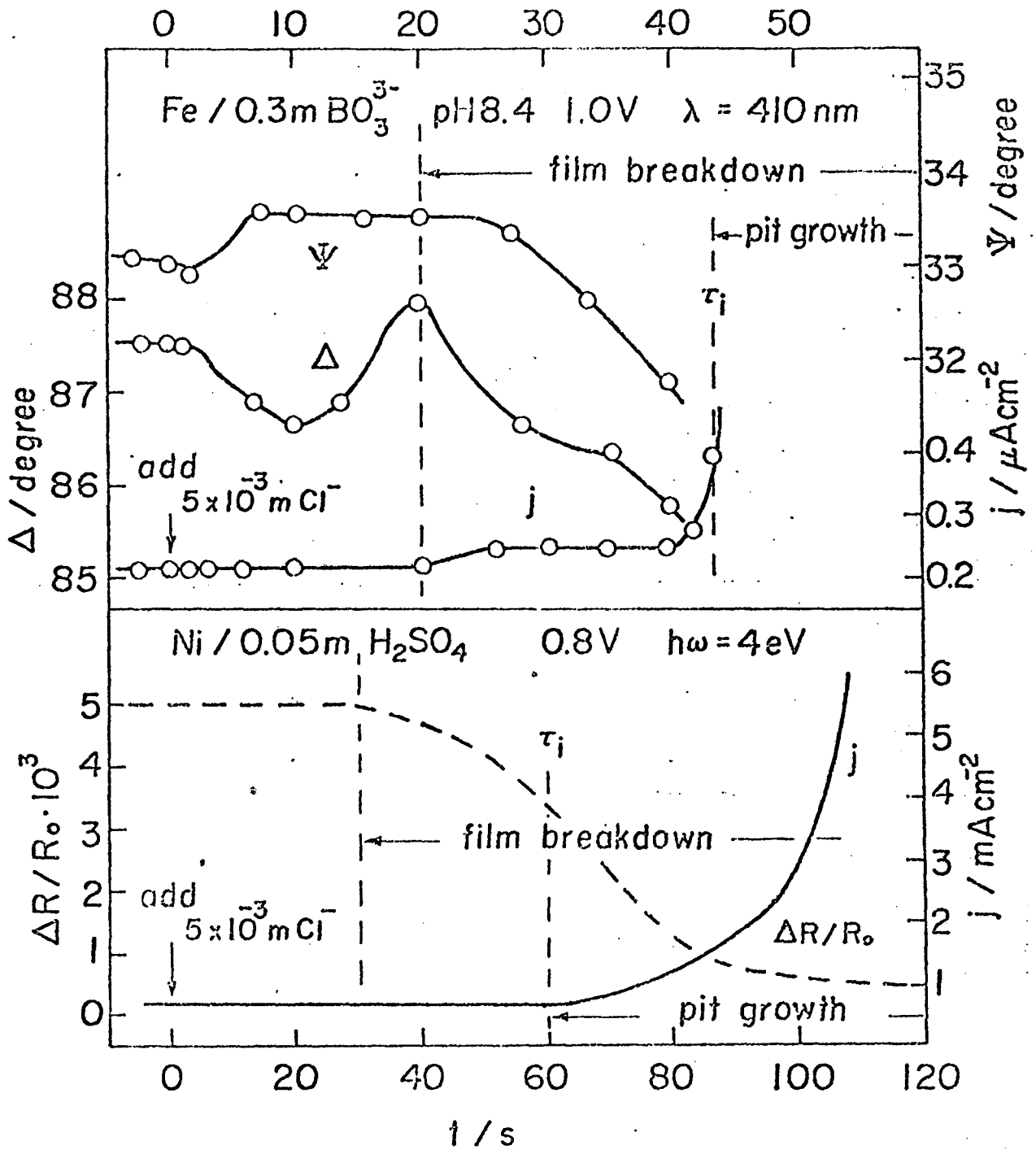

Fig. 8-5. Ellipsometric parameters Δ and Ψ and anodic dissolution current of a passive iron electrode at constant potential in borate solution (Kruger et al., 1971), and modulated electroreflectance and anodic dissolution current of a passive nickel at constant potential in H_2SO_4 solution (Paatsch, 1973) after introduction of chloride ions.

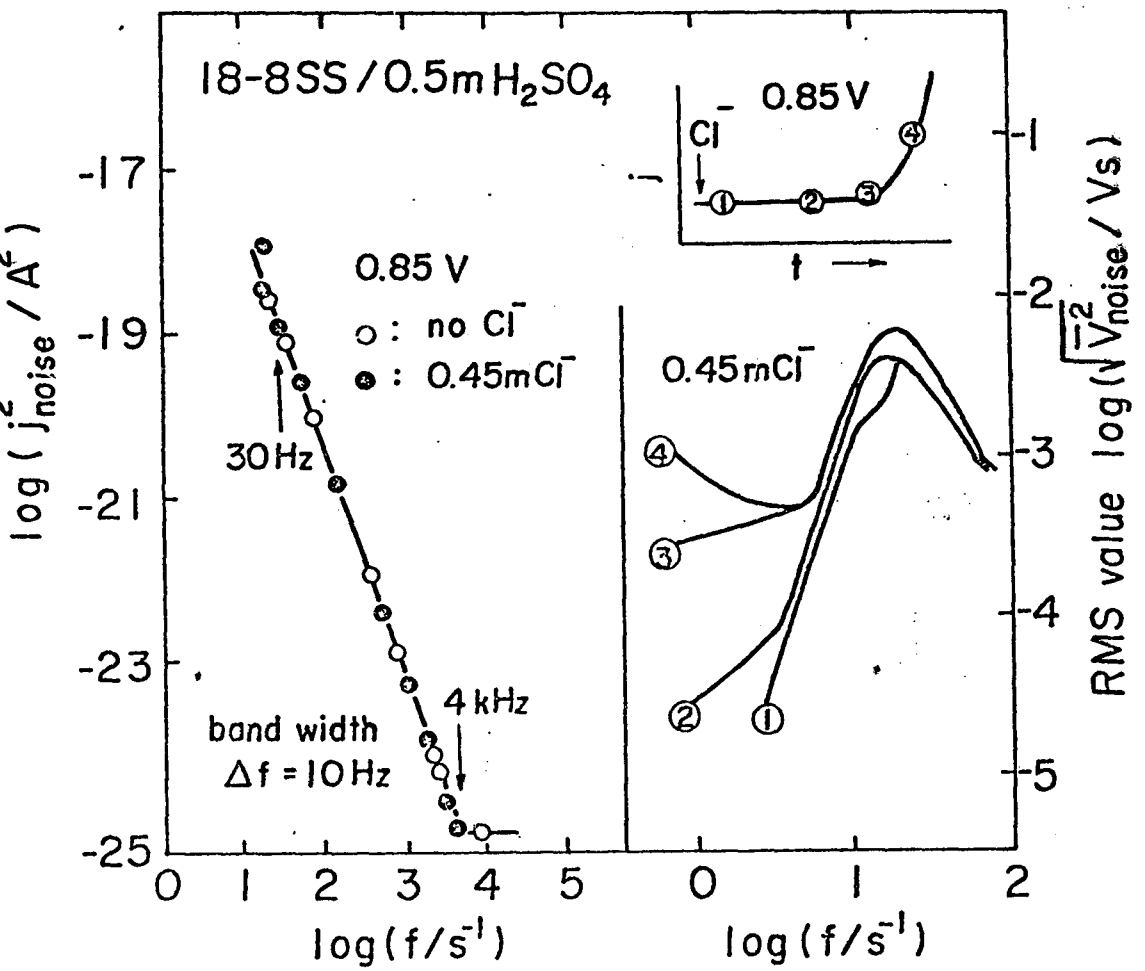

Fig. 8-6. Noise spectra of passive current of stainless steel in 0.5 M H_2SO_4 with and without chloride. The left shows the mean square of noise current versus noise frequency and the right is the root mean square of noise voltage versus noise frequency at different stages of film breakdown during induction for pitting (Okamoto, 1975).

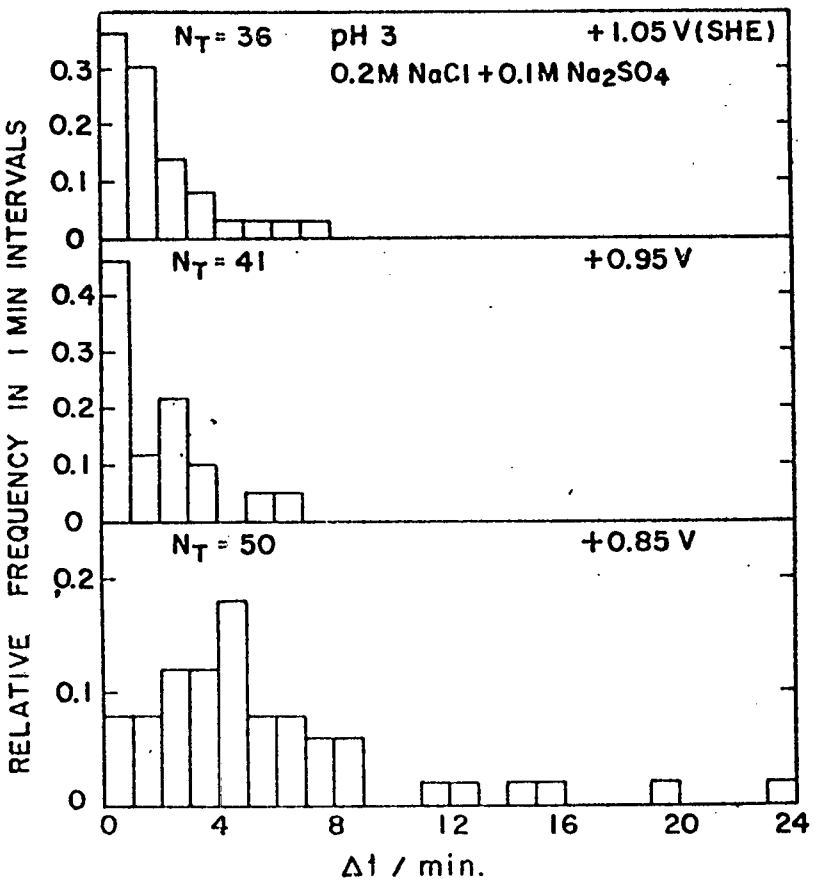

Fig. 8-7. Frequency histogram of potentiostatic pit generation on a rotating 18 Cr - 8 Ni stainless steel electrode in a NaCl + $NaSO_4$ solution (Sato, 1976).

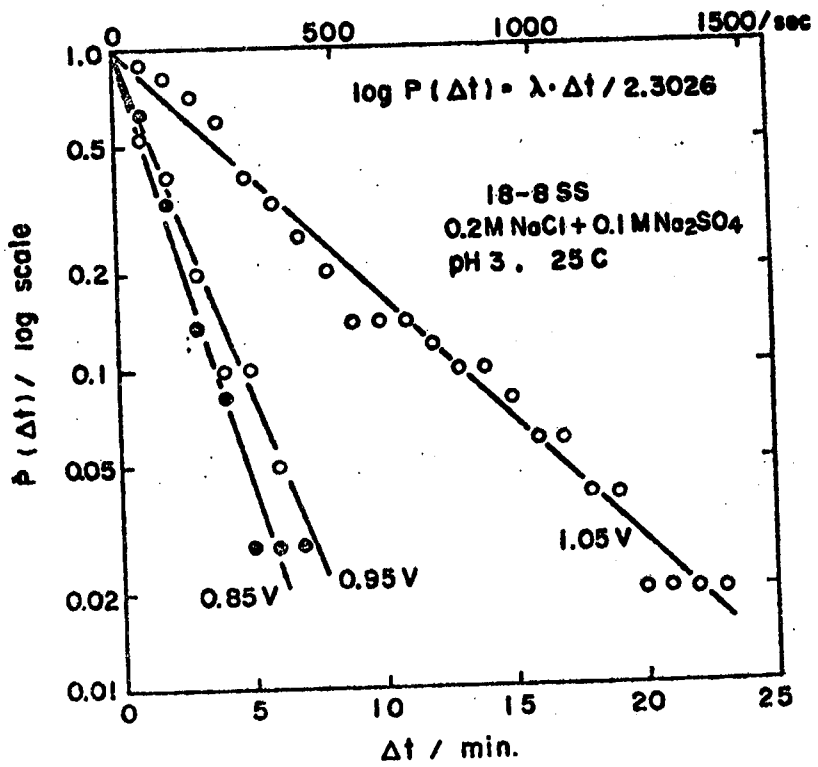

Fig. 8-8. Cumulative relative frequency curves for pit generation time interval at three different potentials of a rotating 18 Cr - 8 Ni stainless steel in a NaCl + $NaSO_4$ solution (Sato, 1976).

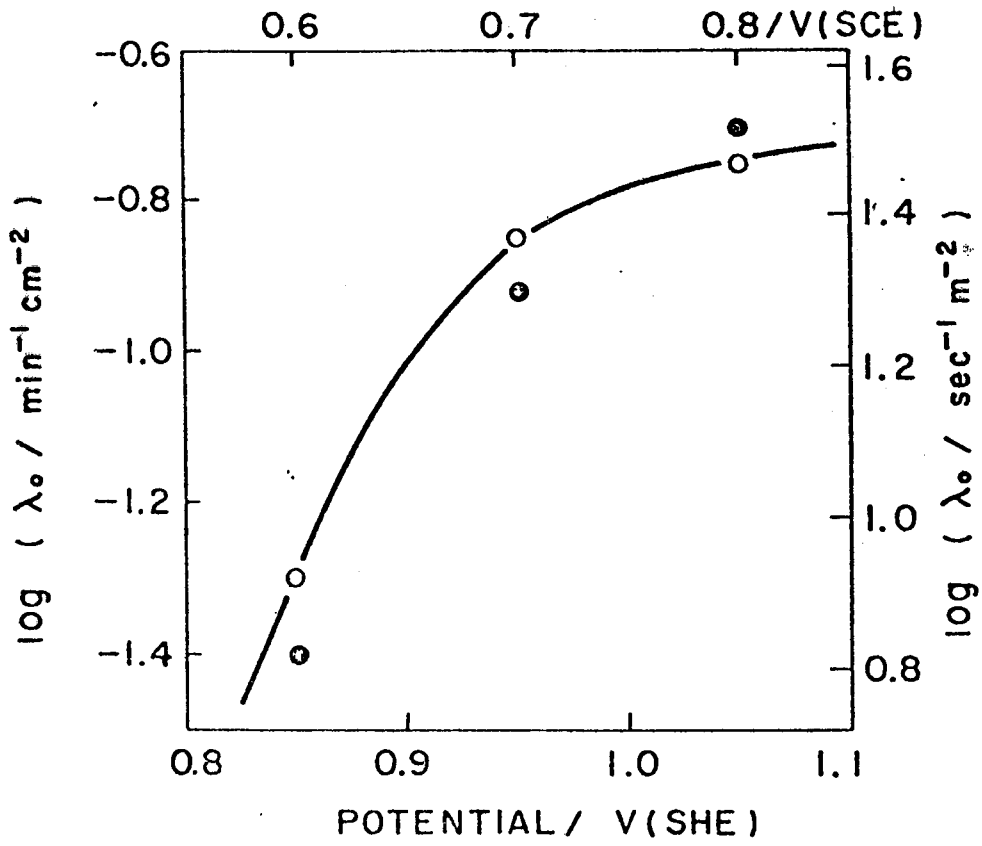

Fig. 8-9. Pit generation intensity for unit surface area of a rotating stainless steel in a NaCl + Na_2SO_4 solution as a function of potential (Sato, 1976). Data are based on the result in Fig. 8 - 8 .

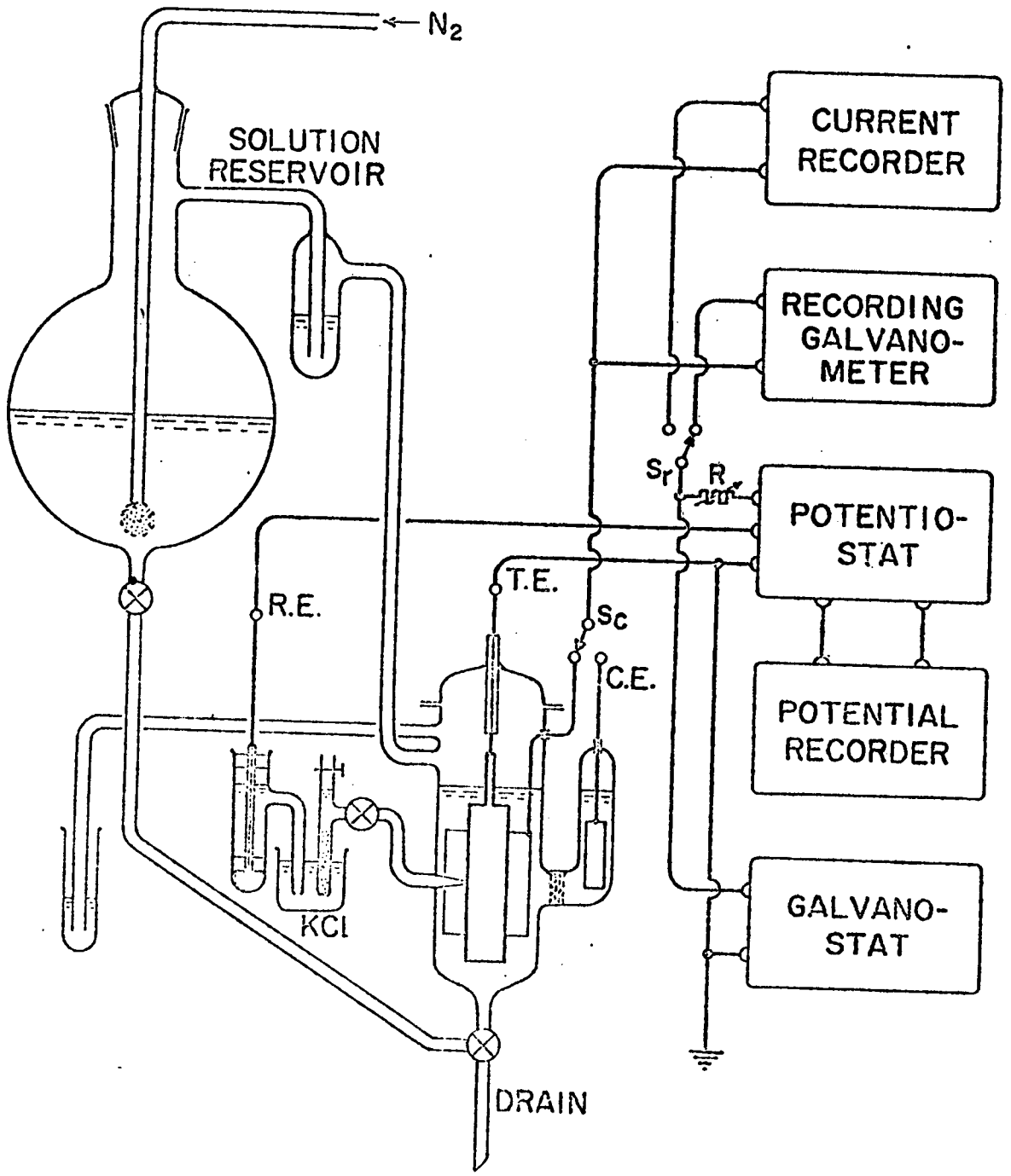

Fig. 9-1. Electrolytic cell and electric wiring diagram for electrochemical measurements.

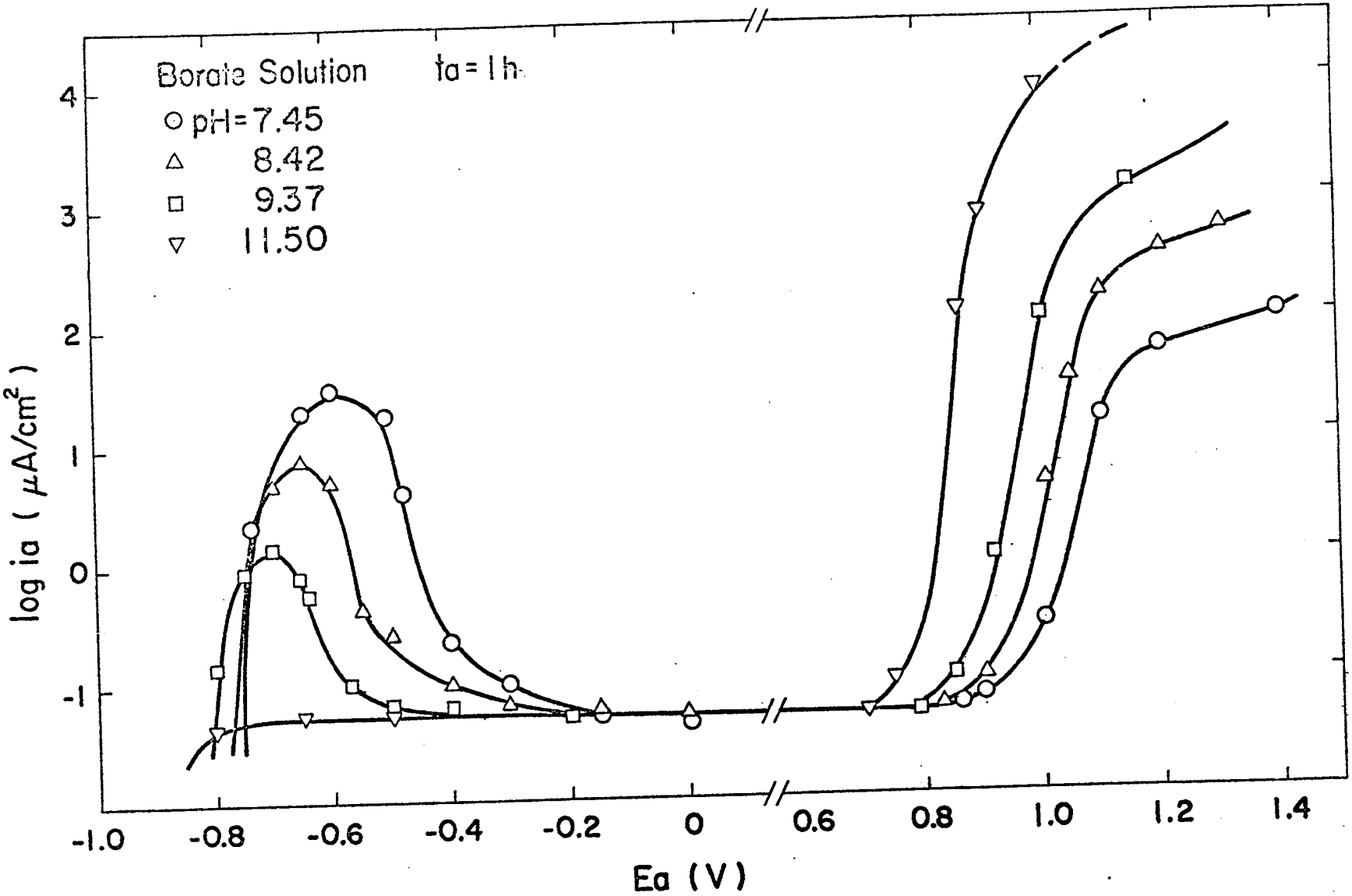

Figure 9 - 2. Anodic polarization curve of iron in sodium borate-buffer solutions at pH from 7.45 to 11.5.

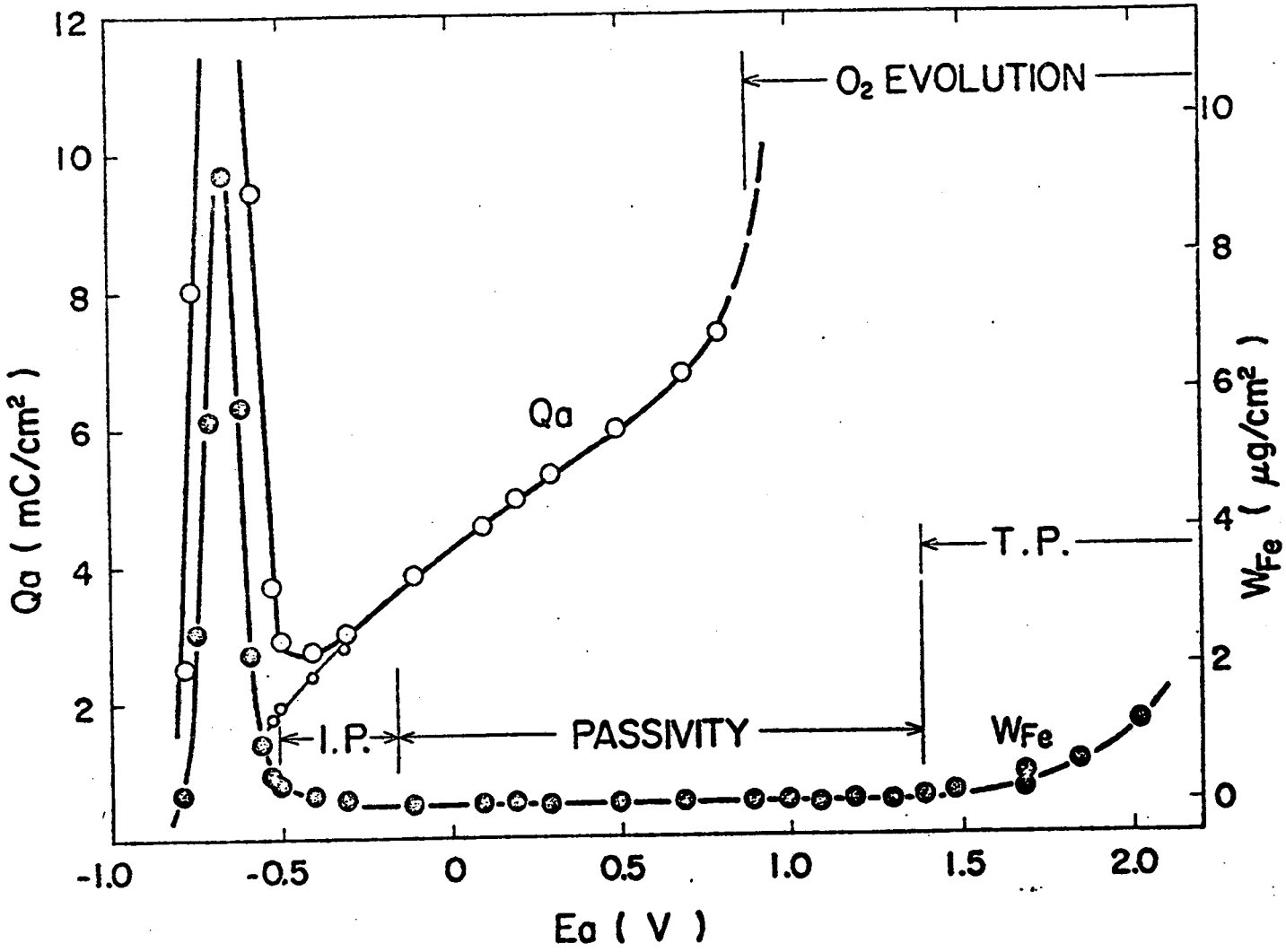

Figure 9-3. Amount of charge passed and iron dissolved during potentiostatic anodic one-hour oxidation as functions of potential in borate-buffer solution at pH 8.42 at 25°C. IP = incomplete passivity, TP = transpassivity.

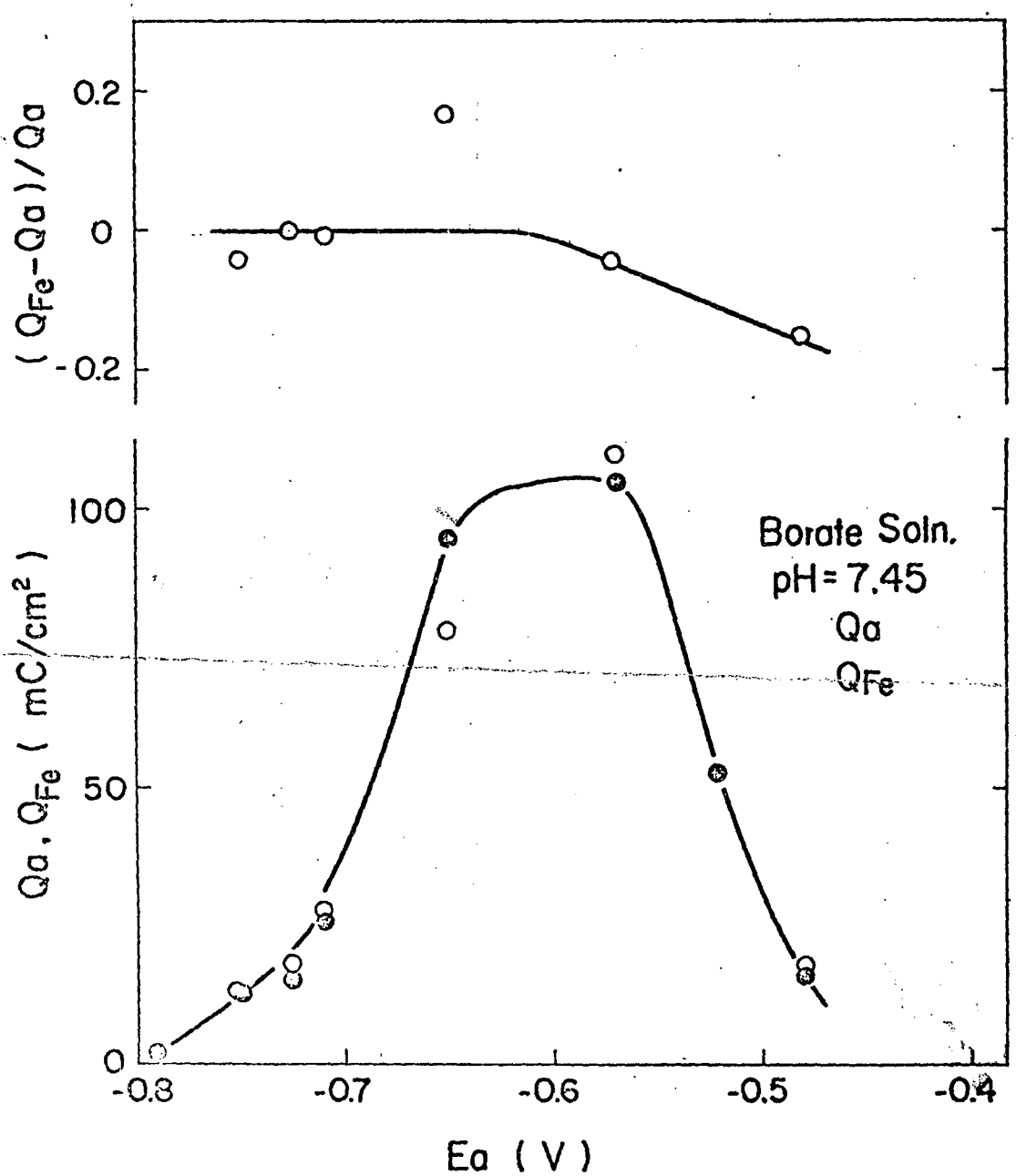

Figure 9-4. Amount of charge passed, Q_a, and charge equivalent to Fe^{2+} dissolution, Q_{Fe}, during anodic one-hour oxidation at constant potential in the active region in deaerated 0.15N borate-buffer solution at pH 7.45 at 25°C.

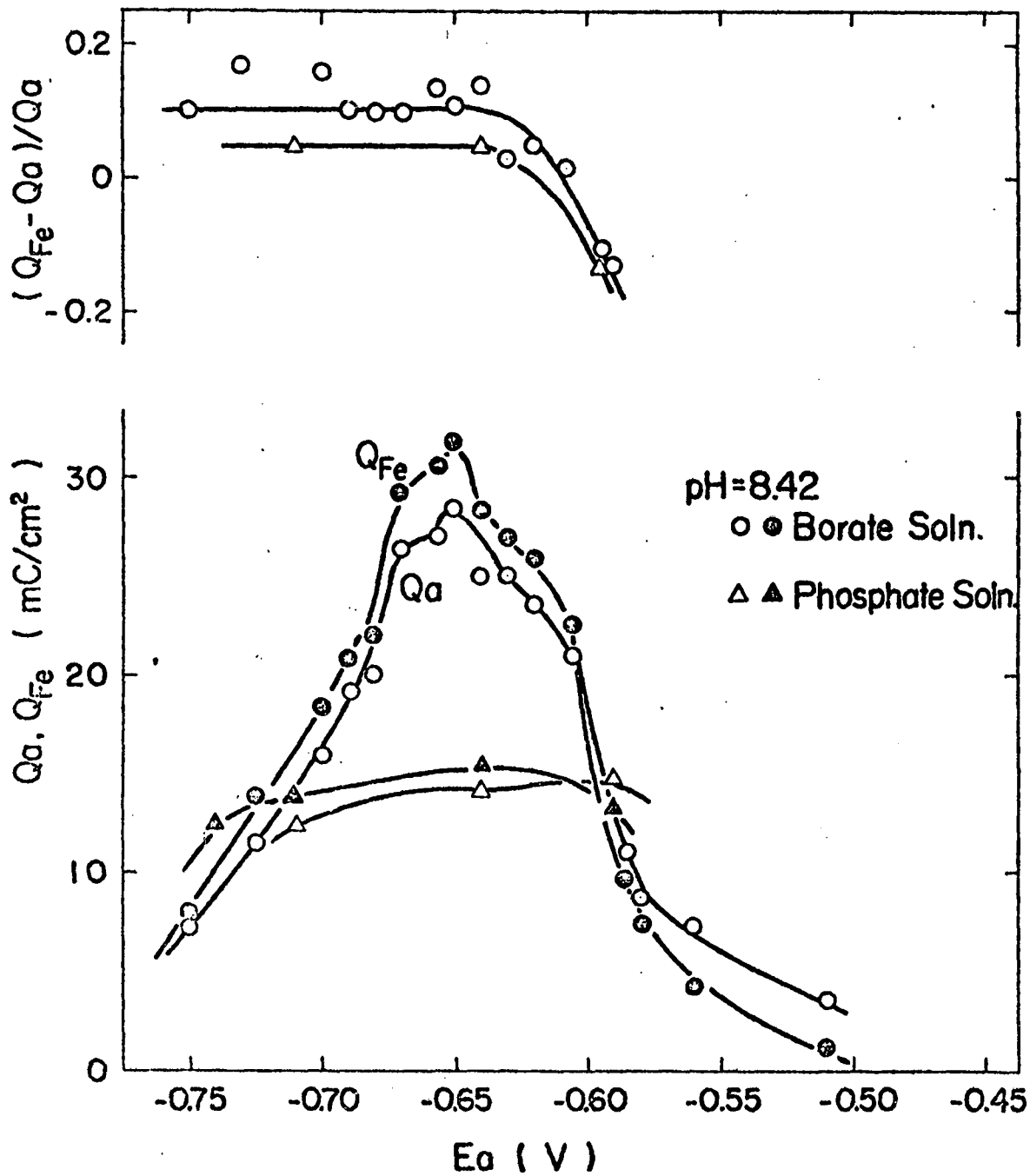

Figure 9-5. Amount of charge passed, Q_a, and charge equivalent to Fe^{2+} dissolution, Q_{Fe}, during anodic one-hour oxidation at constant potential in the active region in deaerated 0.15N borate-buffer solution and 0.15M phosphate buffer solution at pH 8.42 at 25°C.

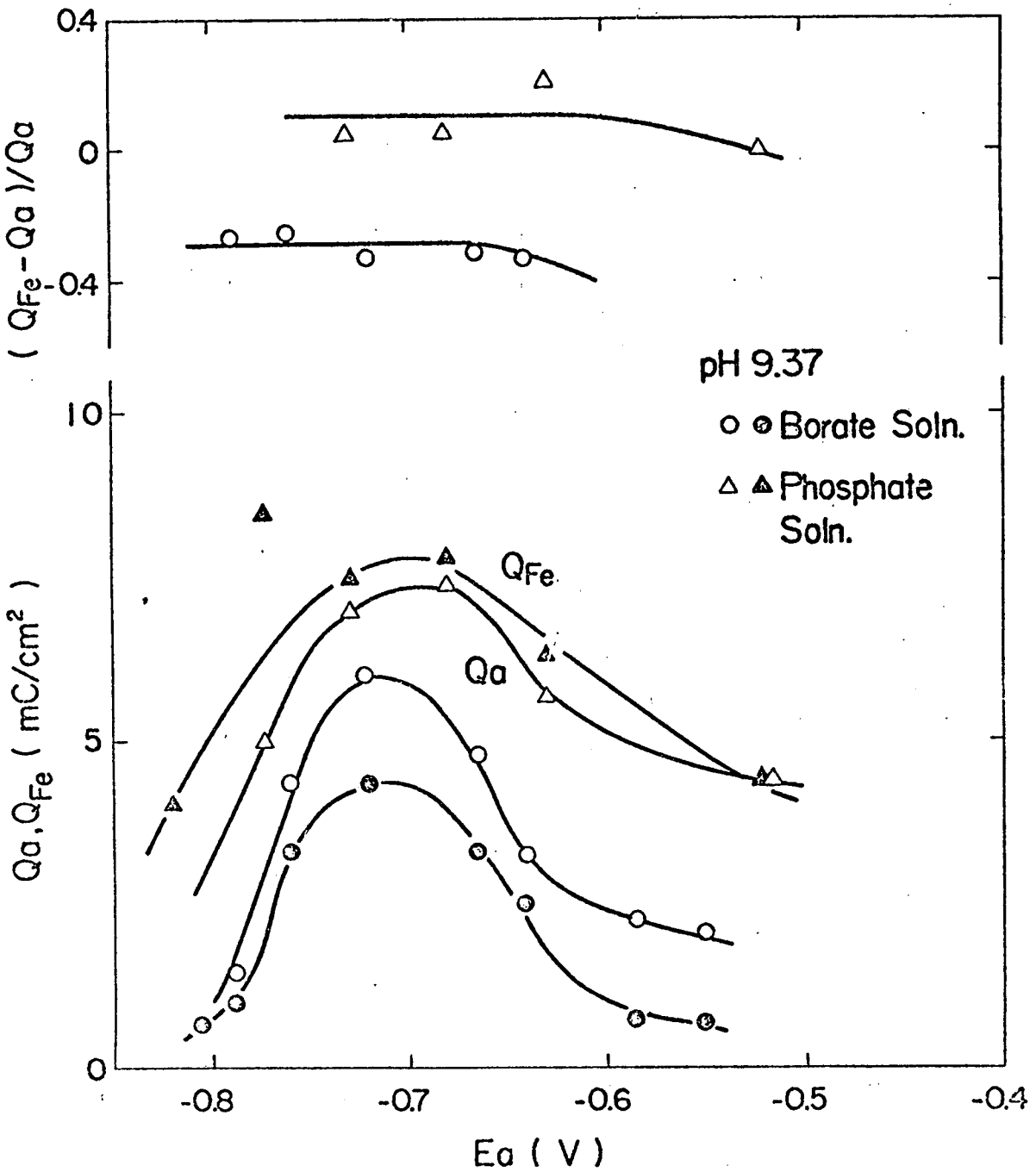

Figure 9-6. Amount of charge passed, Q_a, and charge equivalent to Fe^{2+} dissolution, Q_{Fe}, during anodic one-hour oxidation at constant potential in the active region in deaerated 0.15N borate-buffer solution and 0.15M phosphate buffer solution at pH 9,37 at 25°C.

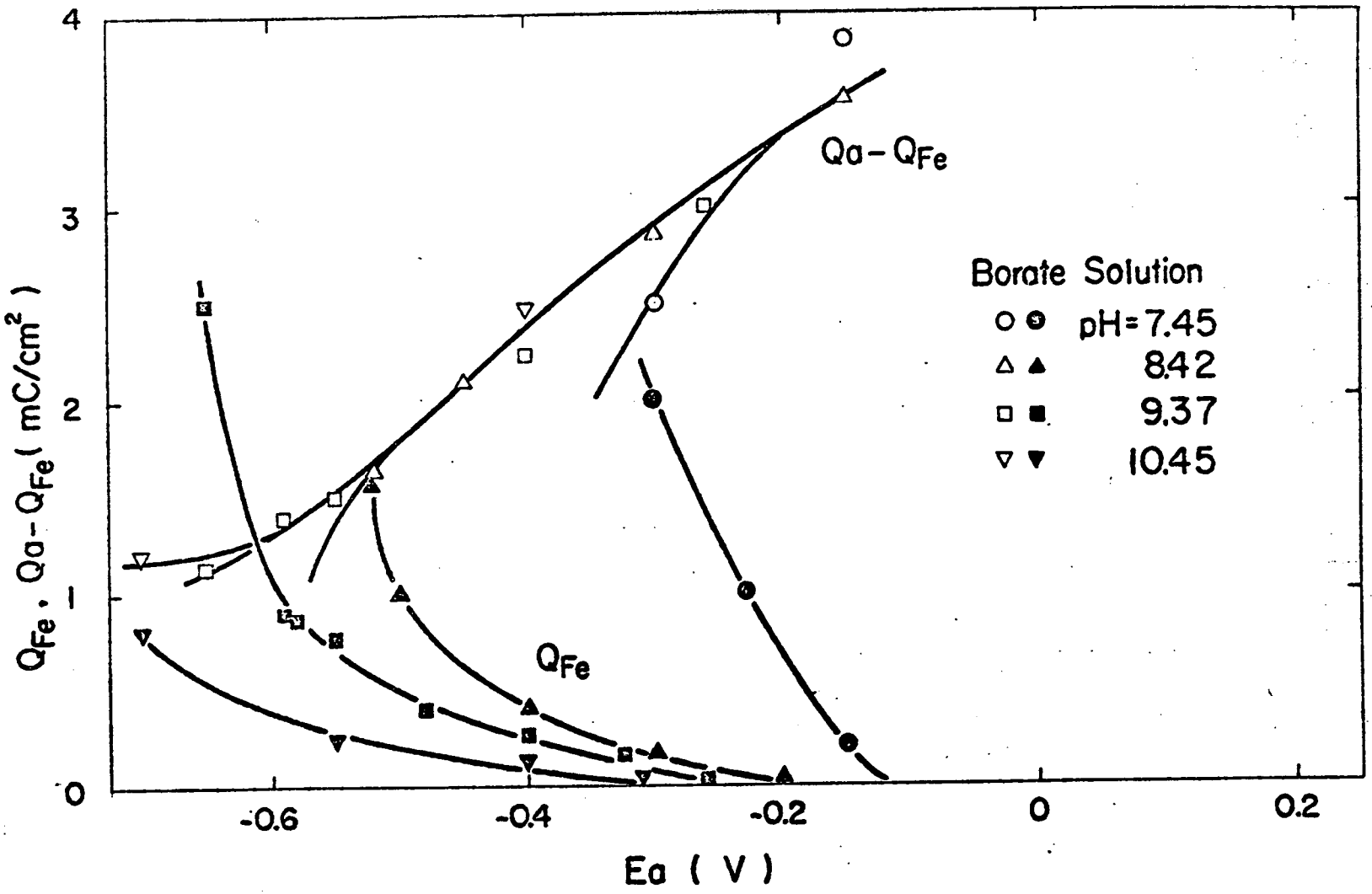

Figure 9-7. Amount of charge equivalent to Fe^{2+} dissolution, Q_{Fe}, and of charge for anodic oxide film, Q_a-Q_{Fe}, in the incomplete passivity region during potentiostatio one-hour oxidation of iron in deaerated 0.15N borate-buffer solution at pH from 7.45 to 10.45 at 25°C.

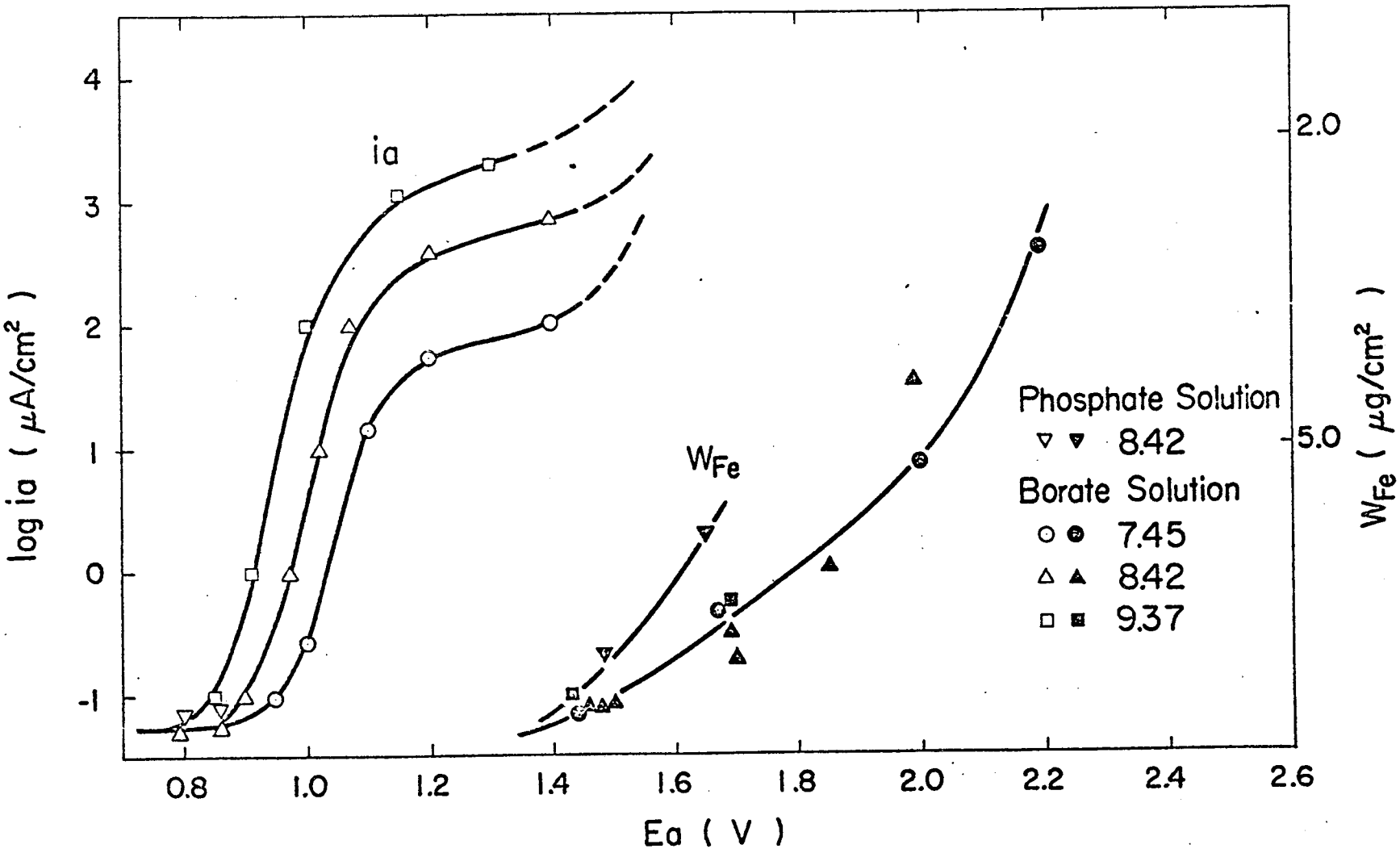

Figure 9-8. Amount of iron dissolution W_{Fe} during potentiostatic one-hour oxidation of iron in deaerated 0.15N borate-buffer solution at different pH values at 25°C.

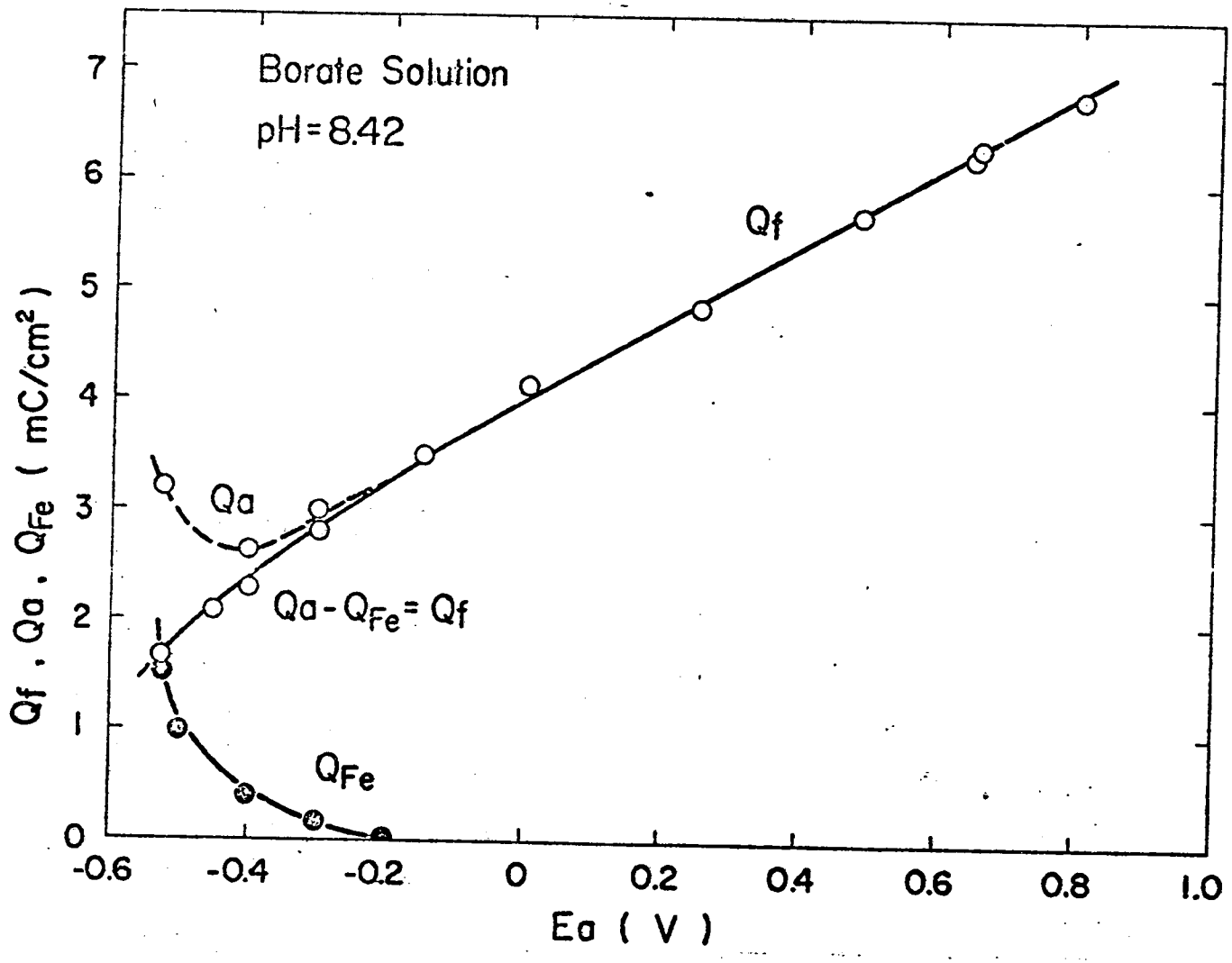

Figure 9-9. Amount of anodic charge Q_a and charge Q_{Fe} equivalent to Fe^{2+} dissolution in the potential regions of incomplete and complete passivity in deaerated 0.15N borate-buffer solution at pH 8.42 at 25°C; $Q_a - Q_{Fe} = Q_f$, which is the charge consumed for formation of the anodic oxide film.

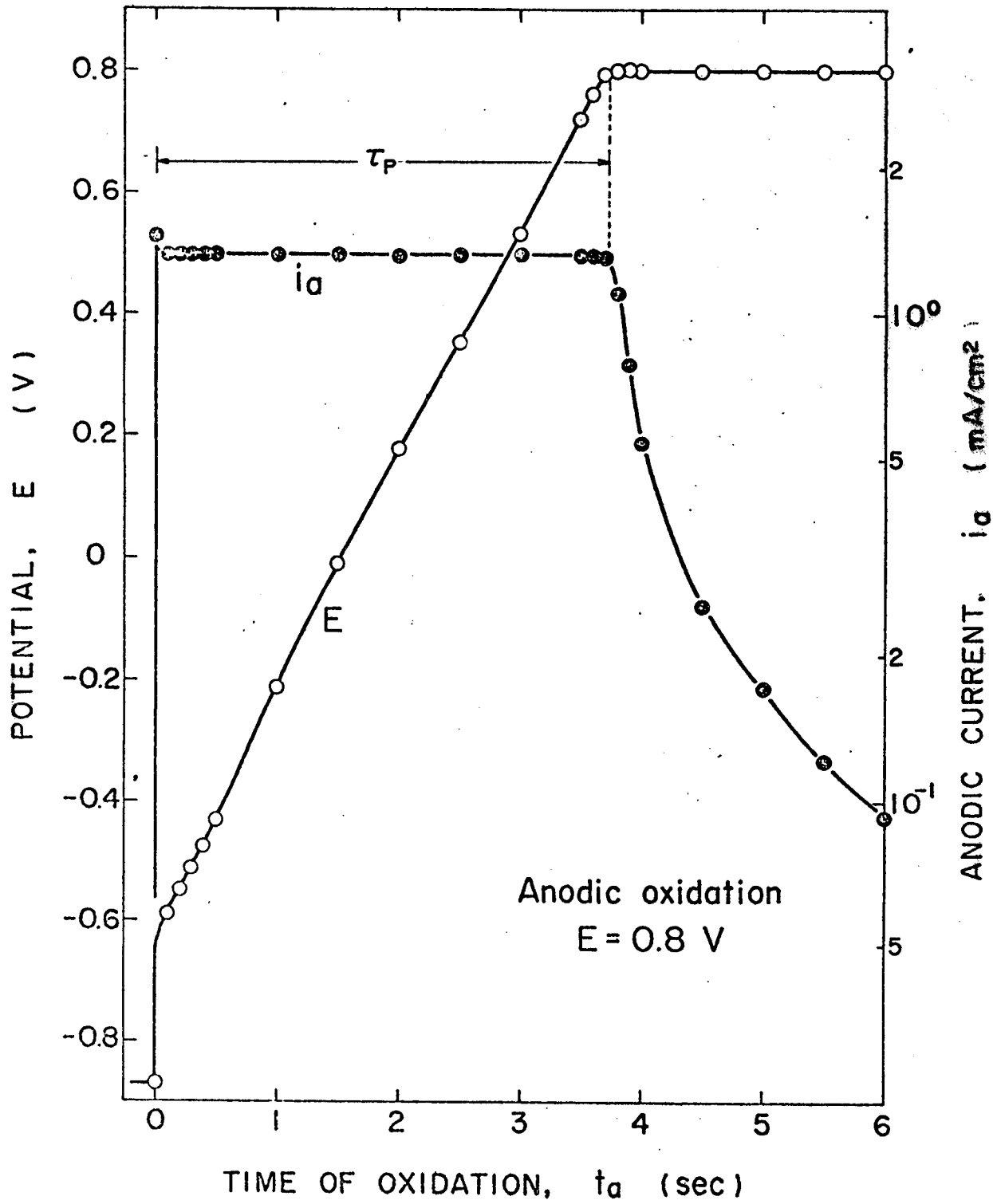

Figure 9-10. Potential and current transients of iron from galvanostatic-cathodic reduction at $i = 5\mu A/cm^2$ to potentiostatic-anodic oxidation at E = 0.8V.

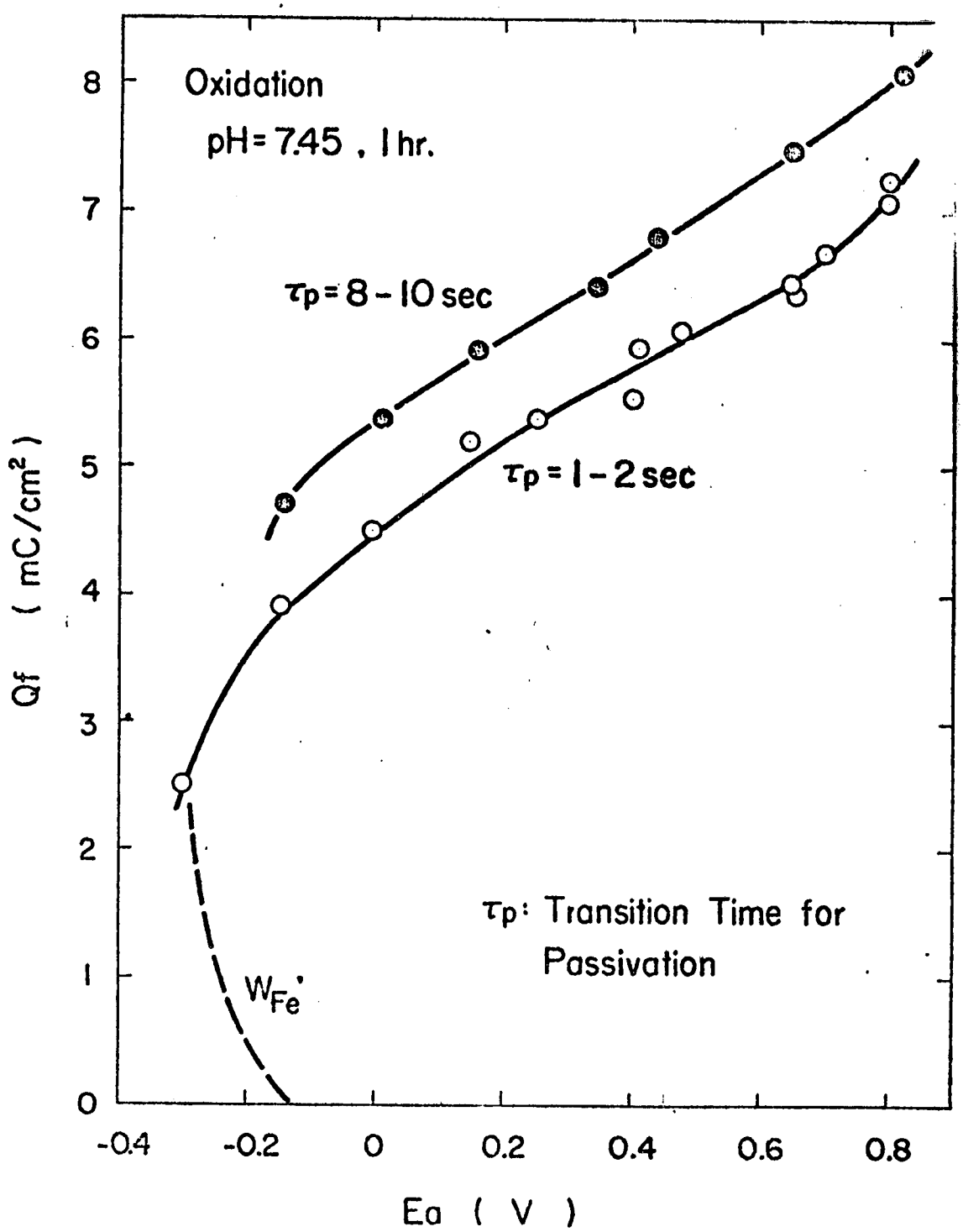

Figure 9-11. Effect of the speed of passivation on the amount of charge Q_f consumed for formation of the anodic oxide film. W_{Fe}' is amount of iron dissolved during anodic one-hour oxidation.

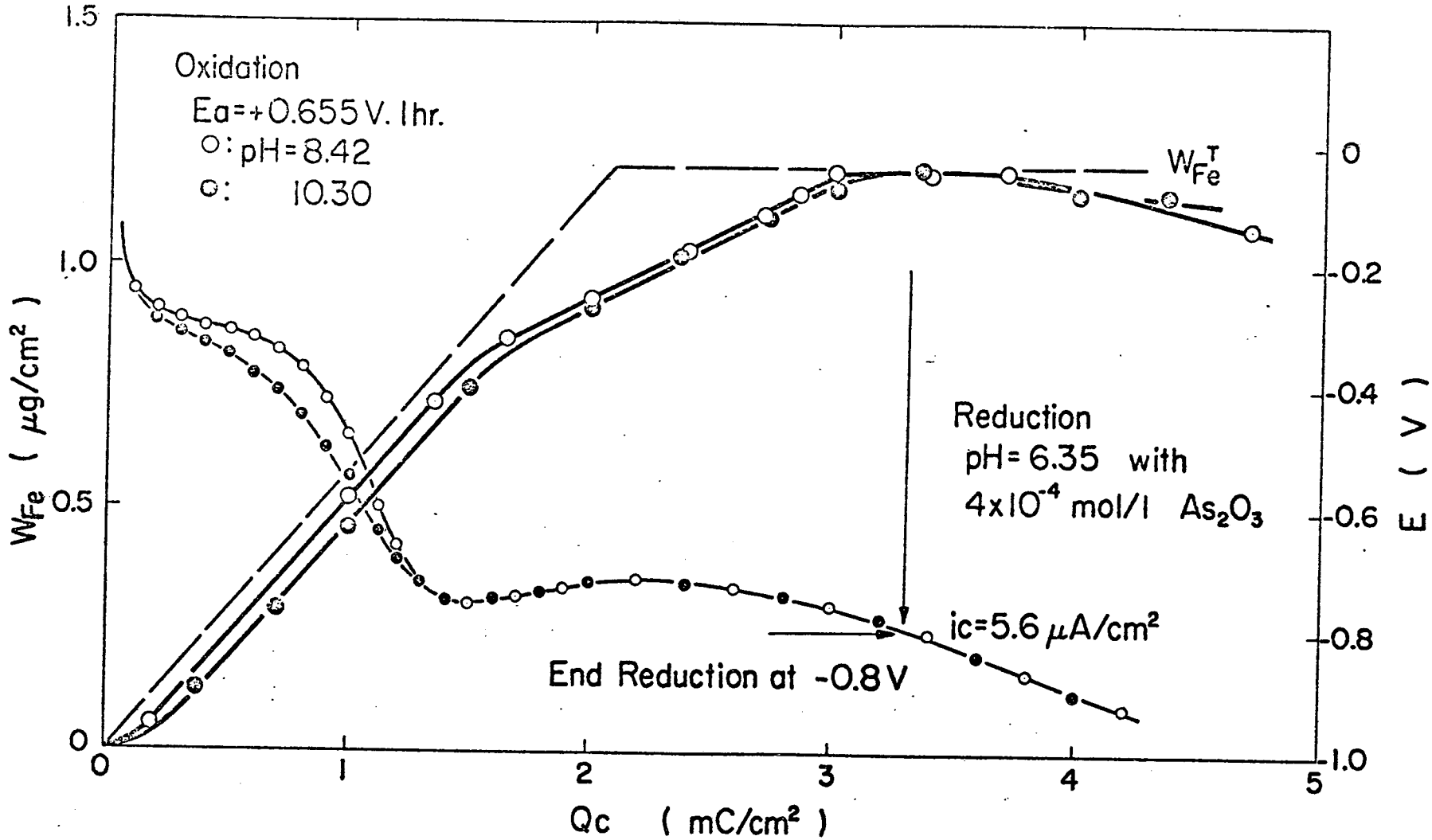

Figure 9-12. Cathodic reduction of anodic oxide film in 0.15N borate-buffer solution of pH 6.35 containing 4×10^{-4} mol/l As_2O_3 as inhibitor, showing establishment of $W_{Fe(max)} = W_{Fe}^T$.

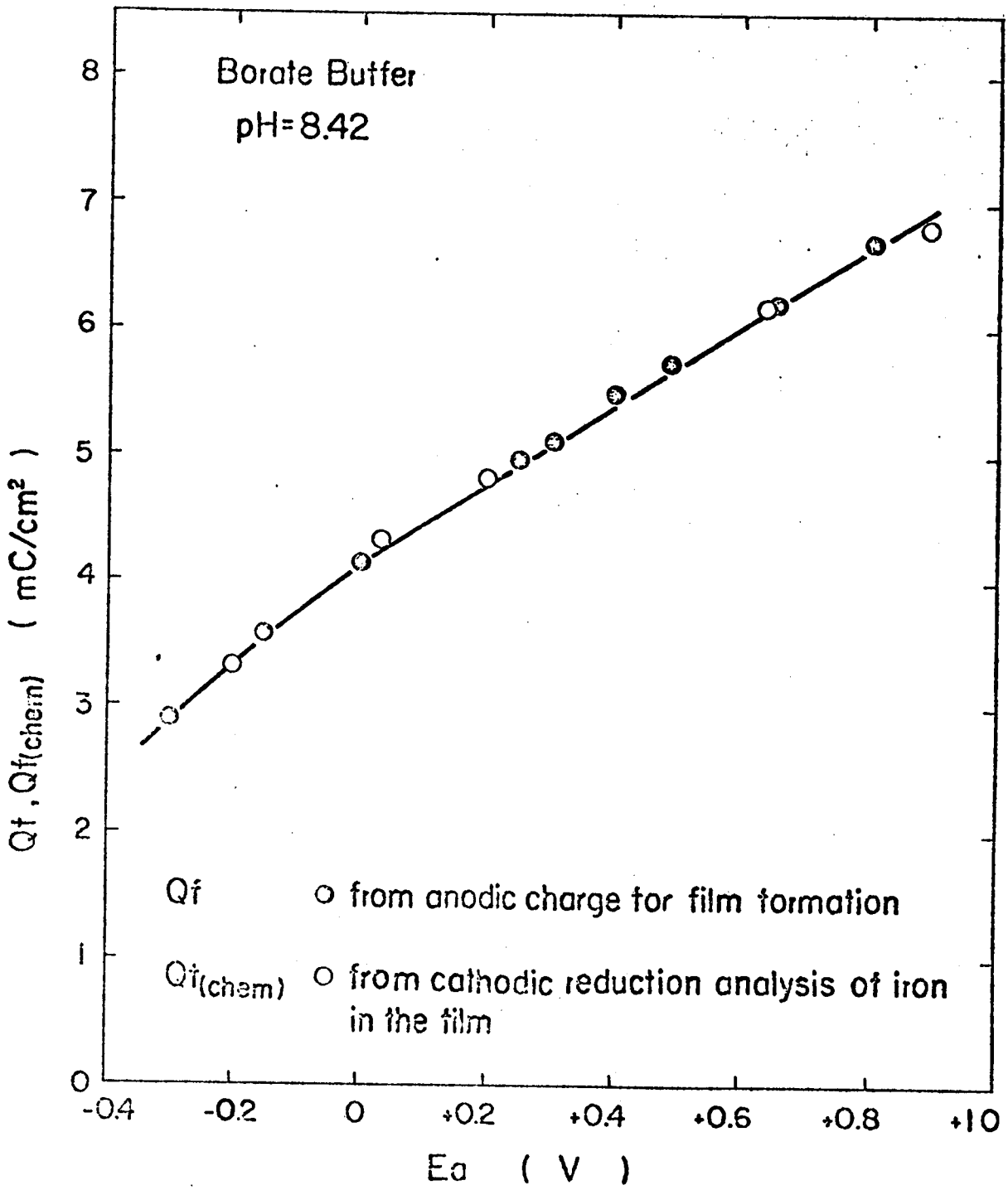

Figure 9-13. Comparison of the film charge Q_f coulometrically estimated by anodic oxidation, with the film charge $Q_{f(chem)}$ calculated from $W_{Fe(max)}$ in the film, assuming Fe(III) oxide. $W_{Fe(max)}$ was estimated by the cathodic reduction at 5.6 μ A/cm^2 in borate-buffer solution of pH 6.35 containing 4 x 10^{-4} mol/l As_2O_3 as inhibitor.

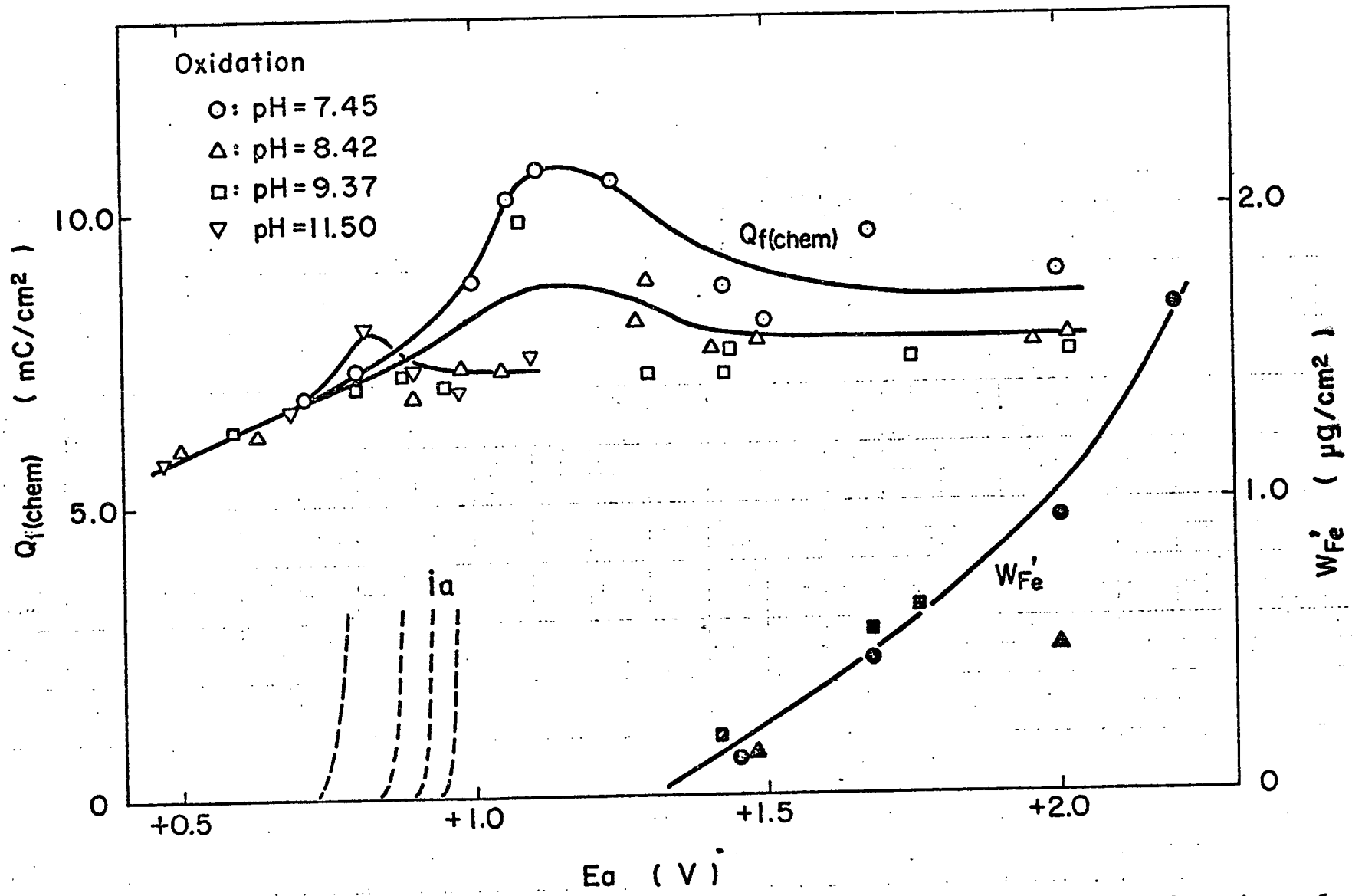

Figure 9-14. Anodic oxide film and transpassive dissolution of iron as a function of potential in the oxygen – evolution region, $Q_{f(chem)}$ being the anodic charge equivalent to iron in the film estimated by cathodic reduction and W_{Fe}' the amount of iron dissolved during potentiostatic-anodic one-hour oxidation.

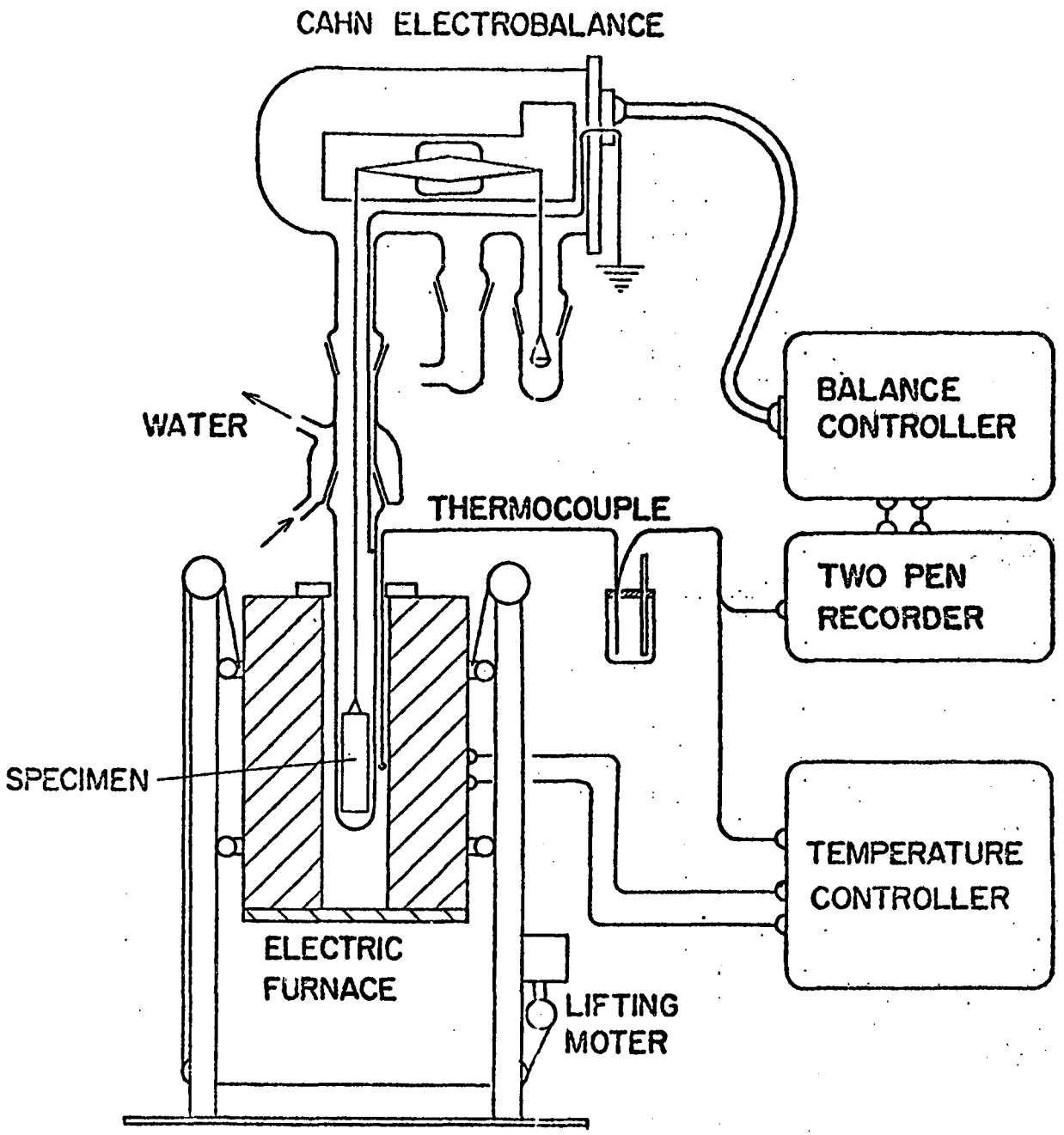

Figure 9-15. Vacuum microbalance.

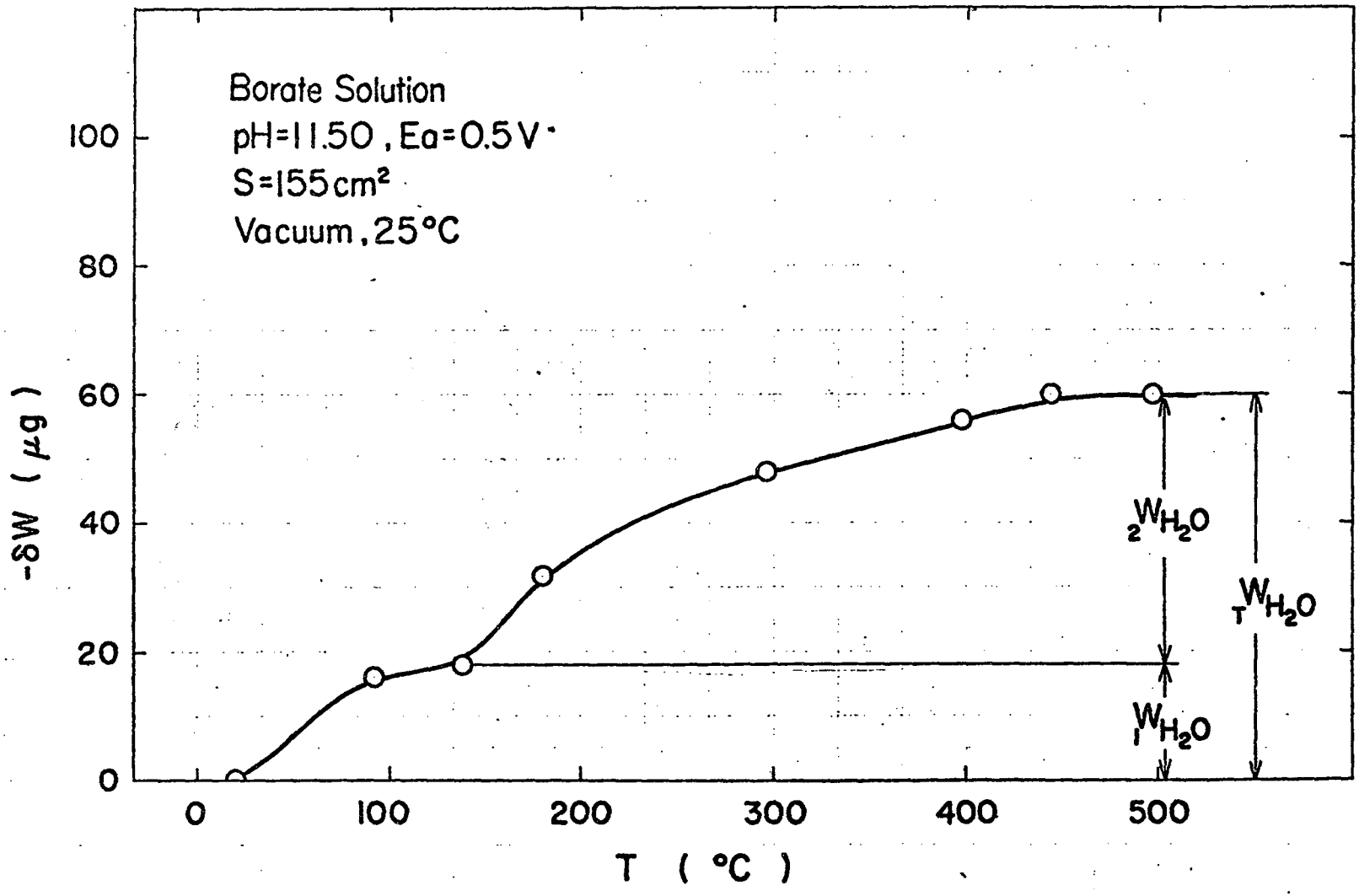

Figure 9-16. Weight decrease during heating in vacuum of an anodically passivated iron specimen.

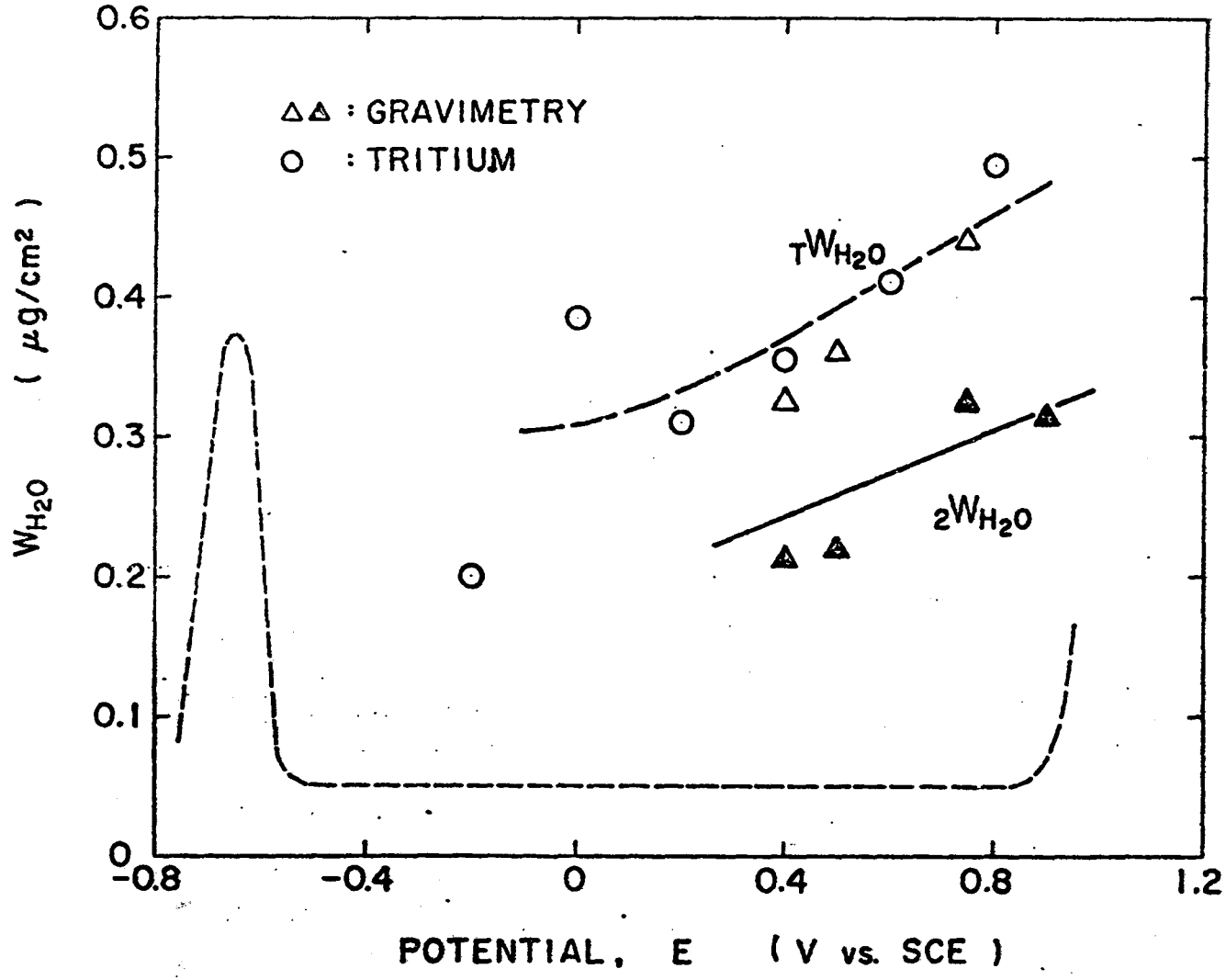

Fig. 9-17. Amount of water in the passive film versus potential of iron in borate solution at pH 8.42.
$_2W_{H_2O}$ = water desorbed above 150°C.

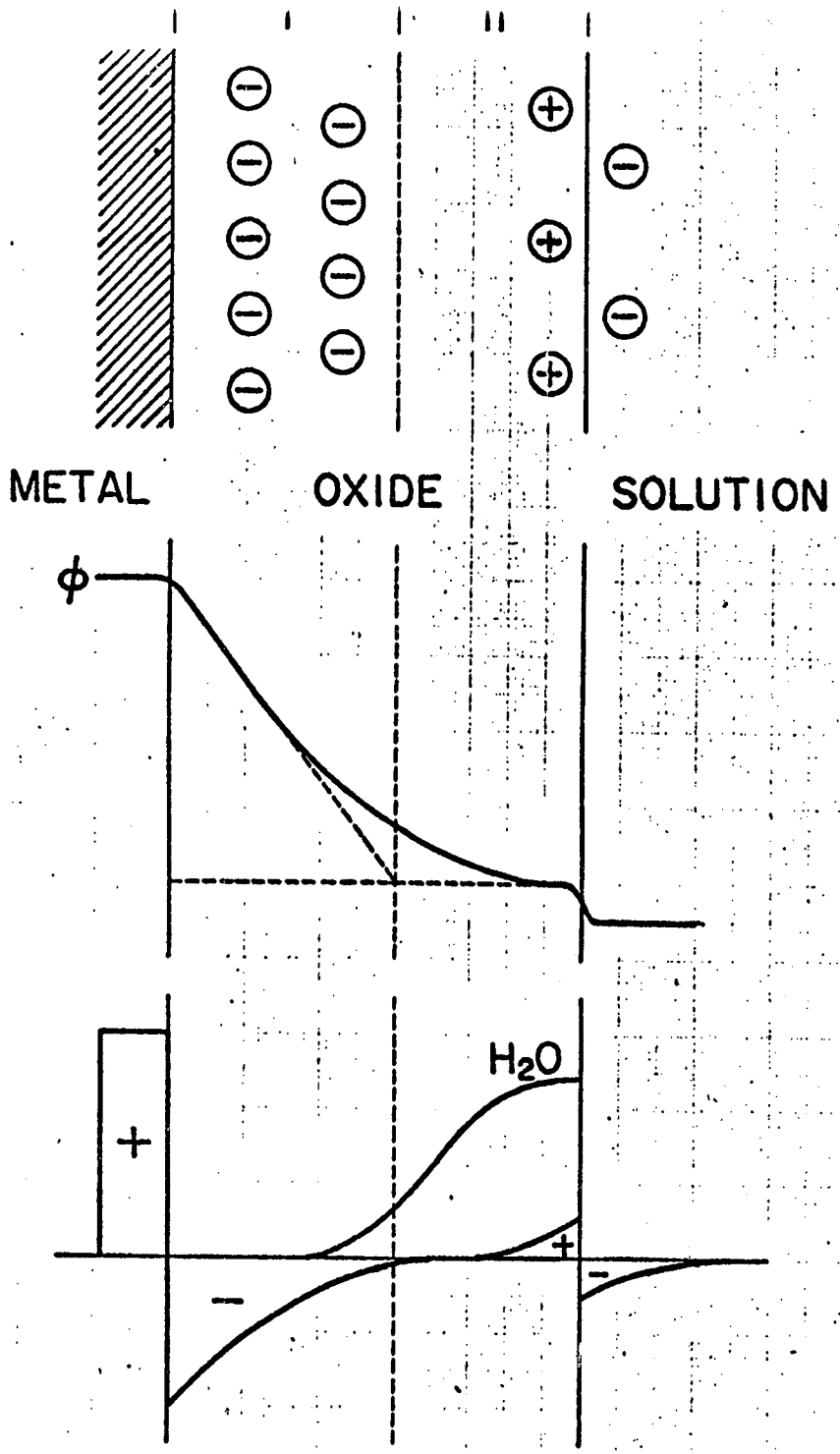

Figure 9-18. Model of the anodic oxide film on iron and the distribution of space charge, potential and bound water.

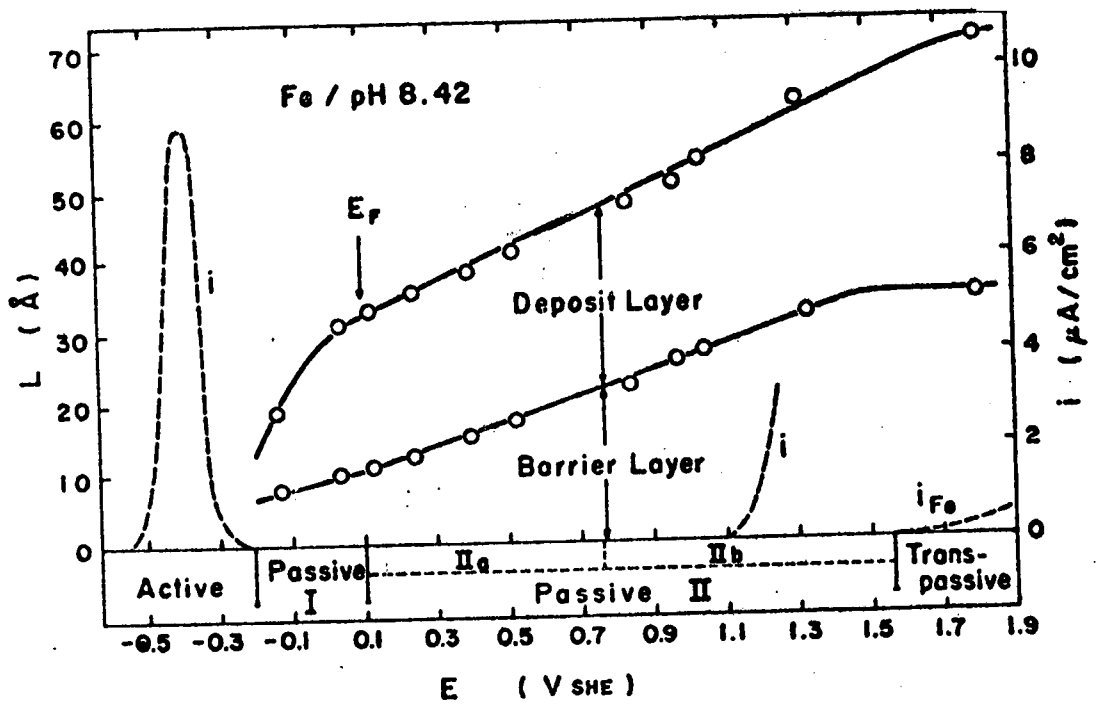

Fig. 9-19. Anodic current-potential curve of iron and thickness-potential curve for the passive film on iron anode in borate solution of pH 8.42. i_{Fe} = transpassive dissolution current, E_F = Flade potential.

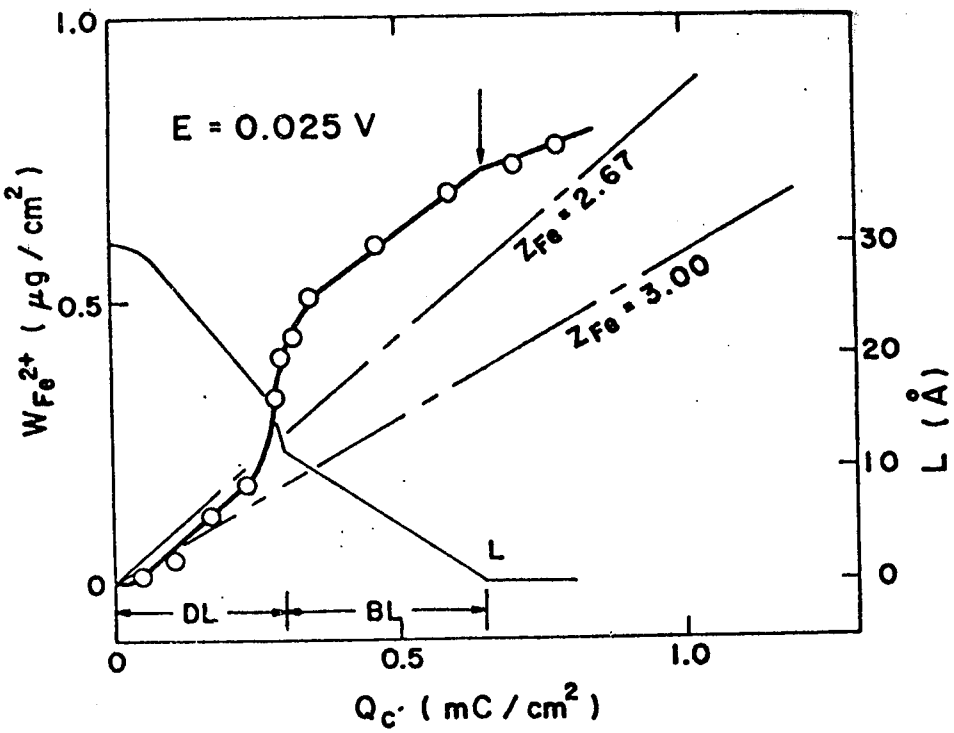

Fig. 9-20. Cathodic dissolution and thickness reduction curves of the passive film formed on iron at +0.025 V in potential region I in borate solution of pH 8.42. Q_c = cathodic charge passed during galvanostatic film reduction at pH 6.35.

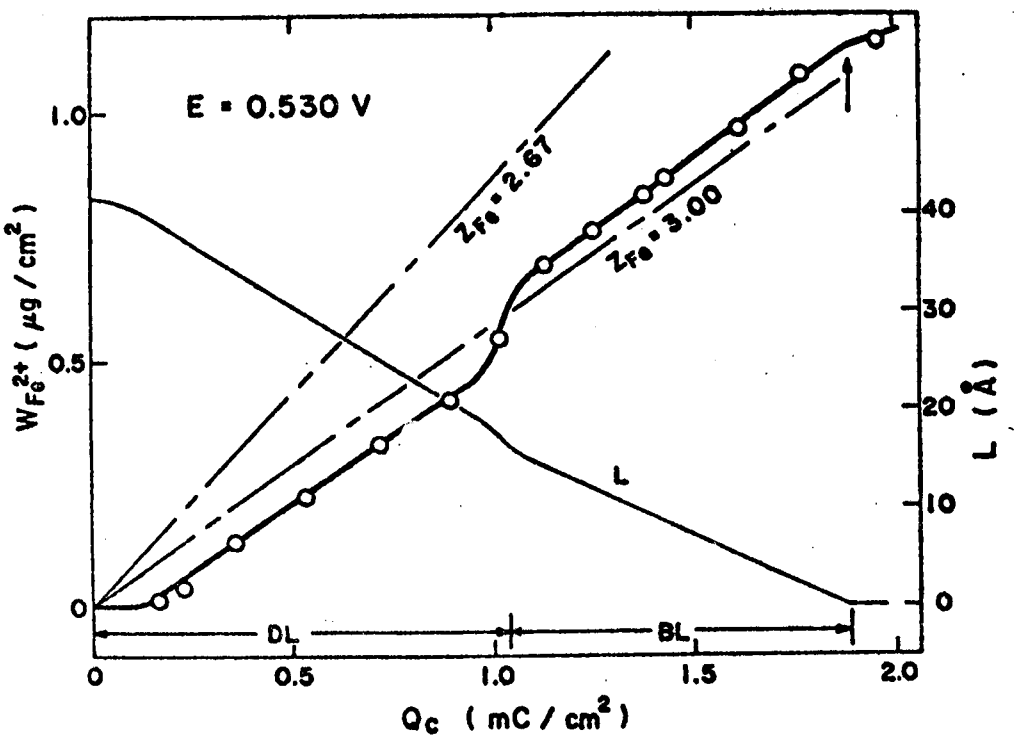

Fig. 9-21. Cathodic dissolution and thickness reduction curves of the passive film formed on iron at +0.53 V in potential region IIa in borate solution of pH 8.42. Q_c = cathodic charge passed during galvanostatic film reduction at pH 6.35.

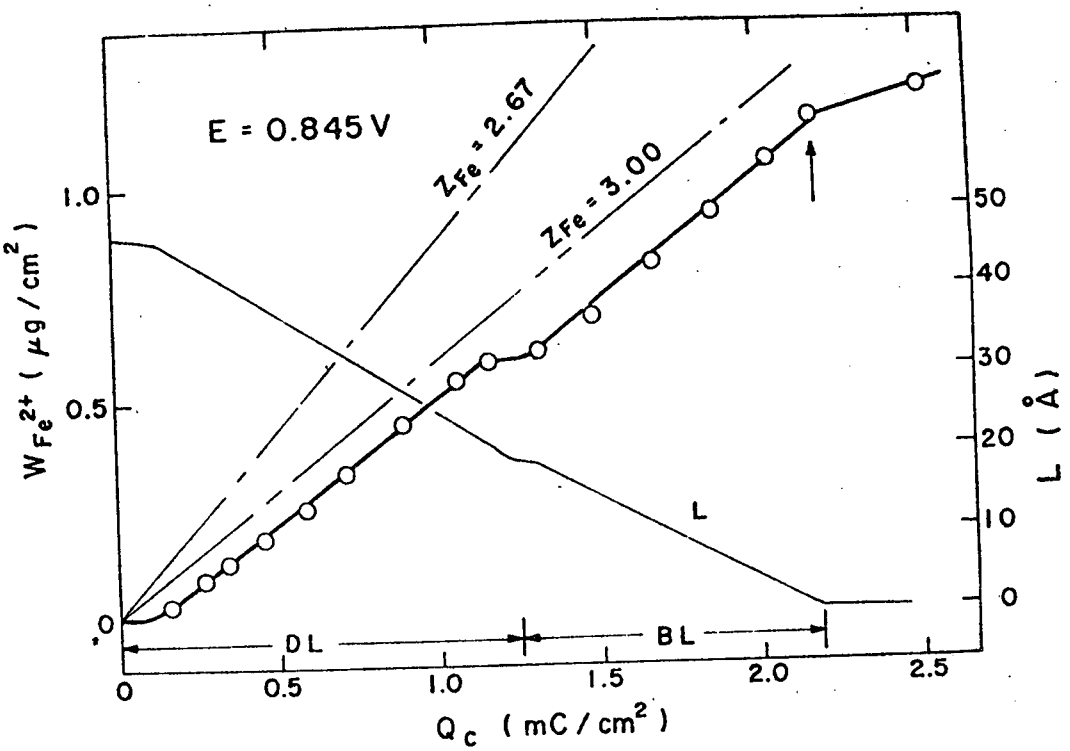

Fig. 9-22. Cathodic dissolution and thickness reduction curves of the passive film on iron at +0.845 V in potential region IIb in borate solution at pH 8.42. Q_c = cathodic charge passed during galvanostatic film reduction at pH 6.35.

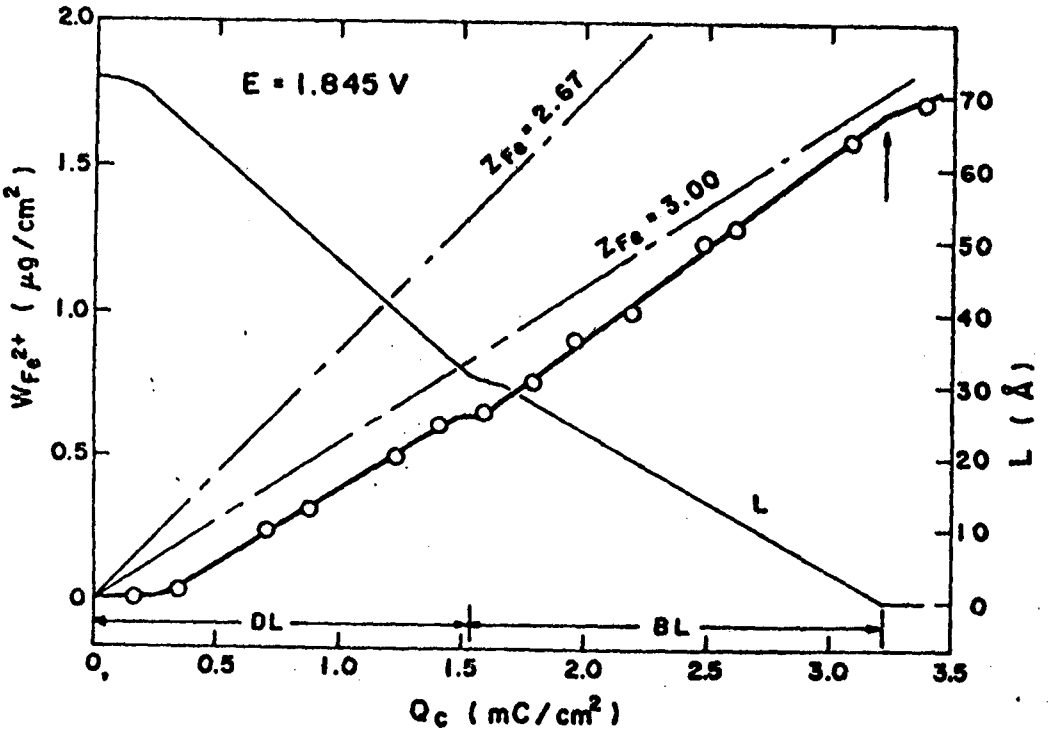

Fig. 9-23. Cathodic dissolution and thickness reduction curves of the passive film formed on iron at +1.845 V in transpassive potential region in borate solution at pH 8.42. Q_c = cathodic charge passed during galvanostatic film reduction at pH 6.35.

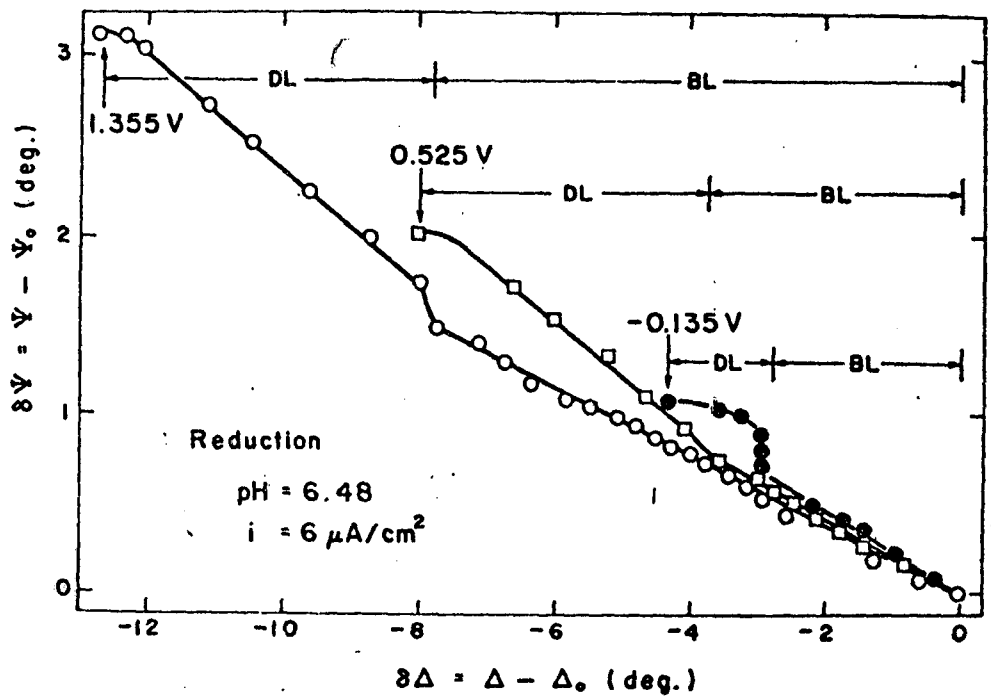

Fig. 9-24. Change in ellipsometric parameters Δ and Ψ during cathodic dissolution at pH 6.48 of the passive film formed at various potentials (-0.135 V, +0.525 V and +1.355V) in borate solution at pH 8.42. The refractive index was N = 3.01-3.47i for the cathodically reduced iron surface (Δ_o, Ψ_o) and n = 1.336 for the solution of pH 6.48.

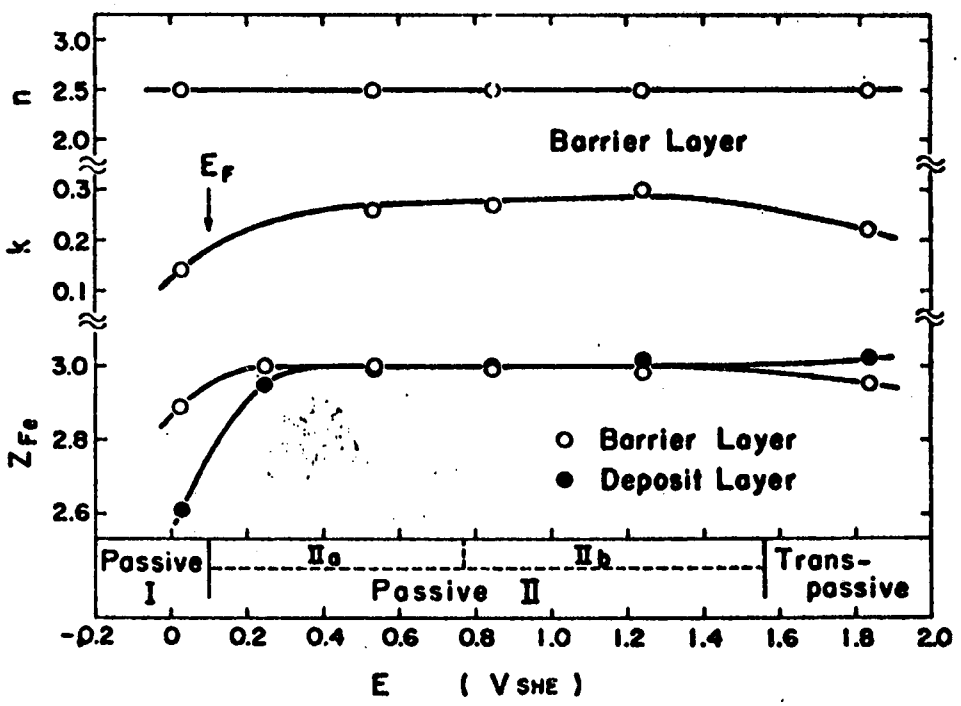

Fig. 9-25. Refractive index of the barrier layer and iron ion valency in the barrier and deposit layers as a function of potential at which the passive film has been formed on iron by potentiostatic one-hour oxidation in borate solution at pH 8.42.

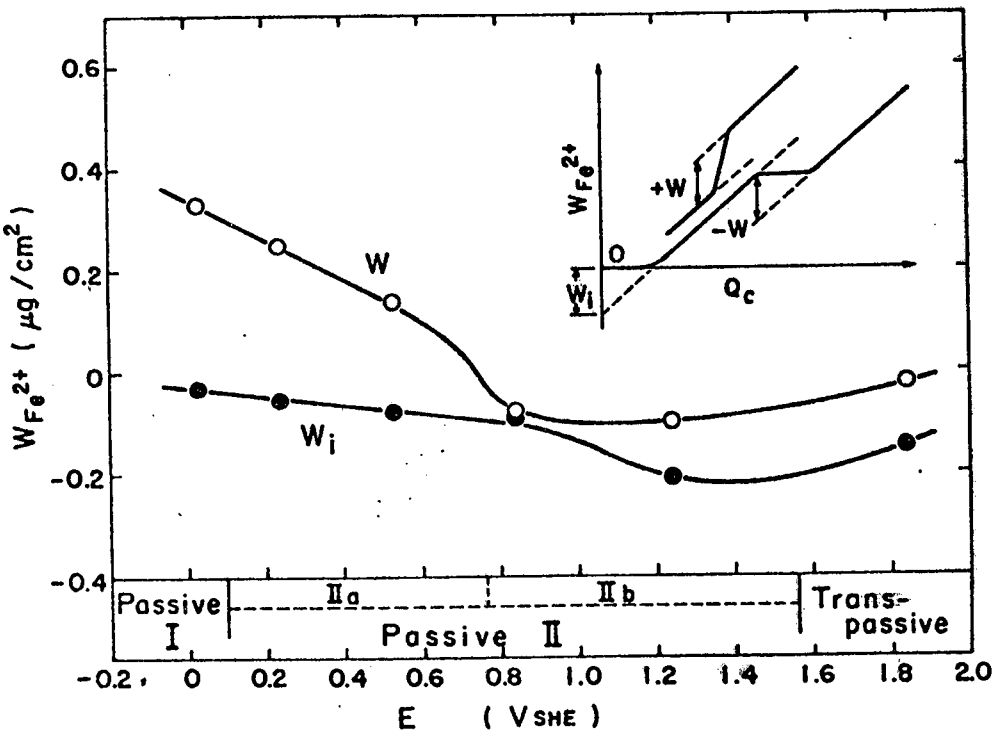

Fig. 9-26. Initial delay and boundary gap in cathodic film dissolution curve as a function of potential at which the passive film has been formed at pH 8.42.

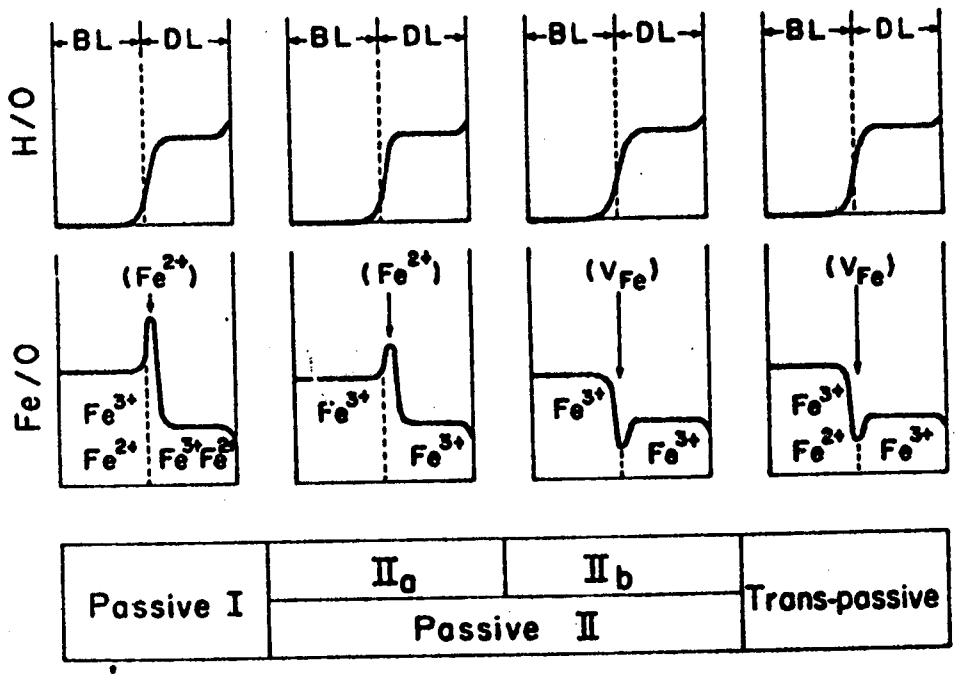

Fig. 9-27. Schematic depth profile of iron and hydrogen in the passive film formed on iron in different potential regions in borate solution of pH 8.42. Iron profile is based on this study and hydrogen profile on previous studies[1,4].

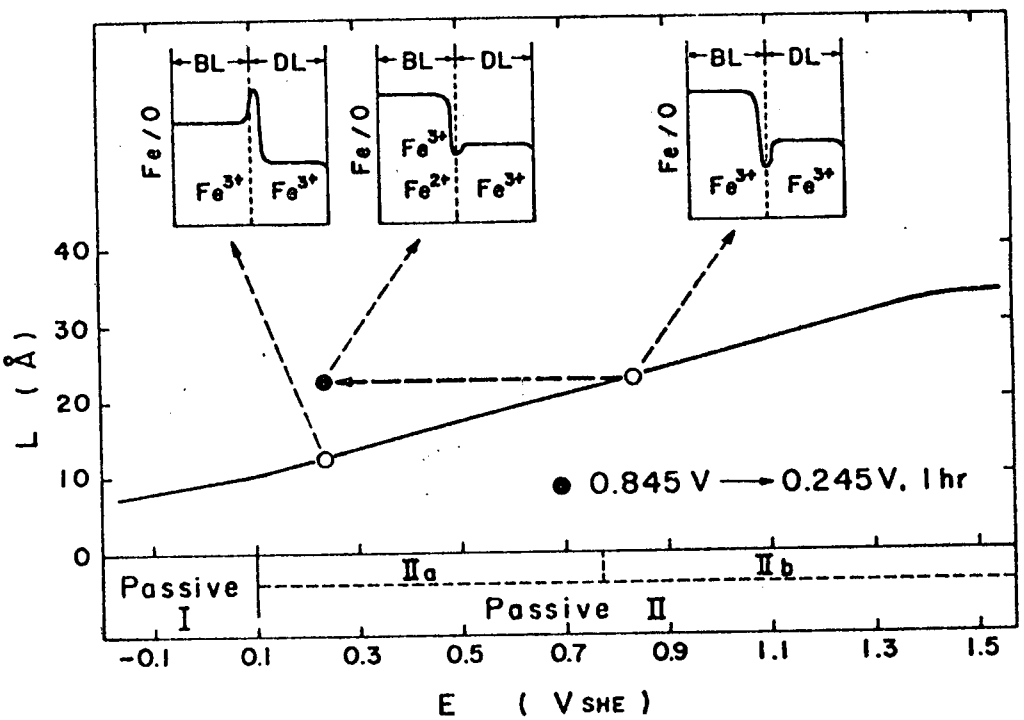

Fig. 9-28. Barrier layer thickness and schematic depth profile of the passive film showing dependence on the process of film formation.

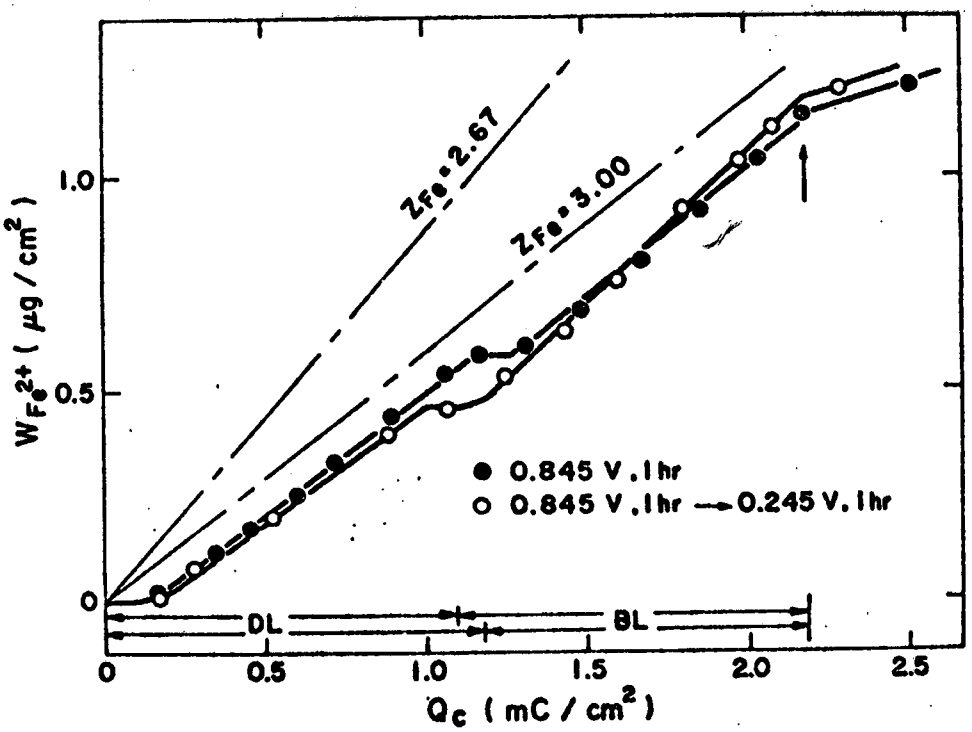

Fig. 9-29. Cathodic dissolution curve of the passive film formed in potential region IIb and of the film subsequently aged in potential region I. Aging causes the oxidized state of the barrier layer to change from $z_{Fe} = +3.0$ to $z_{Fe} < +3$, but no appreciable change occurs at the barrier/deposit boundary.

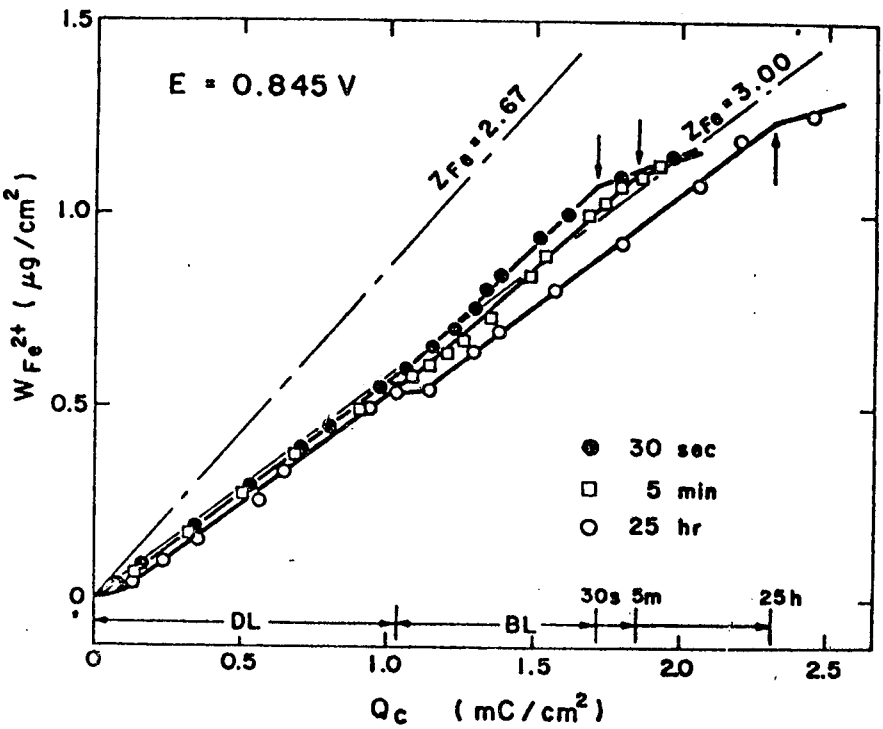

Fig. 9-30. Cathodic dissolution curve of the passive film at different periods of time during potentiostatic film growth in potential region II.

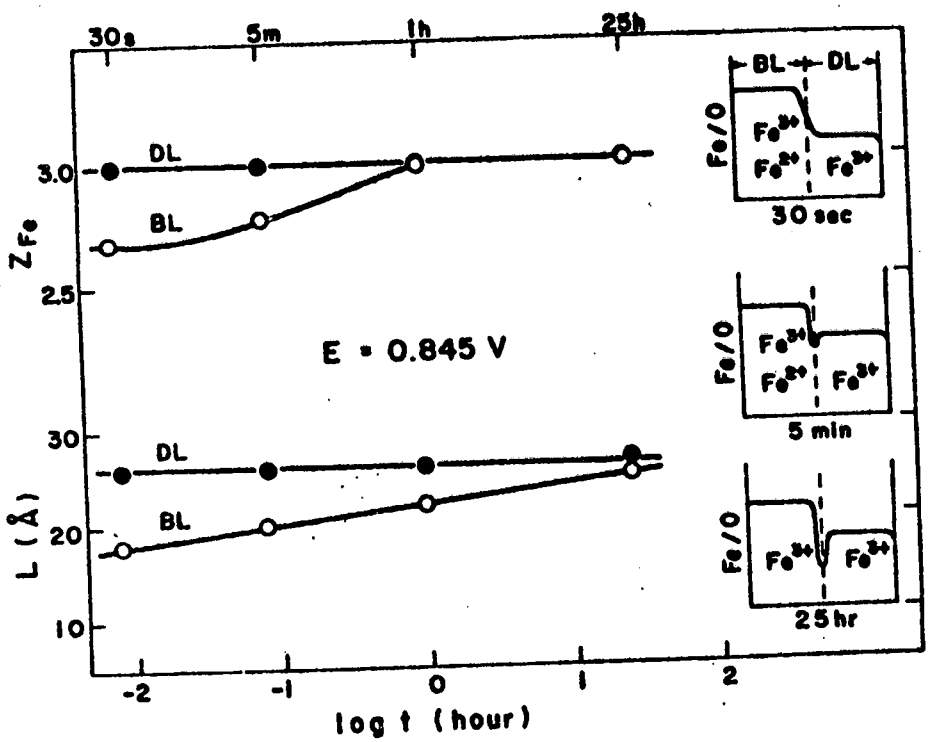

Fig. 9-31. Thickness, iron ion valency, and schematic depth profile of the passive film as a function of time of potentiostatic film growth in potential region II.

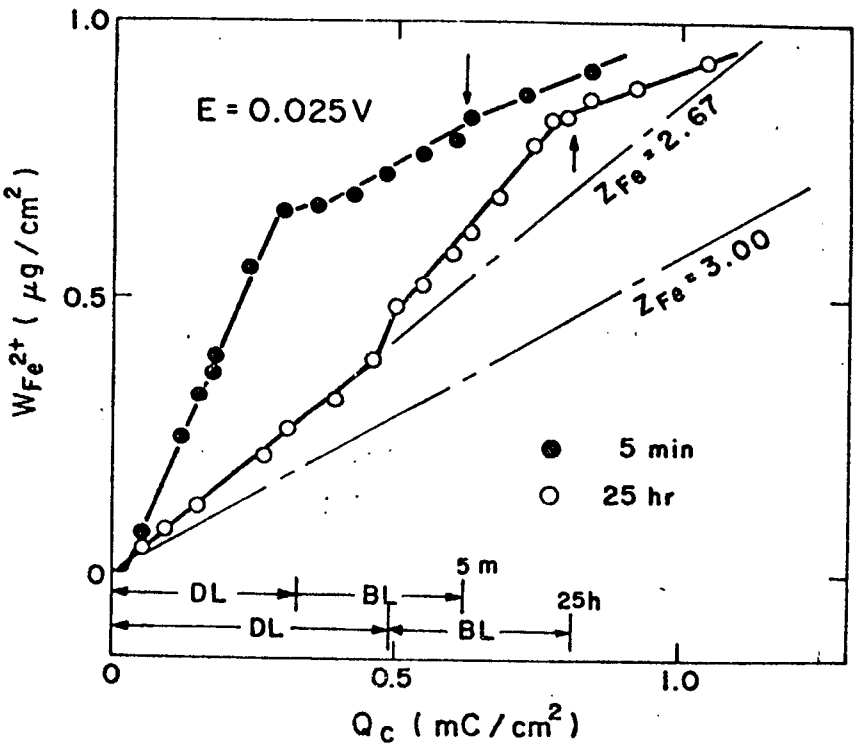

Fig. 9-32. Cathodic dissolution curve of the passive film at different periods of time during potentiostatic film growth in potential region I.

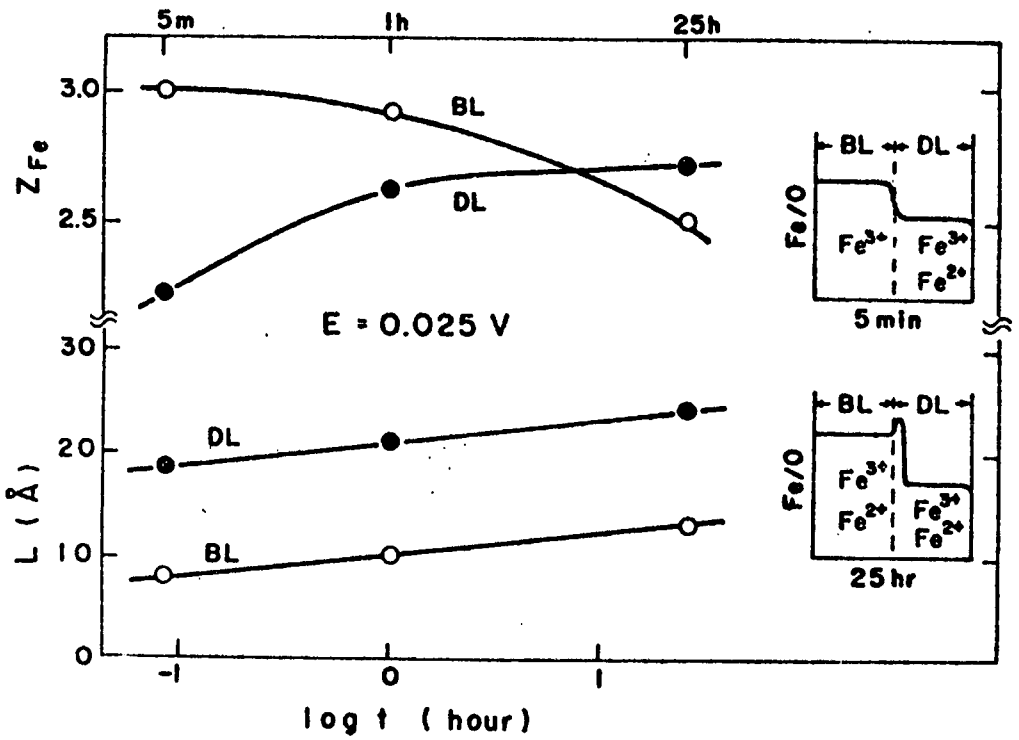

Fig. 9-33. Thickness, iron ion valency, and schematic depth profile of the film as a function of time of potentiostatic film growth in potential region I.

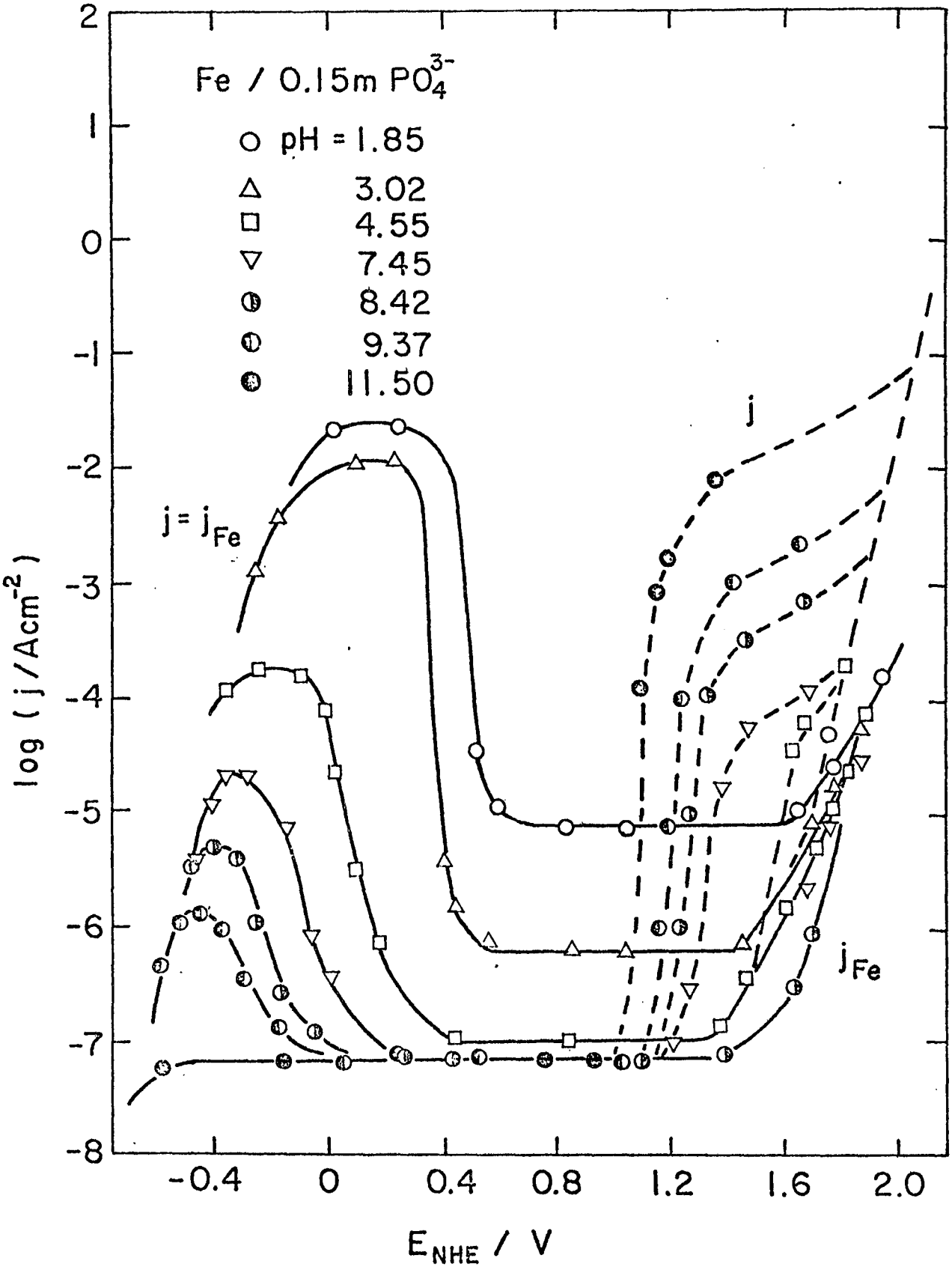

Fig. 9-34. Anodic current j and dissolution current j_{Fe} versus potential of iron in acid, neutral, and alkaline phosphate solutions.

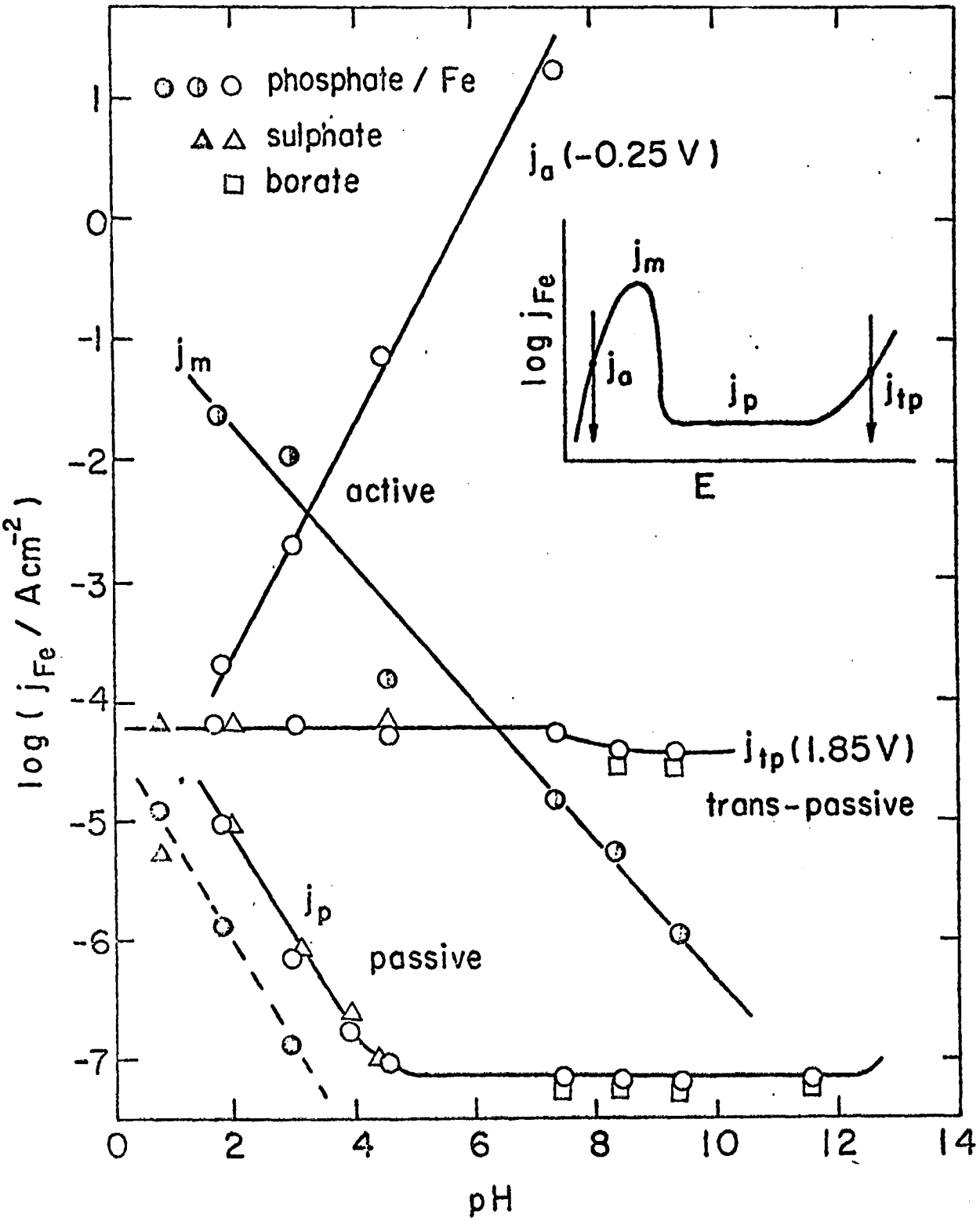

Fig. 9-35. pH-dependenceof active dissolution current j_a at a constant potential, active dissolution current peak j_m, passive dissolution current j_p, and transpassive dissolution current j_{tp} at a constant potential of iron in phosphate solutions.

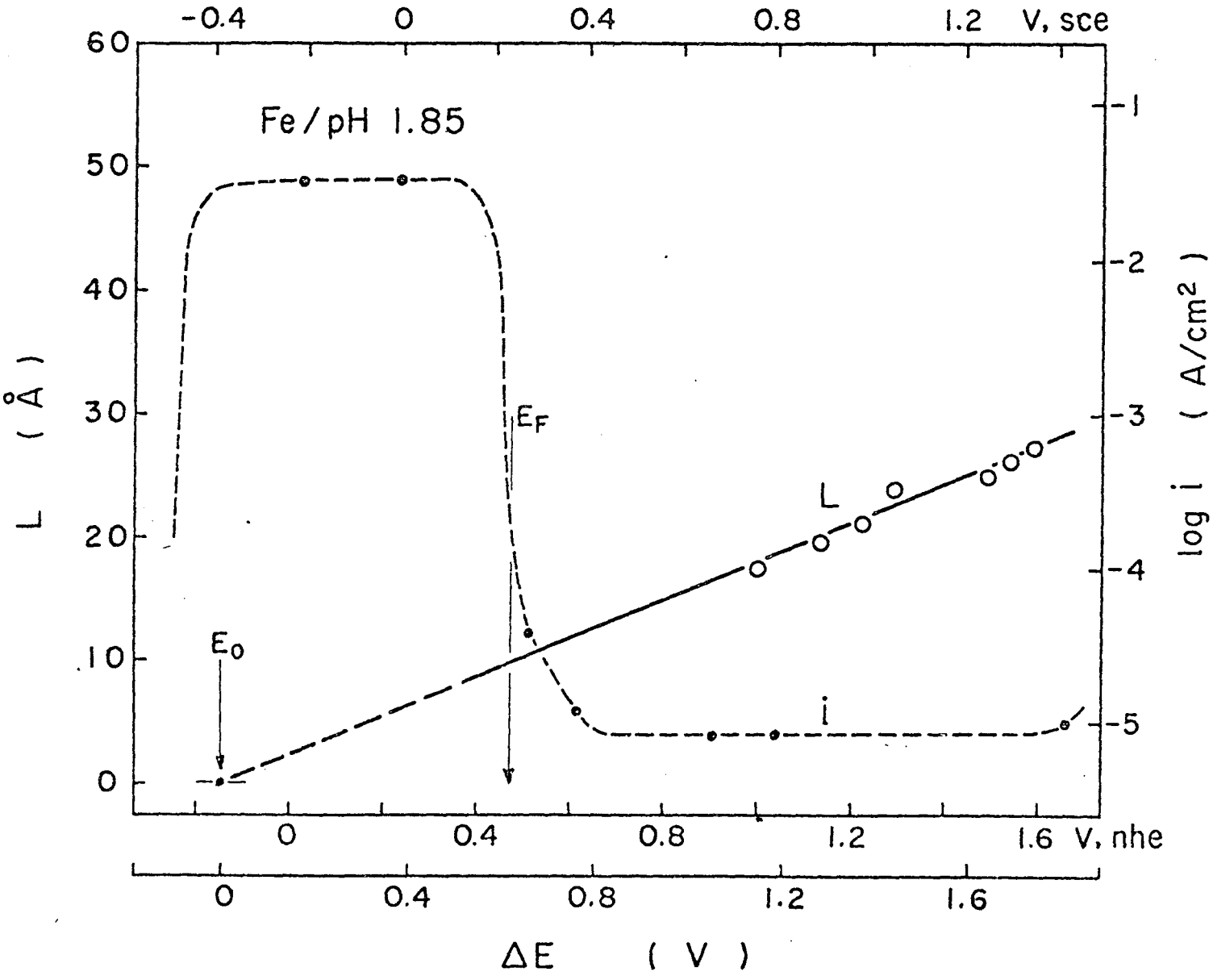

Fig. 9-36. Thickness measured by ellipsometry versus potential of the passive film on iron, in sulphuric acid solution.

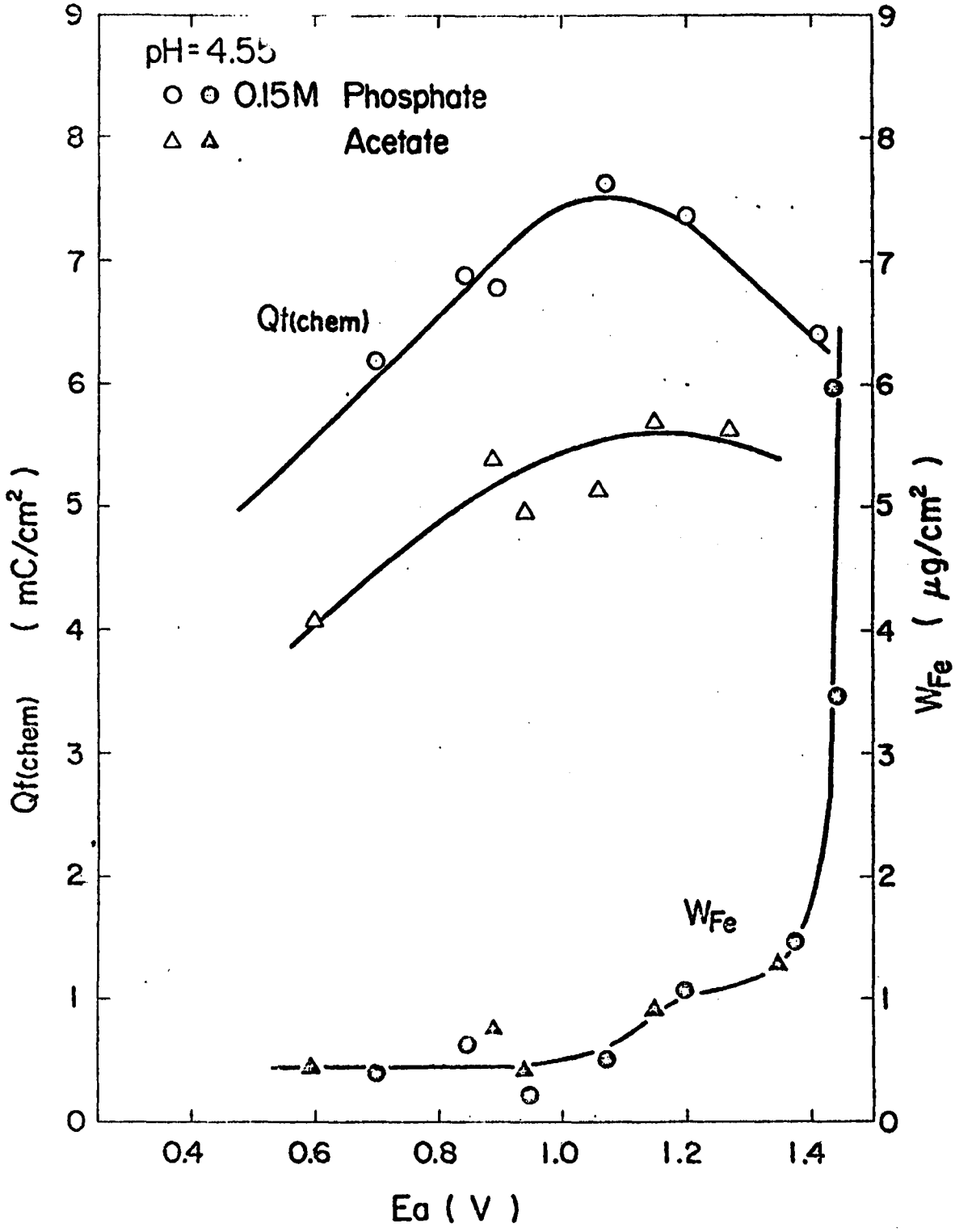

Fig. 9-37. Amount of film charge measured by chemical analysis and amount of dissolved iron for one hour versus potential of iron in acidic phosphate and acetate solutions.

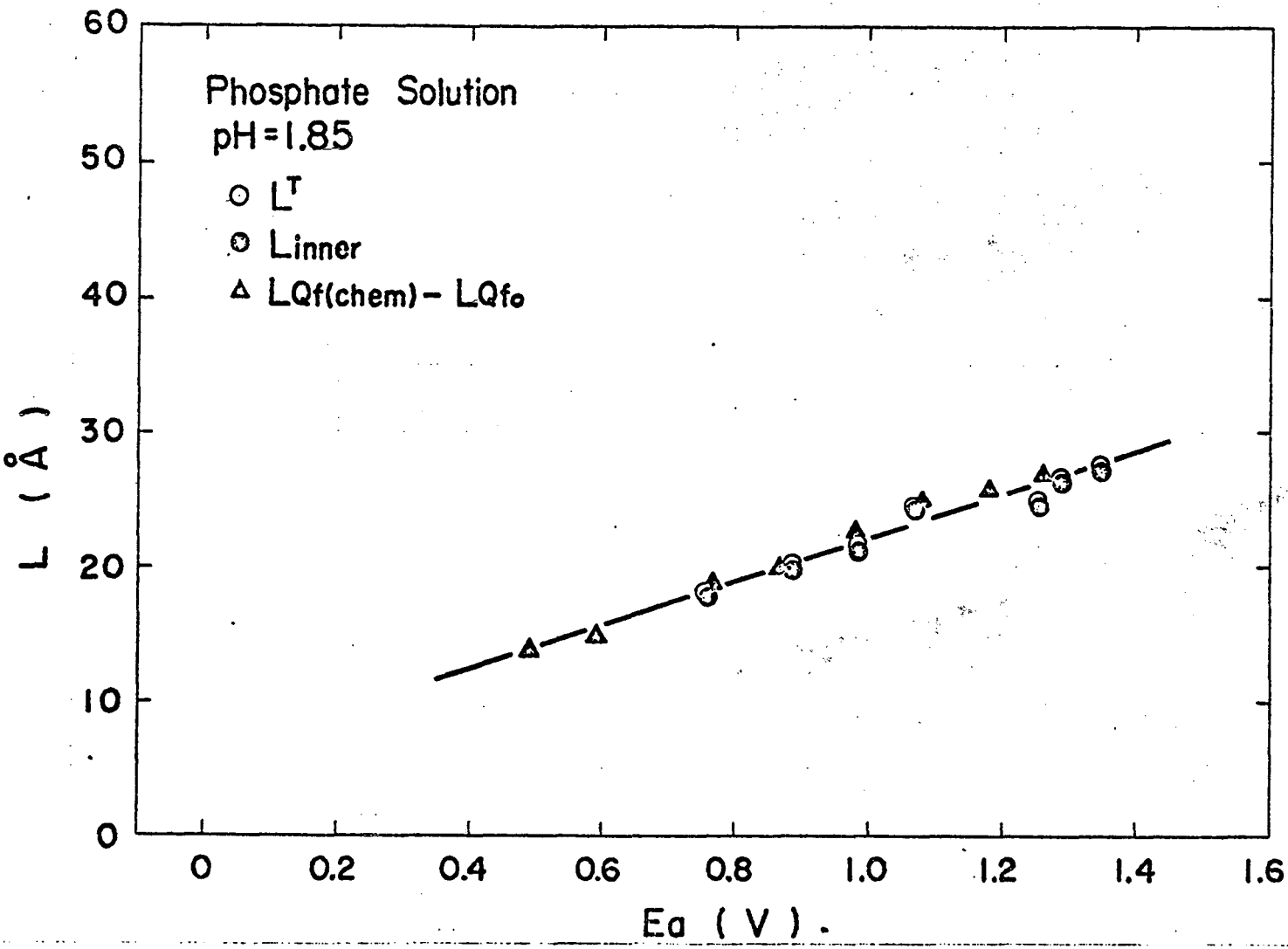

Figure 9-38. Thickness of the film formed on iron by potentiostatic one-hour oxidation in phosphate solution at pH 1.85 as functions of potential. L^T and Linner are respectively the total thickness and the inner layer thickness estimated by ellipsometry. $LQ(chem) - LQ_{fo}$ is the thickness calculated from the anodic charge for the inner layer shown in Figure 4-10.

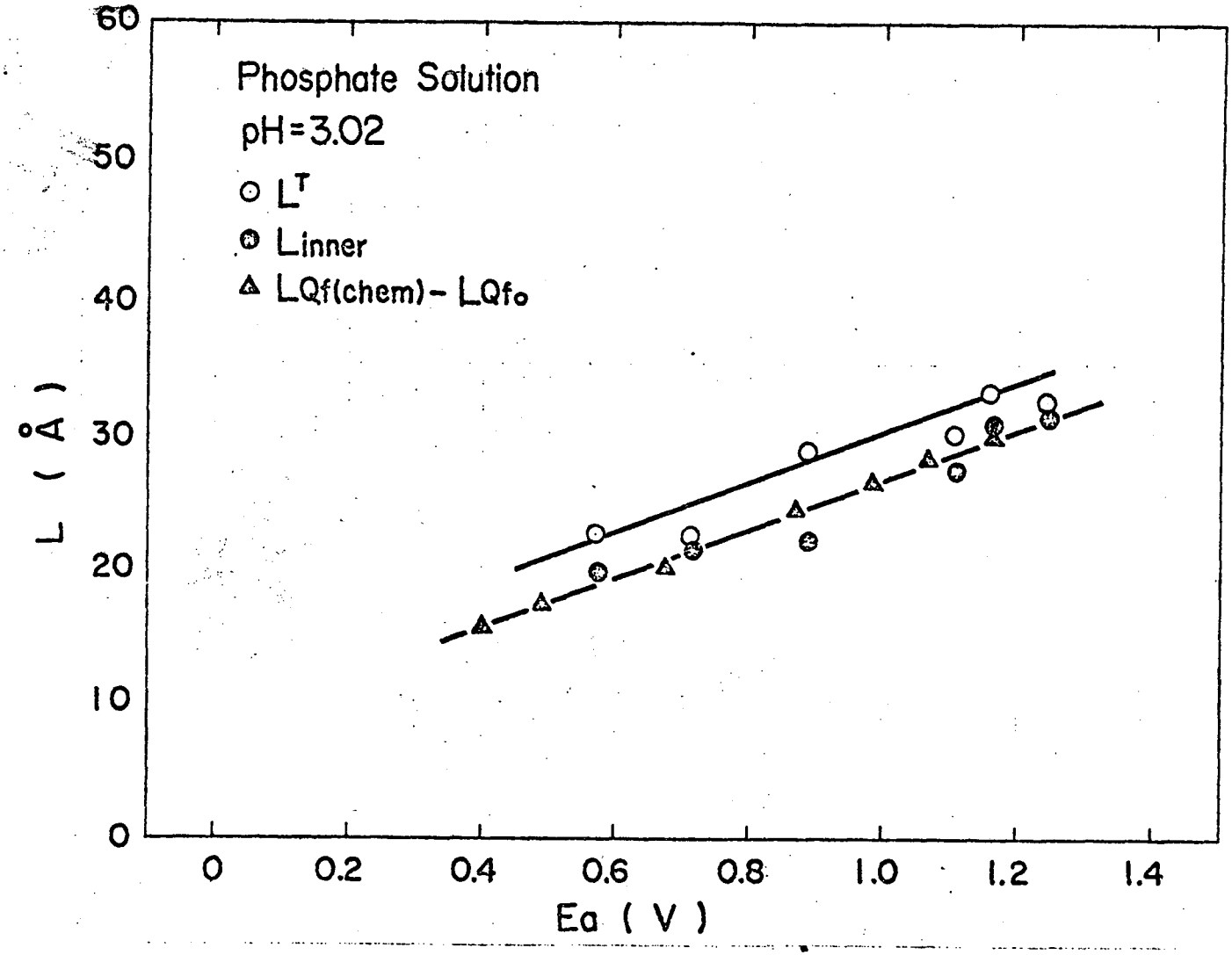

Figure 9-39. Thickness of the film formed on iron by potentiostatic one-hour oxidation in phosphate solution at pH 3.02 as functions of potential. L^T and L_{inner} are respectively the total thickness and the inner layer thickness estimated by ellipsometry. $L_{Qf(chem)} - L_{Qfo}$ is the thickness calculated from the anodic charge for the inner layer shown in Figure 4-10.

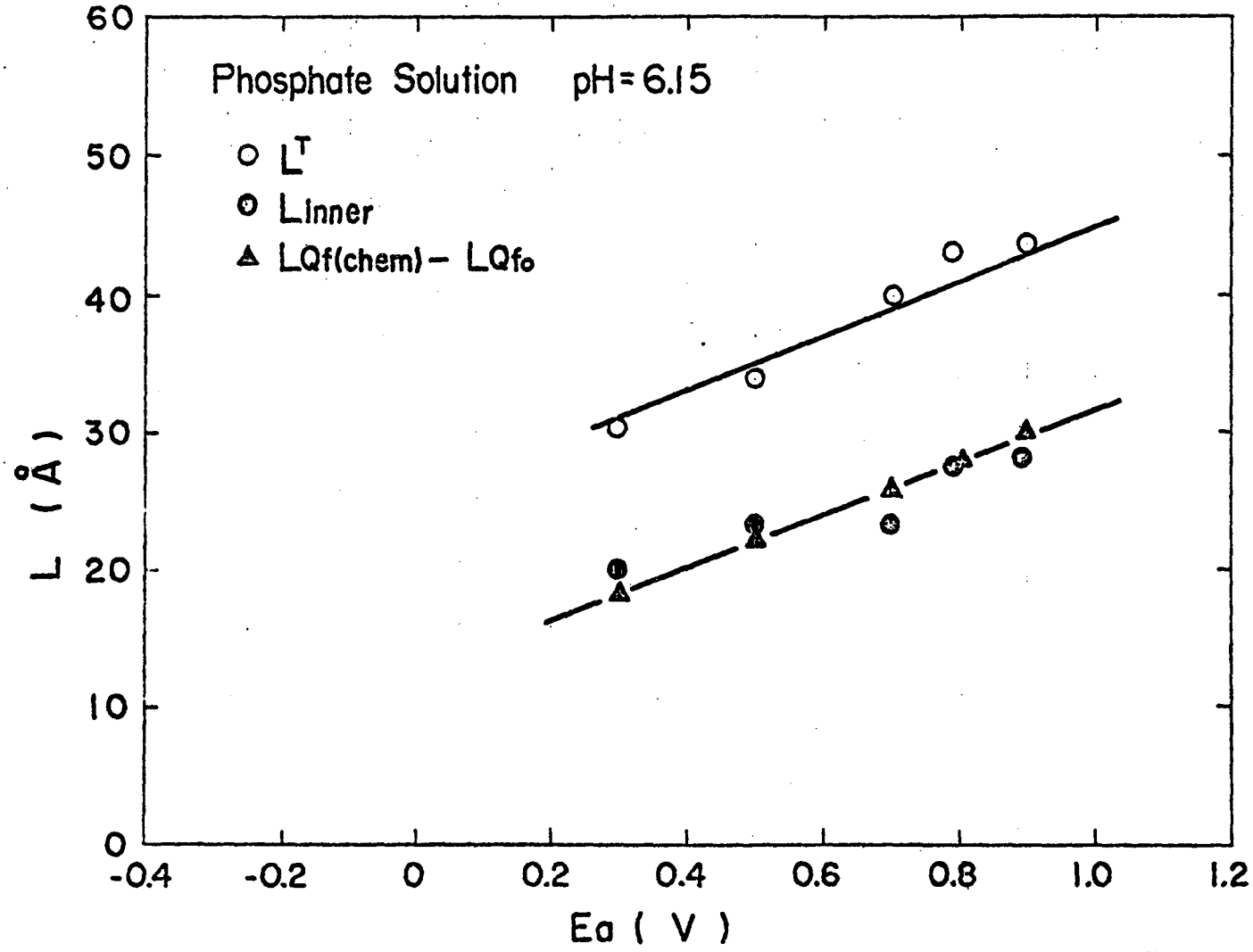

Figure 9-40. Thickness of the film formed on iron by potentiostatic one-hour oxidation in phosphate solution at pH 6.15 as functions of potential. L^T and L_{inner} are respectively the total thickness and the thickness of the inner layer estimated by ellipsometry. $L_{Qf(chem)} - L_{Qfo}$ is the thickness calculated from the anodic charge for the inner layer shown in Figure 4-10.

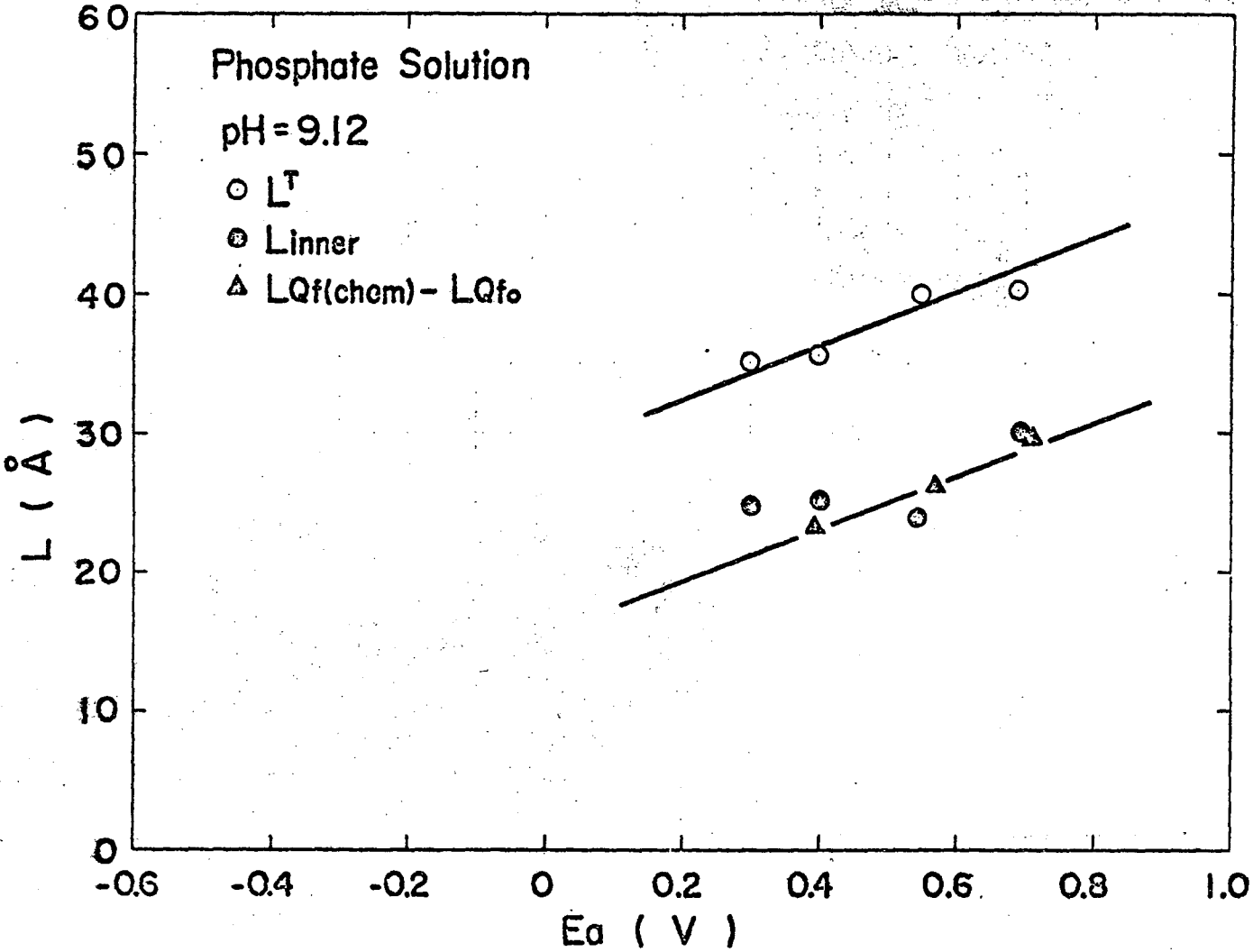

Figure 9-41. Thickness of the film formed on iron by potentiostatic one-hour oxidation in phosphate solution at pH 9.12 as functions of potential. L^T and Linner are respectively the total thickness and the thickness of the inner layer estimated by ellipsometry. $L_{Qf(chem)} - L_{Qfo}$ is the thickness calculated from the anodic charge for the inner layer shown in Figure 4-10.

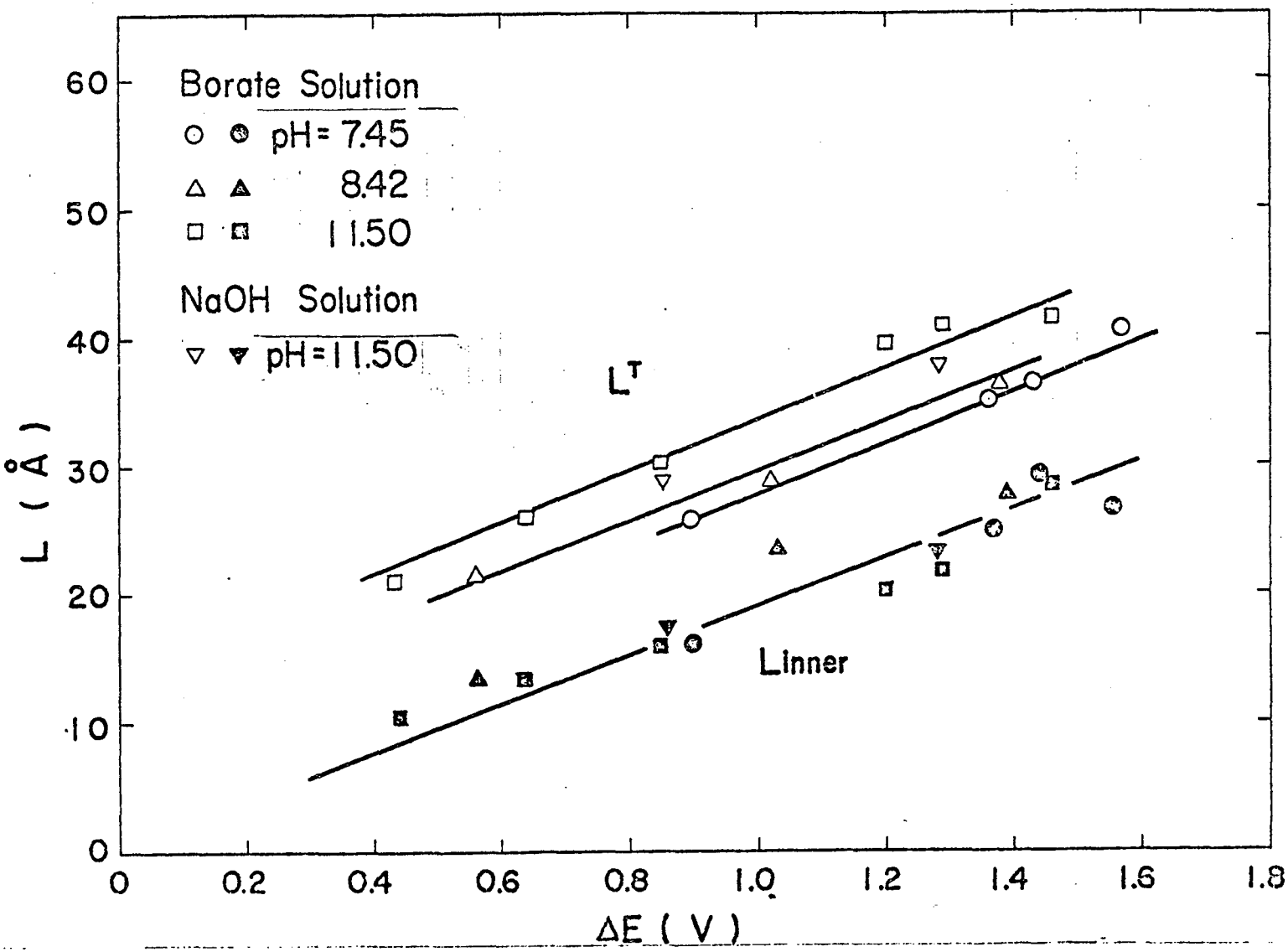

Figure 9-42. Total thickness, L^T, and the thickness of the inner layer, L_{inner}, of the film formed on iron by potentiostatic one-hour oxidation in borate-buffer solution at various pH and sodium hydroxide solution at pH 11.50 as a function of over voltage ΔE.

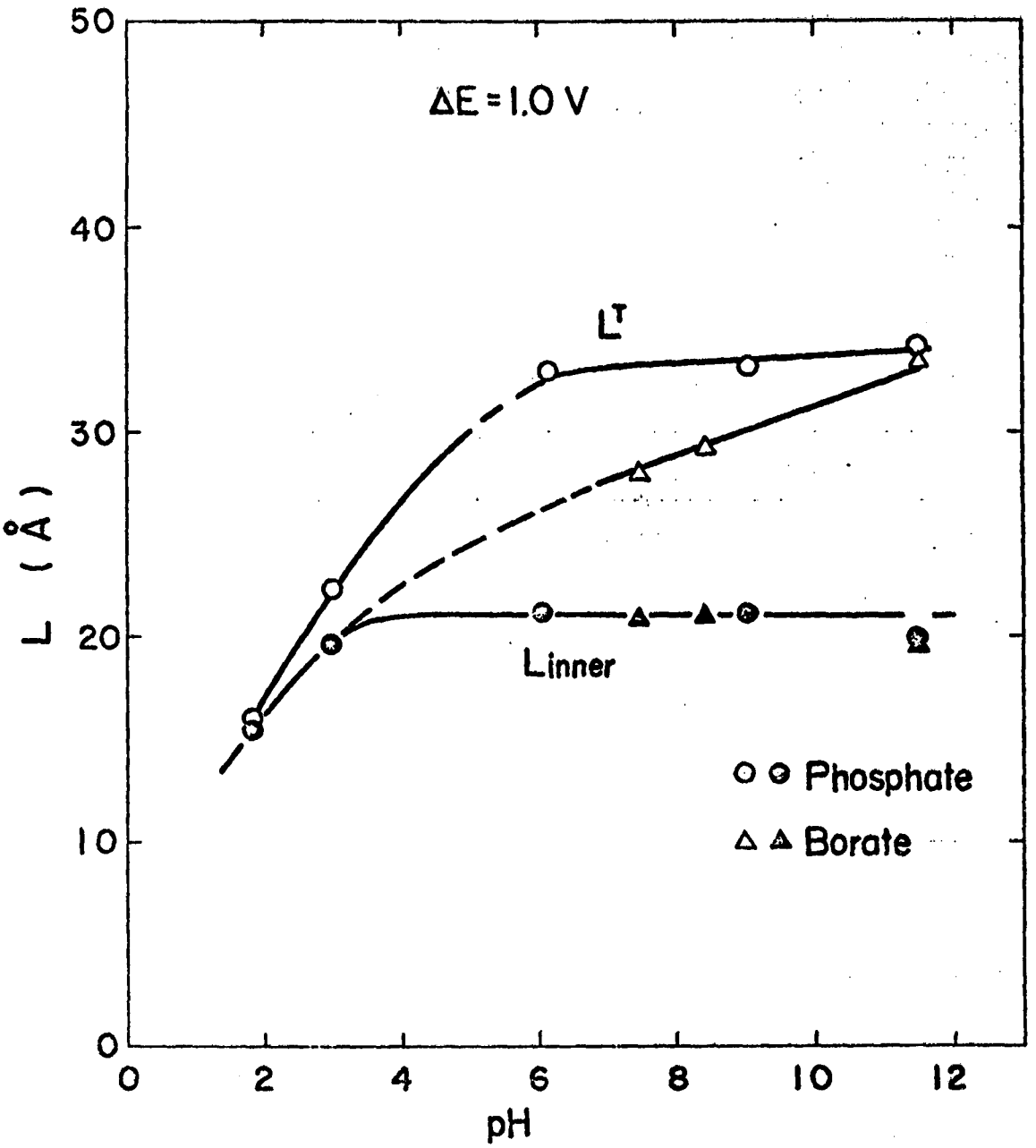

Figure 9-43. Total thickness L^T and inner layer thickness L_{inner} of the film formed on iron by potentiostatic one-hour oxidation in various solutions at a constant over voltage of 1.0V as functions of pH.

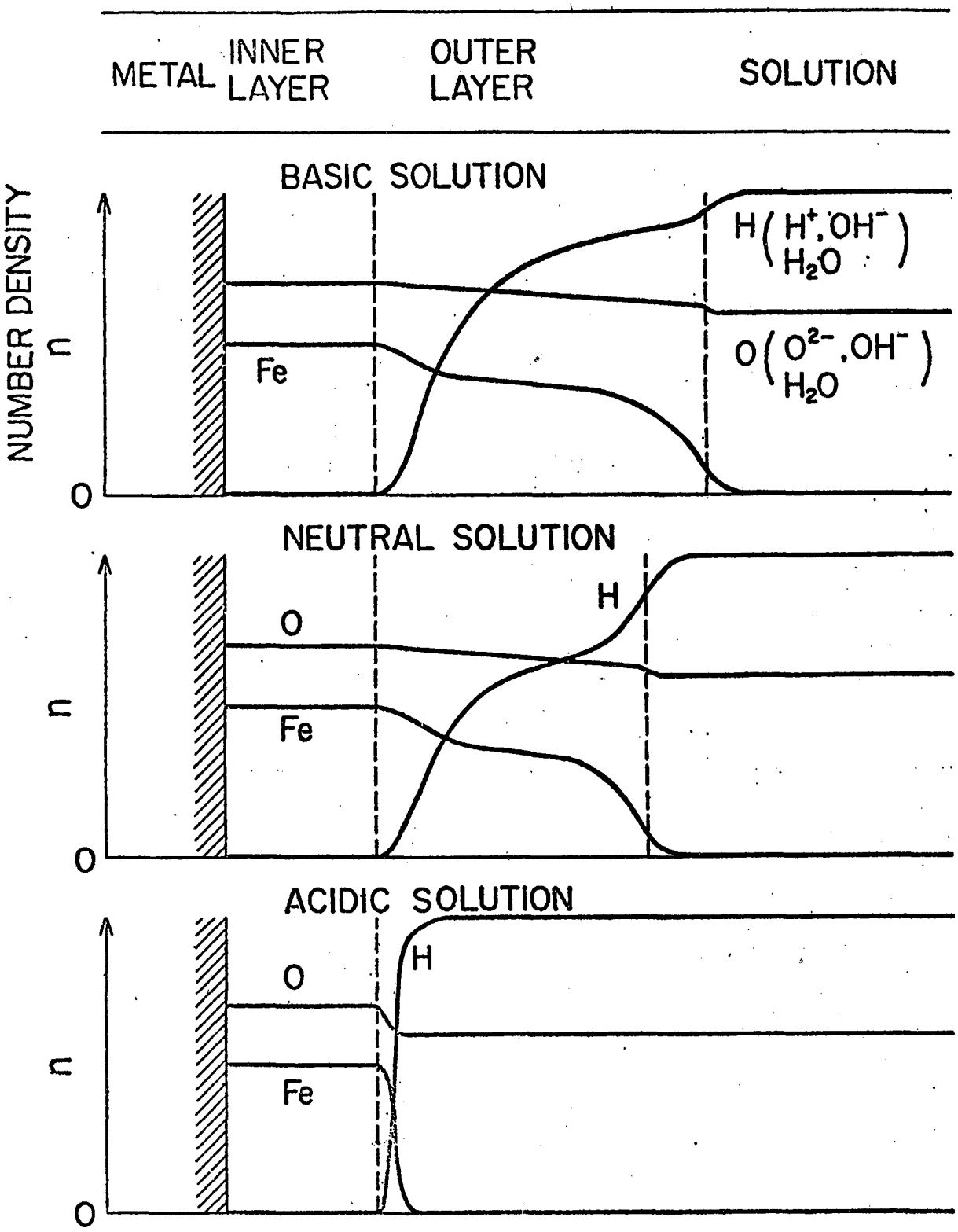

Fig. 9-44. Schematic model for the barrier layer and deposit layer of the passive film on iron.

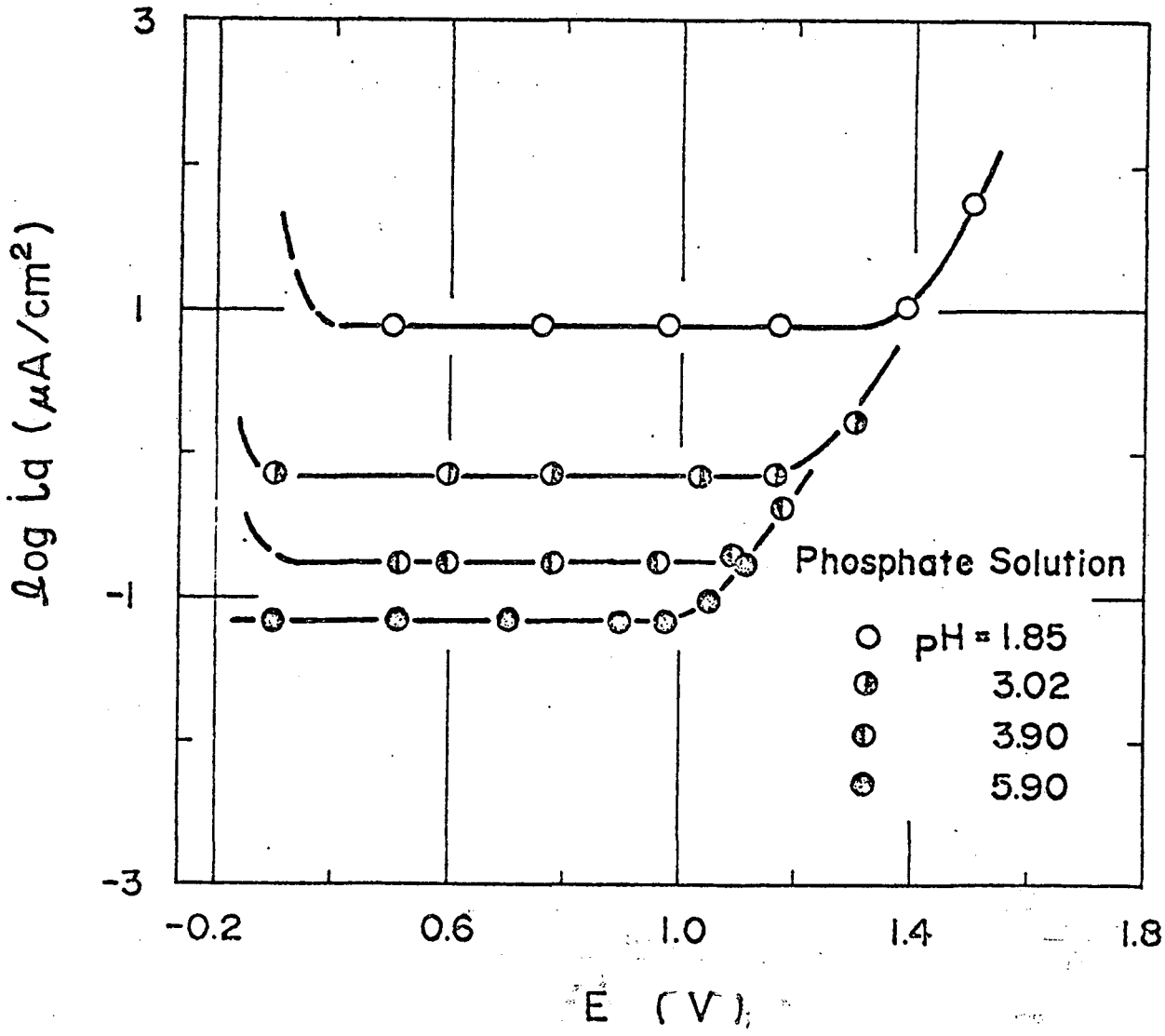

Fig. 9-45. Anodic steady state polarization curve of iron in acidic oxygen-free sodium phosphate solutions at 25°C. Potential is in SCE scale.

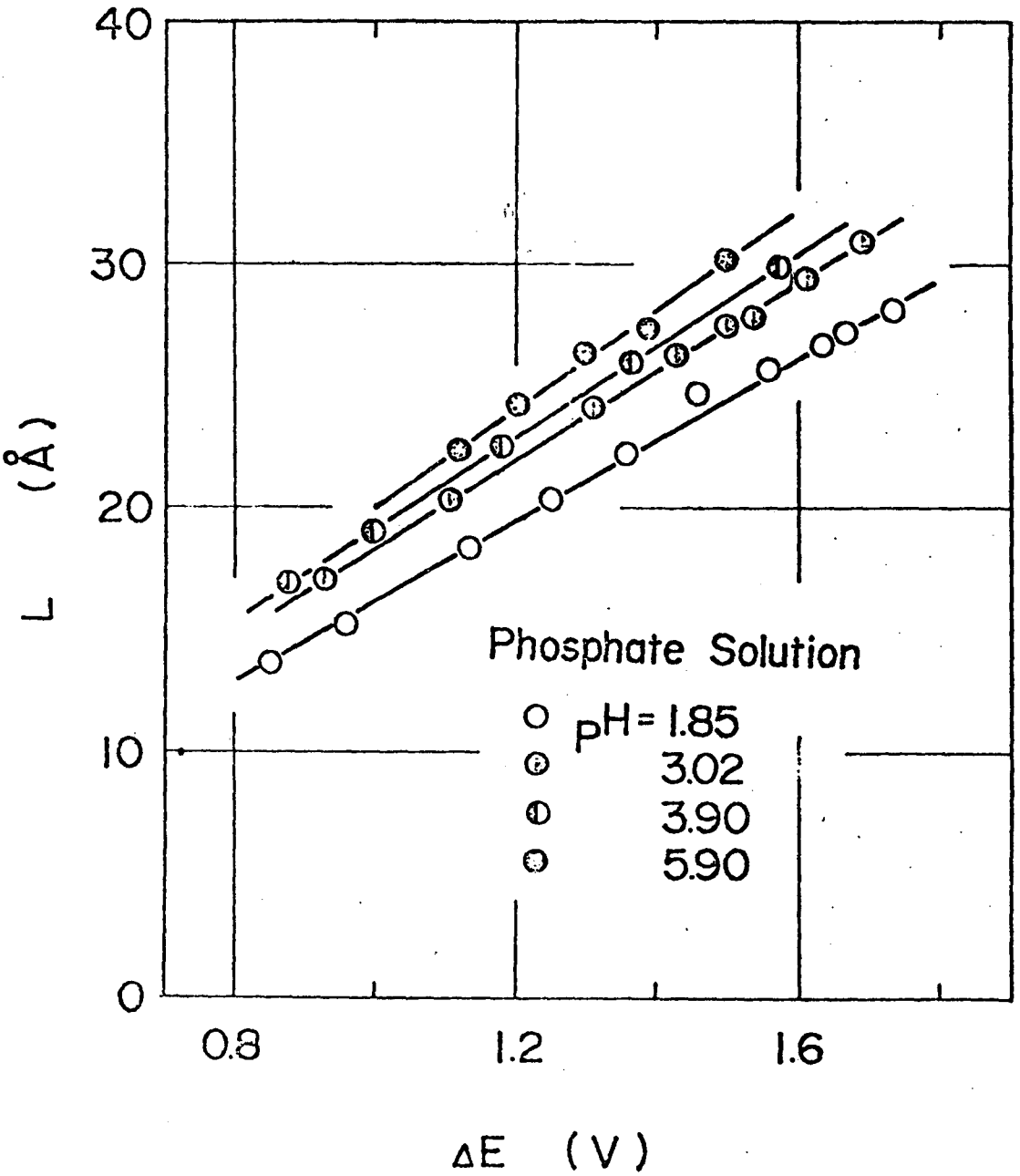

Fig. 9-46. Thickness of the barrier oxide layer of anodic oxide films on iron in acidic phosphate solutions as a function of overpotential in the layer.

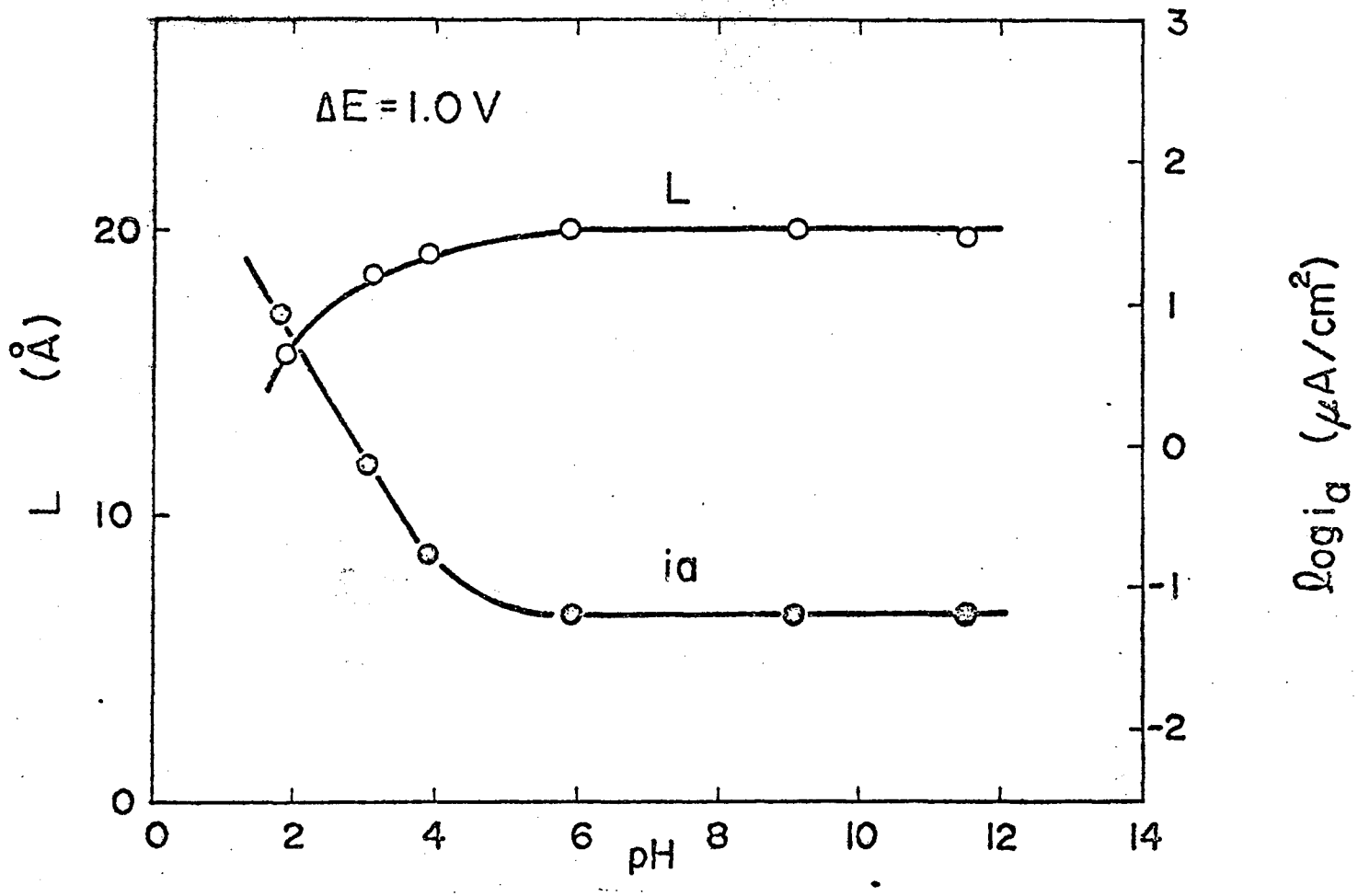

Fig. 9-47. Anodic potential-independent steady state current i_a and barrier oxide layer thickness L at a constant overpotential of anodic oxide films on iron in acidic phosphate solutions as a function of solution pH.

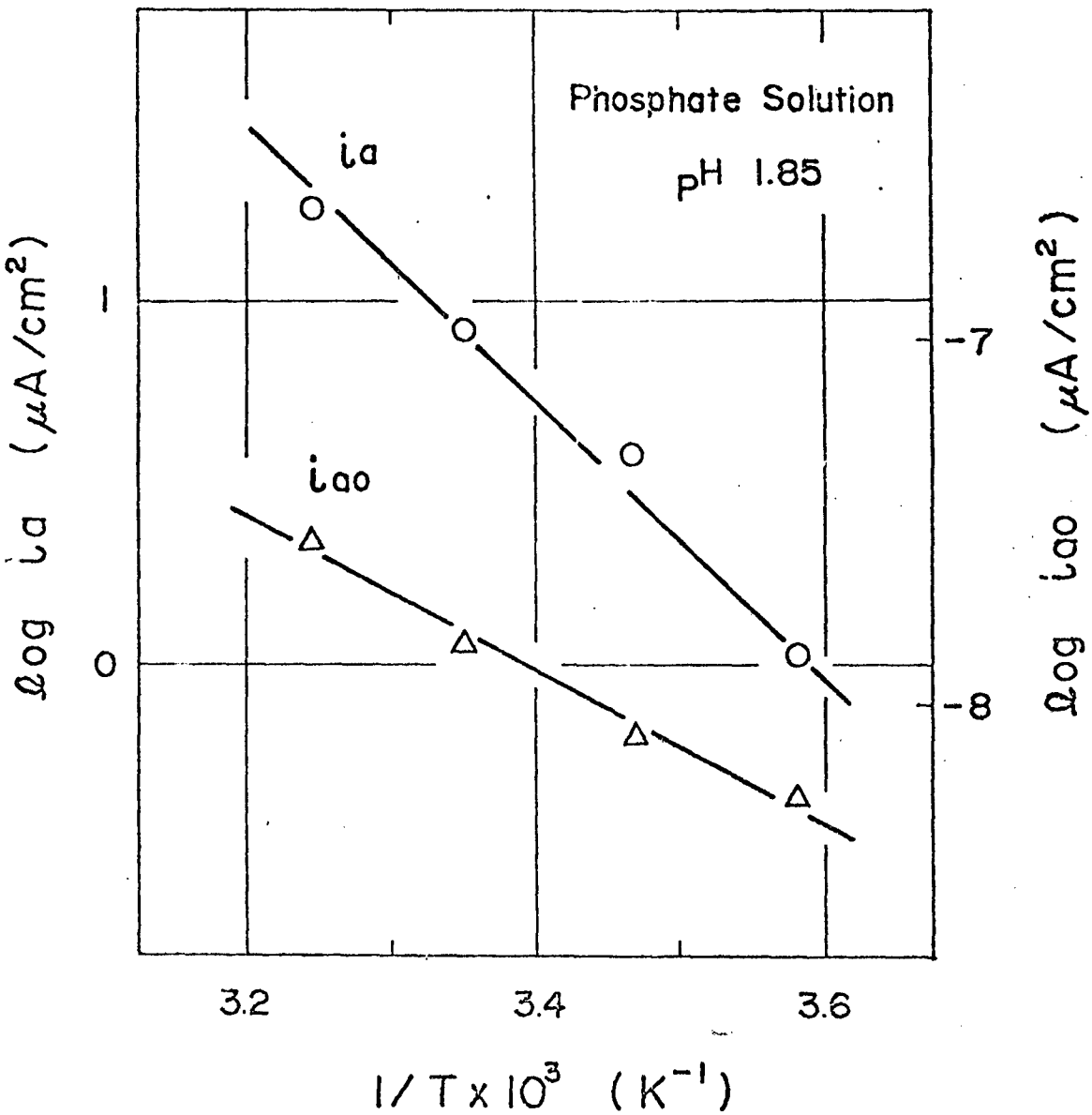

Fig. 9-48. Arrhenius plot of anodic potential-independent steady state current i_a and pre-exponential parameter i_{ao} in equation (6).

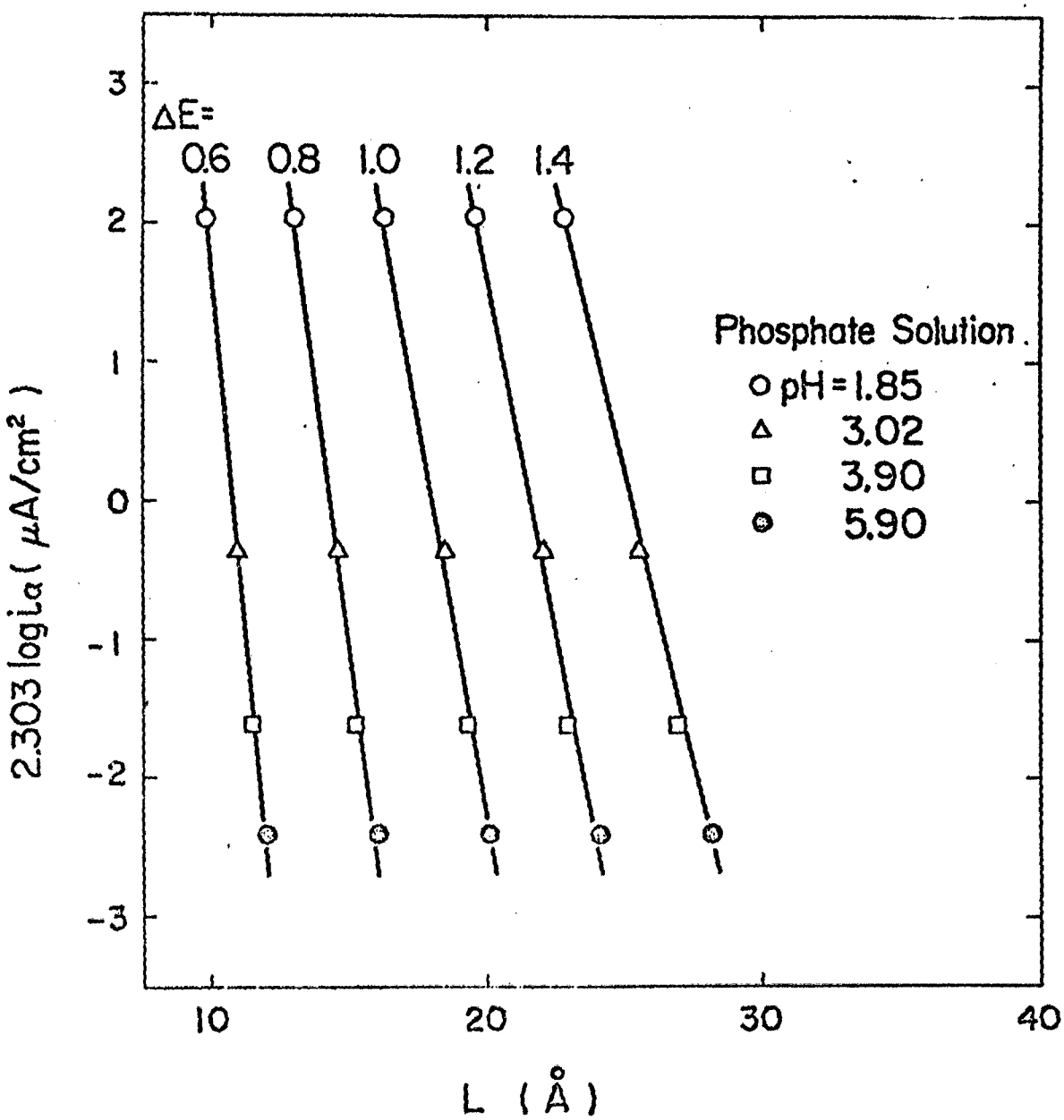

Fig. 9-49. Plot of logarithm of i_a against barrier oxide layer thickness L at constant overpotential.

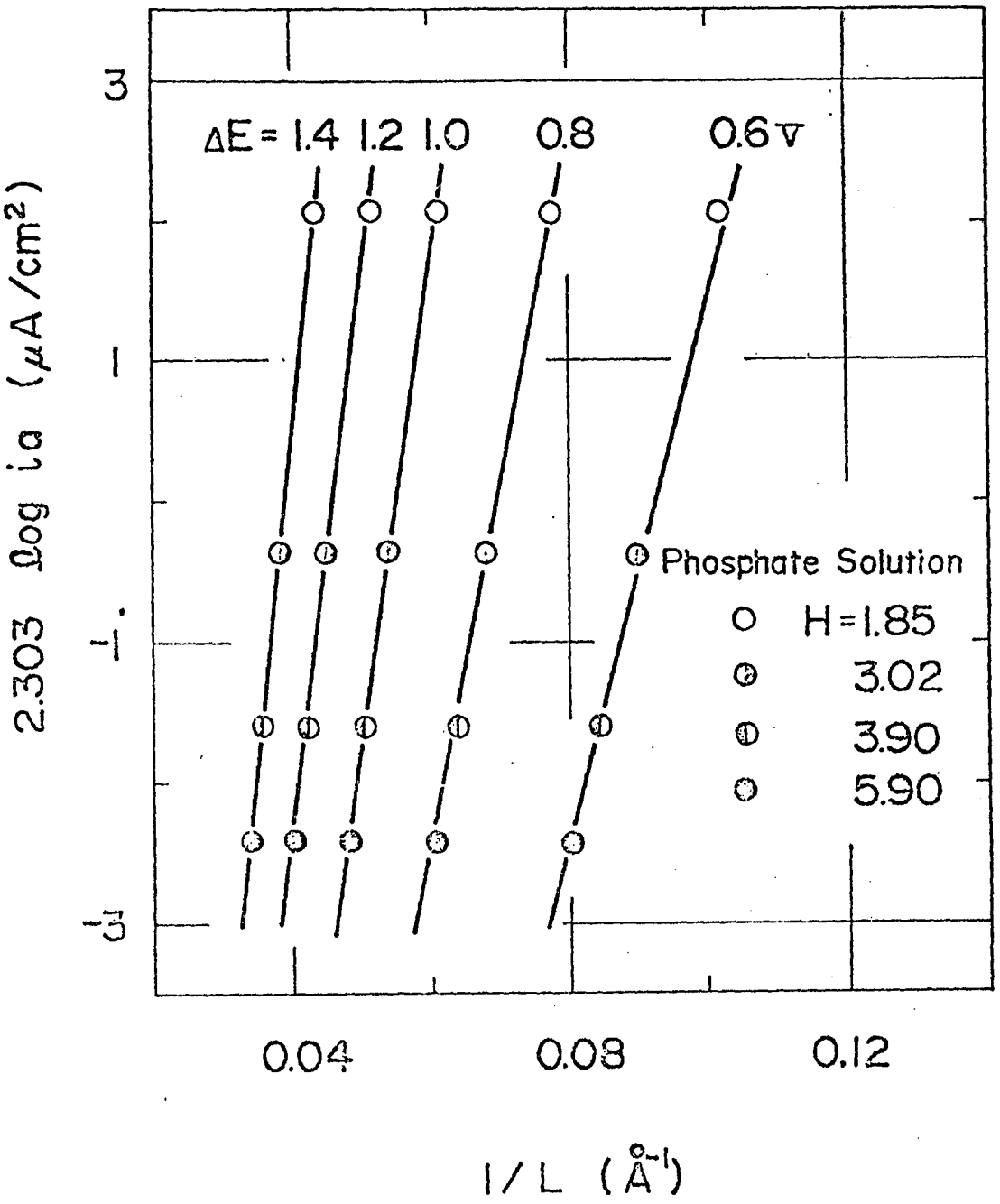

Fig. 9-50. Plot of logarithm of i_a against reciprocal of barrier oxide layer thickness 1/L at constant overpotential.

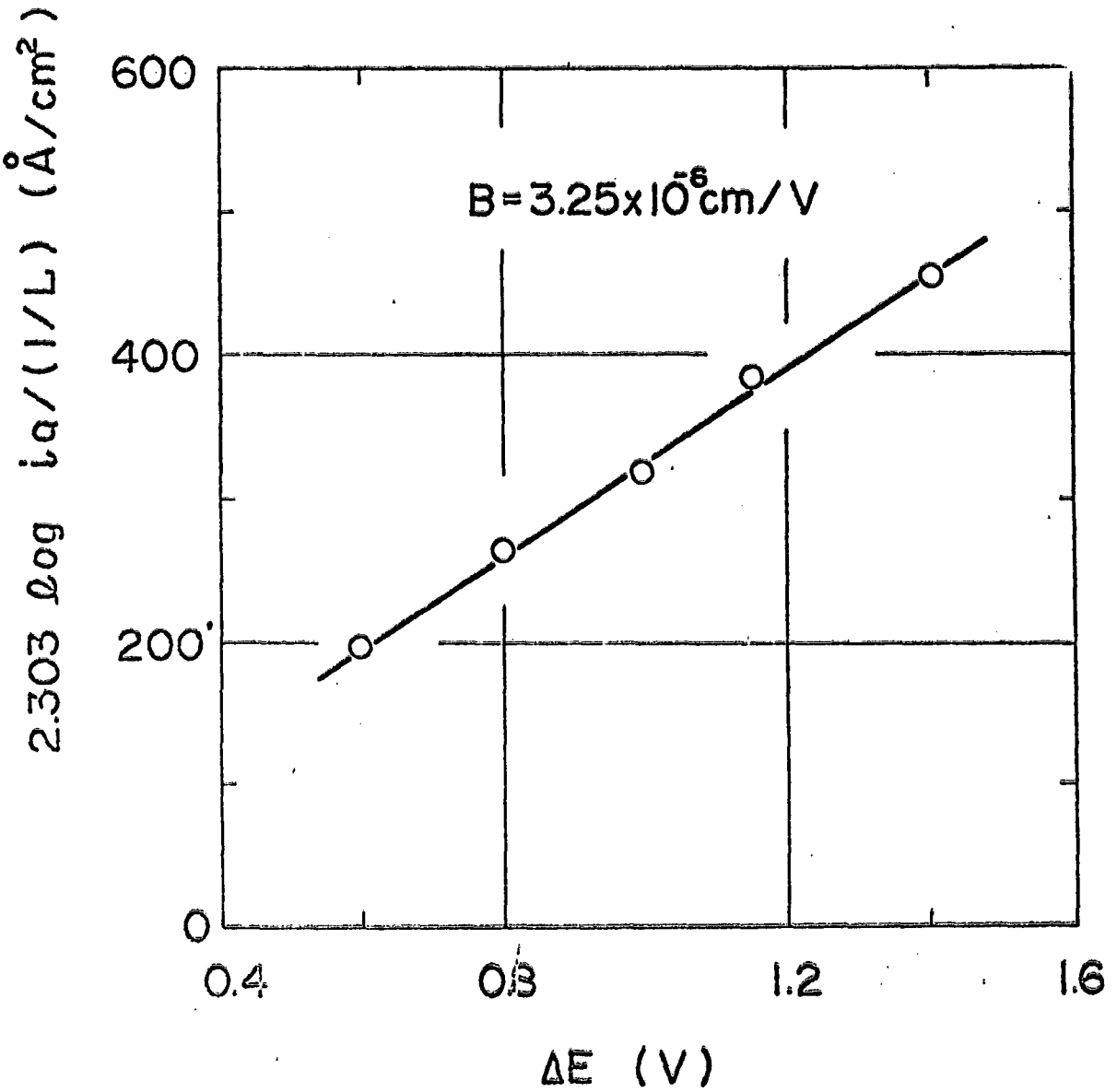

Fig. 9-51. Slope of log i_a versus 1/L plot (Fig.6) as a function of overpotential.

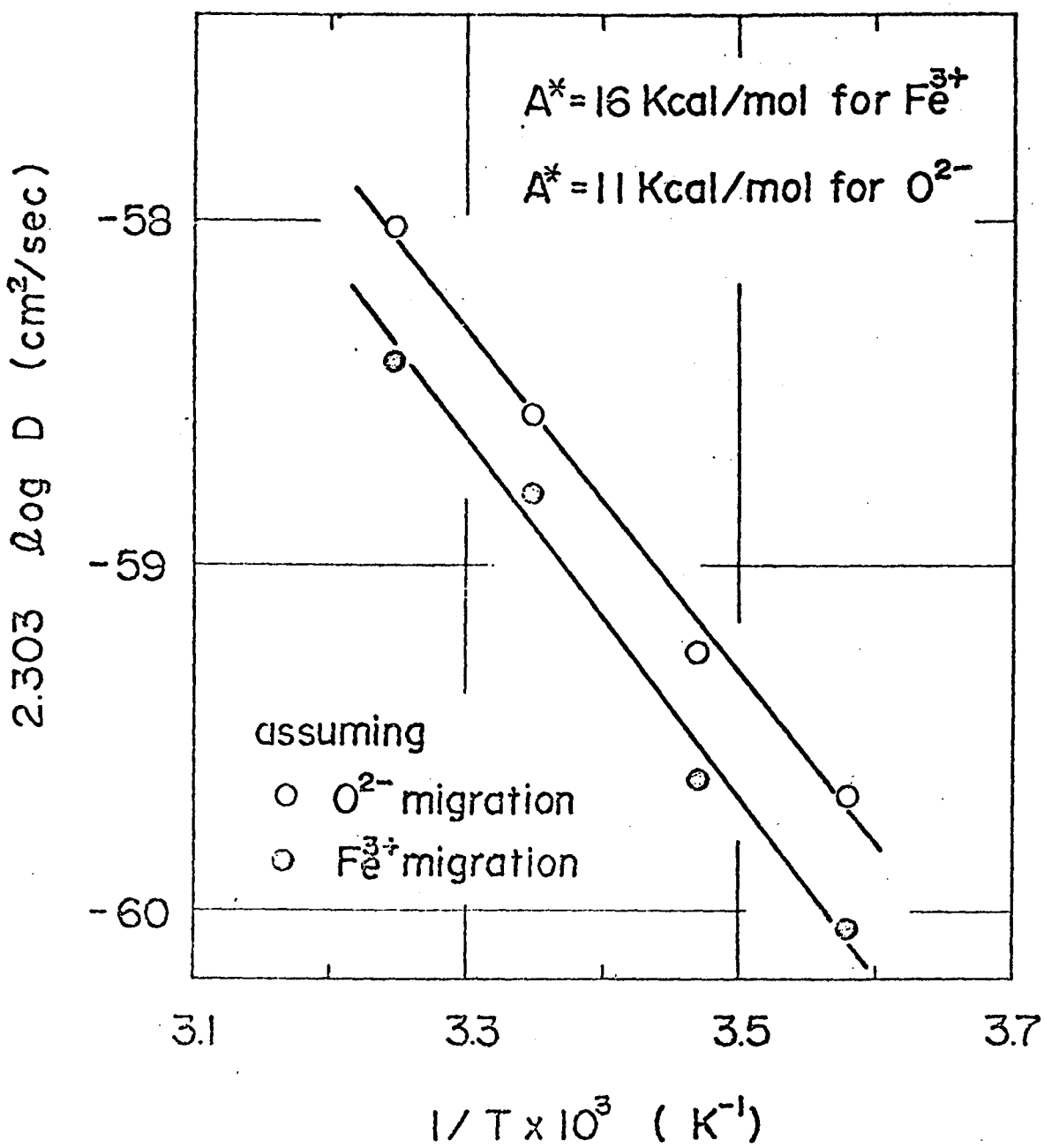

Fig. 9-52. Arrhenius plot of diffusion coefficient of migrating ion in the barrier oxide layer of anodic oxide films on iron in acidic phosphate solutions, migrating ion being iron(III) ion or oxygen(II) ion.

Fig. 9-53.

Table 1 Diffusion data for iron oxide at 25°C.

Compound	Diffusing element	D (cm^2/se)	A* (kcal/mol)	Reference
Dry Fe_3O_4	Fe	3.9×10^{-34}*	45	[18]
Dry Fe_3O_4	Fe	2.4×10^{-40}*	55	[19]
Dry α-Fe_2O_3	Fe	2.9×10^{-77}*	112	[19]
Wet Fe_3O_4	O	9.3×10^{-27}*	17	[20]
passive film (γ-Fe_2O_3)	if assuming Fe diffusion	3.1×10^{-26}	16	present work
	if assuming O diffusion	4.6×10^{-26}	11	present work

*extrapolated.

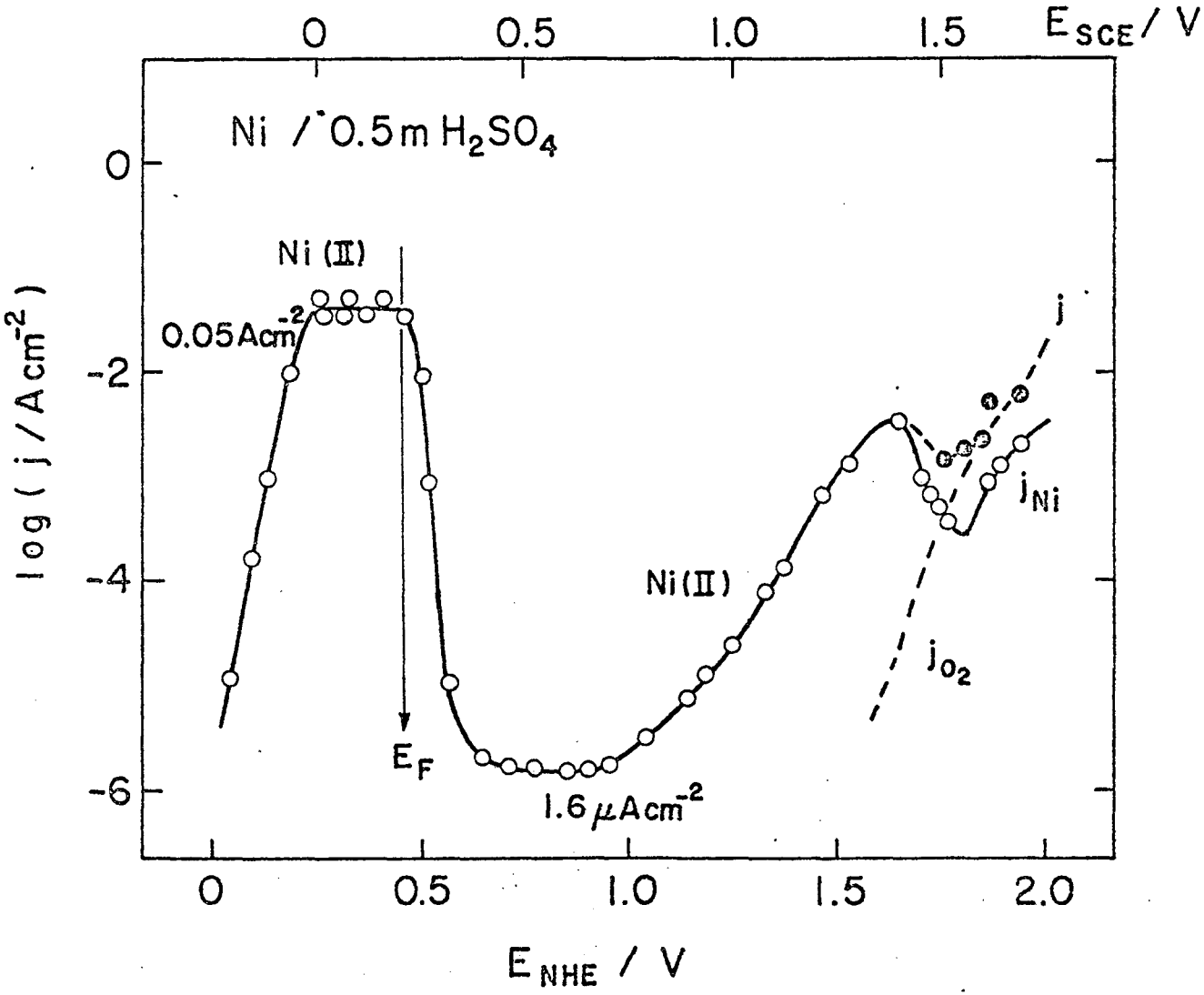

Fig. 10-1. Anodic polarization curve of Ni in 0.5 M H_2SO_4 solution (Sato, 1957).

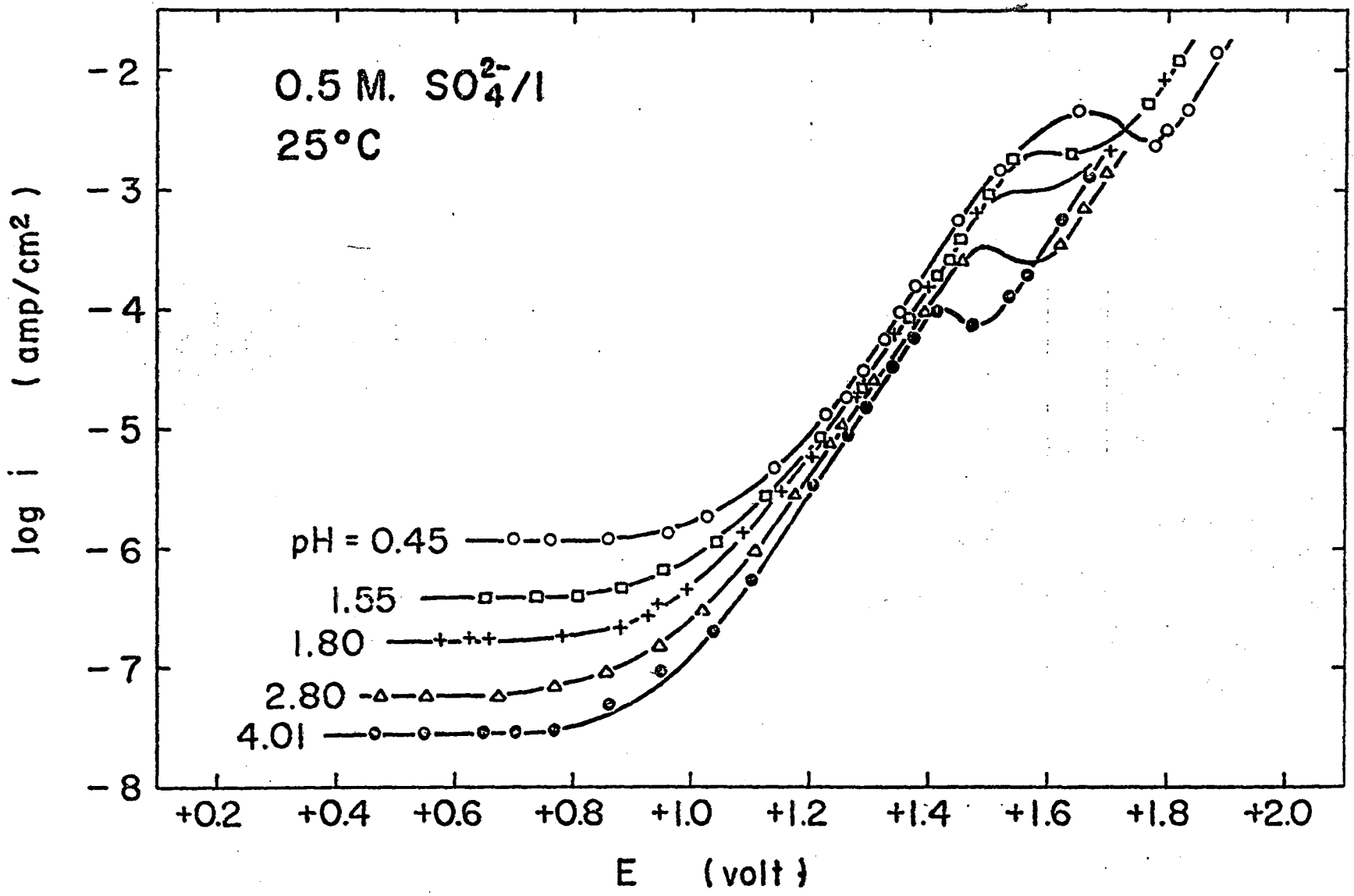

Fig. 10-2. Effect of the concentration of hydrogen-ion upon the stationary anodic polarization curve of nickel in the passive and over-passive region.

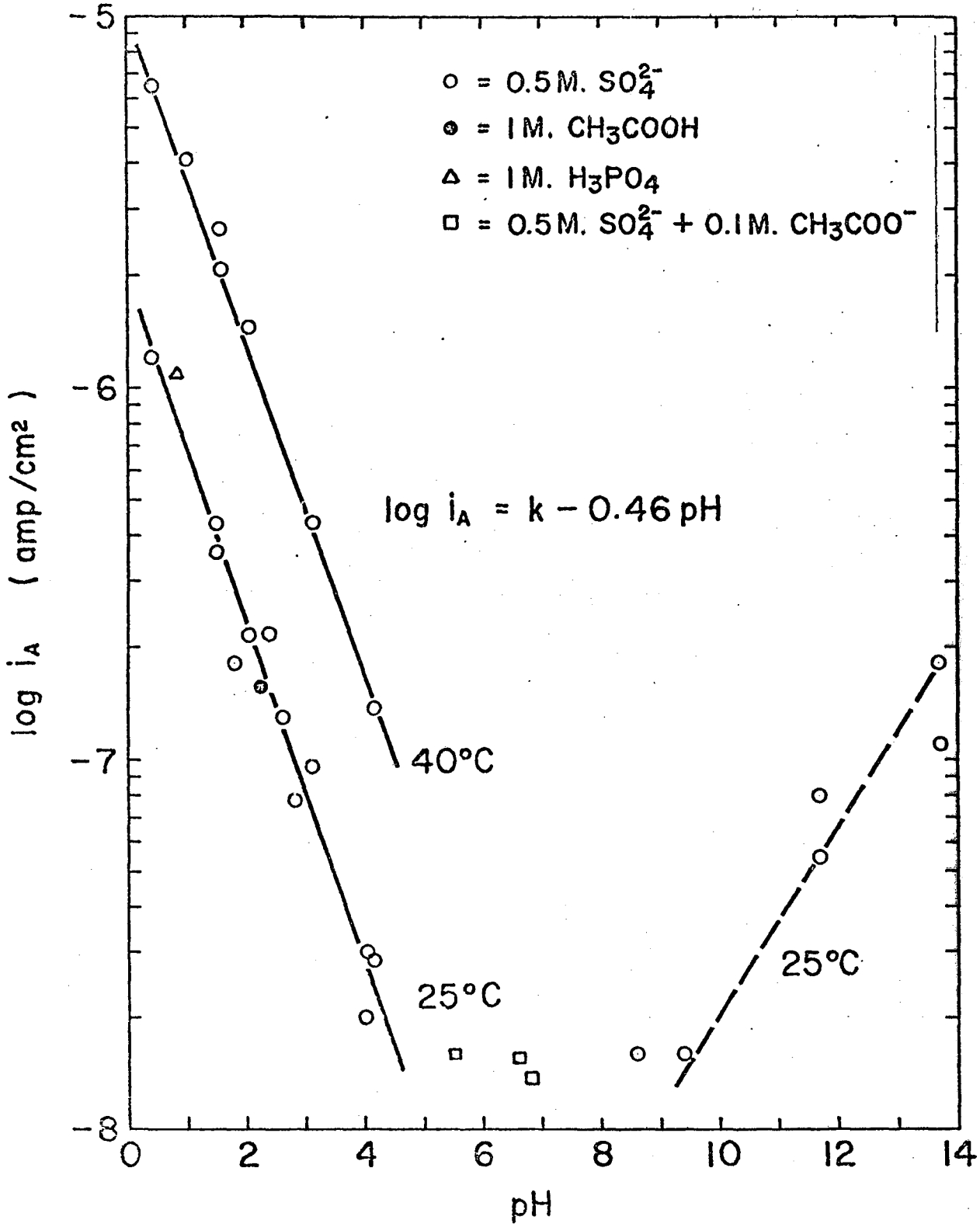

Fig. 10-3. Effect of pH on the dissolution current of passive nickel.

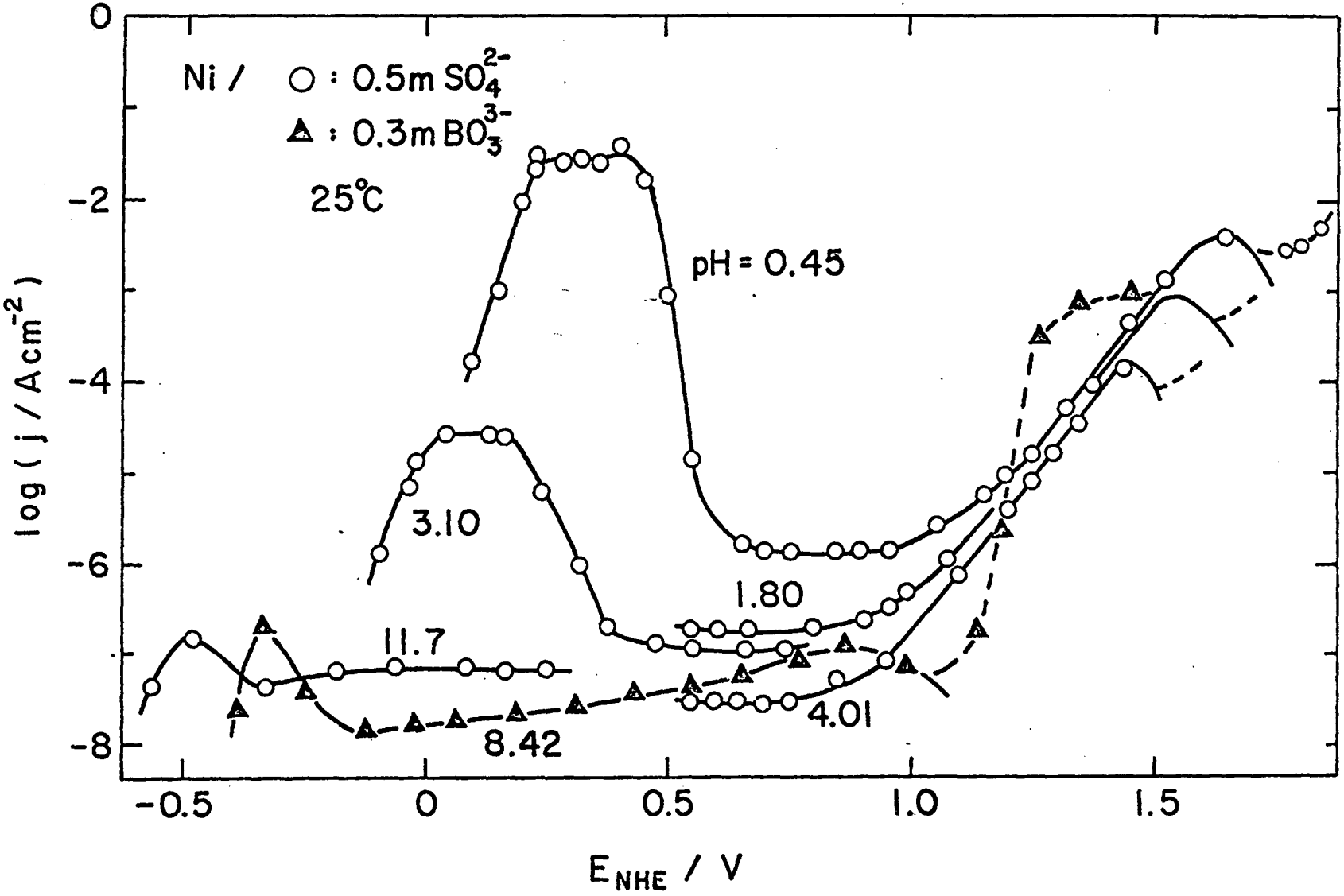

Fig. 10-4. Anodic polarization curve of Ni in verious pH solutions.

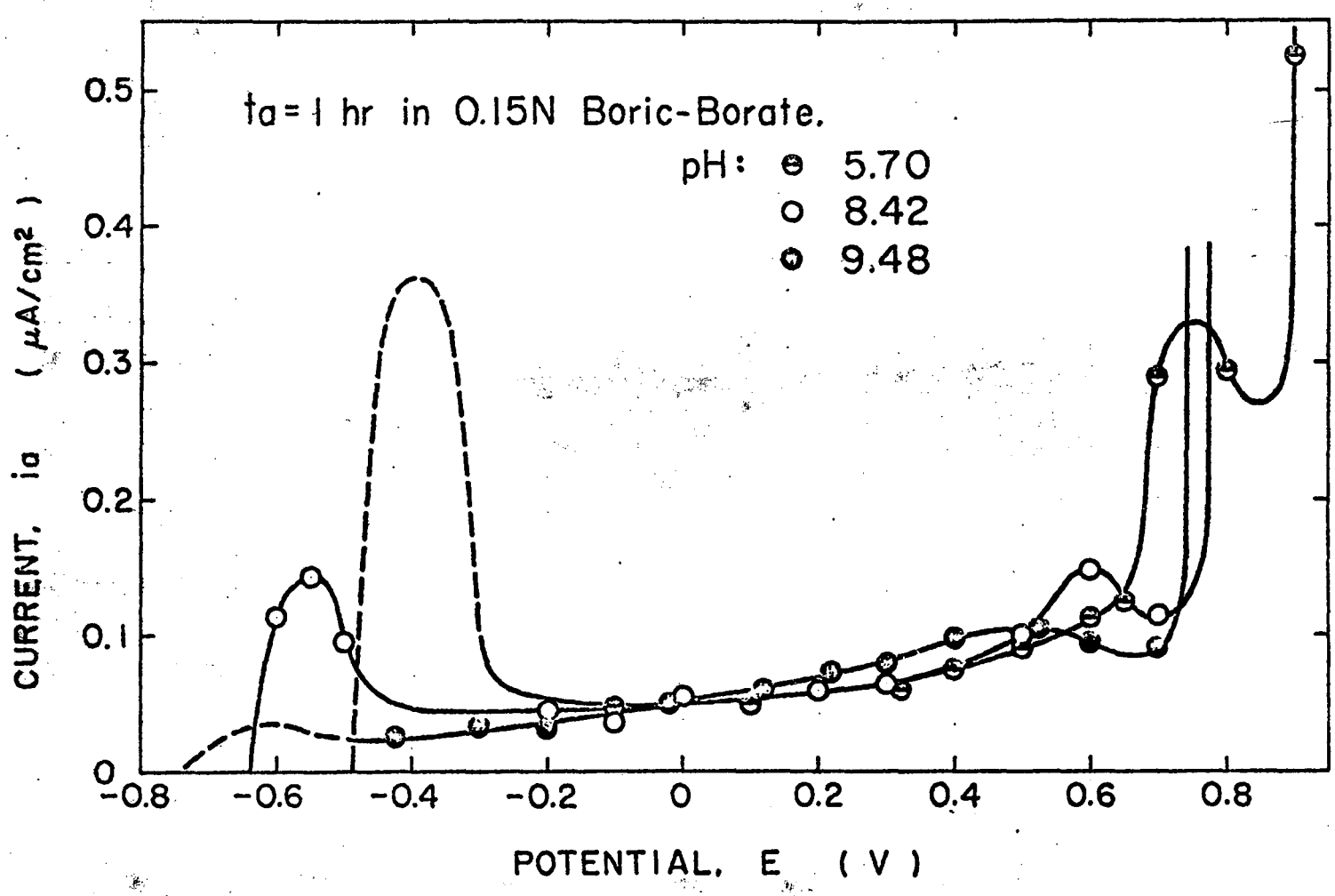

Fig. 10-5. Anodic polarization curves of nickel in sodium borate-boric acid solutions.

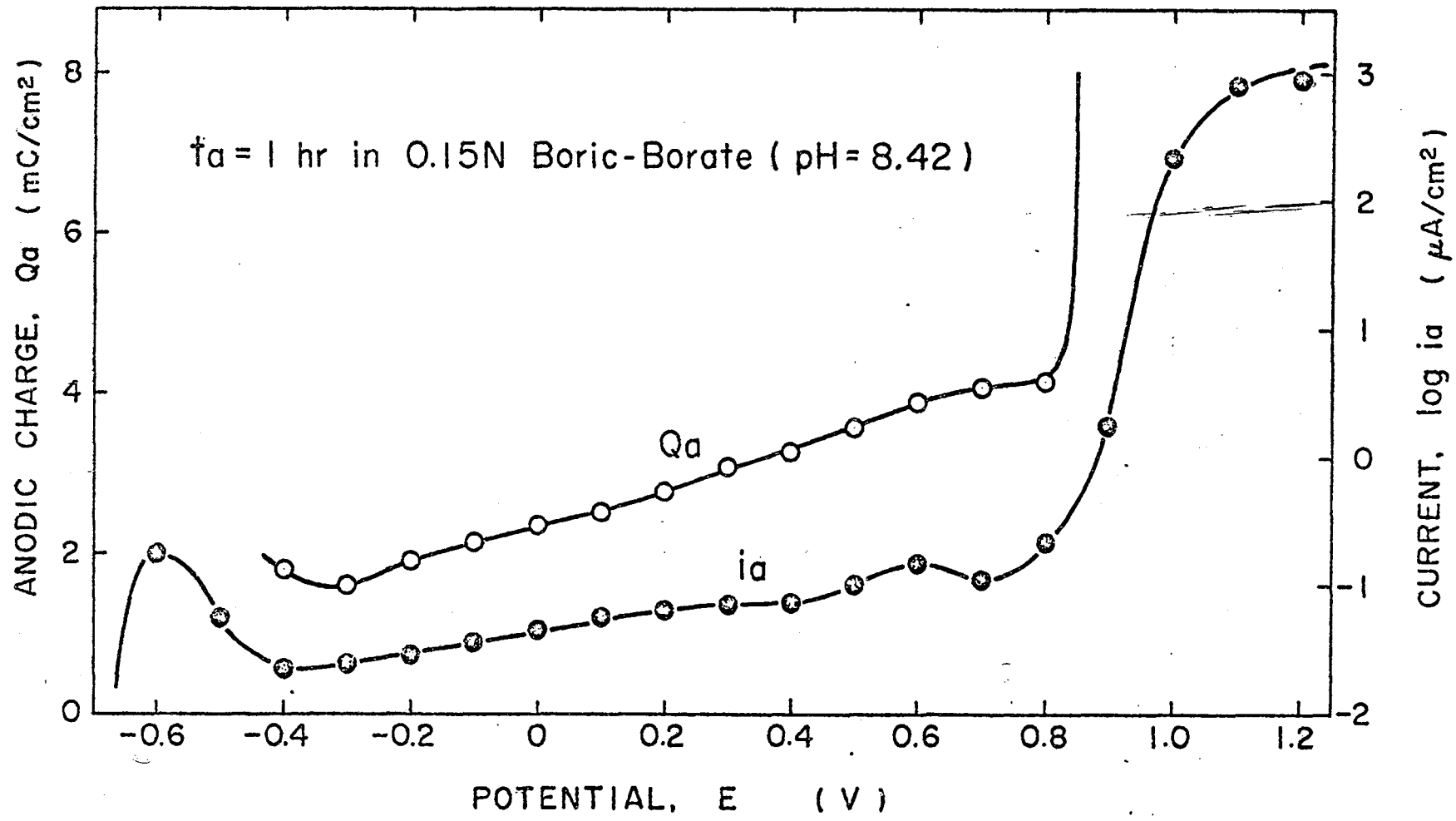

Fig. 10-6. Anodic current dencity and charge passed of nickel measured by 1 hr potentiostatic axidation at each potential in sodium borate-boric acid solution.

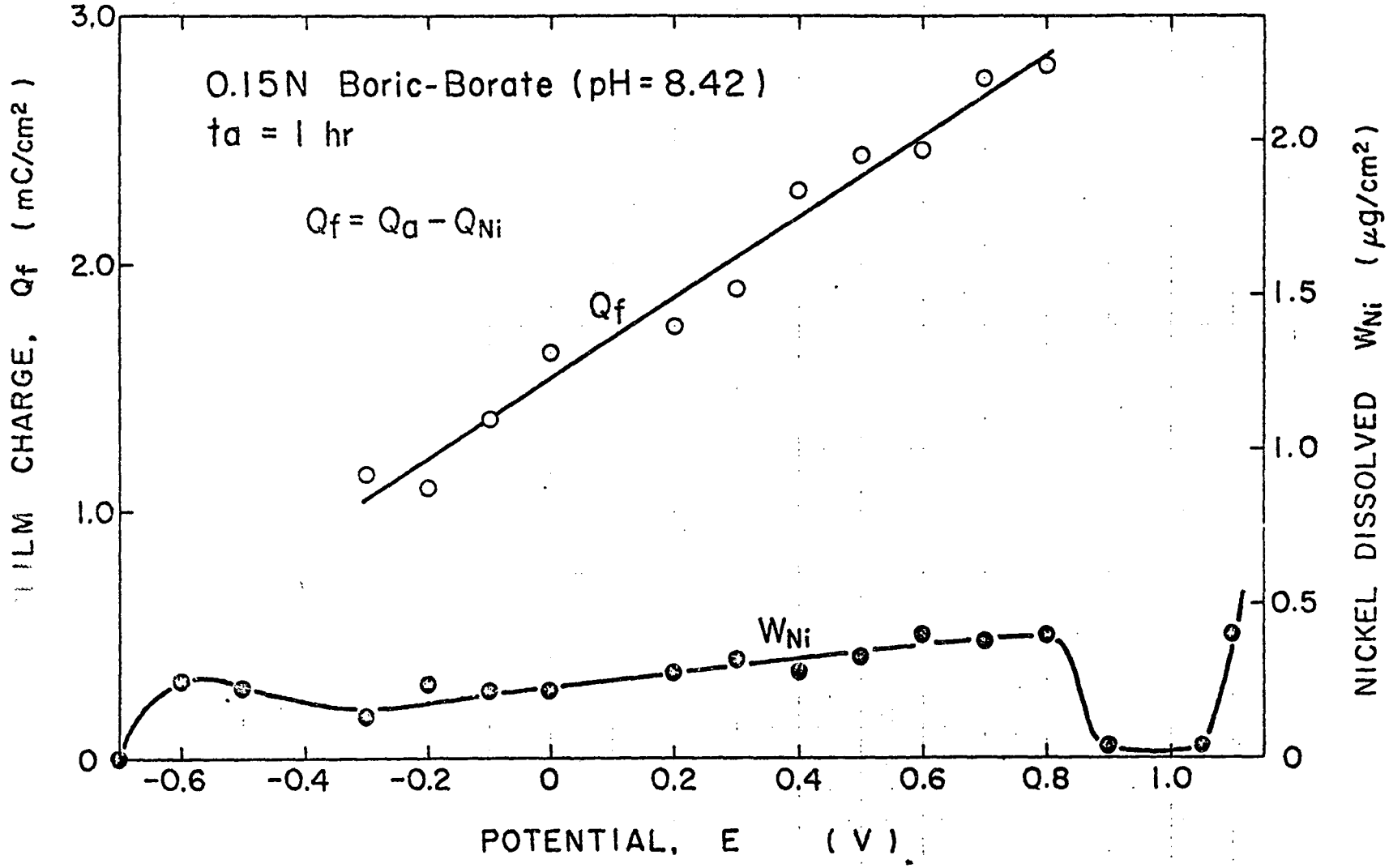

Fig. 10-7. Amount of charge accumulated in the film, Q_f, and of nickel dissolved, W_{Ni}, during 1 hr potentiostatic oxidation of nickel as a function of potential.

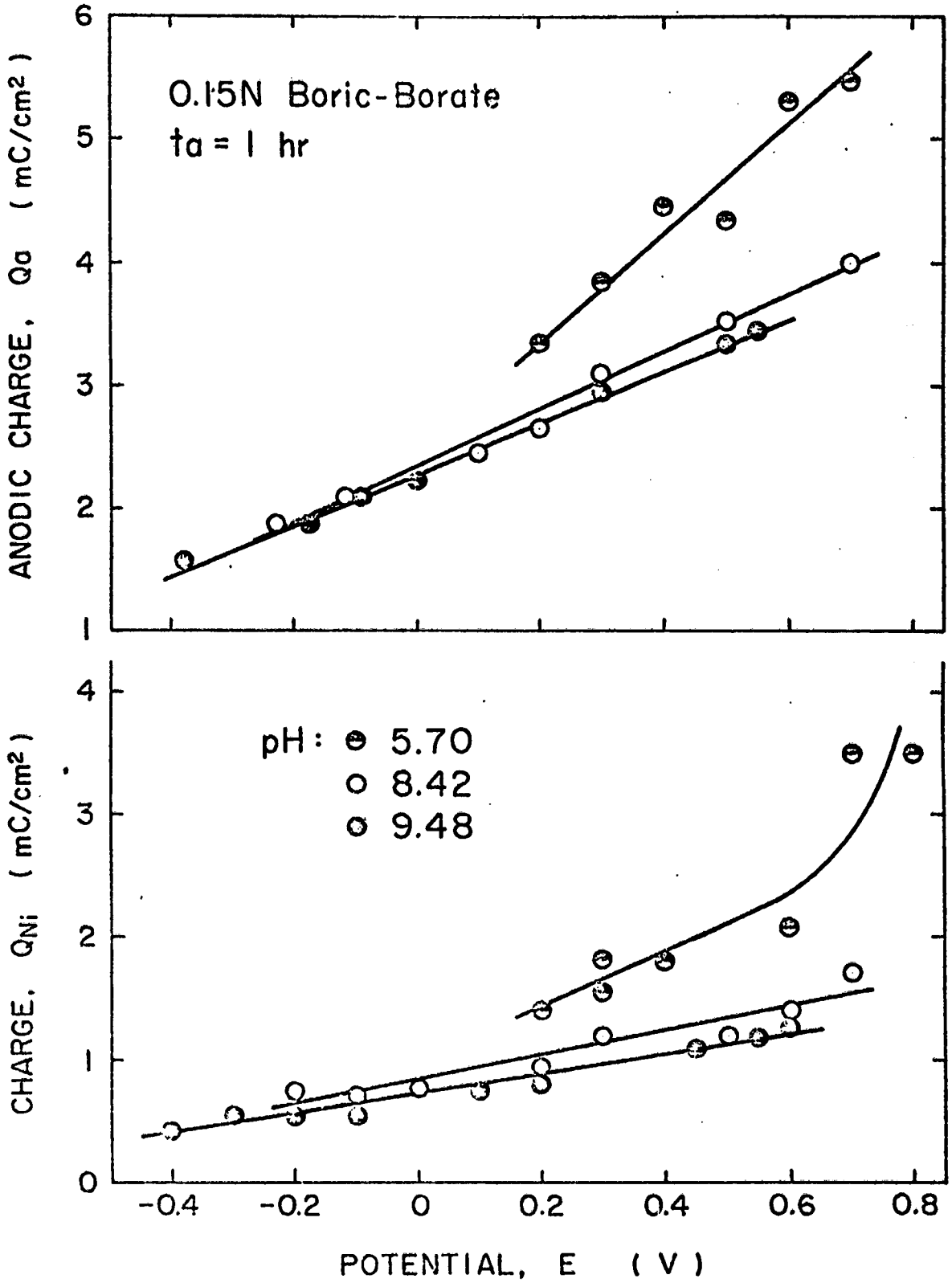

Fig. 10-8. Amount of anodic charge passed, Qa, and charge equivalent to dissolved Ni^{2+}, Q_{Ni}, during 1 hr potentiostatic oxidation of nickel.

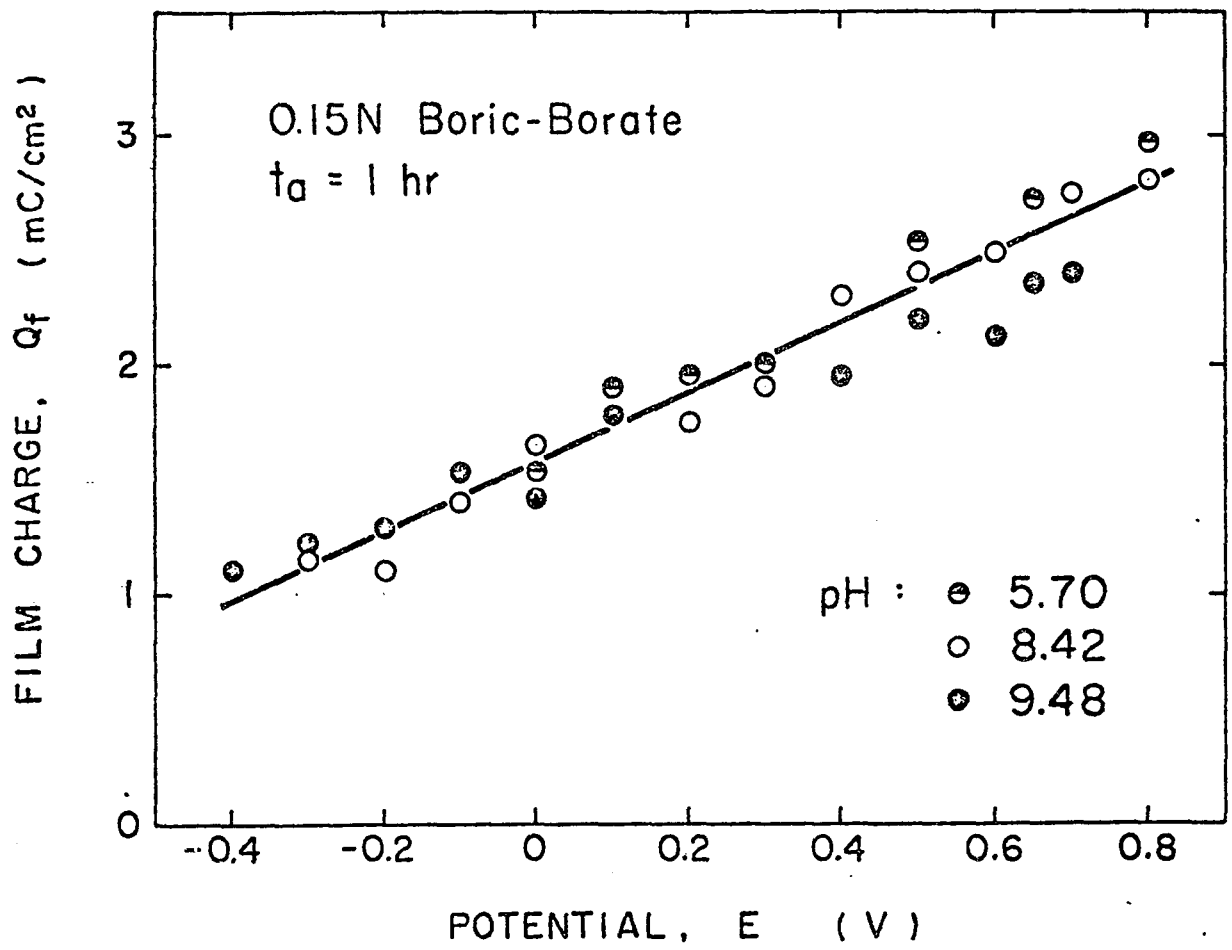

Fig. 10-9. Film charge Q_f obtained by 1 hr potentiostatic oxidation of nickel in 0.15N sodium borate-boric acid solutions.

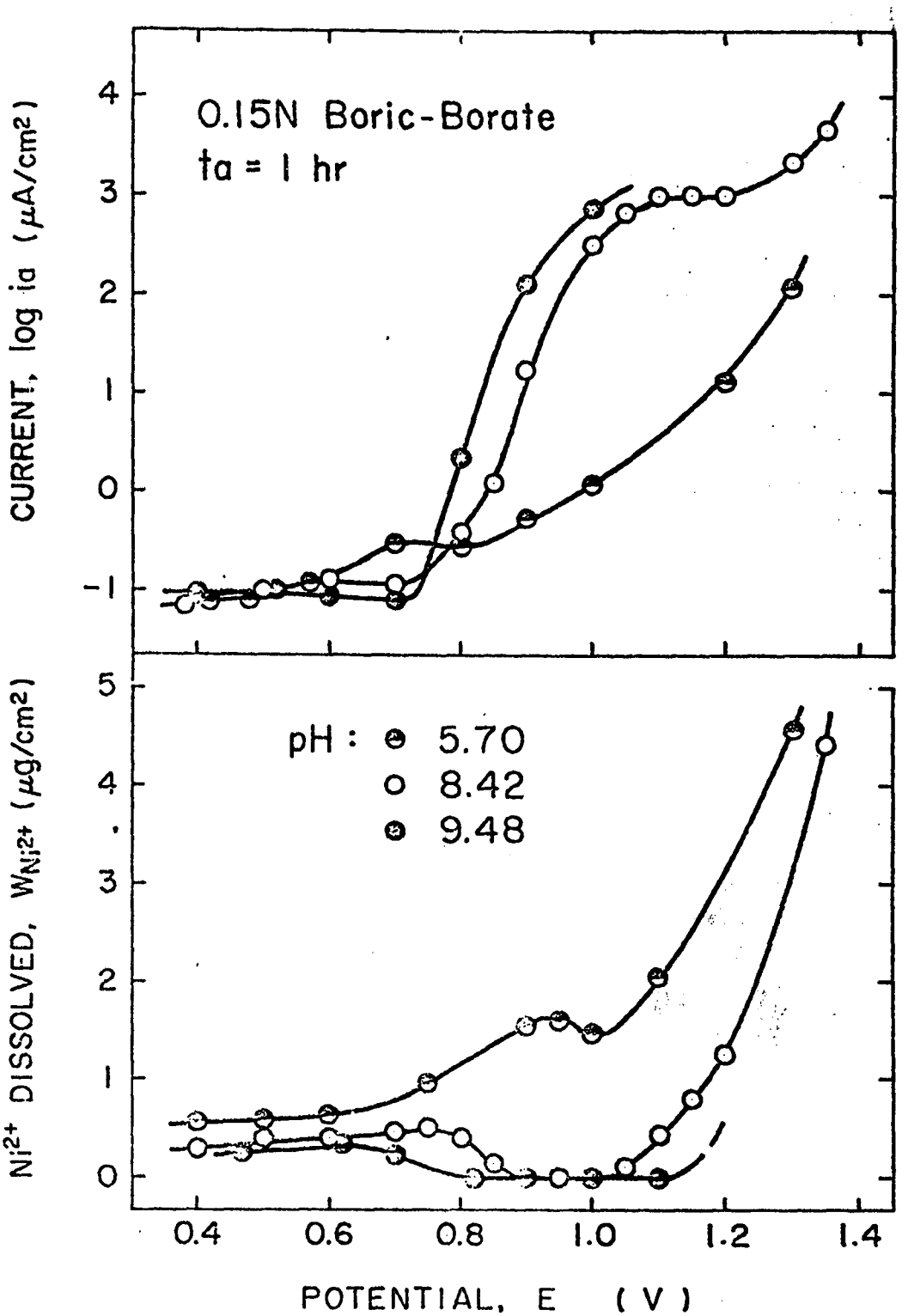

Fig. 10-10. Anodic current at nearly steady state and amount of Ni^{2+} dissolved during 1 hr potentiostatic oxidation of nickel as a function of potential.

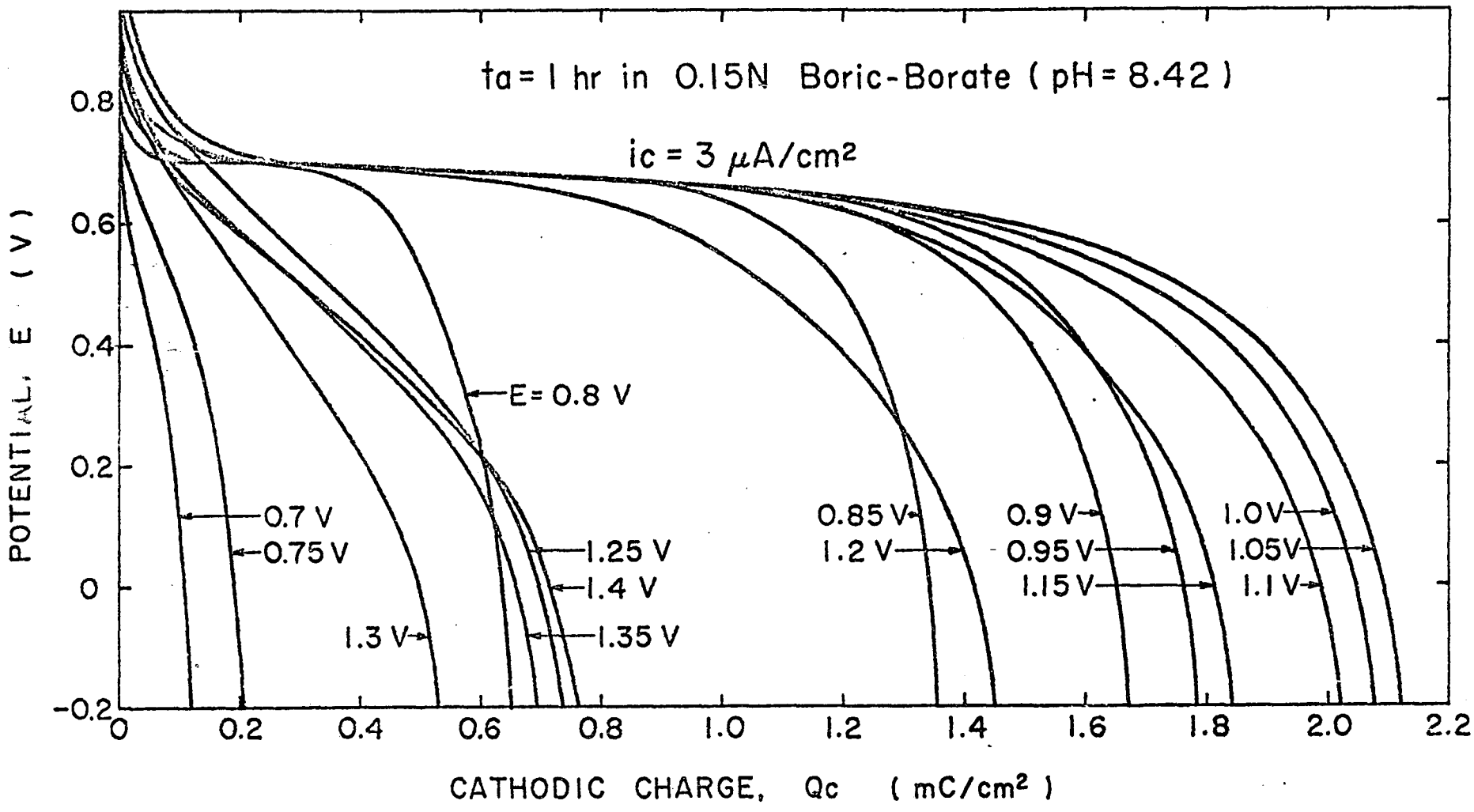

Fig. 10-11. Potential decay curves during galvanostatic cathodic reduction of anodic oxide films formed on nickel by 1 hr potentiostatic oxidation at the potential of secondary passivation, transpassivation and oxygen evolution regions.

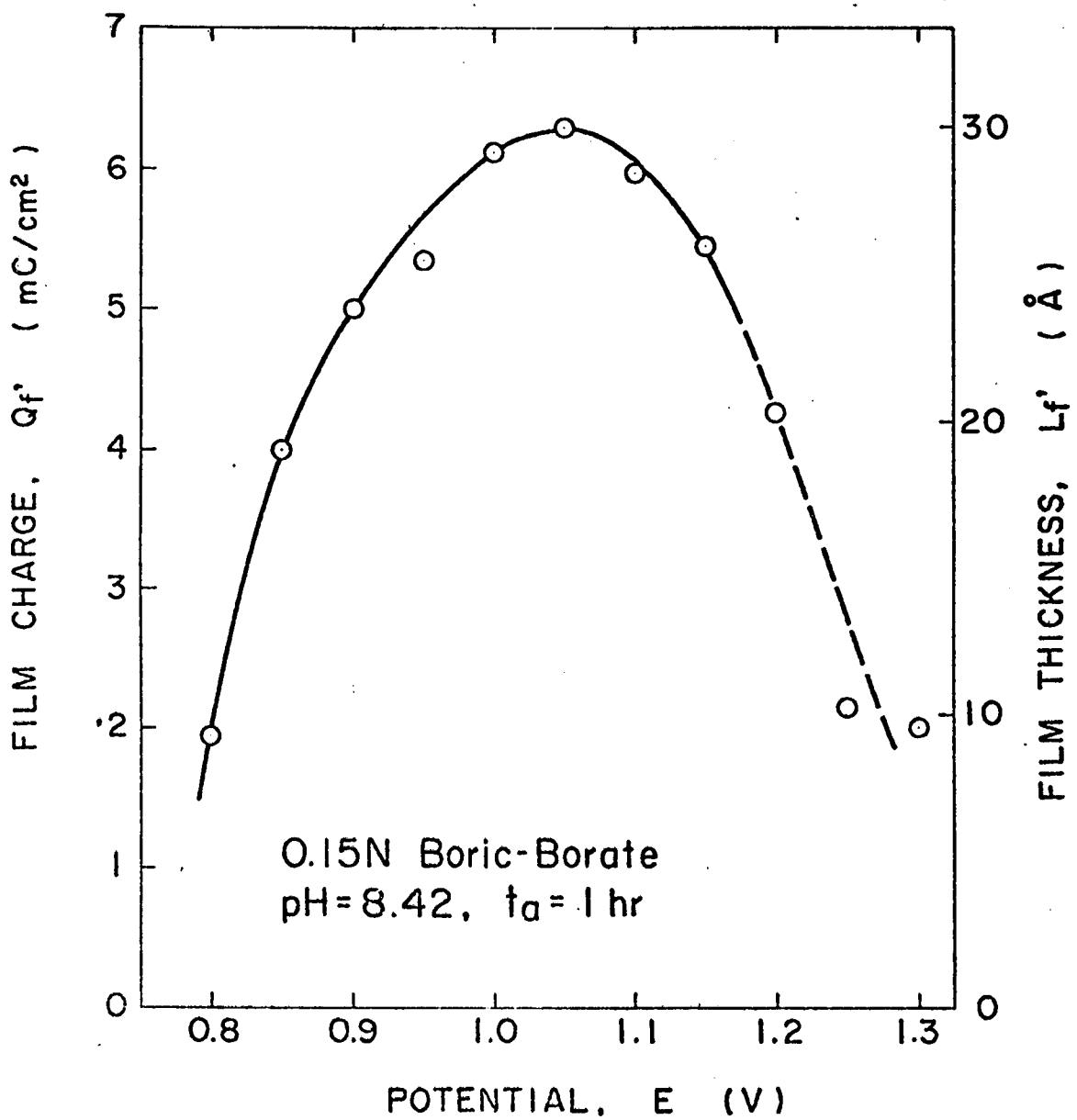

Fig. 10-12. Film charge Q_f' and thickness L_f' of Ni_2O_3 formed on nickel by 1 hr potentiostatic oxidation, Q_f' and L_f' being estimated from cathodic charge required for a potential arrest of potential decay curve assuming reduction of Ni_2O_3 to NiO.

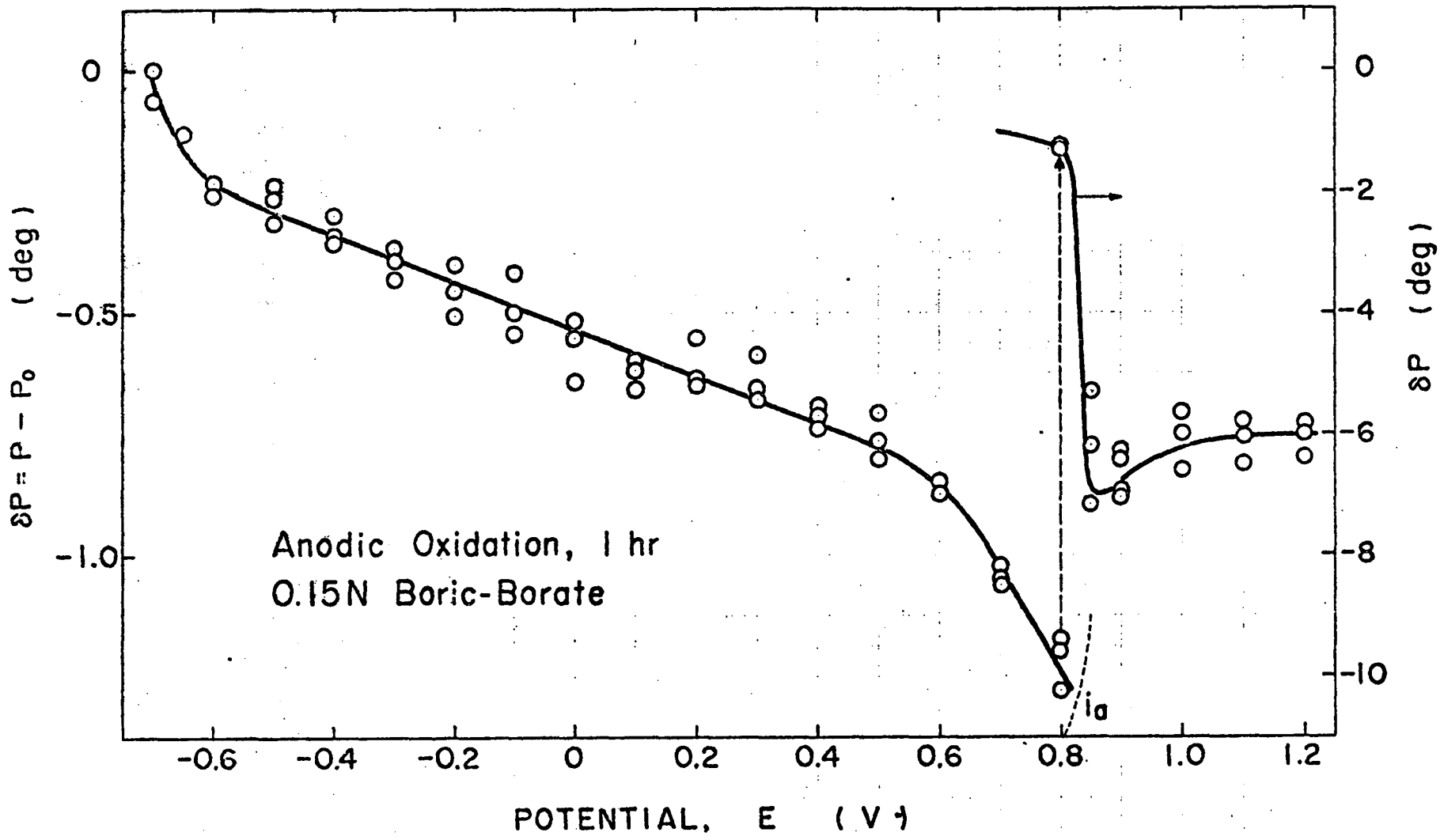

Fig. 10-13. The departure of polarizer settings δP obtained by potentiostatic oxidation of nickel for 1 hr at various potentials.

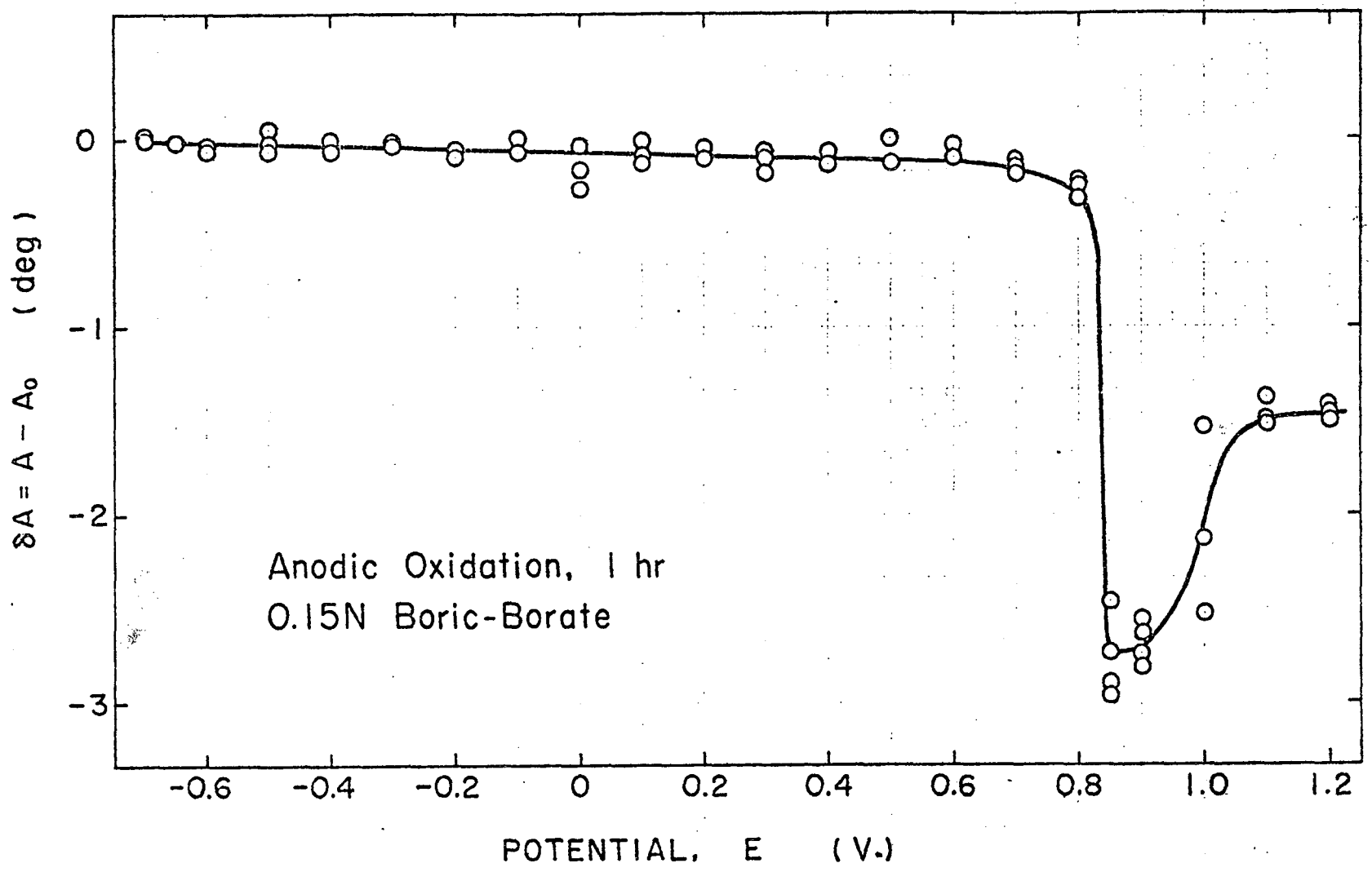

Fig. 10-14. The departure of analyzer settings δA obtained by potentiostatic oxidation of nickel for 1 hr at various potentials.

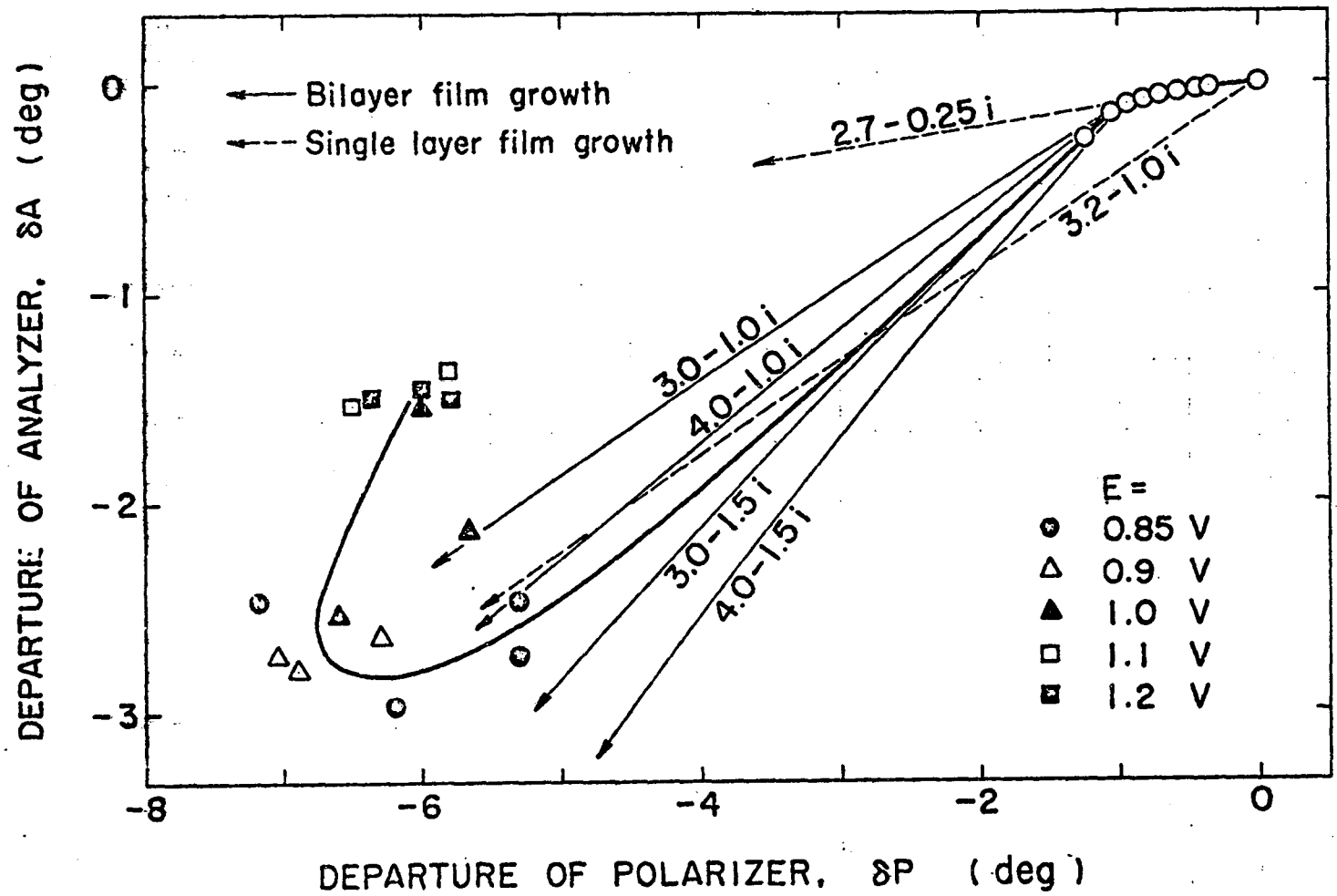

Fig. 10-15. Experimental changes of δA and δP in oxygen evolution region compared with theoretical changes computed for various optical constants and for single and double films.

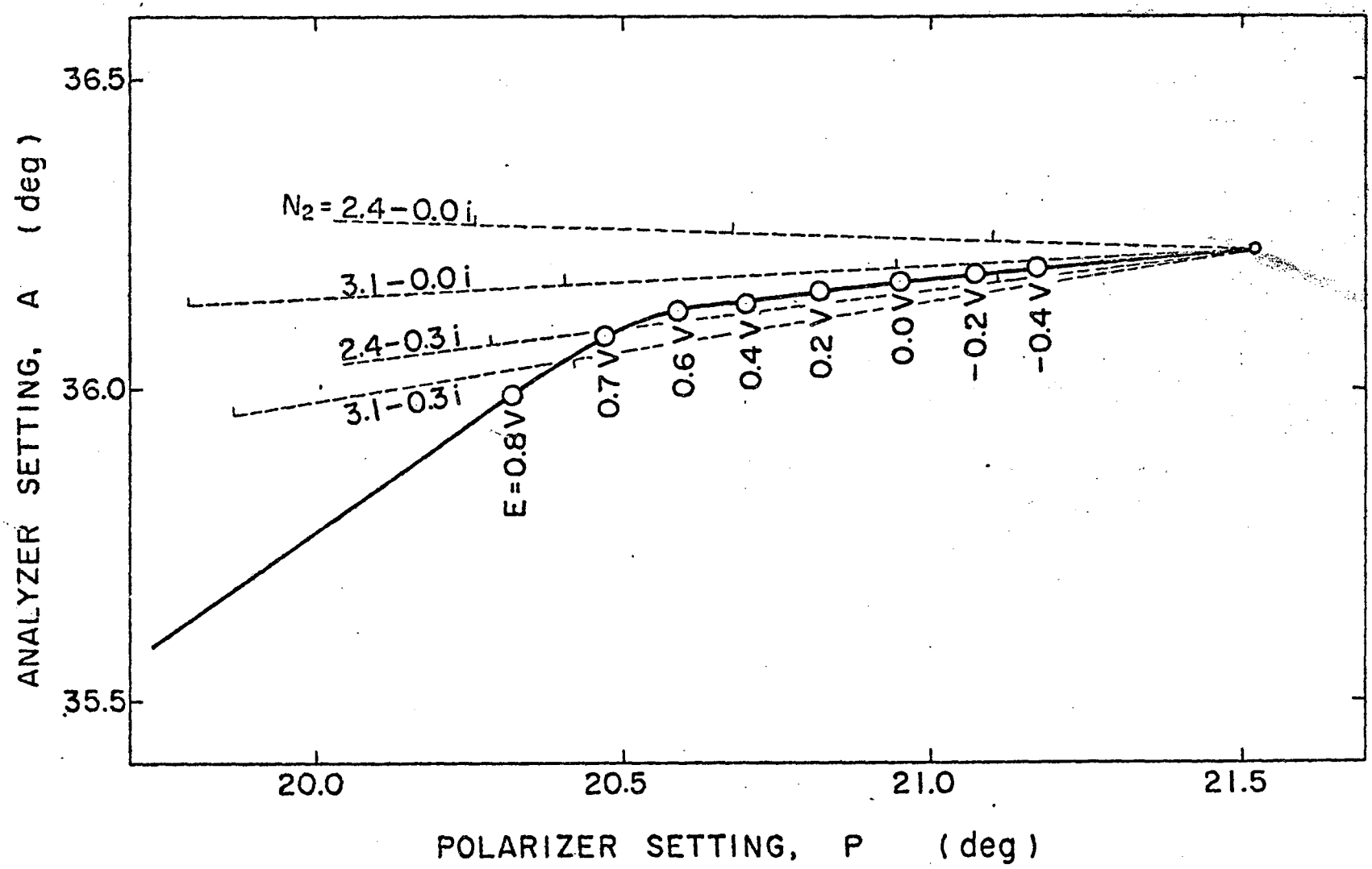

Fig. 10-16. A comparison between experimental change of P and A in passive region and theoretical changes of a film with various optical constants.

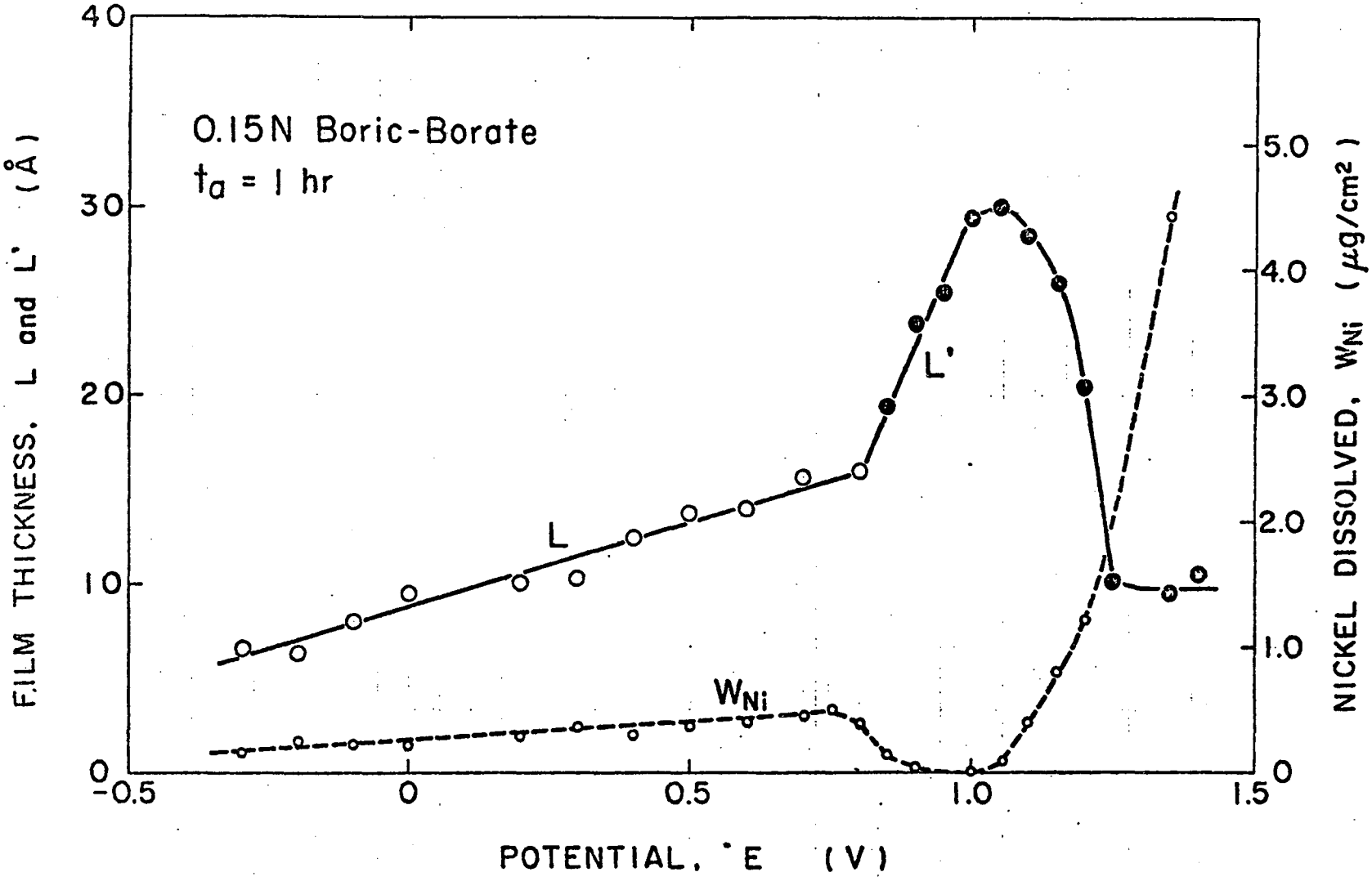

Fig. 10-17. Film thickness and dissolution versus potential of passive nickel in borate solution of pH 8.42.

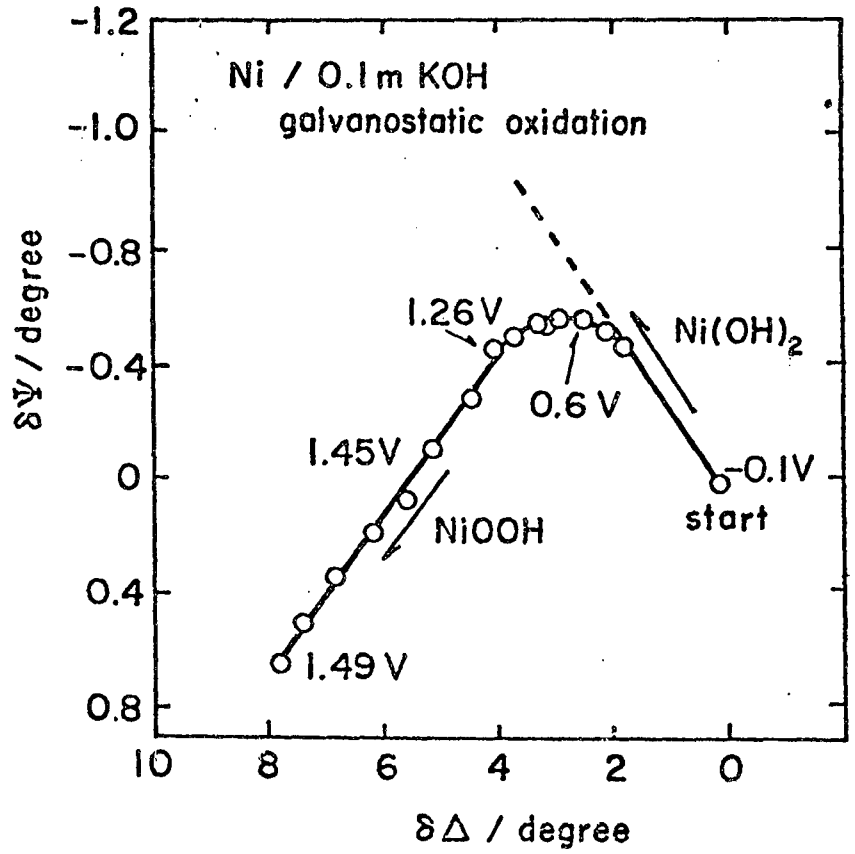

Fig. 10-18. Ellipsometric parameters changing during galvanostatic oxidation of Ni in 0.1 M KOH solution (Wisscher et al., 1976).

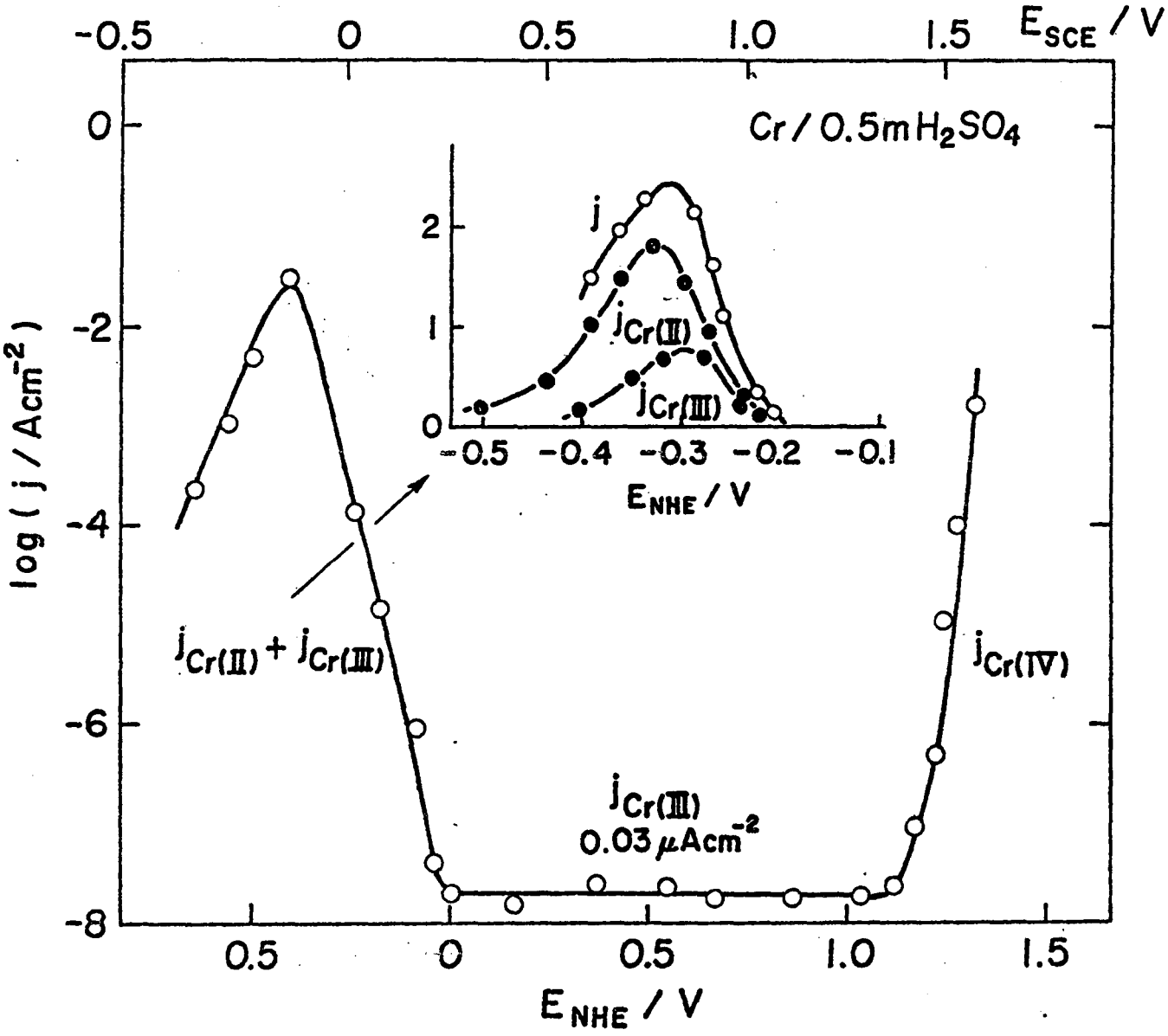

Fig. 11-1. Anodic polarization curve of Cr in 0.5 M H_2SO_4 (Kolotyrkin, 1958) and ionic valency of dissolution in the active state (Armstrong et al., 1972).

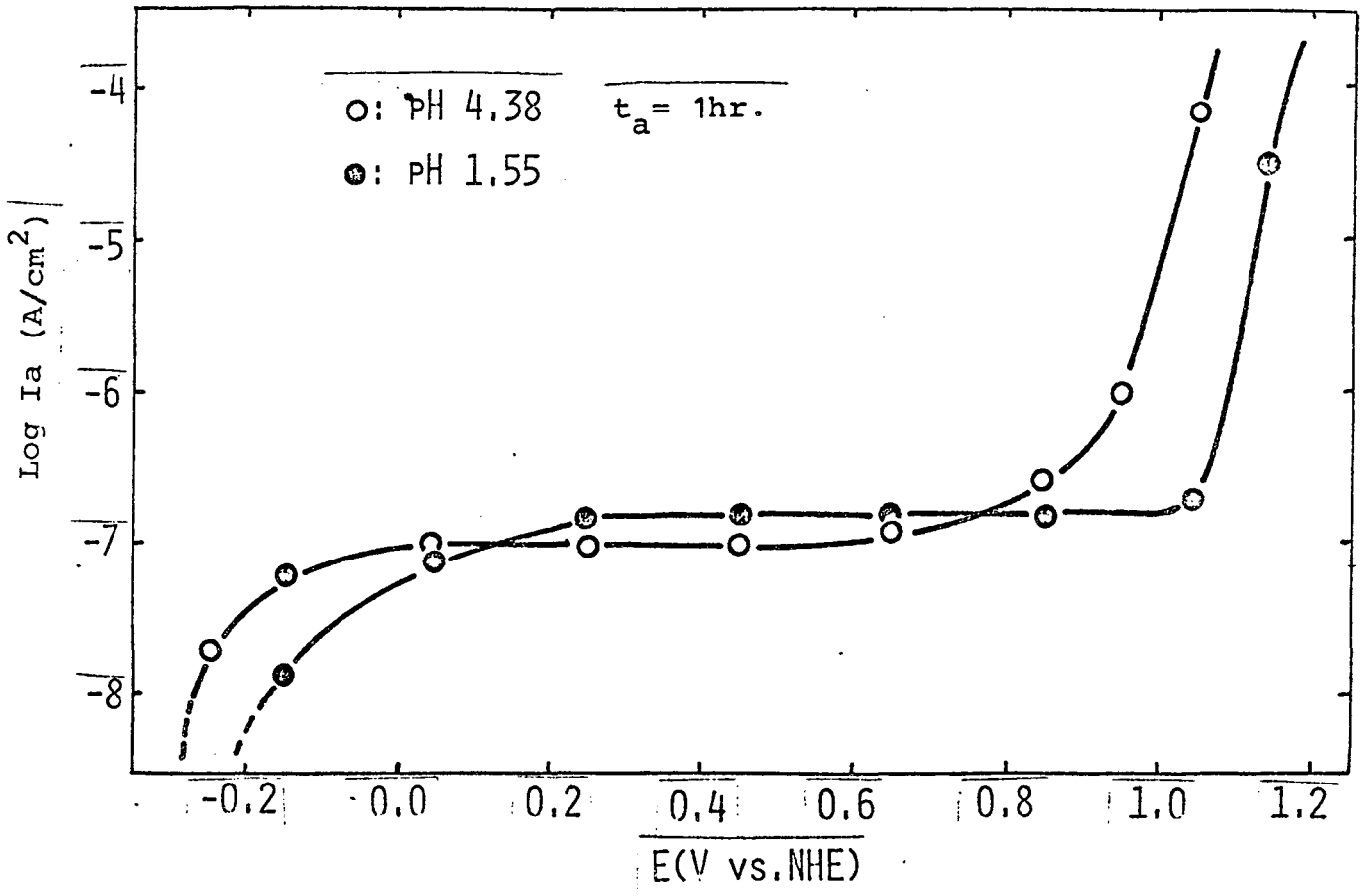

Fig. 11-2. Anodic polarization curves of Cr in 0.15 M PO_4^{3-} solutions. A bare surface was obtained by a cathodic reduction at -1.45 V for 15 min in a 0.15 M PO_4^{3-} solution at pH 4.38.

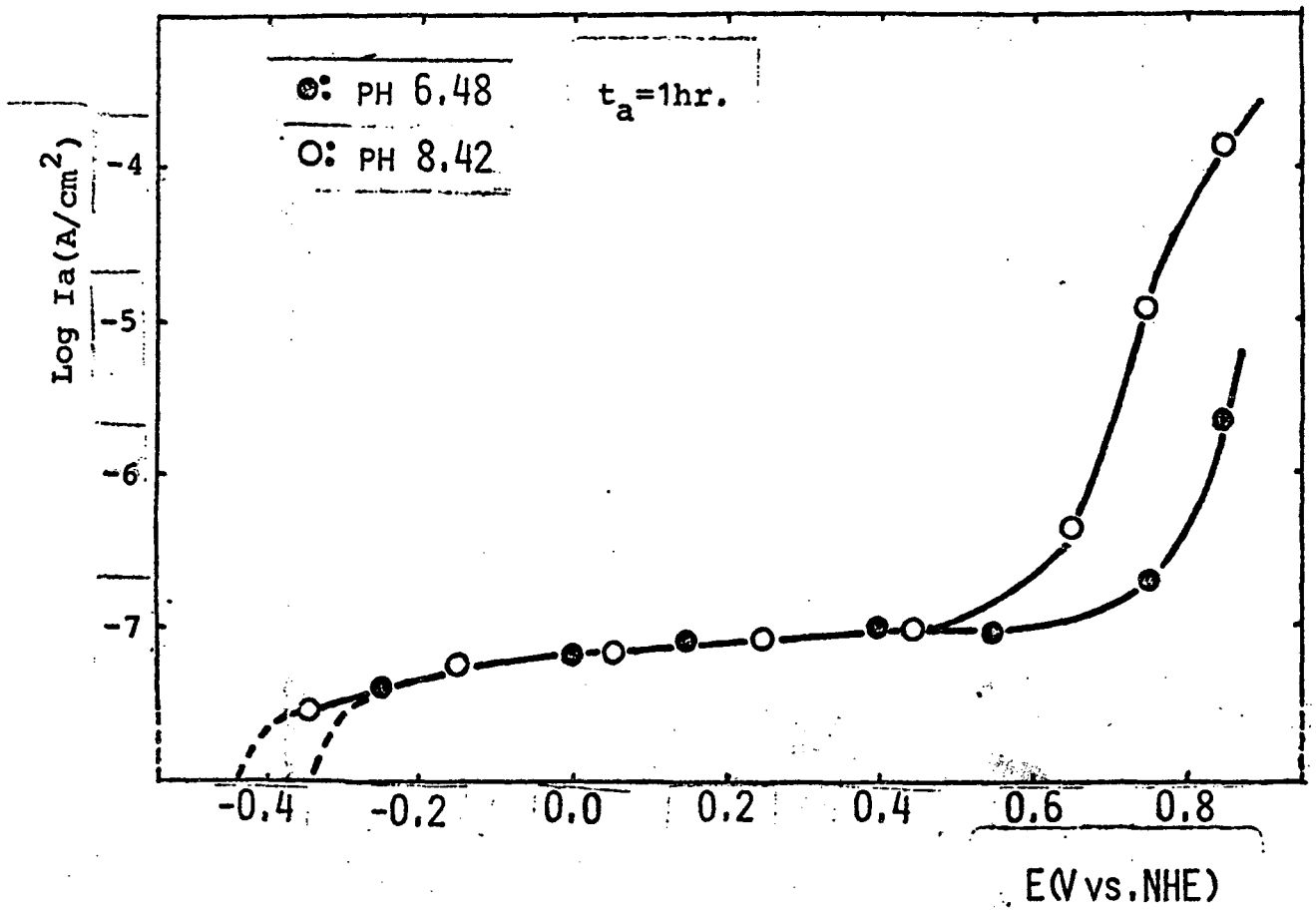

Fig. 11-3. Anodic polarization curves of Cr in 0.3 M BO_3^{3-} solutions.

Fig. 11-4. Anodic charge and dissolution charge of Cr versus potential in 0.15 M PO_4^{3-} solution.

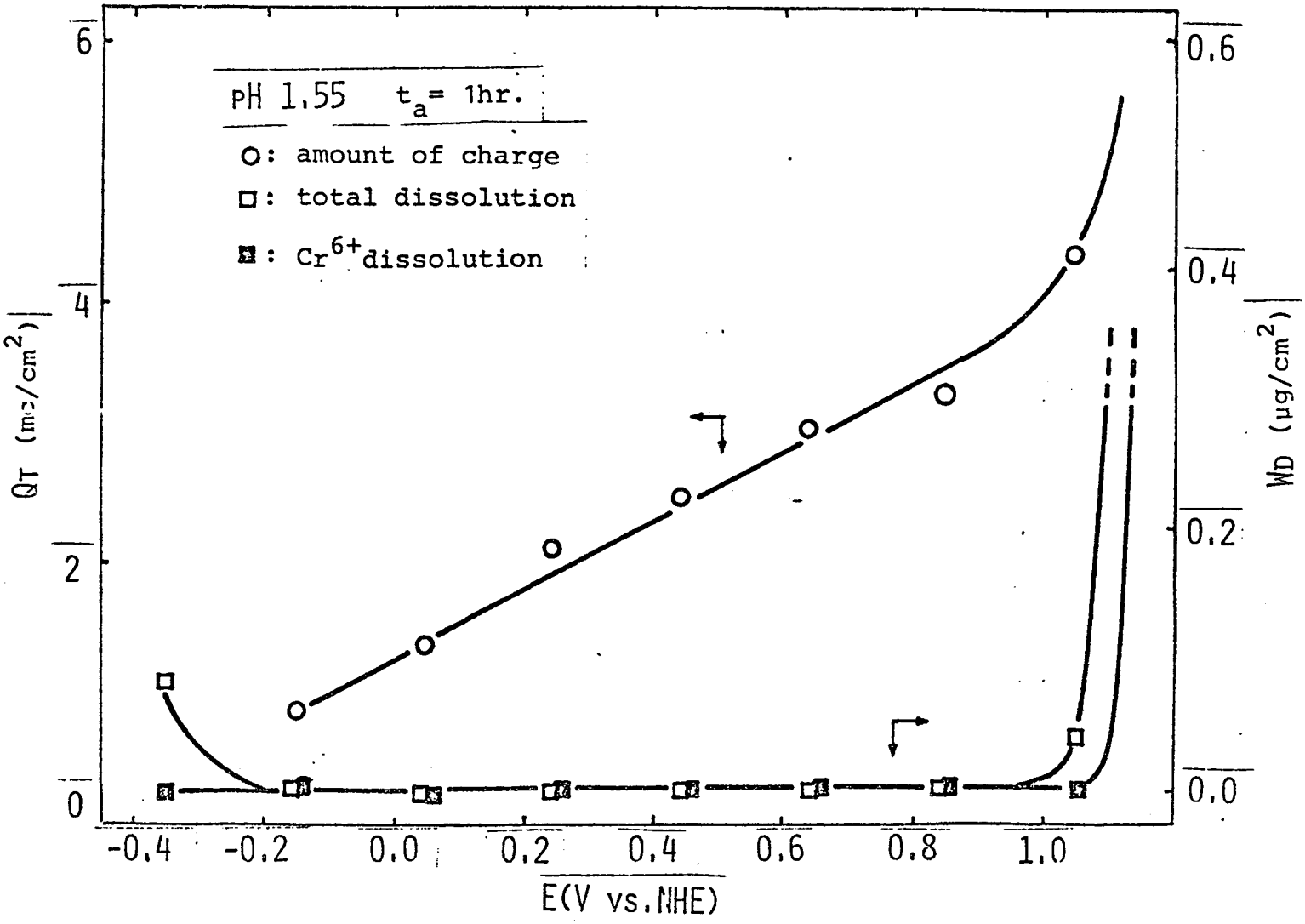

Fig. 11-5. Anodic charge and dissolution charge of Cr versus potential in 0.15 M PO_4^{3-} solution.

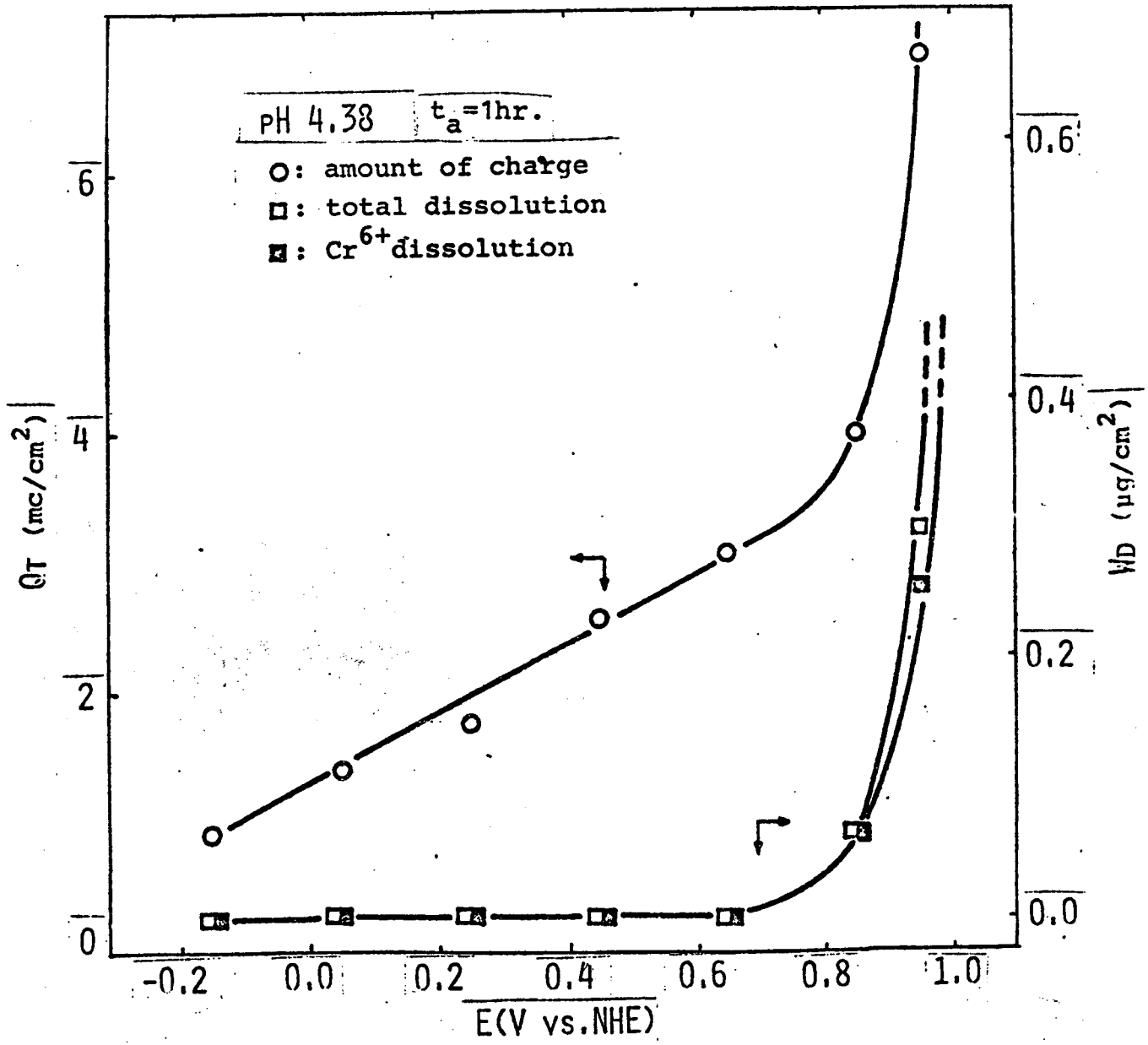

Fig. 11-6. Anodic charge and dissolution charge of Cr versus potential in 0.3 M BO_3^{3-} solutions.

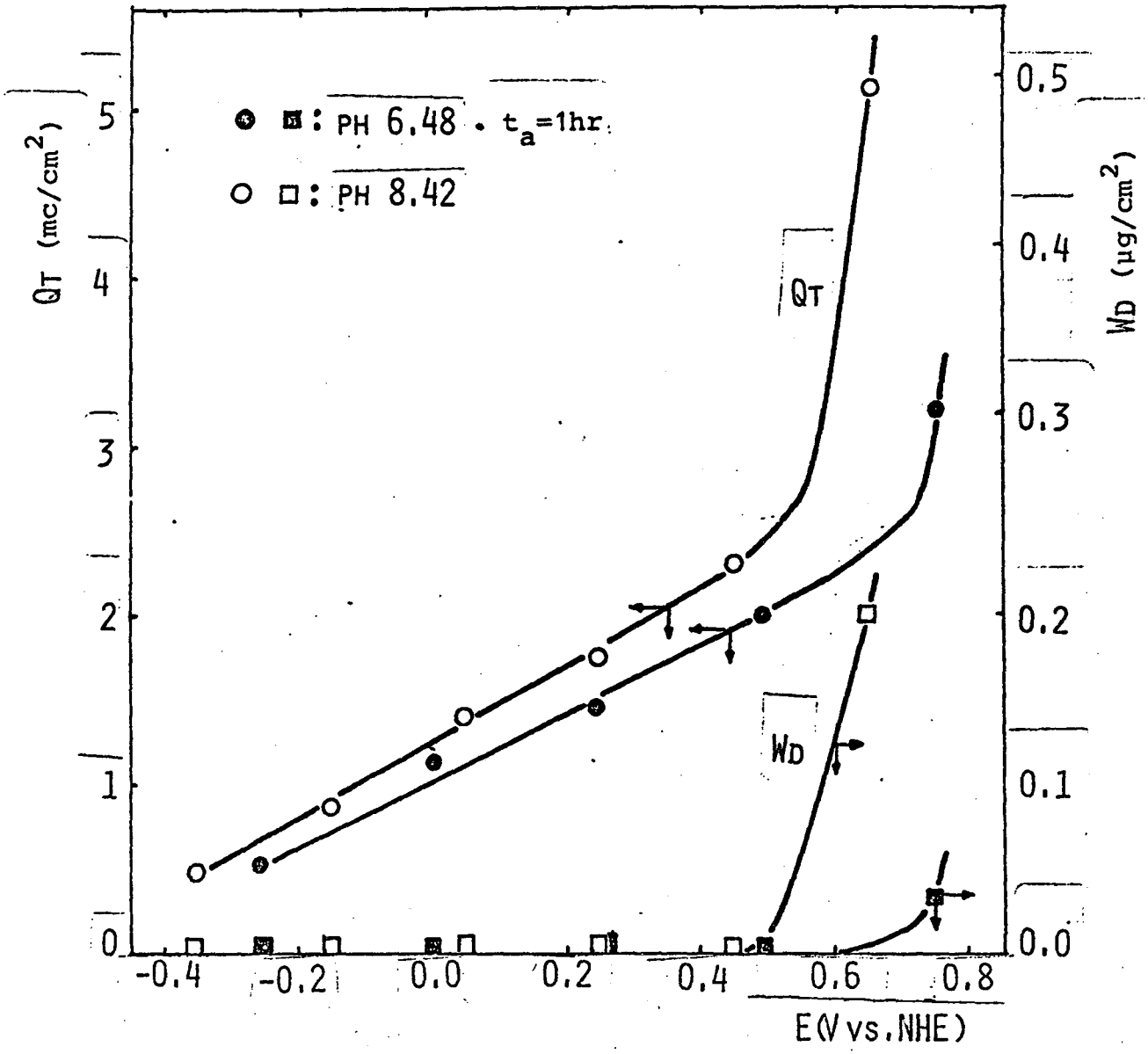

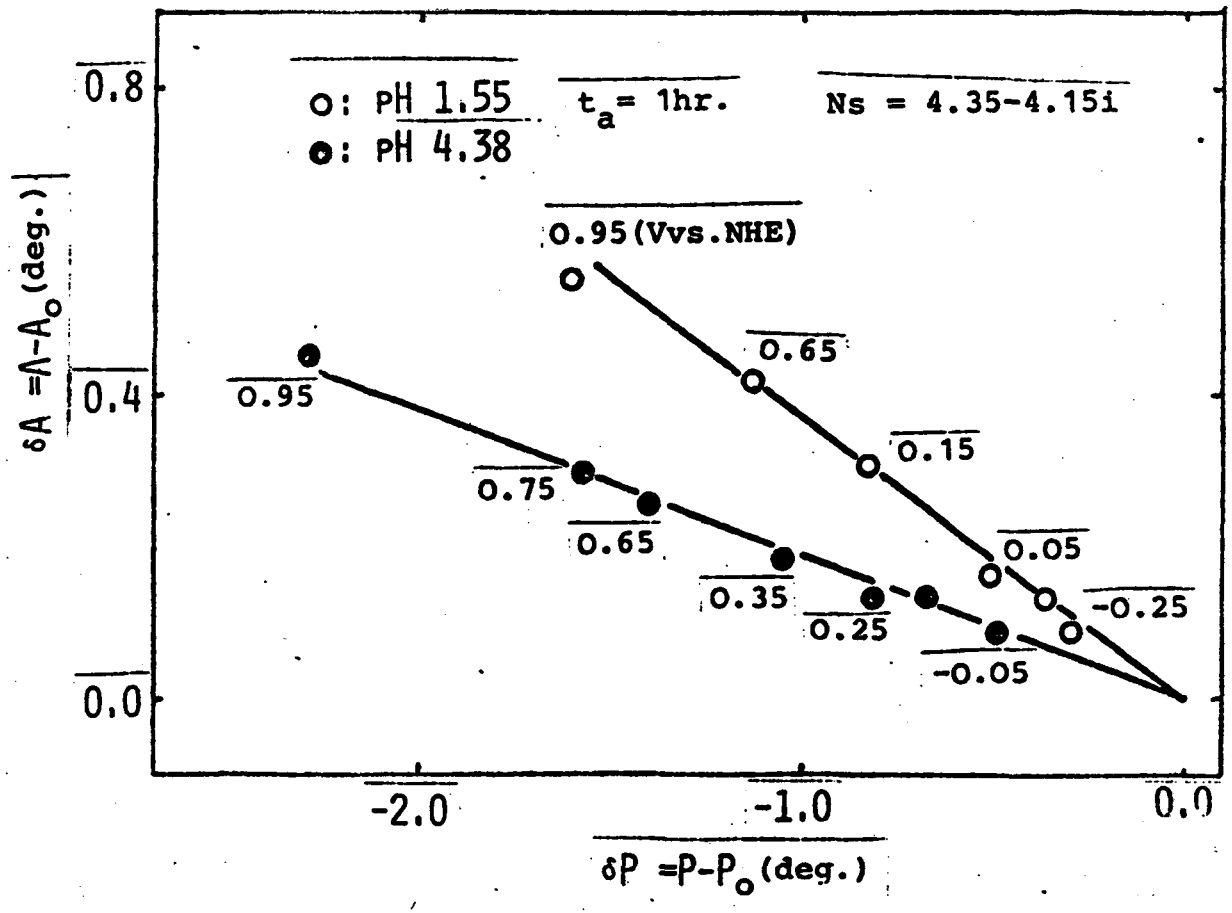

Fig. 11-7. Ellipsometric parameters of the passive films on Cr at versus potentials in 0.15 M PO_4^{3-} solutions.

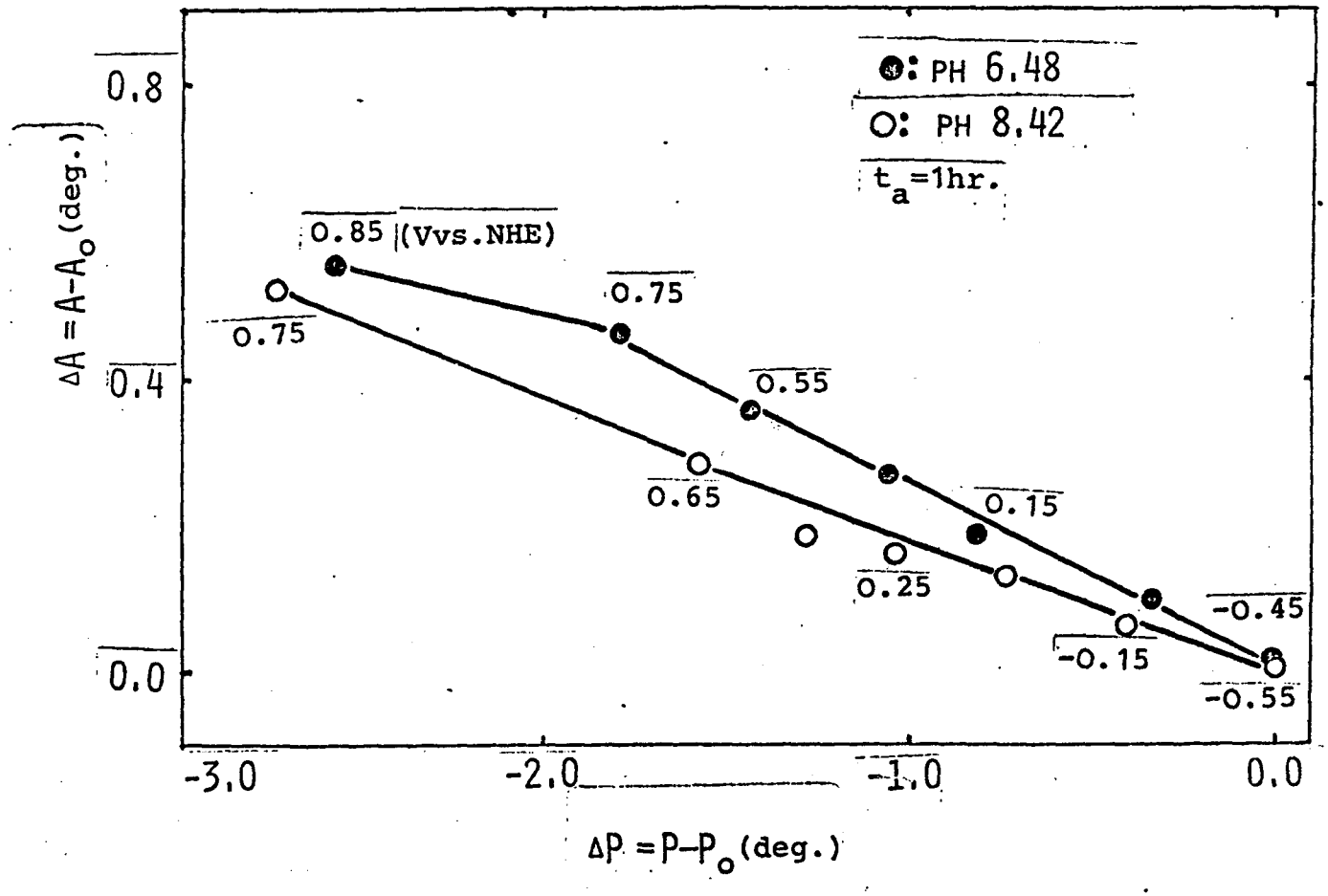

Fig. 11-8. Ellipsometric parameters of the passive films on Cr at versus potentials in 0.15 M PO_4^{3-} solutions.

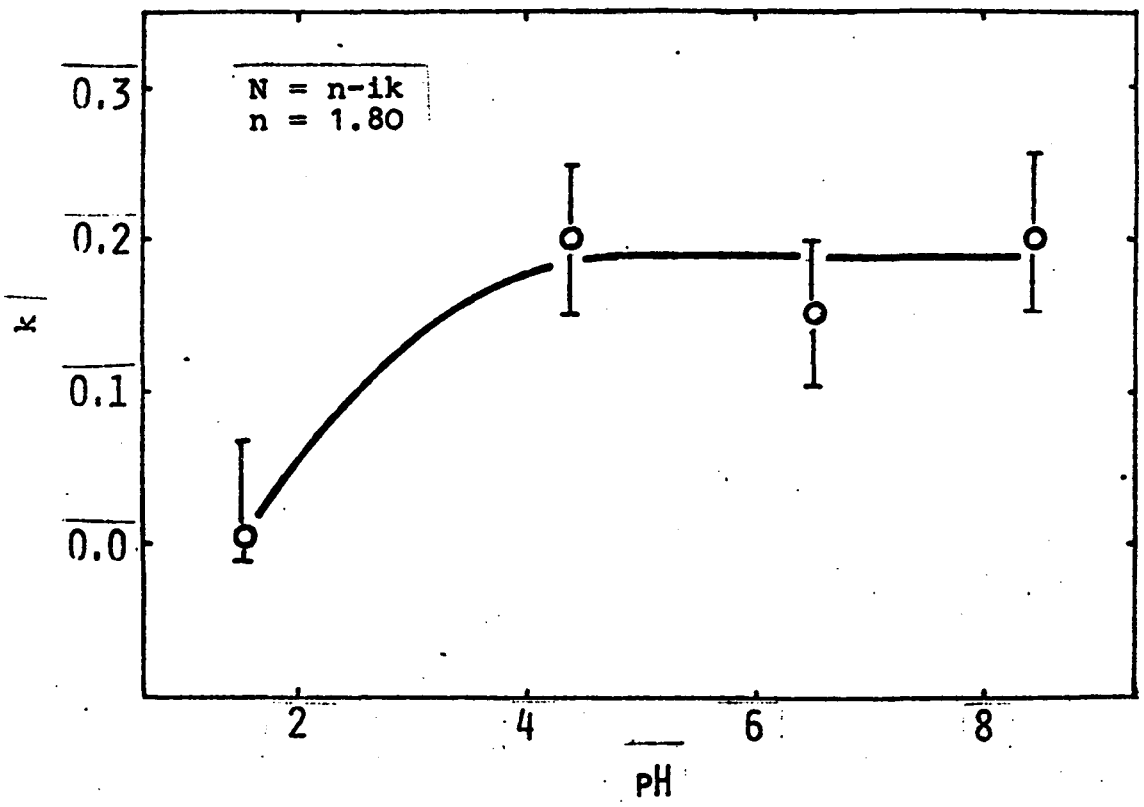

Fig. 11-9. Optical constant of the passive film on Cr versus pH.

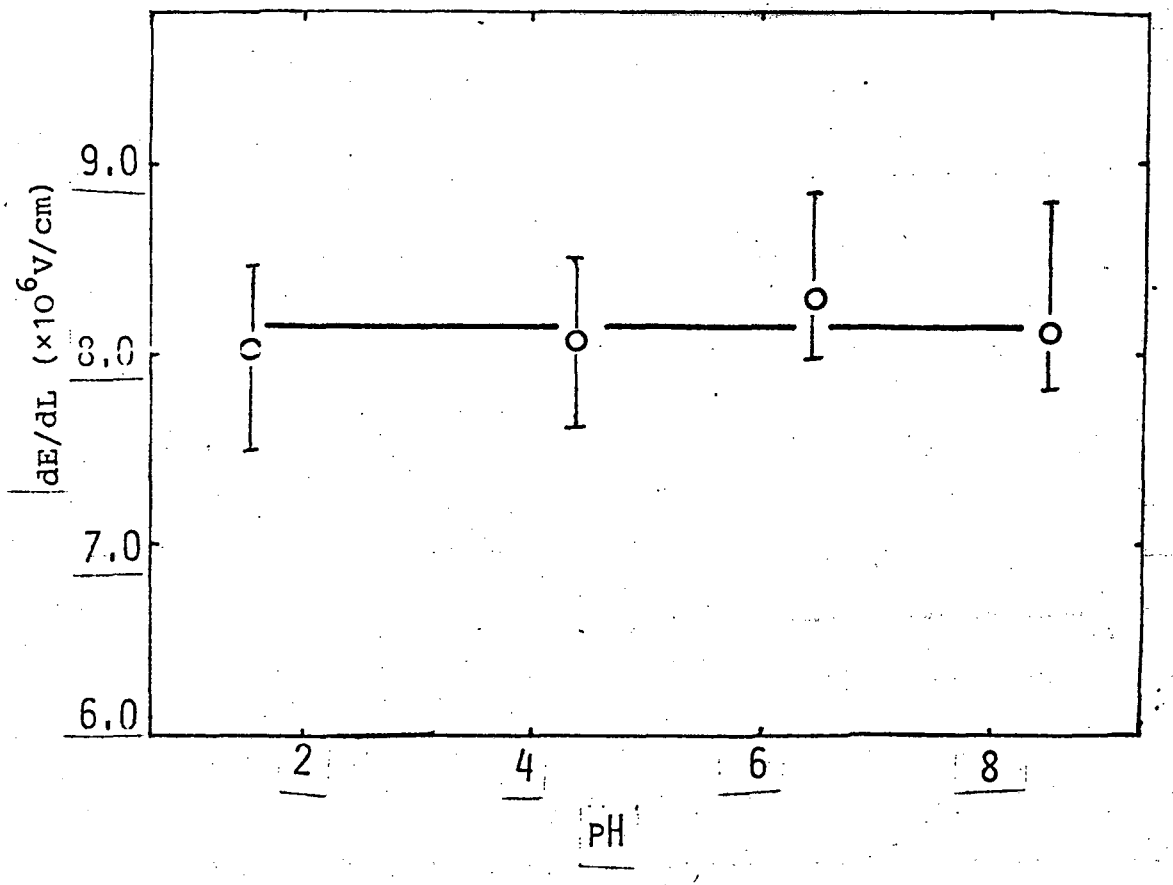

Fig. 11-10. Field strength in the passive film on Cr versus pH.

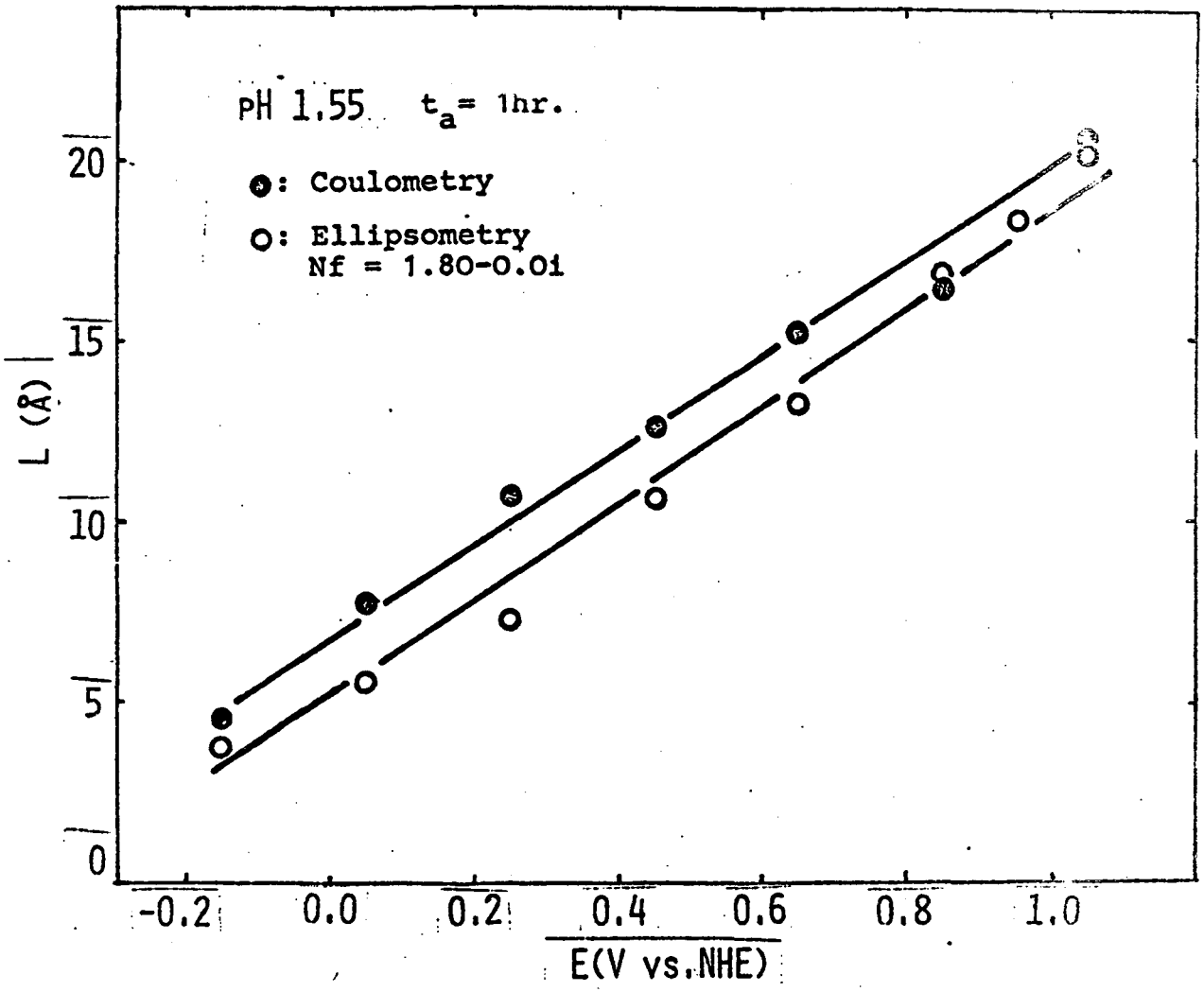

Fig. 11-11. Film thickness versus potential of the passive film on Cr in 0.15 M PO_4^{3-} solution.

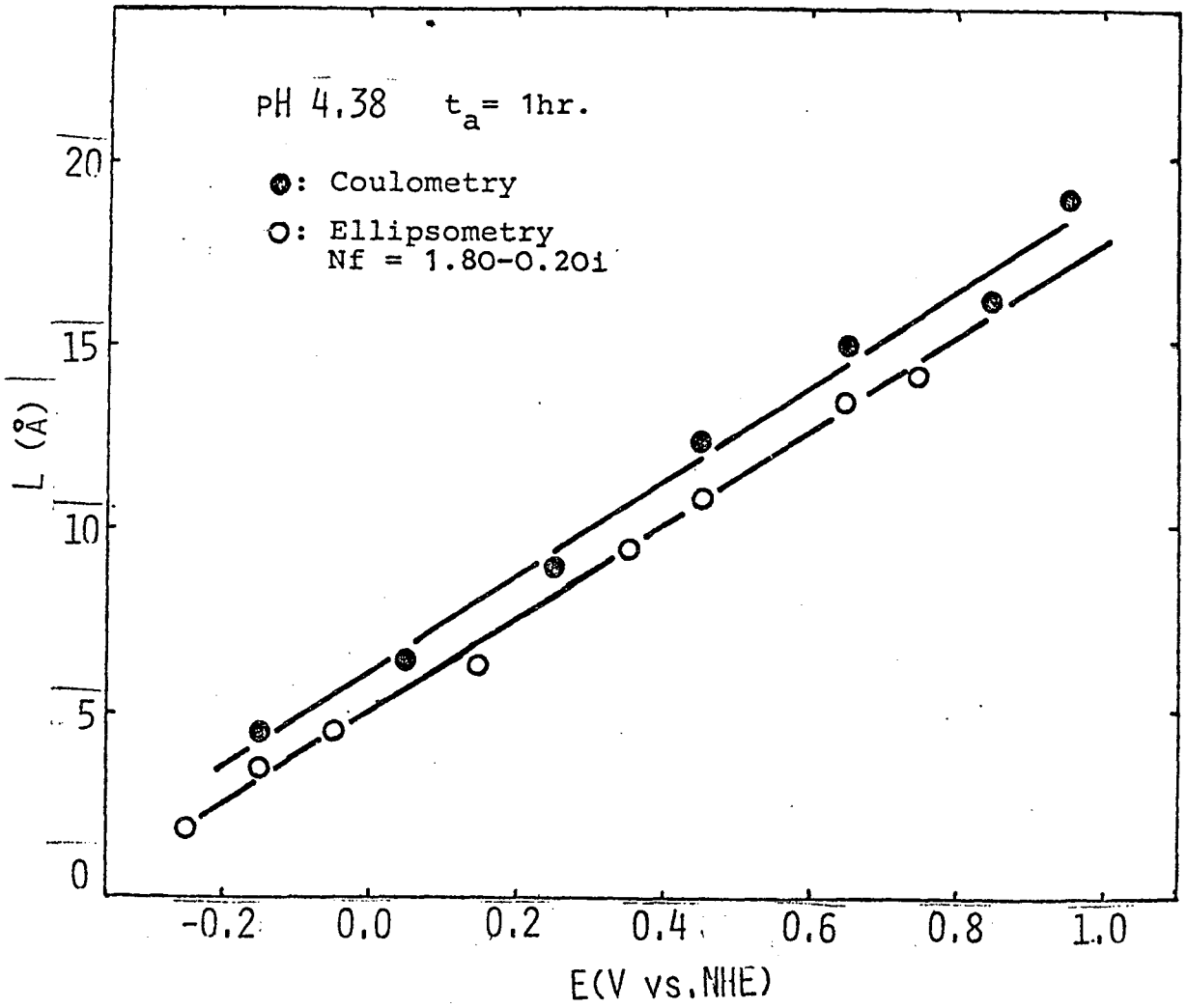

Fi g. 11-12. Film thickness versus potential of the passive film on Cr in 0.15 M PO_4^{3-} solution.

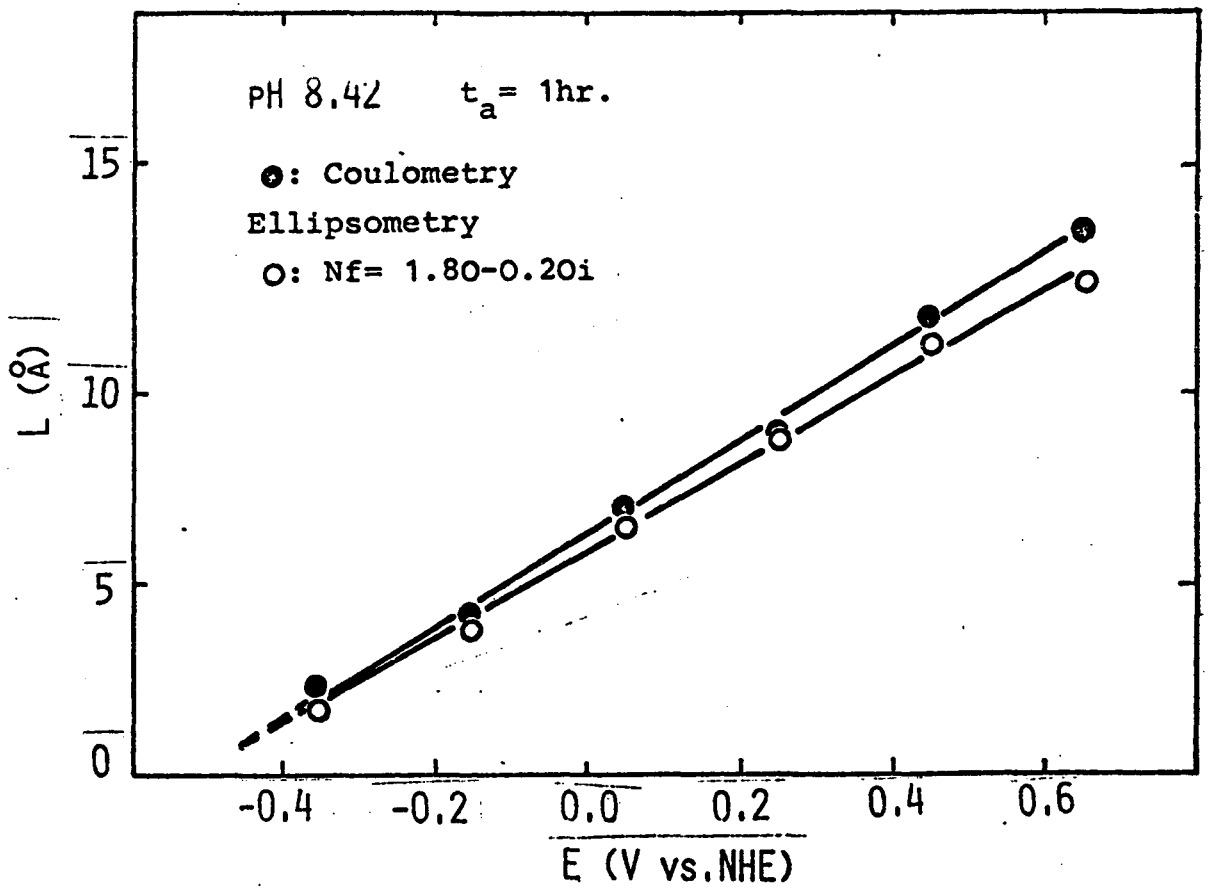

Fig. 11-13. Film thickness versus potential of the passive film on Cr in 0.3 M BO_3^{3-} solution.

Fig. 12-1. Anodic current, anodic charge, and amount of dissolution of Co versus potential in one-hour steady state borate solution at pH 8.42.

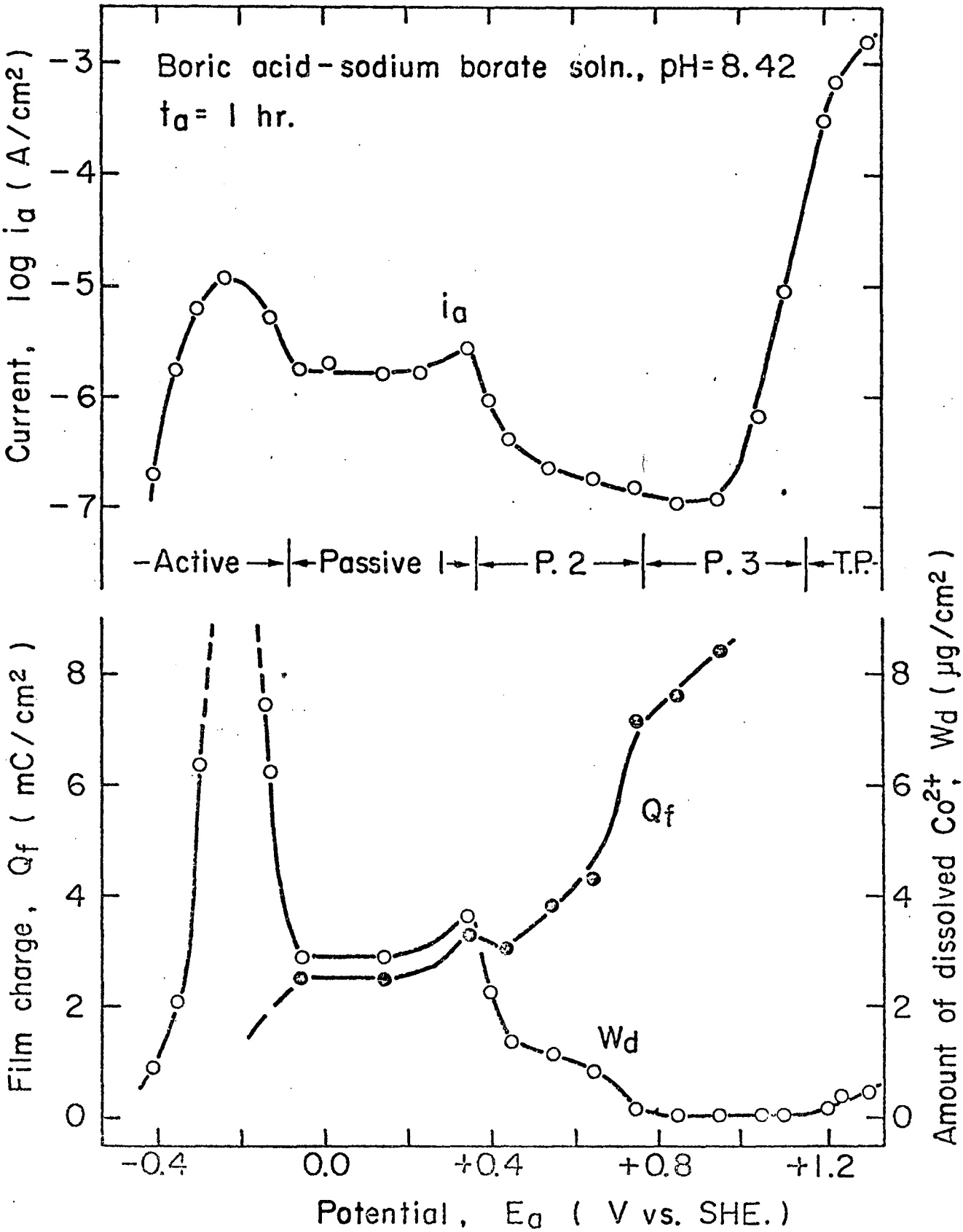

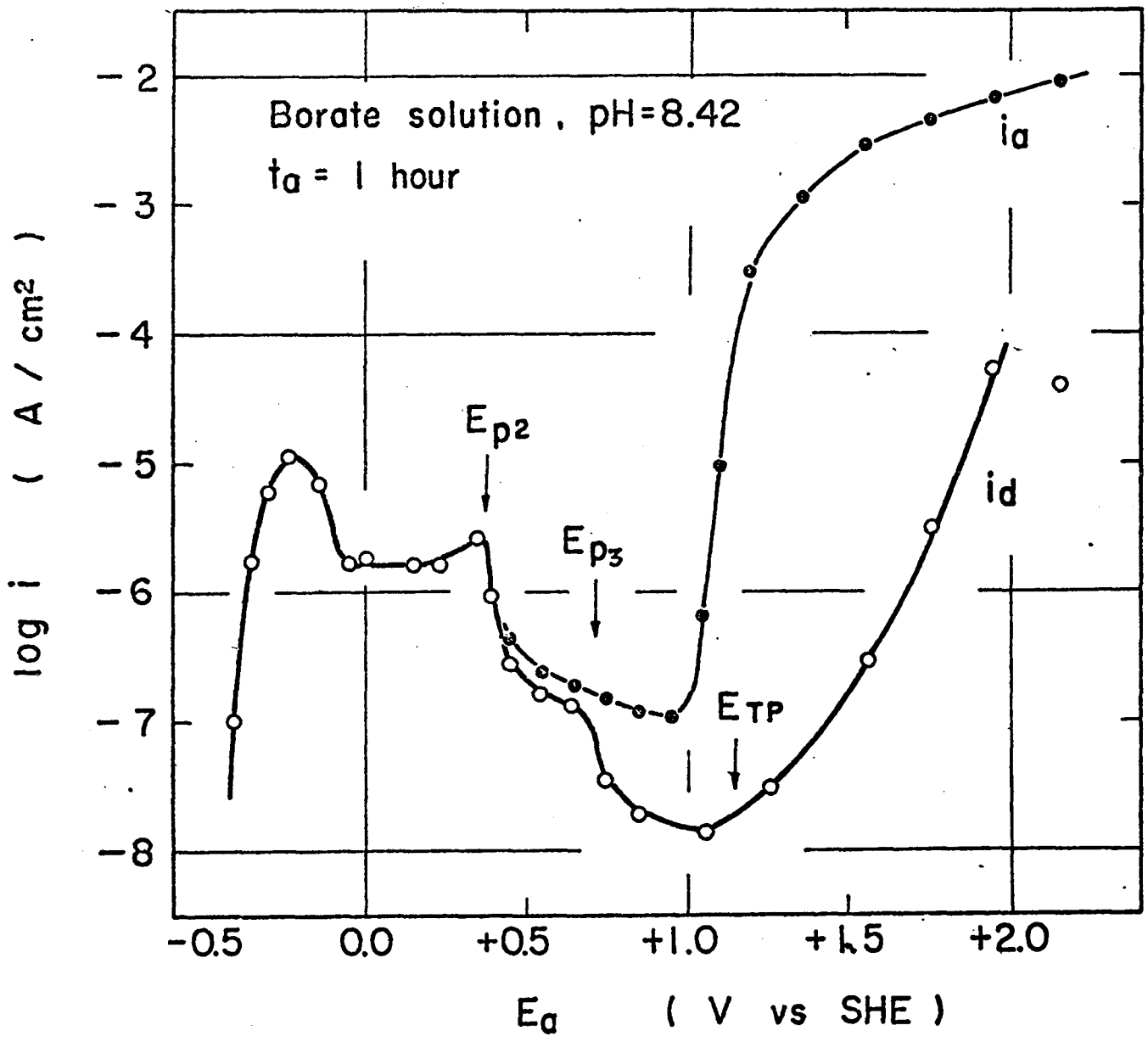

Fig. 12-2. Anodic current and dissolution current of Co in borate solution of pH 8.42.

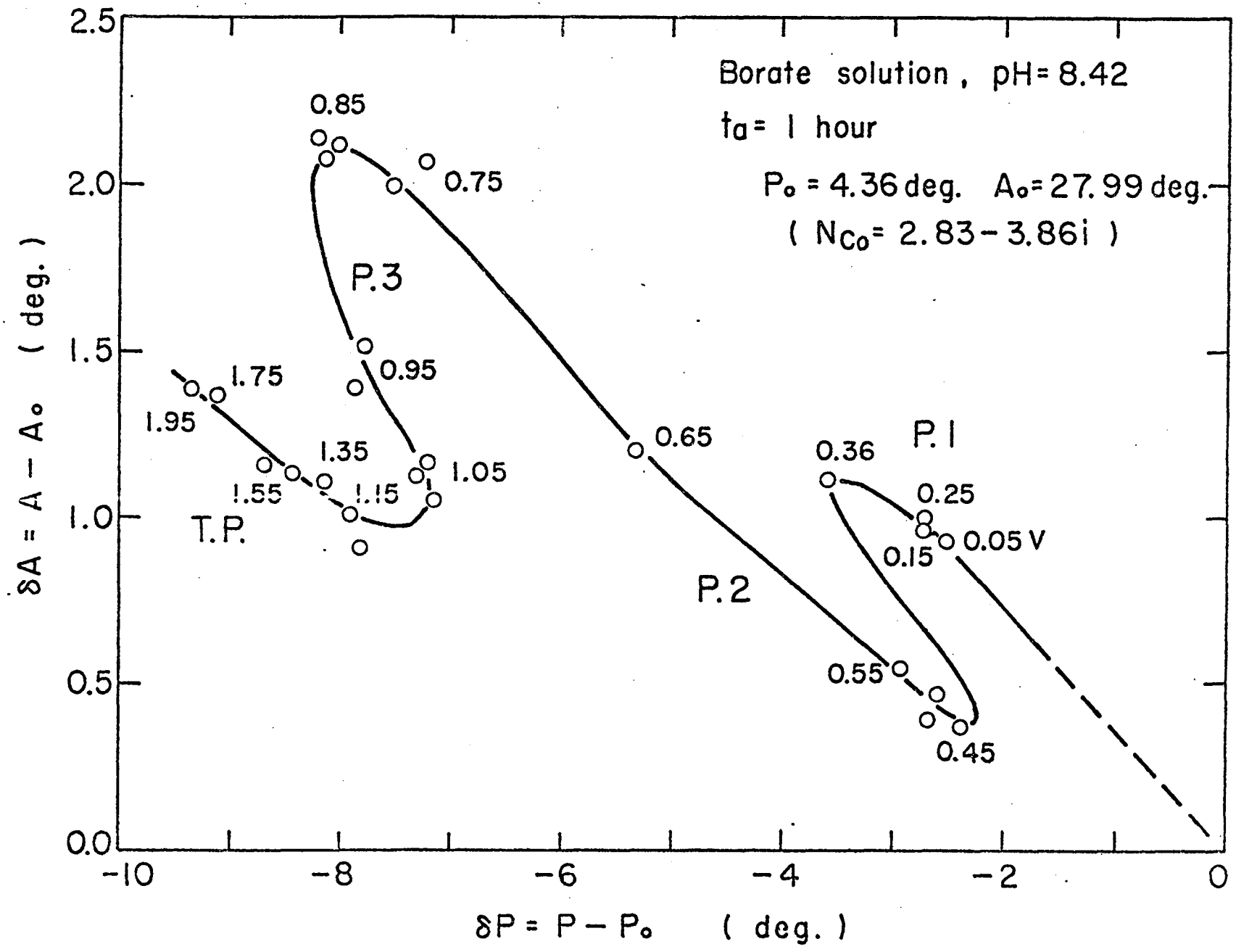

Fig. 12-3. Ellipsometric parameters P and A for passive Co in borate solution.

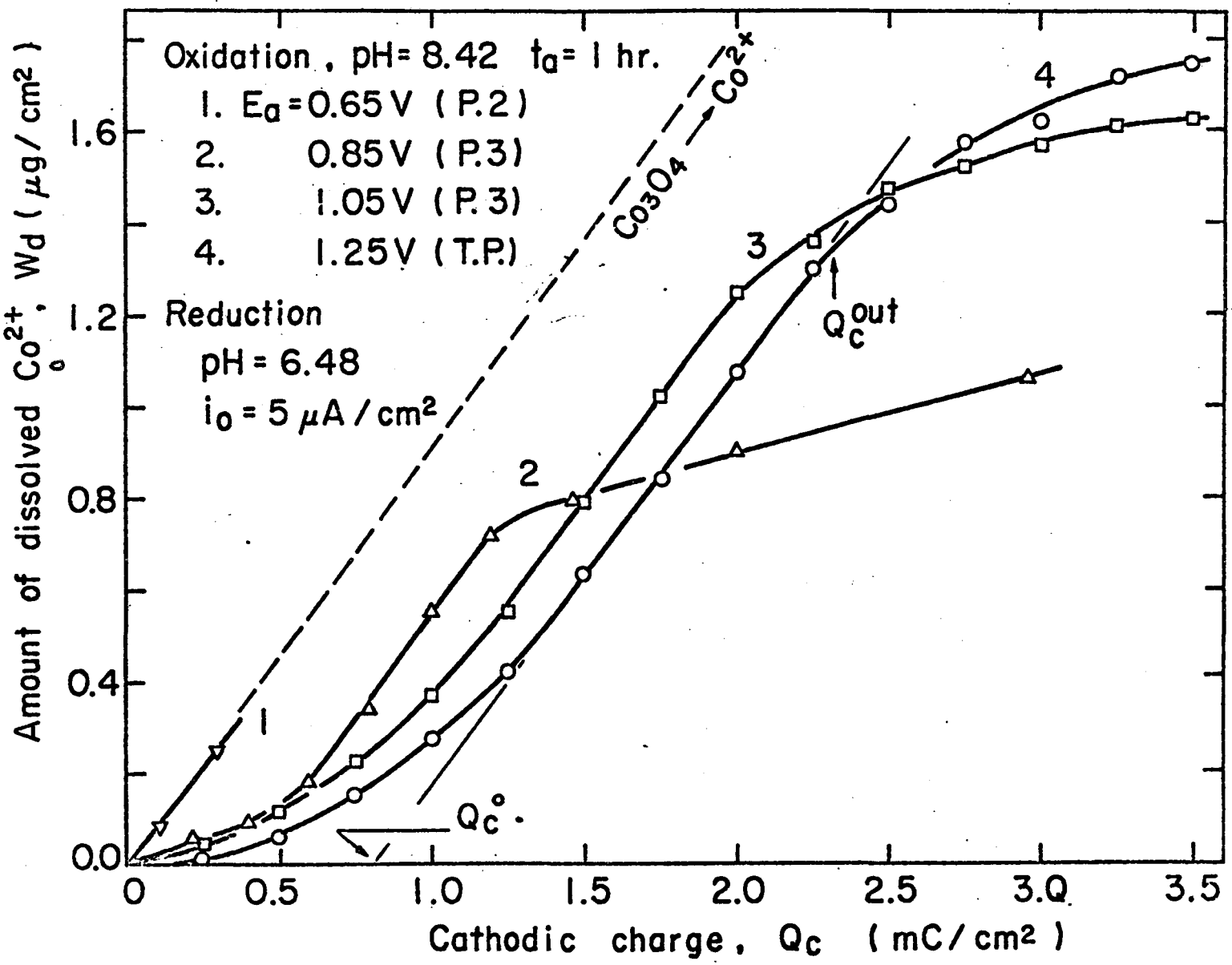

Fig. 12-4. Cathodic dissolution in borate solution at pH 6.48 of the passive film formed on cobalt at various potentials in borate solution at pH 8.43.

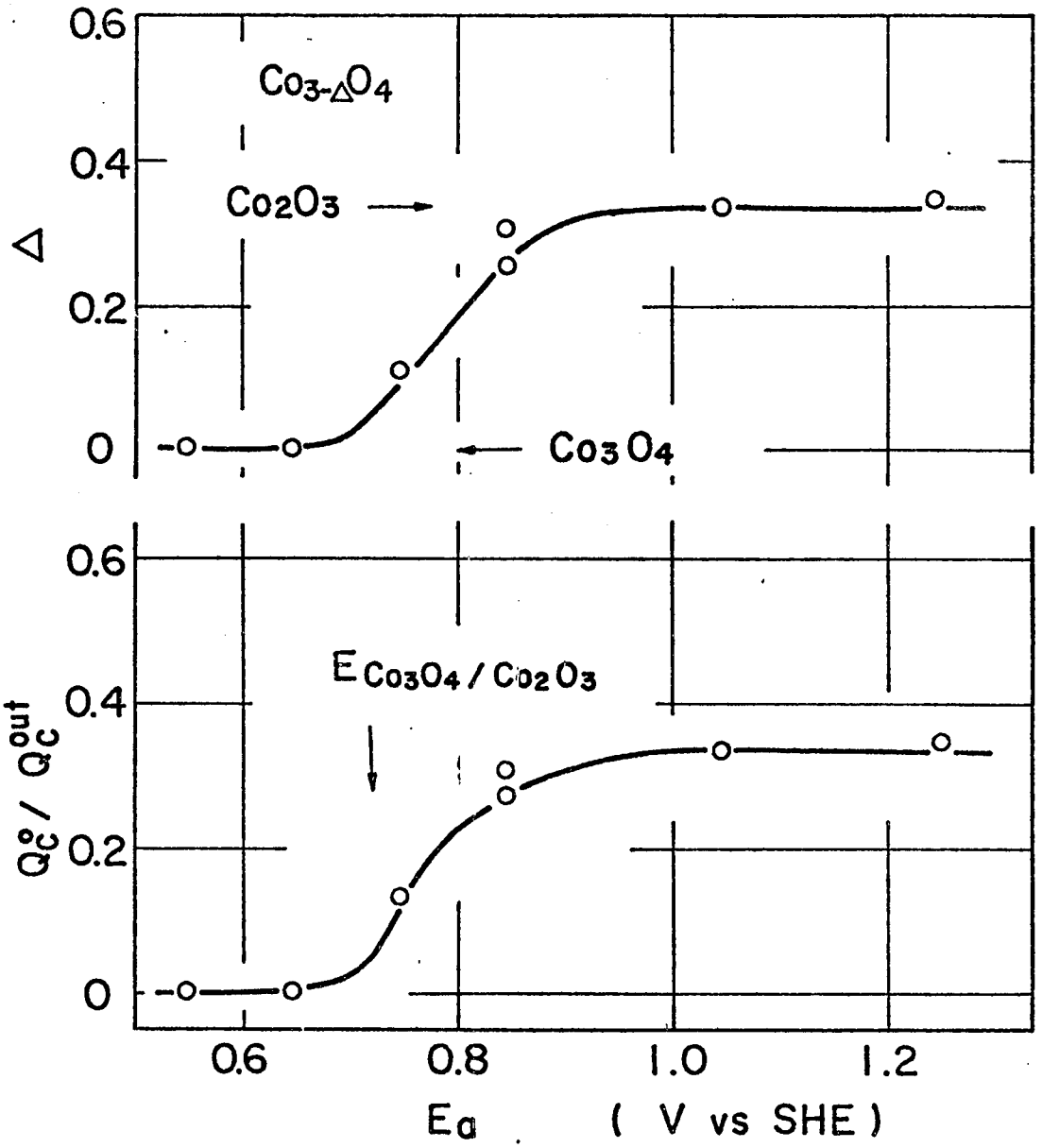

Fig. 12-5. Ratio of Q_c^o/Q_c^{out} and nonstoichiometry Δ for the barrier layer of $Co_{3-\Delta}O_4$ on Co versus potential in borate solution at pH 8.42: Q_c^o is the charge required for the induction stage of cathodic dissolution and Q_c^{out} the charge for the complete reduction of $Co_{3-\Delta}O_4$ layer.

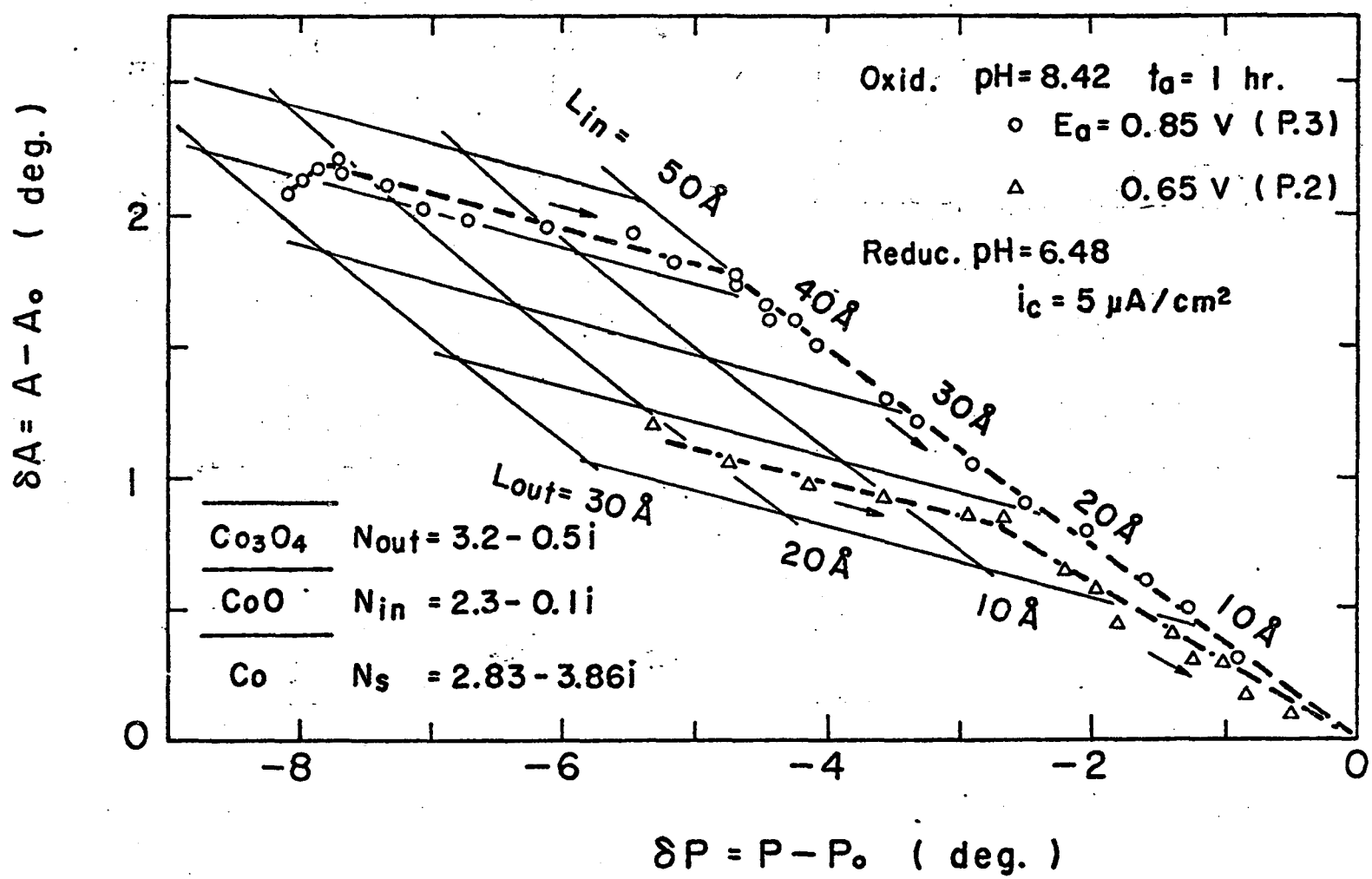

Fig. 12-6. Change in ellipsometric parameters P and A during galvanostatic reduction of passive films on Co.

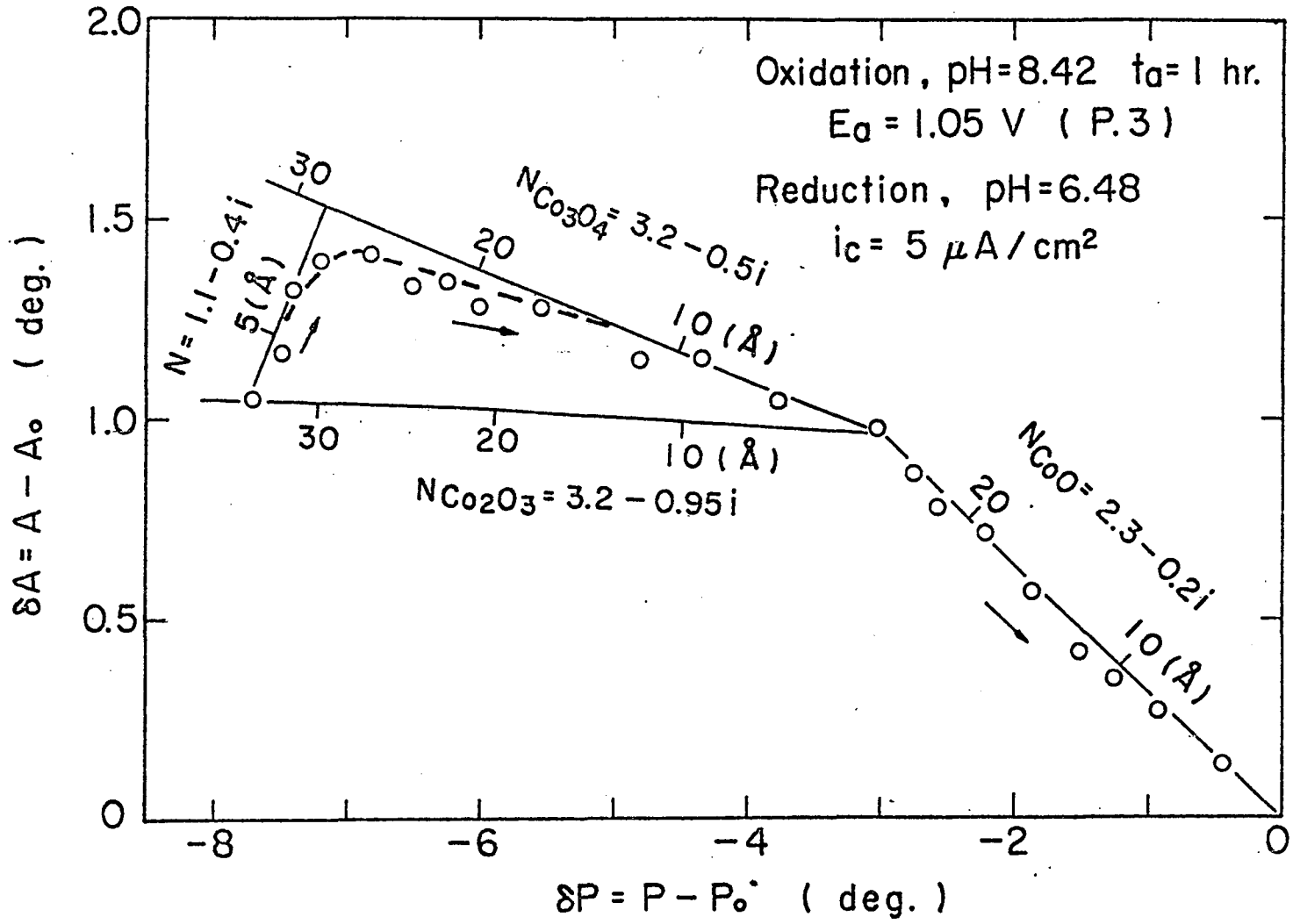

Fig. 12-7. Change in ellipsometric parameters P and A during galvanostatic reduction of a passive film formed on Co at a high potential.

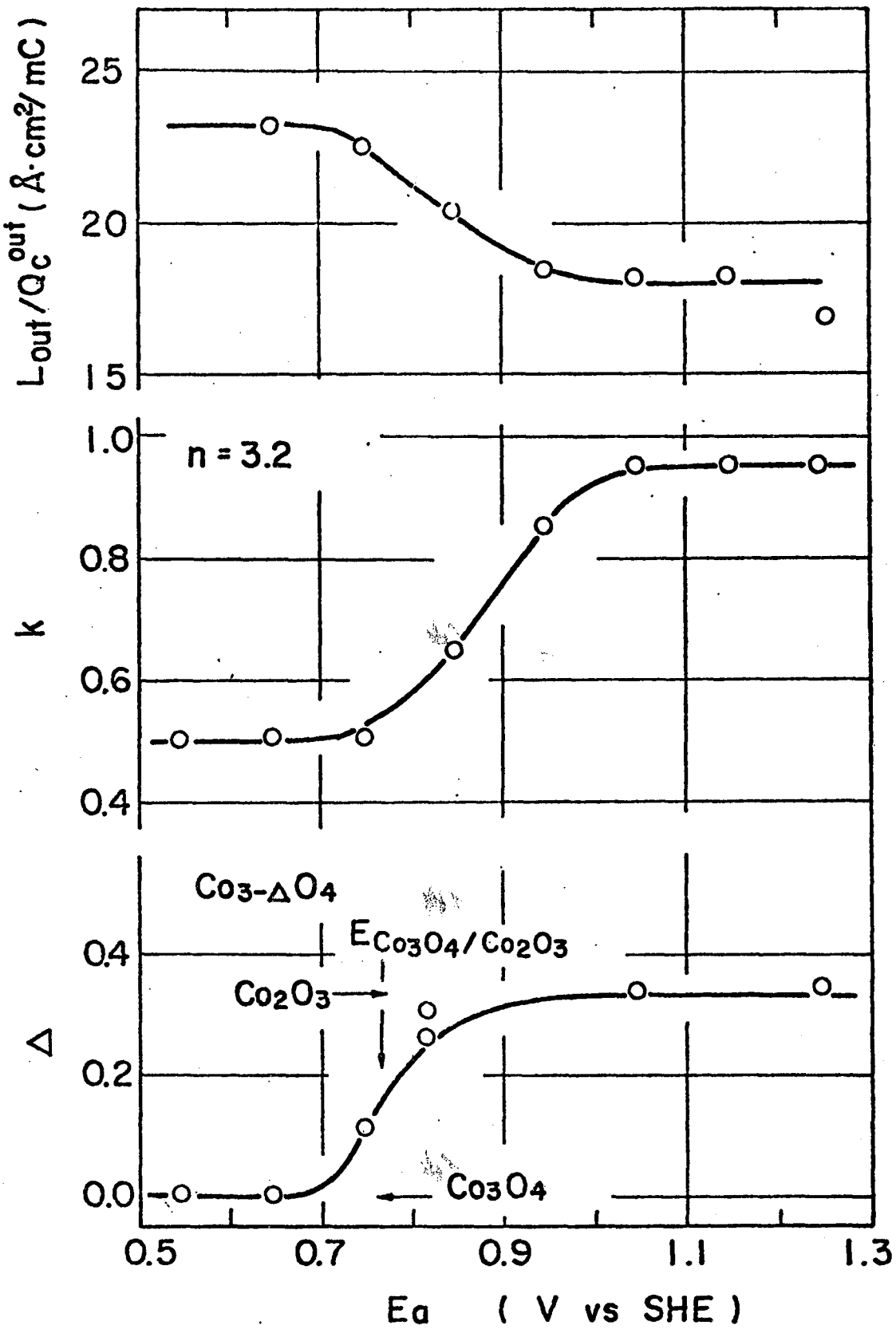

Fig. 12-8. Imaginary park k of optical constant and non-stoichiometry versus potential for the $Co_{3-\Delta}O_4$ layer on Co.

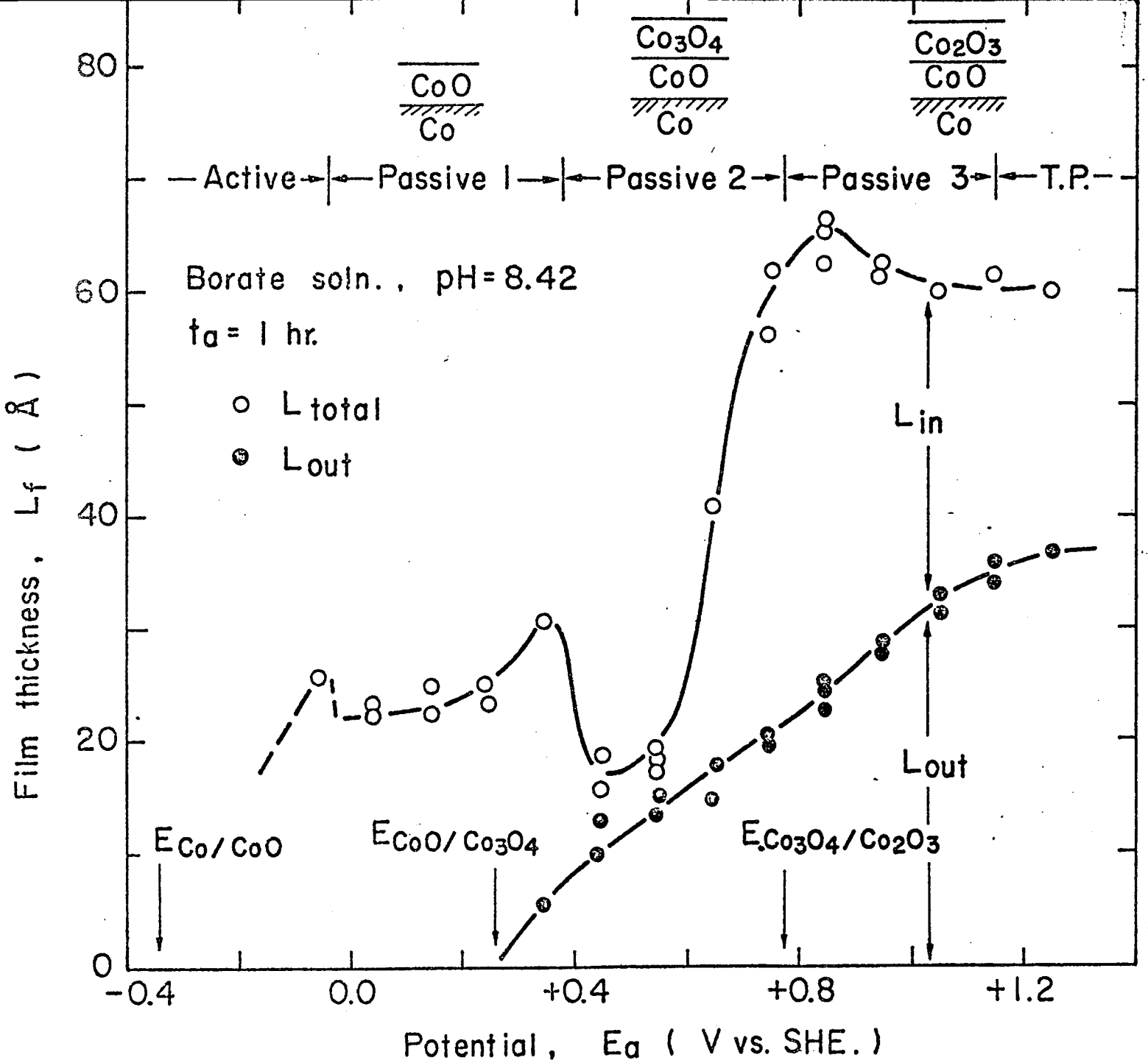

Fig. 12-9. Film thickness versus potential for the passive film on Co in borate solution at pH 8.42.

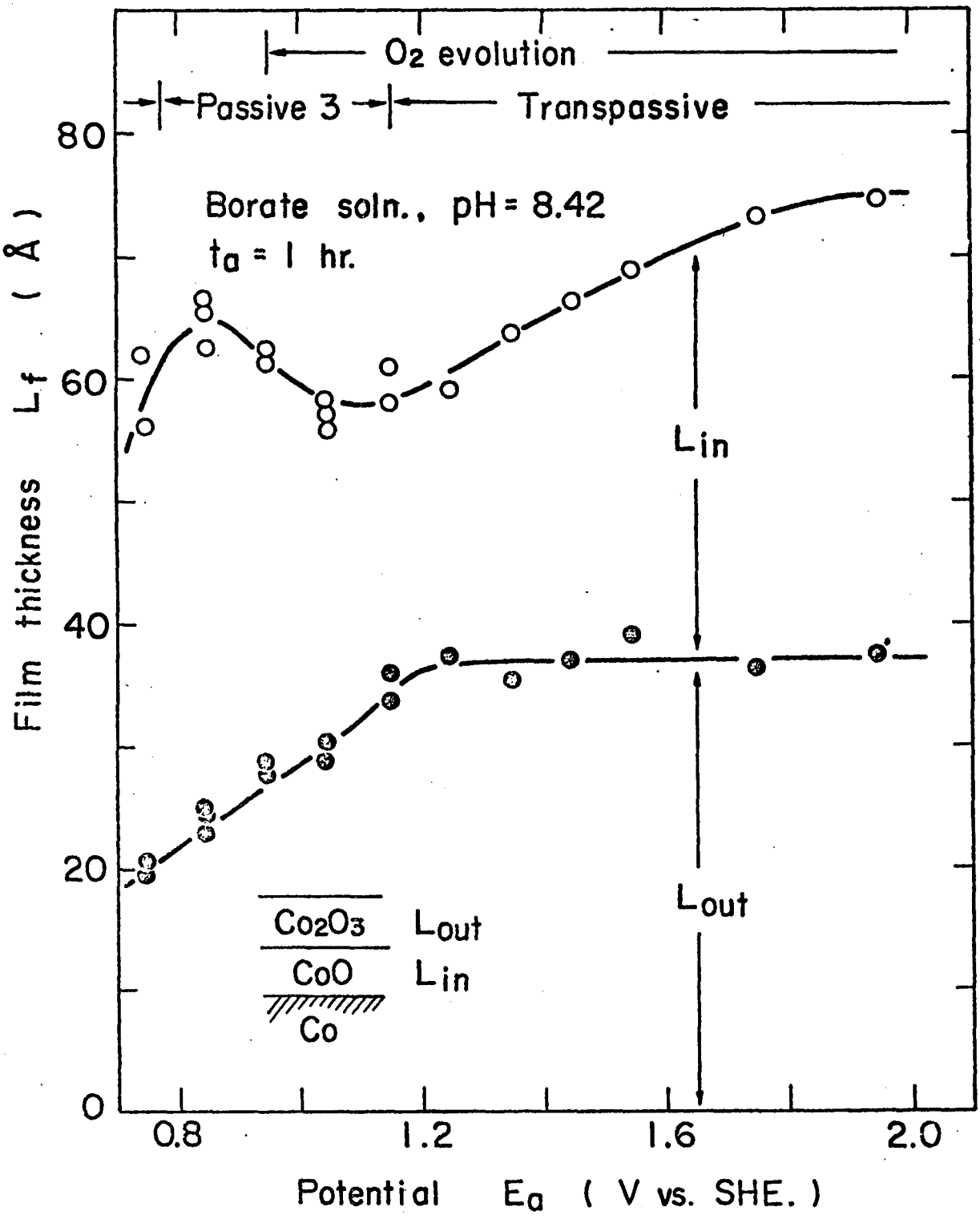

Fig. 12-10. Film thickness versus potential for the passive film formed on Co at transpassive potentials.

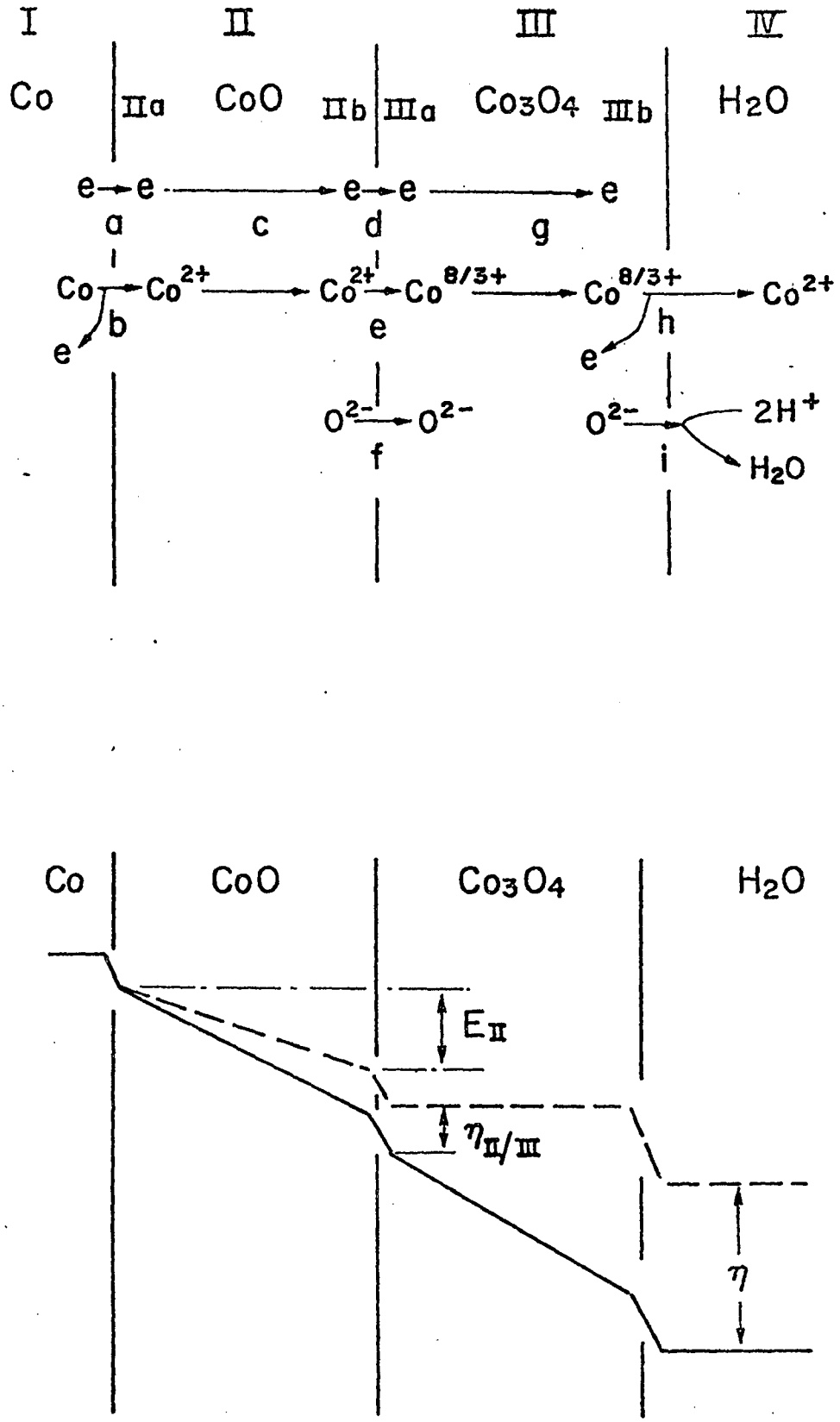

Fig. 12-11. Bilayer film model of CoO and $Co_{3-\Delta}O_4$.

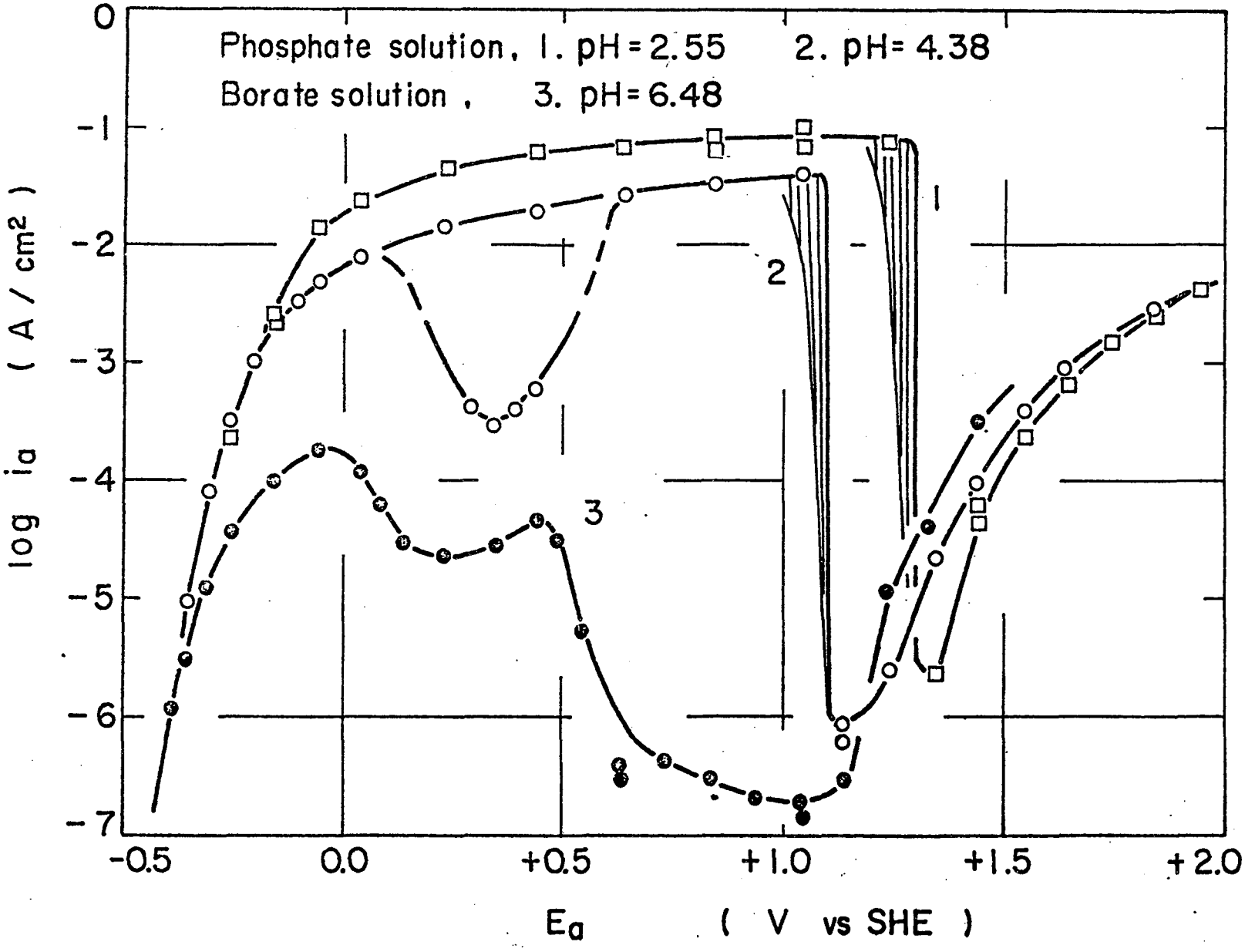

Fig. 12-12. Anodic polarization curves of Co in acid solutions.

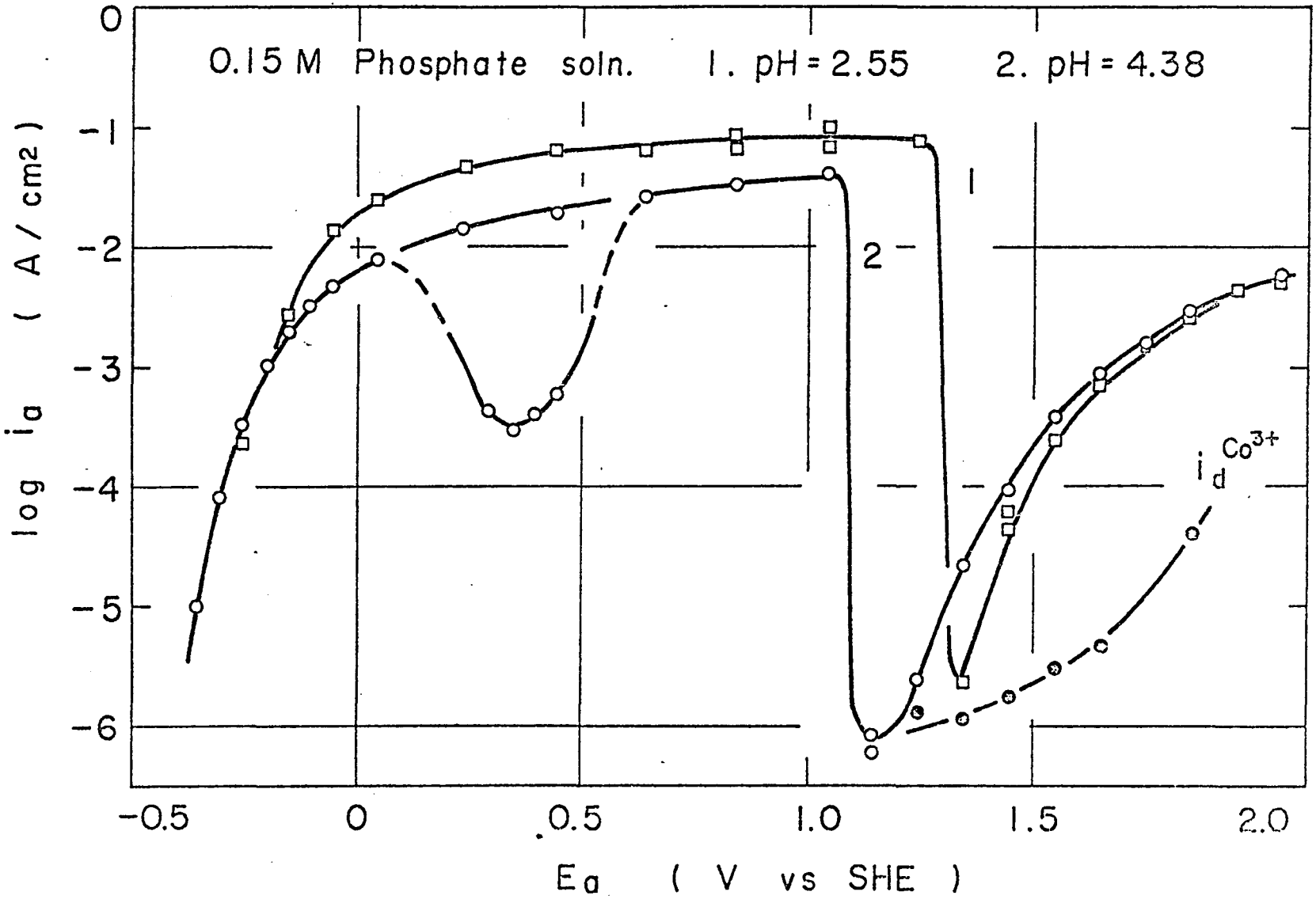

Fig. 12-13. Anodic current and dissolution current versus potential of Co in 0.15 M PO_4^{3-} solution.

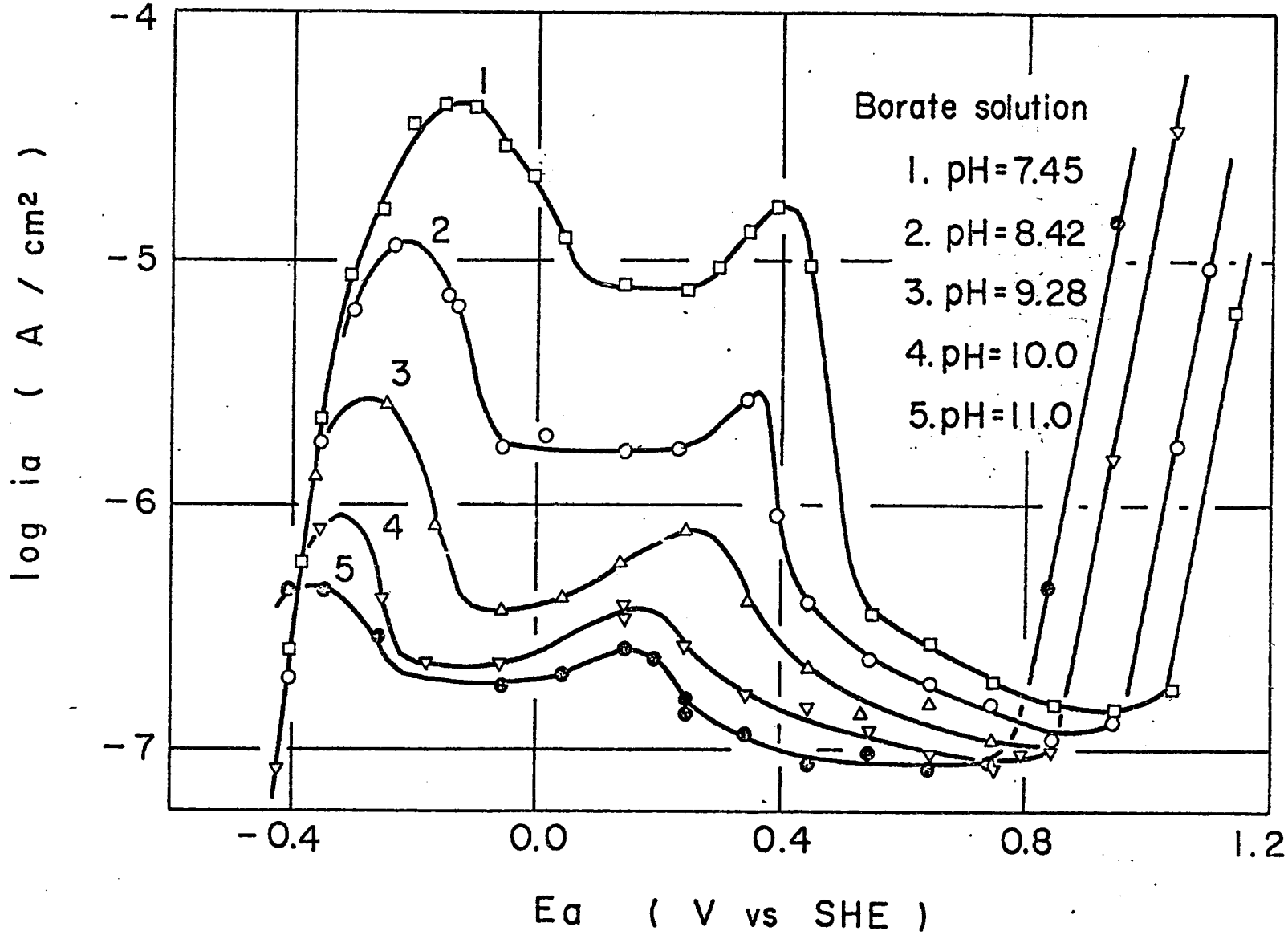

Fig. 12-14. Anodic polarization curve of Co in neutral and alkaline solutions.

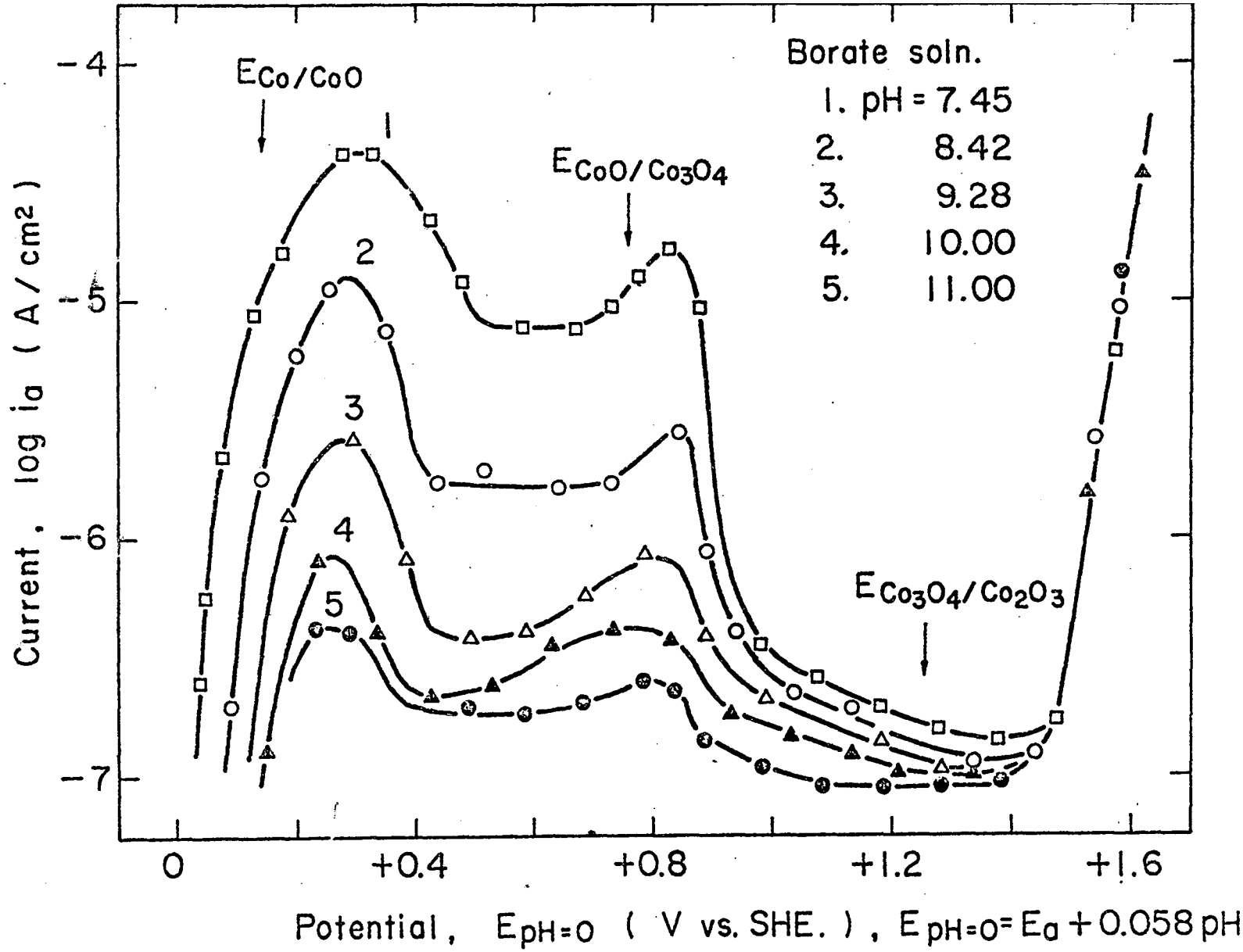

Fig. 12-15. Anodic polarization curve of Co in neutral and alkaline solutions.

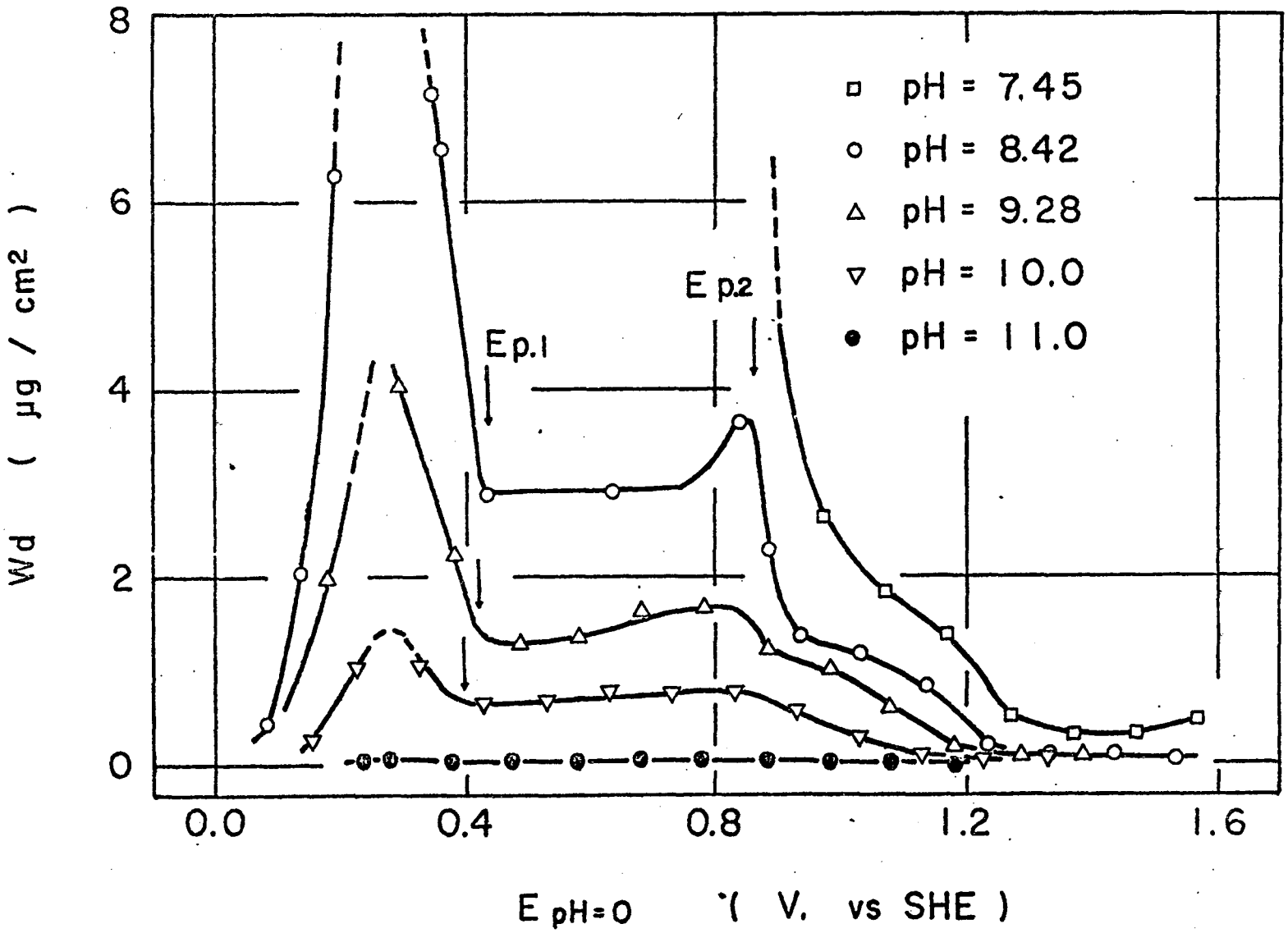

Fig. 12-16. Amount of dissolution of Co for one-hour potentiostatic oxidation versus potential in neutral and alkaline solutions.

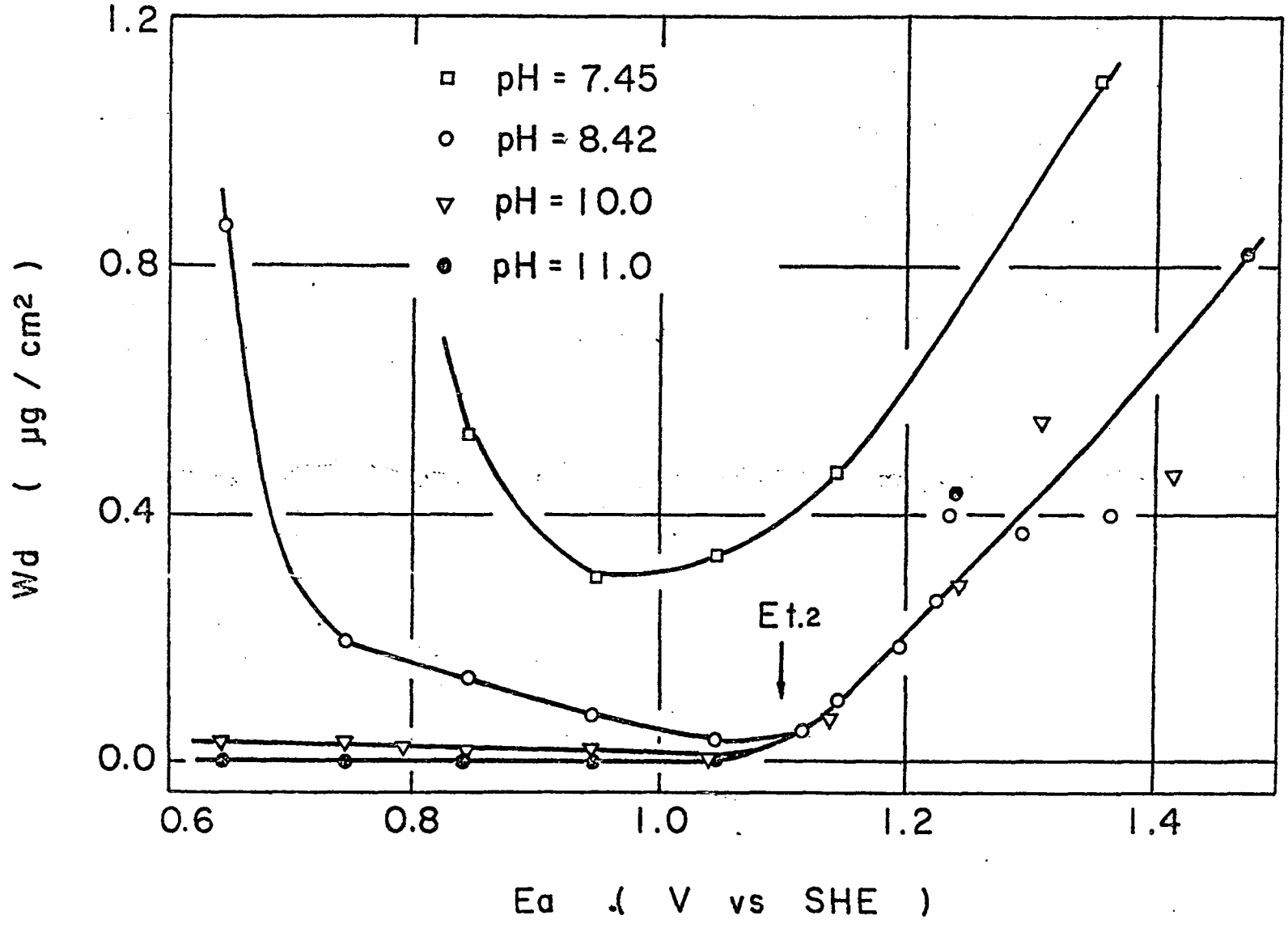

Fig. 12-17. Amount of dissolution of Co for one-hour potentiostatic oxidation in neutral and alkaline solutions.

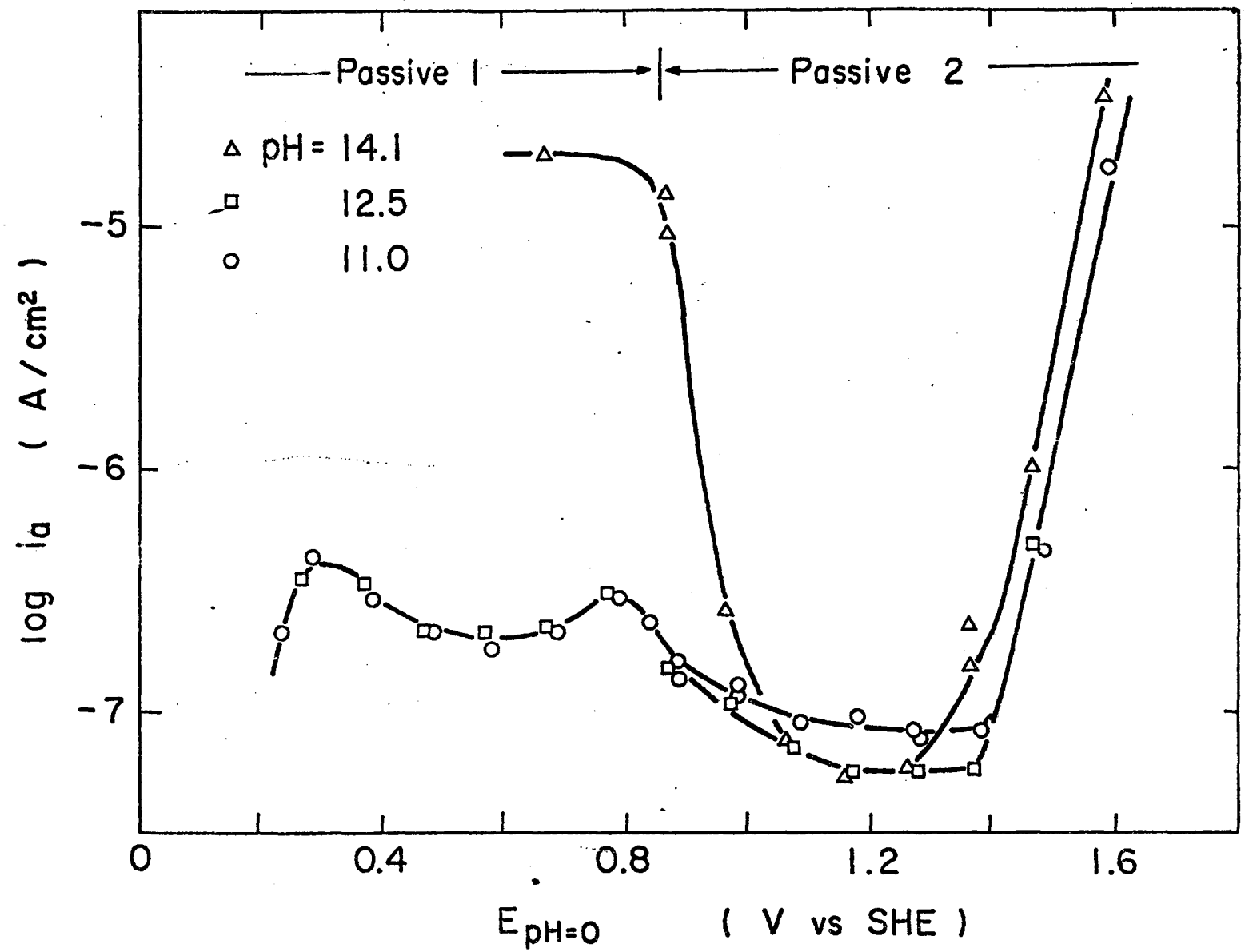

Fig. 12-18. Anodic current versus potential of Co in alkaline solutions.

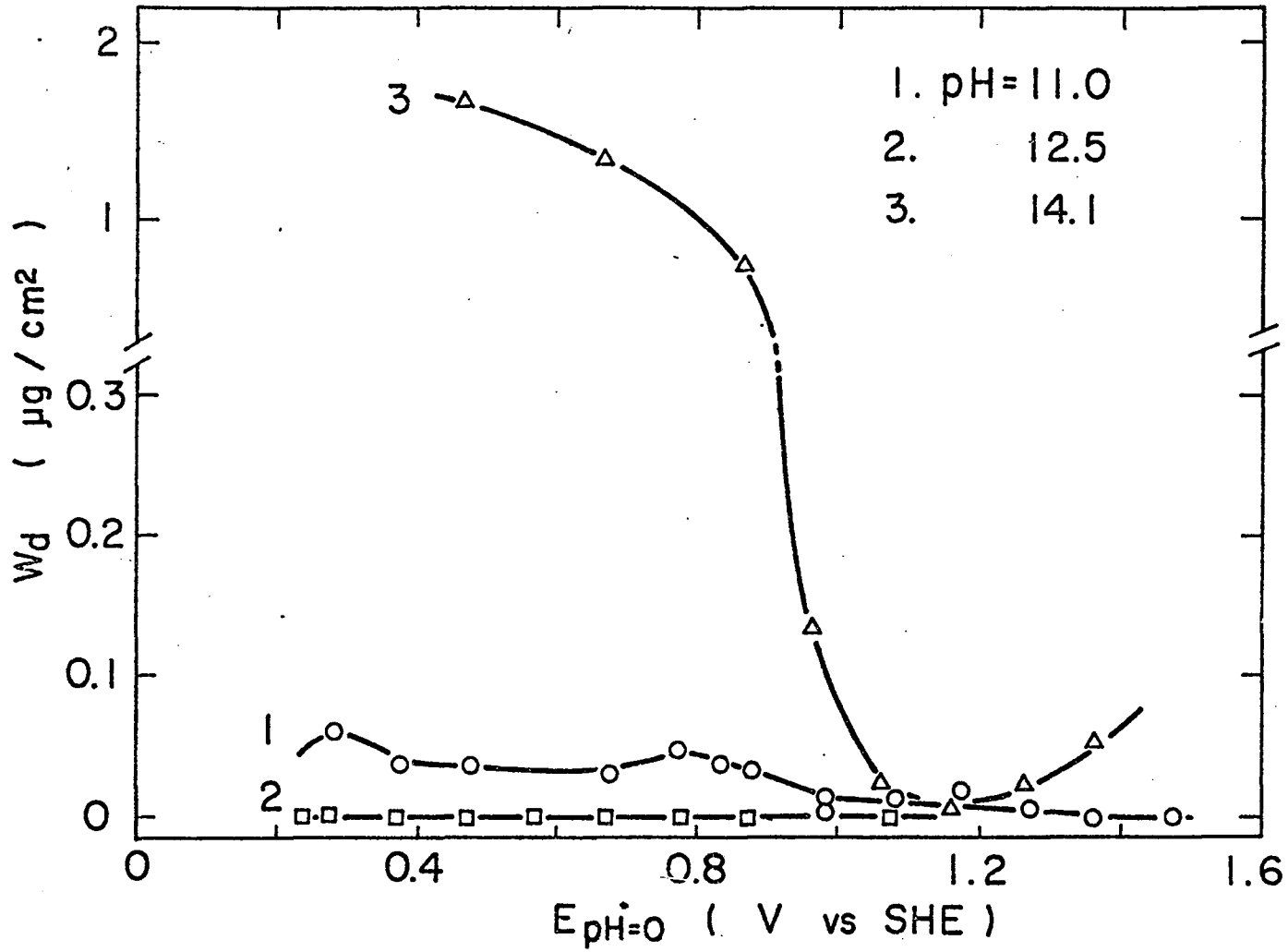

Fig. 12-19. Amount of dissolution of Co versus potential of Co in Alkaline solutions.

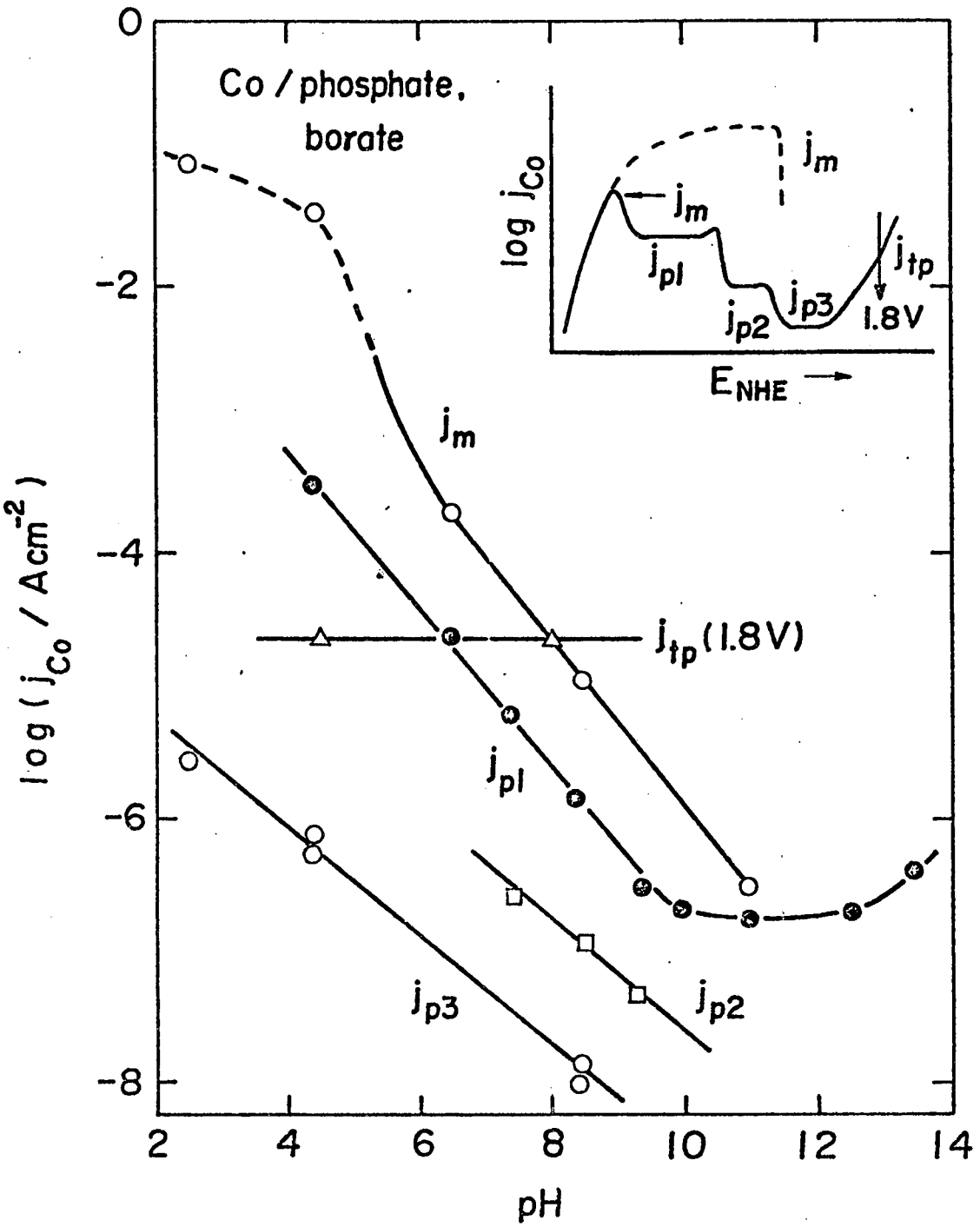

Fig. 12-20. Anodic dissolution current of Co versus pH.

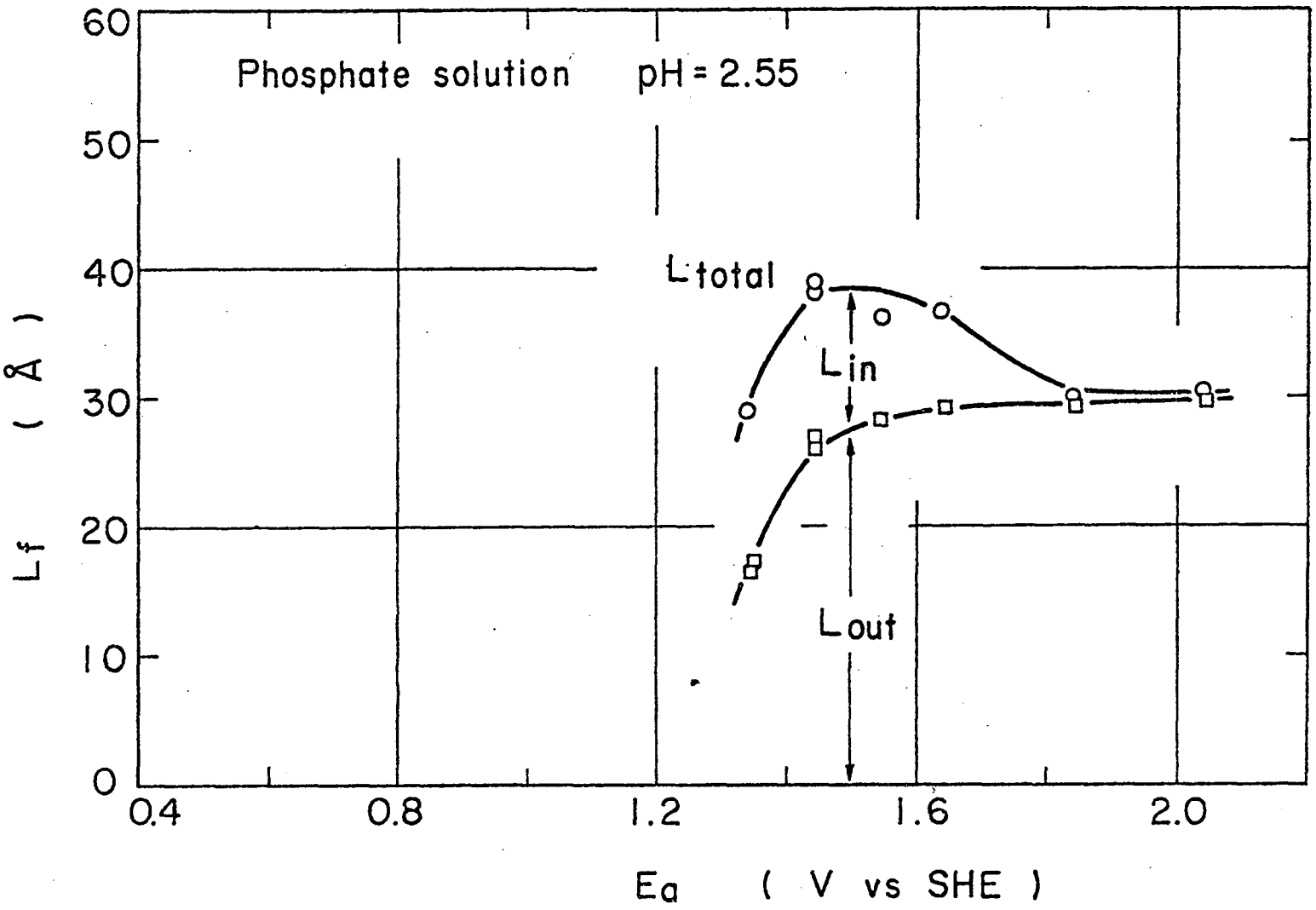

Fig. 12-21. Film thickness versus potential for the passive film on Co in acid solution at pH 2.55.

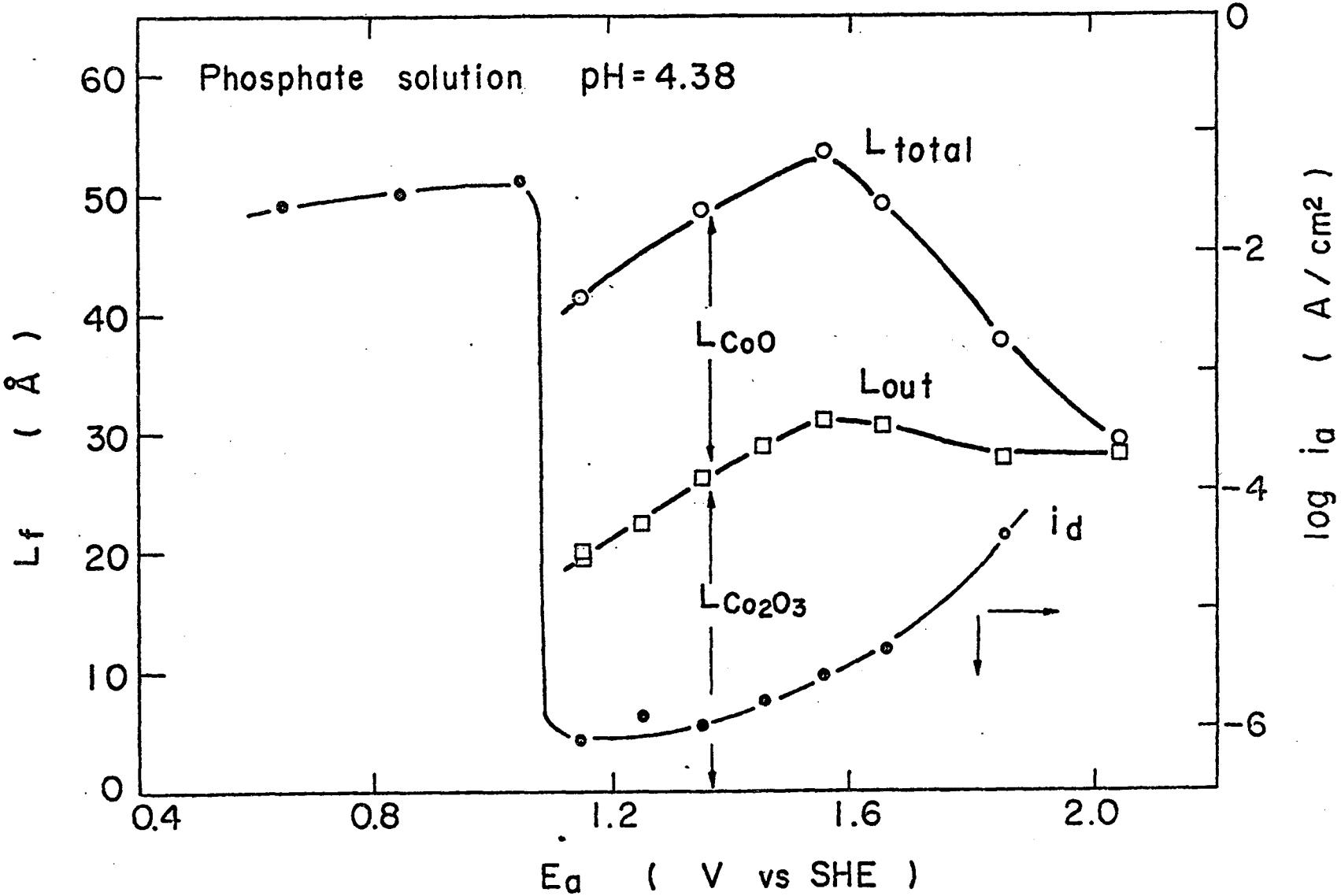

Fig. 12-22. Film thickness versus potential for the passive film on Co in acid solution at pH 4.38.

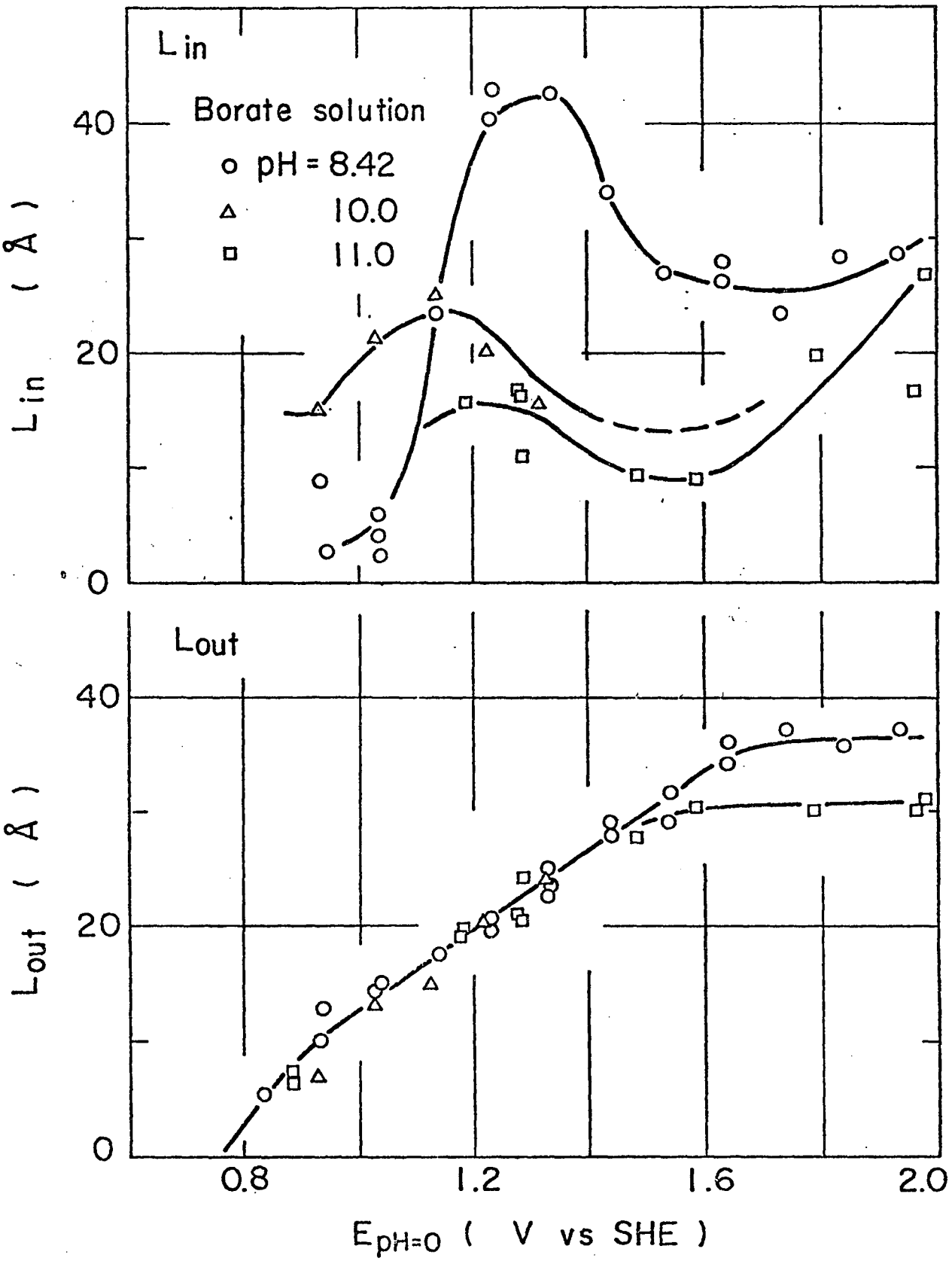

Fig. 12-23. Film thickness versus potential for the passive film on Co in alkaline solutions.

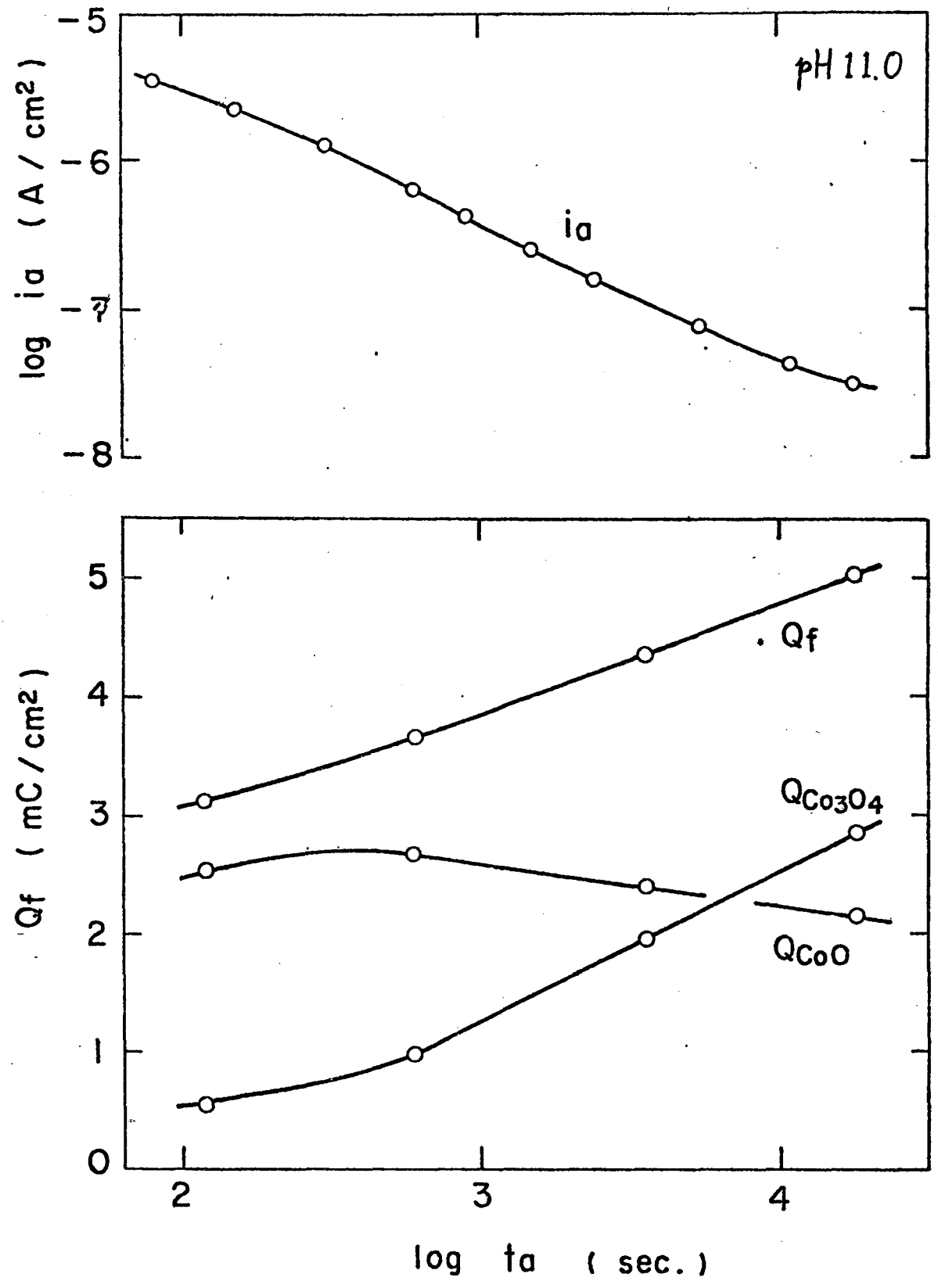

Fig. 12-24. Anodic current and layer thicknesses versus time during potentiostatic oxidation of Co at 0.32 V in borate solution at pH 11.0.

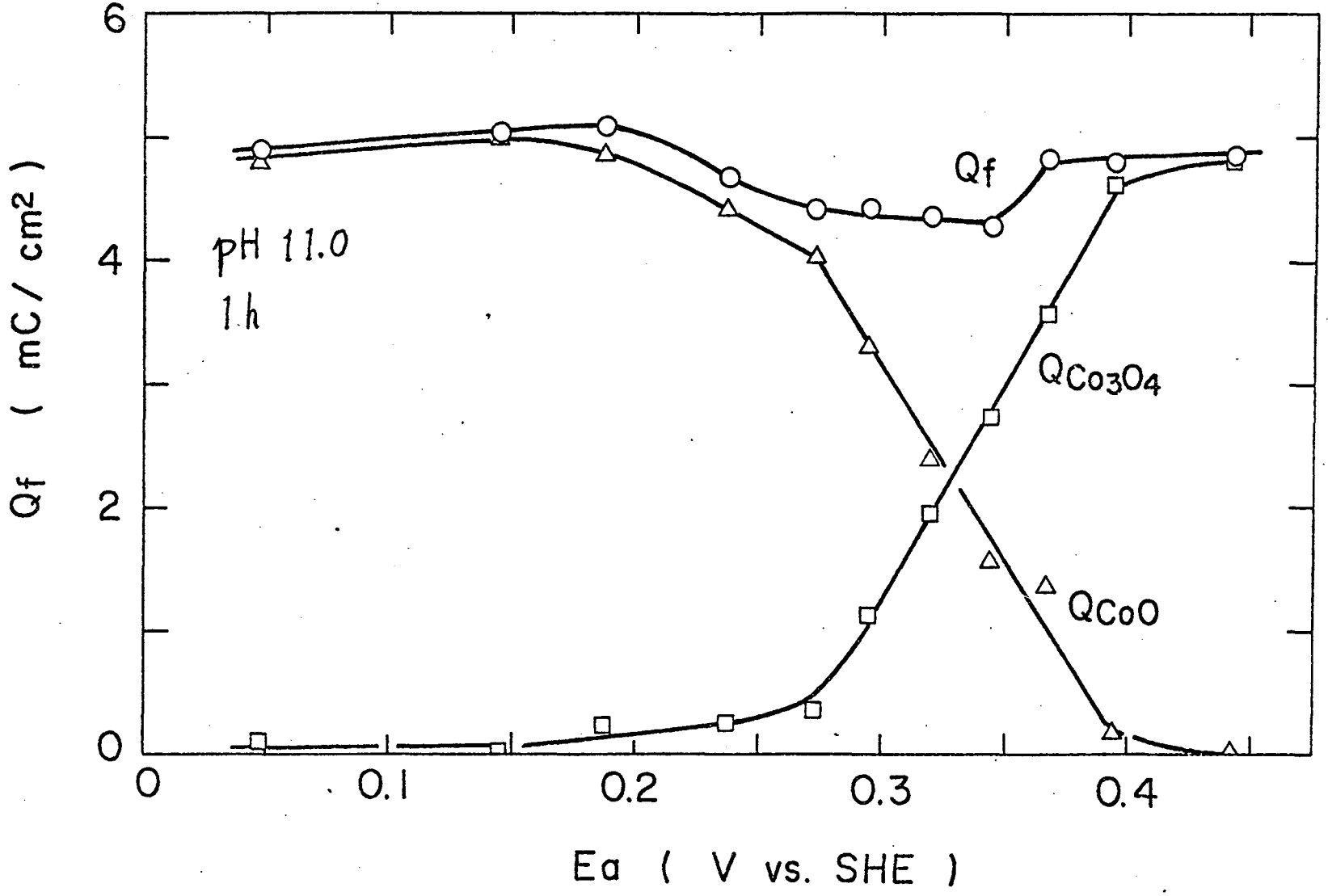

Fig. 12-25. Layer thicknesses versus potential for the passive oxide film on Co in alkaline solution of pH 11.0.

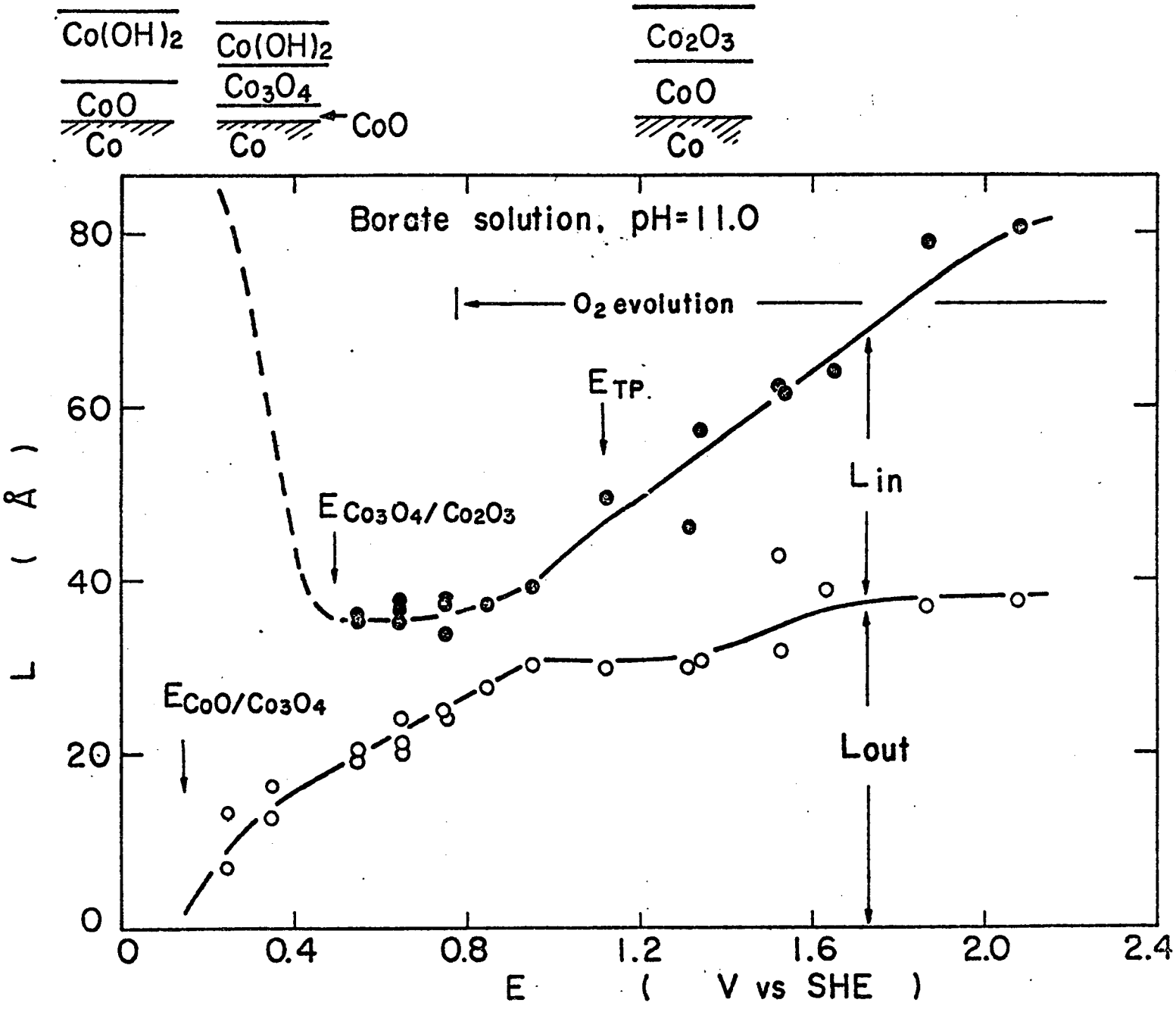

Fig. 12-26. Film thickness versus potential for the passive oxide film on Co in alkaline solution of pH 11.0

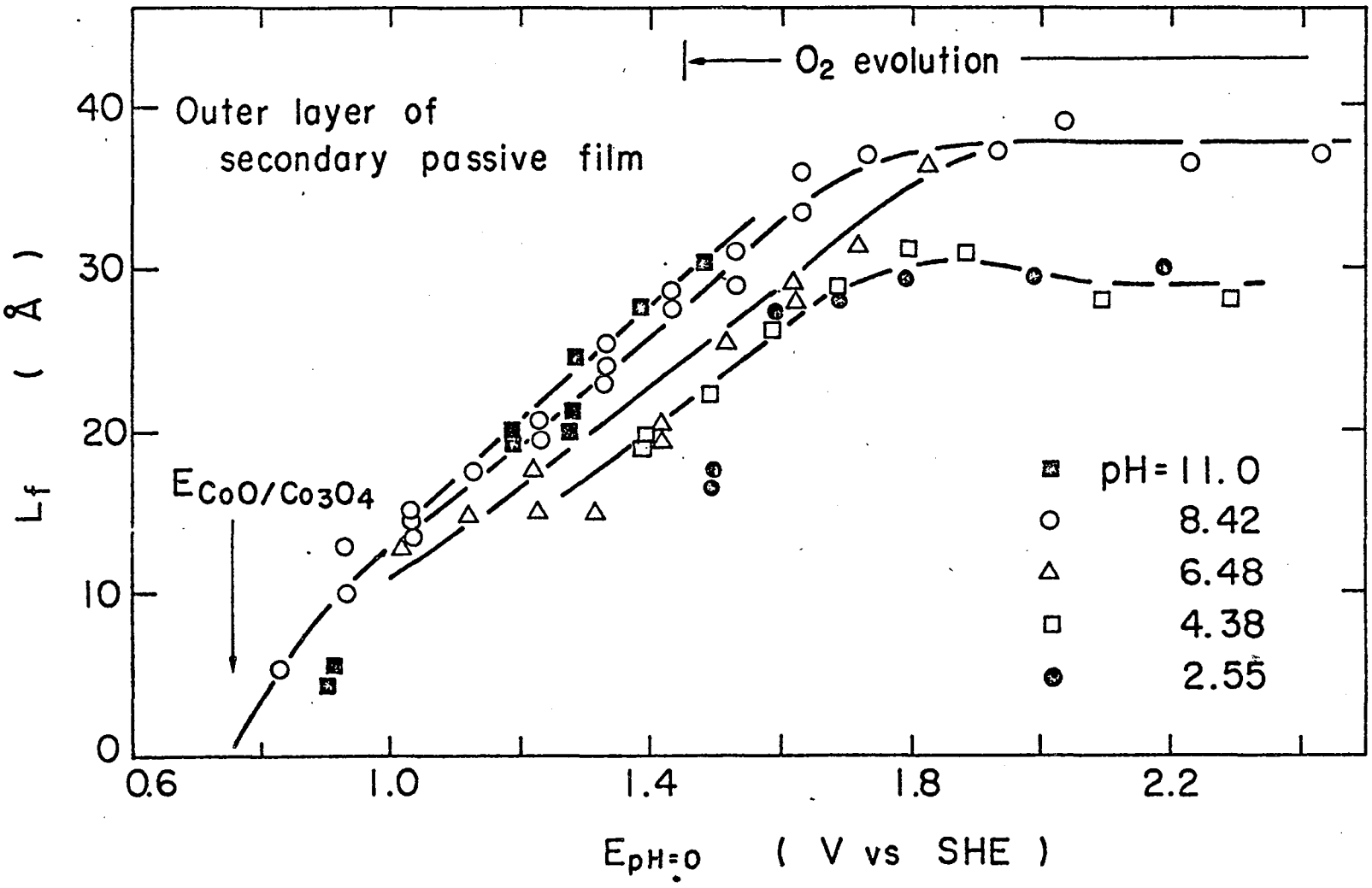

$$\frac{dL}{dE} = 33 \pm 5\,(Å/V), \quad \frac{dE}{dL} = (3.0 \pm 0.5) \times 10^6 \ (V/cm)$$

Fig. 12-27. Outer barrier layer thickness versus potential for passive oxide film on Co in various pH solutions.

Fig. 12-28. Film thickness versus potential for the passive oxide film on Co in acid and alkaline solutions.

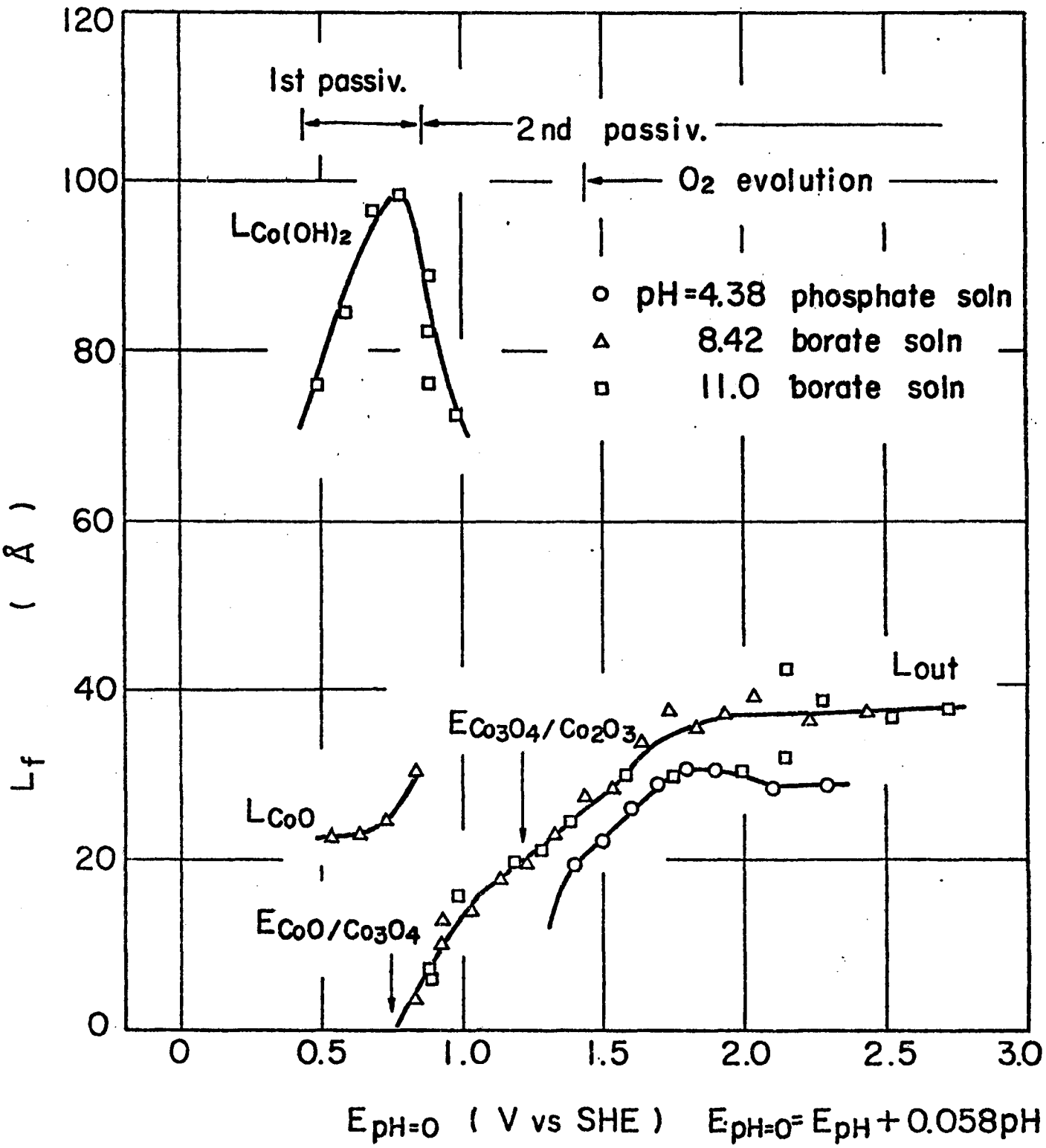

Fig. 12-29. Film thickness and anodic dissolution current versus pH for the passive film on Co in potential region I.

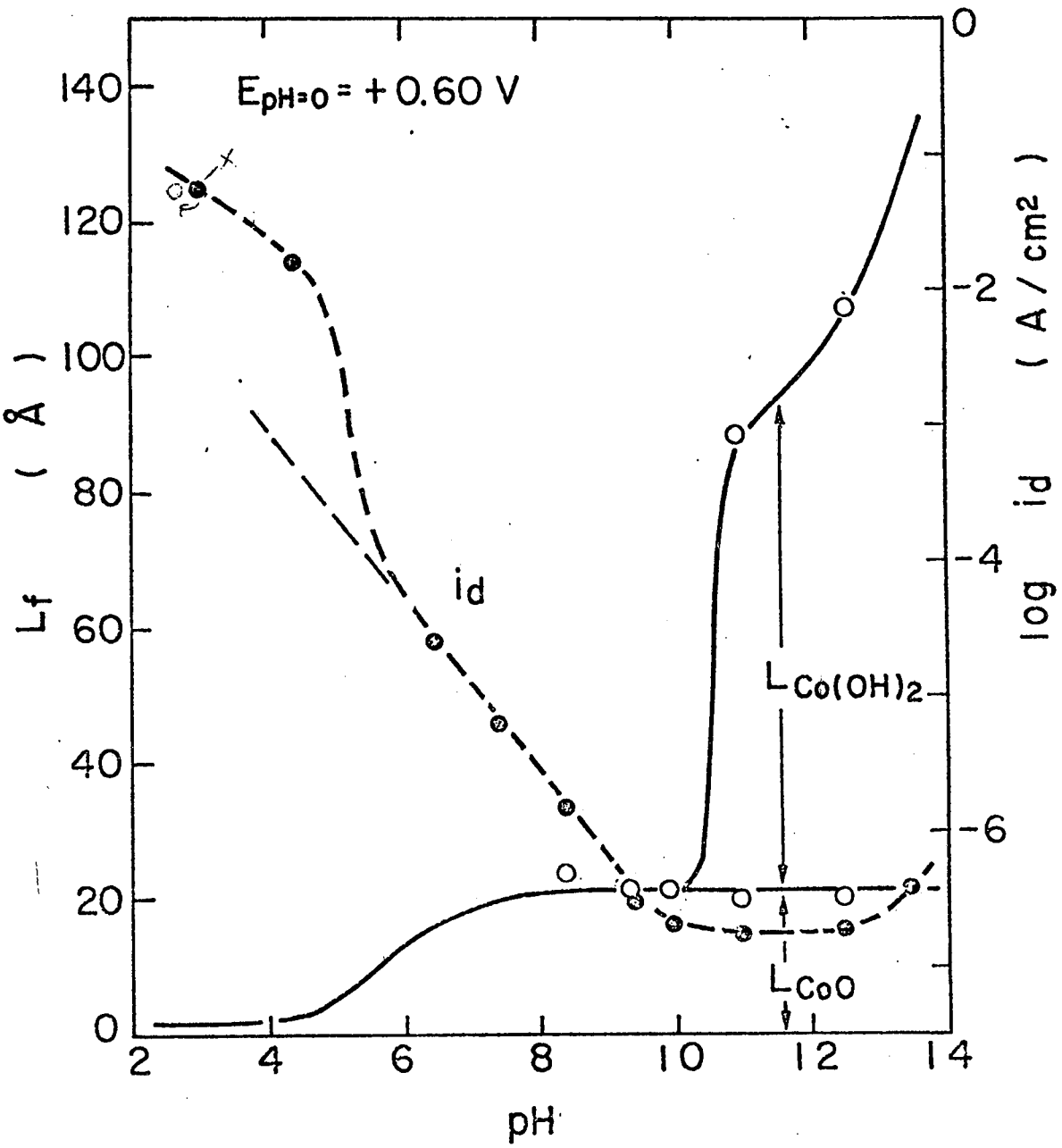

Film thickness and dissolution current of primary passivity.

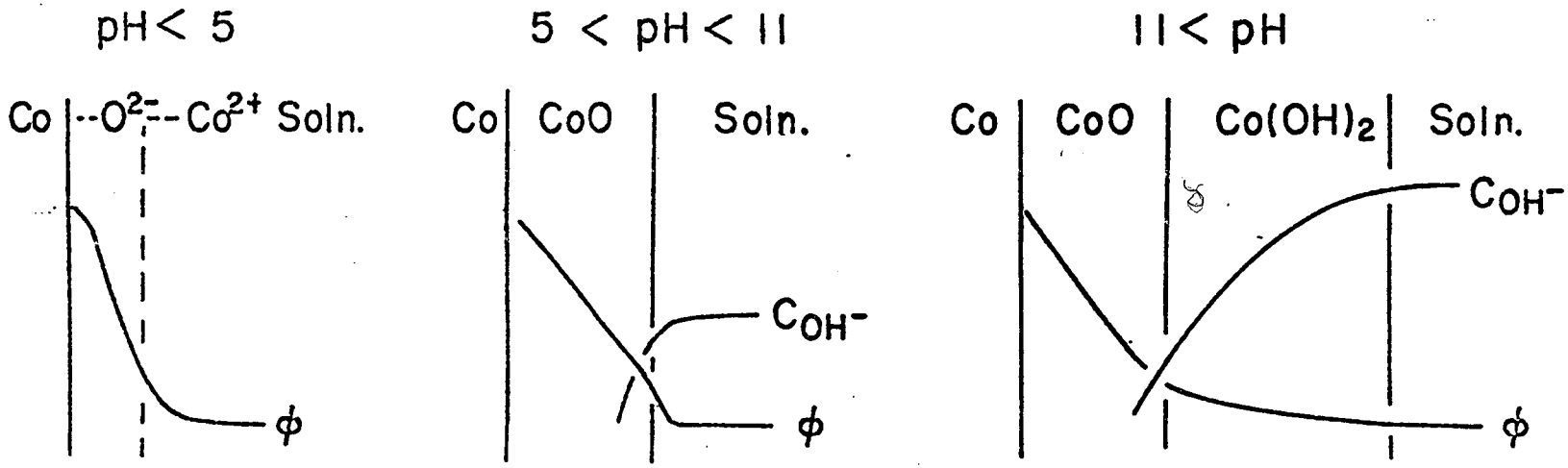

Fig. 12-30. Film model for the passive film on Co in potential region I in acid, neutral and alkaline solutions.

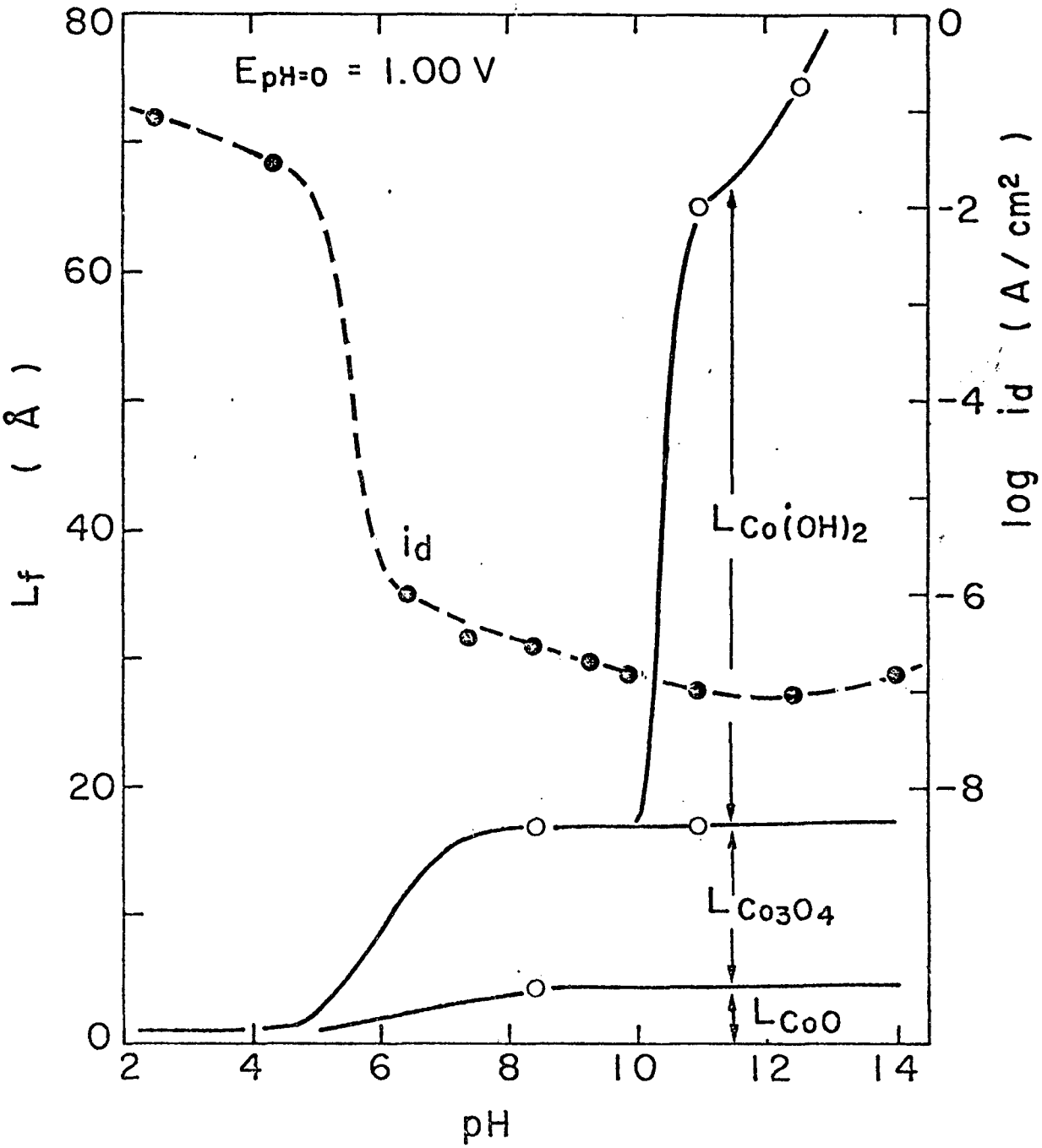

Fig. 12-31. Film thickness and dissolution current of secondary passivity.

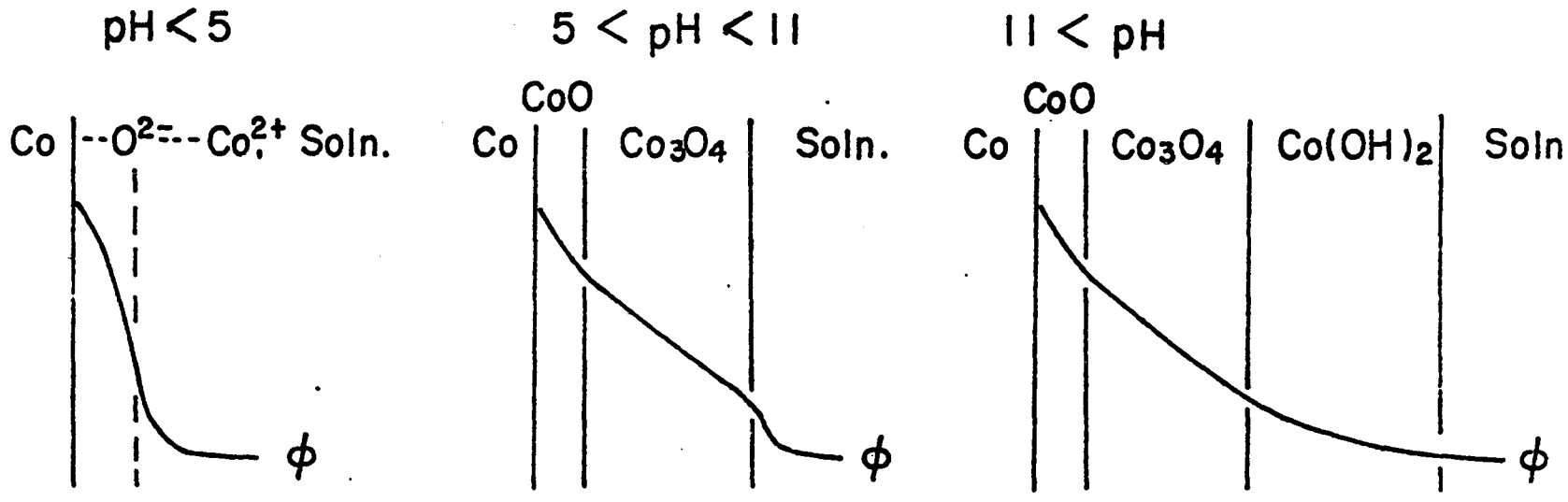

Fig. 12-32. Film model for the passive film on Co in potential region II in acid, neutral, and alkaline solutions.

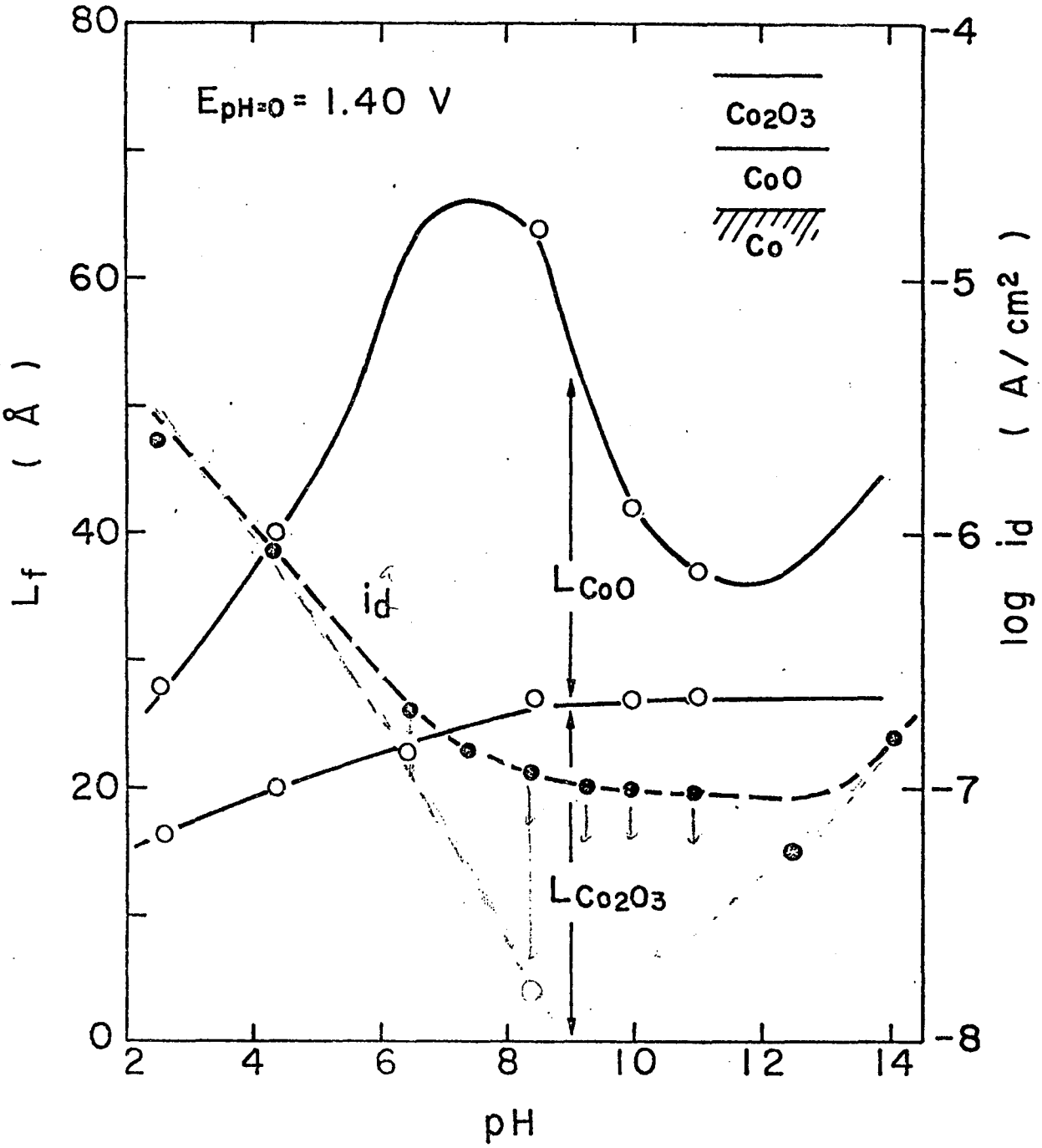

Fig. 12-33. Film thickness and dissolution current of tertiary passivity.

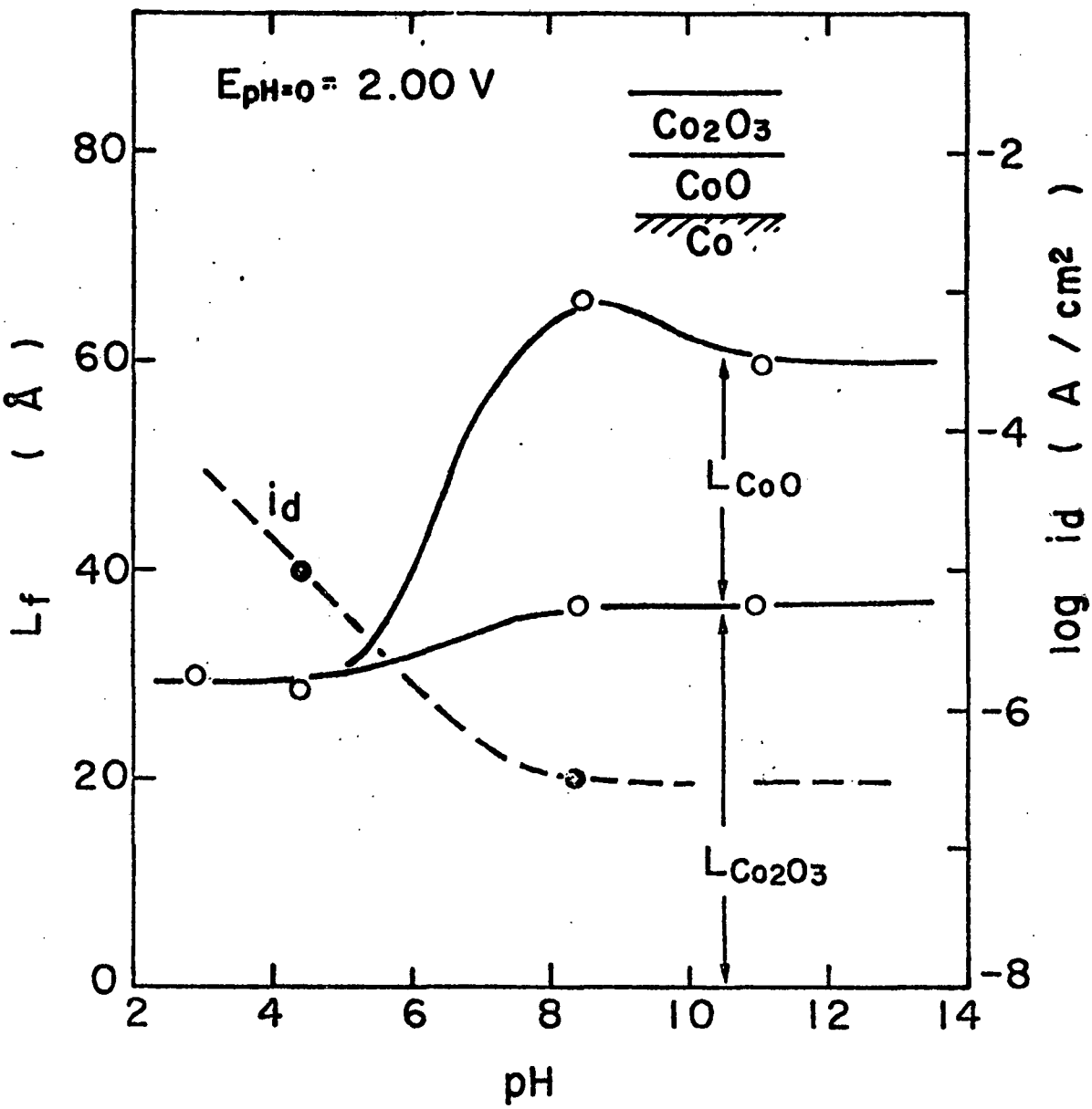

Fig. 12-34. Film thickness and dissolution current of transpassivity

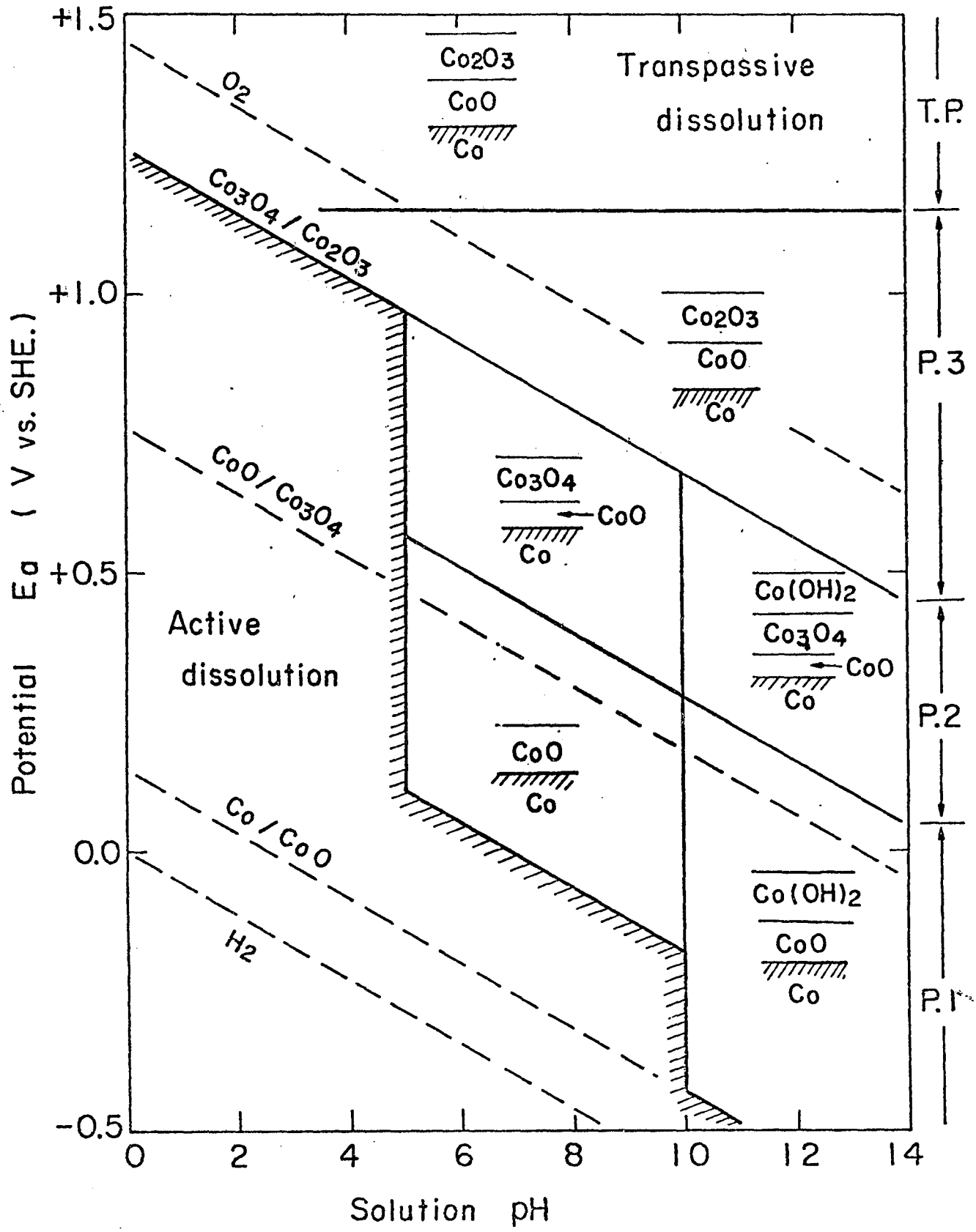

Fig. 12-35. Potential-pH diagram showing the composition of passive oxide films on Co which depends on pH and potential.

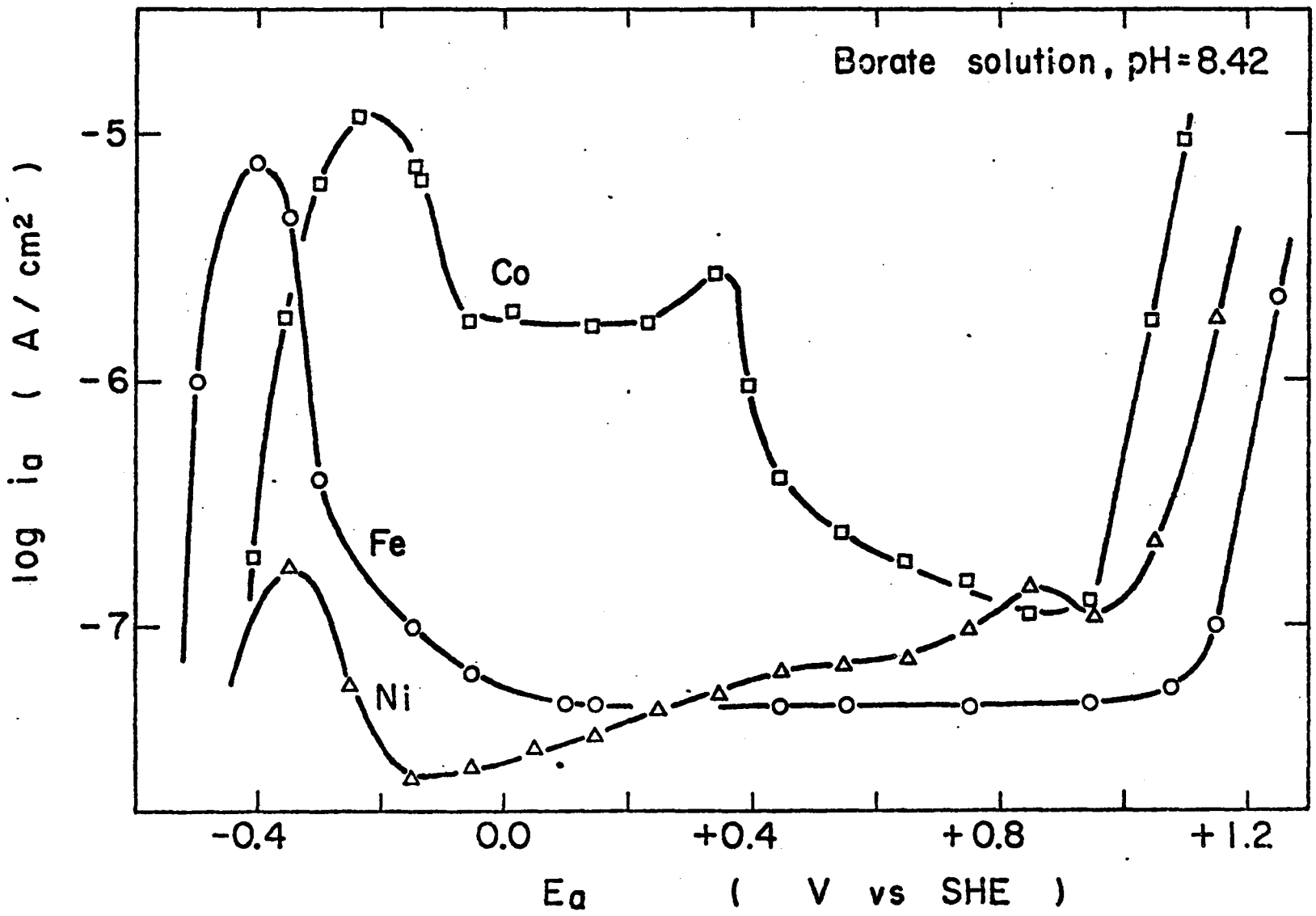

Fig. 12-36. Anodic polarization curve of Fe, Ni and Co in borate solution at pH 8.42.

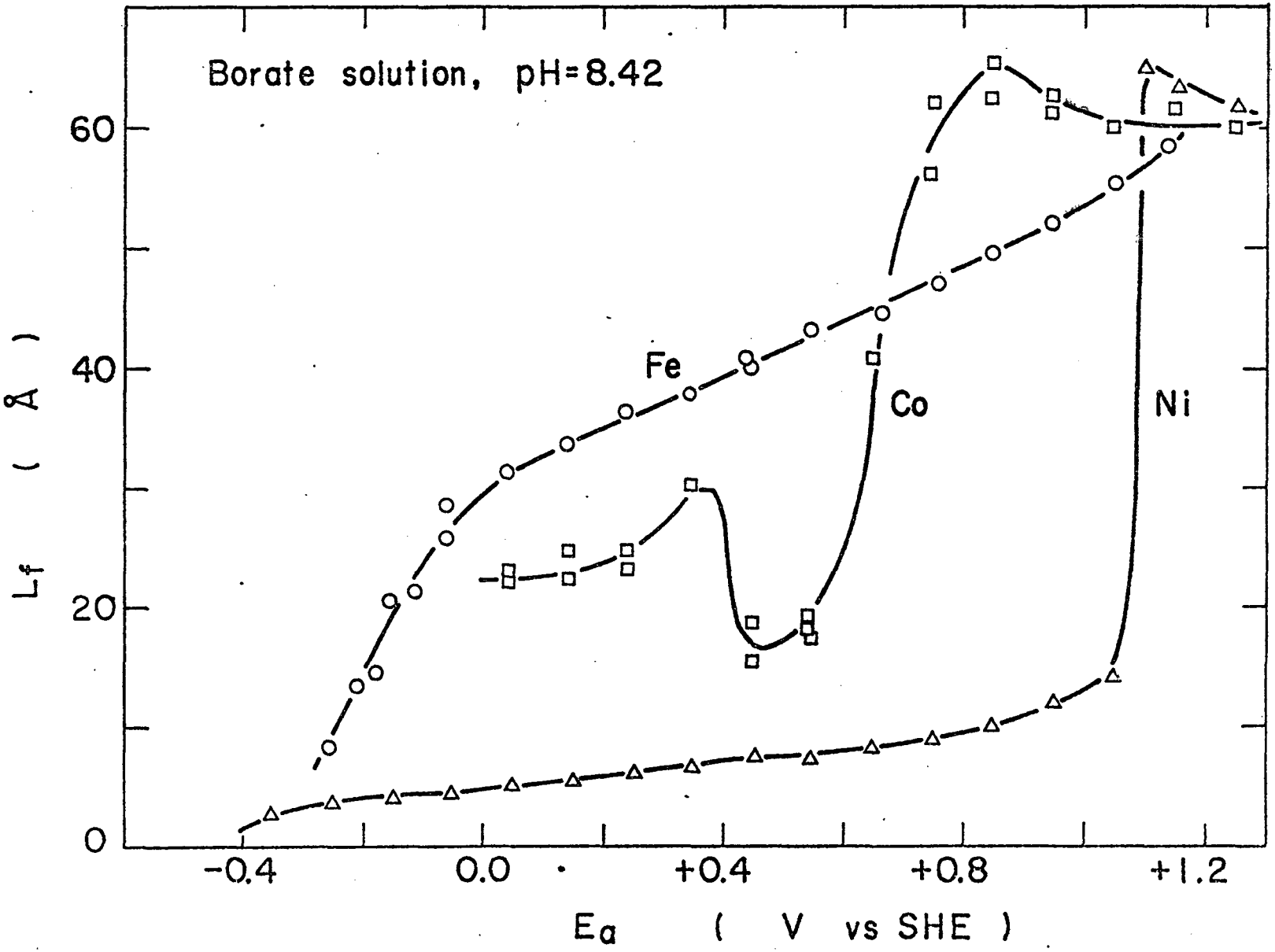

Fig. 12-37. Film thickness versus potential for passive film on Fe, Ni and Co in borate solution at pH 8.42.

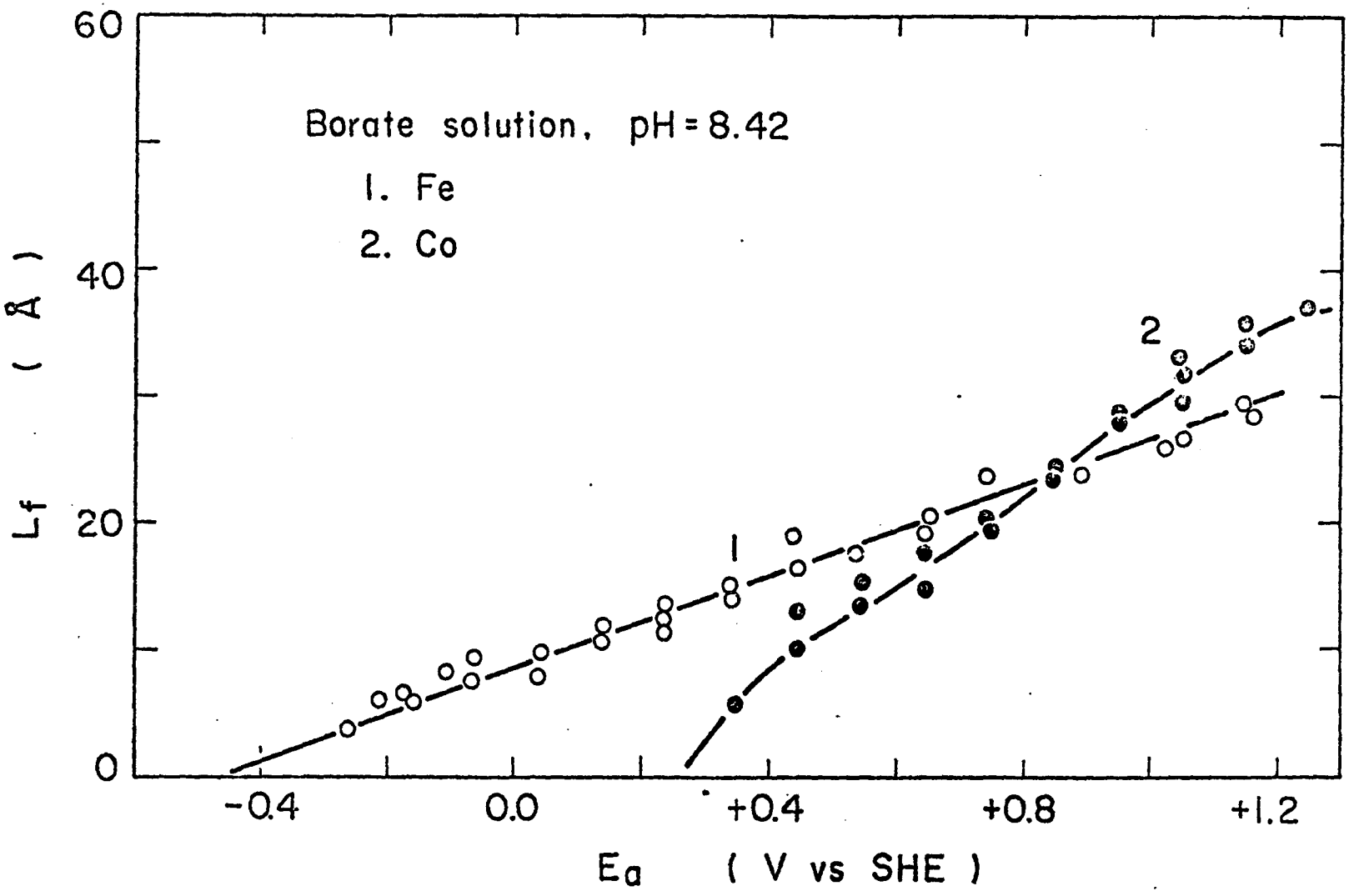

Fig. 12-38. Barrier layer thickness versus potential for passive oxide films on Fe and Co in borate solution at pH 8.42.

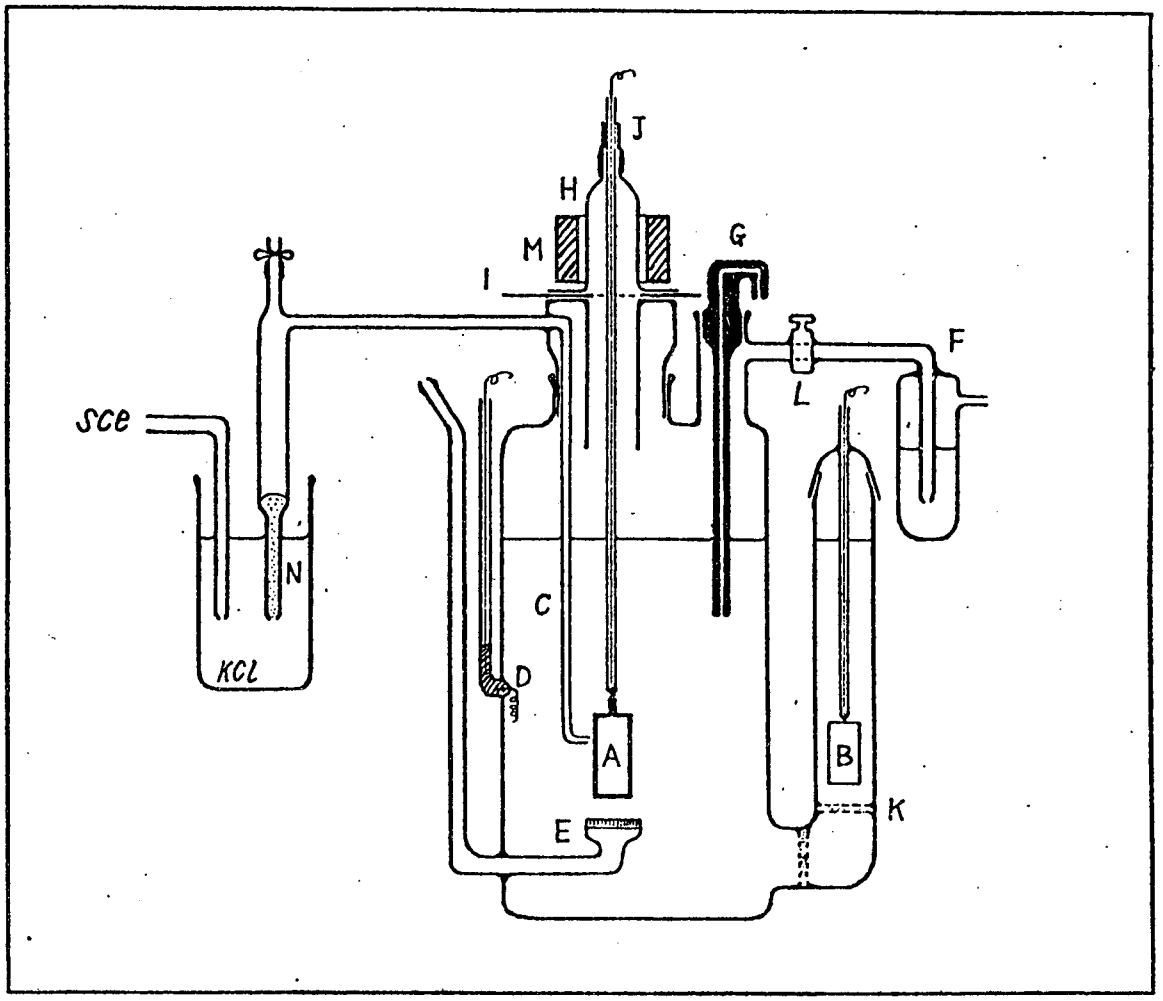

Fig. 13-1. Electrolytic cell

A: test specimen B: subsidary Pt electrode for current supply C: tip of liquid bridge D: auxiliary Pt electrode for setting potential of specimen E: nitrogen gas inlet F: gas outlet G: capillary tube for sampling the solution H: cap of the cell I: glass plate J: rubber tube for supporting the specimen K: sintered glass filter L: stop cock M: weight N: agar saturated with KCl

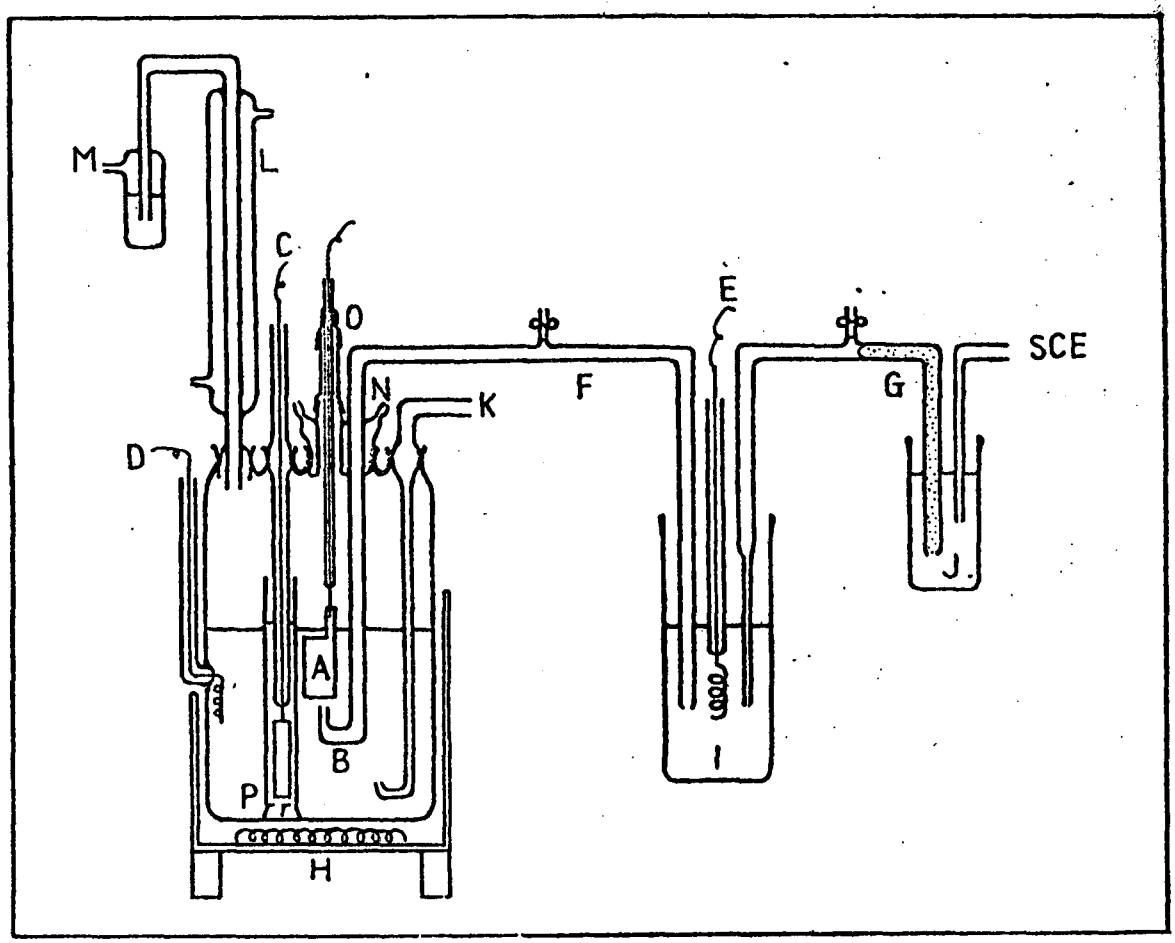

Fig. 13-2. Electrolytic cell.

A: test specimen B: tip of liquid bridge C: subsidary Pt electrode for current supply D: auxiliary Pt electrode for setting potential of specimen E: subsidary Pt electrode for pre-electrolysis F: liquid bridge G: agar saturated with KCl H: heater I: 10% H_2SO_4 solution J: saturated KCl solution K: nitrogen gas inlet L: condenser M: water sealed gas outlet N: condenser cap O: rubber tube for supporting the specimen P: glass chimney

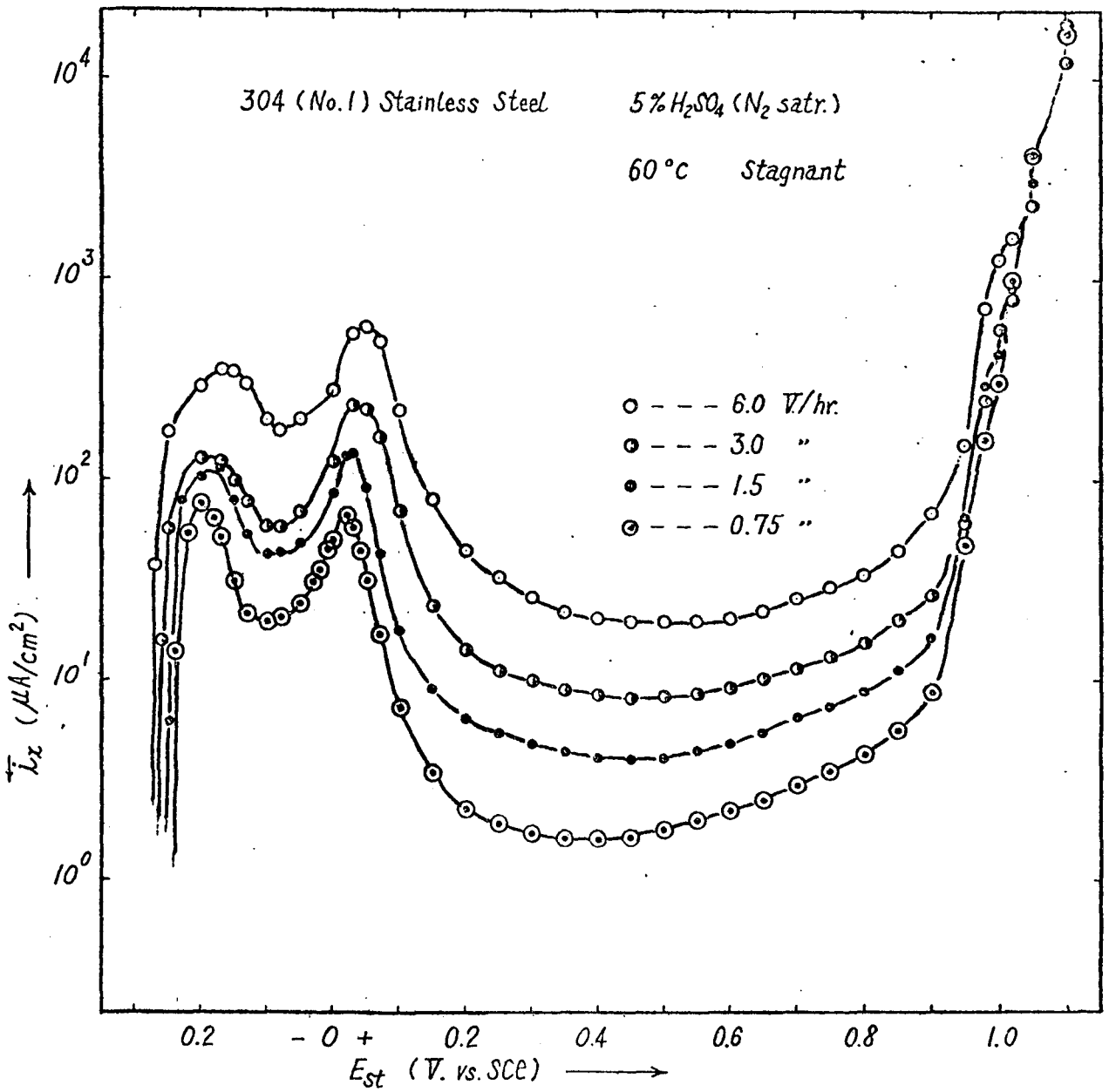

Fig. 13-3. Effect of shifting rate of potential on the anodic polarization curves of stainless steel.

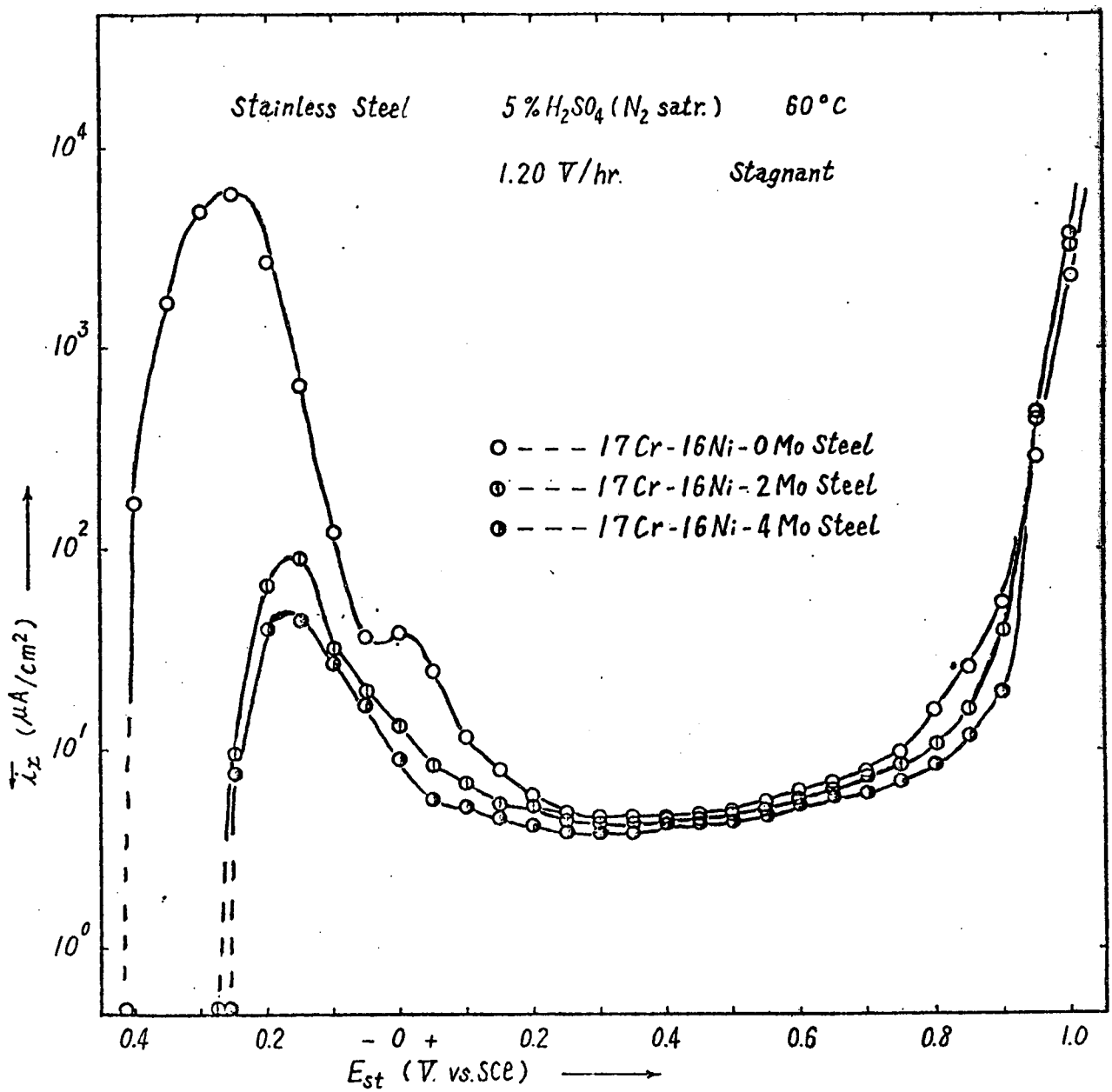

Fig. 13-4. Effect of Molybdenum content on the anodic polarization curves obtained by potentiodynamic method.

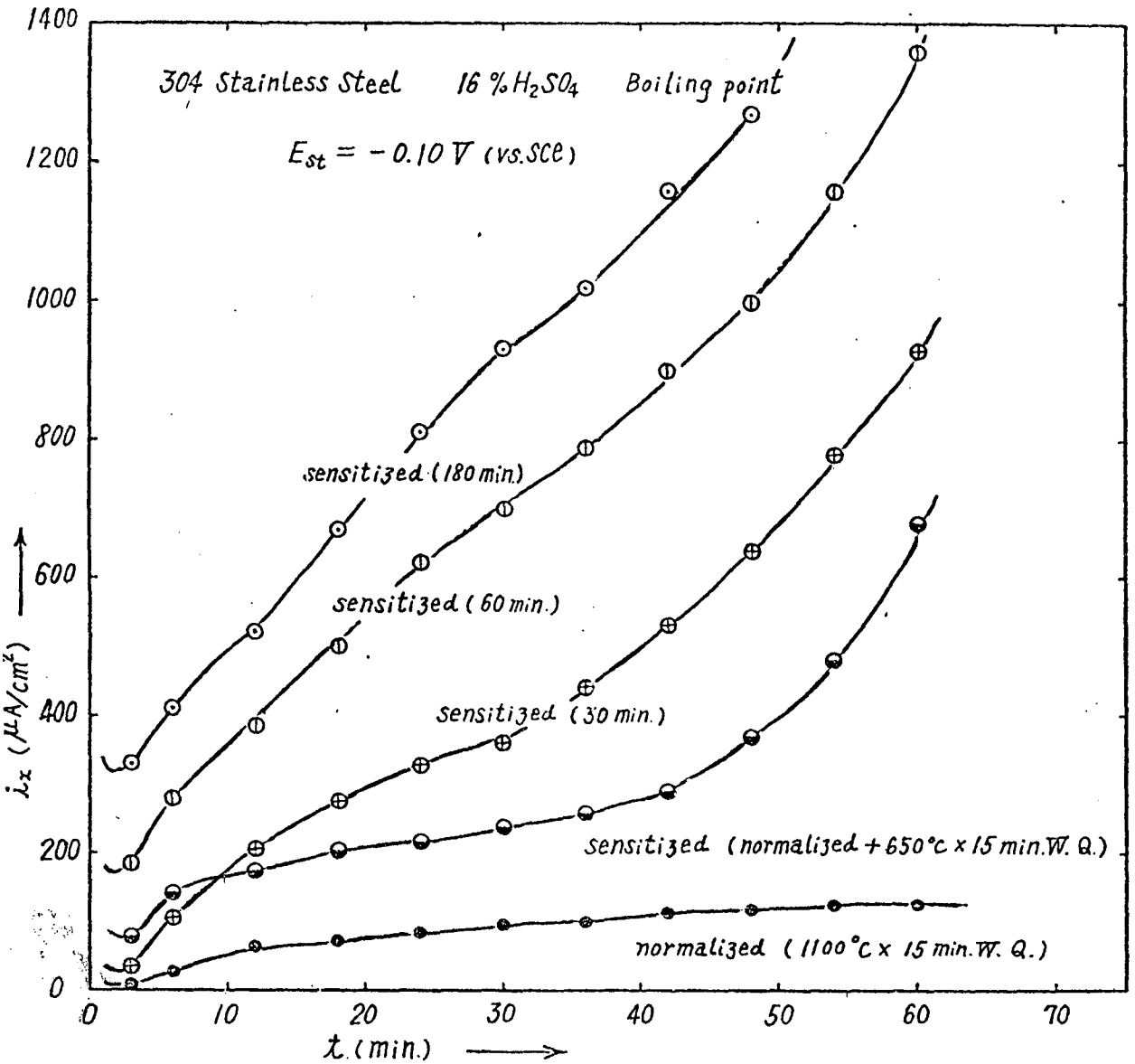

Fig. 13-5. Effect of heat treatment on the time-variation of external current at E_{st} = - 0.10 V vs.SCE.

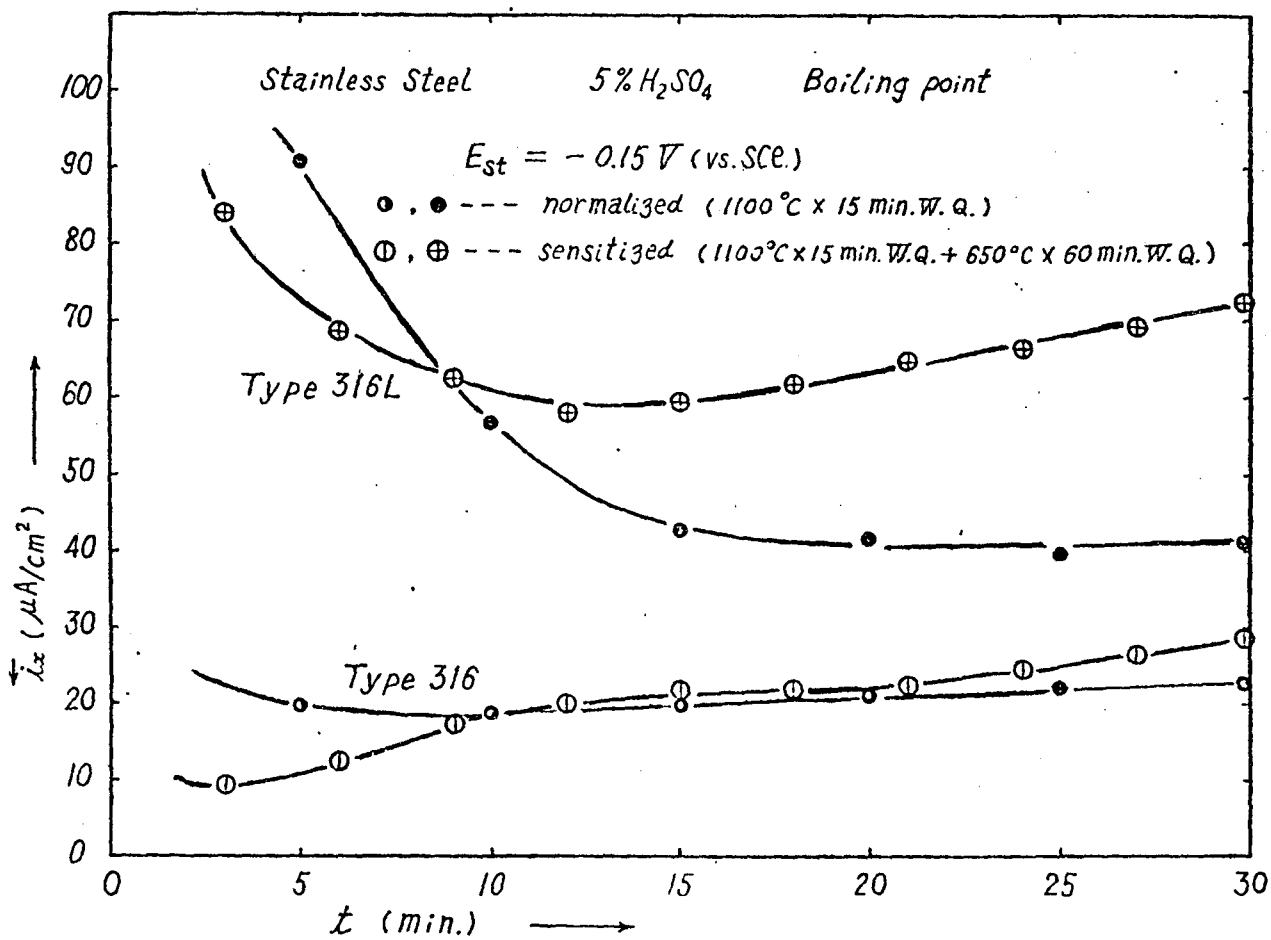

Fig. 13-6. Effect of heat treatment on external current of stainless steel at a constant potential in active-passive transitional region.

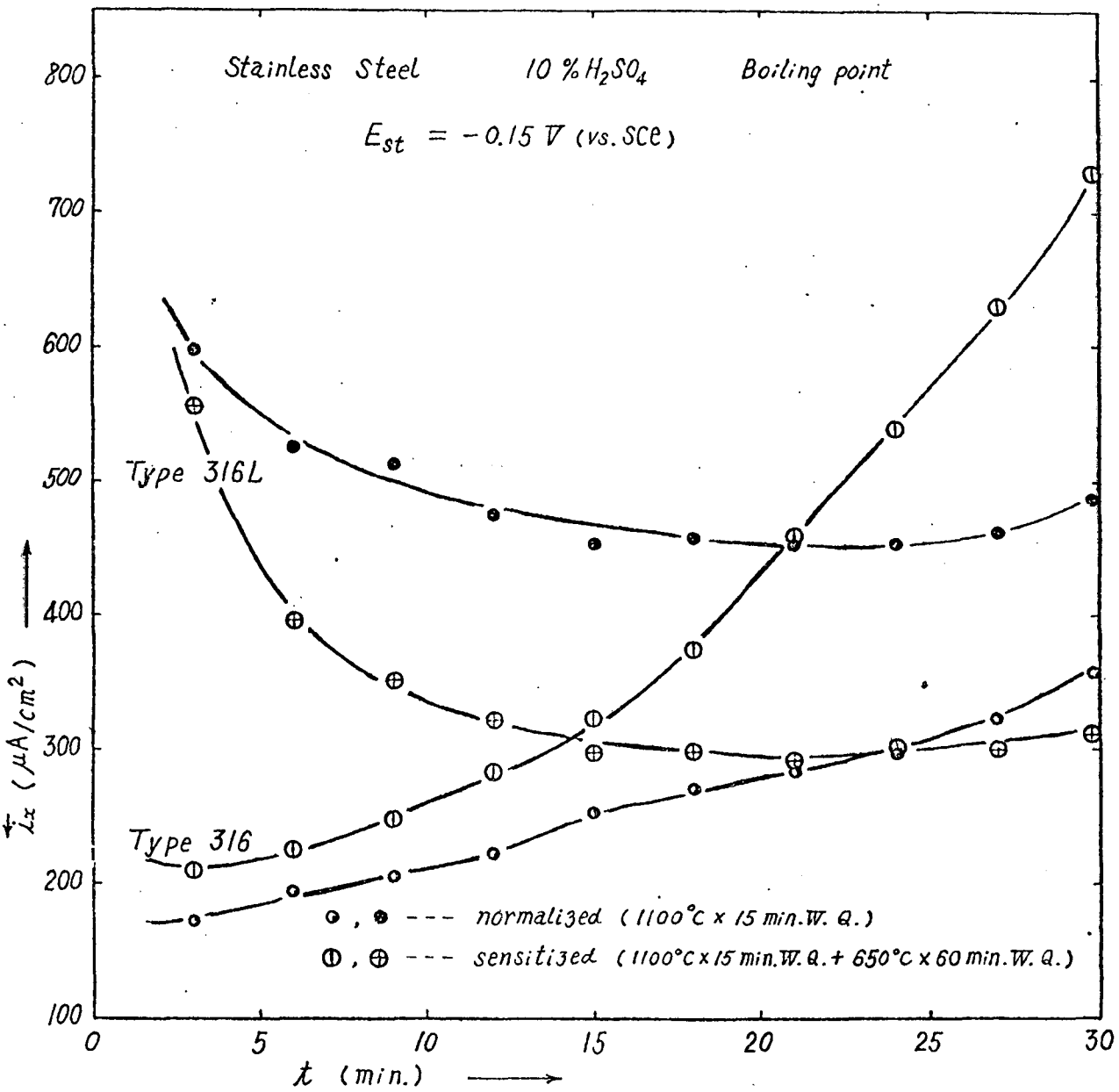

Fig. 13-7. Effect of heat treatment on external current of stainless steel at a constant potential in active-passive transitional region.

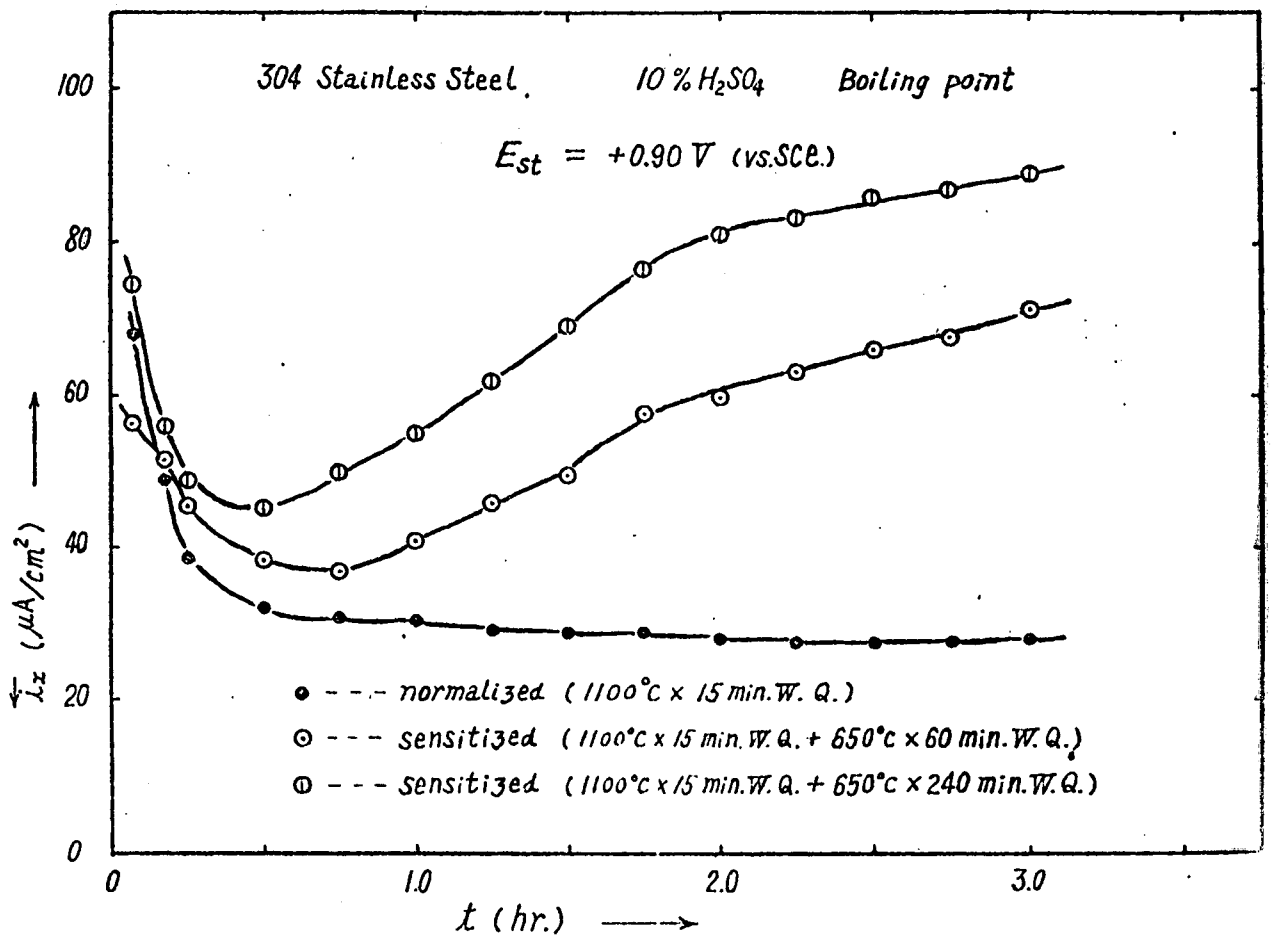

Fig. 13-8. Effect of heat treatment on the time-variation of external current at E_{st} = - 0.90 V. vs. SCE.

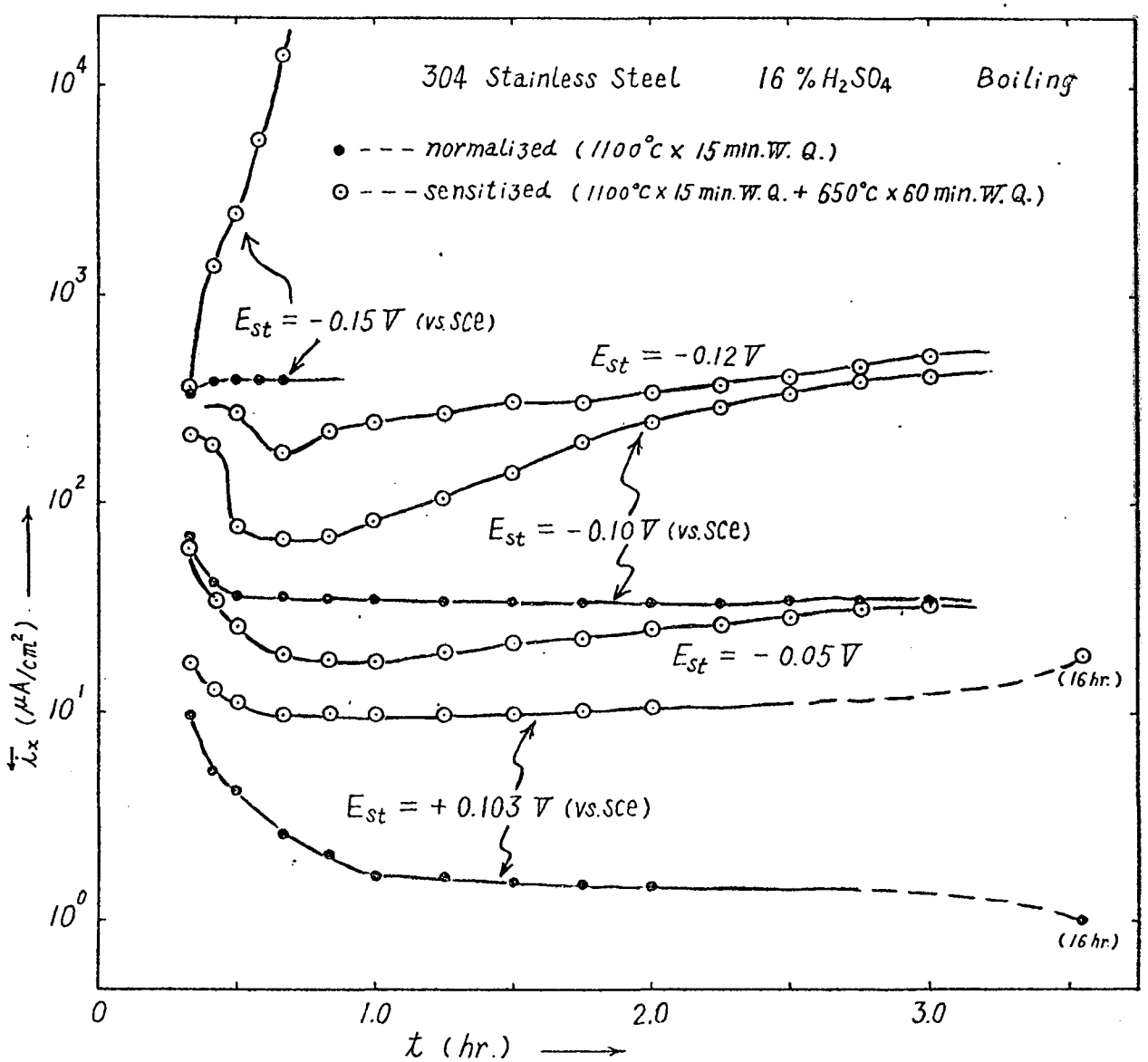

Fig. 13-9. Effect of heat treatment on external current of stainless steel at a constant potential in potential region of Strauß test.

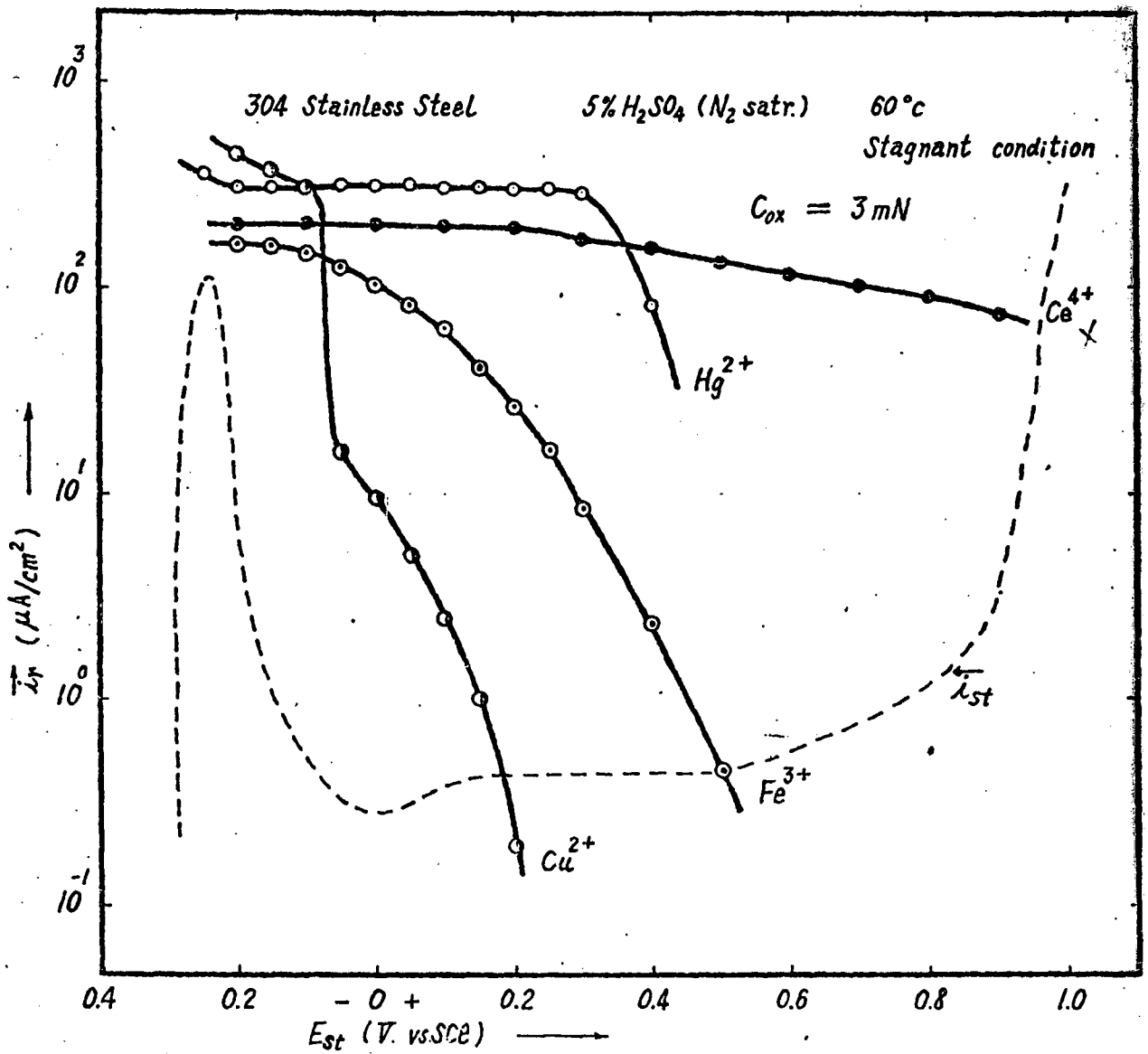

Fig. 13-10. Potential-dependence of reduction current of an oxidizing agent on the surface of stainless steel.

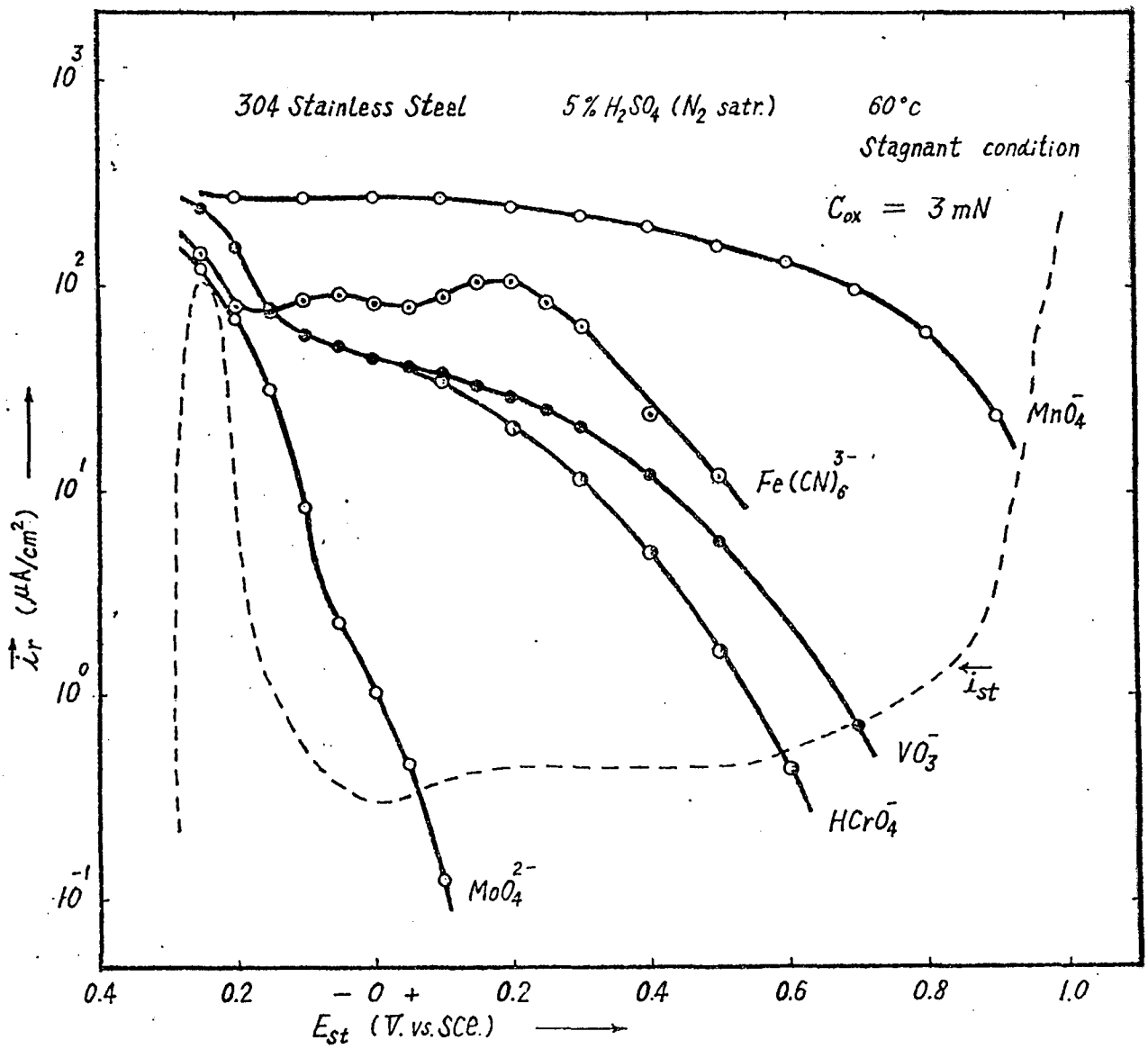

Fig. 13-11. Potential-dependence of reduction current of an oxidizing agent on the surface of stainless steel.

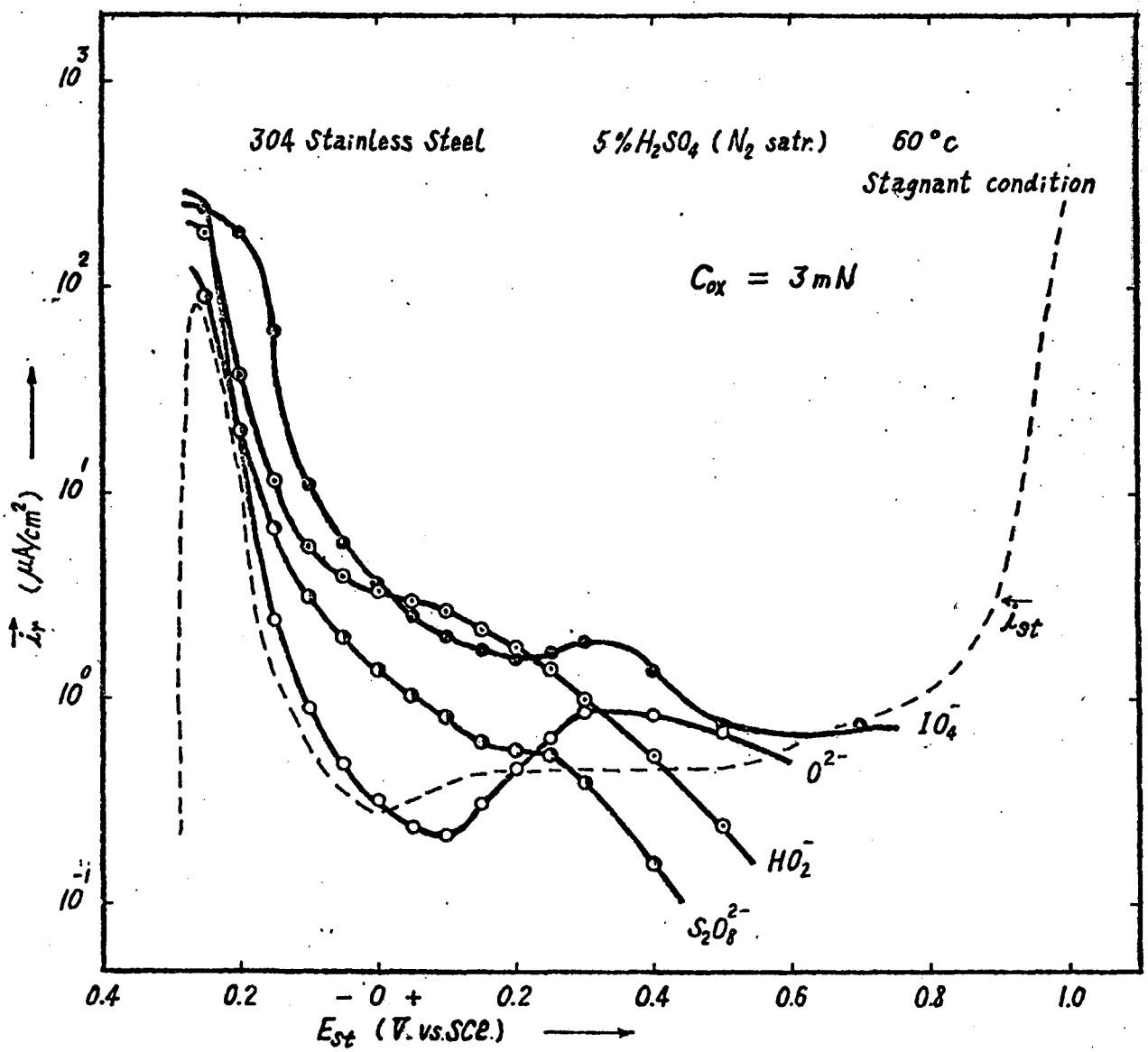

Fig. 13-12. Potential-dependence of reduction current of an oxidizing agent on the surface of stainless steel.

Oxidizing agents	GROUP A Fe^{3+}, Cu^{2+}, Hg^{2+}, Ce^{4+} MnO_4^-, VO_3^- ...	GROUP B O^{2-}, HO_2^-, $HCrO_4^-$ $S_2O_8^{2-}$, IO_4^-, UO_2^- ...
Reduction on passive steel	easy	difficult
Stability for cathodic pulse	stable	unstable
Resistance to Cl^- ion	good	no good
Surface of passive stainless steel (speculative) ⊕ ---positive hole (higher oxide) (OX) --Oxidizing agent (Red) --Reduced product	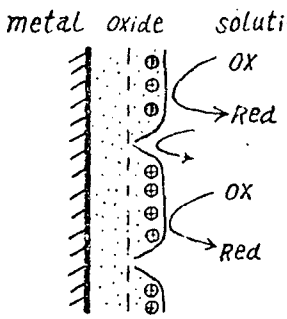	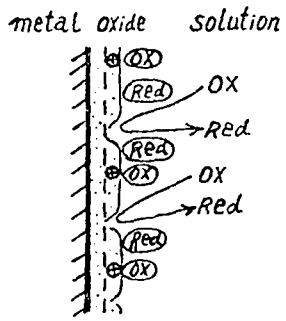

Fig. 13-13. Classification of oxidizing agent with respect to cathodic reduction behaviour and speculative figure of passive surface of stainless steel.

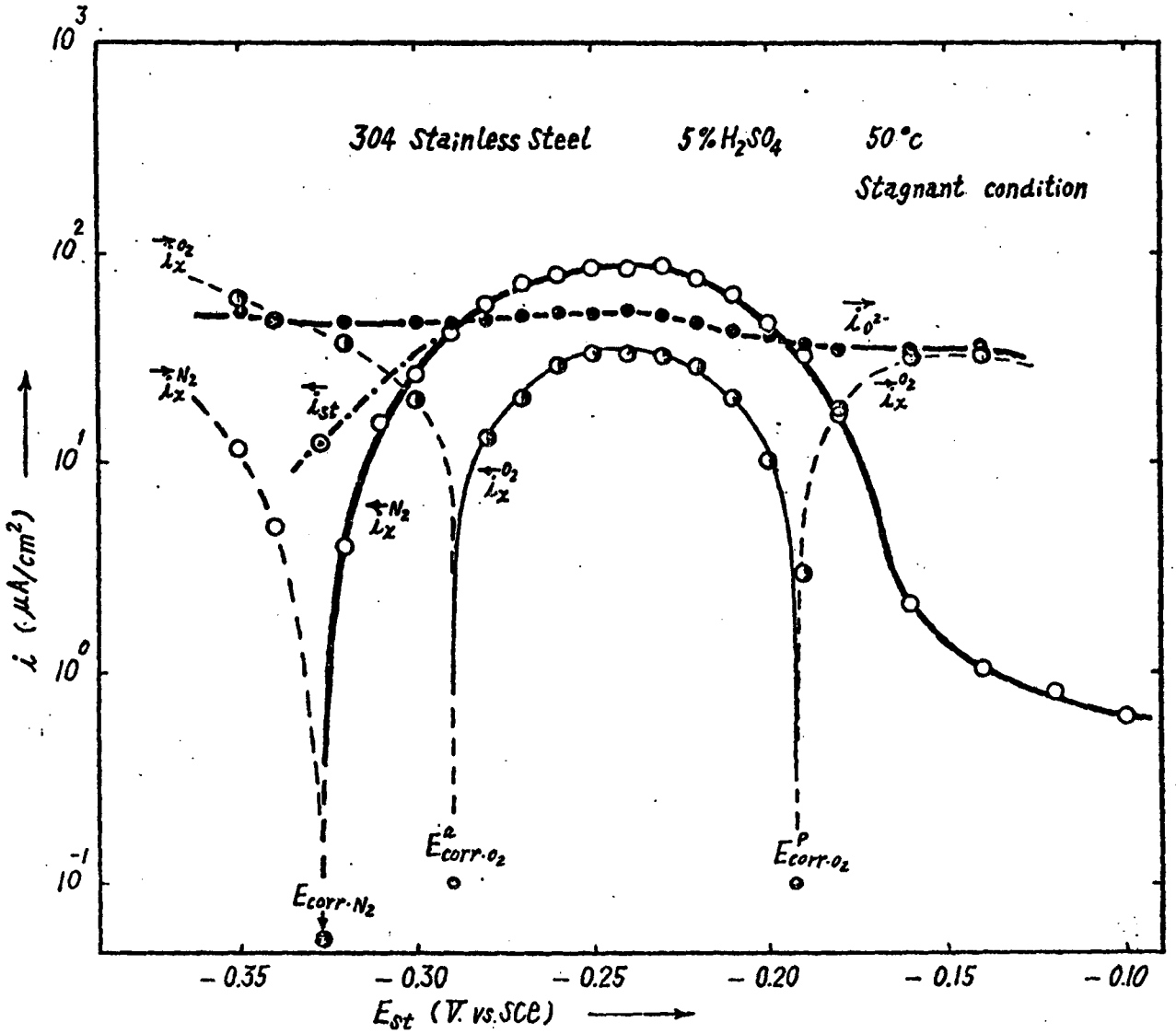

Fig. 13-14. Polarization curves of $\overleftarrow{i}_{st}$, $\vec{i}_r$ and i_x of 304 stainless steel in aerated 5% H_2SO_4 solution at 50°C.

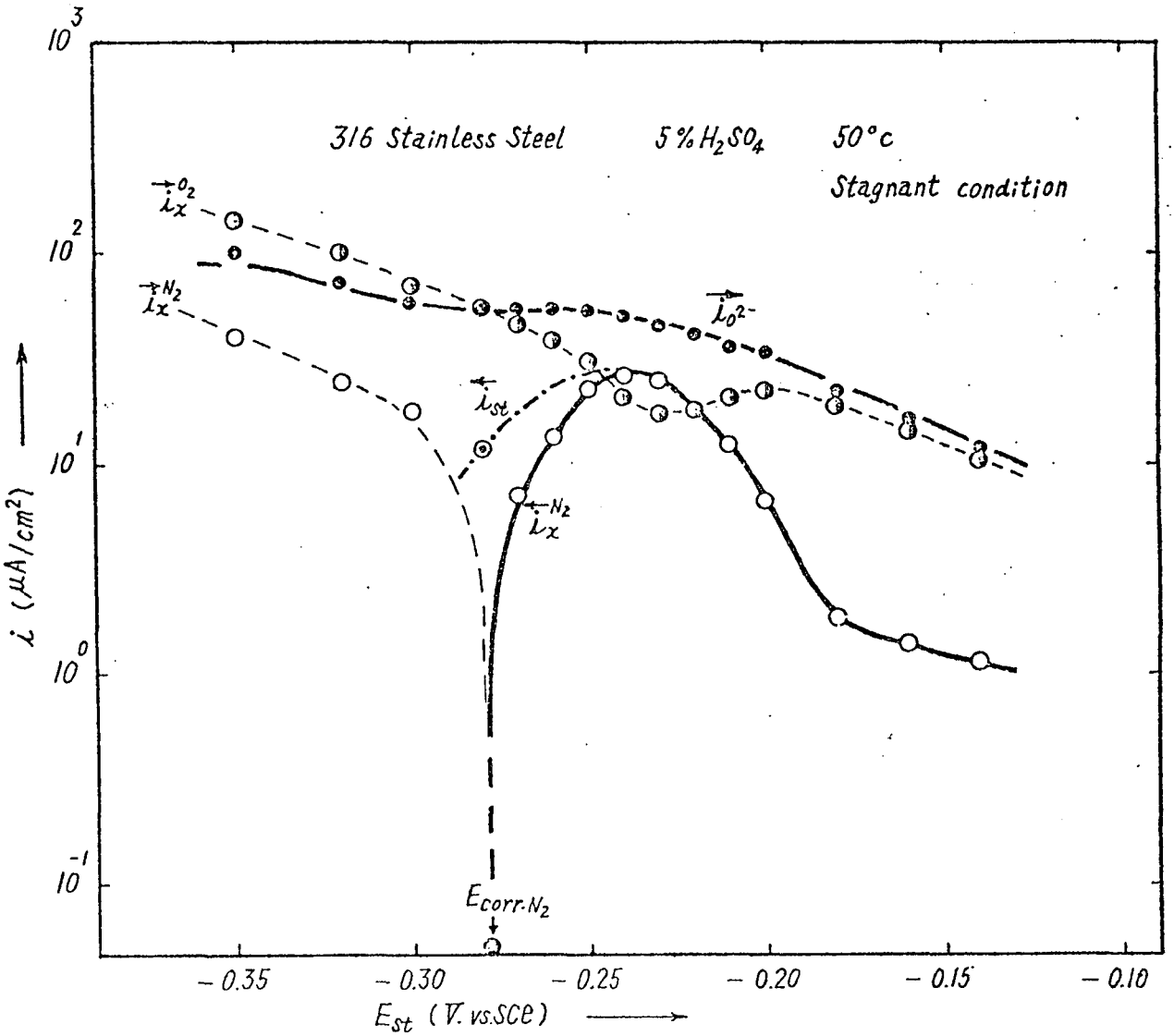

Fig. 13-15. Polarization curves of $\overleftarrow{i}_{st}$, $\vec{i}_r$ and i_x of 316 stainless steel in aerated 5% H_2SO_4 solution at 50°C.

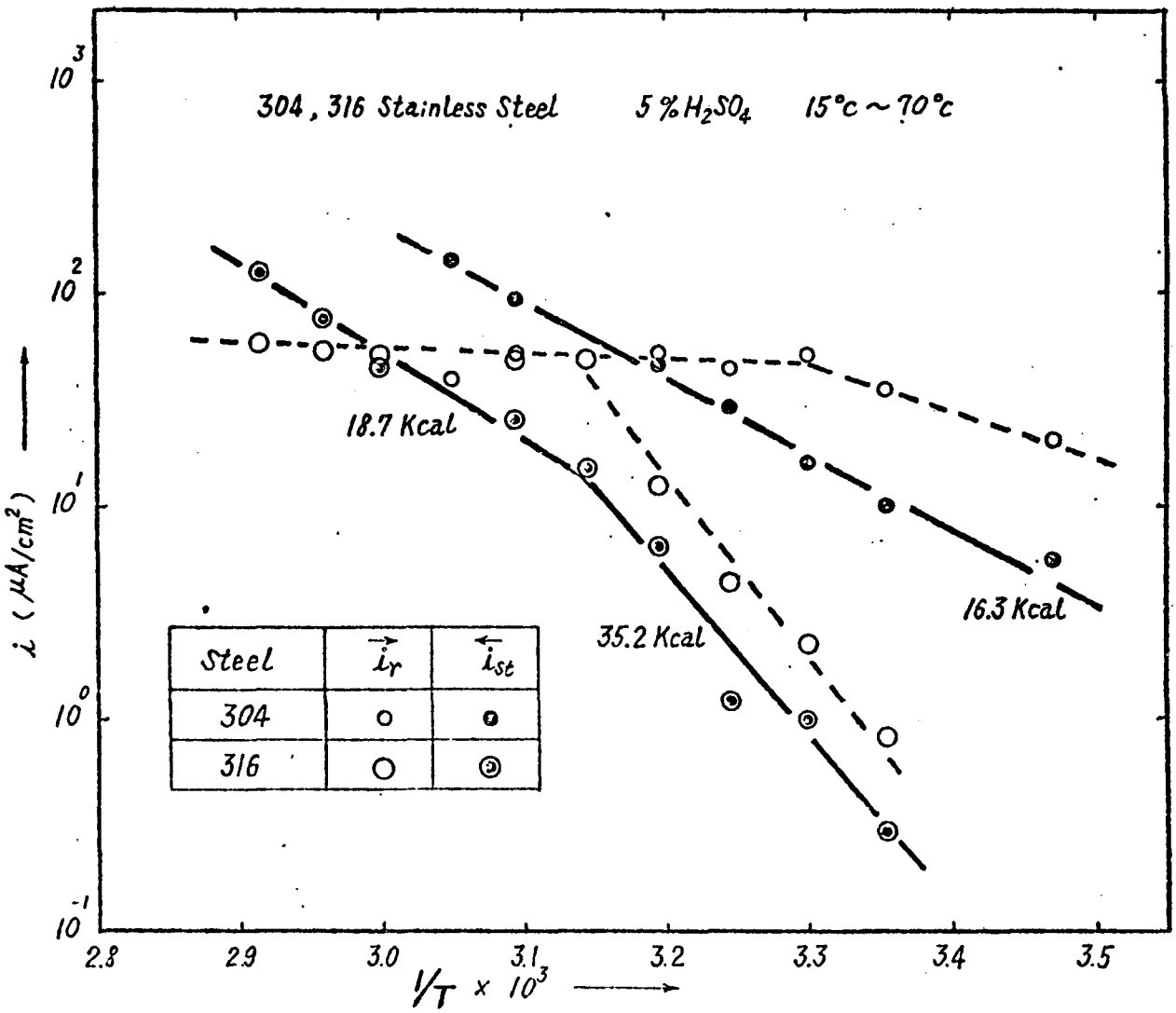

Fig. 13-16. Temperature dependency of $\overleftarrow{i}_{st}$ and $\vec{i}_r$ at a constant potential in active-passive transitional region.

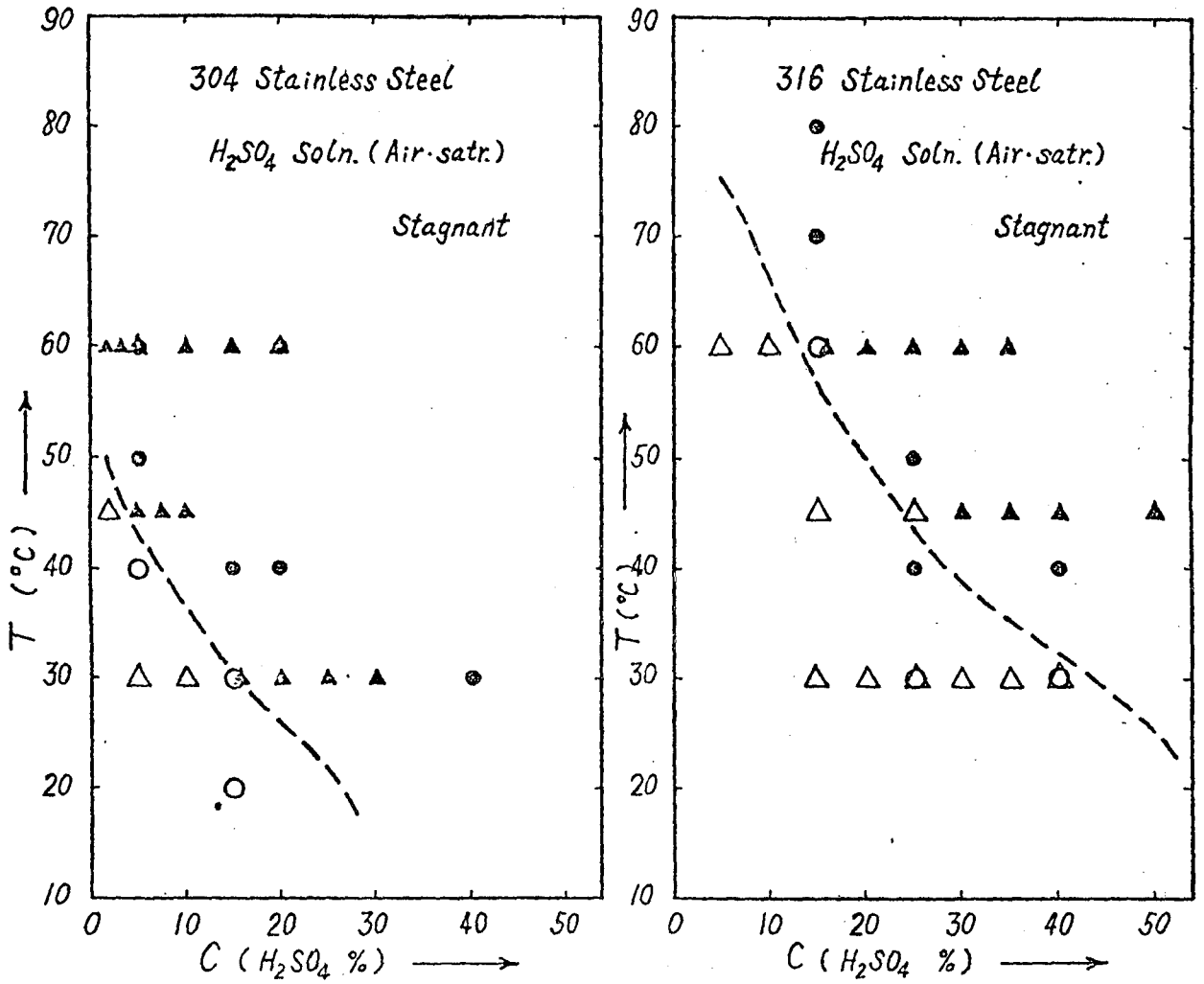

Fig. 13-17. Safety-region of austenitic stainless steel in aerated sulphuric acid solution.

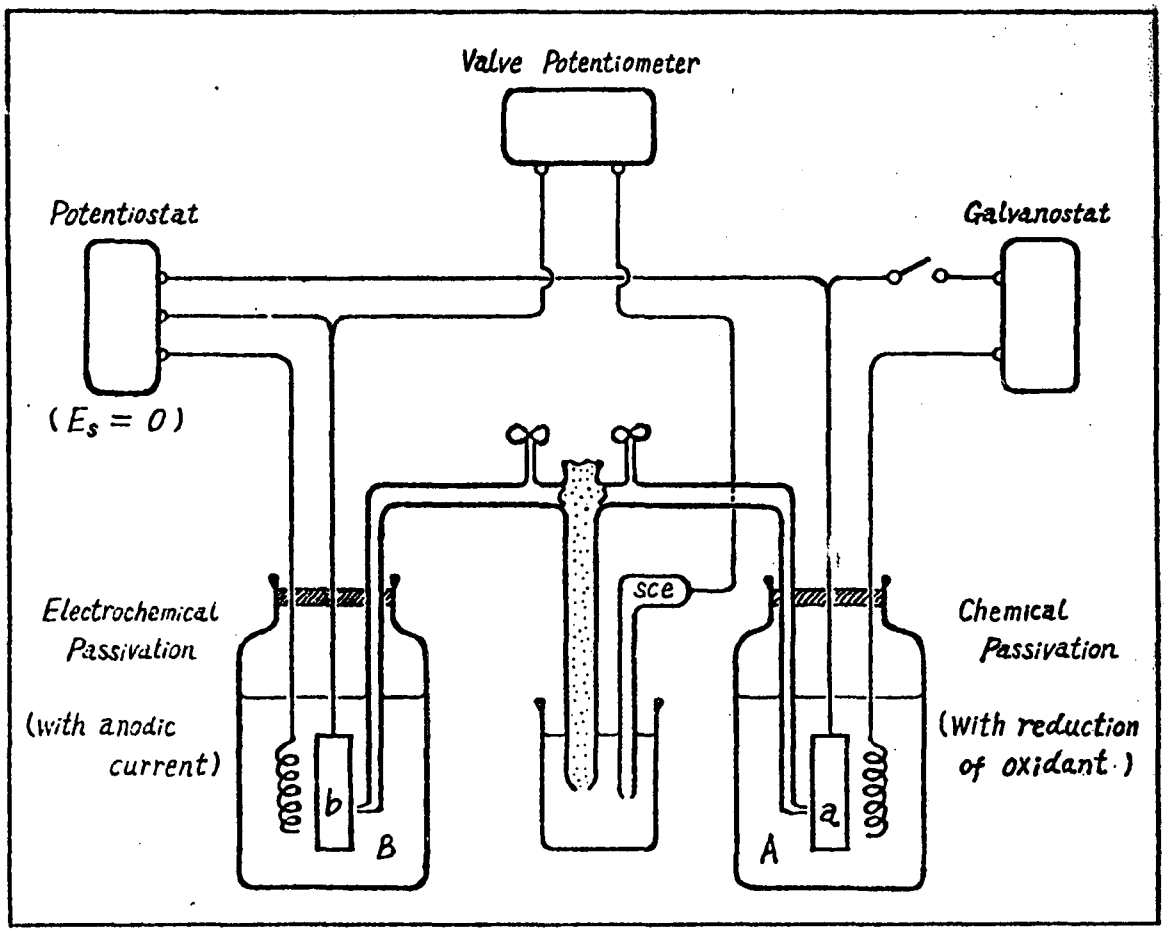

Fig. 13-18. Circuit for the measurement of transitional polarization curve.

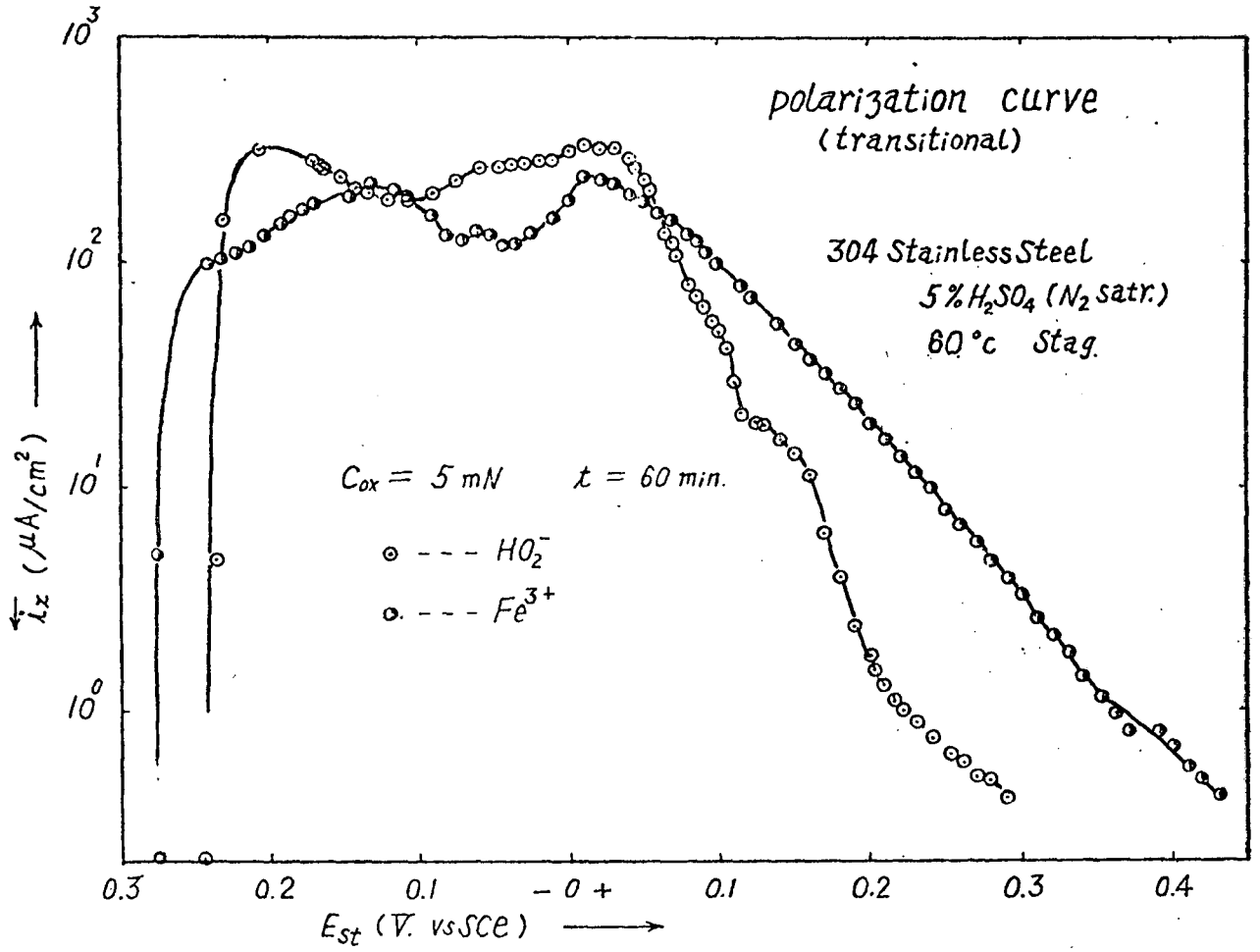

Fig. 13-19. Transitional polarization curve obtained by using the circuit shown in Fig. 13-18.

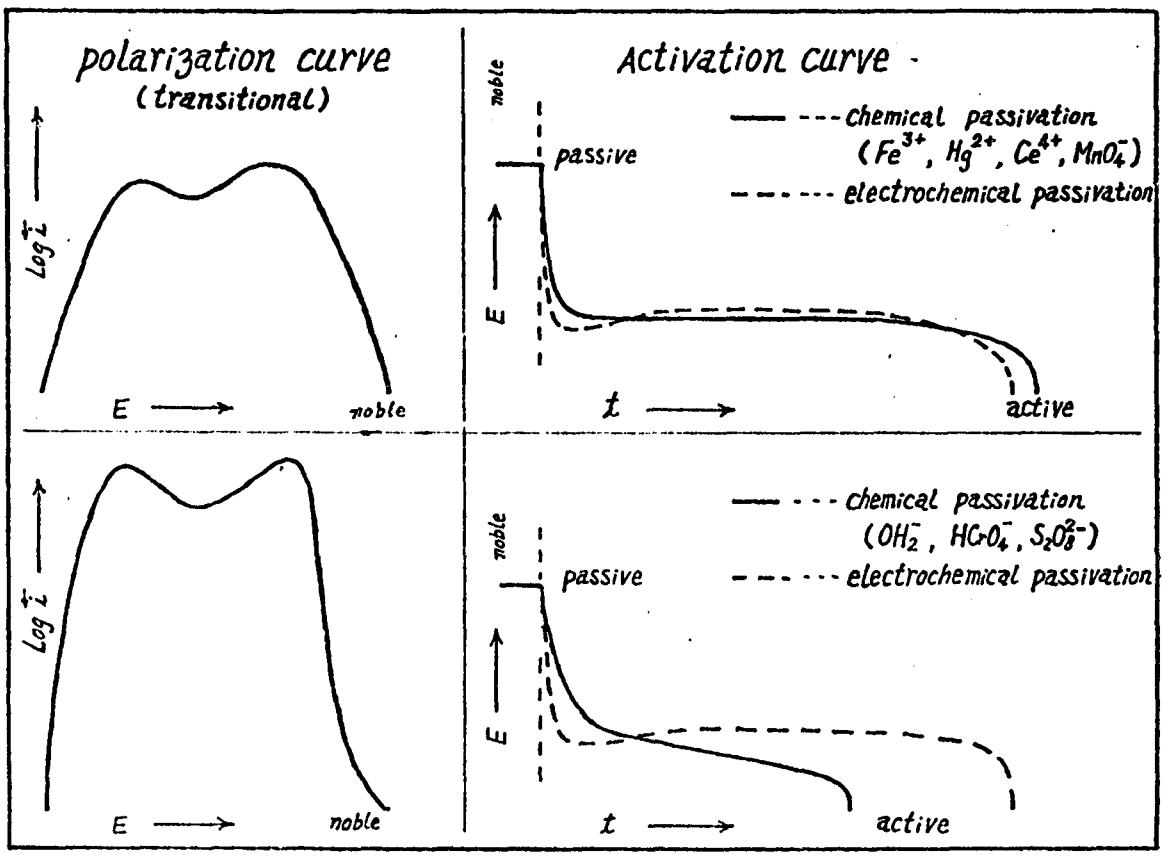

Fig. 13-20. Comparison between chemical passivation and electrochemical passivation with relation to their activation characteristics.

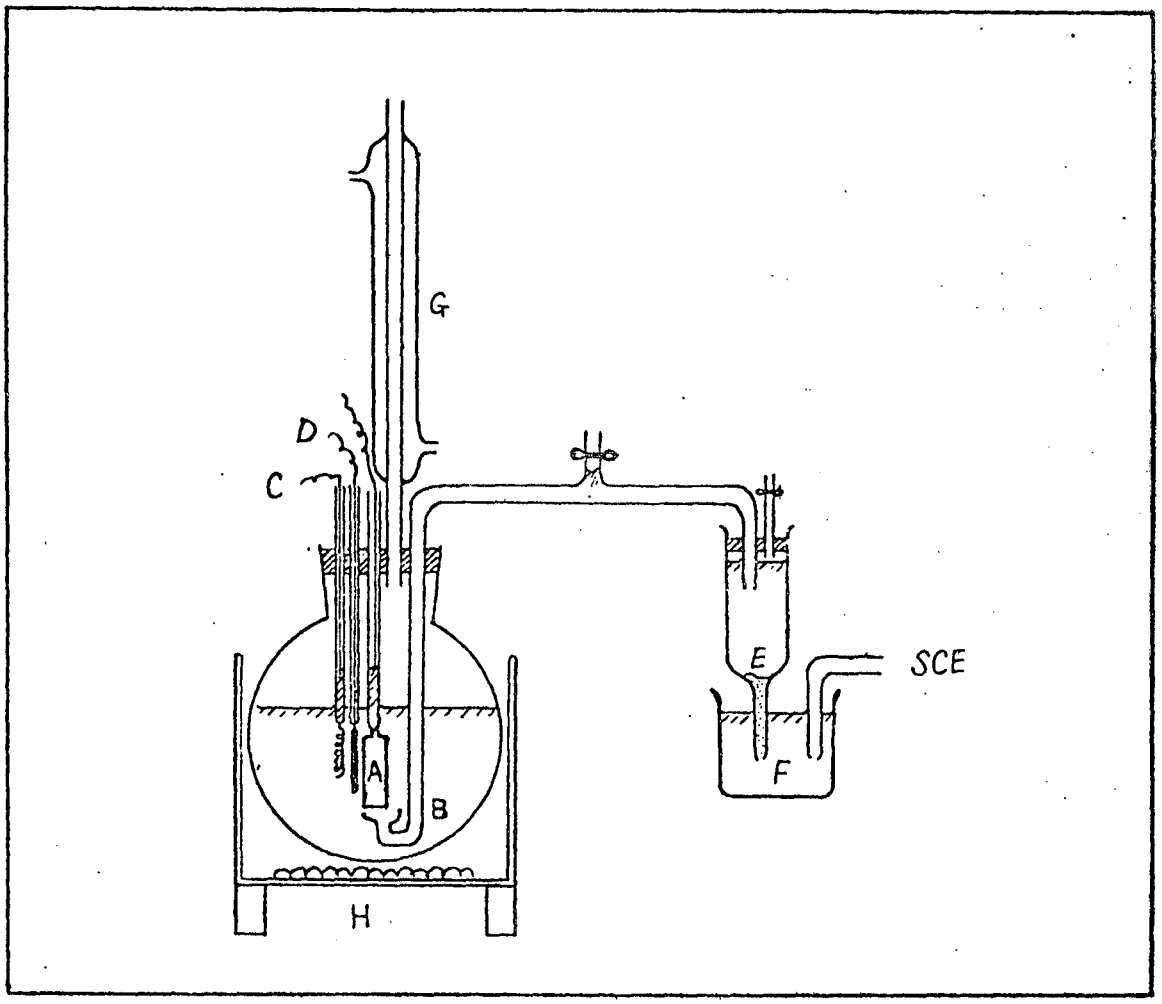

Fig. 13-21. Electrolytic cell for Strauß test.

A: test specimen

B: tip of liquid bridge

C: Pt electrode

D: Cu electrode

E: agar saturated with KCl

F: saturated KCl solution

G: condenser

H: heater

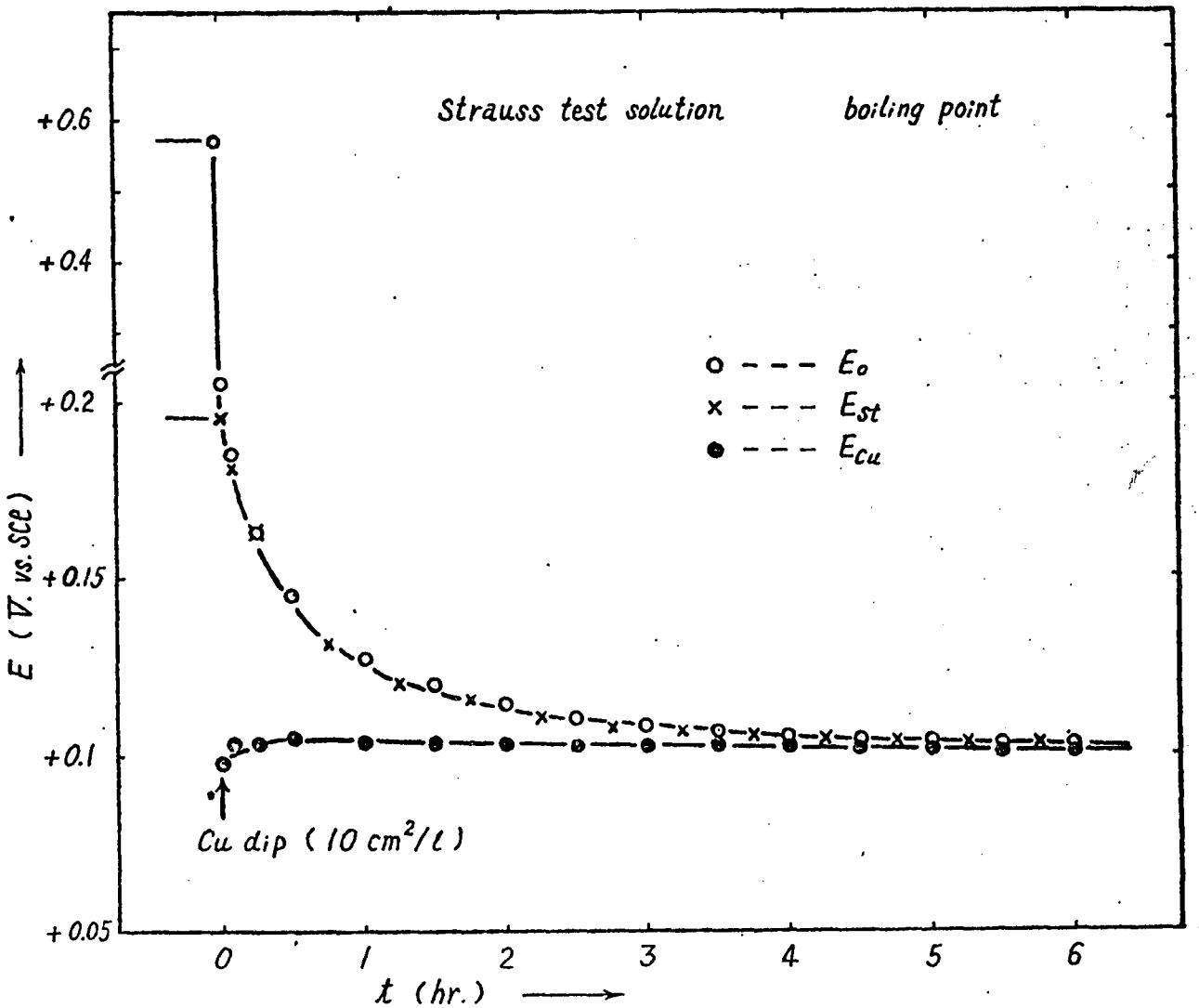

Fig. 13-22. Time-variation of E_o, E_{st} and E_{cu} (in case of no contact with metallic cupper and stainless steel).

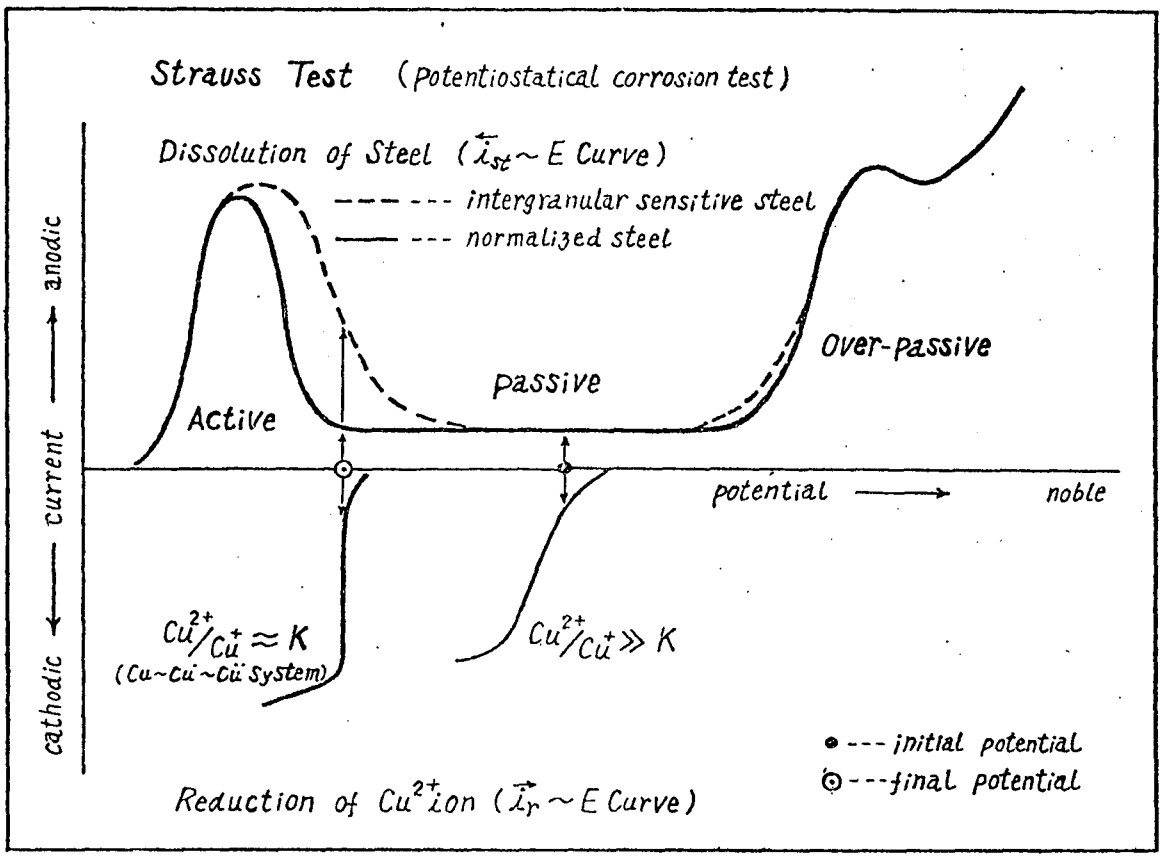

Fig. 13-23. Significance of Strauß test.

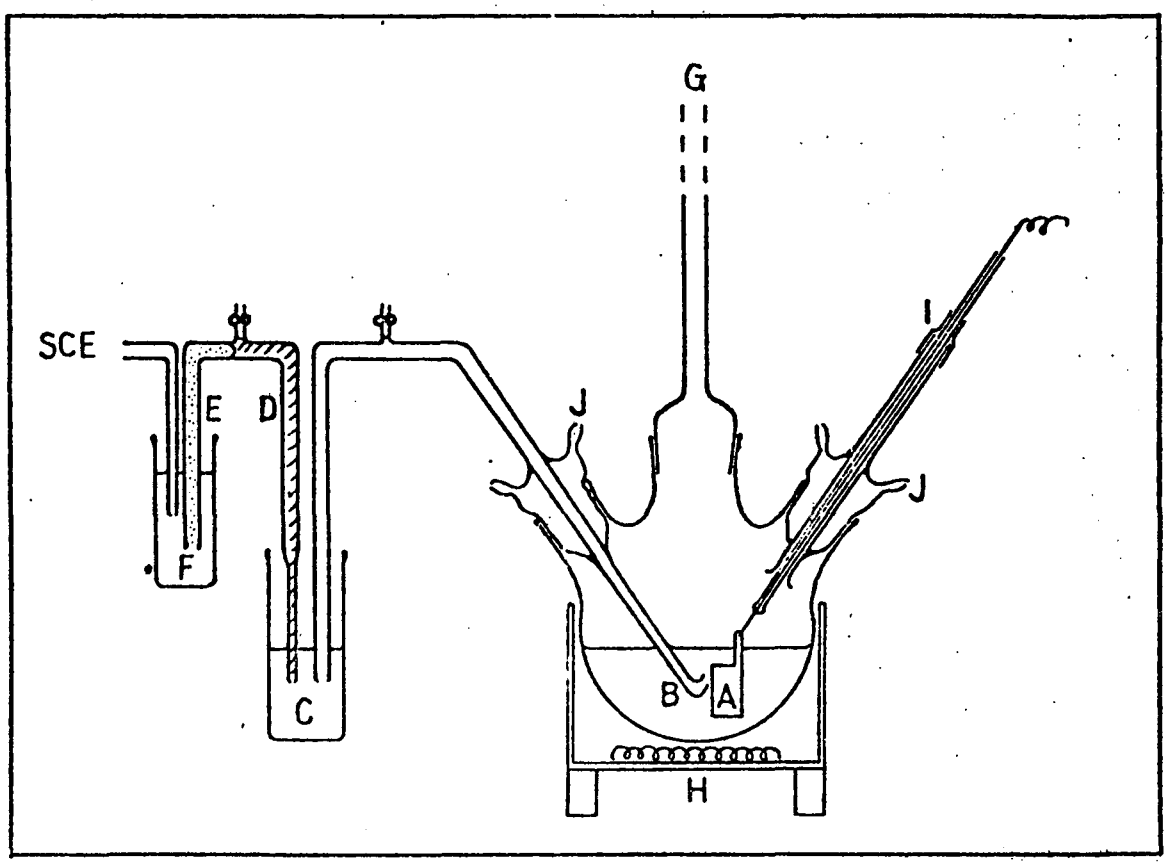

Fig. 13-24. Electrolytic cell for Huey test.

A: test specimen

B: tip of liquid bridge

C: 65% HNO_3 solution

D: saturated KNO_3 solution

E: agar saturated with KCl

F: saturated KCl solution

G: condenser

H: heater

I: rubber tube for supporting the specimen

J: cooling water inlet

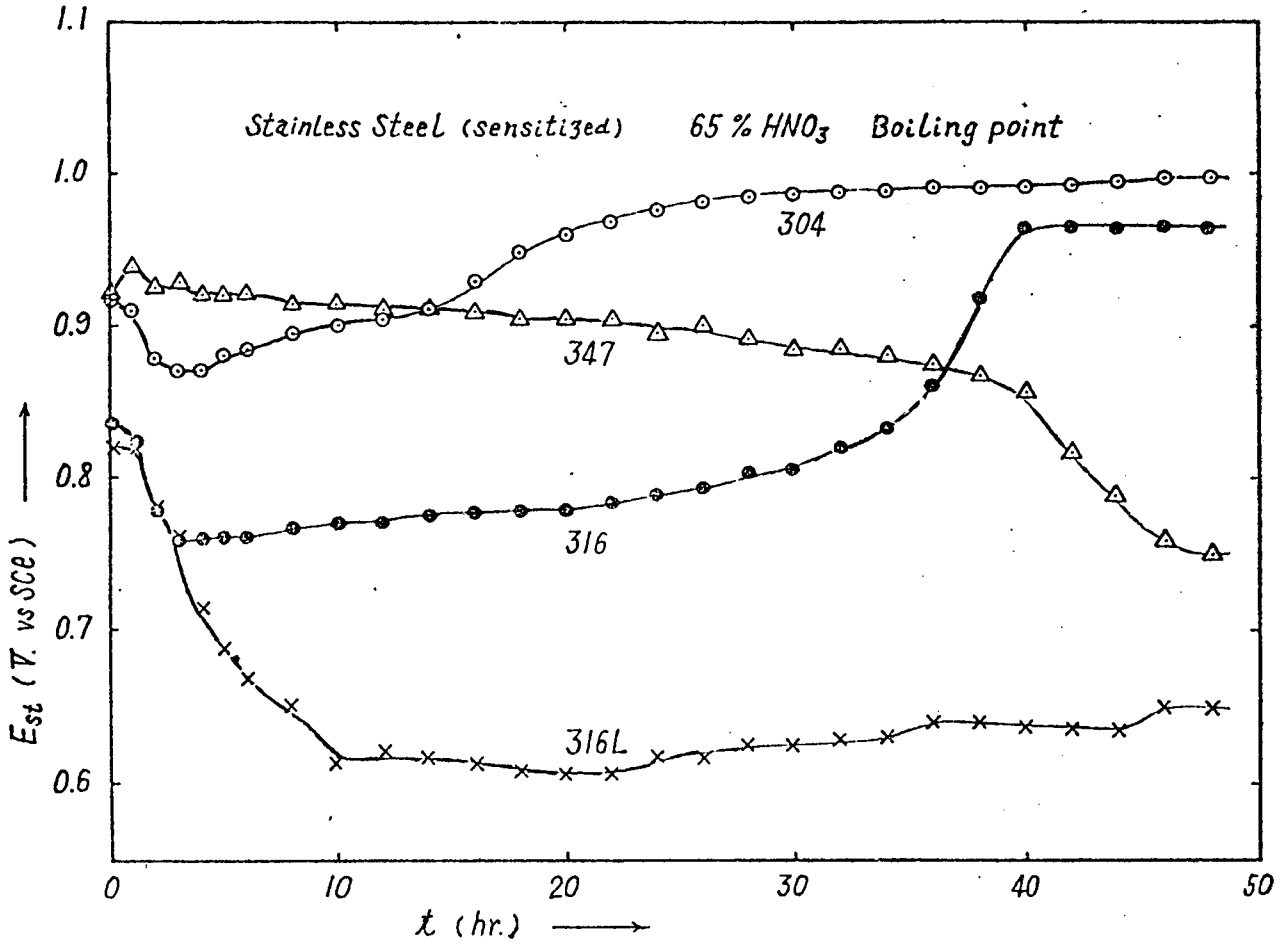

Fig. 13-25. Corrosion potentials of various kinds of stainless steels during Huey test.

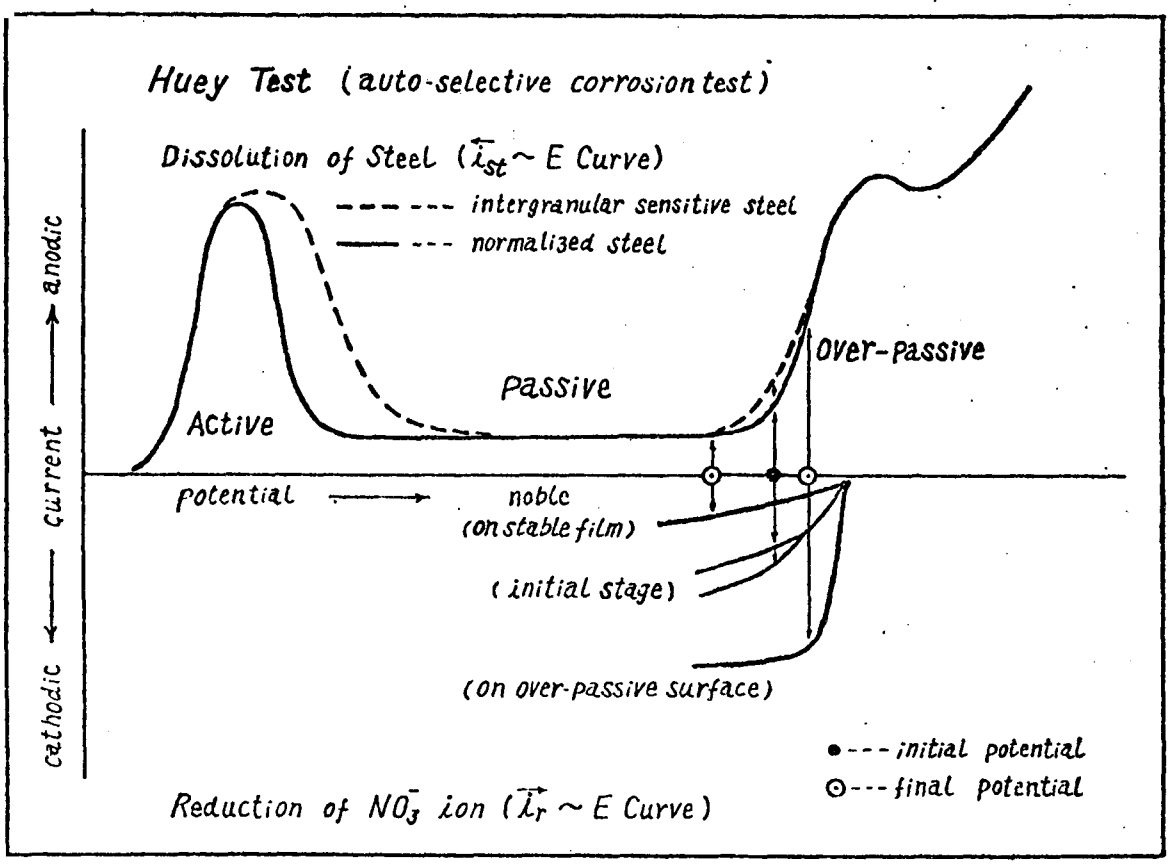

Fig. 13-26. Significance of Huey test.

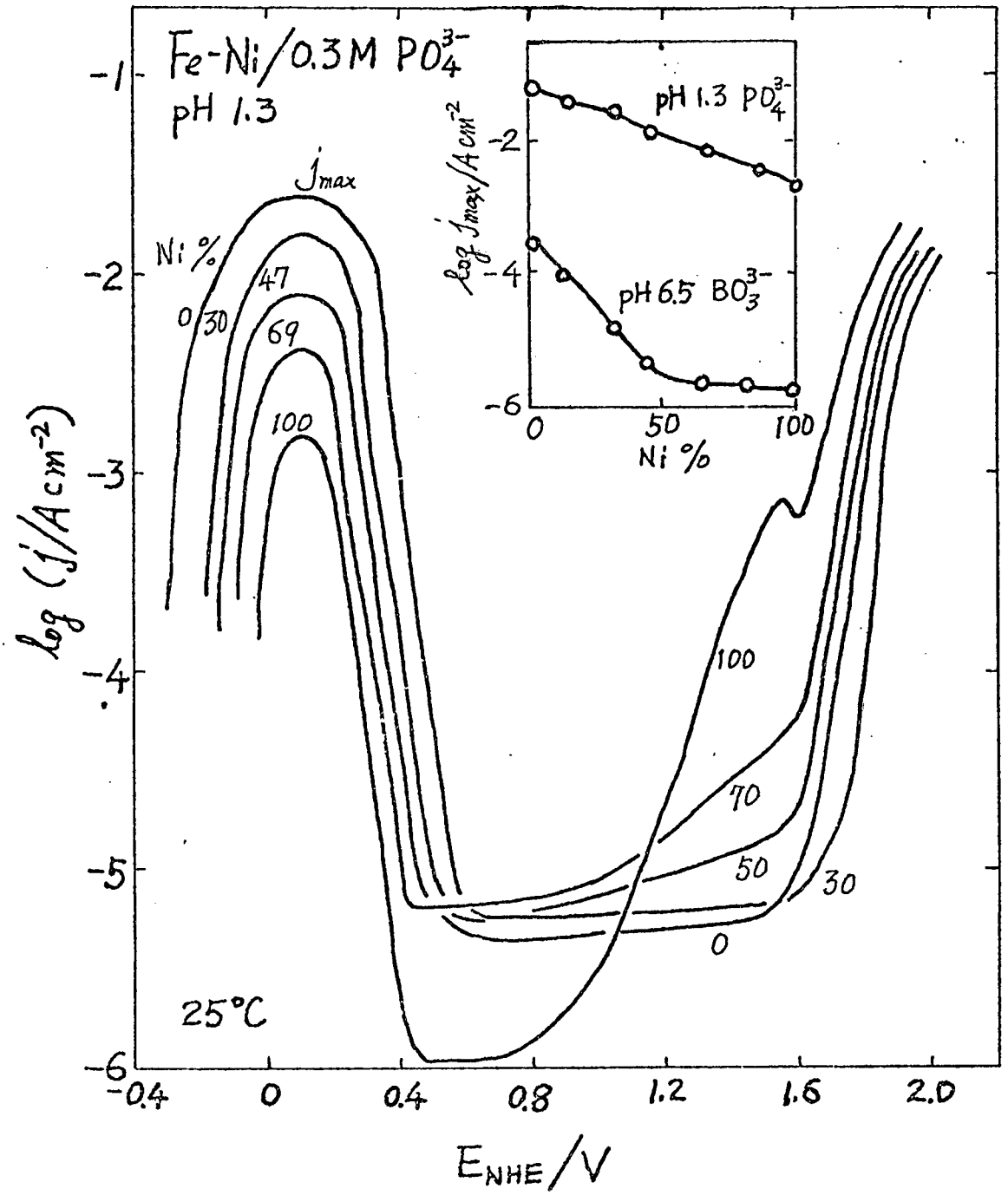

Fig. 14-1. Anodic polarization curve of Fe-Ni alloys and active dissolution current peak in acidic phosphate and neutral borate solutions as a function of nickel content.

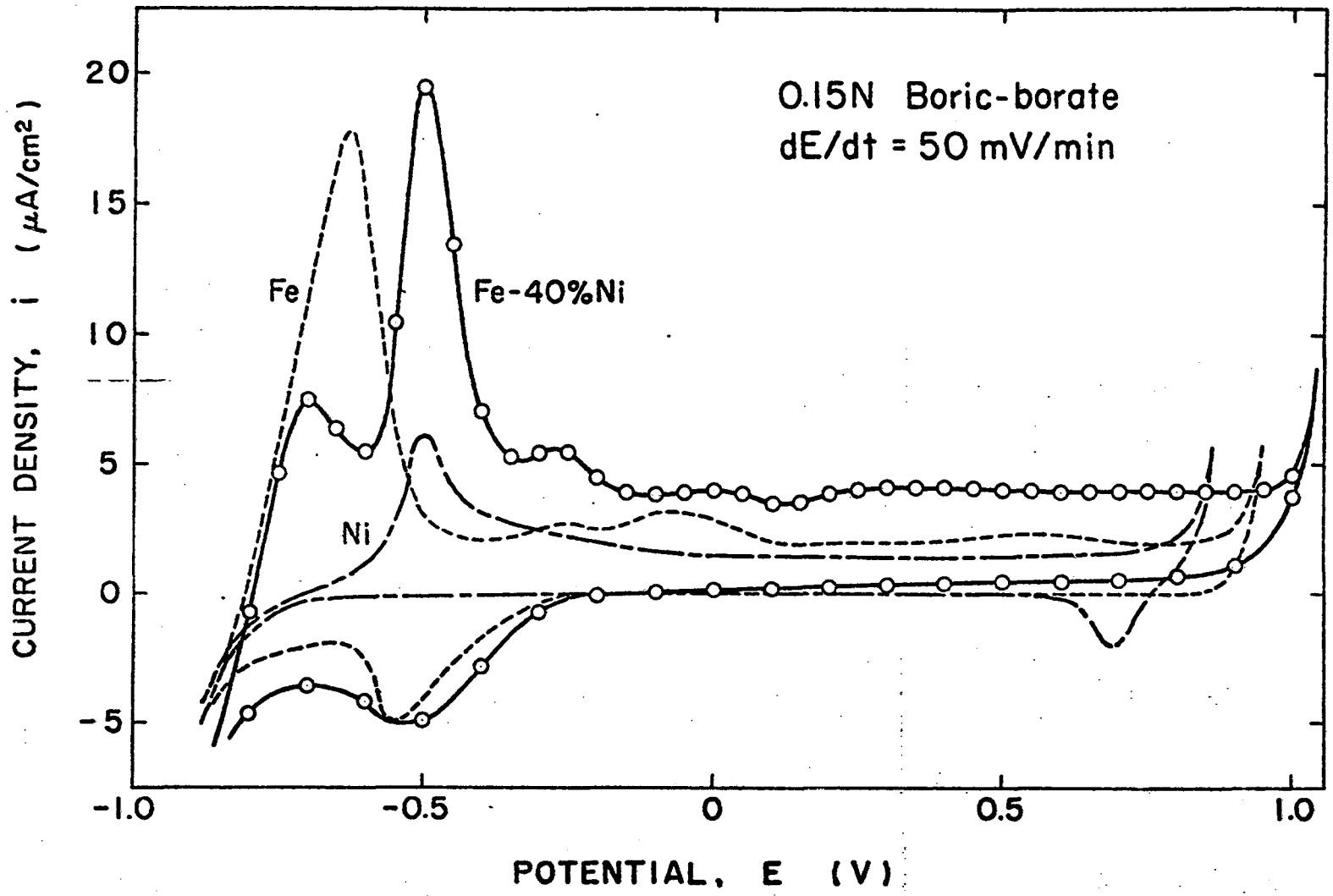

Fig. 14-2. Anodic poiarization curve of Fe-40%Ni alloy in 0.15N sodium borate-boric acid solution of pH=8.42 obtained by potential sweep method at the rate of 50mV/min from -0.9V to oxygen evolution region and then reverse.

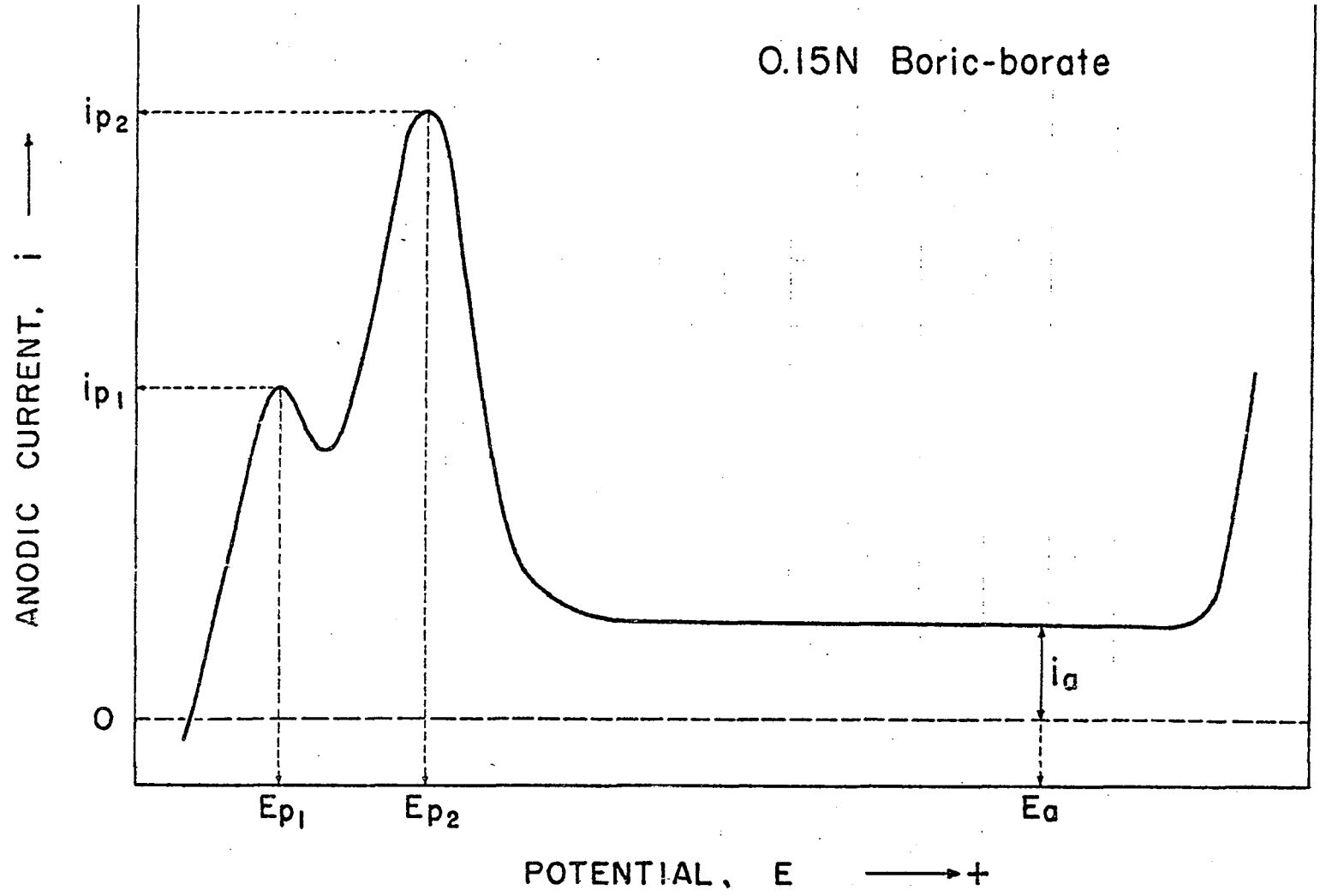

Fig. 14-3. Schematic representation of anodic polarization curve of Fe-Ni alloys obtained by potential sweep method.

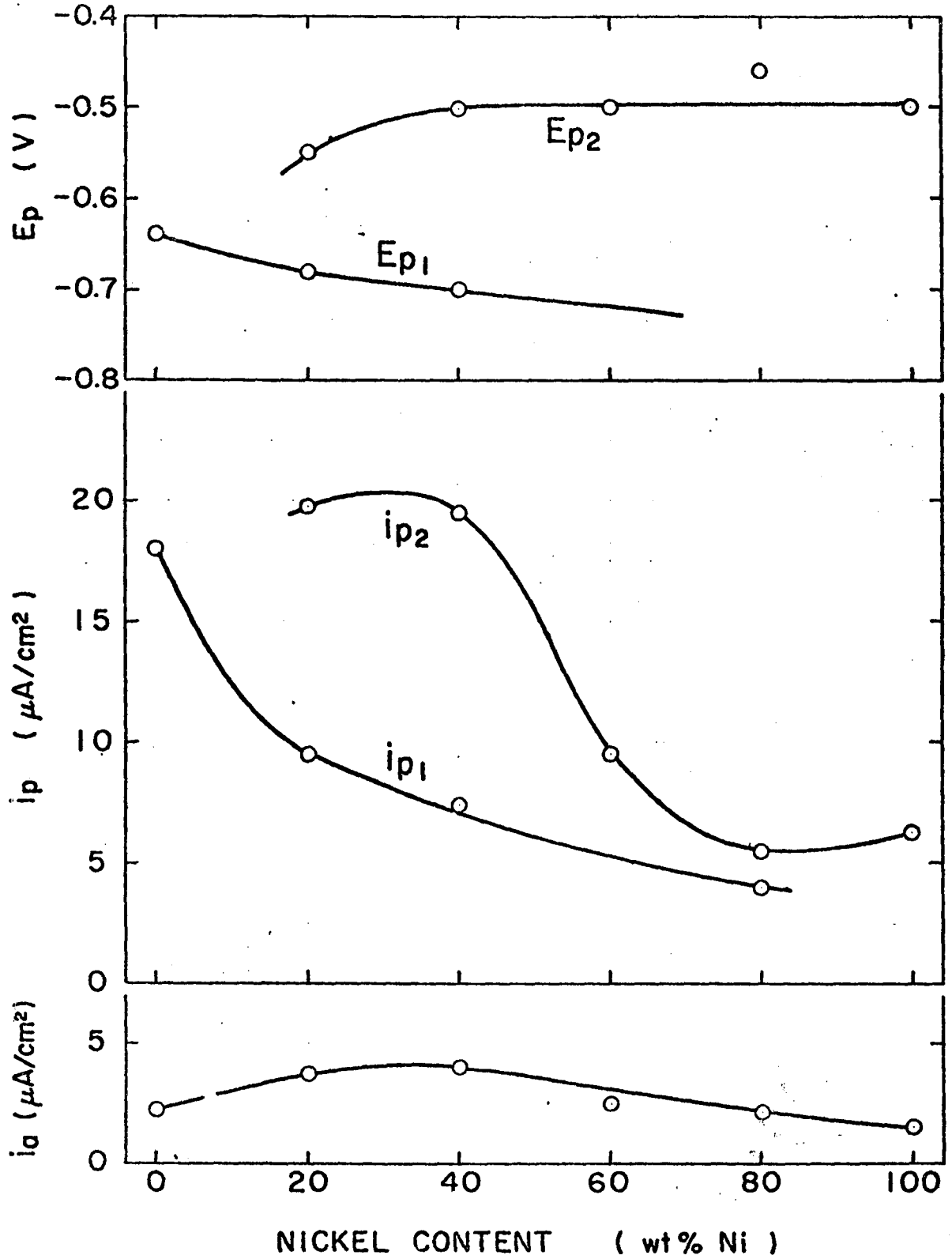

Fig. 14-4. Polarization parameters of Fe-Ni alloys obtained by potential sweep method. i_p is the peak current density at the potential of Ep and i_a is the current density at E=0.6 V.

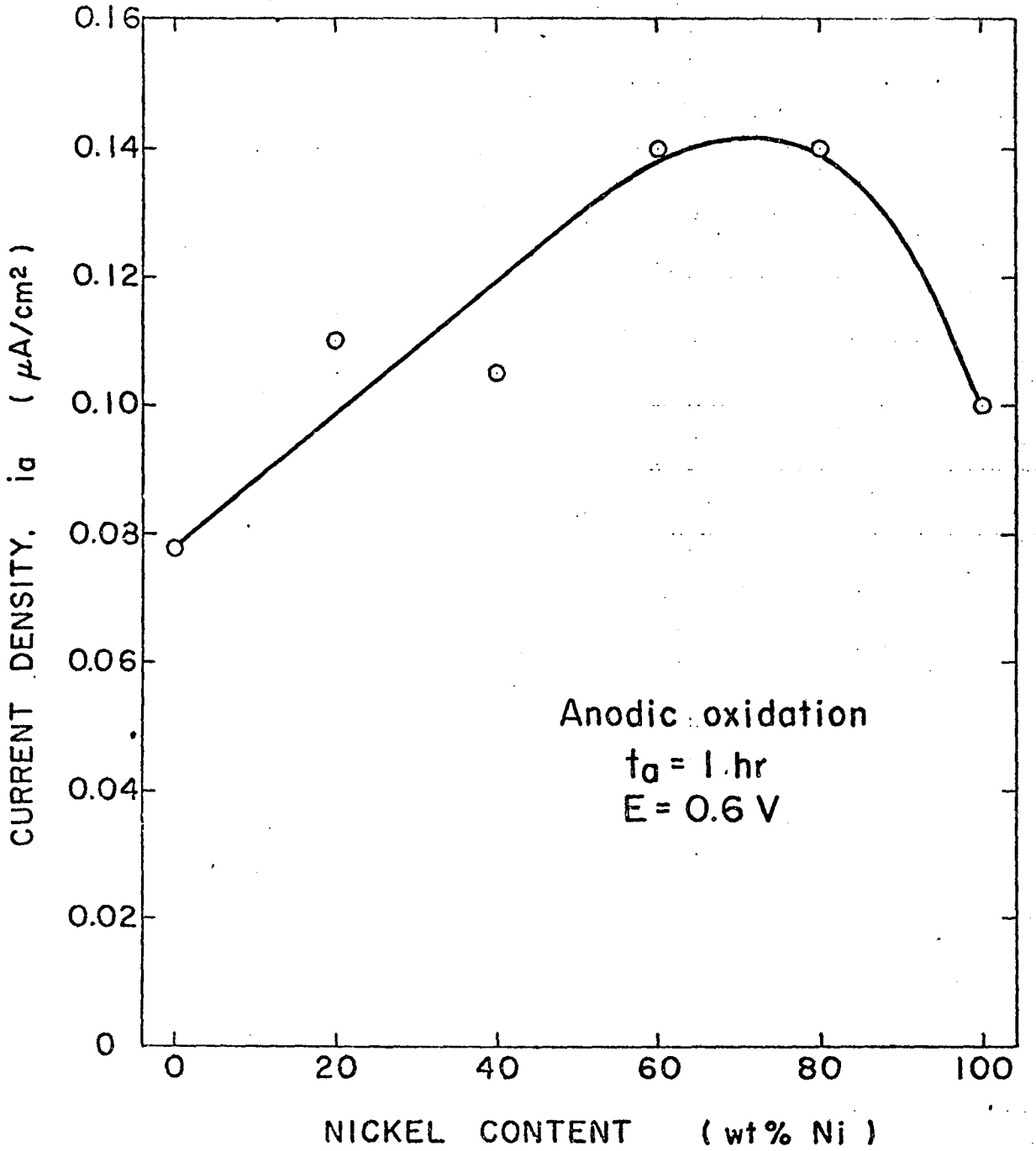

Fig. 14-5. Anodic current density of Fe-Ni alloys after 1 hr potentiostatic-anodic oxidation at E = 0.6 V.

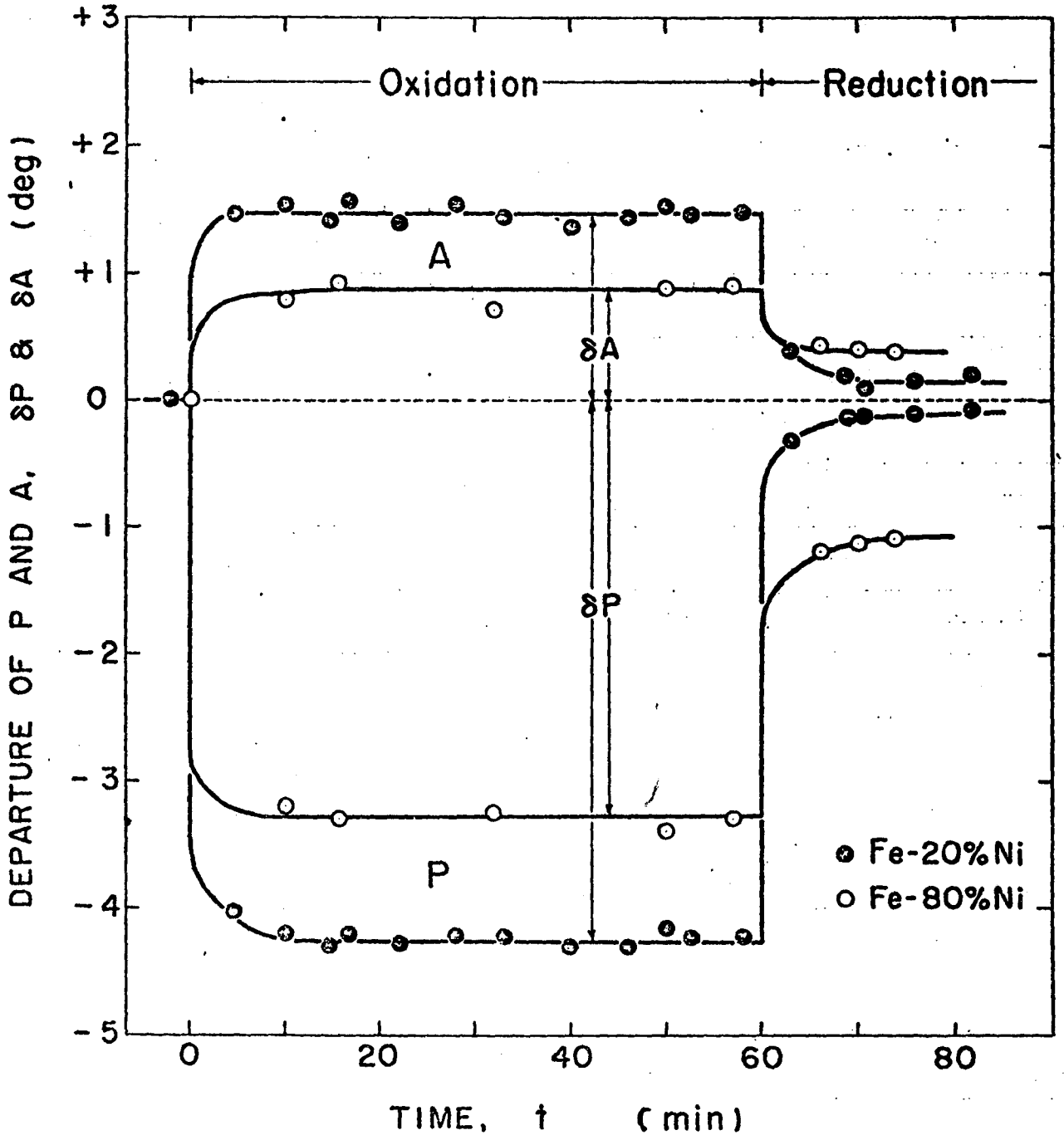

Fig. 14-6. Changes in the departure of P and A of Fe-Ni alloys from cathodically reduced surface values during potentiostatic-anodic oxidation at 0.6V and cathodic reduction at -0.9V.

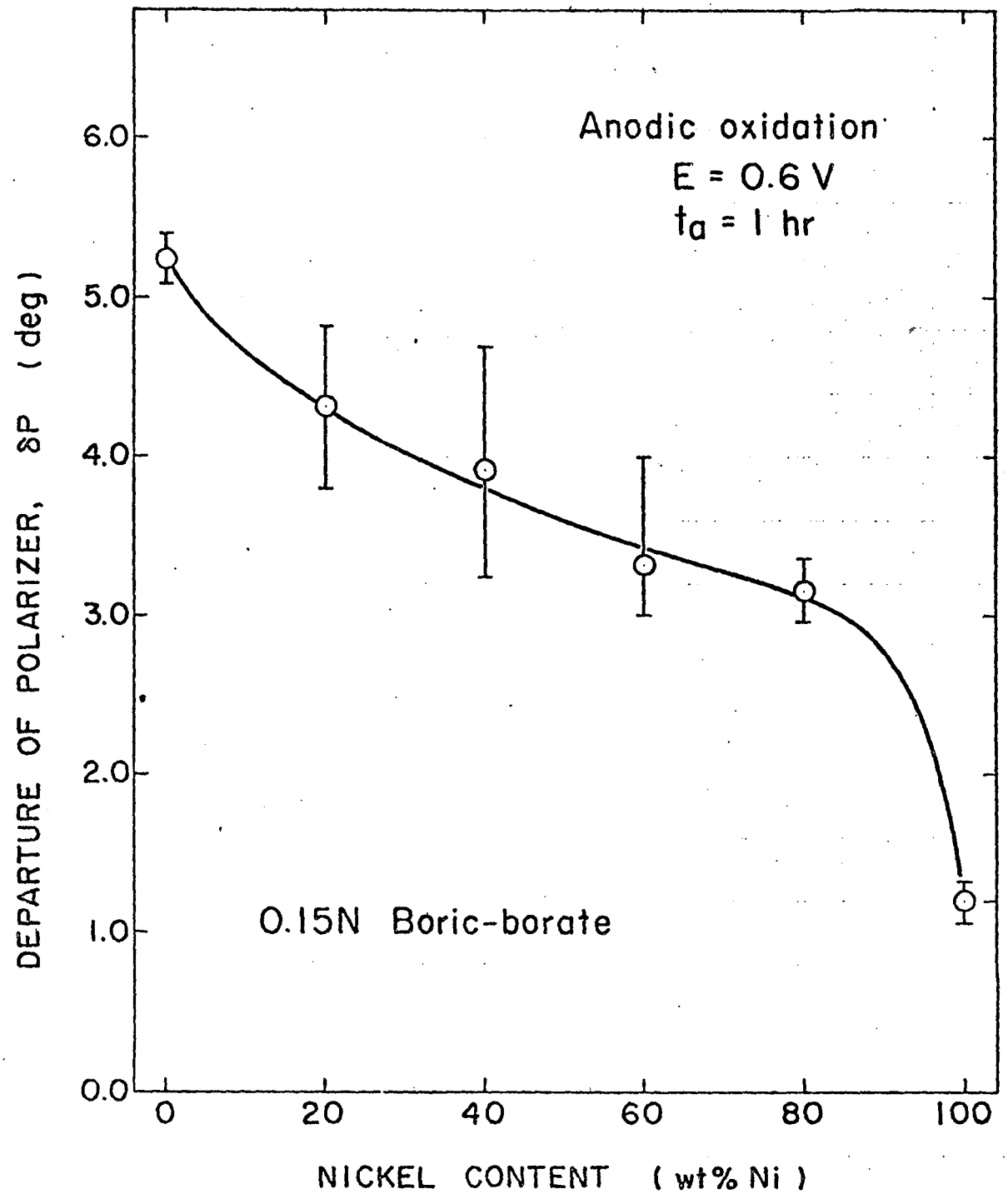

Fig. 14-7. The departure of polarizer settings obtained by potentiostatic oxidation of Fe-Ni alloys at the potential of 0.6V for 1 hr as a function of nickel content.

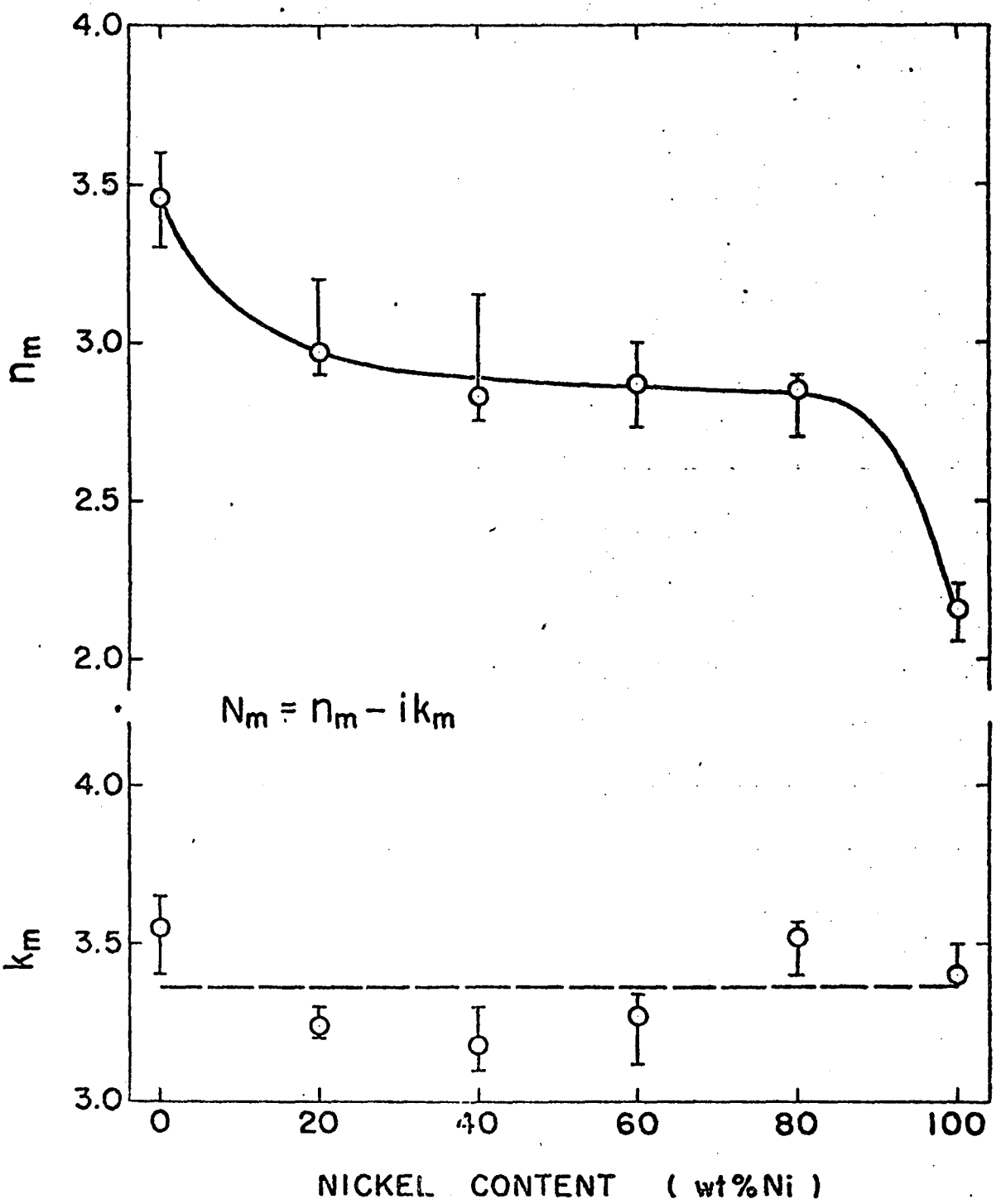

Fig. 14-8. Optical constants of Fe-Ni alloys calculated from measured P and A on the cathodically reduced surface after electropolishing.

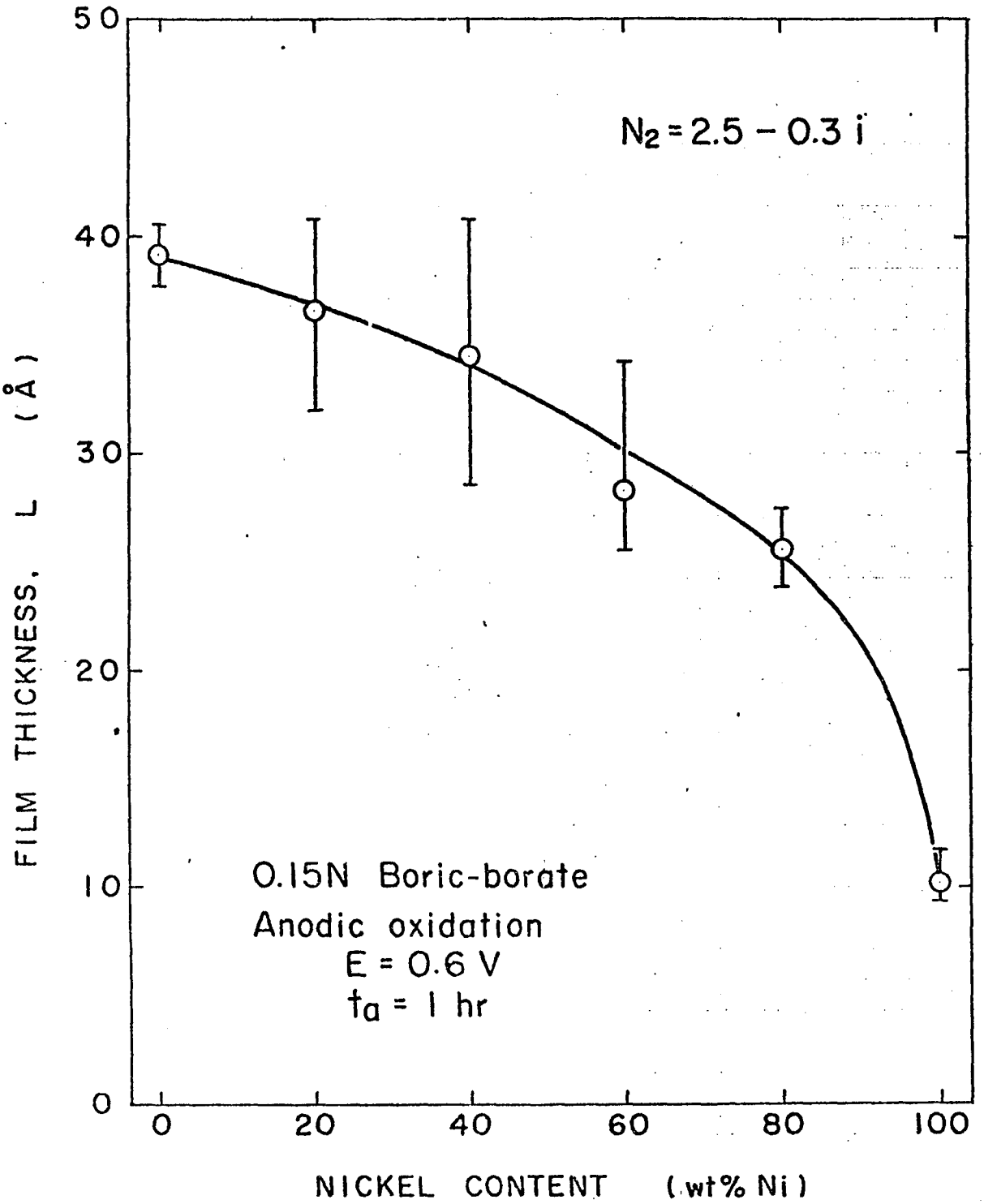

Fig. 14-9. Film thicknesses formed on Fe-Ni alloys obtained by ellipsometry for films formed in 1 hr potentiostatic-anodic oxidation at E=0.6 V.

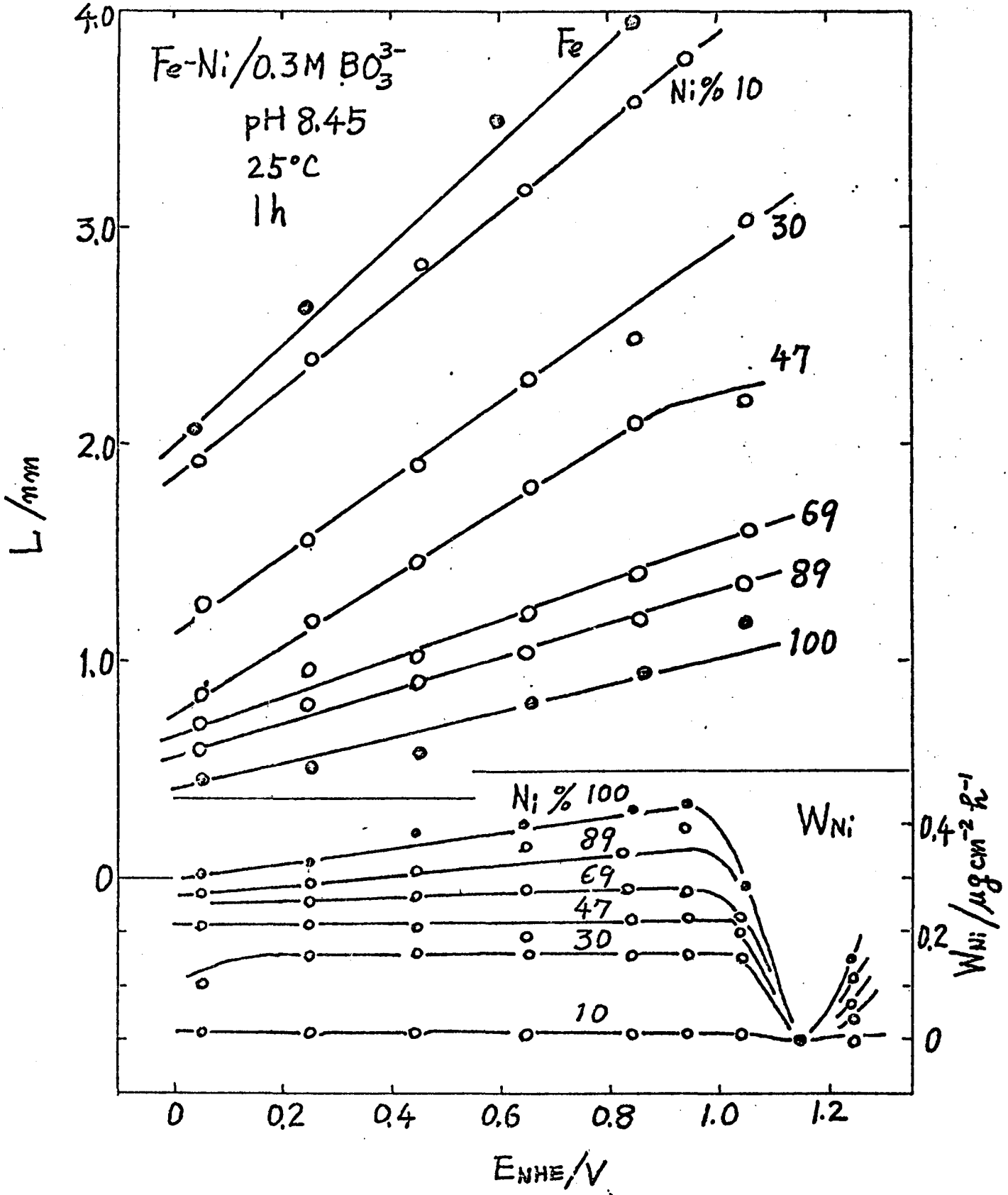

Fig. 14-10. Passive film thickness and amount of Ni dissolved during potentiostatic one hour oxidation of Fe-Ni alloys.

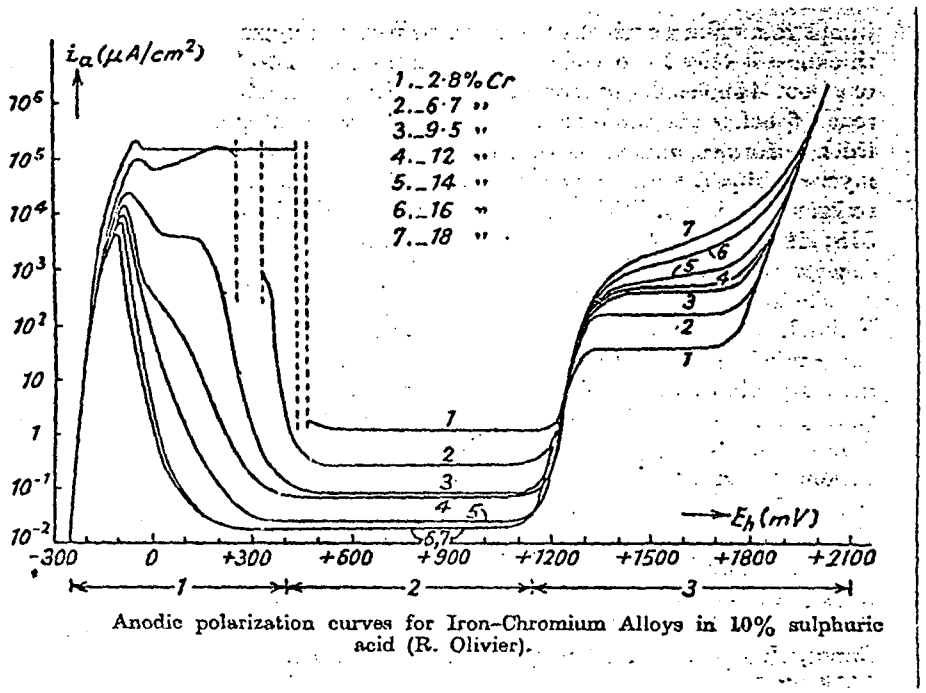

Anodic polarization curves for Iron-Chromium Alloys in 10% sulphuric acid (R. Olivier).

Fig. 14-11. Anodic polarization curves of Fe-Cr alloys in 10 % H_2SO_4 solution.

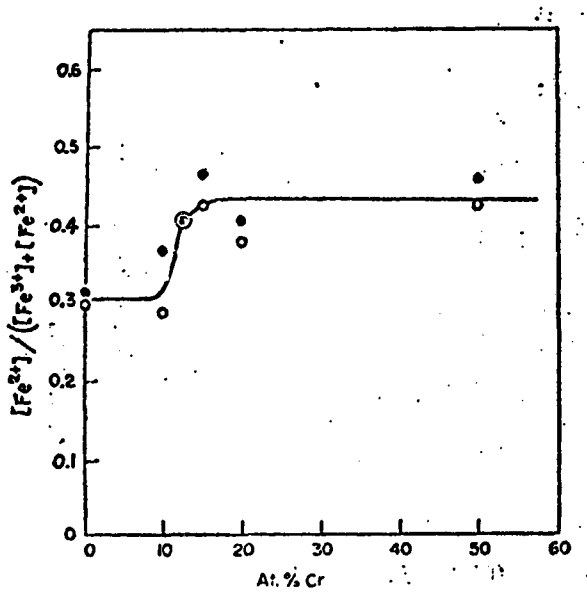

Change in the ratio of Fe^{2+} species to the total iron species in the films as a function of chromium content of Fe-Cr alloys polarized at + 500 mV (— o —) and + 100 mV (— • —) in de-aerated 1M H_2SO_4.

Fig. 14-12. Iron valency in the passive film versus Cr content for Fe-Cr alloys in acid solution: ESCA measurements.

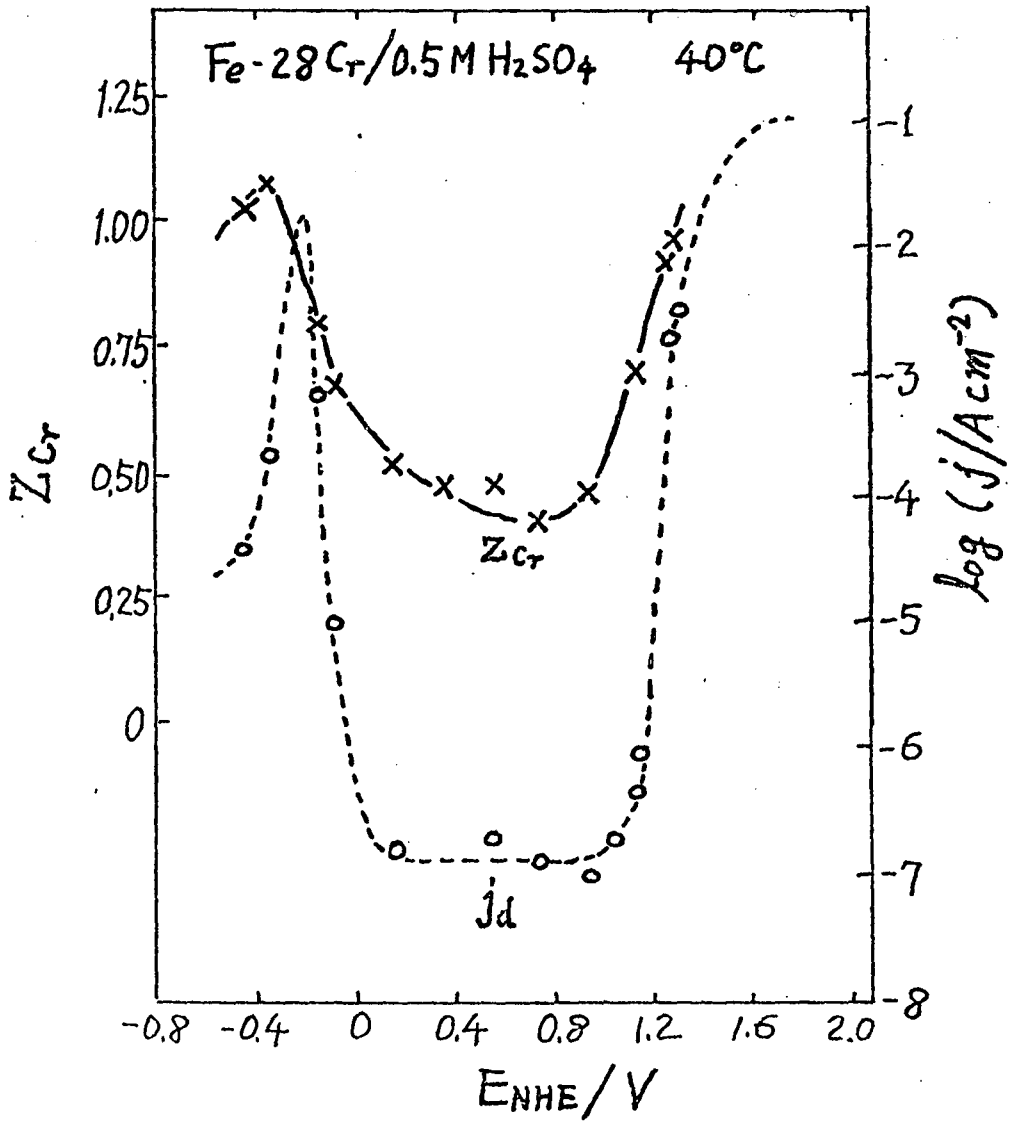

Fig. 14-13. Preferential dissolution of an Fe-Cr alloy in 0.5 M H_2SO_4: Z_{Cr} = Cr/Fe + Cr.

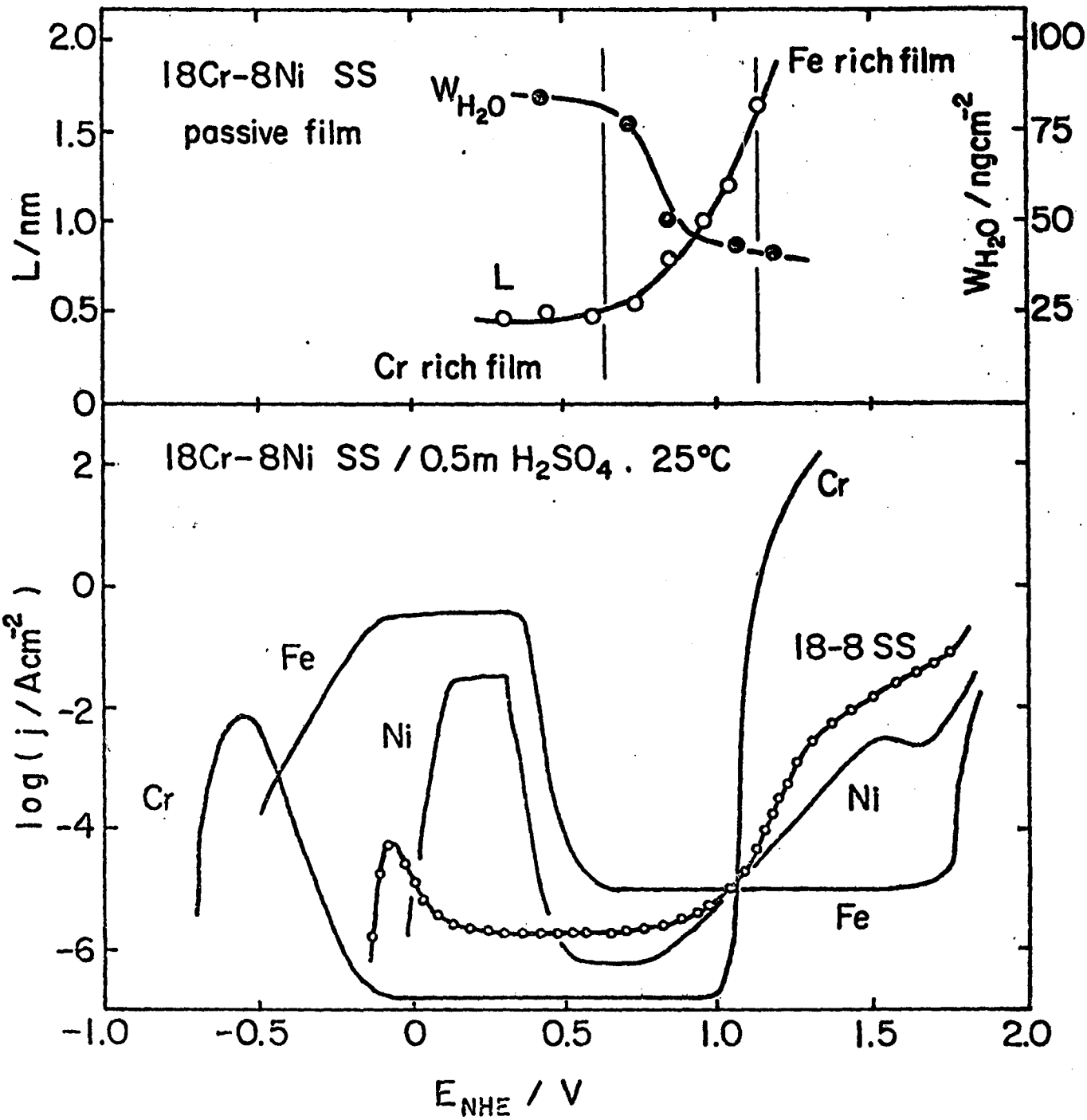

Fig. 14-14. Thickness and water content for the passive film on 18-8 stainless steel in 0.5 M H_2SO_4, and anodic polarization curves of Fe, Ni, Cr and stainless steel.

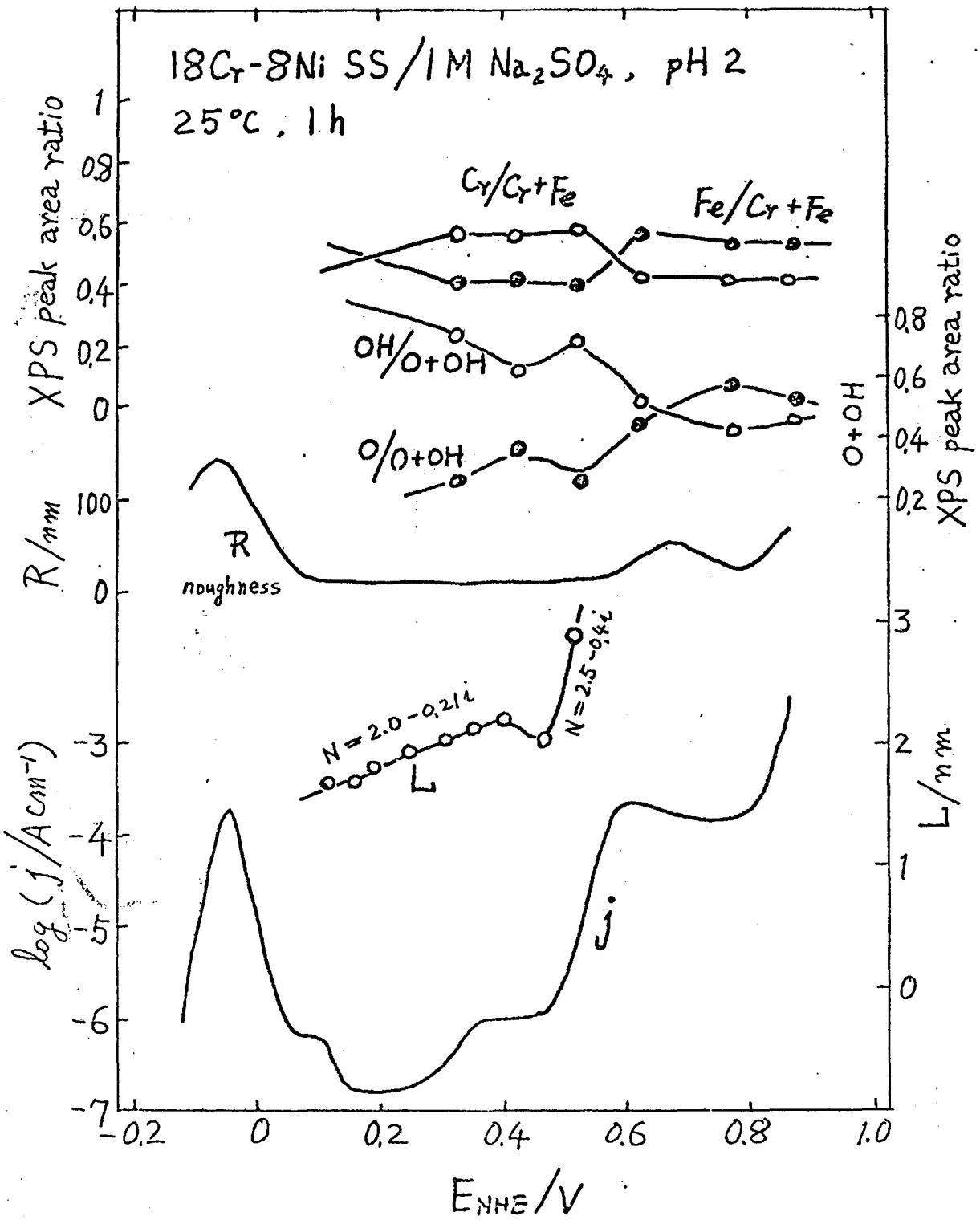

Fig. 14-15. Anodic polarization curve, passive film thickness, surface roughness, and composition of passive films for 18-8 stainless steel in a sulphate solution of pH 2.

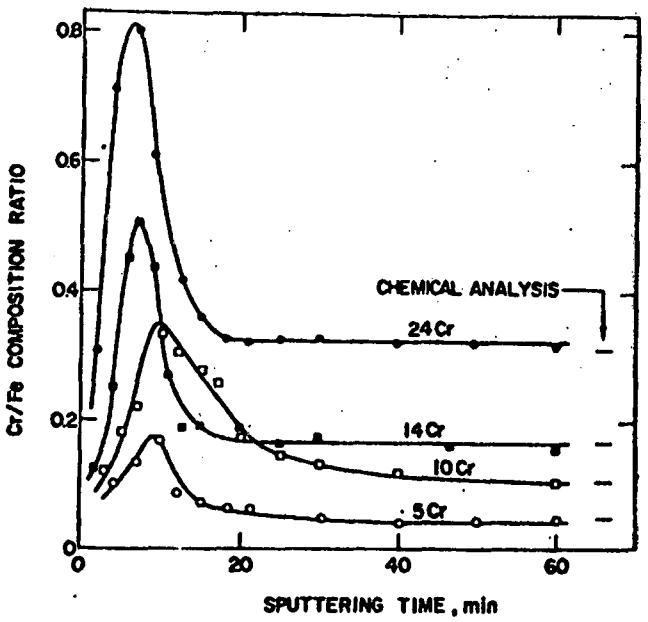

Fig. 14-16

The Cr/Fe composition ratio for a series of iron-chromium alloys as a function of sputtering time. Ratios were obtained from ^{20}Ne spectra and were corrected for relative sensitivities of Fe and Cr. Cr-content of alloy indicated on each curve. Short line to right of each curve is Cr/Fe ratio obtained from chemical analysis.

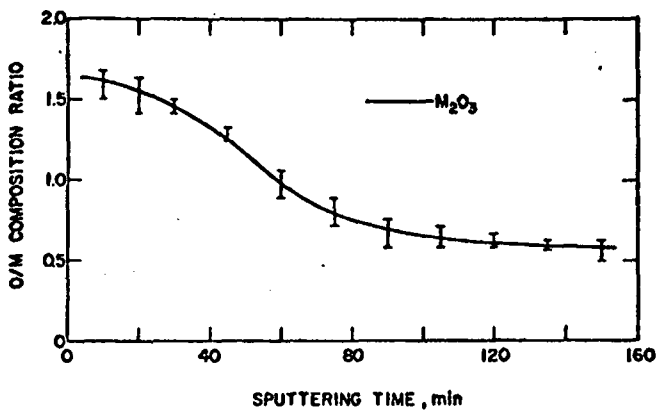

Fig. 14-17

The atomic O/M ratios for the iron-chromium alloys as a function of sputtering time. Ratios were obtained from the ^{3}He spectra and have been corrected for relative sensitivities and Cr/Fe ratio variations within the oxide film, assuming sputtering rates of ^{3}He and ^{20}Ne are proportional to their masses. Error bars at each time represent extremes from all specimens.

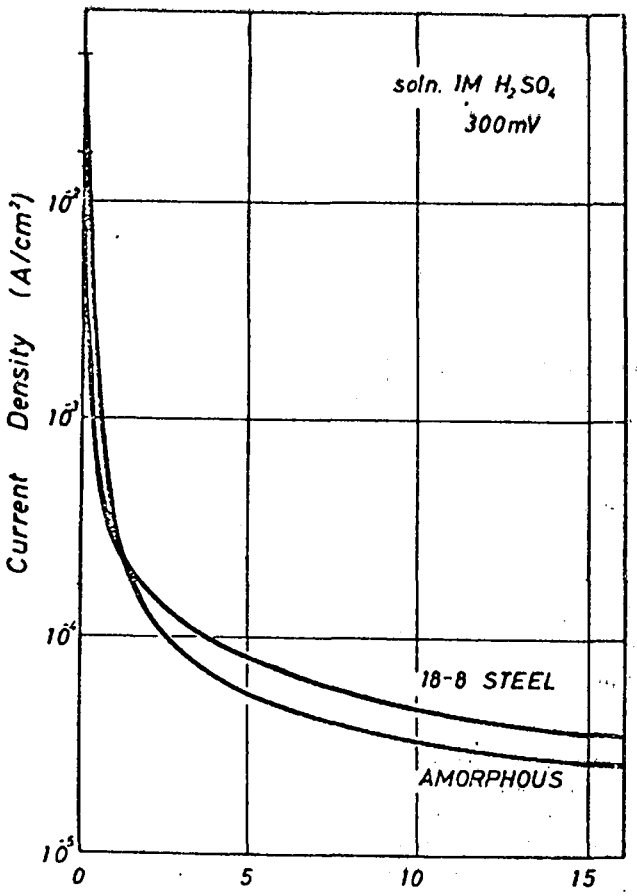

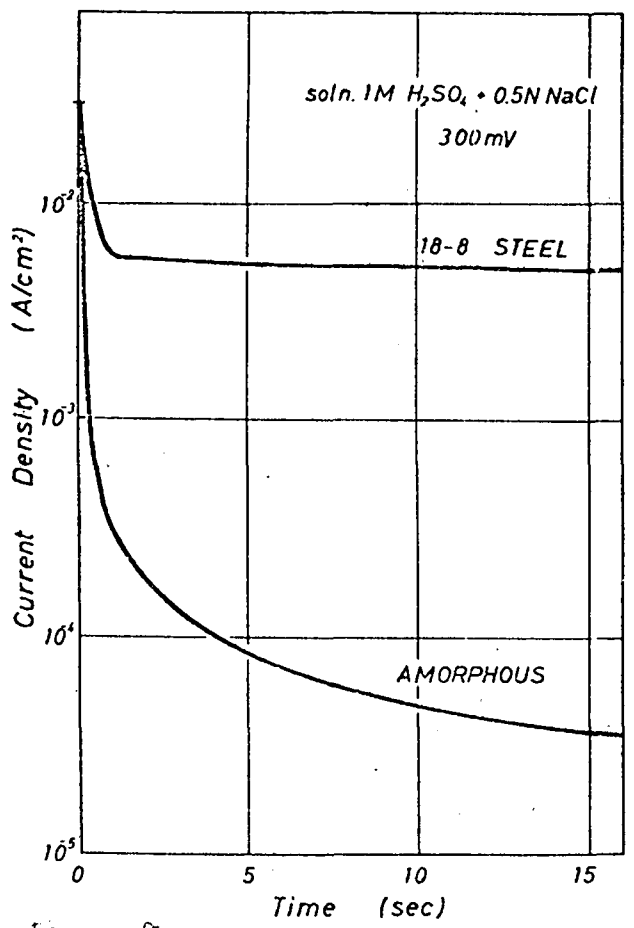

Fig 14-18 — Current density-time curves of the amorphous $FeCr_{10}P_{13}C_7$ alloy and 304 stainless steel measured after abrasing the specimens during anodic polarization at 300 mV vs SCE. (a) in 1M H_2SO_4; (b) in 1M H_2SO_4 + 0.5N NaCl.

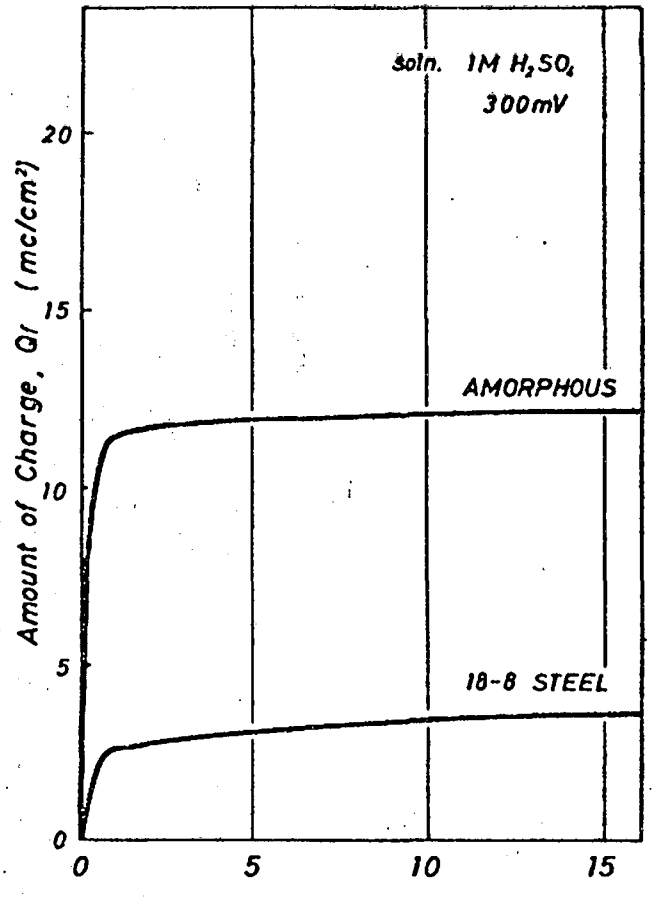

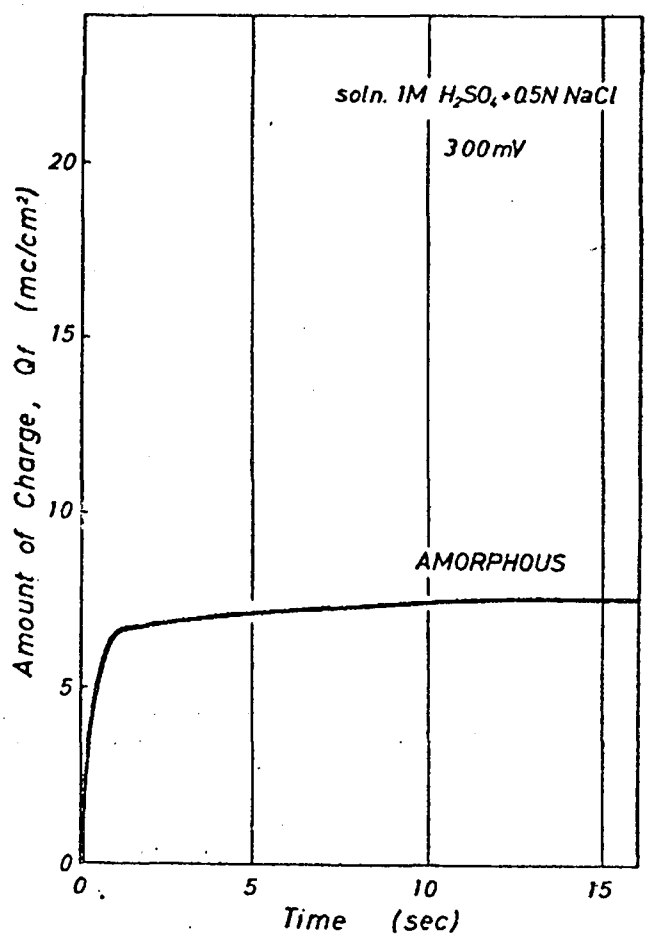

Fig 14-19 — Change in amount of charge passed with time obtained by integration of Figure 14-18 (a) in 1M H_2SO_4; (b) in 1M H_2SO_4 + 0.5N NaCl.